

Dual-Axis Tilting Quadrotor Aircraft

Dynamic modelling and Control of Dual-Axis Tilting Quadrotor Aircraft



Nicholas Von Klemperer

Department of Electrical Engineering
University of Cape Town
Rondebosch, Cape Town
South Africa

October 2018

MSc dissertation submitted in fulfillment of the requirements for the degree of Masters of Science in
the Department of Electrical Engineering at the University of Cape Town

Keywords: Nonlinear Control, Control Allocation, Quadrotor, UAV

“We’re gonna have a superconductor turned up full blast and pointed at you for the duration of this next test. I’ll be honest, we’re throwing science at the wall here to see what sticks. No idea what it’ll do.

Probably nothing. Best-case scenario, you might get some superpowers...”

Cave Johnson -Founder & CEO of Aperture Science

Declaration

I, Nicholas Von Klemperer, hereby:

1. grant the University of Cape Town free license to reproduce the above dissertation in whole or in part, for the purpose of research only;
2. declare that:
 - (a) This dissertation is my own unaided work, both in concept and execution, and apart from the normal guidance from my supervisor, I have received no assistance except as stated below:
 - (b) Neither the substance nor any part of the above dissertation has been submitted in the past, or is being, or is to be submitted for a degree at this University or at any other university, except as stated below.
 - (c) Unless otherwise stated or cited, any and all illustrations or diagrams demonstrated in this work are my own productions.
 - (d) All the content used to compile this report and complete the investigation revolving around the whole project is collectively hosted on the following GIT repositories:
 - L^AT_EXreport: <https://github.com/nickvonklem/Masters-Report>
 - STM32F303 projects: <https://github.com/nickvonklem/Code>
 - Hardware Schematics: <https://github.com/nickvonklem/visio> &
 - EagleCad Schematics <https://github.com/nickvonklem/Eagle>
 - MatLab Simulink Code: <https://github.com/nickvonklem/Simulink>
 - Results & Simulation Data: <https://github.com/nickvonklem/results>
 - All CAD design files & assemblies: <https://grabcad.com/nick.vk-1>



Nicholas Von Klemperer
Department of Electrical Engineering
University of Cape Town
Saturday 6th October, 2018

Abstract

Dual-Axis Tilting Quadrotor Aircraft

Nicholas Von Klemperer

Saturday 6th October, 2018

This dissertation aims to apply non-zero attitude and position setpoint tracking to a quadrotor aircraft, achieved by solving the problem of a quadrotor's inherent underactuation. The introduction of extra actuation aims to mechanically accommodate for stable tracking of non-zero state trajectories. The requirement of the project is to design, model, simulate and control a novel quadrotor platform which can articulate all six degrees of rotational and translational freedom (*6-DOF*) by redirecting and vectoring each propeller's individually produced thrust.

Considering the extended articulation, the proposal is to add an additional two axes (degrees) of actuation to each propeller on a traditional quadrotor frame. Each lift propeller can be independently pitched or rolled relative to the body frame. Such an adaptation, to what is an otherwise well understood aircraft, produces an over-actuated control problem. Being first and foremost a control engineering project, the focus of this work is plant model identification and control solution of the proposed aircraft design. A higher-level setpoint tracking control loop designs a generalized plant input (net forces and torques) to act on the vehicle. An allocation rule then distributes that *virtual* input in solving for explicit actuator servo positions and rotational propeller speeds.

The dissertation is structured as follows: First a schedule of relevant existing works is reviewed in Ch:1 following an introduction to the project. Thereafter the prototype's design is detailed in Ch:2, however only the final outcome of the design stage is presented. Following that, kinematics associated with generalized rigid body motion are derived in Ch:3 and subsequently expanded to incorporate any aerodynamic and multibody nonlinearities which may arise as a result of the aircraft's configuration (changes). Higher-level state tracking control design is applied in Ch:4 whilst lower-level control allocation rules are then proposed in Ch:5. Next, a comprehensive simulation is constructed in Ch:6, based on the plant dynamics derived in order to test and compare the proposed controller techniques. Finally a conclusion on the design(s) proposed and results achieved is presented in Ch:7.

Throughout the research, physical tests and simulations are used to corroborate proposed models or theorems. It was decided to omit flight tests of the platform due to time constraints, those aspects of the project remain open to further investigation. The subsequent embedded systems design stemming from the proposed control plant is outlined in the latter of Ch:2, Sec:2.4. Such implementations are not investigated here but design proposals are suggested. The primary outcome of the investigation is ascertaining the practicality and feasibility of such a design, most importantly whether or not the complexity of the mechanical design is an acceptable compromise for the additional degrees of control actuation introduced. Control derivations and the prototype design presented here are by no means optimal nor the most exhaustive solutions, focus is placed on the whole system and not just a single aspect of it.

Acknowledgements

Firstly, I would like to thank Prof Edward Boje for the supervision he provided throughout this research. Secondly, without the support of everyone in the Mechatronics Lab (Room 6.00) at the University of Cape Town, this project would not have been possible. And last, but certainly not least, I would like to thank my parents who supported and guided me throughout the tenure of my studies.

Nomenclature

In order of appearance:

- 3-D : Three-dimensional vector components in Cartesian XYZ axial
4-DOF : 4 Degrees of freedom, reduced attitude control
- 6-DOF : 6 Degrees of freedom, full attitude and position states
- ABC - Adaptive backstepping control
- BLDC : Brushless-DC, motor
- BEM : Blade element theory, calculation for produced thrust from propeller
- CMG : Control moment gyroscope, satellite actuator
- CH: Channel, number of PWM lines or RC channels
- DIY : Do it yourself, quadcopter assembly kit in context example
- dOAT : Dual-axis opposed active tilting, two-axis birotor rotation
- ESC : Electronic speed controller
- FTC : Fault tolerant control
- GCS : Ground control station, supplements onboard control loops for UAVs
- IBC - Ideal backstepping control
- IMU : Inertial measurement unit, an MEM 9-DOF accelerometer/gyroscope/magnetometer
- ITAE : Integral time absolute error, cost function used for optimization
- KV : Kilo-volt, thousand RPM per V applied, BLDC motor rating
- LQR : Linear quadratic regulator control structure
- LCF : Lyapunov candidate function
- MPC : Model predictive control
- MEMS : Micro-electromechanical system, accelerometer or gyroscopes
- OAT : Opposed active tilting, single-axis birotor rotation
- PD : Proportional + derivative controller
- P.D : Positive definite
- PWM : Pulse width modulation
- PID : Proportional + integral + derivative controller
- PSO : Particle swarm optimization
- QFT : Quantitative feedback theory
- RPM : Revolution per minute, units for propeller rotational velocity
- RPS : Revolution per second, units for propeller speed when calculating BEM thrust
- Rx : Receiver channel, comms line input
- S.bus : Serial.Bus, proprietary encoding of UART comms
- SISO : Single input single output, typical control loop
- STP : Standard temperature and pressure
- TSK : Takagi-Sugeno-Kang, fuzzy logic paradigm
- Tx : Transmitter channel, comms line output μ C : Micro-controller
- UAV : Unmanned aerial vehicle, any autonomous aircraft
- USART : Universal synchronous/asynchronous receiver transmitter, 2 wire comms
- VTOL : Vertical takeoff/landing. Helicopter or quad/bi-rotor directions

Symbols

- An arrowed overbar implies vector quantity (column vector)
- A vector with an T superscript refers to that vector's transpose
- A subscript μ denotes a control input quantity
- A subscript i refers to a quantity associated with the i^{th} motor module
- Any subscript numbered $1 \rightarrow 4$ refer to quantities associated with a particular motor module
- Axes are referred to with hat accents and described as an axis in context
- Estimated quantities are also denoted with a hat accent but are similarly described as an estimate in context
- Lowercase axis quantities are unit vectors in a particular axial direction
- Uppercase axis quantities refer to the axes themselves
- Bold faced vectors are lumped state variables
- Dot accents denote derivatives of vectors or quantities
- Subscripts M_i imply reference to the i^{th} motor module's frame
- The frame \mathcal{F}^i refers to the i^{th} reference frame
- An origin of a frame is given by $\vec{\mathbf{O}}_i$
- Lowercase body vectors imply state trajectories
- Uppercase bold vectors represent Euler-Lagrange generalized forces acting as a result of the same case's lowercase trajectory

Where possible, typical conventions for quantities and notations have been adhered to

- α_i motor module rotation about the $\hat{Y}_{M'_i}$ axis
- $\delta(\varepsilon)$ stable trajectory's maximum bound
- ε stable trajectory initial bounding manifold
- $\vec{\eta} = [\phi \ \theta \ \psi]^T \in \mathcal{F}^{I,v_1,v_2}$ Euler angle set
- $\vec{\eta}_b \in \mathcal{F}^b$ transformed Euler angles in common shared body frame
- θ pitch rotation about \hat{Y} axis in [rad]
- λ_i motor module rotation about the \hat{X}_{M_i} axis
- $\vec{\nu}_d = [\vec{F}_d \ \vec{\tau}_d]^T \in \mathcal{F}^b$ generalized virtual control input
- ξ generalized position coordinate
- ρ STP airdensity
- σ_i motor module rotation about the $\hat{Z}_{M''_i}$ axis
- $\vec{\tau}_\mu = [\tau_\phi \ \tau_\theta \ \tau_\psi]^T \in \mathcal{F}^b$ input torque in [Nm]
- $\vec{\tau}_d = h(\vec{\eta}_e, \dot{\vec{\eta}}_e, t) \in \mathcal{F}^b$ attitude controller generated torque input in [Nm]
- ϕ roll rotation about \hat{X} axis in [rad]
- ψ yaw rotation about \hat{Z} axis in [rad]
- $\vec{\omega}_b = [p \ q \ r]^T \in \mathcal{F}^b$ angular velocity in body frame with units [rad.s $^{-1}$]
- Ω_i rotational velocity of i^{th} propeller, in [RPM] or [RPS] specified

AS asymptotic stability

b subscript for net multibody assembly

c propeller chord length

- \vec{C}_x center of mass for body x, relative to origin $\vec{\mathbf{O}}_b$
- $C_T(J)$ aerodynamic thrust coefficient, varies as function of the advance ratio
- $C_P(J)$ aerodynamic power coefficient, varies as function of the advance ratio
- D propeller diameter
- $\vec{D}(\vec{v}_b)$ aerodynamic drag as a function of the vehicle's net translational velocity
- $\vec{\mathcal{E}}_I = [x \ y \ z]^T \in \mathcal{F}^I$ inertial position in [m]
- ES** exponential stability
- $\vec{F}_d = g(\vec{\mathcal{E}}_e, \dot{\vec{\mathcal{E}}}_e, t) \in \mathcal{F}^b$ position controller generated force input in [N]
- $\vec{F}_\mu = [F_x \ F_y \ F_z]^T \in \mathcal{F}^b$ input force in [N]
- GUAS** global uniform asymptotic stability
- GUES** global uniform exponential stability
- \vec{H} generalized attitude coordinate
- in* subscript for inner ring assembly *without* rotor body contribution
- J aerodynamic advance ratio, inflow velocity relative to propeller's rotational speed
- J_x moment of inertia for body x, relative to the frame provided in context measured in [kg.m^2]
- \vec{L}_i vector arm length from $\vec{\mathbf{O}}_b$ origin in [m]
- \mathcal{L}_x Lagrangian scalar with respect to body x
- m subscript for middle ring assembly
- m_x mass for body x in [kg]
- $\vec{\mathbf{M}}_i$ i^{th} motor module center of rotation
- n subscript for inner ring assembly
- $\vec{\mathbf{O}}_b$ body frame origin of motion
- p subscript for net motor module assembly
- q_0 and vector \vec{q} components
- $Q_b = [q_0 \ \vec{q}]^T$ attitude quaternion with scalar r subscript for rotor body
- $\vec{r}(t)$ generalized path trajectory for Euler-Lagrange equation
- S** general stability
- T** Kinetic energy
- $T(\Omega_i)$ scalar propeller thrust as a function of rotational speed
- $\vec{u} = [\Omega_1 \dots \alpha_4]^T$ actuator plant input matrix, $\in \mathbb{R}^{12}$
- U** Potential energy **UAS** uniform asymptotic stability
- US** uniform stability
- $\vec{v}_b = [u \ v \ w]^T \in \mathcal{F}^b$ translational velocity in body frame with units [m.s^{-1}]
- $V(\vec{\mathbf{r}})$ Lyapunov function of some trajectory $\vec{\mathbf{r}}(t)$
- x translational position in the \hat{X}_I axis direction
- $\vec{\mathbf{x}}_b$ full 6-DOF state for combined attitude and position
- $\vec{\mathbf{x}}_d$ desired state setpoint
- $\vec{\mathbf{x}}_e$ error state, not necessarily subtractive, quaternion errors are multiplicative
- y subscript for constant body frame structure
- y translational position in the \hat{Y}_I axis direction
- z translational height in the \hat{Z}_I axis direction

Contents

Declaration	ii
Abstract	iii
Acknowledgements	iv
Nomenclature	v
Symbols	vii
1 Introduction	1
1.1 Foreword	1
1.1.1 A Brief Background to the Study	1
1.1.2 Research Questions and Hypotheses	2
1.1.3 Scope and Limitations	3
1.1.4 Contributions of Study	5
1.2 Literature Review	7
1.2.1 Existing and Related Work	7
1.2.2 Notable Quadrotor Control Implementations	10
2 Prototype Design	15
2.1 Design	15
2.1.1 Actuation Functionality	16
2.2 Reference Frames Used	18
2.2.1 Reference Frames Convention	18
2.2.2 Motor Axis Layout	22
2.3 Inertia Matrices and Masses	25

2.4 Electronics	35
2.4.1 Actuator Transfer Functions	39
3 Kinematics and Dynamics	45
3.1 Rigid Body Dynamics	45
3.1.1 Lagrange Derivation	45
3.2 Aerodynamics	49
3.2.1 Propeller Torque and Thrust	49
3.2.2 Hinged Propeller Conning and Flapping	54
3.2.3 Drag	56
3.3 Quaternion Attitude	56
3.3.1 Rotation Matrix Singularity	56
3.3.2 Quaternion Dynamics	58
3.3.3 Quaternion Unwinding	59
3.4 Multibody Nonlinearities	61
3.4.1 Relative Rotational Gyroscopic and Inertia Torques	61
3.4.2 Verification and simulation of induced model	76
3.5 Consolidated Model	82
4 Controller Development	84
4.1 Control Loop	84
4.2 Control Plant Inputs	85
4.3 Stability	87
4.4 Lyapunov Stability Theory	89
4.5 Model Dependent and Independent Controllers	90
4.6 Attitude Control	91
4.6.1 The Attitude Control Problem	91
4.6.2 Linear Controllers	92
4.6.3 Nonlinear Controllers	98
4.7 Position Control	103
4.7.1 PD Controller	104
4.7.2 Adaptive Backstepping Controller	105

5 Control Allocation Algorithm	109
5.1 Generalized allocation	110
5.2 Thrust vector inversion	110
5.3 Allocators	113
5.3.1 Pseudo Inverse Allocator	113
5.3.2 Priority Norm Inverse Allocator	115
5.3.3 Weighted Pseudo-Inverse Allocator	117
6 Simulations and Discussion of Results	119
6.1 Simulator description	119
6.2 Controller Tuning	121
6.2.1 Particle Swarm Optimization Algorithm	122
6.3 Attitude Controllers	124
6.3.1 PD	125
6.3.2 Auxiliary Plant Controller	130
6.3.3 Ideal and Adaptive Backstepping Controllers	131
6.4 Position Controllers	133
6.4.1 PD	134
6.4.2 Ideal and Adaptive Position Backstepping	135
6.5 Setpoint Control Results	137
6.6 Robust Stability and Disturbance Rejection	140
6.6.1 Torque Disturbance Rejection	141
6.6.2 Disturbance Force Rejection	142
6.7 Allocation Tests	142
6.8 Input Saturation	148
6.9 State Estimation	150
7 Conclusions and Recommendations	152
A Expanded Equations	154
A.1 Standard Quadrotor Dynamics	154
A.2 Blade-Element Momentum Expansion	156
A.3 Euler-Angles from Quaternions	156

B Design Bill of Materials	157
B.1 Parts List	157
B.2 F3 Deluxe Schematic Diagram	162
B.3 Strain Gauge Amplification	163
C System ID Test Data	164
C.1 Thrust and Torque Test Data	164
C.2 Cobra CM2208-200KV Thrust Data	165
C.3 Controller Disturbance Rejection	166
C.3.1 Attitude Controllers	166
C.3.2 Position Controllers	167

List of Figures

1.1	Bell/Boeing V22 Osprey actuation, notations pertinent to patent [105]	2
1.2	Mechanical actuators	5
1.3	General structure for opposed tilting platform, [46]	7
1.4	DJI Inspire1, the notations are with regards to the DJI patent [139]	8
1.5	Tilt-rotor mechanisms	9
1.6	Dual-axis tilt-rotor mechanism used in [41]	9
1.7	ArduCopter PI control structure for pitch angle channel θ ; [82]	10
2.1	Isometric view of the prototype design	15
2.2	Tilting rotor design	16
2.3	Difference between propeller and motor planes	17
2.4	Motor module assembly	17
2.5	Digital and analogue servo timing	17
2.6	Inertial and body reference frames	18
2.7	Aligned motor frame axes	22
2.8	Intermediate motor frames	22
2.9	Body frame axes layout	23
2.10	Motor thrust force	24
2.11	Rotor assembly rotational structure	25
2.12	Inner ring rotational structure	26
2.13	Middle ring rotational structure	27
2.14	Module assembly rotational structure	28
2.15	Complete motor module attached to the body structure	28
2.16	Body structure's center of mass	29
2.17	Inertia, mass and motor modules respective centers	30

2.18 Final constructed prototype	34
2.19 Hardware schematic diagram	35
2.20 SPRacing F3 deluxe layout	36
2.21 SBUS converter & 6CH receiver	36
2.22 S.BUS data stream	37
2.23 BLDC electronic speed controllers	38
2.24 RPM sensor calibration plots	39
2.25 Servo transfer function test rig	39
2.26 Unloaded servo transfer characteristics	40
2.27 Servo block diagram	41
2.28 Inner ring servo characteristics	41
2.29 Middle ring servo characteristics	42
2.30 BLDC RPM speed calibration and transfer function rig	43
2.31 BLDC motor characteristics	43
3.1 Generalized quadrotor net forces and torques	48
3.2 Propeller types	49
3.3 Disc Actuator Propeller Planar Flow	50
3.4 Blade element profile at radius r	51
3.5 Thrust and power coefficients	53
3.6 Propeller thrust tests	53
3.7 Static induced torque results	54
3.8 Propeller blade flapping; [59]	55
3.9 Propeller coning	55
3.10 Mechanical gimbal lock	57
3.11 Exploded inner ring inertial bodies for $\vec{\tau}_\lambda(\lambda_i)$	62
3.12 Exploded middle ring inertial bodies for $\vec{\tau}_\alpha(\lambda_i, \alpha_i)$	65
3.13 Rotating system	69
3.14 Free-body diagram for rotational system	69
3.15 Exploded motor module inertial bodies for $\vec{\omega}_b$ response	71
3.16 Illustration of rotated center of gravity $\vec{C}_p''(\lambda_i, \alpha_i)$	72
3.17 Inner ring torque test rig	76

3.18 Inner ring test rig response	77
3.19 Middle ring torque test rig	78
3.20 Middle ring response	79
3.21 Combined middle ring response	79
3.22 Upward lift test	80
3.23 Differential torque input	81
3.24 Quaternion from yaw torque	81
3.25 Position descent from yaw spin	82
4.1 Generalized control loop with allocation	85
4.2 Extended control loop with overactuation	86
4.3 Trajectory illustrations for S and US	87
4.4 Trajectory illustrations for AS and UAS	88
4.5 Trajectory illustrations for UES and GUES	89
4.6 Adaptive disturbance torque observer example	103
4.7 Adaptive disturbance force observer example	108
5.1 Actuator allocation	109
5.2 Hover conditions with respect to the inertial frame \mathcal{F}^I	116
5.3 Hover conditions with respect to the body frame \mathcal{F}^b	116
5.4 Weighting matrix biasing	117
6.1 Simulation loop	119
6.2 Orbital trajectory	120
6.3 Chirp trajectory plots	121
6.4 Swarm trajectory's velocity direction	122
6.5 Particle swarm flow diagram	123
6.6 Attitude setpoint working space	124
6.7 Independent diagonal PD	126
6.8 Dependent diagonal PD	127
6.9 Dependent symmetric PD	128
6.10 Increased gain PD	129
6.11 Unconstrained Error Quaternion attitude step	129

6.12 Auxiliary Plant PD	131
6.13 Ideal backstepping controller	132
6.14 Position setpoint workspace	134
6.15 Position PD	135
6.16 Position backstepping controller	136
6.17 Increased gain PD position	137
6.18 Independent PD attitude controller	138
6.19 Dependent PD attitude controller	138
6.20 Auxiliary PD attitude controller	139
6.21 Ideal backstepping attitude controller	139
6.22 PD position controller	140
6.23 Backstepping position controller	140
6.24 Attitude torque disturbance observer	141
6.25 Adaptive backstepping attitude trajectory tracking	141
6.26 Position force disturbance observer	142
6.27 Adaptive backstepping position trajectory tracking	142
6.28 Pseudo inverse step response plot	143
6.28 Pseudo inverse step actuator response	144
6.29 Inertial hover preferred actuator step response	145
6.30 Body frame hover preferred actuator step response	146
6.31 Weighted actuator allocation step response	147
6.32 Step response without servo limits	148
6.33 Servo inputs without limits	149
6.34 Step response with servo limits	149
6.35 Servo inputs with limits	150
6.36 Discretized state steps	151
B.1 Bearing Bracket Inner Ring Assembly	159
B.2 Servo Bracket Inner Ring Assembly	159
B.3 Servo Bracket Middle Ring Assembly	159
B.4 Bearing Holder Middle Ring Assembly	159
B.5 Servo Mount Middle Ring Assembly	159

B.6 Bearing Shaft Middle Ring Assembly	159
B.7 Bearing Holder Damping Assembly	160
B.8 Servo Mount Damping Assembly	160
B.9 Servo Mount Damping Bracket	160
B.10 Bearing Holder Damping Bracket	160
B.11 Arm Mount Damping Bracket	160
B.12 Frame Brackets	160
B.13 F3 Deluxe Flight Controller Hardware Schematic	162
B.14 Strain gauge full bridge amplifier	163
C.1 Clockwise and counterclockwise rotation tests	164
C.2 Official Test Results for Cobra Motors	165
C.3 Disturbances on Attitude Controllers	166
C.4 Disturbances on Position Controllers	167

List of Tables

1.1	A breakdown of common attitude controllers	11
B.1	Parts List	157
B.2	3D Printed Parts	158
B.3	Inner & Middle Ring Assemblies	159
B.4	Damping Assemblies	160
B.5	Laser Cut Damping Brackets	160
B.6	Laser Cut Parts	161

Chapter 1

Introduction

1.1 Foreword

1.1.1 A Brief Background to the Study

A popular topic for current control and automation research is that of quadrotor unmanned aerial vehicles (*UAVs*). Attitude control of a quadrotor poses an unique 6-DOF control problem, to be solved with an underactuated 4-DOF system. As a result the pitch, ϕ , and roll, θ , plants are not directly controllable. The attitude plant is often linearized around a stable operating point. The trimmed operating region is always at the inertial frame's origin, resulting in a zero setpoint tracking problem. The highly-coupled nonlinear dynamics of a rigid body's translational and angular motions arise from gyroscopic torques and Coriolis accelerations (Sec: 3.4.1). Such effects are mostly negligible around the origin, hence the origin trim point decouples the system's nonlinearities. The control system can therefore reduce each first order tracking state variable, $\vec{x}_b = [x \ y \ z \ \phi \ \theta \ \psi]^T$, to independent single-input single-output (*SISO*) plants. Those simplifications are derived in the App:A.1.

As almost every quadrotor research paper mentions, the recent interest in the platform is due to increased availability of micro-electromechanical systems (*MEMS*) and low-cost microprocessor systems. These technical advancements accomodate onboard state estimation and control algorithm processes in real time. Developmental progress in quadrotors and, to a lesser extent UAVs in general, has led to rapidly growing enthusiast communities. For example HobbyKing [58] is now a name synonymous with providing custom DIY hobbyist quadrotor assembly kits and frames, no longer retailing only prebuilt commercial products like DJI's Phantom [36] or Parrot's AR [1] drones.

The avenue for potential application of both fixed-wing and vertical take-off and landing (*VTOL*) UAVs is expansive; supporting civil [99], agricultural [104] and security [144] industries and not just recreational hobbyists. The quadrotor design provides a mechanically simple platform on which to test advanced aerospace control algorithms. Commercial drone usage in industry is already emerging as a prolific sector, especially in Southern Africa. Subsequently, following the 8th amendment of civil aviation laws [108], commercial use of UAVs is now both legalized and regulated. Research into any non-trivial aspect of the field will therefore be to extremely valuable to the field as a whole.

Large scale quadrotor, hexrotor and even octocopter UAVs are popular intermediate choices for aerial cinematography and other high-payload capacity applications. The cost of commercial drones such as the SteadiDrone Maverik [85] is significantly less than a chartered helicopter, used to achieve the same panoramic aerial scenes or on-site inspections. One foreseeable issue which may hinder commercial drone progress in the agricultural and civil sectors is the consequential inertia damping effects from scaling up a vehicle's structure. When increasing the size of any vehicle, its performance is adversely affected if actuation rates are not proportionately increased.

1.1.2 Research Questions and Hypotheses

The difficulty with quadrotor control is that fundamentally, from their uncertainty and underactuation, they are ill-posed for 6-DOF setpoint tracking. A quadrotor inherently has only four controllable inputs; each propeller's rotational speed $\Omega_{1,2,3,4}$ which are then abstracted to a net virtual control input net torque $\vec{\tau}_\mu = [\tau_\phi \ \tau_\theta \ \tau_\psi]^T$ and a scalar perpendicular heave thrust projection $\vec{F}_\mu = \sum_{i=1}^4 T(\Omega_i) \cdot \hat{z}_b$ in the \hat{Z}_b direction. Those four inputs are then used to effect both the translational XYZ positions $\vec{E}_I = [x \ y \ z]^T$ and angular pitch, roll and yaw attitude rotations $\vec{\eta}_b = [\phi \ \theta \ \psi]^T$. Pitch and roll torques, τ_ϕ and τ_θ respectively, are produced from differential thrusts of each opposing propeller. Yaw torque τ_ψ is induced from the net aerodynamic drag about each propeller's rotational axis. Aerodynamic drag and differential thrust responses are highly nonlinear (detailed later in Sec:3.2.1) and difficult to approximate as sources of control action. As a result the body's yaw channel control is depreciated. Stemming from the system's underactuation, the attitude control problem is a zero setpoint problem, attempting to track attitudes is ill-posed and will only ever be locally stable (in the Lyapunov sense, Sec:4.4).

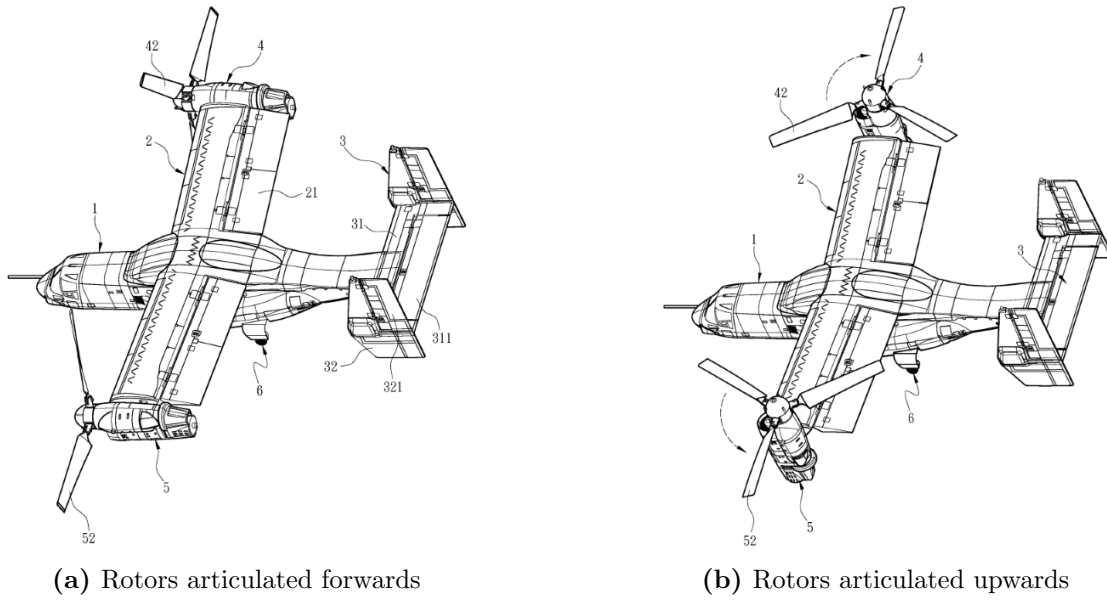


Figure 1.1: Bell/Boeing V22 Osprey actuation, notations pertinent to patent [105]

The aim of this research is to implement non-zero attitude and position state setpoint tracking on a quadrotor by solving the problem of its inherent underactuation. Inspired by Boeing/Bell Helicopter's V22 Osprey (Fig:1.1) and the tilting articulation of its propellers, the prototype design proposed here (described in Sec:2.1) introduces two additional actuators for each of the quadrotor's four lift propellers, specifically adding rotations about the \hat{X} and \hat{Y} axes for each motor/propeller pair. The result is four individually articulated 3-D thrust vectors instead of a bound perpendicular net heave force. The control problem is then posed as the design and allocation of net input forces $\vec{F}_\mu = [F_x \ F_y \ F_z]^T$ and torques $\vec{\tau}_\mu = [\tau_\phi \ \tau_\theta \ \tau_\psi]^T$ to act on a general 6-DOF body, such that for any desired trajectory $\vec{x}_d(t) = [x \ y \ z \ \psi \ \theta \ \phi]^T$ the error state $\vec{x}_e(t) \triangleq \vec{x}_d(t) - \vec{x}_b(t)$ is asymptotically stable. Mathematically:

$$\lim_{t \rightarrow \infty} \vec{x}_e(t) = \vec{0} \quad \forall \vec{x} \in \mathbb{R}^n \quad (1.1)$$

where n is the number of the degrees of freedom the system has, typically a 6-DOF plant for rigid bodies. Trajectory stability is explicitly defined later (Sec:4.3) in the context of Lyapunov stability analysis (Sec:4.4). The overactuation brings about the need for a control allocation scheme, one which distributes the six commanded system inputs (net torques and forces) among the twelve actuators in order to optimize some objective function secondary to that of Eq:1.1. The potential improvement(s) for exploiting those overactuated elements is the most novel outcome which the project could yield.

Part of the control research is the multivariable dynamic modelling of the system, making as few assumptions as possible about the nonlinear dynamics involved in the quadrotor's motion and its operational conditions. Common linearizations applied to the quadrotor's control plant will not hold true for more aggressive attitude maneuvers because they are dependent on small angle approximations and neglect second or higher-order effects. To produce a stabilizing control solution, there first needs to be a plant model that incorporates both multibody and actuator dynamics, against which the controller efficacy can be tested. The final key outcomes for the project are; the prototype design, its mathematical plant model and simulation analysis, the resultant control law produced and finally conclusions drawn on all of the above.

For a rigidly-connected multibody system with revolute joints between sub-bodies, the induced relative motion between those sub-bodies will produce complex dynamics like inertia and gyroscopic responses, amongst others. A rotating propeller will respond to pitching or rolling much like a Control Moment Gyroscope [138] or a flywheel, producing a precipitating torque cross product. A less trivial aspect, which is occasionally considered, is the aerodynamic effects produced from the propeller's aerofoil profile. Such induced responses manifest normal to the propeller's rotational axis. Those aspects are not typically compensated for due to a quadrotor's fundamental co-planar propeller counter-rotating pairs which mostly negate such effects. A strongly plant-dependent control law is needed for dynamic compensation, reducing potential fragility associated with the subsequent stability proof. Unmodelled dynamics could push the plant out of the range of stability with regards to the Lyapunov proof.

1.1.3 Scope and Limitations

Scope

Critical to this project is the conceptualized design, prototyping and modelling of a novel actuation suite to be used on a quadrotor platform. The control research question is to apply dynamic setpoint control to the quadrotor platform. Stemming from this is an investigation into the kinematics that are potentially influenced by such a design and the structure's configuration changes. In order to apply correct control theory to achieve the state tracking on the physical prototype, plant dynamics must first be identified for the controller to be designed and optimized correctly. Aspects of the mechanical design are detailed in the next chapter, Ch:2.1. There is no scope beyond the cursory investigation for materials analysis or stress testing of the design. This dissertation's scope focuses on deriving the vehicle's equations of motion and subsequent control design, not the structural integrity of the proposed frame given the forces it may undergo. No flight tests were performed but physical measurements were made on the platform for kinematic inertia measurements (Sec:2.3) and experiments were conducted for corroboration of second order gyroscopic and inertia dynamic responses relating to the novel actuation block (Sec:3.4.2).

Despite aiming to track first-order trajectory setpoints, flight path planning and the trajectory generation thereof are not ubiquitous with this dissertation. Derivations for the differential equations for a 6-DOF body's motion, throughout Ch:3, are applicable to any aerospace body, rigid or multibody. Some particular standards are used, like ZYX Euler Aerospace rotational matrix sequences, all of which are covered in Sec:2.2. The control plant is stabilized with nonlinear state-space control techniques in the time domain, aided and justified by Lyapunov stability theorem [18, 111]. Alternative solutions using model predictive control (*MPC*) or quantitative feedback theory (*QFT*) could perhaps yield more refined or effective controllers, however they are not discussed here and remain open to further investigation. Quadrotor attitude control is commonly stabilized with feedback linearizations, decoupling the plant around a trim point so that SISO techniques can be applied. A derivation of such a linearization is included in App:A.1 but beyond that there are no further discussions. Any comparisons between non-zero and zero setpoint attitude controller efficacy for quadrotors are difficult as the fundamental objectives are in stark contrast with one another.

Arguably the most important and potentially novel aspect of this project is the control allocation. The system has twelve plant inputs and six output variables to be controlled. There is then an entire set of compatible actuator solutions, $\vec{u} \in \mathbb{U} \in \mathbb{R}^{12}$, which each satisfy commanded virtual input. Such a plant is classified as overactuated. There must be some logical process as to how those twelve actuators are combined to achieve the desired six control plant inputs, specifically input force \vec{F}_μ and torque $\vec{\tau}_\mu$ acting on the system.

Appropriate allocation rules are first derived in Ch:5 then simulated and compared in Ch:6 before the final solution is reviewed in Ch:7. It is not a comprehensive survey of every possible allocation or control scheme but rather an analysis of the sub-set of problems and design of what is regarded as a logical and pertinent approach. With regards to the prototype design in Sec 2.1, it is assumed that certain aspects are readily available and require no design/development. Particularly the position and attitude state estimation, which is assumed to be updated through a five-camera positioning system and fused with an on-board 6-axis inertial measurement unit (*IMU*) using some discretized filtration, is assumed to be accurate and readily disposable at a consistent 50 Hz. Hence state estimation and its discretization effects are included in Sec:6.9 but are bereft of intricate detail. State estimation for quadrotors and aerial vehicles is a thoroughly researched subject [9, 80, 110].

Limitations

The biggest constraint faced by the design is the net weight of the assembled frame. Lift thrusts which are required to keep an aircraft aloft and oppose the net gravitational force are obviously dependent on the body's net weight. The steady-state actuator positions and rates ought to be far less than their respective saturation limits to ensure sufficient actuator headroom to implement control actuations. Conversely, the structure's net weight is mostly dependent on the lift motors which are often the heaviest part of the vehicle (batteries included).

A trade-off between net weight and actuator bandwidth/headroom makes designing the prototype a balancing act of compromise, added actuation is needed to produce the desired thrust vectoring. The added actuation increases the weight which then requires more thrust force to ensure the vehicle remains airborne. Larger motors therefore need stronger actuators to effect the rotational motion applied to the sub-bodies to overcome their inertia responses. There is a compromise between the weight of the body and the strength/quality of the actuation.

To forego the deliberation detailed above, reducing the possibility of unbounded scope creep, a design limitation is self-imposed on the prototype design. Restricting the propeller diameter, and hence maximum thrust/frame size, will provide a constraint upon which all other design considerations must adhere to. Smaller propellers require far greater rotational speeds to produce similar levels of thrust than their larger diameter counterparts could provide. Electing to use three bladed 6×4.5 inch diameter propellers constrained the maximal overall dimensions of the prototype, but as a consequence required very high revolution per minute (*RPM*) motors. Specifically a set of four Cobra-2208/2000 KV [33] brushless direct current (*BLDC*) motors are proposed for lift actuation (Fig:1.2a).

A direct consequence of that decision is (provisionally based on official thrust tests of the motor included in App:C.2) the net thrust disposable to the control loop is limited to around 950 [g] \approx 9.3 [N], per motor at 14.1 [V]. That thrust test data is provided from the official Cobra motor's website, [33], but further verification is done through physical testing in Sec:3.2.1. The frame weight should ideally remain below 50% of the maximum available thrust, or roughly below 2 [kg].

Another aspect of limitations produced by design decisions made, mostly to reduce the prototype's cost, is the use of 180° rotation servo motors. Here Corona DS-339MG metal gear digital servos (Fig:1.2b) were selected as they were readily available from university stores. The servos are used for each individual motor's \hat{X}_{M_i} and \hat{Y}_{M_i} axial pitch and roll actuators respectively, terms λ_i and α_i represent those respective rotations for the i^{th} motor set to differentiate from body pitch θ and roll ϕ .



(a) Cobra CM2208/2000KV BLDC motor [43]

(b) Corona DS-339MG digital servo [58]

Figure 1.2: Mechanical actuators

Servos act in place of either BLDC gimbal or stepper motors with closed-loop position control to articulate actuator rotations. The latter pair could both accommodate for continuous ($> 2\pi$) rotations of the actuation modules (Sec:2.1.1) but would need their own control design which includes some element of position feedback. Continuous rotation (velocity controlled) servos could otherwise be used but would similarly require rotational feedback, making the design even more complex. Any rotations beyond 2π would similarly require slip rings to transmit power throughout rotational movement to avoid mechanical interference from connection lines.

Implementing such a design and maintaining an acceptable weight would prove too costly and would provide no additional insight attained from experimental testing. The effect of servo rotational limits can be evaluated in simulation and if it proves to be significant, continuous rotation could be implemented. The initial design was constructed with flight tests in mind, however subsequent dynamic and control derivations proved too time consuming and the project led to a close before final tests could be completed. Throughout the design stage in Ch:2 practical implementation was always considered. Certain elements of the whole system could potentially limit performance but were mitigated where possible. For example analogue, servos have an associated 1 [ms] dead time from their 50 [Hz] refresh rate. That can be addressed by using faster but more expensive digital servos which sample at 330 [Hz].

An important element of consideration was the prototype's proposed flight controller which needs to provide a total of twelve pulse-width modulated (*PWM*) output compare channels for the eight servos and four BLDC speed controllers. Moreover the system needs some form of primary state update from a ground control station and a secondary fail safe radio control receiver module, both to be processed by the micro-controller system. Particular attention is paid to the proposed embedded system design and layout in Sec:2.4.

1.1.4 Contributions of Study

Owing to the huge popularity of quadrotor platforms as research tools (i.e [10, 23, 48]), any work that builds on UAV and quadrotor fundamentals will prove to be valuable. With that being said, there is already a plethora of research on the subject of linear and nonlinear control techniques for quadrotor platforms (surveyed in Table:1.1). Attitude control loops are the most common topic for research, requiring a unique underactuated solution and mostly linearized around the origin (App:A.1). Far less common is the application of optimal flight path and trajectory planning to a quadrotor's (*augmented*) autopilot system. The difficulty and ill-posed aspect of a quadrotor's attitude control does not hold true for its position plant, so standard techniques can be applied for waypoint and trajectory planning once the attitude control problem has been addressed.

The most significant aspect of this project is the attitude control, discussed later in Sec:4.6. The overactuation of the proposed design and, more critically, the manner in which the controller's commanded (virtual) output is distributed among those control effectors would, at the time of writing, appear to be the first of its kind. Otherwise known as control allocation, the requirements of the distribution algorithm(s) are outlined in Sec:5.1. Dynamic setpoint attitude control for aerospace bodies is not a subject heavily researched outside the field of satellite attitude control. Even papers that propose similarly complicated mechanical overactuation (expanded upon in next in the lit review, Sec:1.2) hardly broach the topic of tracking attitude setpoints away from the origin.

The control plant presented in this dissertation, developed in Ch:4, does indeed close both the position and attitude control loops. There is, however, no consideration of trajectory generation nor flight path planning as such topics are well discussed elsewhere. Once closed-loop position and attitude control have been achieved, the control algorithms can be adjusted to incorporate higher-order state derivative (acceleration, jerk and jounce) tracking needed for nodal waypoint planning. The heuristics involved with flight path planning are well documented and their application is an easily implemented task [50, 52, 117]. Where possible, the system identification and control (both *design* and *allocation*) for this project is kept as generally applicable as possible. The intention is the project's pertinence falls not only within the UAV field but also to any aerospace attitude control plant, rigid or otherwise.

The primary contributions of this work, presented subsequently, start with a mechanical design for a novel quadrotor platform. Then a unique non-linear multibody dynamic model is derived for the vehicle's complex equations of motion. A series of presented control laws are (in some cases) designed and shown to be stable using Lyapunov stability analysis, thereafter higher-level commanded control inputs are allocated to lower-level actuator modules using derived static allocation laws. The controller coefficient selection exploits an iterative swarm algorithm to optimize each specific set of control coefficients, and finally a simulation environment tests the efficacy of all of the above. Ideally the investigation can be expanded upon with more focused research into one of the above subsystems without compromising the stability of the remainder of the plant. Provisionally, an obvious outcome which the project could yield is improved yaw control of a quadcopter's attitude. However, if the express purpose was just to improve yaw control, it could be done with a dramatically less complicated design.

Moreover, this dissertation could provide greater insight into higher bandwidth actuation and hence faster control responses for larger aerospace bodies. Any standard quadrotor uses differential thrusts to develop a torque about its body. Such actuation suffers a second-order inertia response when the propellers accelerate or decelerate. For a propeller of rotational inertia J_p about its axis of rotation at an angular speed of Ω_i radians per second, the response torque from rotational accelerations induced in the propeller's frame M_i is given by:

$$\vec{\tau}_p = J_p \dot{\Omega}_i \cdot \hat{z}_{M_i} \quad \in \mathcal{F}^{M_i} \quad (1.2)$$

Where $i \in [1 : 4]$ is for each of the four propeller speeds found on a quadrotor. A typical quadrotor helicopter has fixed propellers so each propeller's frame is shared with the body frame \mathcal{F}^b . Framing conventions are expanded on in Sec:2.2. Prioritizing pitching the propeller away from its principle axis of rotation in lieu of changing the rotational speed could potentially improve the actuator plant rate response. This is entirely dependent on how the allocator block is prioritized (presented in Ch:5). The exact effects of different actuator prioritization and distribution in the context of aerospace control are, at the time of writing, unique to this research.

1.2 Literature Review

1.2.1 Existing and Related Work

The field of transformable aerospace frames is not new, with many commercial examples seeing successes over their operational life span. The most notable tilting-rotor vehicle is the Boeing/Bell V22 Osprey [42] aircraft. First introduced into the field in 2007, the Osprey has the ability to pitch its two lift propellers forward to aid translational flight after vertically taking off or landing. In addition to this, there have been many papers published on similar tilting bi-rotor UAVs for research purposes.

Birotors

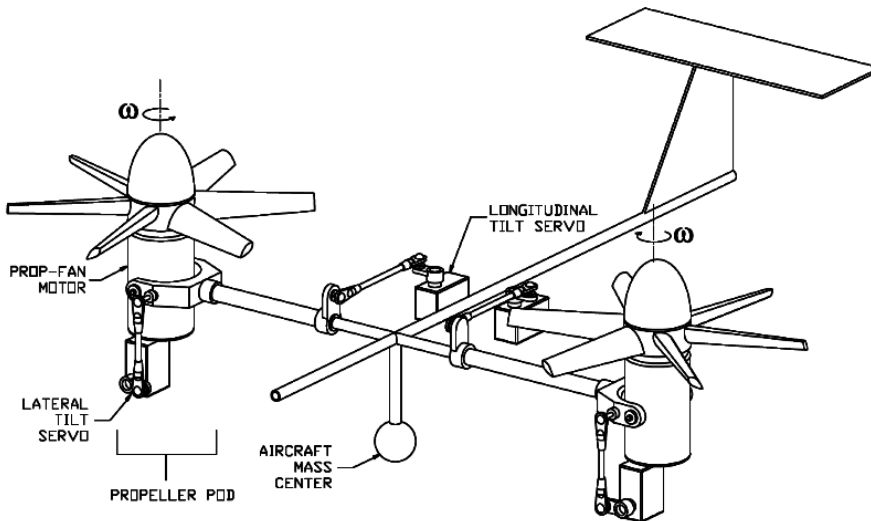


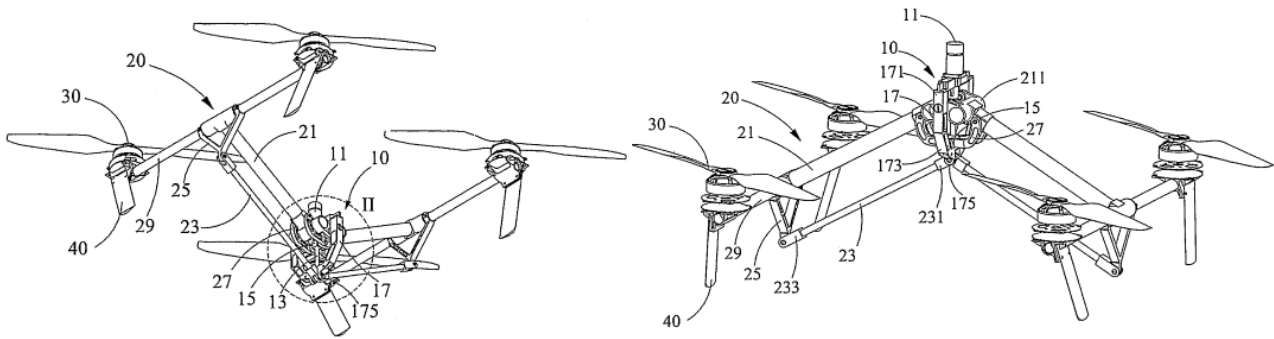
Figure 1.3: General structure for opposed tilting platform, [46]

Research into bi-rotor vehicles (Fig:1.3) with ancillary lift propeller actuation is often termed *Opposed Active Tilting* or *OAT*. Such a rotorcraft's mechanical design applies either a single *oblique* 45° tilting axis relative to the body [16, 71], or a *lateral* tilting axis, adjacent to the body [30, 73, 103, 119]. Leading research is currently focussed on applying doubly actuated tilting axes to bi-rotor UAVs. *Dual axis Opposed Active Tilting* or *dOAT* introduces vectored thrust with independent propeller pitch and roll actions to further expand the actuation suite [3, 46]. A bi-rotor is sometimes considered preferable to higher degree of freedom multi-rotor platforms due to its reduced controller effort, however the controller plant derivation (typically requiring feedback linearization and virtual plant abstraction) often detracts from the quality and effectiveness of its stability solution as a result of the bi-rotor's underactuation.

Bi-rotor attitude control mostly introduces plant independent PD [16] and PID [103] stabilizing controller schemes. Sometimes more computationally intensive and plant dependent *ideal* or *adaptive* backstepping controllers are implemented, presented in [71, 119] and [73] respectively. The gyroscopic response of a bi-rotor vehicle's attitude system is more pronounced than that of a quadrotor, derived in Sec:3.4, and so feedback linearisation is almost always used. In an interesting progression from the norm, [79] proposed a unique PID coefficient selection algorithm for a bi-rotor control block. Using a particle swarm optimization (*PSO*) technique, similar to [142], the coefficients were globally optimized around a given performance metric. Their performance criterion is a standard integral time-weighted absolute error (*ITAE*) term and nothing more appropriate involving effects unique to flight systems was used. *PSO* algorithms iteratively search for a globally optimized solution and offer independent, gradient free based optimization. In subsequent chapters, controller coefficients are optimized for this project using *PSO* algorithms, shown later in Sec:6.2.

Quadrrotors

Expanding on bi-rotor vehicles, the quadrotor UAV is a popular and well researched multirotor platform due to its mechanical simplicity. The current popularity of quadrotors as research platforms started in 2002 with a control algorithm implemented on what is now known as the X4-Flyer quadrotor [48, 109]. Alternative iterations then followed; like the Microraptor [112] and STARMAC [59] quadcopters which have subsequently been built and tested. A plethora of literature exists around quadrotor kinematics and their control [5, 12, 23], however dedicated rigid body 6-DOF mechanical derivations [89, 106] offer better explanations of the kinematics. Often the plant's dynamics are simplified around an origin trim point and assumed to reduce to six SISO plants for each degree of freedom (App:A.1). Recent research projects have begun to incorporate nonlinear aerodynamic effects like drag and propeller blade-element momentum (*BEM*) theory into the plant model [7, 26, 59, 114]. The higher fidelity models for thrust and propeller responses offer more precision as they make fewer linearisations and assumptions.



(a) Inspire1 articulated upwards

(b) Inspire1 articulated downwards

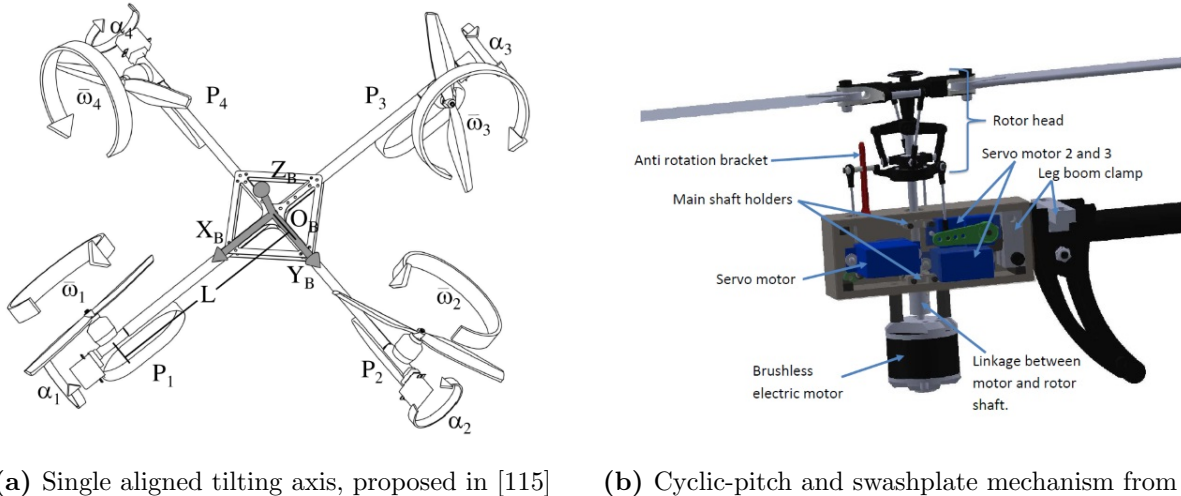
Figure 1.4: DJI Inspire1, the notations are with regards to the DJI patent [139]

At the time of writing, the only commercial UAV multirotor capable of structural transformation is the DJI Inspire1 quadrotor [35], manufactured by Shenzhen DJI Technologies. DJI are better known for their hugely successful DJI Phantom commercial quadrotor [36]. The Inspire1 can articulate its supporting arms up and down as shown in Fig:1.4, the purpose of which is to both alter the center of gravity and to further expose a belly mounted camera gimbal for panoramic viewing angles. This changes the body's inertia matrix about its center of gravity, affecting the second-order inertia response opposed to changes in angular velocity $\vec{\tau} = J\dot{\vec{\omega}}$. Variable inertia is a detrimental consequence which makes researchers apprehensive of reconfigurable aerospace frames. The range of transformations which the Inspire1 frame can undergo is limited to just articulating its arms up and down.

In a similar fashion to the progression seen in bi-rotor state-of-the-art, quadrotor research is engaging the topics of single and dual-axis propeller tilting articulations. The extra actuation scheme(s) were first conceptualized and implemented on a prototype related to an ongoing project covered in two reports [115, 116]. Those authors modified and tested a QuadroXL four rotor helicopter, produced by MikroKopter [44], to actuate a single axis of tilting aligned with the frame's arms (Fig:1.5a). Their proposed control solution, detailed next in Sec:1.2.2, assumes no nominal linearised conditions around hover flight, unlike a similar single-axis tilting quadrotor prototype presented in [95]. The latter is simulated but remains as yet untested.

One approach to improving quadrotor flight response is to alter the manner in which the thrust is mechanically actuated, potentially improving actuator bandwidth (demonstrated in [2, 41]). Drawing from helicopter design, [94] purported a novel quadrotor UAV prototype that used swashplates for varying the propeller pitch and generating torque moments. The aim was a design which was independent of propeller rotational speed power electronics (*ESCs*) for thrust force actuation.

Petrol motors were intended for use in place of BLDC motors. Furthermore, the design proposed a single axis of tilt actuation to each of the four motor modules. Whilst mechanically complex, that prototype made use of existing off-the-shelf hobbyist helicopter components to design a rotor actuation bracket (Fig:1.5b). The cyclic-pitch swashplates [98] used could apply pitching and rolling torques, τ_ϕ and τ_θ , about each propeller's hub, its *principle axis of rotation*. The torques were induced by cycling the blade's angle of attack throughout the propeller's rotational cycle. The actuation rate of such a configuration is far greater than that of a differential torque produced rolling/pitching motion.



(a) Single aligned tilting axis, proposed in [115] (b) Cyclic-pitch and swashplate mechanism from [94]

Figure 1.5: Tilt-rotor mechanisms

Irrespective of the strong initial design in the early stages of [94], it would appear that the research suffered due to time constraints. The introductory derivation on aerodynamic effects and deliberation over the design provide clear insight into the project's goals, however the control solution and system architecture are severely lacking in detail. A brief introductory proposal of an MPC attitude control system detracted from the comprehensive dynamics discussed. The project ended before testing, simulation or results could be obtained. Unfortunately, despite the novel overactuated design, there was no discussion about how the actuator allocation would be achieved.



Figure 1.6: Dual-axis tilt-rotor mechanism used in [41]

Finally, the most crucial research to mention is [41], which was a dual presented masters dissertation together with [2]. Currently, this appears to be the only project published pertaining to overactuation in aerospace bodies implemented and tested on a quadrotor platform. The research was split between the two authors who completed the electronic/control design and the mechanical design for their respective research projects. Shown in Fig:1.6, the dual-axis articulation is achieved using an RC helicopter tail bracket and servo push-rod mechanism reducing the mass of the articulated components but limiting the range of its possible actuation. The propellers are treated as energy storing flywheels whose induced gyroscopic response act as a controllable actuator plant. Thrusts produced by the propellers were not vectored, but the controller's commanded virtual input is distributed to the actuator set by weighted pseudo-inversion, Sec:1.2.2. The extra actuation is justified as fault tolerance redundancy (*FTC*) but the project does not necessarily detail how such a redundancy could be beneficial.

1.2.2 Notable Quadrotor Control Implementations

Quadcopter Attitude Control

Note that here $\vec{\eta}$ is not necessarily an Euler angle set but any attitude representative state variable.

Attitude control of a 6-DOF aerospace body, quadrotor or otherwise, is best described by [131] and referred to as *the attitude control problem*. For a rigid body that has an instantaneous (Euler) attitude state $\vec{\eta}$ and a desired state $\vec{\eta}_d$, the problem is to then find a stabilizing torque control $\vec{\tau}_\mu$. The control law is dependent on some feedback error state $\vec{\eta}_e$. Quaternion attitude states later replace Euler angles for attitude representation, $\vec{\eta} \Rightarrow Q_b$. A general attitude control law h designs an input torque $\vec{\tau}_\mu$:

$$\vec{\tau}_\mu \triangleq h(\vec{\eta}_d, \dot{\vec{\eta}}_d, \vec{\eta}, \dot{\vec{\eta}}, t) \in \mathcal{F}^b \quad (1.3a)$$

$$= h(\vec{\eta}_e, \dot{\vec{\eta}}_e, t) \text{ given some error state } \vec{\eta}_e \quad (1.3b)$$

where the control law designs a net torque such that both the angular position and velocity rates are stabilized with the bounded limits; $\lim \vec{\eta} \rightarrow \vec{\eta}_d$ and $\lim \dot{\vec{\eta}} \rightarrow \dot{\vec{\eta}}_d$ respectively as $t \rightarrow \infty$. Stability definitions are expanded upon later in Sec:4.3. A distinction must be made between Euler angular rate vector $\dot{\vec{\eta}} = [\dot{\phi} \ \dot{\theta} \ \dot{\psi}]^T$ and the angular velocity vector $\vec{\omega}_b = [p \ q \ r]^T$. Depending on how the attitude is posed: with rotation matrices [75, 89, 106], quaternions [39, 47, 75] or otherwise (direct cosine matrix etc ...) the error state $\vec{\eta}_e = \vec{\eta}_d - \vec{\eta}$ could then differ to a (Hamilton) multiplicative relationship. [131] describes these conventionally different error states.

Simulation and modelling papers often rely on Euler angle-based rotation matrices for attitude representation, [19, 23, 87, 95, 113], without addressing the inherent singularity associated with such an attitude representation (known as gimbal lock, [122], Sec:3.3.1). The alternative quaternion attitude representation, first implemented in 2006 on a quadrotor UAV platform in [128], is often used in lieu of rotation matrices. Quaternions do have their own caveat of *unwinding* as a result of the dual-coverage in \mathbb{R}^3 space, discussed in [92] and derived mathematically later in Sec:3.3.3. Quaternions are $\in \mathbb{R}^4$ variables for attitude representations in \mathbb{R}^3 and so a mapping $\mathbb{R}^4 \rightarrow \mathbb{R}^3$ produces an infinite coverage set for each unique attitude state in \mathbb{R}^3 .

Quadrotor plant dynamics are often simplified, especially when represented with a 3-variable Euler angle set, $\vec{\eta} = [\phi \ \theta \ \psi]^T$. The cross-coupled gyroscopic and Coriolis terms are both neglected when the body's angular velocity is small, $\vec{\omega}_b \approx \vec{0}$, and the inertia matrix J_b is approximately diagonal, $\text{rank}(J_b) = x$ for $x \in \mathbb{R}^x$. The consequence of such simplifications is the depreciation of both the gyroscopic torque term, $\vec{\tau}_{gyro} = -\vec{\omega}_b \times J_b \vec{\omega}_b \approx \vec{0}$ and the Coriolis force term, $\vec{F}_{cor} = -\vec{\omega}_b \times m\vec{v}_b \approx \vec{0}$ in the body's dynamics (Ch:3 for context).

Once the coupled cross-product terms are no longer of consequence, the 6-DOF state trajectory, $\vec{x}_b = [x \ y \ z \ \phi \ \theta \ \psi]^T$, can be treated as a series of independent SISO plants each controlled by an appropriate technique. Quaternion-represented attitude plants cannot easily be decomposed into individual SISO channels (quaternion dynamics in Sec:3.3.2). A quaternion-combined four variable attitude state-space vector is then used, $Q_b \triangleq [q_0 \ \vec{q}]^T$, for the major loop trajectory plant of $\vec{x}_b(t)$.

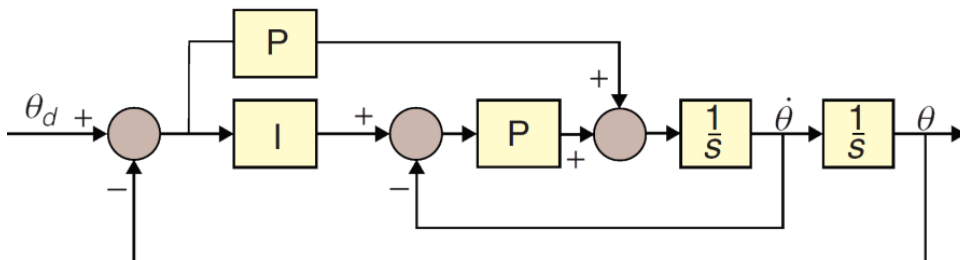


Figure 1.7: ArduCopter PI control structure for pitch angle channel θ ; [82]

Opensource and hobbyist flight controller software (Arducopter [4], Openpilot [81] whose firmware stack is now maintained by LibrePilot, CleanFlight [31], BetaFlight [14], etc ...) for custom fabricated UAV platforms all apply their own flavour of structured attitude controllers and state estimation algorithms, based on onboard hardware sensor fusion. [82] summarizes the control structures implemented on a range of popular flight controllers.

The most popular of these, ArduCopter, implements a feed-forward PI compensation controller, whose single channel control loop for an attitude pitch channel θ is shown in Fig:1.7. PI, PD and PID controllers are all popular and effective plant independent control solutions for general attitude plants. Table:1.1 lists the common attitude control blocks (not exclusively quadrotors UAVs but MAVs too) and which projects they've been implemented in, after which a critique of the more unique adaptations is given. One ideal backstepping controller listed in Table:1.1, presented in [119], applies an algorithm derived through Hurwitz polynomials unlike the Lyapunov based backstepping control laws used here, derived later in Ch:4.

Controller Type	Independent	Dependent	Total Examples
PI	[131]	[131]	2
PD	[2]	[39, 95]	3
PID	[12, 19, 21, 115, 131]	[59, 113, 131]	8
Lead	[109]	N/A	1
LQR	[21]	N/A	1
Backstepping controllers			
Ideal	[87, 119]	[87]	3
Adaptive	[10, 34, 73, 93]		4

Table 1.1: A breakdown of common attitude controllers

In a collection of papers, written by early quadrotor authors S. Bouabdallah and R. Siegward [21–23], a range of different attitude control implementations is surveyed and tested on the OS4 platform. The final paper, [23], derived and practically tested an integral backstepping attitude controller on the OS4 quadrotor platform. It builds on their research presented earlier in [21] which provides an analysis of PID vs linear quadratic regulator (*LQR*) attitude controllers, specifically in the context of underactuated quadrotor attitude control. LQR controllers aim to optimize the controller effort with actuator inputs $u \in \mathbb{U}$, controller effort is then $\|u\|_2$ or the Euclidean norm (magnitude) of the plant input. Although, in theory, solving the associated Riccati cost function may produce a cost optimal, stable and efficient control law, it needs exact plant matching. In reality, exact plant matching is difficult to achieve for a quadcopter or any aerospace body for that matter. The resultant controller in [21] achieved asymptotic stability but had poor steady-state performance due to low accuracy of the identified actuator dynamics and poor-confidence inertia measurements.

Adaptive Backstepping Control (in [136] or any other example in Table:1.1) expands on nominal ideal backstepping fundamentals by introducing disturbance and plant uncertainty terms into the Lyapunov energy function to be used for the backstepping suppression. For Lyapunov iteration, the adaptive backstepping process requires a disturbance estimate derivative or *update law* which is often difficult to quantify. Approximation of plant disturbances without *a priori* information is a complex subject. At some point in the design, an approximation heuristic must be adopted and that typically involves some compromise of performance over accuracy. One example of disturbance approximation in [34] proposes using a statistical projection operator (or *proj(.)*, [28]). When used in adaptive control, presented similarly in [29], the statistical projection operator ensures a derivative-based estimator can be bound for adaptive regression approximationnonlinearregression.

Although the control implementation is not explicitly backstepping, in [143] a sliding mode controller was used to compensate for the disturbances in an Unmanned Submersible Vehicle attitude plant. The underwater current disturbances were approximated using a fuzzy logic system, specifically a *zero-order Takagi-Sugeno-Kang* (TSK) fuzzy approximator.

The TSK system has been shown in [90] to mimic an artificial neural network approximator, where the fuzzy TSK system is more comprehensible than the latter. Statistical analysis and investigation of approximators without *a priori* knowledge of a system are well beyond the scope of this research but are worth mentioning.

Single/Dual Axis Control and Allocation

The additional control actuation introduced with either single or dual axis articulation provides room for secondary control goals to be achieved. Of the few papers published on tilting-axis quadrotors, PD controllers (used in [95] and again in both [2, 41]) and PID controllers (collectively [115, 116]) are the standard fare for attitude control blocks. For either of these systems, there needs to be an allocation rule to distribute a commanded input amongst the actuator set. In a control allocation survey, [65] describes the control allocation problem for a dynamic plant:

$$\dot{\vec{x}} = f(\vec{x}, t) + g(\vec{x}, \vec{\nu}, t) \quad \vec{x} \in \mathbb{R}^n, \vec{\nu} \in \mathbb{R}^m \quad (1.4a)$$

$$\vec{y} = c(\vec{x}, t) \quad (1.4b)$$

State variables of [65] were changed to match this dissertation's conventions. In the state-space equation Eq:1.4a, it is assumed that the plant input, $\vec{\nu}$, has a linear multiplicative relationship with the input response, $g(\vec{x}, t, \vec{\nu}) \equiv g'(\vec{x}, t)\vec{\nu}$. That linear relationship is a prerequisite for most allocation inversion rules but is not a necessity.

In Eq:1.4a the state $\vec{x} \in \mathbb{R}^n$ has associated plant dynamics $f(\vec{x}, t)$ and an input response $g(\vec{x}, \vec{\nu}, t)$. Setpoint tracking control equates the output variable with the state, in practice only state estimates (denoted by a hat accent) are available:

$$\vec{y} = c(\vec{x}, t) = A(\vec{x}) = \hat{\vec{x}} \quad (1.5)$$

Therefore the output \vec{y} has the same dimension as the state variable \vec{x} , or rather both $\vec{x}, \vec{y} \in \mathbb{R}^n$. In an ideal, well posed system the number of actuator inputs equals the number of outputs; that being $\dim(\vec{x}) = \dim(\vec{\nu}) \in \mathbb{R}^n$ in the case where the control input $\vec{\nu}$ has a dimension m , for m different actuator plants $\vec{\nu} \in \mathbb{R}^m$. If $m > n$ the problem is then overactuated and a level of abstraction is needed. The system mechanically commands a physical control input $\vec{\nu}_c$, dependent on explicit actuator positions $\vec{u} \in \mathbb{U} \in \mathbb{R}^m$ as per some *effectiveness* function derived from the actuator plant's dynamics:

$$\vec{\nu}_c = B(\vec{x}, \vec{u}, t) \quad \in \mathbb{R}^n \quad (1.6)$$

where it is assumed that some higher-level control law designs well a satisfactory stabilizing virtual control input from the error state(s) $\vec{\nu}_d = h(\vec{x}_d, \dot{\vec{x}}_d, \vec{x}_b, \dot{\vec{x}}_b, t) \in \mathbb{R}^n$. The allocation rule then aims to solve for an explicit actuator position $\vec{u} \in \mathbb{U} \in \mathbb{R}^m$ derived from $\vec{\nu}_d$ which actuates the physically commanded control input $\vec{\nu}_c$, minimizing the deviation or slack \vec{s} between virtual desired and physical commanded inputs $\vec{\nu}_d$ and $\vec{\nu}_c$ respectively.

Allocation is effectively a paradigm which transforms dimensions $\mathbb{R}^m \rightarrow \mathbb{R}^n$ using a commanded actuator matrix position $u \in \mathbb{R}^m$. An overactuated plant can be summarized into a nonlinear state space form as:

$$\dot{\vec{x}} = f(\vec{x}, t) + g(\vec{x}, \vec{\nu}_c, t) \quad \vec{x} \in \mathbb{R}^n \quad (1.7a)$$

$$\vec{\nu}_c = B(\vec{x}, \vec{u}, t) \quad \vec{\nu}_c \in \mathbb{R}^n \quad (1.7b)$$

$$\text{with } \vec{u} \in \mathbb{U}^m \text{ subject to some } \min(\vec{s}) \text{ such that } \vec{s} = \vec{\nu}_d - \vec{\nu}_c \quad (1.7c)$$

$$\text{using a generalized control law: } \vec{\nu}_d = \mathcal{H}(\vec{x}_d, \dot{\vec{x}}_d, \vec{x}_b, \dot{\vec{x}}_b, t) \quad \vec{\nu}_d \in \mathbb{R}^n \quad (1.7d)$$

$$\vec{y} = c(\vec{x}, t) = \vec{x} \quad (1.7e)$$

The effectiveness function $B(\vec{x}, \vec{u}, t)$ quantifies how actuator inputs $\vec{u} \in \mathbb{U}$ correlate to the physically commanded plant input $\vec{\nu}_c$. Inversion based allocation rules which solve for explicit actuator solutions (Sec:5.2) require that $B(\vec{x}, \vec{u}, t)$ can be abstracted to a linear multiplicative relationship $B'(\vec{x}, t)\vec{u}$ with $B'(\vec{x}, t) \in \mathbb{R}^{n \times m}$, such that a generalized inverse of $B'(\vec{x}, t)$ can be found. For generic setpoint tracking the control law \mathcal{H} will design a desired virtual control input $\vec{\nu}_d$, the allocation rule then has to solve \vec{u} for $\vec{\nu}_c$ such that for some slack variable $\vec{s} \triangleq \vec{\nu}_c - \vec{\nu}_d$ is minimized:

$$\min_{\vec{u} \in \mathbb{R}^m, \vec{s} \in \mathbb{R}^n} \|\vec{s}\|_2 \text{ subject to } \vec{\nu}_c - \vec{\nu}_d = B(\vec{x}, \vec{u}, t) - \mathcal{H}(\vec{x}_e, \dot{\vec{x}}_e, t) = \vec{s} \quad \vec{u} \in \mathbb{U} \quad (1.8)$$

which ensures the commanded input $\vec{\nu}_c$ tracks the desired control input $\vec{\nu}_d$, $\vec{\nu}_c \rightarrow \vec{\nu}_d$ as per some cost function of the slack variable. Mostly the Euclidean norm $\|\vec{s}\|_2$ is used, but alternatively could be some different cost metric. In an overactuated system it then follows that there is a whole set of possible inputs for each commanded $\vec{\nu}_c$. An unique actuator solution (rather than a family of solutions) to Eq:1.8 needs a secondary objective function, $j(\vec{x}, \vec{u}, t)$ to be solved explicitly. Eq:1.8 expands to:

$$\min_{\vec{u} \in \mathbb{R}^m, \vec{s} \in \mathbb{R}^n} (\|\vec{s}\|_2 + j(\vec{x}, \vec{u}, t)) \text{ subject to } \vec{\nu}_c - \vec{\nu}_d = \vec{s} \quad \vec{u} \in \mathbb{U} \quad (1.9)$$

The same authors from [65–67] proposed multiple control allocation solutions to a variety of systems. Following [65], in a subsequent paper [66], the authors introduced a secondary cost function, driving the solution away from the typical linear quadratic programming pseudo and weighted inverse solutions. Aiming for actuator efficiency and not just input saturation, a subsequent paper [67] proposed adaptively allocating actuator positions online. Using a Lyapunov energy equation as the online cost function, the adaptive law settles to a feasible solution.

Overactuation is not often applied to quadrotors and rather than providing a comprehensive literature review of associated papers here (which are all mostly theoretical derivation), the contextual application and solutions are expanded upon later in Ch:5. The only overactuated quadrotor literature which covers allocation of the extra actuators is [2, 41], where the authors apply a weighted pseudo inverse (otherwise known as the Moore-Penrose Inverse [77]) allocation rule. Birotor dual-axis tilting, detailed earlier, results in a critically actuated system and so requires no allocation. As mentioned before, a prerequisite for (*pseudo*) inversion is a multiplicative *linear* control effectiveness relationship for Eq:1.7b.

The only overactuated quadcopter paper which addressed its required control allocation was that of the combined project in [2, 41]. That proposed solution applied weighted inversion, relying on some very specific assumptions to achieve the required input actuator linearity for the system in Eq:1.7b. The gyroscopic torque response to extra actuator η pitching or γ rolling movement, applied to each rotating propeller about the body's \hat{X}_b and \hat{Y}_b axes respectively, gives:

$$\vec{\tau} = (\dot{\eta} \cdot \hat{X}_b) \times J(\Omega \cdot \hat{Z}_b) \in \mathcal{F}^b \quad (1.10)$$

with Ω being that propeller's rotational speed and $\dot{\eta}$ being the inducing servos rate. Projections onto body axes were used in Eq:1.10 because the resultant thrust/responses *were not vectored* or assumed to be redirected. The authors assumed the extra actuators pitch and roll angular rates, $\dot{\eta}$ and $\dot{\gamma}$ respectively, were both proportionally related to their positions η and γ as follows:

$$\dot{\eta} \approx \frac{1}{t_{settle}} \Delta\eta \quad \text{and} \quad \dot{\gamma} \approx \frac{1}{t_{settle}} \Delta\gamma \quad (1.11)$$

where t_{settle} is a constant derived in the actuator transfer function's settling time from a unit input step. Such an assumption holds true so long as $\Delta\eta$ or $\Delta\gamma$ is smaller than the initial step used to evaluate t_{settle} , a restrictive and unrealistic assumption but implemented nonetheless. It then follows that the gyroscopic first-order torque $\vec{\tau} = -\vec{\omega}_b \times J_b \vec{\omega}_b$ and second-order inertia torque $\vec{\tau} = J_b \vec{\omega}_b$ responses are both functions of their associated servo positions η and γ and not their respective derivatives. The extent of that consequence is contrasted with the allocation solution proposed later in Ch:5.

Satellite Attitude Control

Unconstrained attitude setpoint tracking for 6-DOF bodies, quaternion based or otherwise, is a topic well covered in the field of satellite attitude control [64, 74, 133]. The *status quo* for recent research is on nonlinear adaptive backstepping attitude control systems, wherein the adaptive update rule is the novel contribution. Plant uncertainty always adversely affects the confidence in inertia measurements critical to the attitude control of a satellite. In [64] the authors proposed applying adaptive backstepping to compensate for steady-state plant uncertainty errors of the (asymmetric) inertia estimations.

Alternatively, instead of deliberating on costly non-orbital prelaunch inertia measurements, [17] suggested an algorithm for estimating the inertia matrix using controlled single-axis perturbations. Such an approach does assume any initial estimates are sufficiently close to true body measurements such that estimates will settle and stability can be ensured, irrespective of how unacceptable the transient performance may be.

Satellite actuator suites mostly include additional redundant effectors, to ensure fault tolerance, and thus require control allocation. Often the extra allocators are control moment gyroscopic actuators (flywheels driven by DC motors) to produce rotational torques. Thrusters have a limited amount of fuel and can actuate the system only a finite number of times. The thrusters can then be scheduled with a lower priority, preferring bias of electronic CMG actuators. In [74] the authors address the overactuation with direct pseudo inversion before applying quaternion based backstepping for attitude control. Such an inversion solves for Eq:1.9 as follows:

$$\vec{u} = B^\dagger \vec{\nu}_d \quad (1.12a)$$

$$B^\dagger = B^T (BB^T)^{-1} \quad (1.12b)$$

$$\vec{u} \in \mathbb{R}^m, \vec{\nu}_d \in \mathbb{R}^n, B \in \mathbb{R}^{m \times n}, B^\dagger \in \mathbb{R}^{n \times m} \quad (1.12c)$$

where B is the effectiveness matrix which is a static effector form of the effectiveness function $B(\vec{x}, \vec{u}, t)$. The generalized inverse B^\dagger is such that $BB^\dagger \equiv \mathbb{I}_{n \times n}$. Specifically B^\dagger is the general *pseudo* inversion matrix of B (inversions included in Ch:5). Moreover there is an assumed *affine* multiplicative relationship between the input, $\vec{u} \in \mathbb{U}$, and the input effectiveness matrix from Eq:1.7b.

The higher-level controller designs actuator torques $\vec{\nu}_d$, which are then used to solve for explicit actuator positions \vec{u} as per the inversion equation Eq:1.12a. Much like the overactuation previously discussed with respect to quadcopters, the pseudo inversion method of actuator distribution applies linear quadratic programming optimization to the allocation slack cost function, Eq:1.8. The resultant quaternion attitude backstepping controller developed in [74] demonstrated global uniform asymptotic stability. The strength of that backstepping stability lies in the choice of trajectory aiming to be stabilized; $z \rightarrow \vec{0}$.

The first candidate Lyapunov trajectory was defined as:

$$z_1 = \begin{bmatrix} 1 - |q_0| \\ \vec{q}_e \end{bmatrix} \quad (1.13a)$$

such that the Lyapunov energy function candidate is always positive definite and its derivative is positive definite decrescent. The particulars of that stability proof are omitted but it is worth detailing their chosen candidate function:

$$V_1(z) = z_1^T z_1 > 0 \quad \forall [q_0, \vec{q}_e] \quad (1.13b)$$

The absolute quaternion error scalar used in Eq:1.13a ensures a global trajectory's asymptotic stability (Sec:4.6.3), not just local stability that would otherwise be gained. The stable equilibrium points at $Q_e = [\pm 1 \ 0]^T$ apply settling of the trajectory's *error*, allowing the satellite to track its setpoint. Considering that the controller is an ideally compensating controller, the disturbance rejection and uncertainty compensation of the attitude controller could potentially disrupt that achieved stability. This was not discussed in the original paper.

Chapter 2

Prototype Design

2.1 Design

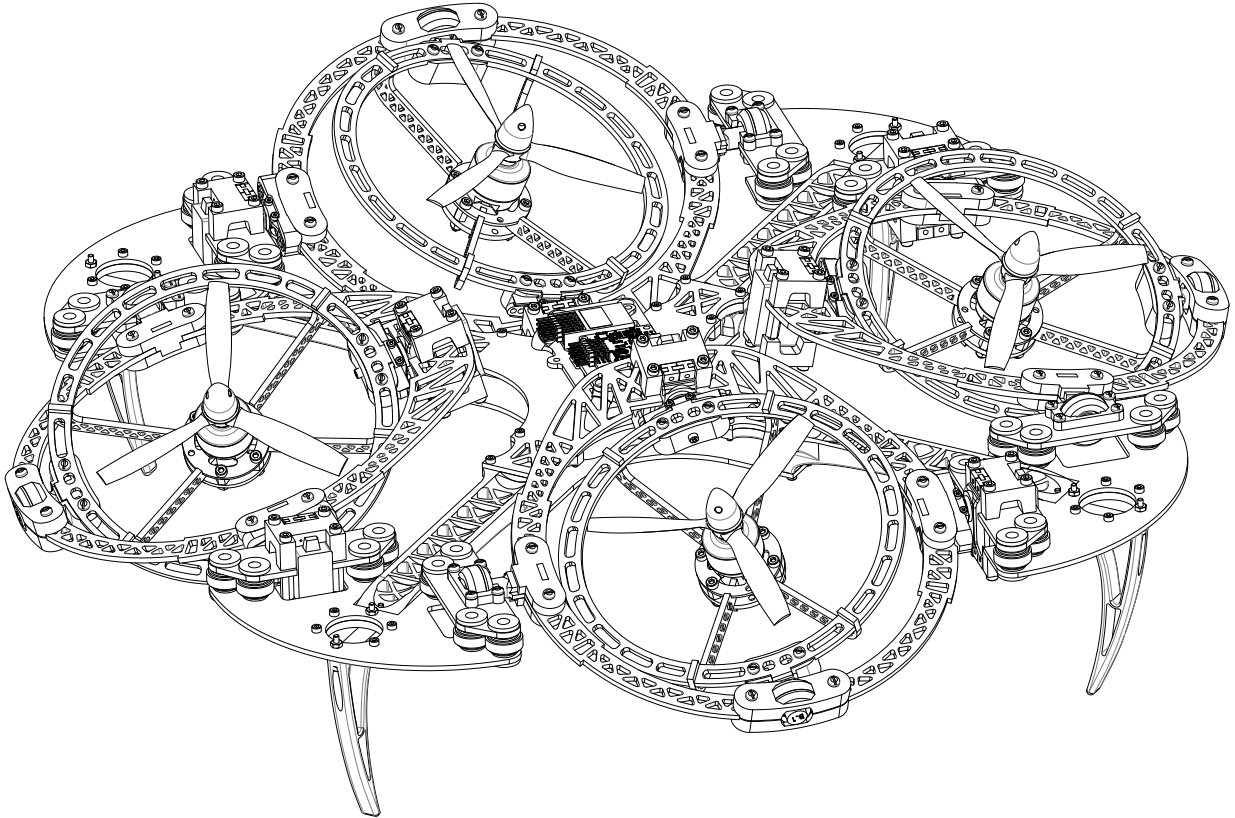


Figure 2.1: Isometric view of the prototype design

The final prototype (Fig:2.1) went through a series of different design iterations, aimed at optimizing engineering time spent on construction and reducing the associated component costs. Significant consideration for the design process was the net weight whose upper limit is inherently limited by the thrust produced from lift motors. Some of the more important design factors, like inertia matrices and associated masses (Sec:2.3), are discussed here in order to give context for the dynamics derived later in Ch:3. The reference frame orientations (which those dynamics are developed with respect to) are detailed here. A brief overview of the electrical systems layout is then given with the associated components and their electrical characteristics included. Finally, the actuator suite's functionality and transfer characteristics are quantified.

2.1.1 Actuation Functionality

The most important component of the design is the articulation for each of the four vectored thrust forces. A concentric gimbal ring structure (Fig:2.2a) independently redirects each lift propeller/motor about two separate rotational axes. Within each module are servos affixed onto sequential gyroscope-like support rings to accommodate pitching and rolling of the propeller's direction. Aligned with each servo is a coaxial support bearing. The bearing and actuator servos have a mass disparity which results in an eccentric center of mass, producing a net gravitational torque arm. Unfortunately, due to weight constraints, counter balance measures cannot be introduced. Consequences from the center of mass variations must be either compensated for (*plant dependent solution*) or exploited in the dynamics (*additional nonlinear actuator plants*). The precise effects are quantified numerically later in Sec:2.3.

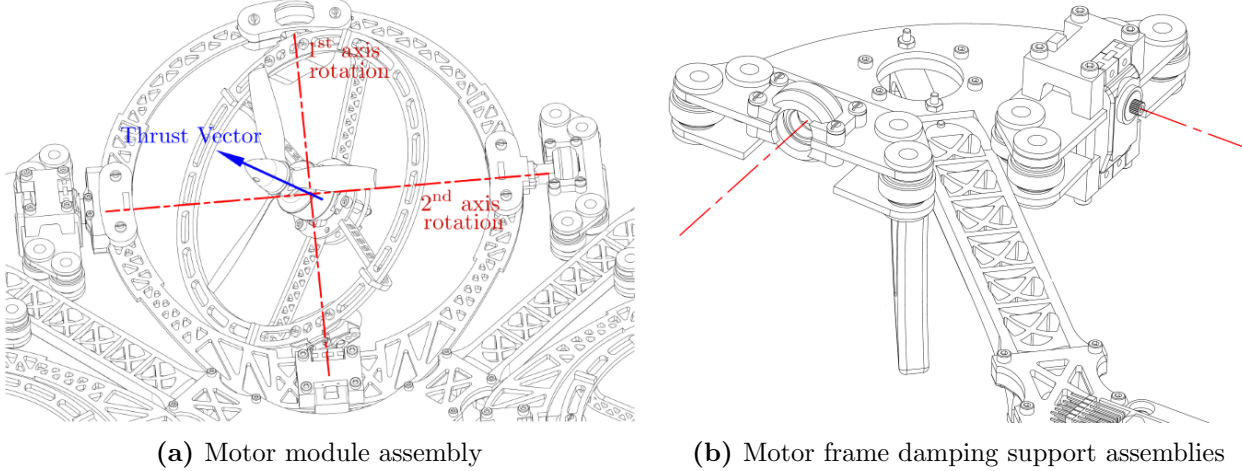


Figure 2.2: Tilting rotor design

Each motor module is positioned such that its produced thrust vector coincides with the intersection of its two rotational axes (Fig:2.2a). As a result there is only a perpendicular displacement of the thrust vector, $L_{arm} = 195.16$ [mm], co-planar to the body frame's XYZ origin \vec{O}_b (see subsequent Fig:2.8). That length directly affects the differential torque plant, $\vec{\tau}_{diff} \triangleq \sum \vec{L}_i \times \vec{T}_i$. An eccentric thrust vector line would make the torque arm displacement a non-orthogonal vector. The center of gravity for each module is time varying and depends on the two servo rotational positions. It is more prudent to ensure intersection of the thrust vector with the rotational center than to balance the masses undergoing rotation. A thrust varying torque is harder to approximate and hence compensate for than a gravitational torque, given the complexity of modelling a propeller's aerodynamic thrust (Sec:3.2.1).

The primary body structure is similar to a traditional quadcopter '+' configuration with adjacent propellers spinning in opposite directions. Each motor module's rotational assembly is suspended by silicone damping balls (Fig:2.2b). A smaller damping assembly in the center of the frame houses all the electronics and power distribution circuitry. All the mounting brackets affixing the motor module rings are 3D printed from CAD models using an Ultimaker V2+ [134]. A complete bill of materials for all parts used, including working drawings for each 3D printed bracket and the laser cut frame(s), is presented in App:B.

The propeller's rotational plane is not aligned exactly with the plane made by the \hat{X}_{M_i} and \hat{Y}_{M_i} rotational servo axes (Fig:2.3). The offset is approximately 23.0 [mm] and must be considered when evaluating pitch/roll inertia and gyroscopic torque responses later in Sec:3.4.1. The propellers are six inch (6×4.5) three-bladed plastic Gemfam propellers, powered by Cobra CM2208-2000 KV Brushless DC (BLDC) motors (Fig:2.4a). The thrust produced as a function of angular velocity (in revolutions per second) for the propellers is derived later in Sec:3.2.1.

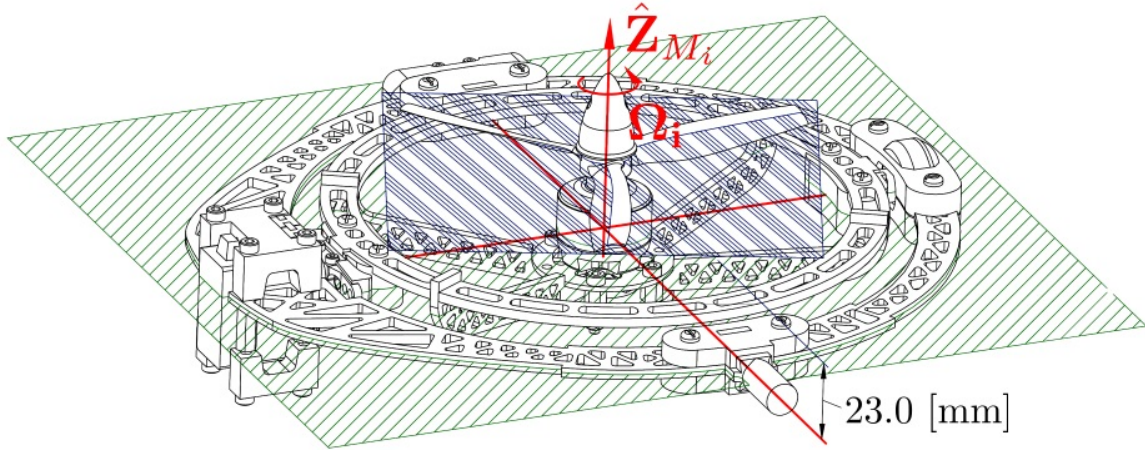
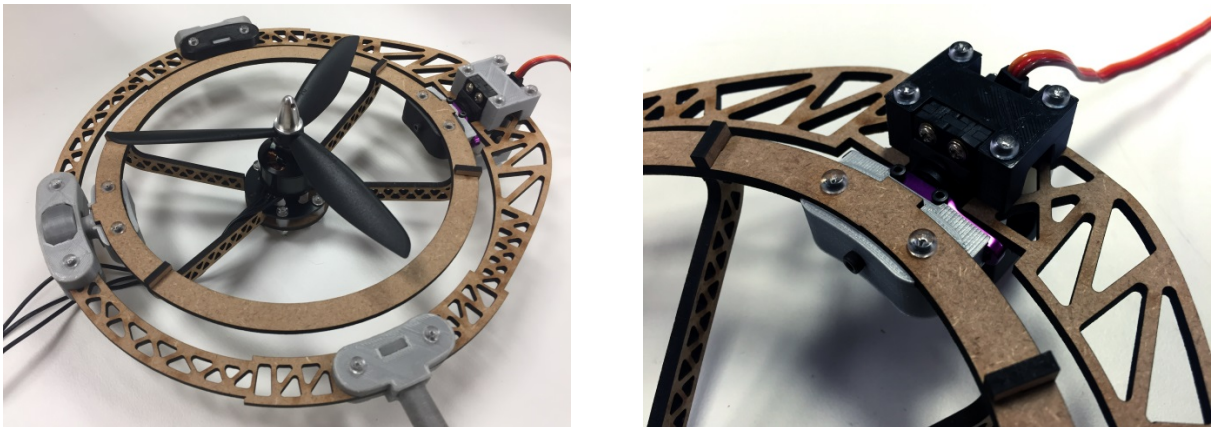


Figure 2.3: Difference between propeller and motor planes

The BLDC motors are controlled with LDPower 20A ESC modules with an in-line OrangeRx RPM Sensor. The ESCs were reflashed with BLHeli [15] firmware. The default firmware on the speed controllers had an unsatisfactory exponentially approaching, nonlinear input speed curve, in contrast to the linear unloaded speed curve in Fig:2.24. The net transfer functions for both ESC modules and the servos are detailed later in Sec:2.4.1. Power for the quadrotor is supplied from a power tether (not from a battery bank). Power lines to both the BLDC motors and servos are supplied through conventional wiring, however an ideal and more flexible design would see slip-rings for each module's power supply.



(a) Cobra CM2208-2000KV BLDC motor module

(b) Corona DS-339MG servo bracket

Figure 2.4: Motor module assembly

Metal gear Corona DS-339MG digital servos are used for the two axes of rotation (Fig:2.4b). Each servo has a rotational range of $\approx 180^\circ$, positioned such that a zeroth offset aligns the motor modules, adjacent to the body frame, and has a $\pm 90^\circ$ rotational range. A digital servo updates at 330 Hz, faster than a 50 Hz analogue servo equivalent (Fig:2.5). This means the otherwise 20 ms zero-order “analogue” sampling effect is a less significant 3.30 ms zero-order holding time. Both the \hat{X}_{M_i} and \hat{Y}_{M_i} axis servos will be rotating differing bodies, so their open-loop transfer functions are individually determined through testing in Sec:2.4.1.

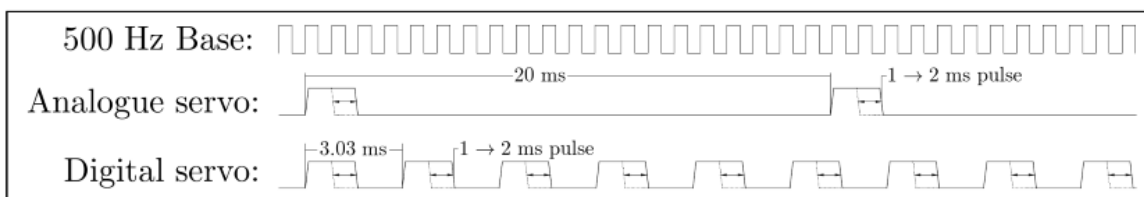


Figure 2.5: Digital and analogue servo timing

2.2 Reference Frames Used

Attitude conventions used for deriving the system's dynamics in Ch:3 are first discussed here. Often these aspects are assumed and are omitted. It is important to clearly and unambiguously define a standard set of framing conventions to avoid uncertainty later. Rotation matrices are included but the focus is on the *contrast* between rotation and transformation operations. Both [47] and [106] provide an in-depth and thorough explanation of rotation matrices and direction cosine matrix (*DCM*) attitude representation. Later, quaternions are used to replace rotation matrix notation for the dynamics in Sec:3.3.2.

2.2.1 Reference Frames Convention

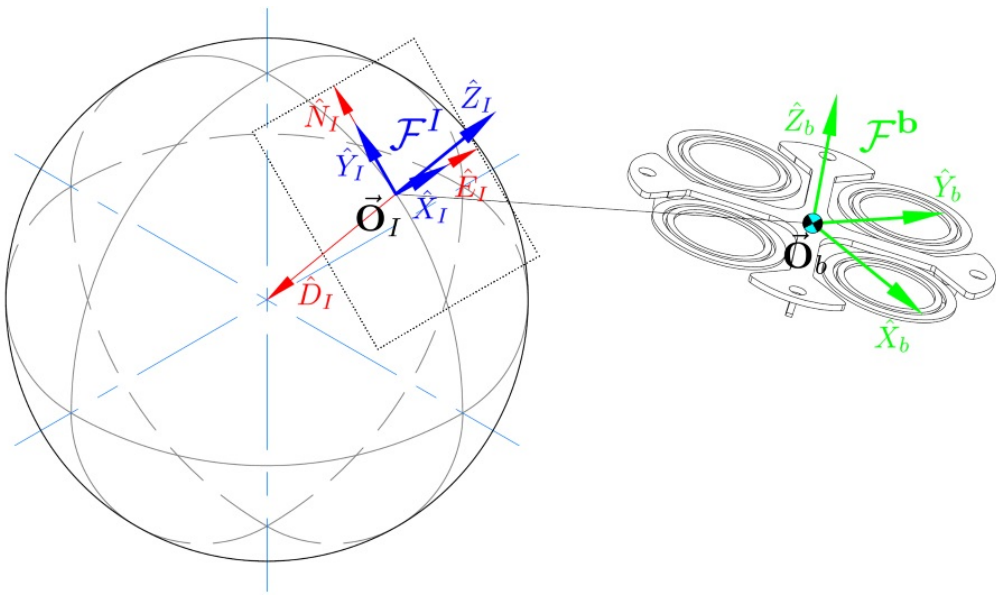


Figure 2.6: Inertial and body reference frames

NASA aerospace frames are used for principle Cartesian inertial and body coordinate representation (Fig:2.6). The inertial frame, \mathcal{F}^I with an origin \vec{O}_I , is aligned such that the \hat{Y}_I axis is in the \hat{N} direction, \hat{X}_I is in the \hat{E} direction and $-\hat{Z}_I$ is in the \hat{D} direction. In Euler orbital sequences the \hat{Z} direction would be toward the Earth's center, sometimes referred to as the NED convention which differs from the NASA frames used here. The body frame, \mathcal{F}^b centered on the point \vec{O}_b , then has both \hat{X}_b and \hat{Y}_b aligned obliquely between two perpendicular arms of the quadrotor's body and the \hat{Z}_b axis in the body's normal upward direction (illustrated in Fig:2.9).

The body frame's axes and center of motion relative to the prototype design's center of mass are both detailed next in Sec:2.2.2. Frame superscripts I and b represent inertial and body frames respectively whilst vector subscripts imply the reference frame in which the vector's coordinates exist or are taken relative to. The function $R_I^b(\eta)$ represents a rotation operator of the Euler set $\vec{\eta}$ (expanded on in Eq:2.11) rotating from subscript frame \mathcal{F}^I to superscript frame \mathcal{F}^b .

A vector $\vec{\nu}$ has the relationship between the body and inertial frames:

$$\vec{\nu}_I \equiv R_b^I(\eta) \vec{\nu}_b \quad \vec{\nu}_b \in \mathcal{F}^b, \vec{\nu}_I \in \mathcal{F}^I \quad (2.1)$$

Displacement between the inertial and body frames is given by $\vec{\mathcal{E}}_I$, defined in the inertial frame:

$$\vec{\mathcal{E}}_I \triangleq [x \ y \ z]^T \quad \in \mathcal{F}^I \quad (2.2)$$

An axial hat and upper case differentiates axis unit vectors $\hat{X}, \hat{Y}, \hat{Z}$ from inertial position quantities x, y, z in Eq:2.2. The body position's time derivative $\dot{\vec{\mathcal{E}}}_I$ refers to the *inertial frame* rate:

$$\frac{d}{dt} \vec{\mathcal{E}}_I = [\dot{x} \quad \dot{y} \quad \dot{z}]^T \quad \in \mathcal{F}^I \quad (2.3)$$

whereas the body's translational velocity \vec{v}_b is with respect to the body frame \mathcal{F}^b . Velocity and the inertial position time derivative are related as follows:

$$\vec{v}_b \triangleq R_I^b(\eta) \dot{\vec{\mathcal{E}}}_I \quad \in \mathcal{F}^b \quad (2.4a)$$

$$= R_I^b(\eta) [\dot{x} \quad \dot{y} \quad \dot{z}]^T \quad (2.4b)$$

Relative angular displacement between two frames is commonly measured by the three angle Euler set. The Euler angle set $\vec{\eta} \triangleq [\phi \ \theta \ \psi]^T$ represents pitch ϕ , roll θ and yaw ψ rotations about sequential \hat{X}, \hat{Y} and \hat{Z} axes respectively. Depending on how the rotation sequence is formulated, those angles can be used to construct rotation matrices which give relation to vectors or can transform coordinates.

The general rotation equation to *rotate* some vector \vec{v} about a normalized unit axis \hat{u} through a rotation angle θ is given by the rotation formula, derived in [40]:

$$\vec{v}' = (1 - \cos(\theta))(\vec{v} \cdot \hat{u})\hat{u} + \cos(\theta)\vec{v} + \sin(\theta)(\hat{u} \times \vec{v}) \quad (2.5)$$

In Eq:2.5, when the unit vector \hat{u} is in the direction of either \hat{X}, \hat{Y} or \hat{Z} axes the equation is simplified to produce the three fundamental rotation matrices $R_x(\phi), R_y(\theta)$ and $R_z(\psi)$. The set of three principle rotation matrices about a Cartesian frame's XYZ axes is defined as:

$$R_x(\phi) \triangleq \begin{bmatrix} 1 & 0 & 0 \\ 0 & \cos(\phi) & -\sin(\phi) \\ 0 & \sin(\phi) & \cos(\phi) \end{bmatrix} \quad (2.6a)$$

$$R_y(\theta) \triangleq \begin{bmatrix} \cos(\theta) & 0 & \sin(\theta) \\ 0 & 1 & 0 \\ -\sin(\theta) & 0 & \cos(\theta) \end{bmatrix} \quad (2.6b)$$

$$R_z(\psi) \triangleq \begin{bmatrix} \cos(\psi) & -\sin(\psi) & 0 \\ \sin(\psi) & \cos(\psi) & 0 \\ 0 & 0 & 1 \end{bmatrix} \quad (2.6c)$$

The notation for a rotation matrix operation is multiplication of the matrix $R_u(\theta)$, applying a left-handed *rotation* operator about some axis \hat{u} by θ . The resultant vector of a rotation operation still exists in the same reference frame. For example an \hat{X} axis rotation by ϕ of some vector \vec{v} is given by:

$$\vec{v}' = R_x(\phi)\vec{v} \quad \vec{v}', \vec{v} \in \mathcal{F}^1 \quad (2.7a)$$

No subscripts are used in Eq:2.7 to indicate reference frame ownership because all vectors are in the same frame. The time derivative of a rotation matrix about some axis \hat{u} by a rotation θ , $\dot{R}_u(\theta)$ is shown in [12] to be:

$$\frac{d}{dt}(R_u(\theta)) \triangleq (\dot{\theta} \cdot \hat{u}) \times R_u \equiv [\dot{\theta} \cdot \hat{u}]_{\times} R_u \quad (2.8a)$$

Where $\dot{\theta} \cdot \hat{u}$ is the projection of the angular rate $\dot{\theta}$ onto the \hat{u} axis. Furthermore, for some vector \vec{a} , the operator $[\vec{a}]_{\times}$ denotes the cross-product matrix or *skew* matrix. The symmetric skew matrix is a matrix multiplication to replace the cross-product operator. For some other vector \vec{b} :

$$\vec{a} \times \vec{b} \equiv [\vec{a}]_{\times} \vec{b} \quad (2.8b)$$

$$[\vec{a}]_{\times} \triangleq \begin{bmatrix} 0 & -a_3 & a_2 \\ a_3 & 0 & -a_1 \\ -a_2 & a_1 & 0 \end{bmatrix} \quad (2.8c)$$

A vector *transformation* changes the resultant vector's reference frame. The transformation is then a rotation by an angle of the *difference* (or negative angle) between the resulting and principle reference frames. A transformation from frame \mathcal{F}^1 to \mathcal{F}^2 , differing by an angle of ϕ about the \hat{X} axis is then a negative rotation operation:

$$\vec{\nu}_2 = R_x(-\phi)\vec{\nu}_1 \quad (2.9a)$$

$$\vec{\nu}_2 \in \mathcal{F}^2 \text{ and } \vec{\nu}_1 \in \mathcal{F}^1 \quad (2.9b)$$

The distinction between Eq:2.7 and Eq:2.9 is the directional sense of the angular operand ϕ , and hence the effect it has on the argument vector. The transformation or rotation of a vector from the inertial frame \mathcal{F}^I to the body frame \mathcal{F}^b is the product of three sequential operations about each principle axis. Each subsequent rotation is applied relative to a new intermediate frame, hence each Euler angle is taken relative to a specific intermediate frame and *not a global one*. The order of those axial rotation operations indeed effects the Euler set, any consequences of which are detailed in [75]. This dissertation uses the ZYX or yaw, pitch, roll rotation sequence. A *rotation* of the vector $\vec{\nu}$ from the inertial to the body frame, $\mathcal{F}^I \rightarrow \mathcal{F}^b$, is then applied by sequential yaw, ψ , pitch, θ , and roll ϕ operations about the \hat{Z} , \hat{Y} and \hat{X} axes respectively:

$$R_I^b(\eta) = R_I^b(\phi, \theta, \psi) \triangleq R_z(\psi)R_y(\theta)R_x(\phi) \quad (2.10a)$$

$$\vec{\nu}' = R_I^b(\phi, \theta, \psi)\vec{\nu} \in \mathcal{F}^I \quad (2.10b)$$

$$= R_z(\psi)R_y(\theta)R_x(\phi)\vec{\nu} \quad (2.10c)$$

It is important to note that in Eq:2.10 both the operand $\vec{\nu}$ and output vector $\vec{\nu}'$ are both in the inertial frame. A *transformation* of a vector from the inertial to the body frame is the negative counterpart of Eq:2.10, a distinction which is not always explicitly specified.

$$\vec{\nu}_b = R_I^b(-\eta)\vec{\nu}_I \triangleq R_I^b(-\phi, -\theta, -\psi)\vec{\nu}_I \quad \vec{\nu}_b \in \mathcal{F}^b, \quad \vec{\nu}_I \in \mathcal{F}^I \quad (2.11a)$$

$$\therefore \vec{\nu}_b = R_z(-\psi)R_y(-\theta)R_x(-\phi)\vec{\nu}_I \quad (2.11b)$$

$$= R_x(\phi)R_y(\theta)R_z(\psi)\vec{\nu}_I = R_b^I\vec{\nu}_I \quad (2.11c)$$

$$R_I^b = (R_b^I)^{-1} \equiv (R_b^I)^T \quad (2.11d)$$

The relationship in Eq:2.11d is an inversion property (*transpose*) of the rotation matrix. A rotation matrix's inverse can be used interchangeably with its negative counterpart to maintain a positive sense of the argument angle. To ensure clarity throughout this dissertation's mathematics, a negative angular sense implies a *transformation* to a different reference frame. Where applicable, the order of rotation will indicate the sequence direction whilst the angular sign differentiates the rotation or transformation operations.

The body frame's angular velocity is taken relative to the inertial frame, represented by $\vec{\omega}_{b/I}$ mostly just simplified to $\vec{\omega}_b$. Because each Euler angle is measured with respect to an intermediary frame, a distinction must then be made between $d\vec{\eta}/dt$ and $\vec{\omega}_b$. All three Euler angles need to be transformed to a common frame $\vec{\eta}_b \in \mathcal{F}^b$ to define the relationship between Euler and angular rates. Exploiting vehicle frames 1 and 2, or rather \mathcal{F}^{v1} and \mathcal{F}^{v2} , as intermediary frames to retrospectively describe frames after $R_x(\phi)$ and $R_y(\theta)$ operations and using the rotation matrix derivative from Eq:2.8, the angular velocity $\vec{\omega}_b$ is the time derivative of Euler angles in the body frame:

$$\vec{\eta} = [\phi \quad \theta \quad \psi]^T \in \mathcal{F}^{I,v_1,v_2} \quad (2.12a)$$

$$\vec{\omega}_b = [p \quad q \quad r]^T \triangleq \frac{d}{dt}\vec{\eta} \equiv \frac{d}{dt}\vec{\eta}_b \in \mathcal{F}^b \quad (2.12b)$$

$$\vec{\eta}_b \triangleq R_{v_2}^b(\phi)\vec{\phi} + R_{v_2}^b(\phi)R_{v_1}^{v_2}(\theta)\vec{\theta} + R_{v_2}^b(\phi)R_{v_1}^{v_2}(\theta)R_I^{v_1}(\psi)\vec{\psi} \in \mathcal{F}^b \quad (2.12c)$$

$$\therefore \vec{\omega}_b = \left[\dot{\vec{\phi}} \right]_x R_{v_2}^b(\phi) + R_{v_2}^b(\phi) \left[\dot{\vec{\theta}} \right]_x R_{v_1}^{v_2}(\theta) + R_{v_2}^b(\phi)R_{v_1}^{v_2}(\theta) \left[\dot{\vec{\psi}} \right]_x R_I^{v_1}(\psi) \in \mathcal{F}^b \quad (2.12d)$$

Euler vectors $\vec{\phi}$, $\vec{\theta}$ and $\vec{\psi}$ are axis projections onto \hat{X} , \hat{Y} and \hat{Z} axes respectively $\phi \cdot \hat{i}$, $\theta \cdot \hat{j}$ and $\psi \cdot \hat{k}$. The vehicle frames used for Eq:2.12b and the subsequent rotations between each frame do not necessarily have to be in that order. The equation could change depending on the rotation sequence used, here ZYX rotation sequences were used. The Euler rate Eq:2.12f then simplifies to the formal relationship between two rotating frames, with $\vec{\omega}_b = [p \ q \ r]^T$:

$$\begin{bmatrix} p \\ q \\ r \end{bmatrix} \equiv \begin{bmatrix} 1 & 0 & -\sin(\theta) \\ 0 & \cos(\phi) & \sin(\phi)\cos(\theta) \\ 0 & -\sin(\theta) & \cos(\phi)\sin(\theta) \end{bmatrix} \begin{bmatrix} \dot{\phi} \\ \dot{\theta} \\ \dot{\psi} \end{bmatrix} \quad (2.12e)$$

$$\therefore \vec{\omega}_b = \Psi(\eta) \dot{\vec{\eta}} \in \mathcal{F}^b \quad (2.12f)$$

$$\Psi(\eta) \triangleq \begin{bmatrix} 1 & 0 & -\sin(\theta) \\ 0 & \cos(\phi) & \sin(\phi)\cos(\theta) \\ 0 & -\sin(\theta) & \cos(\phi)\sin(\theta) \end{bmatrix} \quad (2.12g)$$

$$\therefore \dot{\vec{\eta}} = \Psi^{-1}(\eta) \vec{\omega}_b \equiv \Phi(\eta) \vec{\omega}_b \in \mathcal{F}^{v1,v2,I} \quad (2.12h)$$

$$\Phi(\eta) \triangleq \begin{bmatrix} 1 & \sin(\phi)\tan(\theta) & \cos(\phi)\tan(\theta) \\ 0 & \cos(\phi) & -\sin(\phi) \\ 0 & \sin(\phi)\sec(\theta) & \cos(\phi)\sec(\theta) \end{bmatrix} \quad (2.12i)$$

The *Euler* matrix $\Psi(\eta)$ contains a well known and problematic singularity at $\theta = \pm 90^\circ$, where the determinant of the Euler transformation matrix is zero. The mathematical manifestation of that singularity and its physical consequences are expanded on in Sec:3.3.1. The singularity is present in the middle roll angle θ , which is a direct consequence of the chosen ZYX rotation sequence adopted. Each Euler angle is potentially singular depending on the rotation order used. In later dynamics, quaternions are used in lieu of Euler angles (Sec:3.3.2). Attitude in \mathbb{R}^3 , or $SO(3)$, is intuitive and well suited to the conventions defined here.

Quaternions (Sec:3.3.2), despite being in \mathbb{R}^4 , are similarly constructed in the ZYX order following a three rotation sequence. Combined quaternion operations are additive but non-commutative, thus the order is important. The constructed attitude quaternion order will produce the same resultant frame orientation however the quaternion and its rotation path will differ. A quaternion Q_b , representing the body's attitude, and some vector $\vec{\nu}_I$ in the inertial frame is related to the body frame \mathcal{F}^b as follows:

$$\vec{\nu}_b = R_I^b(-\eta) \vec{\nu}_I \iff Q_b \otimes [0 \ \vec{\nu}_I]^T \otimes Q_b^* \quad (2.13a)$$

$$Q_b \triangleq Q_z \otimes Q_y \otimes Q_x \text{ and its inverse } Q_b^* \triangleq Q_x^* \otimes Q_y^* \otimes Q_z^* \quad (2.13b)$$

The symbol \otimes represents the Hamilton product, or quaternion multiplication operator. Later the Hamilton product is used again for inertia tensor transformations (Sec:2.3). Each quaternion Q_i is always the *unit* quaternion about the i^{th} axis. For the body quaternion Q_b it is the unit quaternion rotation about the body's Euler axis, [75]. A quaternion rotation operates on an argument vector with a zero quaternion scalar component, thus for some vector $\vec{\nu}$, the quaternion rotation operation in Eq:2.13a is equivalent to:

$$Q_{\vec{\nu}'} = Q \otimes (Q_{\vec{\nu}}) \otimes Q^* \quad (2.14a)$$

$$\text{where } Q_{\vec{\nu}} \triangleq [0 \ \vec{\nu}]^T \text{ and } Q_{\vec{\nu}'} \triangleq [0 \ \vec{\nu}'] \quad (2.14b)$$

Quaternion representation in Eq:2.14b ensures that the operation is entirely in \mathbb{R}^4 space. It is typically omitted, despite \mathbb{R}^4 being implied, and as such, Eq:2.14a is then simply:

$$\vec{\nu}' = Q \otimes (\vec{\nu}) \otimes Q^* \quad (2.15)$$

Quaternion dynamics, and the quaternion operator, are later expanded upon to replace the use of Euler angles and rotation matrices as a convention for attitude representation in Chapter:3.

2.2.2 Motor Axis Layout

The whole structure (previously in Fig:2.1) consists of multiple rigidly connected bodies with only relative rotations between each body permitted by its revolute joints, illustrated in the design description in Sec:2.1. Those rigid bodies are categorized into four inter-connected motor modules $\mathbf{M}_{1,2,3,4}$ or \mathbf{M}_i , $i \in [1 : 4]$ and a single body structure \mathbf{B} (*frame* structure, not reference frame). Each module contains two sequential gimbal rings, where each ring has one degree of relative rotation, actuated by a servo, between itself and the subsequent ring. There needs to be distinct nomenclature used for describing these motor modules such that the dynamic derivations later are clear and logical despite the complicated multibody system.

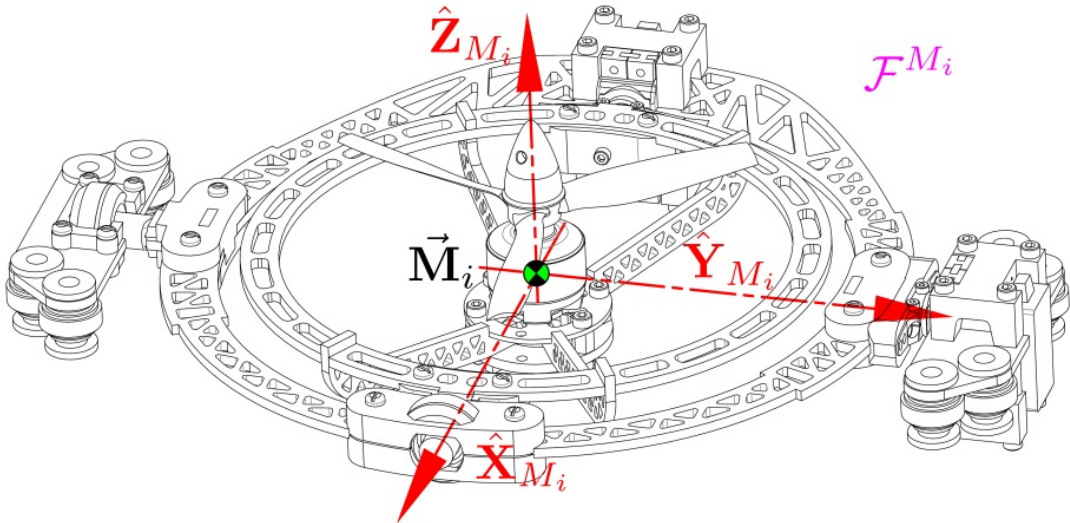


Figure 2.7: Aligned motor frame axes

Every propeller/motor is actuated by a pair of two servos about two subsequent rotational axes (Fig:2.7) in a similar fashion to an Euler rotation sequence. A motor module frame \mathcal{F}^{M_i} is attached to the innermost ring, the BLDC motor's stator is affixed to that frame and its rotor has a rotational velocity Ω_i about the \hat{Z}_{M_i} stator axis. Fig:2.8 shows the sequential relative module frames.

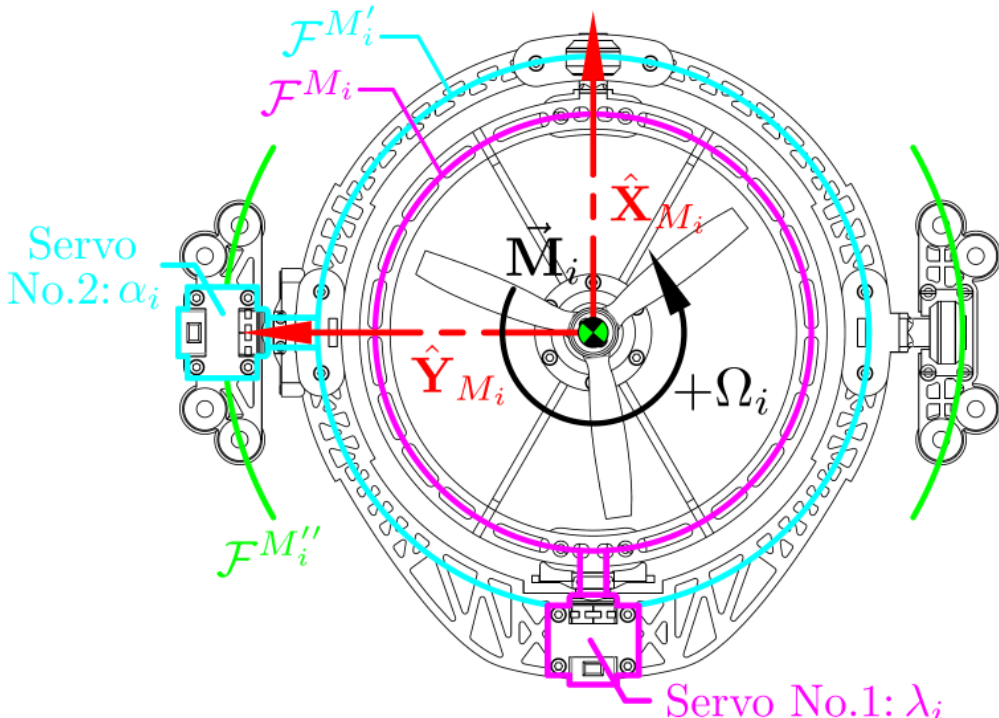


Figure 2.8: Intermediate motor frames

The inner ring frame rotates about its \hat{X}_{M_i} axis by an angle λ_i from the module's first servo. The first servo is attached to the middle ring assembly with the frame $\mathcal{F}^{M'_i}$. The middle ring assembly and frame then rotates by an angle α_i about its $\hat{Y}_{M'_i}$ axis actuated by the second servo. That second servo is affixed to an intermediate $\mathcal{F}^{M''_i}$ frame. Finally there is an orthogonal rotation about that intermediate frame's $\hat{Z}_{M''_i}$ axis to the body frame \mathcal{F}^b . Each module's actuation state is fully described by the propeller's rotational speed Ω_i , both servo positions λ_i and α_i and all their respective rates, $\vec{u}_i \triangleq [\Omega_i, \lambda_i, \alpha_i, \dot{\Omega}_i, \dot{\lambda}_i, \dot{\alpha}_i]^T$ for $i \in [1 : 4]$.

Fig:2.9 shows how the axes of each motor module align with the body frame's axes at rest. The body frame \mathcal{F}^b has the origin \vec{O}_b at the \hat{X}_b and \hat{Y}_b intersect of the structure, co-planar to each motor modules' centers. *Neither* the body frame's origin *nor* each module's center of rotation are coincidental with the body's center of mass. The exact disparity between the origin(s) of motion and the respective body's center of mass are quantified subsequently in Sec:2.3.

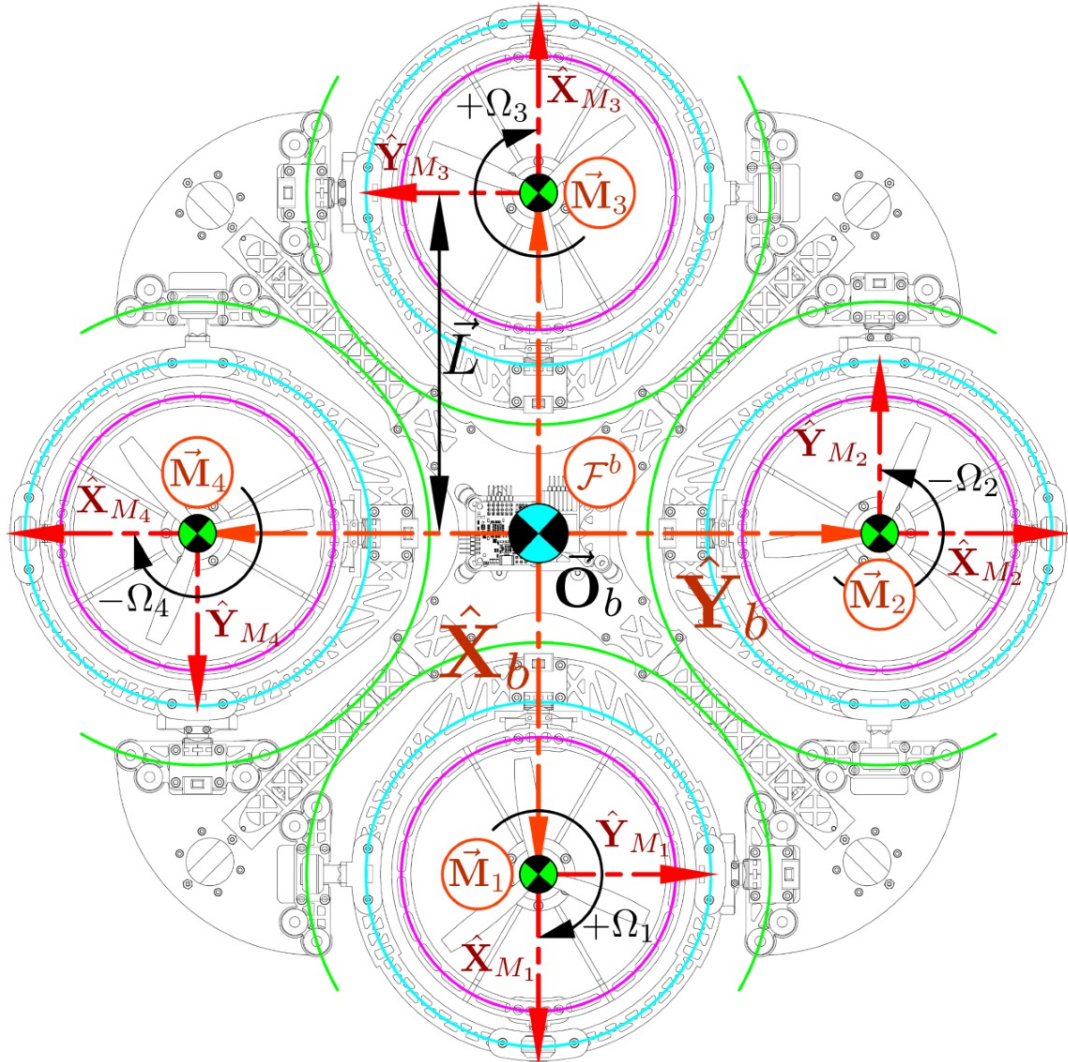
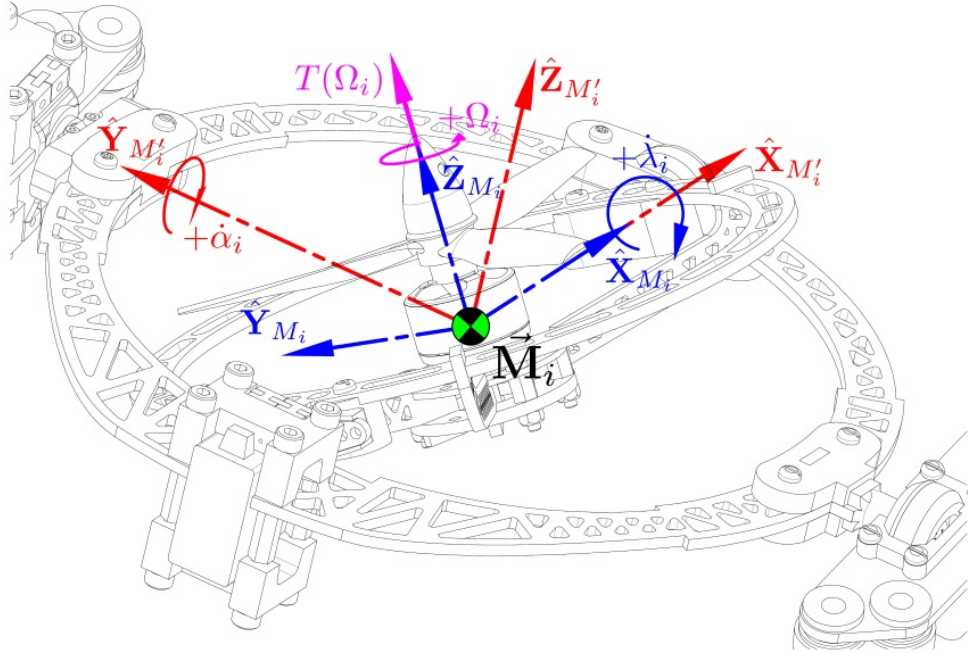


Figure 2.9: Body frame axes layout

The motor modules pair 1 and 3 have their $\hat{X}_{M_{1,3}}$ axes in the positive and negative \hat{X}_b directions of the body frame respectively. Similarly Modules 2 and 4 have their $\hat{X}_{M_{2,4}}$ axes in the positive and negative \hat{Y}_b directions of the body frame. Motor modules 1 and 3 have clockwise rotating propellers, denoted by a positive superscript or $\Omega_{[1,3]}^+$. Conversely modules 2 and 4 have counter-clockwise rotations, denoted by a negative superscript or $\Omega_{[2,4]}^-$.

Not shown in Fig:2.9 is the relative \hat{Z}_b origin position of \vec{O}_b with respect to the entire assembly. The ΔZ height of the body's motion centroid is such that its origin is co-planar with the four motor modules' rotational centers. The center of motion is not coincidental with the center of mass.

**Figure 2.10:** Motor thrust force

Each motor module's rotational center \vec{M}_i is displaced from the body frame origin \vec{O}_b by the distance $L_{\text{arm}} = 195.16$ [mm] (shown in Fig:2.9). Transformation of some vector \vec{v}_{M_i} in the motor frame \mathcal{F}^{M_i} to the body frame \mathcal{F}^b is given as three sequential rotation operations:

$$\vec{v}_b = R_{M_i}^b \vec{v}_{M_i} = R_z(-\sigma_i) R_y(-\alpha_i) R_x(-\lambda_i) \vec{v}_{M_i} \quad \in \mathcal{F}^b, \text{ for } \sigma_i \in [0 \quad \frac{\pi}{2} \quad \pi \quad \frac{2\pi}{3}] \quad (2.16a)$$

The constant orthogonal σ_i rotations about $\hat{Z}_{M''_i}$ are independent of actuator positions, σ_i is determined by the motor module's location, illustrated in Fig:2.9. The rotation matrices $R_z(\sigma_i)$ for $\sigma_i = (i-1)\pi/2$, $i \in [1 : 4]$ are:

$$R_z = \begin{bmatrix} 1 & 0 & 0 \\ 0 & 1 & 0 \\ 0 & 0 & 1 \end{bmatrix}, \begin{bmatrix} 0 & -1 & 0 \\ 1 & 0 & 0 \\ 0 & 0 & 1 \end{bmatrix}, \begin{bmatrix} -1 & 0 & 0 \\ 0 & -1 & 0 \\ 0 & 0 & 1 \end{bmatrix}, \begin{bmatrix} 0 & 1 & 0 \\ -1 & 0 & 0 \\ 0 & 0 & 1 \end{bmatrix} \text{ for } i \in [1 : 4] \text{ respectively} \quad (2.16b)$$

If the propeller's rotation Ω_i produces some thrust force $T(\Omega_i)$ in the motor module frame (Fig:2.10) which acts through the center of rotation \vec{M}_i , that force is similarly transformed to the body frame through Eq:2.16a. A thrust vector for $\vec{T}_i \in \mathcal{F}^{M_i}$ in the body frame \mathcal{F}^b is calculated:

$$\vec{T}_i = R_z(-\sigma_i) R_y(-\alpha_i) R_x(-\lambda_i) [0 \quad 0 \quad T(\Omega_i)]^T \quad \in \mathcal{F}^b \quad (2.17)$$

The actuator space, including propeller speed Ω_i , is then $\in \mathbb{R}^{12}$, or rather $\mathbb{U} \in \mathbb{R}^{12}$, in contrast to $\mathbb{U} \in \mathbb{R}^4$ for a standard quadrotor. The actuator input set $\vec{u} \in \mathbb{U}$ is then structured as:

$$\vec{u}_{\mathbb{U}} = [\Omega_1^+ \quad \lambda_1 \quad \alpha_1 \quad \dots \quad \Omega_4^- \quad \lambda_4 \quad \alpha_4]^T \quad \in \mathbb{R}^{12} \quad (2.18)$$

2.3 Inertia Matrices and Masses

When transforming inertias between reference frames it is more appropriate to use rotation matrices to apply the transformation and not quaternions. Spatial rotations of inertia matrices are ill suited to quaternion parametrization.

An undesirable consequence of relative rotations within a non-rigid body is the inertia response associated with such movements. Newton's Second Law of Rotational Motion states that each applied rotation is going to produce an equal but opposite reaction onto the principally inducing body. Similarly a gyroscopic cross-product from rotational velocities is also present when rotating bodies have their own relative rotation. Typically for most rigid body dynamics (Sec:3.1), such first and second order effects are negligible given that the angular rates on which they depend are small enough to approximate as zero, $\vec{\omega}_b \approx \vec{0}$. A dynamic setpoint (non-zero) attitude tracking plant is, however, going to produce time varying body angular velocities and accelerations that must be accounted for.

The dynamic effects of those torque responses are derived later in Sec:3.4.1. Both inertia and gyroscopic effects are dependent on the considered body's rotational inertia about each respective axis. The magnitude of those inertias is ostensibly a by-product of the structure's design and also the vehicle's instantaneous configuration.

The following inertias presented are all calculated from a SolidWorks model with masses to match physical measurements taken of the constructed prototype. Each connected body affected by the same angular velocity is grouped together. Every motor module then contains 3 independent inertial bodies; the propeller/rotor body, the inner ring, and the middle ring assemblies, each of which are now described in detail.

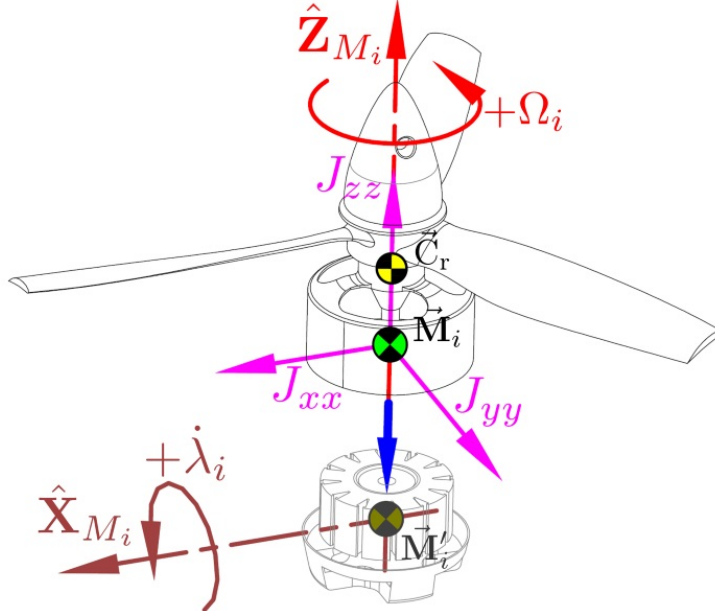


Figure 2.11: Rotor assembly rotational structure

The first rotational body to consider is that of the propeller and rotor assembly (Fig:2.11, excluding the motor's stator). The *rotor* assembly, with subscript r, has a net mass $m_r = 27$ [g] with a center of mass $\vec{C}_r = [0.0 \ 0.0 \ 15.5]^T$ [mm] relative to the entire motor module's center of rotation \vec{M}_i . The propeller's rotation plane is similarly $[0.0 \ 0.0 \ 23.0]^T$ [mm] relative to \vec{M}_i (previously illustrated in Fig:2.3).

At high speeds, the propeller's inertia contribution to the rotor assembly can be approximated as a solid disc. It follows that the inner ring's inertia components can then be regarded as constant with respect to Ω_i , moreover its center of mass is independent of that propeller's rotation.

The entire rotor assembly then has a rotational constant inertia J_r , with principle inertial axes centered and aligned as in Fig:2.11:

$$J_r = \begin{bmatrix} 105.5 & 0.0 & 0.0 \\ 0.0 & 105.5 & 0.0 \\ 0.0 & 0.0 & 41.8 \end{bmatrix} \quad [\text{g.cm}^2] \quad (2.19)$$

The net angular velocity of the rotor assembly $\vec{\omega}_{r/b}$ relative to the body frame is produced by the BLDC motor's rotational velocity Ω_i and both servo rates, $\dot{\lambda}_i$ and $\dot{\alpha}_i$. Here Ω_i and both servo rates are measured in rad.s^{-1} , later Ω_i is used in rev.s^{-1} for Blade-element momentum theory thrust calculations (Sec:3.2.1). Each servo's angular velocity is *transformed* onto the motor frame \mathcal{F}^{M_i} .

$$\vec{\omega}_{r/b} = \begin{bmatrix} 0 \\ 0 \\ \Omega_i \end{bmatrix} + \frac{d\lambda_i}{dt} R_x(-\lambda_i) \begin{bmatrix} \lambda_i \\ 0 \\ 0 \end{bmatrix} + \frac{d\alpha_i}{dt} R_y(-\alpha_i) R_x(-\lambda_i) \begin{bmatrix} 0 \\ \alpha_i \\ 0 \end{bmatrix} \in \mathcal{F}^{M_i} \quad (2.20)$$

Eq:2.20 is later replaced with a quaternion operator. That equation and the remaining angular velocity equations for each body derived here are therefore not expanded further in their current rotation matrix form(s)...

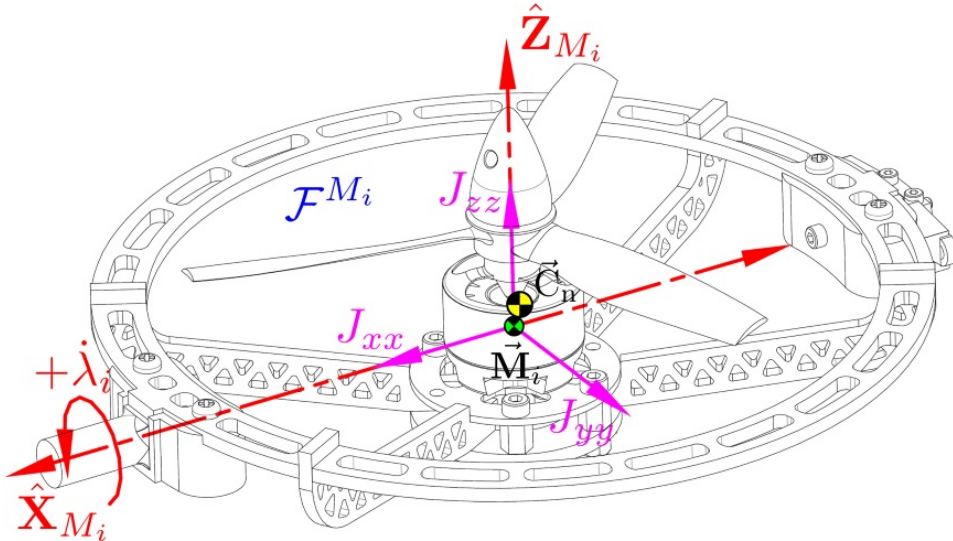


Figure 2.12: Inner ring rotational structure

The next assembly, to which the motor frame \mathcal{F}^{M_i} is attached, is the *inner ring* assembly denoted with subscript n. The inner ring structure has a mass $m_n = 92 \text{ [g]}$, including the rotor assembly in that calculation. The center of mass is positioned $\vec{C}_n = [-1.44 \ 00.0 \ 5.14]^T \text{ [mm]}$ relative to the module's center of rotation \vec{M}_i . The inner ring, being rotated by the λ_i servo about the \hat{X}_{M_i} axis, then has an inertia matrix which includes J_r from Eq:2.19 centered and aligned with axes as in Fig:2.12:

$$J_n = J_{M_i} = \begin{bmatrix} 520.9 & -31.7 & -0.3 \\ -31.7 & 1826.3 & 0.0 \\ -0.3 & 0.0 & 2050.8 \end{bmatrix} \quad [\text{g.cm}^2] \quad (2.21)$$

The rotational velocity of the collective inner ring assembly $\vec{\omega}_{n/b}$ for the angular velocity of frame \mathcal{F}^{M_i} , is similar to that of Eq:2.20. They both occur in the same frame, however the inner ring's angular velocity has no velocity contribution from Ω_i :

$$\vec{\omega}_{n/b} = \frac{d\lambda_i}{dt} R_x(-\lambda_i) \begin{bmatrix} \lambda_i \\ 0 \\ 0 \end{bmatrix} + \frac{d\alpha_i}{dt} R_y(-\alpha_i) R_x(-\lambda_i) \begin{bmatrix} 0 \\ \alpha_i \\ 0 \end{bmatrix} \in \mathcal{F}^{M_i} \quad (2.22)$$

That first actuating servo for λ_i and its coaxial support bearing are both affixed to the intermediate *middle ring* assembly, with subscript m (middle ring only Fig:2.13). The intermediate frame $\mathcal{F}^{M'_i}$ is attached to the middle ring body with a mass $m_m = 98$ [g], *excluding* the inner most ring's contribution. That middle ring body alone has a center of mass $\vec{C}_m = [-4.70 \quad 0.37 \quad -0.36]^T$ [cm] relative to \vec{M}_i .

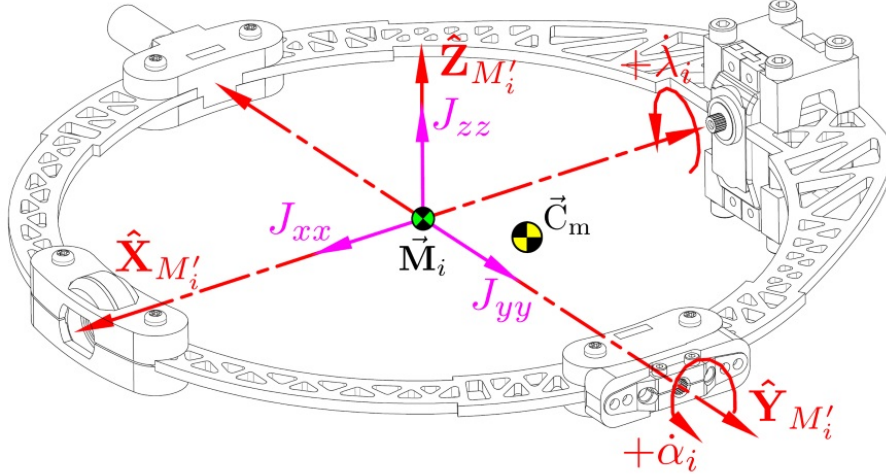


Figure 2.13: Middle ring rotational structure

Together the inner and middle rings make the whole motor module assembly (Fig:2.14), with a subscript p. The net module has a mass $m_p = 190$ [g]. The center of mass for the entire module \vec{C}_p is a function of the inner ring's rotational position λ_i relative to the middle frame $\mathcal{F}^{M'_i}$. That module's center of mass is calculated:

$$\vec{C}'_n(\lambda) \triangleq R_x(\lambda)(\vec{C}_n) \quad (2.23a)$$

$$\vec{C}_p(\lambda) \triangleq \frac{m_m(\vec{C}_m) + m_n(\vec{C}'_n(\lambda))}{m_p} \quad (2.23b)$$

Substituting physical values into Eq:2.23b for the inner and middle rings' center of masses respectively:

$$\vec{C}_p(\lambda) = \frac{98 [-4.70 \quad 0.37 \quad -0.36]^T \times 10^{-7} + 92R_x(\lambda) [-1.44 \quad 0.00 \quad 3.06]^T \times 10^{-8}}{190 \times 10^{-3}} \quad (2.23c)$$

which then has a value at rest, for reference, with the servo $\lambda_i = 0^\circ$ relative to the center of rotation \vec{M}_i :

$$\vec{C}_p(0) = [-2.49 \quad 0.19 \quad 0.04]^T \Big|_{\lambda_i=0} \quad [\text{cm}] \quad (2.23d)$$

The complete motor module is finally rotated by the α_i servo about its $\hat{Y}_{M'_i}$ axis. The module's compound inertia J_p is a combination of the middle ring's inertia J_m and the inner ring's inertia J_n rotated by λ_i about \hat{X}_{M_i} (Fig:2.14). The latter's contribution is dependent on the *rotation*, not transformation, angle λ_i as per the conservation of angular momentum theory, detailed in [107]. The motor module's net rotational inertia J_p , is then calculated from J_m :

$$\text{with } J_m = \begin{bmatrix} 2905.7 & 0.0 & 390.9 \\ 0.0 & 8446.4 & 0.0 \\ 390.9 & 0.0 & 11125.7 \end{bmatrix} \quad [\text{g.cm}^2] \quad (2.24a)$$

$$J_p(\lambda_i) \triangleq J_m + R_x(\lambda_i)(J_n)R_x^{-1}(\lambda_i) \quad (2.24b)$$

That net inertia for the complete motor module, with $\lambda_i = 0^\circ$ and relative to the middle ring frame $\mathcal{F}^{M'_i}$, has a reference value:

$$J_p(0) = \begin{bmatrix} 3365.4 & -0.1 & 390.6 \\ -0.1 & 10210.1 & 0.0 \\ 390.6 & 0.0 & 13118.0 \end{bmatrix} \Big|_{\lambda_i=0^\circ} \quad [\text{g.cm}^2] \quad (2.24c)$$

The rotation matrix R_x in Eq:2.24b is a full rank square matrix, its inverse R_x^{-1} always exists. The module's inertia could be further divided into constant and variable components $J_p(\lambda_i) = J_{const} + J_{M_i}(\lambda_i)$. The variable terms, if small enough, or under certain conditions, could be simplified or neglected.

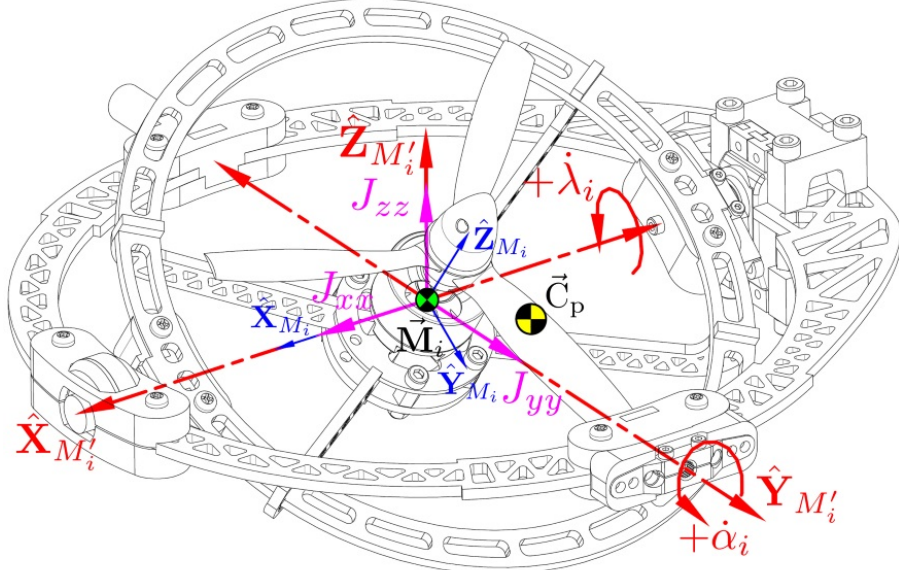


Figure 2.14: Module assembly rotational structure

Fig:2.15 shows how the complete motor module and its rotational axes (in Fig:2.14) are attached and centered relative to the body structure. The second α_i servo is fixed to the body structure and rotates the entire motor module about the $\hat{Y}_{M''_i}$ axis.

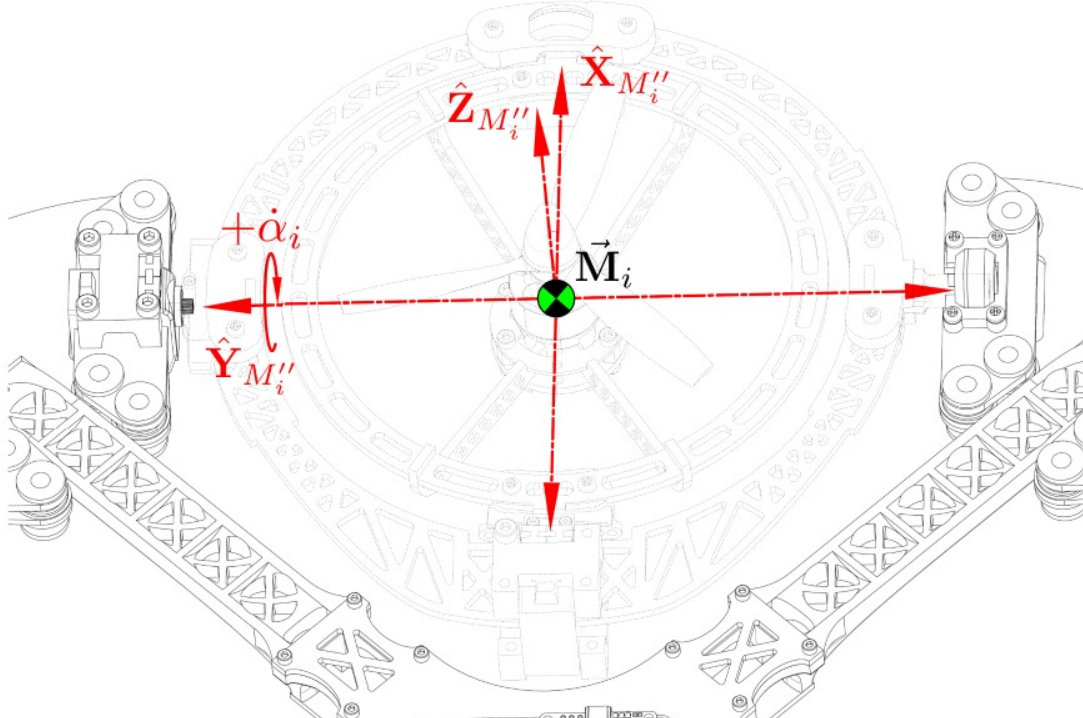


Figure 2.15: Complete motor module attached to the body structure

Finally, the angular velocity experienced by the net motor assembly relative to the body frame, $\vec{\omega}_{p/b}$ in frame $\mathcal{F}^{M'_i}$, is entirely as a result of the α_i servo actuation:

$$\vec{\omega}_{p/b} = \frac{d\alpha_i}{dt} R_y(-\alpha_i) \begin{bmatrix} 0 \\ \alpha_i \\ 0 \end{bmatrix} \in \mathcal{F}^{M'_i} \quad (2.24d)$$

That α_i servo is affixed to the body structure and so its inertia and that of the outer coaxial bearing support contributes then to the body structure's inertia, whose value excludes any of the four motor modules. Attached to that servo is an intermediate frame $\mathcal{F}^{M''_i}$ (Fig:2.15) which differs from the middle ring frame by an $R_y(-\alpha_i)$ transformation and differs from the body frame F^b by an orthogonal $R_z(\sigma_i)$ rotation.

The motor modules are suspended from the body frame with a set of silicone damping balls. The *body structure* which includes those connecting masses, with a subscript y , has center of mass C_y (without any motor modules attached, Fig:2.16). The center of mass coincides with the \hat{X}_b and \hat{Y}_b axis intercepts but lies $\Delta Z = -9.52$ [mm] below the body frame's origin of motion $\vec{O}_b \in \mathcal{F}^b$.

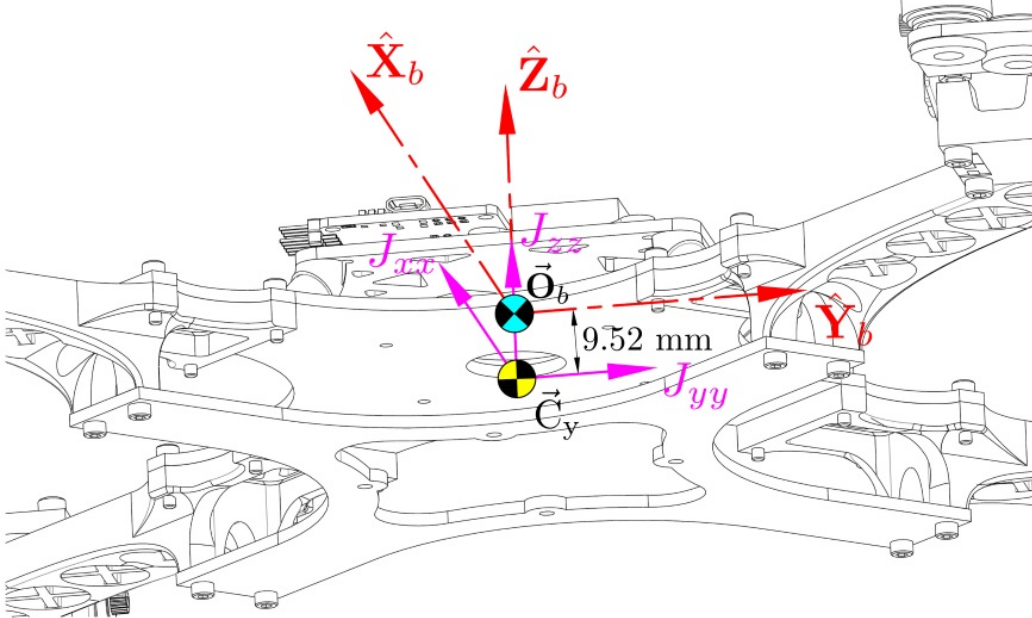


Figure 2.16: Body structure's center of mass

Note: that body frame origin \vec{O}_b which all motion is calculated with respect to is co-planar to the motor module's rotational centers, not the net center of mass.

The body structure's weight, including all four damping assemblies and electronics, totals to $m_y = 814.70$ [g]. Similarly the body structure's net inertia (*sans* motor modules) J_y , about its center of mass (Fig:2.16), is:

$$J_y = \begin{bmatrix} 181569.7 & 0.4 & -19.4 \\ 0.4 & 181692.2 & 8.9 \\ -19.4 & 8.8 & 360067.2 \end{bmatrix} \times 10^{-7} \quad [\text{kg.m}^2] \quad (2.25a)$$

Using the Parallel Axis theorem to translate that inertia to the origin of motion by $\Delta Z = +9.52$ [mm], the inertia about the origin, \vec{O}_b , is:

$$J' \triangleq J + m(\vec{d} \cdot \vec{d} - \vec{d} \otimes \vec{d}) \approx J + md^2 \quad (2.25b)$$

For the general parallel axis transformation in Eq:2.25b, \otimes represents the Hamilton product of two $[3 \times 1]$ matrices. It is used later to indicate quaternion multiplication. The vector \vec{d} is the displacement from the center of mass \vec{C}_y to the body frame origin \vec{O}_b .

$$J'_y \triangleq J_y + m_y(\Delta \vec{Z} \cdot \Delta \vec{Z} - \Delta \vec{Z} \otimes \Delta \vec{Z}) \quad (2.25c)$$

That body's constant inertia J_y at the origin $\vec{\mathbf{O}}_b$ and aligned with the body frame \mathcal{F}^b is then:

$$\therefore J'_y = \begin{bmatrix} 182307.7 & 0.4 & -14.5 \\ 0.4 & 182430.1 & 6.5 \\ -14.5 & 6.5 & 360067.2 \end{bmatrix} \times 10^{-7} \text{ [kg.m}^2\text{]} \quad (2.25d)$$

Net inertia for the complete multibody vehicle, $J_b(\vec{u})$ about the origin $\vec{\mathbf{O}}_b$, is a combination of all the relative attached bodies as a function of all actuator positions $\vec{u} \in \mathbb{U}$. The entire assembly's inertia $J_b(\vec{u})$ is the *net* body frame's inertia, different from J_y , which is the inertia for *only* the body structure. The collective assembly consisting of; the four motor modules each rotated first by λ_i then α_i and finally translated to the body frame origin, and the body structure's contribution itself.

Those motor modules' inertia transformations from their respective centers of rotation, in frames \mathcal{F}^{M_i} for $i \in [1 : 4]$, to the body frame \mathcal{F}^b are analogous to that of Eq:2.16. Reiterating that $\vec{\mathbf{O}}_b$ is *co-planar* to each module's center of rotation, each motor module's inertia $J_p(\lambda_i)$, defined in Eq:2.24b, is further rotated by α_i about the $\hat{Y}_{M'_i}$ axis and finally an orthogonal $\hat{Z}_{M''_i}$ axis rotation (aligned with \hat{Z}_b) onto \mathcal{F}^b .

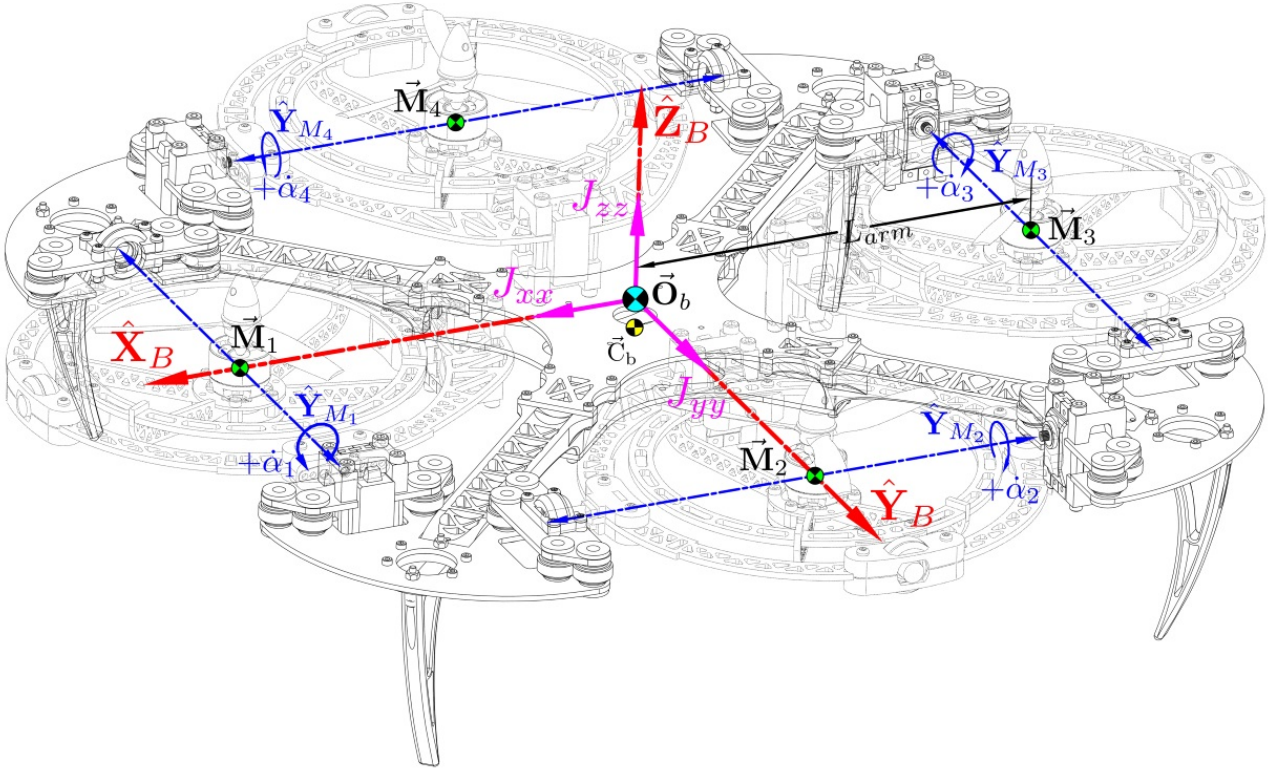


Figure 2.17: Inertia, mass and motor modules respective centers

For the entire body's net inertia, each contributing assembly's inertia must be defined with respect to the body's origin, first aligned parallel to the common set of body frame axes \hat{X}_b , \hat{Y}_b and \hat{Z}_b and then translated to the origin $\vec{\mathbf{O}}_b$. Each motor module's inertia, still centered relative to each individual rotational center $\vec{\mathbf{M}}_i$ in Fig:2.17, but re-orientated to align parallel to the origin $\parallel \vec{\mathbf{O}}_b$ with rotations about axes $\hat{X} \in \mathcal{F}^{M_i}$, $\hat{Y} \in \mathcal{F}^{M'_i}$, $\hat{Z} \in \mathcal{F}^{M''_i}$, is calculated:

$$J_{\vec{\mathbf{M}}_i}(\vec{u}_i) = R_z(\sigma_i)R_y(\alpha_i)(J_p(\lambda_i))R_y^{-1}(\alpha_i)R_z^{-1}(\sigma_i) \text{ for } i \in [1 : 4] \quad (2.26a)$$

The argument (\vec{u}_i) in Eq:2.26a is the i^{th} projection of the actuator space $([\Omega_i \ \lambda_i \ \alpha_i]^T)$. Furthermore the rotation $R_z(\sigma_i)$ was defined as an orthogonal \hat{Z}_b rotation previously in Eq:2.16b. Expanding each module's inertia to individual inner and middle ring contributions then yields:

$$J_{\vec{\mathbf{M}}_i}(\vec{u}_i) = R_z R_y(\alpha_i)(J_m)R_y^{-1}(\alpha_i)R_z^{-1} + R_z R_y(\alpha_i)R_x(\lambda_i)(J_n)R_x^{-1}(\lambda_i)R_y^{-1}(\alpha_i)R_z^{-1} \quad (2.26b)$$

It is at this stage that, despite simplifications, the symbolic inertia equations all become overly cumbersome to include numeric values. For the sake of brevity, exact calculated inertia values for the input dependent plant are omitted.

Each module's rotational center, vectors $\vec{M}_{[1:4]}$, are all equally spaced relative to the origin of motion, \vec{O}_b , with a parallel axis arm $L_{arm} = 195.16$ [mm] (Fig:2.17). To avoid notational confusion, the terms $\vec{L}_{[1,3]} = [\pm 195.16 \ 0 \ 0]^T$ and $\vec{L}_{[2,4]} = [0 \ \pm 195.16 \ 0]^T$ are used to represent the vector displacements between the origin \vec{O}_b and each motor module's center of rotation $\vec{M}_{[1:4]}$. The vehicle's net inertia $J_b(\vec{u})$, about the origin \vec{O}_b and depending on the actuator position matrix $\vec{u} \in \mathbb{U}$, can be calculated as:

$$\underset{\vec{O}_b}{J_b}(\vec{u}) = J_y + \sum_{i=1}^4 J'_{\vec{M}_i}(\vec{u}_i) \quad [\text{kg.m}^2], \quad \vec{u} \in \mathbb{U} \quad (2.27a)$$

where $J'_{\vec{M}_i}(\vec{u}_i)$ is the motor module inertia from Eq:2.26 but translated to the origin \vec{O}_b using a parallel axis theorem with $m_p = 190$ [g] and the displacement vector \vec{L}_i :

$$J'_{\vec{M}_i}(\vec{u}_i) \triangleq J_{\vec{M}_i}(\vec{u}_i) + m_p(\vec{L}_i \cdot \vec{L}_i - \vec{L}_i \otimes \vec{L}_i) \quad (2.27b)$$

Although Eq:2.27 produces the net multi-body's inertia, each equation used to calculate $J'_{\vec{M}_i}$ involves cascaded transformations which may deteriorate the result's certainty. Each module's inertia is first translated to their respective centers of rotation, then rotated as per the two servos, and then finally translated again back to the body frame's origin.

Alternatively, the inertia contribution of each sub-assembly can be considered separately and translated directly to the body frame's origin from their respective mass centers. This will improve the accuracy of the produced inertia equations, each translation/rotation has with it an associated floating point concatenation. It is also perhaps more intuitive for the reader to consider each sub-body's contribution individually, despite having been derived as combined inertial bodies in the above. The vehicle's net inertia can then be described as nine separate contributing bodies; four inner rings J_n , four middle rings J_m , and one body structure J_y :

$$\underset{\vec{O}_b}{J_b}(\vec{u}) \equiv J'_y + \sum_{i=1}^4 \underset{\vec{O}_b}{J_n}(\vec{u}_i) + \sum_{i=1}^4 \underset{\vec{O}_b}{J_m}(\vec{u}_i) \quad \vec{u} \in \mathbb{U} \quad (2.28)$$

Note that the rotor's inertia J_r is included in J_n . Each body is isolated and each inertia is independently considered, starting with the inner ring's contribution (having an inertia J_n with respect to its *center of mass*, and not center of rotation) measured *relative* to its center of rotation. The following is then fundamentally different from the process in Eq:2.21, calculating the inner ring's inertia contribution about the origin \vec{O}_b .

For the inner ring only, with a mass m_n and center of mass \vec{C}_n relative to its center of rotation \vec{M}_i , the inner ring's directly transformed inertia contribution then follows:

$$m_n = 92 \quad [\text{g}] \quad (2.29a)$$

$$\vec{C}_n = [-1.44 \ 0.0 \ 5.14]^T \quad [\text{mm}], \quad \in \mathcal{F}^{M_i} \quad (2.29b)$$

The inner ring's inertia matrix about its center of mass (Fig:2.12) is the constant:

$$\begin{matrix} J_n \\ \vec{C}_n \end{matrix} = \begin{bmatrix} 496.6 & -31.7 & 6.6 \\ -31.7 & 1800.1 & 0.0 \\ 6.6 & 0 & 2048.9 \end{bmatrix} \quad [\text{g.cm}^2] \quad (2.29c)$$

Relative to the body frame's origin \vec{O}_b , the inner ring has a center of mass rotated by λ_i and α_i servos about their respective axes with a relative orthogonal R_z rotation where σ_i for the i^{th} module is implied:

$$\vec{C}_n'''(\lambda_i, \alpha_i) = R_z R_y(\alpha_i) R_x(\lambda_i)(\vec{C}_n) \quad \in \mathcal{F}^b \quad (2.29d)$$

Transforming the inertia from Eq:2.29c, still about the center of mass \vec{C}_n''' , but with axes aligned parallel to the body frame, or using the shorthand $\parallel \vec{\mathbf{O}}_b$, the inner ring's inertia as a function of both servo angles λ_i and α_i aligned with \mathcal{F}^b is:

$$\begin{aligned} J_n'''(\lambda_i, \alpha_i) &= R_z R_y(\alpha_i) R_x(\lambda_i) (J_n) R_x^{-1}(\lambda_i) R_y^{-1}(\alpha_i) R_z^{-1} \\ &\parallel \vec{\mathbf{O}}_b \end{aligned} \quad (2.29e)$$

The vector difference between the rotated center of mass C_n''' with the body origin $\vec{\mathbf{O}}_b$ is:

$$\Delta \vec{L}_i = \vec{L}_i - \vec{C}_n'''(\lambda_i, \alpha_i) \quad (2.29f)$$

Then using the above with a parallel axis translation, adapted from Eq:2.25b, to move the rotated inertia J_n''' to the center of the body frame $\vec{\mathbf{O}}_b$:

$$\begin{aligned} J_n(\lambda_i, \alpha_i) &\triangleq J_n'''(\lambda_i, \alpha_i) + m_n((\Delta \vec{L}_i \cdot \Delta \vec{L}_i) \mathbb{I}_{3 \times 3} - \Delta \vec{L}_i \otimes \Delta \vec{L}_i) \\ &\parallel \vec{\mathbf{O}}_b \end{aligned} \quad (2.29g)$$

and for reference when both servos are at rest, $\lambda_i = 0^\circ$ and $\alpha_i = 0^\circ$, the inner ring's inertia contribution about the origin is explicitly:

$$\begin{aligned} J_n(\lambda_i, \alpha_i) &= \begin{bmatrix} 520.9 & -31.0 & 922.6 \\ -31.0 & 36348.5 & 0.0 \\ 922.6 & 0.0 & 36573.0 \end{bmatrix} \times 10^{-7} \Big|_{\lambda_i, \alpha_i=0} \quad [\text{kg.m}^2], \in \mathcal{F}^b \\ &\parallel \vec{\mathbf{O}}_b \end{aligned} \quad (2.29h)$$

Similarly, the same process is applied for the middle ring's rotated and translated inertia. The middle ring *only* (Fig:2.13) has a mass and center of mass relative to the module's center of rotation respectively:

$$m_m = 98 \quad [\text{g}] \quad (2.30a)$$

$$\vec{C}_m = [-47.00 \quad 3.74 \quad -3.63]^T \quad [\text{mm}], \in \mathcal{F}^{M'_i} \quad (2.30b)$$

The inertia matrix of the middle ring body, excluding the inner ring, about its center of mass is:

$$\begin{aligned} J_m &= \begin{bmatrix} 2879.1 & 172.3 & 223.6 \\ 172.3 & 6269.0 & 13.3 \\ 223.6 & 13.3 & 8947.5 \end{bmatrix} \quad [\text{g.cm}^2] \\ &\parallel \vec{\mathbf{C}}_m \end{aligned} \quad (2.30c)$$

Rotating the center of mass only by the α_i servo about the $\hat{Y}_{M'_i}$ axis yields the center of mass \vec{C}_m'' relative to $\vec{\mathbf{O}}_b$:

$$\vec{C}_m''(\alpha_i) = R_z R_y(\alpha_i) (\vec{C}_m) \quad \in \mathcal{F}^b \quad (2.30d)$$

Then the rotated inertia matrix, aligned with axes parallel to the body frame origin $\vec{\mathbf{O}}_b$, follows:

$$\begin{aligned} J_m''(\alpha_i) &= R_z R_y(\alpha_i) (J_m) R_y^{-1}(\alpha_i) R_z^{-1} \\ &\parallel \vec{\mathbf{O}}_b \end{aligned} \quad (2.30e)$$

The vector difference from the rotated center of mass to the body frame origin is calculated:

$$\Delta \vec{L}'_i = \vec{L}_i - \vec{C}_m''(\alpha_i) \quad (2.30f)$$

which then leads to the parallel axis translation of the middle ring's inertia to the body origin:

$$\begin{aligned} J_m(\alpha_i) &\triangleq J_m''(\alpha_i) + m_m((\Delta \vec{L}'_i \cdot \Delta \vec{L}'_i) \mathbb{I}_{3 \times 3} - \Delta \vec{L}'_i \otimes \Delta \vec{L}'_i) \\ &\parallel \vec{\mathbf{O}}_b \end{aligned} \quad (2.30g)$$

For reference, at rest with the middle ring servo $\alpha_i = 0^\circ$ the middle ring's inertia contribution at $\vec{\mathbf{O}}_b$ is:

$$\begin{aligned} J_m(\alpha_i) &= \begin{bmatrix} 2905.7 & 715.4 & -303.9 \\ 715.4 & 27795.7 & 0.0 \\ -303.9 & 0.0 & 30475.0 \end{bmatrix} \times 10^{-7} \Big|_{\alpha_i=0} \quad [\text{kg.m}^2], \in \mathcal{F}^b \\ &\parallel \vec{\mathbf{O}}_b \end{aligned} \quad (2.30h)$$

Then, reiterating Eq:2.28, the instantaneous inertia of the entire body in motion is calculated as the contribution of each connected sub-body, depending on the actuator matrix $\vec{u} \in \mathbb{U}$.

$$\begin{aligned} J_b(\vec{u}) &\equiv J'_y + \sum_{i=1}^4 J_n(\vec{u}_i) + \sum_{i=1}^4 J_m(\vec{u}_i) \quad \vec{u} \in \mathbb{U} \\ \vec{\mathbf{O}}_b & \quad \vec{\mathbf{O}}_b \end{aligned} \quad (2.31a)$$

The net mass for the entire multibody system is $m_b = 1574.7$ [g]. For reference and using Eq:2.31a, the inertia matrix for the assembly when actuators are at rest conditions, $\vec{u} = \vec{0}$, about the origin $\vec{\mathbf{O}}_b$ is:

$$J_b(\vec{0}) = \begin{bmatrix} 317448.2 & 0.4 & -14.5 \\ 0.4 & 317570.7 & 6.5 \\ -14.5 & 6.5 & 628257.5 \end{bmatrix} \times 10^{-7} \Big|_{\vec{u}=\vec{0}} \quad [\text{kg.m}^2], \quad \in \mathcal{F}^b \quad (2.31b)$$

The maximum variation of the body's net inertia is found from the maximum determinant of the inertia matrix in Eq:2.31a for some actuator state $\max(\det|J_b(\vec{u}_\Lambda)|)$, $\vec{u}_\Lambda \in \mathbb{U}$. A maximum $J_b(\vec{u}_\Lambda)$, with a determinant $\det|J_b(\vec{u}_\Lambda)| = 1017.93 \times 10^{-7}$, is:

$$J_b(\vec{u}_\Lambda) = \begin{bmatrix} 384695.4 & 0.4 & -14.5 \\ 0.4 & 384717.9 & 6.5 \\ -14.5 & 6.5 & 687970.7 \end{bmatrix} \times 10^{-7} \Big|_{\vec{u}_\Lambda} \quad [\text{kg.m}^2], \quad \in \mathcal{F}^b \quad (2.32a)$$

The actuator matrix, independent of propeller speeds $\Omega_{[1:4]}$, as follows:

$$\vec{u}_\Lambda = \begin{bmatrix} \Omega_1, \quad \lambda_1 = 178^\circ, \quad \alpha_1 = 260^\circ \dots \\ \Omega_2, \quad \lambda_2 = 178^\circ, \quad \alpha_2 = 260^\circ \dots \\ \Omega_3, \quad \lambda_3 = 178^\circ, \quad \alpha_3 = 0^\circ \dots \\ \Omega_4, \quad \lambda_4 = 0^\circ, \quad \alpha_4 = 0^\circ \end{bmatrix} \quad (2.32b)$$

Conversely, the minimum net inertia for the body is from the smallest determinant of Eq:2.31a, for the actuator state $\min(\det|J_b(\vec{u}_V)|)$, $\vec{u}_V \in \mathbb{U}$. A minimum $J_b(\vec{u}_V)$, with a determinant $\det|J_b(\vec{u}_V)| = 633.48 \times 10^{-7}$, is:

$$J_b(\vec{u}_V) = \begin{bmatrix} 317469.0 & 0.4 & -1219.0 \\ 0.4 & 317591.5 & 1195.3 \\ -1219.0 & 1195.3 & 628298.1 \end{bmatrix} \times 10^{-7} \Big|_{\vec{u}_V} \quad [\text{kg.m}^2], \quad \in \mathcal{F}^b \quad (2.33a)$$

When an actuator matrix for that minimum inertia is:

$$\vec{u}_V = \begin{bmatrix} \Omega_1, \quad \lambda_1 = 178^\circ, \quad \alpha_1 = 0^\circ \dots \\ \Omega_2, \quad \lambda_2 = 0^\circ, \quad \alpha_2 = 260^\circ \dots \\ \Omega_3, \quad \lambda_3 = 0^\circ, \quad \alpha_3 = 0^\circ \dots \\ \Omega_4, \quad \lambda_4 = 0^\circ, \quad \alpha_4 = 0^\circ \end{bmatrix} \quad (2.33b)$$

The inclusion of Eq:2.32 and Eq:2.33 is used to calculate maximum and minimum Eigenvalues of the body's inertia matrix at a later stage in the control derivation, Sec:4.6. It is interesting to note that both extremes of $J_b(\vec{u})$ are still symmetrical, and *roughly* diagonal. Actuator positions hardly affect the skew products of inertia in $J_b(\vec{u})$ but can vary the diagonal moments of inertia by almost 20% of their principle value. Unless otherwise specified, any inertia $J_b(\vec{u})$ indicates an instantaneous calculated solution to Eq:2.31a given a particular $\vec{u}(t) \in \mathbb{U}$. The purpose of the derivations for rotated centers of mass in Eq:2.29 and Eq:2.30 is twofold, highlighting both the inertia contributions *and* the variable center of mass for each sub-body. Seeing that the origin of motion $\vec{\mathbf{O}}_b$ in the body frame \mathcal{F}^b and the body's effective center of mass $\vec{\mathbf{C}}_b$ are not coincidental, it is important to quantify the net center of mass's variation with actuator positions $\vec{u} \in \mathbb{U}$.

In the general case for a collection of n bodies, with each body's center of mass at some position \vec{X}_i and each having a mass m_i , resultant center of mass is:

$$\vec{\mathbf{C}} = \frac{\sum_{i=1}^n m_i \cdot \vec{X}_i}{\sum_{i=1}^n m_i} \quad (2.34a)$$

Using $\vec{C}_n'''(\lambda_i, \alpha_i)$ and $\vec{C}_m''(\alpha_i)$ as rotated centers of mass defined in Eq:2.29d and Eq:2.30d respectively and \vec{C}_y for the body structure, the vehicle has a variable center of mass $\vec{C}_b(\vec{u})$:

$$\vec{C}_b(\vec{u}) = \frac{m_y \vec{C}_y + \sum_{i=1}^4 m_n \vec{C}_n'''(\vec{u}_i) + \sum_{i=1}^4 m_m \vec{C}_m''(\vec{u}_i)}{m_b} \quad (2.34b)$$

So, for reference, the net center of gravity for the entire multibody assembly, when all actuators are at their zero positions is: $\vec{C}_b(\vec{0}) = [0 \ 0 \ -4.94]^T$ [mm]. Using a gravity force vector \vec{G}_b in the body frame as a result of gravitational acceleration $g = -9.81$ [m.s⁻²], acting on the vehicle's center of mass:

$$\vec{G}_b = R_I(\vec{\eta}) {}^b \vec{G}_I \in \mathcal{F}^b \quad (2.35a)$$

$$= R_I^b(\vec{\eta}) [0 \ 0 \ -9.81(m_b)]^T \text{ N} \quad (2.35b)$$

Because Eq:2.35 acts through the body's center of gravity $\vec{C}_b(\vec{u})$, not its center of motion \vec{O}_b , there exists a gravitational torque from the varying center of gravity. The resultant gravitational torque about the origin \vec{O}_b in the body frame \mathcal{F}^b from that eccentric mass center for the vehicle is:

$$\Delta \vec{C}_g = \vec{O}_b - \vec{C}_b(\vec{u}) \quad (2.35c)$$

$$\vec{\tau}_g = \Delta \vec{C}_g \times m_b \vec{G}_b \in \mathcal{F}^b \quad (2.35d)$$

The prototype which was constructed is shown in Fig:2.18. The above mass centers and inertias were calculated from physical values measured on assembled components of the prototype. The listed values includes measurements of fasteners and electronics.



Figure 2.18: Final constructed prototype

Uncertainty with inertia measurements, proven to be destabilizing and detrimental to control efforts in [76, 140], can indeed be incorporated into state dependent plant uncertainty compensation, in [10]. Controllers with strong disturbance and uncertainty rejection, like a well designed H_∞ controller, would be ideally suited to controlling an attitude plant without having to explicitly specify all of the above inertias.

It is, however, worth the mathematical deliberation to detail each inertia's equation given that Lagrange dynamics are later applied to determine the servo actuator dynamic responses (Sec:3.4). Such equations of motion will later need explicit terms defined for instantaneous transformed inertias.

2.4 Electronics

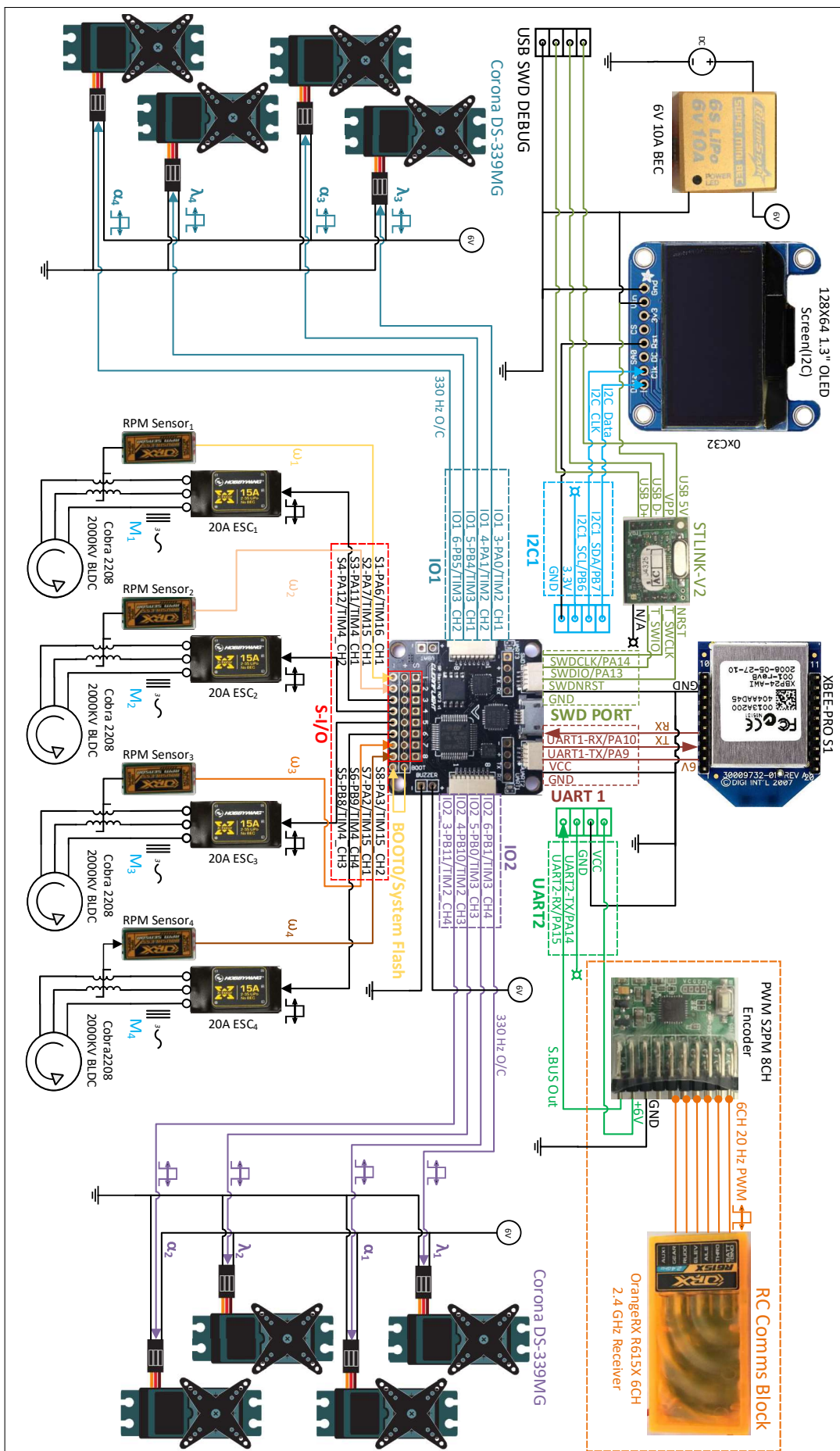
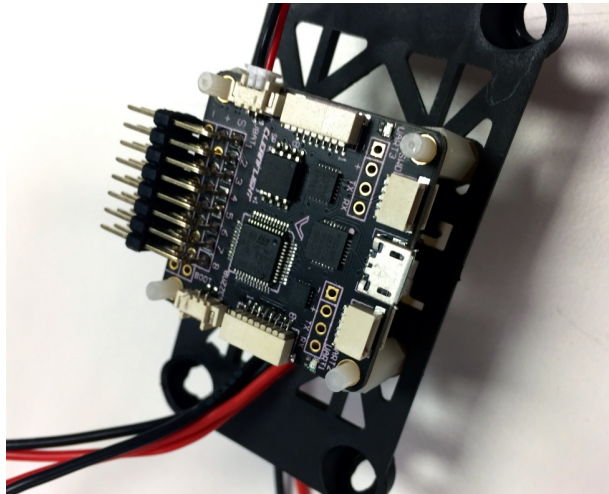
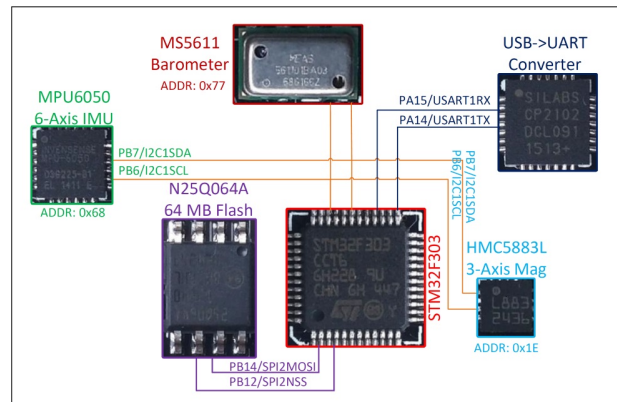


Figure 2.19: Hardware schematic diagram

An abstracted hardware diagram for the proposed (electronic) system layout is shown in Fig:2.19. It is an illustration for the connection of different electronic peripherals to aid the on-board control system. The structure of the implemented autopilot system and control loops are addressed later. This section aims to provide a brief overview of the specific modules intended for the flight controller, their purpose and a description of how they are interfaced. No control loops or code structures are discussed here.



(a) SPRacing F3 deluxe flight controller

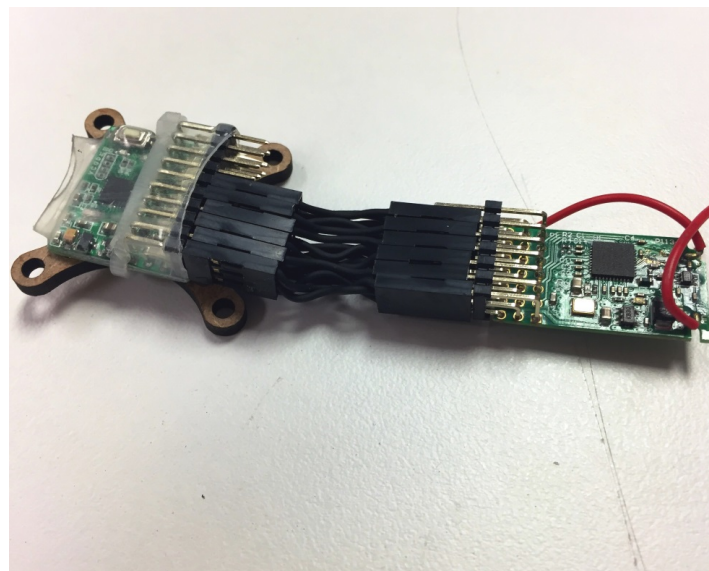


(b) F3 Deluxe on-board connections

Figure 2.20: SPRacing F3 deluxe layout

The embedded system is constructed around an ARM STM32F303 [127] based microcontroller. The micro-processor board is a commercial flight control board, specifically an SPRacing F3 Deluxe [32]. CleanFlight or BetaFlight opensource software (from [31] and [14] respectively) are typically used for this SPRacing F3 board, but despite using open-source software, its hardware specifications are however not openly available. The reverse engineered electrical schematic for the board is included in App:B.2 but a simplified overview of its internal connections is shown in Fig:2.20b.

The flight-controller has the following onboard peripherals; an I2C MPU-6050 6-axis gyroscope and accelerometer [61] with an I2C connected HMC5883 magnetometer compass [38], an I2C MS5611 barometer [125] and finally 64 Mb of SPI flash memory. Consideration of sensor fusion effects of the above state-estimators is discussed subsequently in Sec:6.9. The caveats of Kalman filtering and discretized effects on the simulation loop are similarly discussed in that particular section.

**Figure 2.21:** SBUS converter & 6CH receiver

Two separate wireless communication loops are to be used. Firstly, the system relays full state information for a complete 6-DOF XYZ position and an attitude autopilot system which is sent from an independent ground control station (*GCS*) using 2.4 [GHz] XBEE S1 module(s) [63] which is connected to the flight controller via USART. Full state-estimation, using a multi-camera system ([110]), and basic trajectory generation is performed on the GCS for the vehicle to track that trajectory.

Secondly, a partial trajectory (basic orientation) augmented pilot control input system, fail safe and secondary to the autopilot loop, is transmitted through a six channel 2.4 [GHz] radio frequency module. The secondary system allows for physical control without the need of a trajectory generation loop. The six CH received signals, otherwise permeated as six individual 20 [kHz] PWM signals via an OrangeRx R615x receiver [101], are encoded into a single proprietary S.BUS data stream (Fig:2.21).

The need for a serial bus (S.BUS) encoder, specifically using [56], comes about as a consequence of the introduction of the eight additional servos. As a result, there are no longer six free additional timer input/output channels which can be dedicated to input capture of those RC channels. Encoding the received data to a serial data line means the six CH commands can be processed with a single RX channel by the microcontroller. The encoder implements a USART derivative communications standard called S.BUS. Shown in Fig:2.22, the S.BUS data, captured with a logic analyzer [118], was used to ascertain the data stream's following parameters:

- 25 Bytes per packet
- 8-Bit byte length
- 1 Start byte 0x240
- 1 Byte of state flags
- 1 Stop byte 0x0
- Bytes are:
 - MSB First
 - 1 start & 2 stop bits
 - Even parity bit
 - Inverted
 - 100000 baud [$b.s^{-1}$]
- 22 total bytes of CH data
- Each channel's data is 11 bits long
- 16CH encoded
- Channel data is little Endian prioritized
- 14 [ms] idle time between packets
- Packets are arranged:

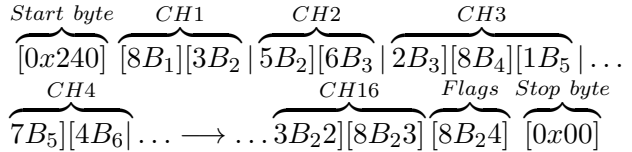


Figure 2.22: S.BUS data stream

The received information from the transmitted six channels should be smoothed with a digital filter, using an infinite impulse response moving average filter. A simple digital filter's difference equation could be implemented as follows:

$$y_n = \left(1 - \frac{1}{N}\right)y_{n-1} + \frac{1}{N}x_n \quad (2.36)$$

Moving over an average of $N = 5$ samples, each with a propagation delay of 14 [ms] due to S.BUS transmission, the filtered input channels will have a 70 [ms] zero order holding time. The signal's sampling delays are sufficiently faster than the transfer times so propagation delay ought not to be of consequence.

Similarly all the measured RPM signals measured by the OrangeRx RPM speed sensors should be filtered over five samples as well. Filtering for state estimation made without using the inertial-measurement unit (using the camera system) could be performed separately on the Ground Control Station computer.

Each of the eight digital servo actuators need to be controlled individually from 330 [Hz] center aligned PWM timer output compare channels (TIM2:CH1→CH4 and TIM3:CH1→CH4). Output pulses range from 1 – 2 [ms] to linearly control the rotational position. The servo's exact range and transfer function(s) is empirically determined next in Sec:2.4.1. The four 20 [A] brushless DC electronic speed controllers (*ESCs*) are each driven from a 20 [Hz] PWM output (TIM4:CH1→CH4), similarly with 1 – 2 [ms] input pulse widths.

There are a total of twelve PWM output compare signals to be drawn from the flight controller, eight for the servos and four for the *ESCs*. The servos are to be powered by a regulated 6 [V] DC 10 [A] power supply [55] whilst the *ESCs* switch unregulated 14.1 [V] DC supplied from an external power tether. The DC supply could be drawn from a battery bank, but that would adversely affect the weight of an already heavy platform.

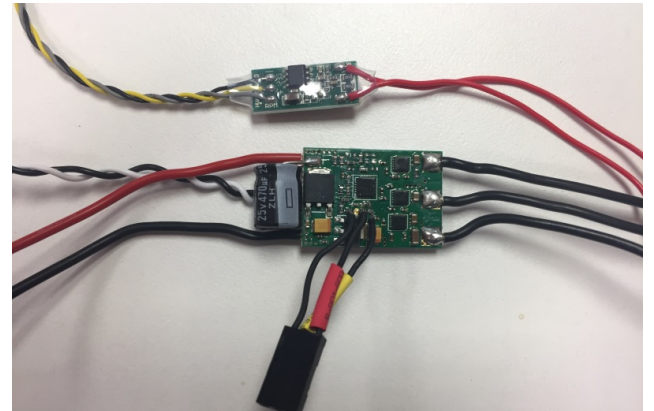
There is no integrated feedback for instantaneous RPM values available from the *ESCs*. Dedicated OrangeRX BLDC RPM sensors, [54], are used to measure each of the four motor's rotational speeds. Despite being termed *brushless DC motors*, the motors are actually 3-phase motors which, when used with an *ESC*, behave like closed-loop DC motors. The RPM sensors physically measure switching phases across two of the three motor phases, following that exact RPM can be ascertained. In general, the switching signal of a 3-Phase induction motor is shown by [84] to be proportional to the rotational velocity:

$$F_{rps} = \frac{2 \times F_{poles}}{\text{No. of rotor poles}} \quad [\text{Hz}] \quad (2.37)$$

The output signal generated by the OrangeRx RPM sensors changes the period of an output 50% duty cycle square wave, that wave frequency is directly proportional to the motor's pole switching frequency. The sensor output signal has a gain of 7 for the 14 pole BLDC Cobra motors. That gain is verified through the linear relationship physically measured using an optical rotation sensor, plotted in Fig:2.24. Knowing exact RPM rates means the subsequent thrust and aerodynamic torques for the control plant inputs can be calculated with greater certainty.



(a) XRotor 20A ESC connection guide [53]



(b) LDPower 20A ESC with RPM sensor

Figure 2.23: BLDC electronic speed controllers

The *ESCs*, although LDPower 20A devices, are re-flashed with BLHeli firmware [15]. The LDPower *ESCs* (Fig:2.23b) match Hobbywing Xrotor 20A ones (Fig:2.23a), which both use SiLabs F396 microcontrollers so the same firmware can be flashed onto both MCUs. Custom BLHeli software provides greater refinement over configurations like the deflection range of inputs, but default values were used for subsequent tests. The plot in Fig:2.24a shows the rotation per second, or otherwise frequency in Hz, speed curve for an unloaded motor, similarly Fig:2.24b shows the speed curve when loaded for a 6 × 4.5 prop.

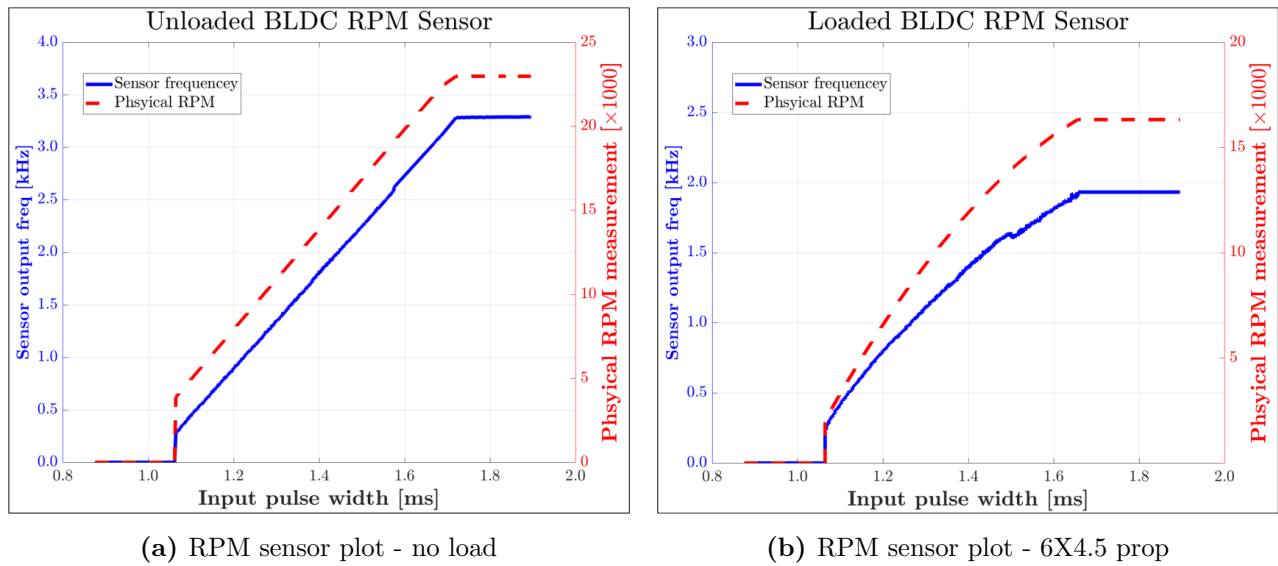


Figure 2.24: RPM sensor calibration plots

The loaded speed plot for a BLDC motor with an attached prop in Fig:2.24b is slightly quadratic. The response is due to second order aerodynamic drag, quadratic with respect to the propeller's rotational speed (expanded on in Sec:3.2.1). Moreover, when the motor is torque loaded by the propeller, the ESC current limits rotational speeds at just over 16×10^3 [RPM]. Timer channels are to be used to measure the varying frequency output from the RPM sensors. General purpose Timers 15 (TIM15:CH1→CH2), 16 (TIM16:CH1) and 17 (TIM17:CH1) should be configured to capture the input PWM signal generated by the speed sensors. Included on the I2C communication line is an I2C O-LED display for debugging and status update purposes.

Any STM32 microcontroller is programmed through a dedicated debugging device. The ST-Link V2 [126] is the current proprietary device which, itself, is a specially programmed STM32F10 chip. The chip connects to the dedicated **Serial Wire Debugging** ports of the target STM (*SWD-CLK*, *SWD-IO* & *SWD-NRST*) and is interfaced via regular USBD+ and USBD- data lines.

2.4.1 Actuator Transfer Functions

Servo Transfer Functions

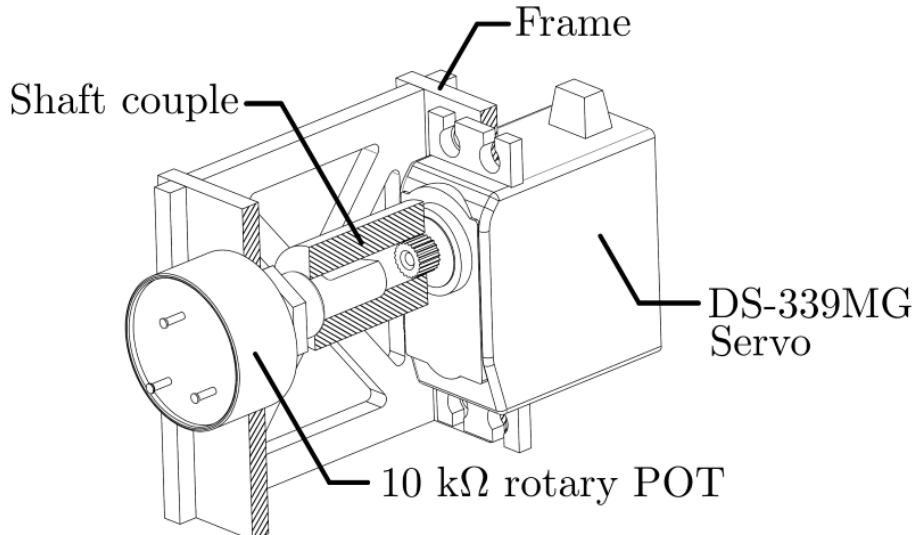


Figure 2.25: Servo transfer function test rig

The range and step transfer functions for an unloaded servo were evaluated with the test rig, illustrated in Fig:2.25. The servo's output shaft was mechanically coupled to a rotatory potentiometer which was sampled to measure the shaft's rotational position. Full scale deflection for the digital servos used are in fact greater than their quoted 180° range, each having an input range of around 230° , plotted in Fig:2.26a. The prototype control loop commands each servo position in open loop, the major loop controller gains designed later in Sec:6.2 are expected to account for such minor loop actuator dynamics. However, the simulation must first accurately represent the servo's transfer characteristics for such an assumption to hold true.

Considering the servo's hard limit of 180° was a design imposed constraint, one point of contention is the effect such a restriction has on the feasible operating trajectories. The control algorithms derived in Ch:4 are first tested with an ideal, continuous rotation servo limited only by the rate and transfer characteristics. Following that, the servo's rotational limitations imposed on the system and the constraints to feasibly achievable trajectories are discussed in Sec:6.8.

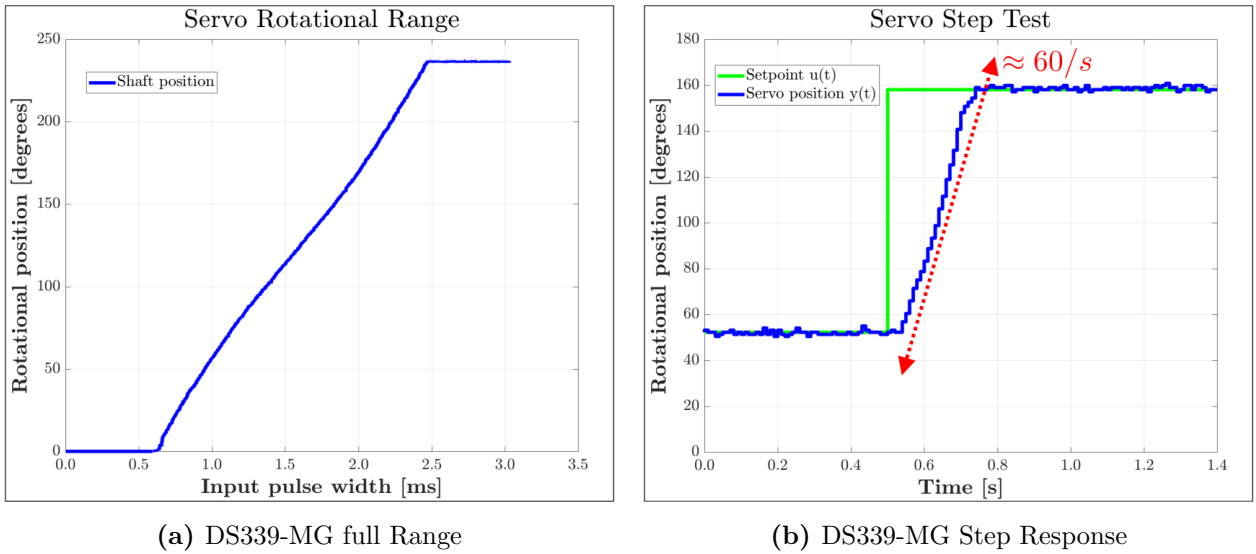


Figure 2.26: Unloaded servo transfer characteristics

For the servo whose particular rotational range and step response is shown in Fig:2.26, the relationship between the input pulse-width x in [m.s] and the rotational output position y in $^\circ$ is governed by the non-linear saturating hybrid system:

$$y(x) = \begin{cases} 0^\circ & x < 0.65 \text{ [ms]} \\ 129.12x - 82.64 & 0.64 \text{ [ms]} \leq x \leq 2.46 \text{ [ms]} \\ 230^\circ & x > 2.46 \text{ [ms]} \end{cases} \quad (2.38)$$

In practice, Eq:2.38 is altered such that a 0° offset is taken at around 50% input, making its operational range $\pm 90^\circ$. Each servo is mechanically rate limited to $60^\circ/0.15\text{s}$ or 400 degrees per second with a dead time of $t_d \approx 1.2$ [ms] and a negligible mechanical deadband of 4 μs . That rate limit begins to manifest itself for large step sizes, shown in Fig:2.26b. Each servo has an approximate *critically damped* second order transfer function, determined from Fig:2.26b:

$$G(s)_{servo} = e^{-t_{ds}} \frac{w_n^2}{s^2 + 2\zeta w_n s + w_n^2} \quad (2.39a)$$

$$= \frac{e^{-0.012s}(14.869)^2}{s^2 + 2(1)(14.869)s + (14.869)^2} \quad (2.39b)$$

with input saturation limits for the PWM input magnitude $|U(s)|$ in [ms]:

$$Y(s)_{servo} = \begin{cases} 0^\circ & |U(s)| < 0.65 \\ G(s) & 0.65 \leq |U(s)| \leq 2.46 \\ 230^\circ & |U(s)| > 2.46 \end{cases} \quad (2.39c)$$

The net second order, critically damped transfer block for a servo is shown in Fig:2.27, including saturating nonlinearities, but neglecting the afore-mentioned mechanical deadband.

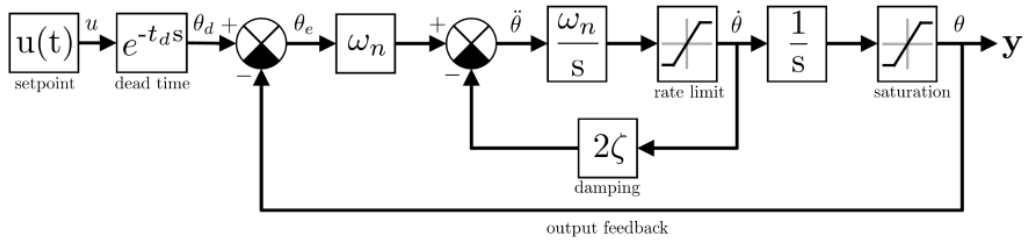
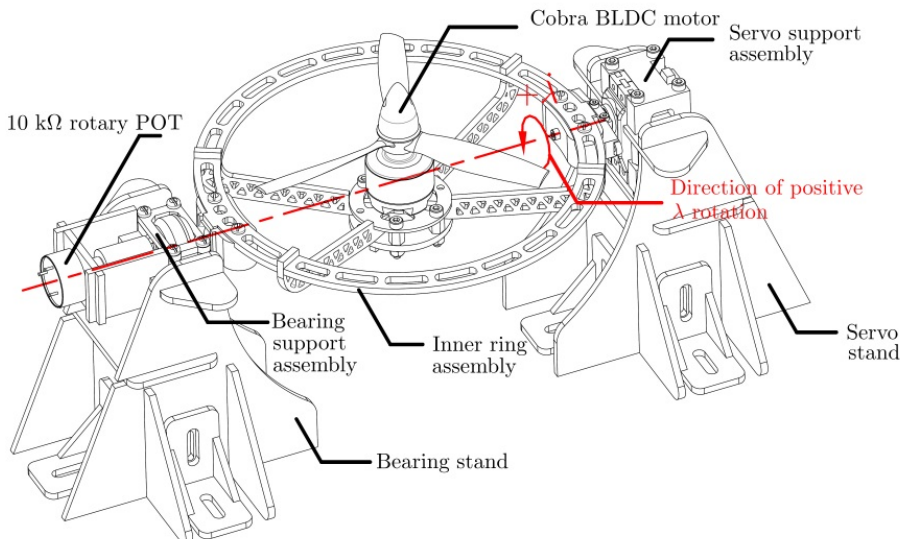
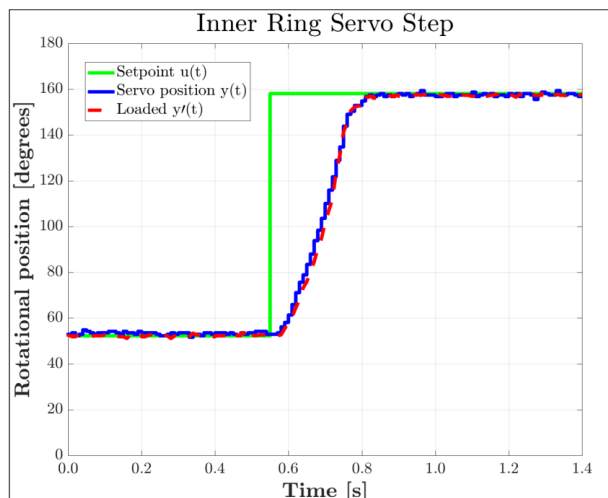


Figure 2.27: Servo block diagram

The plot in Fig:2.26b shows the step response, at the *shaft output*, of an unloaded servo. The servo's transfer characteristics when rotating the inner ring assembly (illustrated in Fig:2.12) are determined from the test rig in Fig:2.28a. Fig:2.28b shows the inner ring servo's step response $y(t)$, which is unchanged from Eq:2.39 and still hits the mechanical rate limit. It then follows that for the inner ring's transfer function $G(s)_{inner} = G(s)_{servo}$. Even when actuating a loaded inner ring assembly with a propeller rotational velocity of $\Omega_i = 6000$ RPM, plotted $y'(t)$, the transfer characteristics are the same in spite of a further increased load on the assembly due to the induced gyroscopic response, Eq:2.19.



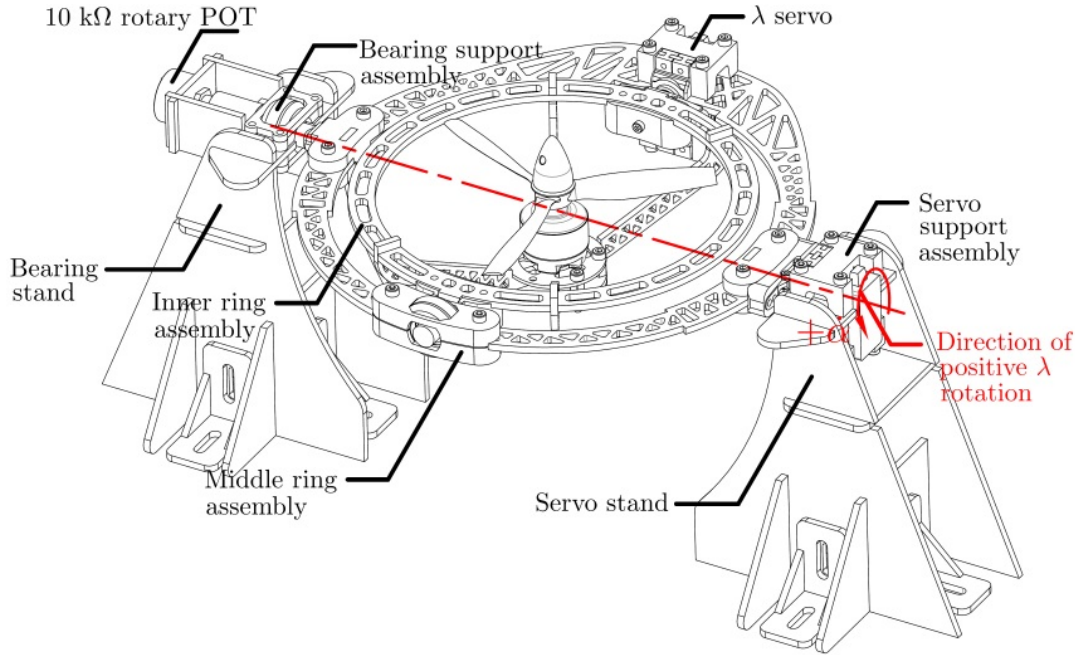
(a) Inner ring servo rig



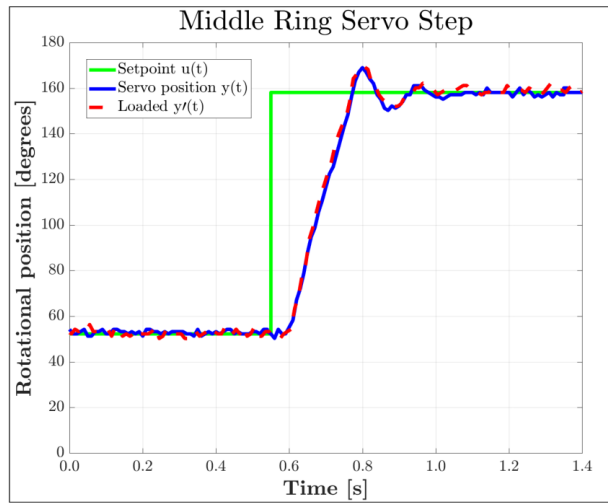
(b) Servo response plot

Figure 2.28: Inner ring servo characteristics

Fig:2.29b plots the step response for the servo actuating the middle ring assembly. Whilst its transients remain the same, oscillations are introduced at the settling point which demonstrates a second order under-damped plant. Those oscillations are as a result of the larger rotational inertia (Eq:2.24) and flexure within the frame structure. It is important to specify that the oscillations are not at the servo's output shaft, the rotational position was measured with respect to the bearing supported shaft, coaxial to the servos (Fig:2.29a). A separate, under-damped transfer function is used for the middle ring's response, the rotational position α_i of the frame is to be used for thrust vectoring calculations in Eq:2.17. Those harmonics are still present under load, plotted in $y'(t)$, despite the frame being tensioned by the thrust.



(a) Middle ring servo test rig



(b) Servo response plot

Figure 2.29: Middle ring servo characteristics

The mechanical structure could indeed be strengthened to reduce the oscillations present in Fig:2.29a. Strengthening the frame would, however, increase the mass of an already weight constrained system. Instead the under-damped transfer function is incorporated into the plant, that transfer function is:

$$G(s)_{middle} = \frac{e^{-0.012s}(12.591)^2}{s^2 + 2(0.454)(12.591)s + (12.591)^2} \quad (2.40)$$

BLDC Transfer Functions

Each Cobra 2208 BLDC motor, when loaded with a 6×4.5 propeller, has a quadratic speed curve (plotted in Fig:2.31a). This is as a result of the propeller's opposing aerodynamic drag, *approximately* proportional to the square of the propeller's angular velocity. Propeller aerodynamics are expanded on further in Sec:3.2.1.

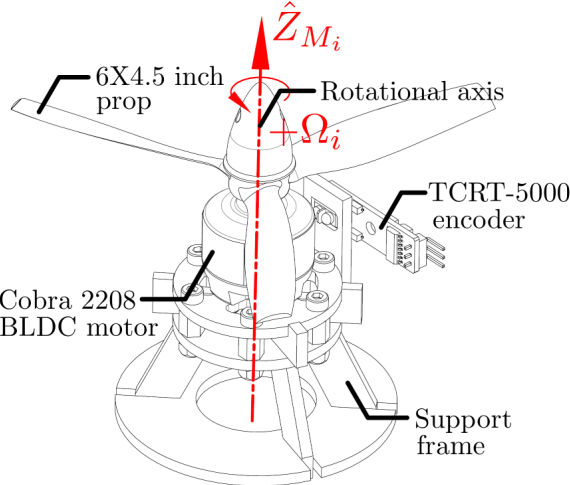


Figure 2.30: BLDC RPM speed calibration and transfer function rig

Using the BLHeli interface, the input range for the motor's speed controllers can be adjusted, but for the purposes of this project were left unchanged. That relationship between input pulse-widths x in [ms] applied to the ESC and output sensor signal y in [RPM] is given by the hybrid state equations for input range limits:

$$y(x) = \begin{cases} 0 \text{ [RPM]} & x < 1.065 \text{ [ms]} \\ -20593x^2 + 80187x - 60004 & 1.065 \text{ [ms]} \leq x \leq 1.655 \text{ [ms]} \\ 16300 \text{ [RPM]} & x > 1.655 \text{ [ms]} \end{cases} \quad (2.41)$$

The upper limit in Eq:2.41 and the motor's step response are both governed by the ESC's maximum current limit; in this case 20 [A]. Artificially imposing 10 [A] current limit, a potential consequence of using lower power ESCs, is plotted $c(t)$ in Fig:2.31b. The current limit significantly restricts the motor's transient and steady-state performance.

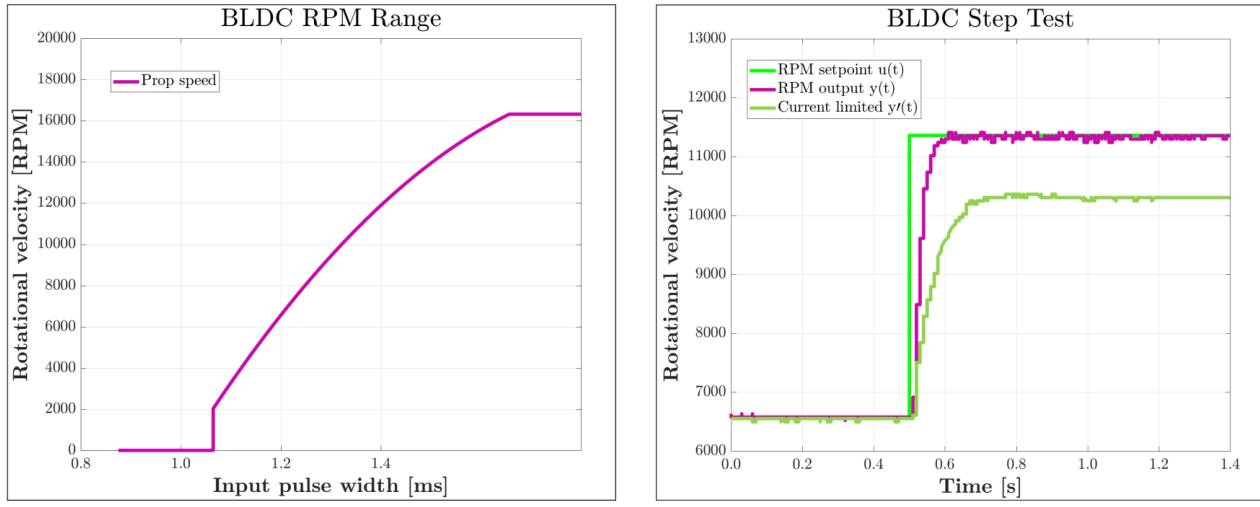


Figure 2.31: BLDC motor characteristics

The motor's step response, $\mathbf{y}(\mathbf{t})$, has a negligible dead time and second order dynamics, with a transient time constant far faster than the servo's plant. The motor's transfer function for speed in [RPM] is:

$$G_{BLDC}(s) = \frac{1}{(1 + 1.7583s \times 10^{-3})(1 + 1.7494s \times 10^{-3})} \quad (2.42a)$$

and saturating input limits on $|U(s)|$ for the PWM input magnitude in [ms]:

$$Y_{BLDC}(s) = \begin{cases} 0 & |U(s)| < 1.065 \\ G(s) & 1.065 \leq |U(s)| \leq 1.655 \\ 16300 & |U(s)| > 1.655 \end{cases} \quad (2.42b)$$

Combined Actuator Transfer

The net transfer characteristics for a complete motor module then combines Eq:2.39 for the inner ring step in λ_i , Eq:2.40 for changes in the middle ring α_i and finally Eq:2.42 for changes in the propeller's rotational speed Ω_i . A single module's transfer function is then bundled in the transfer block $C(s)$:

$$\vec{u}_i \triangleq \begin{bmatrix} \Omega_i(s) \\ \lambda_i(s) \\ \alpha_i(s) \end{bmatrix} = \begin{bmatrix} B(s)_{BLDC} \\ N(s)_{inner} \\ M(s)_{middle} \end{bmatrix} = C(s) \quad (2.43a)$$

Furthermore, the actuator space for the i^{th} motor module $\vec{u}_i \in \mathbb{U}$ is limited by input saturation conditions, where the inputs are *not* in pulse width magnitudes:

$$\mathbb{U}_i \triangleq \begin{bmatrix} 0 & : & 16300 \\ -90^\circ & : & +90^\circ \\ -90^\circ & : & +90^\circ \end{bmatrix} \quad (2.43b)$$

where \mathbb{U}_i is then extended to $\in \mathbb{R}^{12}$ for the entire actuator set. Later, instantaneous actuator positions are used to calculate response dynamics, in which case a commanded $\vec{u}_c \in \mathbb{U}$ is applied, subject to the transfer functions and saturations of Eq:2.43. In the case of control design and feedback compensation, *error free* actuator estimates \hat{u}_c are used, which represent sampled actuator states. A commanded actuator position \vec{u}_c is the instantaneously set actuator value as per some control function but in practice there is an actuator transfer error:

$$\hat{u}_e = \vec{u}_c - \hat{u}_c \quad (2.44)$$

which could lead to plant errors in inertia calculations dependent on those actuator positions, Sec:2.3. Estimates for instantaneous inertial positions \hat{u}_c are further used for dynamic calculations, not the commanded actuator positions \vec{u}_c . Moreover, the actuation error as a result of the minor loop transfer functions produce a deviation in expected actuation effort, those being force and torque inputs. A robust controller with a well designed gain ought to account for those deviations and retain stability.

Chapter 3

Kinematics and Dynamics

The following generally applicable rigid body dynamics are first developed with respect to generalized net forces and torques acting on a rigid vehicle. Following that, dynamics are extended to the nonlinear multibody case wherein constrained relative rotational actuation between interconnected bodies is incorporated, representing the actuator action which the prototype can undergo. Propeller aerodynamic effects are subsequently included into the actuation input model. Finally a consolidated quaternion-based model is presented which is used for the controller development next in Ch:4.

3.1 Rigid Body Dynamics

3.1.1 Lagrange Derivation

Fundamentally any body, rigid or otherwise, can undergo two kinds of motion; namely rotational and translational movement. Often a Lagrangian approach for combined angular and translational movements is used to derive the differential equations of motion for each degree of freedom, [130]. The Lagrangian principle ensures that (translational and rotational) energies are conserved throughout the system's state progression. When combined with Euler-Rotation equations, the Euler-Lagrangian formulation from [132] fully defines the aerospace 6-DOF equations of motion.

Lagrangian formulation is regarded as especially useful in non-Cartesian (*spherical etc...*) coordinate frames and with multibody systems. With that being said, Cartesian coordinates were already defined in Sec:2.2.2 for the plant. Alternatively, relative coordinates could be used for implicit Euler-based dynamics as in [97]. Rigid body dynamics in Cartesian coordinates do lend themselves to Newtonian mechanics. Both Newton-Euler and Euler-Lagrange formulations produce the same resultant differential equations of motion, but follow conceptually different derivations. The Lagrangian operator \mathcal{L} is a scalar term defined as the difference between a trajectory's kinetic and potential energies, T and U respectively. Considering some generalized path trajectory $\vec{r}(t)$ for a body, with both position $\vec{\xi}$ and attitude \vec{H} states:

$$\vec{r}(t) \triangleq \begin{bmatrix} \vec{\xi} & \vec{H} \end{bmatrix}^T \in \mathcal{F}^a \quad (3.1)$$

Coordinates in Eq:3.1 are *generalized* and taken with respect to some hypothetical shared frame \mathcal{F}^a . The generalized coordinates are later refined to Cartesian body coordinates with respect to the inertial frame. The Lagrangian is the difference of the trajectory's kinetic and potential energies, by definition:

$$\mathcal{L}(\vec{r}, \dot{\vec{r}}, t) \triangleq T(\vec{r}, \dot{\vec{r}}) - U(\vec{r}, \dot{\vec{r}}) \quad (3.2a)$$

where the trajectory's kinetic and potential energy functions are T and U respectively, introducing a rigid body's general (translational and rotational) kinetic and potential energies, both defined with respect to that shared reference frame \mathcal{F}^a .

Noting first that there is no attitude contribution for stored potential energy, so $U(\vec{r}, \dot{\vec{r}})$ consists entirely of gravitational potential energy. The gravitational acceleration vector in the inertial frame \mathcal{F}^I is:

$$\vec{G}_I = [0 \ 0 \ -9.81]^T \quad [\text{m.s}^{-2}], \in \mathcal{F}^I \quad (3.2b)$$

where \vec{G}_I acts in the negative \hat{Z}_I , downward, direction. Substituting translational kinetic and potential energies into the Lagrangian yields the following scalar term:

$$\mathcal{L}(\vec{r}, \dot{\vec{r}}, t) = \frac{1}{2} \dot{\xi}^T (m_b) \dot{\xi} + \frac{1}{2} \dot{H}^T (J_b) \dot{H} - m_b \vec{G}_a (h \cdot \hat{Z}_I) \quad (3.2c)$$

The vehicle's mass is m_b and its generalized inertia matrix is similarly J_b , aligned and translated with respect to the common frame \mathcal{F}^a . The Euler-Lagrange formulation equates partial derivatives of the Lagrangian to any generalized forces \vec{R} acting on the system in frame a . In the rigid body motion case those *generalized forces* are net forces \vec{F}_μ and net torques $\vec{\tau}_\mu$ in the shared frame $\in \mathcal{F}^a$.

$$\frac{d}{dt} \left(\frac{\partial \mathcal{L}}{\partial \dot{\vec{r}}} \right) - \frac{\partial \mathcal{L}}{\partial \vec{r}} = \vec{R} = \begin{bmatrix} \vec{F}_\mu \\ \vec{\tau}_\mu \end{bmatrix} \quad \in \mathcal{F}^a \quad (3.3)$$

Evaluating symbolic partial derivatives of Eq:3.2c with respect to the path coordinates $\vec{r}(t)$ and path rates $\dot{\vec{r}}(t)$ respectively produces the two following equations:

$$\frac{\partial \mathcal{L}}{\partial \vec{r}} = \begin{bmatrix} m_b \vec{G}_a \\ 0 \end{bmatrix} \quad \in \mathcal{F}^a \quad (3.4a)$$

$$\frac{d}{dt} \left(\frac{\partial \mathcal{L}}{\partial \dot{\vec{r}}} \right) = \left[\frac{d}{dt} m_b \dot{\xi} \quad \frac{d}{dt} J_b \dot{H} \right]^T \quad \in \mathcal{F}^a \quad (3.4b)$$

where \vec{G}_a in the above is the gravitation force transformed to the common frame \mathcal{F}^a which $\mathcal{L}(\vec{r}, \dot{\vec{r}})$ is defined with respect to. The body mass m_b and inertia J_b could potentially have some non-zero time derivative, but for now are regarded as constants. Time varying inertias are later defined in Sec:2.3 and introduced to the dynamics subsequently in Sec:3.4.1. Here only the general rigid body case is considered. Any vector in some non-Newtonian rotating reference frame \mathcal{F}^a has a time derivative, relative to another frame \mathcal{F}^b with an angular velocity $\vec{\omega}_{a/b}$, as per Rotating Reference Frame or Reynolds Transportation Theorems [49]:

$$\frac{df_b}{dt_a} = \frac{df_b}{dt_b} + \vec{\omega}_{a/b} \times \vec{f}_b \quad \in \mathcal{F}^b \quad (3.5)$$

Applying Eq:3.5 to those partial derivatives in Eq:3.4b and further defining the generalized coordinates $[\dot{\xi}, \dot{H}]^T$ as 6-DOF Cartesian body coordinates with respect to the inertial frame \mathcal{F}^I or the body frame \mathcal{F}^b described in Sec:2.2.

The angular orientations \vec{H} are with respect to a *common frame* \mathcal{F}^a , unlike Euler angles $\vec{\eta} \in \mathcal{F}^{v2,v1,I}$. Recalling the definition of an attitude in a shared frame $\vec{\eta}_b$ from Eq:2.12e, where $\vec{\omega}_b \equiv \dot{\vec{\eta}}_b$ and $\vec{\eta}_b \in \mathcal{F}^b$, the trajectory's definition for \vec{r} is refined:

$$\vec{r}(t) = \begin{bmatrix} \vec{\xi} & \vec{H} \end{bmatrix}^T \triangleq \begin{bmatrix} \vec{\mathcal{E}}_b \\ \vec{\eta}_b \end{bmatrix} \quad \in \mathcal{F}^b \quad (3.6a)$$

Note that the position $\vec{\mathcal{E}}_b$ in Eq:3.6a is the position in the *body frame*, unlike $\vec{\mathcal{E}}_I \in \mathcal{F}^I$ from Eq:2.2. The path rate $\dot{\vec{r}}(t)$ is defined as:

$$\dot{\vec{r}}(t) = \begin{bmatrix} \dot{\xi} & \dot{H} \end{bmatrix}^T \triangleq \frac{d}{dt} \begin{bmatrix} \vec{\mathcal{E}}_b \\ \vec{\eta}_b \end{bmatrix} \equiv \begin{bmatrix} \vec{v}_b \\ \vec{\omega}_b \end{bmatrix} \quad \in \mathcal{F}^b \quad (3.6b)$$

Substituting those changed path coordinates from Eq:3.6 into the Lagrangian Eq:3.2c yields a familiar Lagrangian scalar for a vehicle's energies for \mathcal{F}^b relative to \mathcal{F}^I :

$$\mathcal{L} = \frac{1}{2} \vec{v}_b^T (m_b) \vec{v}_b + \frac{1}{2} \vec{\omega}_b^T (J_b) \vec{\omega}_b - m_b \vec{G}_b z_I \quad (3.7)$$

where \vec{G}_b is the gravitational force vector from Eq:3.2b transformed to \mathcal{F}^b and z_I is the vertical height of the vehicle *in the inertial frame*. The time derivative of the substituted path coordinates in the partial derivative Eq:3.4b is then:

$$\frac{d}{dt} \left(\frac{\partial \mathcal{L}}{\partial \dot{\vec{r}}} \right) = \begin{bmatrix} m_b \frac{d}{dt} \vec{v}_b & J_b \frac{d}{dt} \vec{\omega}_b \end{bmatrix}^T \quad (3.8a)$$

With respective time derivatives of body frame vectors relative to the inertial frame, using the Reynolds transportation theorem:

$$m_b \frac{d}{dt} \vec{v}_b = m_b \dot{\vec{v}}_b + \vec{\omega}_{b/I} \times m_b \vec{v}_b \quad \in \mathcal{F}^b \quad (3.8b)$$

$$J_b \frac{d}{dt} \vec{\omega}_b = J_b \dot{\vec{\omega}}_b + \vec{\omega}_{b/I} \times J_b \vec{\omega}_b \quad \in \mathcal{F}^b \quad (3.8c)$$

which, when substituted back into the Euler-Lagrange formulation in Eq:3.3, yields familiar Newton-Euler rigid body differential equations of translational and rotational motion for generalized net force and torque inputs; \vec{F}_μ and $\vec{\tau}_\mu$ respectively.

$$\begin{bmatrix} m_b \dot{\vec{v}}_b + \vec{\omega}_{b/I} \times m_b \vec{v}_b \\ J_b \dot{\vec{\omega}}_b + \vec{\omega}_{b/I} \times J_b \vec{\omega}_b \end{bmatrix} - \begin{bmatrix} m_b \vec{G}_b \\ 0 \end{bmatrix} = \vec{\mathbf{R}} = \begin{bmatrix} \vec{F}_\mu \\ \vec{\tau}_\mu \end{bmatrix} \quad \in \mathcal{F}^b \quad (3.9a)$$

$$\therefore \vec{F}_\mu = m_b \dot{\vec{v}}_b + \vec{\omega}_b \times m_b \vec{v}_b - m_b R_I^b(-\eta) \vec{G}_I \quad (3.9b)$$

$$\therefore \vec{\tau}_\mu = J_b \dot{\vec{\omega}}_b + \vec{\omega}_b \times J_b \vec{\omega}_b \quad (3.9c)$$

It is important to stress that $\vec{\eta}_b \neq \vec{\eta}$ because each Euler Angle is defined in sequentially rotated reference frames $\in \mathcal{F}^{v2,v1,I}$. Four separate equations are then needed to completely describe a body's position and attitude states:

$$\dot{\vec{\mathcal{E}}}_I = R_b^I(-\eta) \vec{v}_b \quad \in \mathcal{F}^I \quad (3.10a)$$

$$\vec{F}_\mu = m_b \dot{\vec{v}}_b + \vec{\omega}_b \times m_b \vec{v}_b - m_b \vec{G}_b \quad \in \mathcal{F}^b \quad (3.10b)$$

$$\dot{\vec{\eta}} = \Phi(\eta) \vec{\omega}_b \quad \in \mathcal{F}^{v2,v1,I} \quad (3.10c)$$

$$\vec{\tau}_\mu = J_b \dot{\vec{\omega}}_b + \vec{\omega}_b \times J_b \vec{\omega}_b \quad \in \mathcal{F}^b \quad (3.10d)$$

where $\Phi(\eta)$ is the Euler matrix which relates Euler rates $\dot{\vec{\eta}}$ and angular velocity $\vec{\omega}_b$, defined previously in Eq:2.12f. State differentials from Eq:3.10 can be simplified to a pair of equations defined entirely in the reference frames of the variables which they represent. The nonlinear form of those equations substitutes $d\vec{\eta}/dt = \Phi(\eta) \vec{\omega}_b$ into the Lagrangian derivative in Eq:3.4b.

$$\frac{d}{dt} \left(\frac{\delta \mathcal{L}}{\delta \dot{\vec{r}}} \right) = \begin{bmatrix} m_b \frac{d}{dt} \vec{v}_b & J_b \frac{d}{dt} \dot{\vec{\eta}}_b \end{bmatrix}^T \Rightarrow \begin{bmatrix} m_b \frac{d}{dt} \vec{v}_b & J_b \frac{d}{dt} \Phi(\eta) \vec{\omega}_b \end{bmatrix}^T \quad (3.11)$$

which only affects the angular component because the two kinetic energies are independent of one another. Applying the differential chain rule to the angular component of Eq:3.11 yields:

$$J_b \frac{d}{dt} \Phi(\eta) \vec{\omega}_b = J_b (\dot{\Phi}(\eta) \vec{\omega}_b + \Phi(\eta) \dot{\vec{\omega}}_b) \quad (3.12)$$

Drawing from [97] and recognizing that J_b must be transformed to the shared intermediate Euler axes, $J \triangleq \Psi(\eta)^T J_b \Psi(\eta)$. The state differential for the Euler angle acceleration counterpart of Eq:3.9c, defined in intermediate (non-inertial) Euler frames for each respective Euler angle, then becomes:

$$M(\eta) \ddot{\vec{\eta}} + C(\eta, \dot{\eta}) \dot{\vec{\eta}} = \Psi(\eta) \vec{\tau}_\mu \quad \in \mathcal{F}^{v2,v1,I} \quad (3.13a)$$

$$M(\eta) = \Psi(\eta)^T J_b \Psi(\eta) \quad (3.13b)$$

$$C(\eta, \dot{\eta}) = -\Psi(\eta) J_b \dot{\Psi}(\eta) + \Psi(\eta)^T [\Psi(\eta) \dot{\vec{\eta}}] \times J_b \Psi(\eta) \quad (3.13c)$$

The relationship $\dot{\Psi} \equiv \Psi\dot{\Phi}\Psi$ was used to simplify Eq:3.13, the singularity present in Φ remains. The equation in Eq:3.13a completely describes the state derivative $\ddot{\vec{\eta}}$ in its own reference frame(s) $\in \mathcal{F}^{v^2, v^1, I}$. The two differential equations which fully describe the entire body's 6-DOF motion are:

$$\vec{F}_\mu = m_b \dot{\vec{\mathcal{E}}}_I + R_b^I(-\eta) \vec{\omega}_b \times m_b \dot{\vec{\mathcal{E}}}_I - m_b \vec{G}_I \quad \in \mathcal{F}^I \quad (3.14a)$$

$$\vec{\tau}_\mu = \Psi(\eta)^{-1} M(\eta) \ddot{\vec{\eta}} + \Psi(\eta)^{-1} C(\eta, \dot{\eta}) \quad \in \mathcal{F}^{v^2, v^1, I} \quad (3.14b)$$

In most cases the body frame counterparts in Eq:3.10 are used rather than Eq:3.14 when describing states. Eq:3.14 is superfluous when considering that inputs \vec{F}_μ and $\vec{\tau}_\mu$ both act in the body frame \mathcal{F}^b . Irrespective of the differential equation used, some singular transformation will still be performed by either $\Psi(\eta)$ from Eq:2.12g or $\Phi(\eta)$ from Eq:2.12i.

The generalized input forces and torques \vec{F}_μ and $\vec{\tau}_\mu$ respectively are produced by the system's controllable inputs but could include any external disturbances acting on the body. Those control inputs are directly affected by the vehicle's actuators. How actuator action produces the control inputs depends on the actuator's associated *effectiveness* function. In the general case, which is expanded in Sec:3.2, the control inputs for a regular quadrotor (Fig:3.1) are as follows:

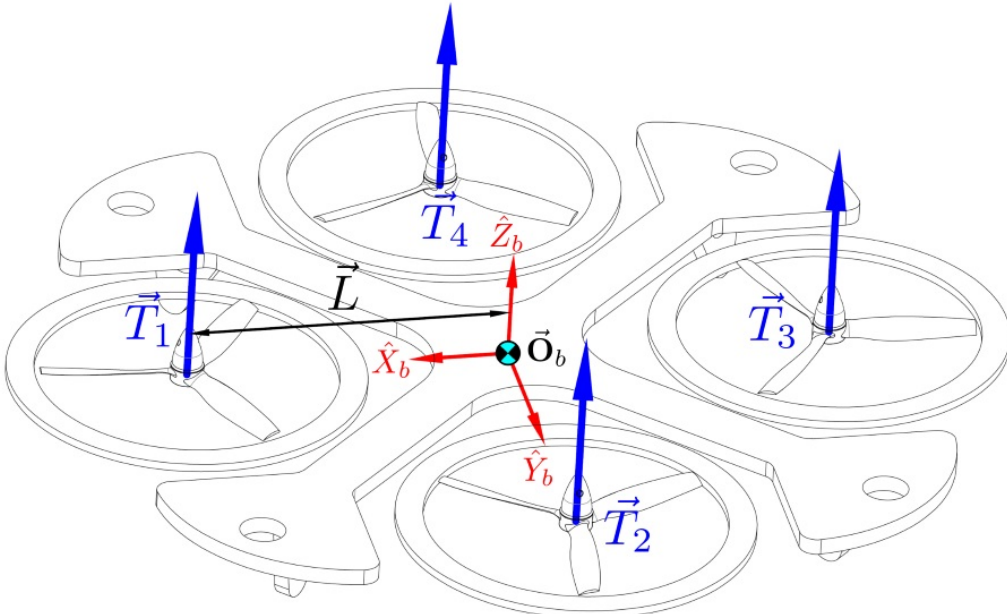


Figure 3.1: Generalized quadrotor net forces and torques

Typically \vec{F}_μ is the net heave force acting on the center of motion \vec{O}_b . The net heave is the sum of all thrust forces produced by rotating propellers, as some function of those rotational speeds, $\vec{T}(\Omega_i)$.

$$\vec{F}_\mu = \sum_{i=1}^4 \vec{T}(\Omega_i) \cdot \hat{Z}_b \quad \in \mathcal{F}^b \quad (3.15a)$$

Similarly net torque $\vec{\tau}_\mu$ is the sum of all *differential* torques produced from opposing propeller thrust vectors. Each torque arm $\vec{L}_{[1:4]}$ is the thrust's orthogonal displacement relative to the origin of *motion*.

$$\vec{\tau}_\mu = \sum_{i=1}^4 \vec{L}_i \times \vec{T}(\Omega_i) \cdot \hat{Z}_b \quad \in \mathcal{F}^b \quad (3.15b)$$

In Eq:3.15, the thrust vector $\vec{T}(\Omega_i)$ is a function of the i^{th} motor's rotational velocity Ω_i , fixed in the \hat{Z}_b direction. Each thrust vector could potentially be $\in \mathbb{R}^3$ such as the redirected vector from Eq:2.17. All of the above equations are still applicable to any 6-DOF body but common simplifications applied to the system for quadrotor control are explored in App:A.1. Aerodynamic components pertinent for thrust and torque generation relative to Eq:3.15 are now introduced and obviously the contextual focus is on quadrotor with dual-tilting axis actuators.

3.2 Aerodynamics

Aerodynamic effects detailed here and subsequent nonlinear multibody responses in Sec:3.4 both affect the generalized forces and torques acting on the body. The relationship between a propeller's rotational speed Ω_i , in revolutions per second or [RPS], and its perpendicular thrust vector $\vec{T}(\Omega_i)$ is more complicated than the quadratic simplification taken at static conditions which some papers assume (e.g [109] etc...). Produced thrust is mostly dependent on the incident air stream flowing through the propeller's rotational plane, typically being the body velocity's component normal to that propeller's plane. Fluid flowing *tangentially* across the propeller's plane contributes toward in-plane aerodynamic drag and hence torque.

The combination of aerodynamic blade-element [102, 114] and fluid-dynamics momentum or *disc actuator* theories equate an integral term generated across the propeller's length with the produced thrust or torque. A schedule of all aerodynamic effects encountered by a quadrotor's propellers is thoroughly detailed in both [8] and [7]. The following is a review of pertinent aerodynamic theories. Vortex ring state and parasitic drag effects are omitted as they will be approximately negligible given the aircraft's proposed flight envelope with low translational velocities.

3.2.1 Propeller Torque and Thrust

A possible situation which the prototype could encounter is where an upstream propeller provides the incident fluid flow to another downstream propeller. Such a situation presents a complicated fluid dynamics and vortex wake effect problem. Propeller overlapping effects are discussed in [129] but remain open to further research in the context of the aircraft considered here.

To expedite the system identification process some simplifications are made on the aerodynamics to construct an approximate model, specifically using coefficients in place of complete local chord and pitch based integrals. Such an assumption holds true given that twisted, fixed pitch propellers are used (Fig:3.2a) and not variable pitch swash-plate actuated propellers (Fig:3.2b).

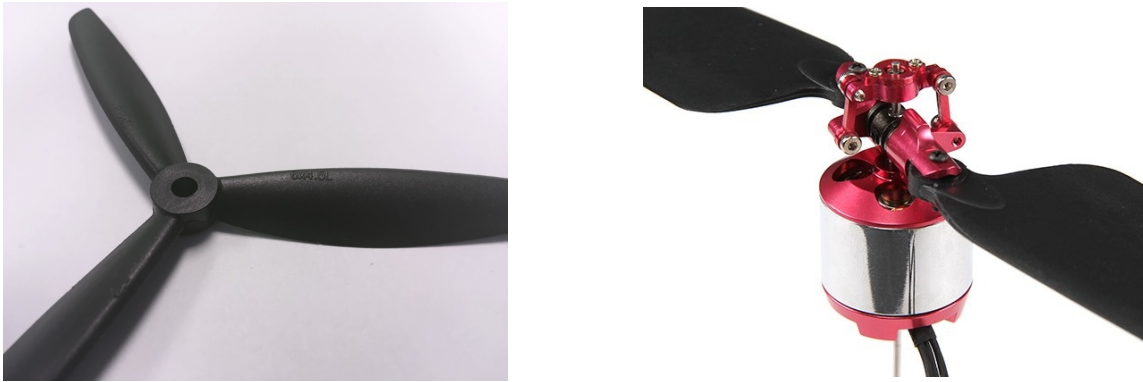


Figure 3.2: Propeller types

A propeller's profile applies a perpendicular scalar thrust force T onto the fluid in which it rotates. To build the following theoretical explanation propellers are first considered in terms of momentum theory and only perpendicular fluid flow through the propeller's plane is regarded. That fluid stream (Fig:3.3) has an incident upstream velocity v_∞ and a resultant slip velocity v_s downstream relative to the rotational plane. The change of fluid flow as a result of the propeller's rotation can be given as:

$$v_s = \Delta v + v_\infty \quad (3.16)$$

where Δv is the net change in fluid velocity caused by the propeller blade's rotating aerofoil profile. The propeller induces a velocity directly in front of its rotational plane v_i , such that the net fluid flow into the plane is $v_b = v_i + v_\infty$. That induced inflowing fluid velocity is different to the net velocity contribution of the propeller; $v_i \neq \Delta v$.

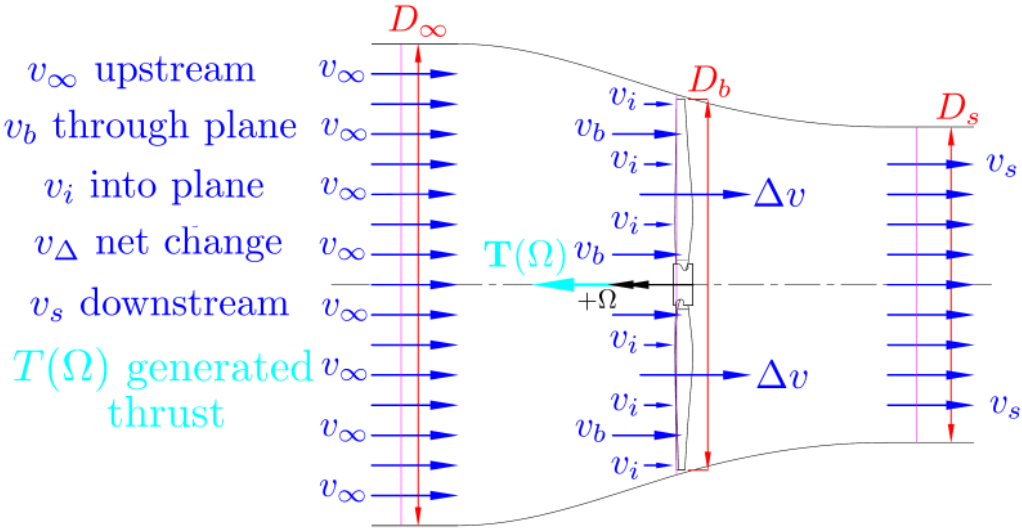


Figure 3.3: Disc Actuator Propeller Planar Flow

It is shown in [8] that at static conditions, using Bernoulli's pressure theorem, the net fluid flow through the propeller's plane is:

$$v_b = \frac{1}{2}(v_s - v_\infty) = \frac{1}{2}\Delta v = \frac{1}{2}v_s|_{v_\infty=0} \quad (3.17)$$

Stemming from classical disc actuator, or fluid *momentum* theory [124, 137], the scalar force $T(\Omega_i)$ acting on the fluid is calculated as a function of mass flow rate with respect to the change in fluid velocity or *pressure differential*:

$$T = (A_b v_b) \Delta v = \rho \pi R_b^2 v_b \Delta v = \rho \pi R_b^2 (v_i + v_\infty) \Delta v = \frac{1}{2} \rho \pi R_b^2 \Delta v^2 \quad (3.18)$$

where R_b is the disc (propeller) radius in m for the fluid stream under consideration, A_b is the swept area of that propeller disc. The fluid density of that stream ρ is typically $1.225 \text{ [kg.m}^{-3}]$ for air at standard temperature and pressure (*stp*). However, the desired form of thrust generated is as a function of propeller rotational velocity, $T(\Omega_i)$ in [RPS], so Eq:3.18 is not yet satisfactory.

Eq:3.18 could be solved from the aerodynamic propulsive power expended using $\Delta P = T \Delta v$. The relationship between rotational kinetic energy of a propeller and its transferred propulsive power is difficult to quantify, compound parasitic losses deteriorate the efficiency of the propeller and motor. Furthermore, the fluid velocity through the propeller's plane is not purely normal but is in fact a vector.

Fluid flow induced by the propeller's rotation v_i directly in front of its plane of rotation has both axial and tangential induced components, termed a and a' respectively. Induced fluid velocity components are abstracted to induction factors which are dependent on the incident fluid velocity entering the propeller's plane of rotation:

$$v_i = av_\infty \text{ in the axial direction} \quad (3.19a)$$

$$v_\theta = a'\Omega_i R_b \text{ in the tangential direction} \quad (3.19b)$$

Using the induction factors to rewrite the fluid's through velocity v_b and its slip stream velocity v_∞ :

$$v_b = (1 + a)v_\infty \quad (3.20a)$$

$$v_s = (1 + 2a)v_\infty \quad (3.20b)$$

A consequence of the tangential fluid flow is that an angular momentum flow rate exists across the propeller plane. This produces a fluid-momentum torque opposing the rotational motion about the propeller's axis, analogous but perpendicular to Eq:3.18:

$$H = \rho \pi R_b^3 (v_\theta - v_\infty) v_b \quad (3.21)$$

Together, Eq:3.18 and Eq:3.21 comprise propeller momentum theory but cannot be solved on their own. Blade-element theory analyses incremental aerofoil sections of width dr of the propeller profile at some radius r , the sectional view of which is illustrated in Fig:3.4. Each aerofoil element has a net local fluid velocity \vec{U} across its profile, calculated as:

$$\vec{U} = \sqrt{(v_\infty + v_i)^2 + (v_\Omega + v_\theta)^2} \quad (3.22)$$

where each profile has a chord length c and an inclination (or *pitch*) θ of the aerofoil *zero-lift line* relative to the horizontal. Local fluid velocities incident to the propeller profile (Fig:3.4) make their own angle of attack ϕ such that a true effective angle of attack α_{eff} is encountered:

$$\phi = \theta - \alpha_{eff} \quad (3.23)$$

That local angle of attack varies with the incident fluid flow magnitude v_∞ and the induced axial velocity v_i . The trigonometric ratio between the two is given as:

$$\phi = \tan^{-1}\left(\frac{v_\infty + v_i}{v_\Omega + v_\theta}\right) = \tan^{-1}\left(\frac{v_\infty(1 + a)}{\Omega r(1 + a')}\right) \quad (3.24)$$

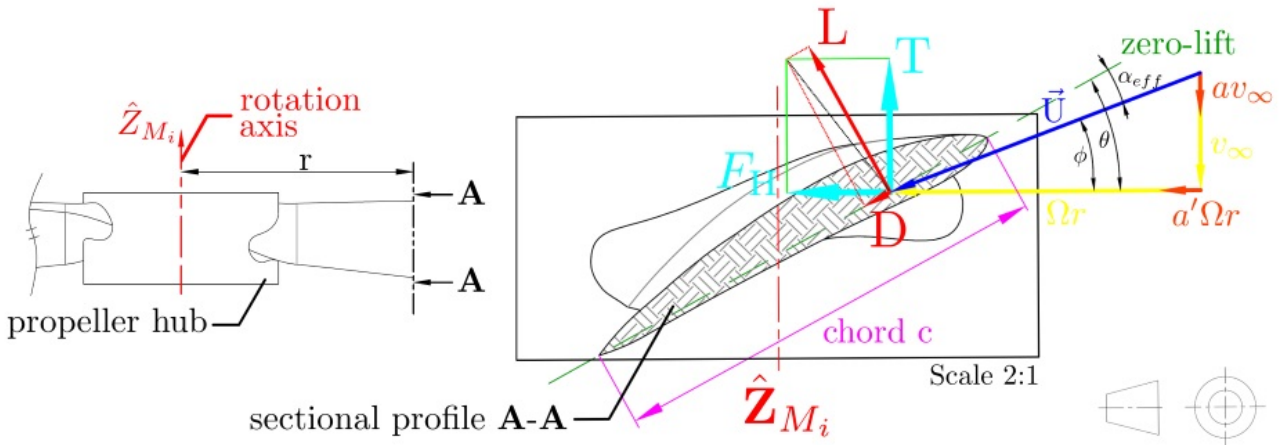


Figure 3.4: Blade element profile at radius r

In-plane fluid flow $\vec{U}(r, \phi)$, for an element at radius r with a local angle of attack ϕ , then contributes towards elemental lift and drag forces as a function of the aerofoil's dimensionless lift, C_L , and drag, C_D , coefficients. Those coefficients are determined by the aerofoil's characteristics, but would be constant across the length of a variable pitch, hinged and untwisted flat propeller (Fig:3.2b).

$$\Delta L = \frac{1}{2} \rho \vec{U}(r, \phi)^2 c C_L \quad (3.25a)$$

$$\Delta D = \frac{1}{2} \rho \vec{U}(r, \phi)^2 c C_D \quad (3.25b)$$

Where air density ρ in Eq:3.25 is taken at *stp*. Lift and drag forces, when taken parallel and perpendicular to the plane of rotation, are thrust T and torque F_H forces (Fig:3.4). The in-plane force applies an aerodynamic torque H at the propeller's hub because the force F_H acts at a radius r , [59].

$$dT = \frac{1}{2} \rho \vec{U}(r, \phi)^2 c (C_L \cos(\theta) + C_D \sin(\theta)) . dr \quad (3.26a)$$

$$dF_H = \frac{1}{2} \rho \vec{U}(r, \phi)^2 c (C_L \sin(\theta) + C_D \cos(\theta)) . dr \quad (3.26b)$$

$$\therefore dH = \frac{1}{2} \rho \vec{U}(r, \phi)^2 c (C_L \sin(\theta) + C_D \cos(\theta)) r . dr \quad (3.26c)$$

$$\therefore dP = \Omega r dF_H . dr \quad (3.26d)$$

Rotational power expended is a product of angular velocity and the opposing in-plane torque, Eq:3.26d. Power is mostly used instead of torque or drag terms in Eq:3.26c or Eq:3.26b respectively. Calculating forces and power terms as per momentum theory for each element, in terms of axial and tangential induction factors:

$$dT = \rho 4\pi r^2 v_\infty (1 + a) a dr \quad (3.27a)$$

$$dP = \rho 4\pi r^2 v_\infty (1 + a) \Omega r (1 + a') dr \quad (3.27b)$$

Equating momentum and element terms produces the blade-element momentum equation(s) for aerodynamic thrust and power from a propeller. Following a few assumptions, most importantly that the lift coefficient C_L is a linear function of the effective angle of attack α_{eff} is typically characterized as:

$$C_L = a_L(\theta - \phi) \quad (3.28)$$

Firstly the lift coefficient curve gradient a_L is shown in [60] for an ideally twisted blade, like the fixed pitch propellers under consideration, to be 2π . An ideal lift coefficient is then a function:

$$C_L = 2\pi(\theta - \phi) \quad (3.29)$$

Secondly, assuming tangentially induced velocities v_θ are small when compared to the propeller's translational speed at radius r , $v(\Omega_i) = \Omega_i r$. The tangential induction factor a' is then the ratio:

$$a' = \frac{v_\theta}{\Omega_i r} \ll 1 \quad (3.30)$$

Small angle approximations then apply to Eq:3.26a-3.26c; $\cos(\phi + \alpha_{eff}) \approx 1$ and $\sin(\phi + \alpha_{eff}) \approx \phi + \alpha_{eff}$. Similarly net inflow and axial velocities are $(v_\infty + v_i) \ll \Omega_i r$, the following integrals are then found:

$$T(\Omega_i) = \int_{r=0}^R \frac{1}{2} a_L b c \rho (\Omega_i r)^2 \left[\theta - \frac{v_\infty + v_i}{\Omega_i r} \right] dr \quad (3.31a)$$

$$P(\Omega_i) = \int_{r=0}^R \frac{1}{2} a_L b c \rho (\Omega_i r)^3 \left[\left(\theta - \frac{v_\infty + v_i}{\Omega_i r} \right) \left(\frac{v_\infty + v_i}{\Omega_i r} \right) + C_d \right] dr \quad (3.31b)$$

where b is the number of blades the propeller has. In practice, knowing exact pitch and chord values as a function of r/R is difficult and calculating integrals at each process step is cumbersome. Both Eq:3.31a and Eq:3.31b can be solved by equating element and momentum terms, a full solution of which is given in App:A.2. Often dimensionless thrust and power coefficients are defined across the entire blade's length:

$$C_T(J) \triangleq \frac{T}{\rho \Omega_i^2 D^4} \quad (3.32a)$$

$$C_P(J) \triangleq \frac{P}{\rho \Omega_i^3 D^5} \quad (3.32b)$$

where the propeller's diameter is D in [m], then Ω_i is the propeller's rotational speed in *revolutions per second* [RPS] and different from other inertial equations like Eq:3.63, with units [rad.s^{-1}]. For fixed pitch propellers the thrust and power coefficients are easily determined and remain consistent. Both Eq:3.32a and Eq:3.32b vary as a function of the dimensionless *advance ratio* J .

$$J \triangleq \frac{v_\infty}{\Omega_i R} \quad (3.33)$$

Typically the net upstream velocity v_∞ in Eq:3.33 is simply the perpendicular component (projected onto the plane's normal vector \hat{n} , shown later in Eq:3.35) of the vehicle's translational velocity in the body frame; $\vec{v}_b \perp \hat{n}$. For the case of a zero advance ratio $J = 0$, the conditions are regarded as static. Static thrust and power coefficients are nominal in their values.

Propeller databases like [25] provide comprehensive coefficient values for a range of small and medium diameter propeller types at different advance ratios. Included in the database are blade profiles, pitch angles and chord lengths. All the results are outcomes of the investigation [26].

The introduction of those coefficients drastically reduces thrust estimation complexity. For a typical 6×4.5 inch propeller the following coefficients were linearly interpolated from similar pitched database results in [25] to match subsequent physical test values. Static thrust and power coefficients determined from tests subsequently in Fig:3.6b and Fig:3.7b are respectively:

$$C_{T0} = 0.191 \quad (3.34a)$$

$$C_{P0} = 0.0877 \quad (3.34b)$$

Fig:3.5 plots interpolated coefficients for thrust C_T and power C_P as a function of the advance ratio J . As the incident upstream fluid velocity v_∞ increases, the thrust coefficient decreases. So too does the power coefficient and hence the aerodynamic torque. The thrust and power coefficients can be assumed constant for low advance ratios, or in the case considered here, translational velocities.

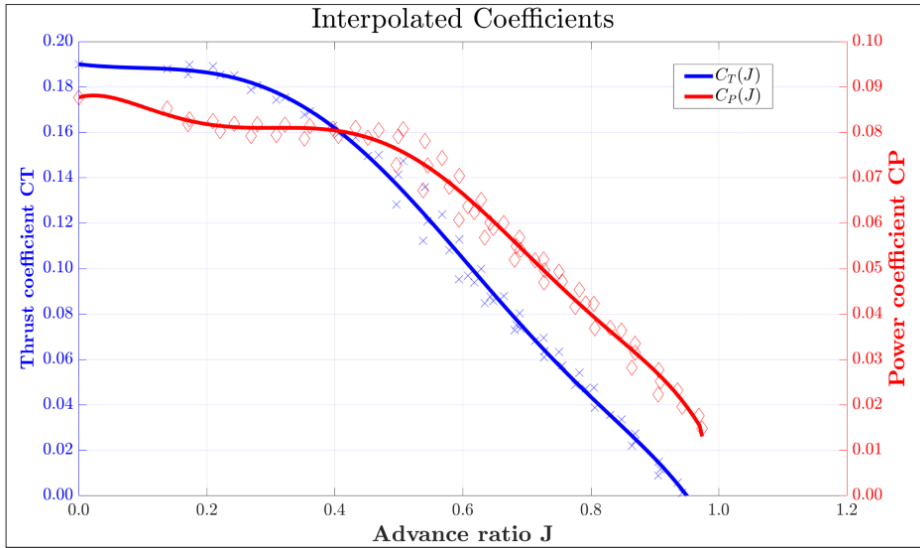
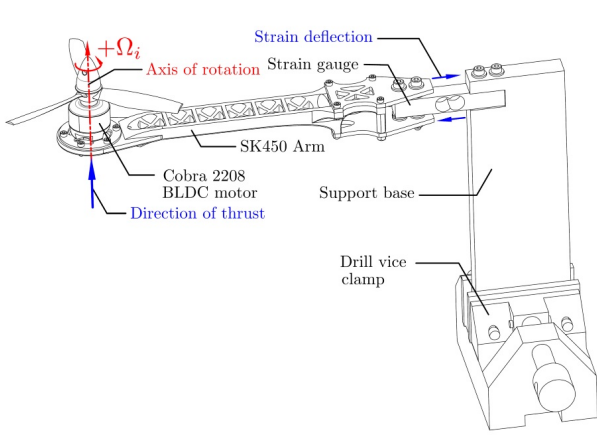
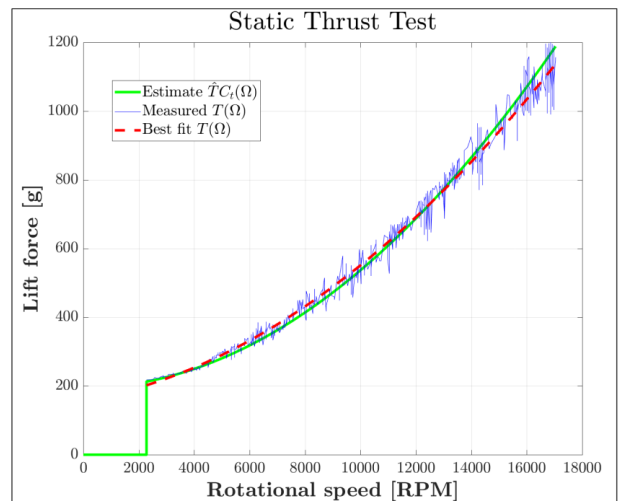


Figure 3.5: Thrust and power coefficients

Static thrust and torque tests were respectively performed on test rigs in Fig:3.6a and Fig:3.7a. Measured values for each test are plotted; $T(\Omega)$ in Fig:3.6b for thrust and $H(\Omega)$ in Fig:3.7b for torque. The physically tested values are fitted with quadratic trend-lines and plotted against static coefficient estimates using Eq:3.32a for thrust $\hat{T}C_t(\Omega)$ and Eq:3.32b for calculated torque $\hat{H}C_p(\Omega)$. Results from Fig:3.5 are used as a lookup table and values from Eq:3.32 are calculated. Induced propeller thrust and torques can be accurately modelled quadratically, power is cubic with respect to rotational velocity.



(a) Propeller thrust test rig



(b) Static lift force results

Figure 3.6: Propeller thrust tests

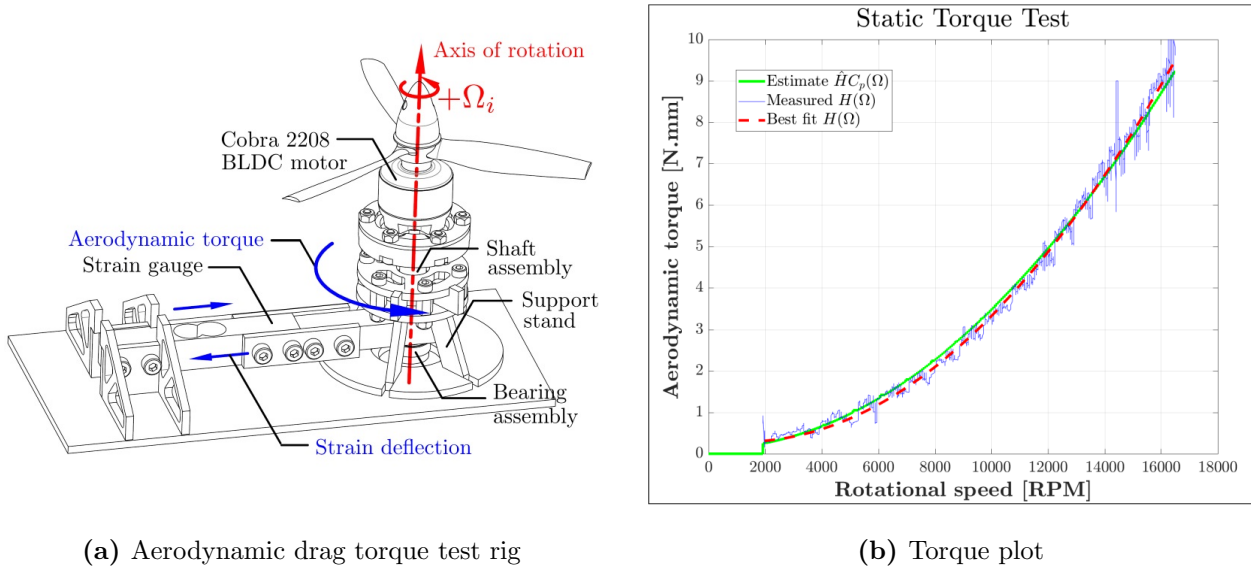


Figure 3.7: Static induced torque results

Advance ratios, Eq:3.33, or rather the propeller incident fluid flows are dependent on the vehicle's net translational and angular velocity. The fluid velocity's normal component to the propeller plane is given by:

$$v_\infty = (\vec{v}_b' + \vec{L}_{arm} \times \vec{\omega}_b') \cdot \hat{n}(\lambda_i, \alpha_i) \in \mathcal{F}^{M_i} \quad (3.35)$$

where \vec{v}_b' in $[\text{m.s}^{-1}]$ is the body's translational velocity and $\vec{\omega}_b'$ in $[\text{rad.s}^{-1}]$ is the body's angular velocity, both transformed to the propeller's frame, $\in \mathcal{F}^{M_i}$. Furthermore $\hat{n}(\lambda_i, \alpha_i)$ is the unit vector normal to the propeller's rotational plane, relative to the body velocity. Then J is calculated from Eq:3.33.

It is worth reiterating that the above static coefficients are indeed calculated from physical static tests, but advance ratio coefficient dependencies are linearly interpolated from the closest available matching data (APC Thin-Electric 8X6 propellers) cited from [25].

Clockwise and anti-clockwise propellers and rotations were used for both thrust and torque tests. Despite both test rigs (Fig:3.6a and Fig:3.7a respectively) having been designed to specifically isolate each response, results from opposing directional tests were averaged in the hopes that stray opposing effects would cancel each other out. Both clockwise and anti-clockwise rotational testing results for thrust and torque measurements are included in App:C.1

Discrepancies which exist between the model or coefficient values derived can be accounted for with lumped uncertainty disturbance terms. Model uncertainty compensation can easily be incorporated into adaptive backstepping or H_∞ control algorithms. The deviation of the modelled thrust or torques from their true values would be simple to incorporate into a plant dependent Lyapunov candidate function; Sec:4.6.3.

3.2.2 Hinged Propeller Conning and Flapping

Aerodynamics which adversely affect a propeller's performance have all been well documented in their own right, mostly in the context of helicopter aerodynamic and propeller fields [24, 120]. Typically such effects are more pronounced when observing hinged variable pitch propellers (Fig:3.2b), fixed pitch propellers with small radii have a diminished effect. Moreover, low translational velocities suppress such responses but they're worth mentioning.

Conning and flapping are the two most significant aerodynamic effects encountered by a propeller. Other phenomena like cyclic vortex ring states are deemed to be inapplicable here and fall outside the scope of the investigation.

In translational flight, for a propeller without shrouding or a ducting, each blade encounters varying incident fluid flow throughout its cycle. The advancing blade relative to the body's translational direction encounters a greater fluid flow than the retreating blade, constructive and destructive interference from the body's translational velocity adds to local fluid flows. The effective local angles of attack, sectional view in Fig:3.4, for advancing and retreating propeller blades are then asymmetrical. Unbalanced angles of attack produce a dissymmetry of lift across the propeller blade's surface.

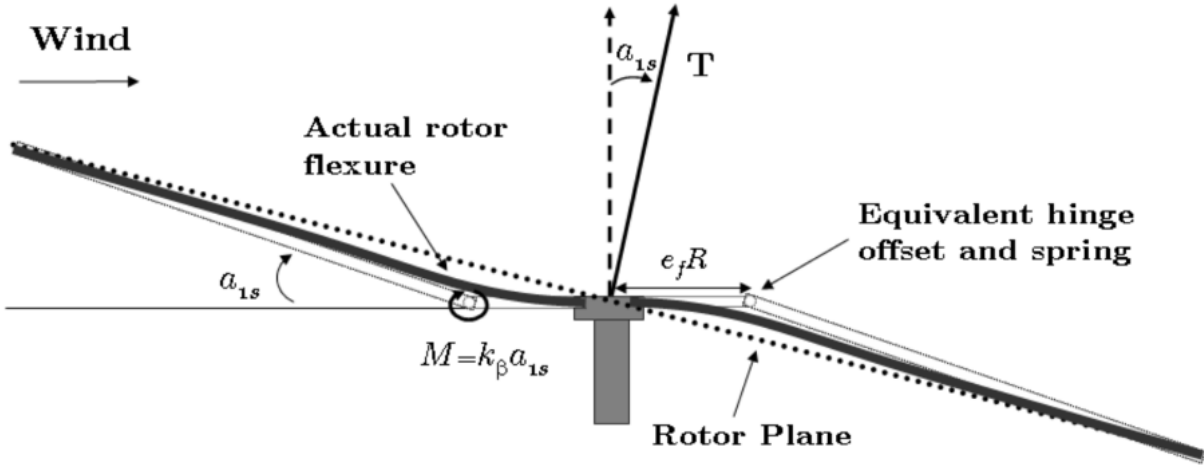


Figure 3.8: Propeller blade flapping; [59]

Throughout each rotation the blade is forced up and down as it cycles through a varying fluid velocity field, applying a torque moment about the propeller's hub. That torque's magnitude is a function of the body's net translational velocity and the propeller material's stiffness and hence its susceptibility to deflection. The flapping pitches the effective propeller plane or *tip-path plane*, and hence the thrust vector line, away from its principle axis; shown in Fig:3.8.

The propeller's resultant thrust vector is pitched away from its perpendicular normal by some deflection angle, α_{1s} in Fig:3.8, toward the direction of translational movement or wind disturbance. Propeller flapping is diminished at low translational velocities with small wind disturbances relative to propeller rotational speed. As such flapping is not applicable to the feasible flight envelope envisaged for the prototype here.

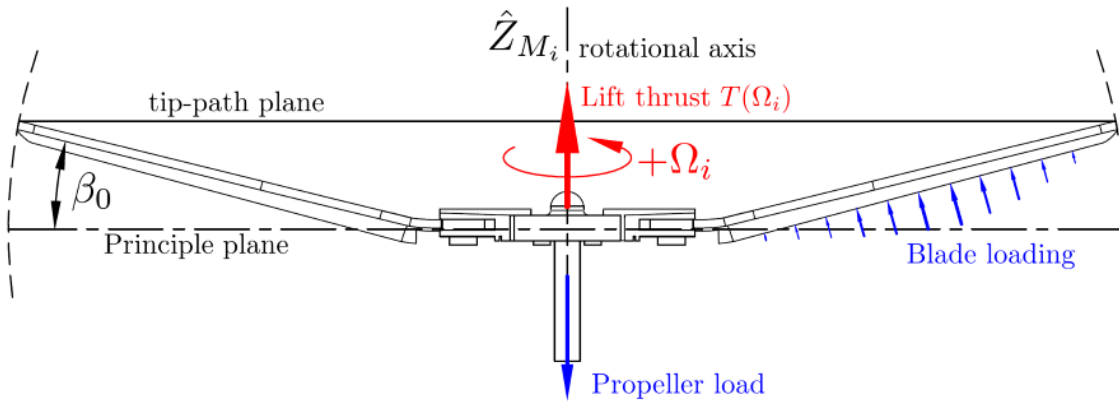


Figure 3.9: Propeller coning

Coning is another form of propeller deflection, illustrated in Fig:3.9, which again is dependent on the blade material's stiffness. Coning causes both advancing and retreating propeller blades to both deflect upward. Distributed loading on the propeller surface from supporting a body's weight causes the upward deflection. The coning reduces the effective propeller disc's radius, adversely affecting thrust produced, Eq:3.31a. Increased loading accentuates the coning angle experienced by the propellers and as such reduces the tip-path plane.

Both aerodynamic propeller deflections can be quantified numerically. Their derivation and resultant equations are cumbersome. In practice, both effects on the produced prototype are not significant enough to affect the derived plant model. The frame could potentially be affected in more adverse ways given certain flight conditions with higher translational velocities or incident wind and fluid flow disturbances.

3.2.3 Drag

For any solid body with some non-zero relative translational velocity through a fluid, that fluid has a second-order damping response opposing the body's movement. Net drag \vec{D}_{net} is locally dependent on individual component cross-sections. For a vehicle's velocity $\vec{v}_b = [u \ v \ w]^T$ in \mathcal{F}^b , the drag force is:

$$\vec{D}_{net}(\vec{v}_b) = \begin{bmatrix} D_{ii} & D_{ij} & D_{ik} \\ D_{ji} & D_{jj} & D_{jk} \\ D_{ki} & D_{kj} & C_{kk} \end{bmatrix} \begin{bmatrix} u \\ v \\ w \end{bmatrix}^2 \in \mathcal{F}^b \quad (3.36)$$

Each drag coefficient's subscript i, j and k is dependent on the body's directional cross-section area for each $\hat{X}_b, \hat{Y}_b, \hat{Z}_b$ axis respectively. Given a well designed and symmetrical frame, it can be assumed the off-diagonal elements are of little or no consequence and as such the drag equation can be simplified to the diagonal:

$$\vec{D}_{net}(\vec{v}_b) \approx \text{diag}(D_{ii}, D_{jj}, D_{kk}) \vec{v}_b^2 \in \mathcal{F}^b \quad (3.37)$$

Due to the second-order degree of translational velocity on the drag force, such terms can be relegated to a lumped disturbance term which is compensated for in the control loop, Sec:4.6.3. The time scale separation between velocity and wind drag effects within the control loop accommodates such an assumption. Analogous rotational drag-like effects opposing angular rates exist but, for the intents and purposes of most practical flight envelopes, can be disregarded.

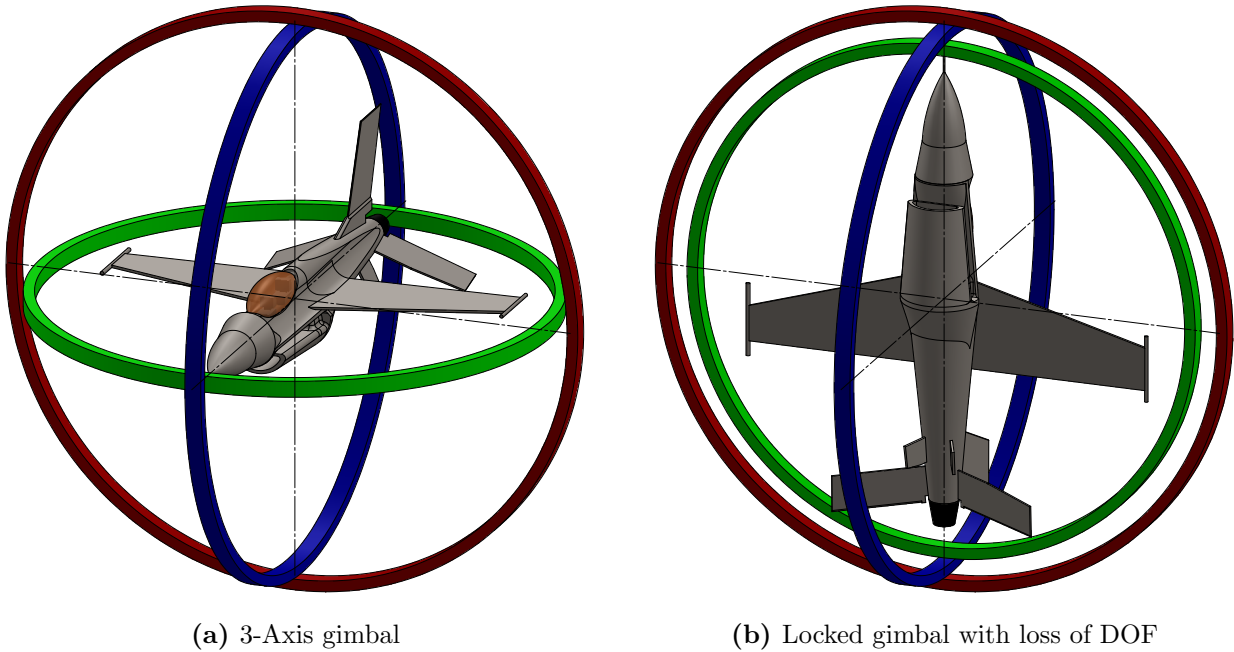
In simulation if the plant has sufficient disturbance rejection then the drag term in Eq:3.36 would be easily accounted for in an adaptive backstepping algorithm. Drag, much like wind turbulence, is shown later in Sec:6.6 to be not consequentially destabilizing. Furthermore, it is possible to physically test for the drag coefficients to attain a higher-certainty model but, given the flight conditions proposed for this research, such effects will be small, if not negligible. As such those tests are outside the scope of investigation here.

3.3 Quaternion Attitude

3.3.1 Rotation Matrix Singularity

The singularity inherent to Euler angle parametrization is often mentioned but far less common is the mathematical demonstration of how that singularity manifests itself. In general, a singularity occurs for some matrix A in $\vec{y} = A\vec{x}$ when the matrix has a zero determinant, losing rank and hence differentiability of \vec{y} in terms of \vec{x} . The combined rotation matrix from the inertial frame \mathcal{F}^I to the body frame \mathcal{F}^b is the singular component of an Euler parametrized sequence.

Consider the case of a rotational 3-axis gimbal system, illustrated in Fig:3.10a, which mimics the sequential nature of the Euler set. When the intermediary sequenced rotational angle is at $\pi/2$ rad, the remaining two axes become co-linear, Fig:3.10b. In a ZYX rotation sequence, as adopted in this work, the singularity occurs from the pitching angle θ about the \hat{Y} axis. Both the roll ϕ and yaw ψ rotations will subsequently have the same rotational effect. Such a situation results in a loss of a degree of freedom.

**Figure 3.10:** Mechanical gimbal lock

What is clear physically is not necessarily as obvious mathematically. A loss of rank occurs in the Euler matrix $\Phi(\eta)$, defined previously in Eq:2.12h from Sec:2.2.1. That relation between angular velocity, in the inertial frame or inversely in the body frame, and the angular rates of the Euler Angles has a determinant:

$$\begin{bmatrix} \dot{\phi} \\ \dot{\theta} \\ \dot{\psi} \end{bmatrix} = \begin{bmatrix} 1 & \sin(\phi)\tan(\theta) & \cos(\phi)\tan(\theta) \\ 0 & \cos(\phi) & -\sin(\phi) \\ 0 & \sin(\phi)\sec(\theta) & \cos(\phi)\sec(\theta) \end{bmatrix} \begin{bmatrix} p \\ q \\ r \end{bmatrix} = \Phi(\eta)\omega_b \in \mathcal{F}^{v_1, v_2, I} \quad (3.38)$$

$$\det(\Phi(\eta)) = \cos(\phi)(\cos(\phi)\sec(\theta)) + \sin(\phi)(\sin(\phi)\sec(\theta)) = \sec(\theta) \quad (3.39)$$

$$\therefore \lim_{\theta \rightarrow \pi/2} |\Phi(\eta)| = \sec(\theta) \rightarrow \infty \quad (3.40)$$

The Euler matrix $\Phi(\eta)$ loses rank as $\theta \rightarrow \pi/2$ rad, losing differentiability as well. The physical consequence of this is the loss of a degree of freedom. More specifically, considering how the ZYX rotation or transformation matrices are formulated, from Eq:2.6:

$$R_I^b(\eta) \triangleq R_z(\psi)R_y(\theta)R_x(\phi) = \begin{bmatrix} c_\psi & -s_\psi & 0 \\ s_\psi & c_\psi & 0 \\ 0 & 0 & 1 \end{bmatrix} \begin{bmatrix} c_\theta & 0 & s_\theta \\ 0 & 1 & 0 \\ -s_\theta & 0 & c_\theta \end{bmatrix} \begin{bmatrix} 1 & 0 & 0 \\ 0 & c_\phi & -s_\phi \\ 0 & s_\phi & c_\phi \end{bmatrix} \quad (3.41a)$$

$$\therefore R_I^b(\eta) = \begin{bmatrix} c_\psi c_\theta & c_\psi s_\theta s_\phi - s_\psi c_\phi & c_\psi s_\theta c_\phi + s_\psi s_\phi \\ s_\psi c_\theta & s_\psi s_\theta s_\phi + c_\psi c_\phi & s_\psi s_\theta c_\phi - c_\psi s_\phi \\ -s_\theta & c_\theta s_\phi & c_\phi c_\theta \end{bmatrix} \quad (3.41b)$$

In the case where $\theta = \pi/2$ rad, and using trigonometric double angles, the following can be reduced:

$$R_I^b(\eta) = \begin{bmatrix} 0 & c_\psi s_\phi - s_\psi c_\phi & c_\psi c_\phi + s_\psi s_\phi \\ 0 & s_\psi s_\phi + c_\psi c_\phi & s_\psi c_\phi - c_\psi s_\phi \\ -1 & 0 & 0 \end{bmatrix} \Big|_{\theta=\pi/2} \quad (3.41c)$$

$$= \begin{bmatrix} 0 & s(\phi - \psi) & c(\phi - \psi) \\ 0 & c(\phi - \psi) & s(\phi - \psi) \\ -1 & 0 & 0 \end{bmatrix} \quad (3.41d)$$

$$\therefore R_I^b(\eta) \Big|_{\theta=\pi/2} \equiv R_{x'}(\phi - \psi) \quad (3.41e)$$

where the resultant in Eq:3.41e represents an \hat{X}' -axis rotation in a new intermediate frame, following a $\pi/2$ rotation about the \hat{Y} -axis. Through trigonometric double angles, a degree of freedom is lost at $\theta = \pi/2$ when both ϕ and ψ affect the same angle.

3.3.2 Quaternion Dynamics

An algorithm proposed in [122] suggested a solution to avoid Euler Angle singularities. The heuristic proposed involved switching between sequence conventions (ZYX,ZYZ etc...there are 12 in total) such that the singularity is always avoided. However the implementation of such an algorithm is cumbersome and computationally exhaustive. Far more elegant is the use of *quaternion* attitude representations in \mathbb{R}^4 , used in [47, 75] amongst other, but most notably made popular by [121] for use in animation.

A quaternion is analogous to a rotation matrix in that it represents an attitude difference between two reference frames. An \mathbb{R}^3 attitude is parameterized as one rotation θ about a single unit *Euler* axis \hat{u} , demonstrated using the Rodriguez Formula in [92]. In brief, a quaternion consists of a scalar component q_0 and complex vector component $\vec{q} \in \mathbb{C}^3$ such that:

$$Q \triangleq \begin{bmatrix} q_0 \\ \vec{q} \end{bmatrix} \in \mathbb{R}^4 \quad (3.42)$$

The relationship between an Euler angle rotation matrix $R_I^b(\eta)$ and a quaternion attitude Q_b is given by the Rodriguez formula:

$$R_I^b(\eta) \equiv R(Q_b) \triangleq \mathbb{I}_{3 \times 3} + 2q_0[\vec{q}]_{\times} + 2[\vec{q}]_{\times}^2 \quad (3.43)$$

where $[.]_{\times}$ is the cross-product matrix, defined previously in Eq:2.8c, and $\mathbb{I}_{3 \times 3}$ is an identity matrix as per convention. All quaternions, unless otherwise specified, are unit quaternions $Q \in \mathbb{Q}_u$. Quaternions with a unity magnitude ensure that rotational operations maintain the vector operand's magnitude. A unit quaternion is defined as follows:

$$\|Q\| \triangleq \sqrt{q_0^2 + \vec{q}^2} = 1 \quad (3.44)$$

Quaternion multiplication is distributive and associative, but not commutative. Specifically a quaternion multiplication operator is equivalent to the Hamilton product. For two quaternions, Q and P :

$$Q \otimes P = \begin{bmatrix} q_0 \\ \vec{q} \end{bmatrix} \otimes \begin{bmatrix} p_0 \\ \vec{p} \end{bmatrix} \quad (3.45a)$$

$$\triangleq \begin{bmatrix} q_0 p_0 - \vec{q} \cdot \vec{p} \\ q_0 \vec{p} + p_0 \vec{q} + \vec{q} \times \vec{p} \end{bmatrix} \quad (3.45b)$$

$$= \underbrace{q_0 p_0}_{\text{scalar}} - \underbrace{\vec{q} \cdot \vec{p}}_{\text{scalar}} + \underbrace{p_0 \vec{q} + q_0 \vec{p} + \vec{q} \times \vec{p}}_{\text{vector}} \quad (3.45c)$$

Because the vector component of a quaternion is complex valued, it is natural that a quaternion complex conjugate Q^* exists, defined:

$$Q^* \triangleq \begin{bmatrix} q_0 \\ -\vec{q} \end{bmatrix} \quad (3.46)$$

It follows that the fundamental quaternion identity is:

$$Q \otimes Q^* = \mathbb{I}_{4 \times 4} \quad (3.47)$$

A right handed quaternion rotation applied to some vector $\vec{v} \in \mathbb{R}^3$ involves multiplication by two unit quaternions Q and its conjugate Q^* .

$$\begin{bmatrix} 0 \\ \vec{v}' \end{bmatrix} = Q \otimes \begin{bmatrix} 0 \\ \vec{v} \end{bmatrix} \otimes Q^* \quad (3.48)$$

Mostly, the zero scalar components are omitted in a rotation (*or transformation*) operation, it is implied that vector operands are substituted with zero scalar quaternions.

$$\vec{v}' = Q \otimes (\vec{v}) \otimes Q^* \quad (3.49)$$

In the case of rigid body attitude parametrization using quaternions, Q_b is the quaternion which represents the difference between body and inertial frames \mathcal{F}^b and \mathcal{F}^I respectively. A quaternion operator is equivalent to a rotation matrix operation, for some vector $\vec{\nu}_I \in \mathcal{F}^I$:

$$\vec{\nu}_b = R_I^b(\eta)\vec{\nu}_I \iff Q_b \otimes (\vec{\nu}_I) \otimes Q_b^* \in \mathcal{F}^b \quad (3.50)$$

Since quaternions are non-commutative, the construction of a body quaternion Q_b from an Euler angle set $\vec{\eta}$ is *sequence dependent*. Euler angles, despite being singular, are conceptually simpler for describing a body's orientation. A ZYX sequenced body quaternion Q_b relative to the inertial frame can be constructed from its Euler angle counterparts using:

$$Q_b \triangleq Q_z \otimes Q_y \otimes Q_x = \begin{bmatrix} \cos(\psi/2) \\ 0 \\ 0 \\ \sin(\psi/2) \end{bmatrix} \otimes \begin{bmatrix} \cos(\theta/2) \\ 0 \\ \sin(\theta/2) \\ 0 \end{bmatrix} \otimes \begin{bmatrix} \cos(\phi/2) \\ \sin(\phi/2) \\ 0 \\ 0 \end{bmatrix} \quad (3.51)$$

A quaternion's time derivative, defined in [39], with Q_ω being a quaternion with a vector component equal to angular velocity $\vec{\omega}_{b/I}$ and a zero scalar component, is:

$$\frac{d}{dt} Q_b \triangleq \frac{1}{2} Q_b \otimes Q_\omega = \frac{1}{2} Q_b \otimes \vec{\omega}_b \quad (3.52a)$$

$$= \begin{bmatrix} -\frac{1}{2} \vec{q}^T \vec{\omega}_b \\ \frac{1}{2} ([\vec{q}]_\times + q_0 \mathbb{I}) \vec{\omega}_b \end{bmatrix} \quad (3.52b)$$

Using quaternions to represent attitudes negates the need for an Euler Matrix, $\Phi(\eta)$ from Eq:2.12i, to represent attitudes and their rates. A body quaternion is fully defined in the inertial frame with respect to the body frame or inversely so. The first quaternion time derivative replaces angular velocity rate differentials in Eq:3.10a and Eq:3.10c respectively:

$$\dot{\mathcal{E}} = R_b^I(-\eta)\vec{v}_b \in \mathcal{F}^I \iff Q_b(-\eta) \otimes \vec{v}_b \otimes Q_b^*(-\eta) = Q_b^* \otimes \vec{v}_b \otimes Q_b \quad (3.53a)$$

$$\dot{\eta} \triangleq \Phi(\eta)\vec{\omega}_b \in \mathcal{F}^{v2,v1,I} \iff \dot{Q}_b = \frac{1}{2} Q_b \otimes \vec{\omega}_b \quad (3.53b)$$

Second order time derivatives for quaternion acceleration are not as useful as their higher order, velocity counterparts. The second order derivative is provided here for the sake of completeness. If at all possible, quaternion accelerations are avoided due to their complexity. The quaternion analogue for angular acceleration Eq:3.14b, dependent on net torque acting on a body $\vec{\tau}_\mu$, is given by:

$$\ddot{Q}(\dot{Q}, Q, t) \triangleq \dot{Q} \otimes Q^* \otimes \dot{Q} + \frac{1}{2} Q \otimes [J_b^{-1}(\vec{\tau}_\mu - 4(Q^* \otimes \dot{Q}) \times (J_b(Q^* \otimes \dot{Q})))] \quad (3.54)$$

An Euler angle attitude error state, used for control input, is defined as the subtracted error between a desired and an existing attitude orientation, $\vec{\eta}_d \in \mathcal{F}^d$ and $\vec{\eta}_b \in \mathcal{F}^b$ respectively, where $\vec{\eta}_d$ is some attitude setpoint produced from a trajectory generator and *both Euler sets are in shared frames*.

$$\vec{\eta}_e \triangleq \vec{\eta}_d - \vec{\eta}_b \quad (3.55)$$

Quaternion attitude control and its stability goals are expanded upon subsequently in Sec:4.6.1. In contrast with Eq:3.55, a quaternion attitude error is a multiplicative term defined as the difference between two quaternions Q_d and Q_b :

$$Q_e \triangleq Q_b^* \otimes Q_d \quad (3.56)$$

3.3.3 Quaternion Unwinding

Although quaternions are indeed better than their Euler angle attitude counterparts and lack the associated singularity, they do contain one caveat. Because a quaternion $Q = [q_0 \ \vec{q}]^T$ represents a body's attitude in \mathbb{R}^3 using \mathbb{R}^4 , there is an infinite coverage of attitude states [92].

Each unit quaternion, stemming from Euler-Rodriguez theorem, represents a single Euler-axis rotation of θ about a unit axis \hat{u} such that:

$$Q = \begin{bmatrix} q_0 \\ \vec{q} \end{bmatrix} \triangleq \begin{bmatrix} \cos(\theta/2) \\ \sin(\theta/2)\hat{u} \end{bmatrix} \quad (3.57)$$

That rotation is applied with a quaternion operator, Eq:3.49. For every attitude state in 3-D there exist two unique quaternions which correspond to the same orientation, differing by their rotational direction about the Euler-axis. The rotation angle θ about the Euler-axis \hat{u} is reciprocal in that $\theta = \theta + 2k\pi$, $k \in \mathbb{N}$. There are then two definitions for Q_b :

$$Q_b = \begin{bmatrix} \cos(\theta/2) \\ \sin(\theta/2)\hat{u} \end{bmatrix} \quad (3.58a)$$

$$Q_b = \begin{bmatrix} \cos(\pi - \theta/2) \\ \sin(\pi - \theta/2)\hat{u} \end{bmatrix} = \begin{bmatrix} -\cos(\theta/2) \\ \sin(\theta/2)\hat{u} \end{bmatrix} \quad (3.58b)$$

$$\therefore \vec{\eta} \in \mathbb{R}^3 \Leftrightarrow \begin{bmatrix} \pm q_0 \\ \vec{q} \end{bmatrix} \in \mathbb{R}^4 \quad (3.58c)$$

Eq:3.58c asserts that for each attitude in \mathbb{R}^3 there are *two* corresponding quaternions in \mathbb{R}^4 , $[\pm q_0 \ \vec{q}]^T$. A consequence of this is that two possible error state trajectories exist for every attitude difference. Both a clockwise $+\theta$ and an anticlockwise $2\pi - \theta$ rotation point to the same quaternion attitude error state. This could lead to an erroneous and unnecessary “unwinding” of a complete counter revolution. So for attitude controllers, the requirement is that for positive and negative quaternion scalars the control input is consistent. That requirement is:

$$\vec{\tau}_d = h([q_0 \ \vec{q}]^T, t) \equiv h([-q_0 \ \vec{q}]^T, t) \quad (3.59)$$

or more simply that $Q_e \triangleq [|q_0| \ \vec{q}]^T$. The simplest solution adhering to that constraint, which is often used, is to neglect the quaternion scalar component altogether. Using a reduced error state, only the quaternion error vector as an argument for the control law $h(\vec{q}_e, t)$. Such a solution is an oversimplification and would only ever be locally stable.

An alternative is to use only the absolute quaternion scalar, which ensures the error state represents a right-handed (clockwise) rotation and not necessarily the shortest path. If the resolution of trajectory coordinates generated is sufficiently fine, the control plant will not encounter a problem.

One proposal presented in [27] suggested using a *signum* operator to design the controller coefficient sign for the desired virtual angular velocity, $\vec{\omega}_d$ control plant input.

$$\vec{\omega}_d = \frac{2}{\Gamma_1} sgn(q_0) \vec{q} \quad (3.60a)$$

with Γ_1 being a proportional error coefficient and signum defining the operator's sign:

$$sgn(q_0) \triangleq \begin{cases} 1 & q_0 \geq 0 \\ -1 & q_0 < 0 \end{cases} \quad (3.60b)$$

Eq:3.60 was shown to be asymptotically stable but only locally in the case where the Euler-axis angle is constrained ($\theta \leq \pm\pi$). That control law would still need the control torques to be calculated from that angular velocity $\vec{\omega}_d$ setpoint using Eq:3.10d.

In [10], the authors used a backstepping controller with a trajectory using the absolute quaternion scalar. The resultant was a global asymptotically stable control law which tracked quaternion setpoints for a satellite's attitude. That satellite's stability proof was difficult given the hybrid nature of the resulting equations. Controllers presented in Sec:4.6.3 all incorporate *signed* quaternion scalars into the control law, the trajectory generation is assumed to specify the preferred quaternion rotational sense.

3.4 Multibody Nonlinearities

The unique component of the prototype's design which facilitates redirection of a propeller's thrust vector (Eq:2.17 and Sec:2.1.1) is also what makes finding the complete equations of motion drastically more complex. The relative (revolute) motion within the multibody system results in torque responses opposing those angular accelerations. Such induced responses, if left unmodelled, would almost definitely destabilize the attitude of the plant. Unmodelled inertia rate responses are shown to be destabilizing in [76]. Typically, multibody dynamics are solved and simulated as a series of interacting torque and force constraints. There are different schools of thought on the subject, each proposing methodologies for stepping through the systems dynamics (*e.g.* Implicit Euler integration [70, 141]).

The prototype investigated here is a multibody system connected with revolute joints, which permit a single degree of relative rotation between each connected rigid body. There are no translational degrees of freedom between each body. Opposed to the angular accelerating actuator action on a body are *gyroscopic* and *inertia* Newtonian torque responses. The responses from each body are solved independently and those excitation induced torque constraints are introduced as additive external torques to the dynamic model derived in Sec:3.1.1. A distinction must be made between torque responses here and those in Eq:3.10d. Recalling the classical differential equation of angular motion already derived:

$$\dot{\vec{\omega}}_b = J_b^{-1}(-\vec{\omega}_b \times J_b \vec{\omega}_b + \vec{\tau}_\mu) \quad \in \mathcal{F}^b \quad (3.61)$$

Eq:3.61 treats the entire body as rigid, included terms are as a result of the entire multibody's *collective motion*. What follows is an extension of that attitude state to incorporate relative movements between each connected body. The objective here is to model the multibody dynamic system with clear responses induced from servo rotations of inner and middle ring bodies, $\Delta\lambda_i$ and $\Delta\alpha_i$ respectively. The subsequent derivations are Lagrangian analytical dynamics applied to the multibody system under consideration. For the purposes of this derivation it is assumed that no potential energy can be stored within the structure from material flexure. The only potential energy contribution is as a result of gravitational potential energy. Moreover, each connected body is first solved as a closed-energy system to ascertain the relative rotational response which is then incorporated in the overall multibody system.

Alternatively, the net dynamics could indeed be derived from a Lagrangian for the *entire* 13 body dynamic system. Those connected bodies are; four rotor/propeller bodies (Fig:2.11), four inner ring bodies (Fig:2.12), four middle ring bodies (Fig:2.13), and the frame structure (Fig:2.17) and each with six degrees of freedom. Constraints on the assembly's joints would eventually reduce the degrees of freedom and simplify solving for net responses. The purpose here is to model the body's response to changes in the actuation servos' positions $\Delta\lambda_i$ and $\Delta\alpha_i$ so independent bodies are analyzed first. The final result is, in fact, a Lagrangian for those collective thirteen bodies, whose partial derivative with respect to the net angular velocity relative to the inertial frame $\partial\vec{\omega}_b$ produces the net torque acting on the system.

3.4.1 Relative Rotational Gyroscopic and Inertia Torques

Rotation matrices are used in the following derivations owing to the fact that induced torque responses are dependent on transformed rotational inertias. Quaternions, as mentioned in Sec:2.3, are ill-suited to inertia transformations.

Each of the four motor modules are symmetrical and so the induced torque response characteristics from one module can be extrapolated simply through a \hat{Z}_b reference frame rotation. Each motor module is positioned relative to the body frame's center of motion \vec{O}_b , as in Fig:2.9. Because each relative rotation from the actuator set $\vec{u} \in \mathbb{U}$ is actuated separately and upon a different body, their responses are calculated independently too.

Drawing again from Lagrangian theory and considering only the angular energy component for the inner ring assembly attached to frame \mathcal{F}^{M_i} , there is no relative translational motion between each connected body and the origin of *motion* $\vec{\mathbf{O}}_b$, the center of the body frame \mathcal{F}^b from Fig:2.9 and Fig:2.16. Relative velocity of each body's center of gravity with respect to $\vec{\mathbf{O}}_b$, from each rotational actuation, is small in relation to the net vehicle's translational velocity. So translational kinetic energy for each module is treated as an extension of the body's net kinetic energy in Eq:3.7 and assumed to be independent of any actuator's position. The following is with regards to the i^{th} motor module, numerical subscripts are implied.

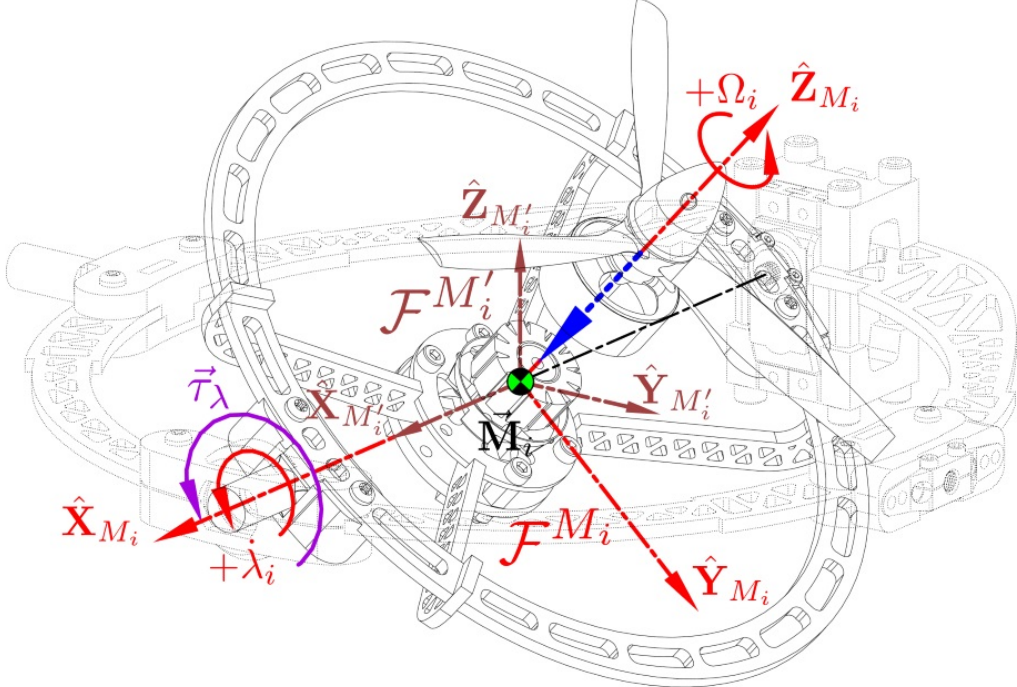


Figure 3.11: Exploded inner ring inertial bodies for $\vec{\tau}_\lambda(\lambda_i)$

Deriving dynamic responses for changes in the λ_i servo, acting on the inner ring frame \mathcal{F}^{M_i} relative to the middle ring frame $\mathcal{F}^{M'_i}$, requires a relative path coordinate to be defined. The only path variable between the two frames is that servo's rotational position λ_i about the $\hat{\mathbf{X}}_{M_i}$ axis. Path coordinates $\vec{\mathbf{u}}(t) = [\lambda_i \ 0 \ 0]^T$ are then used to construct the inner ring's closed energy system Lagrangian with respect to the middle ring frame $\mathcal{L}_{n/m} \in \mathcal{F}^{M'_i}$.

The inner ring assembly consists of two separate bodies, exploded in Fig:3.11. Each body has a relative rotational motion and independent kinetic energies. Those bodies are; the rotor assembly with an inertia J_r defined earlier in Eq:2.19, and the inner ring which has an inertia J_{ir} *without including* the rotor assembly. Reiterating that the rotor's inertia J_r is constant with respect to the propeller's rotational velocity Ω_i , that inner ring inertia is given by:

$$J_{ir} \triangleq J_n - J_r \quad (3.62)$$

where J_n is the net inertia for the inner ring assembly, explicitly defined in Eq:2.21. The rotor assembly has an angular velocity $\vec{\omega}_{r/m}$ relative to the middle ring frame $\mathcal{F}^{M'_i}$ due to the BLDC motor's rotation Ω_i and the inner ring's servo rate $\dot{\lambda}_i$:

$$\vec{\omega}_{r/m} \triangleq R_x(\lambda_i)\vec{\Omega}_i + \dot{\vec{\lambda}}_i \quad \in \mathcal{F}^{M'_i} \quad (3.63)$$

with the propeller's angular velocity vector about the inner ring frame's $\hat{\mathbf{Z}}_{M_i}$ axis $\vec{\Omega}_i \triangleq [0 \ 0 \ \Omega_i]^T \in \mathcal{F}^{M_i}$ and measured in $[\text{rad.s}^{-1}]$ not in *revolutions per second*. The servo position is defined as a vector in the $\hat{\mathbf{X}}_{M'_i}$ axis projected as $\vec{\lambda}_i \triangleq \lambda_i \cdot \hat{\mathbf{X}}_{M'_i} = [\lambda_i \ 0 \ 0]^T$ measured in [rad]. Next, the inner ring's angular velocity $\vec{\omega}_{n/m}$ relative to the middle ring $\mathcal{F}^{M'_i}$ is only as a result of $\dot{\lambda}_i$:

$$\vec{\omega}_{n/m} \triangleq \frac{d}{dt}(\vec{\lambda}_i) = \dot{\vec{\lambda}}_i \quad \in \mathcal{F}^{M'_i} \quad (3.64)$$

The Lagrangian for the inner ring's closed system energy $\mathcal{L}_{n/m}$, in the middle ring frame $\mathcal{F}^{M'_i}$, consists purely of rotational kinetic energy from angular velocities described in Eq:3.63 and Eq:3.64. Stored gravitational potential energy as a result of the rotated center of mass for the inner ring is omitted here as it is already included in Eq:2.35d and is shown to simplify out subsequently in Eq:3.109 when considering the entire system as a whole. The inner ring's Lagrangian is:

$$\mathcal{L}_{n/m} = \frac{1}{2} \vec{\omega}_{r/m}^T (J'_r) \vec{\omega}_{r/m} + \frac{1}{2} \vec{\omega}_{n/m}^T (J'_{ir}) \vec{\omega}_{n/m} \quad (3.65a)$$

Both inertias for the rotor and inner ring bodies, J_r and J_{ir} respectively, are transformed to align with the middle ring frame $\mathcal{F}^{M'_i}$ using an $R_x(\lambda_i)$ rotation to align with the middle ring's frame $\mathcal{F}^{M'_i}$.

$$J'_r = R_x(\lambda_i)(J_r)R_x^{-1}(\lambda_i) \quad \text{and} \quad J'_{ir} = R_x(\lambda_i)(J_{ir})R_x^{-1}(\lambda_i) \quad (3.65b)$$

Then expanding the Lagrangian $\mathcal{L}_{n/m}$ in Eq:3.65a with the above definitions for transformed inertias and relative angular velocities $\vec{\omega}_{r/m}$ and $\vec{\omega}_{n/m}$ yields:

$$\begin{aligned} \mathcal{L}_{n/m} = & \frac{1}{2} \left(R_x(\lambda_i) \vec{\Omega}_i + \dot{\vec{\lambda}}_i \right)^T \left(R_x(\lambda_i) (J_r) R_x^{-1}(\lambda_i) \right) \left(R_x(\lambda_i) \vec{\Omega}_i + \dot{\vec{\lambda}}_i \right) \\ & + \frac{1}{2} \dot{\vec{\lambda}}_i^T \left(R_x(\lambda_i) (J_{ir}) R_x^{-1}(\lambda_i) \right) \dot{\vec{\lambda}}_i \end{aligned} \quad (3.65c)$$

Reiterating J_{ir} is the inner ring's inertia independent of the rotor assembly J_r . Recalling the Euler-Lagrange formulation from Eq:3.3 using path coordinates $\vec{u}(t)$ for the inner ring frame \mathcal{F}^{M_i} relative to the middle ring frame $\mathcal{F}^{M'_i}$, the generalized (torque) forces \vec{U} acting on the middle ring are then:

$$\vec{U}(\lambda_i) = \frac{d}{dt} \left(\frac{\partial \mathcal{L}_{n/m}}{\partial \dot{\vec{u}}} \right) - \frac{\partial \mathcal{L}_{n/m}}{\partial \vec{u}} \quad \in \mathcal{F}^{M'_i} \quad (3.66)$$

Consider first the partial derivative of the Lagrangian $\mathcal{L}_{n/m}$ with respect to the generalized path coordinates $\partial \vec{u}$. The latter part of the Euler-Lagrange formulation with respect to the inner ring in Eq:3.66 then expands from the differential product rule:

$$\begin{aligned} \frac{\partial \mathcal{L}_{n/m}}{\partial \vec{u}} = & \frac{1}{2} \left[\left(\frac{\partial}{\partial \vec{\lambda}_i} R_x(\lambda_i) \vec{\Omega}_i \right)^T (J'_r) \left(R_x(\lambda_i) \vec{\Omega}_i + \dot{\vec{\lambda}}_i \right) + \left(R_x(\lambda_i) \vec{\Omega}_i + \dot{\vec{\lambda}}_i \right)^T \left(\frac{\partial}{\partial \vec{\lambda}_i} J'_r \right) \left(R_x(\lambda_i) \vec{\Omega}_i + \dot{\vec{\lambda}}_i \right) \right. \\ & \left. + \left(R_x(\lambda_i) \vec{\Omega}_i + \dot{\vec{\lambda}}_i \right) (J'_r) \left(\frac{\partial}{\partial \vec{\lambda}_i} R_x(\lambda_i) \right) \right] + \frac{1}{2} \dot{\vec{\lambda}}_i^T \left(\frac{\partial}{\partial \vec{\lambda}_i} J'_{ir} \right) \dot{\vec{\lambda}}_i \end{aligned} \quad (3.67)$$

Partial derivatives with respect to the chosen path variable, $\partial \vec{u} = \partial \vec{\lambda}_i$ in Eq:3.69, only act on rotation matrices $R_x(\lambda_i)$. For the partial derivative of a generalized rotation matrix $R_{\hat{u}}(\theta)$, whose equation is given by Eq:2.5, derived with respect to its angular operand $\partial \theta$:

$$\frac{\partial}{\partial \theta} R_{\hat{u}}(\theta) \triangleq [\hat{u}] \times R_{\hat{u}}(\theta) \quad (3.68a)$$

where $[\hat{u}] \times$ in Eq:3.68a is the cross product matrix from Eq:2.8c of the unit vector \hat{u} in the direction of the axis about which the rotation matrix applies its rotation. In the case of an \hat{X} axis rotation matrix, as in Eq:3.69, the expanded partial derivative is:

$$\frac{\partial}{\partial \vec{\lambda}_i} R_x(\lambda_i) \triangleq [\hat{1}] \times R_x(\lambda_i) = \begin{bmatrix} 0 & 0 & 0 \\ 0 & 0 & -1 \\ 0 & 1 & 0 \end{bmatrix} R_x(\lambda_i) \quad (3.68b)$$

Similarly, the same partial derivative of a rotation matrix transpose $R_x^T(\lambda_i)$ as follows:

$$\frac{\partial}{\partial \vec{\lambda}_i} R_x^T(\lambda_i) \triangleq -[\hat{1}] \times R_x^T(\lambda_i) = \begin{bmatrix} 0 & 0 & 0 \\ 0 & 0 & 1 \\ 0 & -1 & 0 \end{bmatrix} R_x^T(\lambda_i) \quad (3.68c)$$

Applying Eq:3.68 to the Lagrangian's partial derivative in Eq:3.69 reduces and simplifies:

$$\begin{aligned} \frac{\partial \mathcal{L}_{n/m}}{\partial \vec{u}} &= \frac{1}{2} \left[\left([\hat{i}] \times R_x(\lambda_i) \vec{\Omega}_i \right)^T \left(R_x(\lambda_i) (J_r) R_x^{-1}(\lambda_i) \right) \left(R_x(\lambda_i) \vec{\Omega}_i + \dot{\vec{\lambda}}_i \right) \right. \\ &\quad + \left(R_x(\lambda_i) \vec{\Omega}_i + \dot{\vec{\lambda}}_i \right)^T \left([\hat{i}] \times R_x(\lambda_i) (J_r) R_x^{-1}(\lambda_i) - R_x(\lambda_i) (J_r) [\hat{i}] \times R_x^{-1}(\lambda_i) \right) \left(R_x(\lambda_i) \vec{\Omega}_i + \dot{\vec{\lambda}}_i \right) \\ &\quad \left. + \left(R_x(\lambda_i) \vec{\Omega}_i + \dot{\vec{\lambda}}_i \right)^T \left(R_x(\lambda_i) (J_r) R_x^{-1}(\lambda_i) \right) \left([\hat{i}] \times R_x(\lambda_i) \vec{\Omega}_i \right) \right] \\ &\quad + \frac{1}{2} \dot{\vec{\lambda}}_i^T \left([\hat{i}] \times R_x(\lambda_i) (J_{ir}) R_x^{-1}(\lambda_i) - R_x(\lambda_i) (J_{ir}) [\hat{i}] \times R_x(\lambda_i) \right) \dot{\vec{\lambda}}_i = 0 \quad (3.69) \end{aligned}$$

Fortunately the quadratic form of kinetic energies included in Eq:3.65c resulted in symmetrical partial derivatives of rotation matrices in Eq:3.69 simplify out. After some mathematics it follows that partial derivatives of the Lagrangian in Eq:3.65 with respect to \vec{u} are negligible, or that $\partial \mathcal{L}_{n/m} / \partial \vec{u} = 0$. Only the partial derivatives with respect to the path rate $\dot{\vec{u}}$ remain:

$$\vec{U}(\lambda_i) = \frac{d}{dt} \left(\frac{\partial \mathcal{L}_{n/m}}{\partial \dot{\vec{u}}} \right) = \frac{d}{dt} \left((J'_r) \left(R_x(\lambda_i) \vec{\Omega}_i + \dot{\vec{\lambda}}_i \right) + (J'_{ir}) \dot{\vec{\lambda}}_i \right) \quad (3.70)$$

Transformed rates of change for inertias J'_r and J'_{ir} must first be defined before evaluating the simplified Lagrangian derivative in Eq:3.70. Derivatives of those inertias cannot be separated by time scale from the remainder of Eq:3.70 given that $\dot{\lambda}_i$ determines both inertia rates of change J'_r and J'_{ir} , but is also a component of the kinetic energy in Eq:3.65c.

In general for some transformed inertia J to be aligned relative to a frame \mathcal{F}^b where the inertia is originally defined with respect to a frame \mathcal{F}^a , if the two frames differ by some rotation angle θ about an Euler axis \hat{u} , the generalized rotation matrix from frame \mathcal{F}^a to \mathcal{F}^b is given by $R_{\hat{u}}(\theta)$ from Eq:2.7. The transformed inertia is then calculated as:

$$J' = R_{\hat{u}}(\theta)(J)R_{\hat{u}}^{-1}(\theta) \quad (3.71a)$$

which, from the product rule and the rotation matrix time derivative definition previously in Eq:2.8, has a rate of change as a result of the angular velocity $\dot{\theta}$:

$$\dot{J}' = \frac{d}{dt} \left(R_{\hat{u}}(\theta)(J)R_{\hat{u}}^{-1}(\theta) \right) \quad (3.71b)$$

$$= \frac{d}{dt} \left(R_{\hat{u}}(\theta)(J)R_{\hat{u}}^{-1}(\theta) + R_{\hat{u}}(\theta) \left(\frac{d}{dt}(J) \right) R_{\hat{u}}^{-1}(\theta) + R_{\hat{u}}(\theta)(J) \frac{d}{dt} \left(R_{\hat{u}}^{-1}(\theta) \right) \right) \quad (3.71c)$$

$$= [\dot{\vec{\theta}}] \times R_{\hat{u}}(\theta)(J)R_{\hat{u}}^{-1}(\theta) + R_{\hat{u}}(\theta)(\dot{J})R_{\hat{u}}^{-1}(\theta) - R_{\hat{u}}(\theta)(J)[\dot{\vec{\theta}}] \times R_{\hat{u}}^{-1}(\theta) \quad (3.71d)$$

where $\dot{\vec{\theta}} \triangleq \dot{\theta} \cdot \hat{u}$ is the projected angular velocity vector between the two frames. In most cases, the inertia will not be changing in its principle frame, or rather that $\dot{J} = 0$. Both the rotor assembly and inner ring inertias are constant in their principle frames. The transformed inertias then have the following derivatives; first for the rotor assembly:

$$J'_r = \frac{d}{dt} \left(R_x(\lambda_i)(J_r)R_x^{-1}(\lambda_i) \right) \quad (3.72a)$$

$$= [\dot{\vec{\lambda}}_i] \times R_x(\lambda_i)(J_r)R_x^{-1}(\lambda_i) - R_x(\lambda_i)(J_r)[\dot{\vec{\lambda}}_i] \times R_x^{-1}(\lambda_i) \quad (3.72b)$$

Similarly for the inner ring's transformed inertia rate J'_{ir} (again without the rotor's contribution):

$$J'_{ir} = \frac{d}{dt} \left(R_x(\lambda_i)(J_{ir})R_x^{-1}(\lambda_i) \right) \quad (3.73a)$$

$$= [\dot{\vec{\lambda}}_i] \times R_x(\lambda_i)(J_{ir})R_x^{-1}(\lambda_i) - R_x(\lambda_i)(J_{ir})[\dot{\vec{\lambda}}_i] \times R_x^{-1}(\lambda_i) \quad (3.73b)$$

Substituting those transformed inertia rates of change into Eq:3.70 and using Reynolds transportation theorem, Eq:3.5 for a vector's derivative in a rotating reference frame, the product rule then yields:

$$\frac{d}{dt} \left(\frac{\partial \mathcal{L}_{n/m}}{\partial \dot{\mathbf{u}}} \right) = \left[(J'_r) (R_x(\lambda_i) \vec{\Omega}_i + \dot{\lambda}_i) + (J'_r) R_x(\lambda_i) \dot{\vec{\Omega}}_i + \vec{\omega}_{r/m} \times (J'_r) R_x(\lambda_i) \vec{\Omega}_i + (J'_r) \ddot{\lambda}_i \right. \\ \left. + \vec{\omega}_{r/m} \times (J'_r) \dot{\lambda}_i \right] + \left[(J'_{ir}) \dot{\lambda}_i + (J'_{ir}) \ddot{\lambda}_i + \vec{\omega}_{n/m} \times (J'_{ir}) \dot{\lambda}_i \right] = \vec{\mathbf{U}}(\lambda_i) \quad (3.74)$$

Recombining inertial bodies with the same angular velocity ($J'_r + J'_{ir} = J'_n$) and recognizing that, from Eq:3.64 $\vec{\omega}_{n/m} = \dot{\lambda}_i$, the generalized net torque encountered by a $\Delta\lambda_i$ rotation is:

$$\vec{\mathbf{U}}(\lambda_i) = (J'_r) \vec{\Omega}'_i + (J'_r) \dot{\vec{\Omega}}'_i + \dot{\lambda}_i \times (J'_r) \vec{\Omega}'_i + (J'_n) \dot{\vec{\lambda}}_i + (J'_n) \ddot{\vec{\lambda}}_i + \dot{\lambda}_i \times (J'_n) \dot{\vec{\lambda}}_i = \vec{\tau}_\lambda(\lambda_i) \in \mathcal{F}^{M'_i} \quad (3.75a)$$

where both $\vec{\Omega}'_i$ and $\dot{\vec{\Omega}}'_i$ are the respective transformed rotational velocity and acceleration of the propeller in the middle ring frame:

$$\vec{\Omega}'_i \triangleq R_x(\lambda_i) \vec{\Omega}_i \in \mathcal{F}^{M'_i} \quad (3.75b)$$

$$\dot{\vec{\Omega}}'_i \triangleq \frac{d\vec{\Omega}}{dt} (R_x(\lambda_i) \vec{\Omega}_i) = R_x(\lambda) \dot{\vec{\Omega}}_i \in \mathcal{F}^{M'_i} \quad (3.75c)$$

The net torque response, $\vec{\tau}_\lambda(\lambda_i)$ from a $\Delta\lambda_i$ rotation, induced in the middle ring frame $\mathcal{F}^{M'_i}$, can be grouped into *inertia rates*, second order *inertia* and first order *gyroscopic* components:

$$\vec{\tau}_\lambda(\lambda_i) = \underbrace{(J'_r) \vec{\Omega}'_i + (J'_n) \dot{\vec{\lambda}}_i}_{\text{Inertia rates}} + \underbrace{(J'_r) \dot{\vec{\Omega}}'_i + (J'_n) \ddot{\vec{\lambda}}_i}_{\text{Inertia}} + \underbrace{\dot{\lambda}_i \times (J'_r) \vec{\Omega}'_i + \dot{\lambda}_i \times (J'_n) \dot{\vec{\lambda}}_i}_{\text{Gyroscopic}} \in \mathcal{F}^{M'_i} \quad (3.76)$$

Eq:3.76 represents the true torque response $\vec{\tau}_\lambda(\lambda_i)$. Later in control design $\hat{\tau}_\lambda(\lambda_i)$ is used for feedback compensation. The torque $\hat{\tau}_\lambda(\lambda_i)$ is a *modelled estimate* derived from state dynamics and could potentially contain modelling or estimation errors. Moreover, Eq:3.76 assumes instantaneous arguments for the actuator positions λ_i when in practice state estimates for $\hat{\lambda}_i$ are used which are subject to transfer functions from Sec:2.4.1.

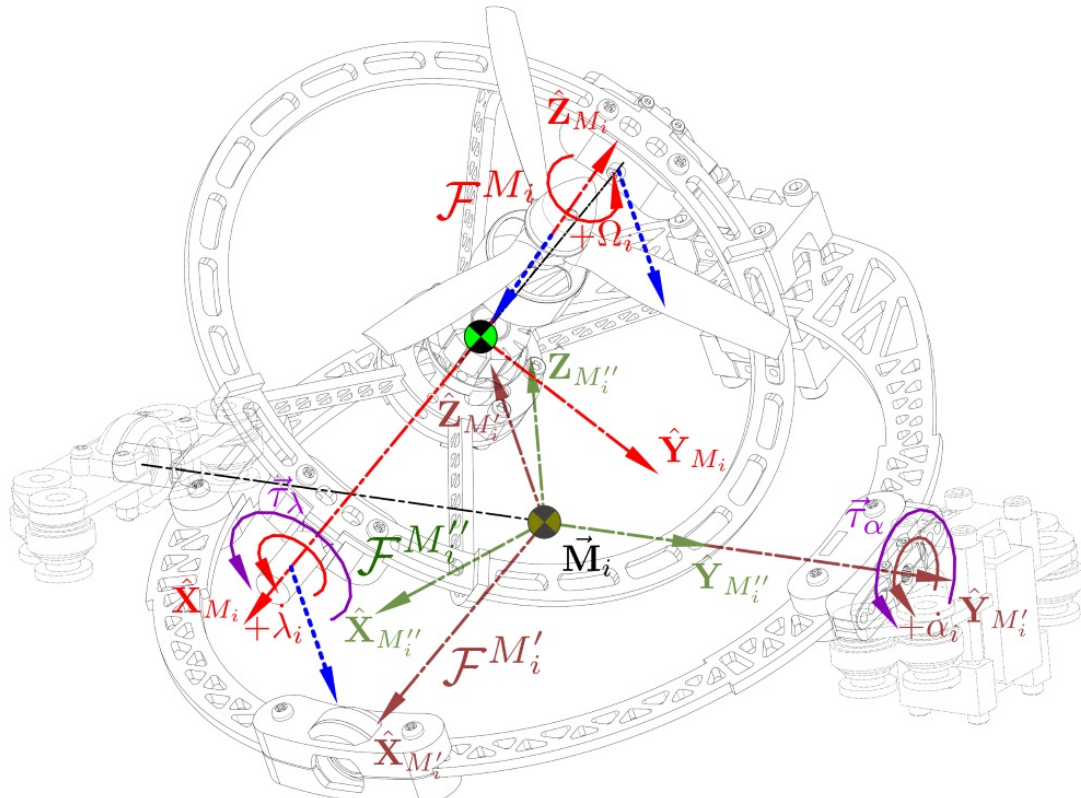


Figure 3.12: Exploded middle ring inertial bodies for $\vec{\tau}_\alpha(\lambda_i, \alpha_i)$

Similarly for the middle ring frame $\mathcal{F}^{M'_i}$ relative to the intermediary frame $\mathcal{F}^{M''_i}$, the only relative path variable is $\vec{v}(t) = [0 \quad \alpha_i \quad 0]^T$. The entire motor module's structure consists of three separate rotating bodies each with their own relative angular velocities; the *rotor* assembly, *inner* and *middle* ring structures (exploded in Fig:3.12).

Applying the same process to evaluate the α_i servo's response, the middle ring assembly Lagrangian $\mathcal{L}_{m/p}$ is constructed but with respect to the intermediary frame $\mathcal{F}^{M''_i}$. First transforming the inertias, the rotor assembly, further rotated by α_i about its $\hat{Y}_{M'_i}$ axis, has an inertia aligned with axes in $\mathcal{F}^{M''_i}$:

$$J''_r = R_y(\alpha_i)(J'_r)R_y^{-1}(\alpha_i) = R_y(\alpha_i)R_x(\lambda_i)(J_r)R_x^{-1}(\lambda_i)R_y^{-1}(\alpha_i) \quad (3.77a)$$

which has a time derivative \dot{J}''_r :

$$\dot{J}''_r = R_y(\alpha_i)(\dot{J}'_r)R_y^{-1}(\alpha_i) + [\dot{\vec{\alpha}}_i] \times R_y(\alpha_i)(J'_r)R_y^{-1}(\alpha_i) - R_y(\alpha_i)(J'_r)[\dot{\vec{\alpha}}_i] \times R_y^{-1}(\alpha_i) \quad (3.77b)$$

The inner ring structure has an inertia, still *without* including the rotor assembly, aligned with $\mathcal{F}^{M''_i}$:

$$J''_{ir} = R_y(\alpha_i)(J'_{ir})R_y^{-1}(\alpha_i) = R_y(\alpha_i)R_x(\lambda_i)(J_{ir})R_x^{-1}(\lambda_i)R_y^{-1}(\alpha_i) \quad (3.78a)$$

Similarly, the time derivative \dot{J}''_{ir} is:

$$\dot{J}''_{ir} = R_y(\alpha_i)(\dot{J}'_{ir})R_y^{-1}(\alpha_i) + [\dot{\vec{\alpha}}_i] \times R_y(\alpha_i)(J'_{ir})R_y^{-1}(\alpha_i) - R_y(\alpha_i)(J'_{ir})[\dot{\vec{\alpha}}] \times R_y^{-1}(\alpha_i) \quad (3.78b)$$

Finally the middle ring structure's inertia from Eq:2.24a, with neither the rotor's nor the inner ring's contributions:

$$J'_m = R_y(\alpha_i)(J_m)R_y^{-1}(\alpha_i) \quad (3.79a)$$

which, when using the collective motor module inertia J_p from Eq:2.24b, expands to:

$$J'_m = R_y(\alpha_i)(J_p)R_y^{-1}(\alpha_i) - R_y(\alpha_i)R_x(\lambda_i)(J_n)R_x^{-1}(\lambda_i)R_y^{-1}(\alpha_i) \quad (3.79b)$$

$$= J'_p - J''_n = J'_p - (J''_{ir} + J''_r) \quad (3.79c)$$

which has a time derivative purely as a result of $\dot{\alpha}$:

$$\dot{J}'_m = [\dot{\vec{\alpha}}_i] \times R_y(\alpha_i)(J_m)R_y^{-1}(\alpha_i) - R_y(\alpha_i)(J_m)[\dot{\vec{\alpha}}_i] \times R_y^{-1}(\alpha_i) \quad (3.79d)$$

The derivative \dot{J}'_m , using \dot{J}''_r and \dot{J}''_{ir} from Eq:3.77b and Eq:3.78b respectively, expands to:

$$\dot{J}'_m = [\dot{\vec{\alpha}}_i] \times R_y(\alpha_i)(J_p)R_y^{-1}(\alpha_i) - R_y(\alpha_i)(J_p)[\dot{\vec{\alpha}}_i] \times R_y^{-1}(\alpha_i) - (\dot{J}''_{ir} + \dot{J}''_r) \quad (3.79e)$$

Note that introducing the relations of Eq:3.79c and Eq:3.79e to the collective body inertia J_p simplifies the subsequent equations. Each body then has its own relative angular velocity with respect to the intermediate frame $\mathcal{F}^{M''_i}$. For the rotor $\vec{\omega}_{r/p}$ is the relative angular velocity of that assembly from the motor Ω_i and both inner and middle servo rates $\dot{\lambda}_i$ and $\dot{\alpha}_i$:

$$\vec{\omega}_{r/p} \triangleq R_y(\alpha_i)R_x(\lambda_i)\vec{\Omega}_i + R_y(\alpha_i)\dot{\vec{\lambda}}_i + \dot{\vec{\alpha}}_i \in \mathcal{F}^{M''_i} \quad (3.80a)$$

$$\therefore \vec{\omega}_{r/p} = \vec{\Omega}''_i + \dot{\vec{\lambda}}'_i + \dot{\vec{\alpha}}_i \quad (3.80b)$$

where $\vec{\Omega}''_i$ and $\dot{\vec{\lambda}}'_i$ are respectively propeller and inner servo velocities transformed to the frame $\mathcal{F}^{M''_i}$. Next, the inner ring has an angular velocity $\vec{\omega}_{n/p}$ relative to the intermediate frame $\mathcal{F}^{M''_i}$ from the two servo rates $\dot{\lambda}_i$ and $\dot{\alpha}_i$:

$$\vec{\omega}_{n/p} \triangleq R_y(\alpha_i)\dot{\vec{\lambda}}_i + \dot{\vec{\alpha}}_i = \dot{\vec{\lambda}}'_i + \dot{\vec{\alpha}}_i \in \mathcal{F}^{M''_i} \quad (3.81)$$

Lastly, the middle ring body has an angular velocity $\vec{\omega}_{m/p}$ relative to the intermediary frame only as a result of the middle ring's servo velocity $\dot{\alpha}_i$:

$$\vec{\omega}_{m/p} \triangleq \dot{\vec{\alpha}}_i \in \mathcal{F}^{M''_i} \quad (3.82)$$

Using the relative path coordinate $\vec{v}(t)$, the Lagrangian $\mathcal{L}_{m/p}$ can be constructed for the complete motor module relative to the intermediate frame $\mathcal{F}^{M''}$ with kinetic energies of the rotor assembly, inner and middle ring structures respectively:

$$\mathcal{L}_{m/p} = \frac{1}{2} \vec{\omega}_{r/p}^T (J_r'') \vec{\omega}_{r/p} + \frac{1}{2} \vec{\omega}_{n/p}^T (J_{ir}'') \vec{\omega}_{n/p} + \frac{1}{2} \vec{\omega}_{m/p}^T (J_m') \vec{\omega}_{m/p} \quad (3.83)$$

where Eq:3.83 again does not include any potential energy gravitational contributions because such quantities are incorporated in Eq:2.35d. The middle ring's Lagrangian $\mathcal{L}_{m/p}$ from Eq:3.83 therefore expands to:

$$\begin{aligned} \mathcal{L}_{m/p} = & \frac{1}{2} \left[R_y(\alpha_i) R_x(\lambda_i) \vec{\Omega}_i + R_y(\alpha_i) \dot{\vec{\lambda}}_i + \dot{\vec{\alpha}}_i \right]^T (J_r'') \left[R_y(\alpha_i) R_x(\lambda_i) \vec{\Omega}_i + R_y(\alpha_i) \dot{\vec{\lambda}}_i + \dot{\vec{\alpha}}_i \right] \\ & + \frac{1}{2} \left[R_y(\alpha_i) \dot{\vec{\lambda}}_i + \dot{\vec{\alpha}}_i \right]^T (J_{ir}'') \left[R_y(\alpha_i) \dot{\vec{\lambda}}_i + \dot{\vec{\alpha}}_i \right] + \frac{1}{2} \dot{\vec{\alpha}}_i^T (J_m') \dot{\vec{\alpha}}_i \end{aligned} \quad (3.84)$$

Extending the path coordinate partial derivative reduction from Eq:3.69, the Euler-Lagrange formulation for the middle ring then simplifies with the partial derivative $\partial \mathcal{L}_{m/p} / \partial \vec{v} = 0$. So the generalized forces (torques) $\vec{V}(\lambda_i, \alpha_i)$ acting on the middle ring are:

$$\vec{V}(\lambda_i, \alpha_i) = \frac{d}{dt} \left(\frac{\partial \mathcal{L}_{m/p}}{\partial \dot{\vec{v}}} \right) - \frac{\partial \mathcal{L}_{m/p}}{\partial \vec{v}} = \frac{d}{dt} \left(\frac{\partial \mathcal{L}_{m/p}}{\partial \vec{v}} \right) \in \mathcal{F}^{M''} \quad (3.85)$$

Finding the partial derivative of $\mathcal{L}_{m/p}$ in Eq:3.84 with respect to the middle ring servo's relative path coordinate rate $\dot{\vec{v}}$ yields:

$$\frac{\partial \mathcal{L}_{m/p}}{\partial \dot{\vec{v}}} = (J_r'') \left[\vec{\Omega}_i'' + \dot{\vec{\lambda}}_i' + \dot{\vec{\alpha}}_i \right] + (J_{ir}'') \left[\dot{\vec{\lambda}}_i' + \dot{\vec{\alpha}}_i \right] + (J_m') \dot{\vec{\alpha}}_i \quad (3.86a)$$

which with relative rotor, inner and middle ring angular velocity definitions from Eq:3.80,3.81 and 3.82 respectively, expands to:

$$\frac{\partial \mathcal{L}_{m/p}}{\partial \dot{\vec{v}}} = (J_r'') \left[R_y(\alpha_i) R_x(\lambda_i) \vec{\Omega}_i + R_y(\alpha_i) \dot{\vec{\lambda}}_i + \dot{\vec{\alpha}}_i \right] + (J_{ir}'') \left[R_y(\alpha_i) \dot{\vec{\lambda}}_i + \dot{\vec{\alpha}}_i \right] + (J_m') \dot{\vec{\alpha}}_i \quad (3.86b)$$

Taking the time derivative of Eq:3.86b and using inertia rates for rotor, inner and middle rings each defined in Eq:3.77b,3.78b and 3.79e respectively, split into product ruled derivative components gives:

$$\begin{aligned} \vec{V}(\lambda_i, \alpha_i) = & \frac{d}{dt} \left(\frac{\partial \mathcal{L}_{m/p}}{\partial \dot{\vec{v}}} \right) = \left[(J_r'') (\vec{\Omega}_i'' + \dot{\vec{\lambda}}_i' + \dot{\vec{\alpha}}_i) \right] \\ & + \left[(J_r'') \dot{\vec{\Omega}}_i'' + \vec{\omega}_{n/p} \times (J_r'') \vec{\Omega}_i'' + (J_r'') \ddot{\vec{\lambda}}_i' + \vec{\omega}_{n/p} \times (J_r'') \dot{\vec{\lambda}}_i' + (J_r'') \ddot{\vec{\alpha}}_i + \vec{\omega}_{m/p} \times (J_r'') \dot{\vec{\alpha}}_i \right] \\ & + \left[(J_{ir}'') (\dot{\vec{\lambda}}_i' + \dot{\vec{\alpha}}_i) \right] + \left[(J_{ir}'') \ddot{\vec{\lambda}}_i' + \vec{\omega}_{n/p} \times (J_{ir}'') \dot{\vec{\lambda}}_i' + (J_{ir}'') \ddot{\vec{\alpha}}_i + \vec{\omega}_{m/p} \times (J_{ir}'') \dot{\vec{\alpha}}_i \right] \\ & + \left[(J_m') \dot{\vec{\alpha}}_i \right] + \left[(J_m') \ddot{\vec{\alpha}}_i + \vec{\omega}_{m/p} \times (J_m') \dot{\vec{\alpha}}_i \right] \end{aligned} \quad (3.86c)$$

with relative frame angular velocities; $\vec{\omega}_{n/p}$ of the inner ring relative to the intermediate frame, and $\vec{\omega}_{m/p}$ of the middle ring relative to the intermediate frame. Both are defined respectively:

$$\vec{\omega}_{n/p} \triangleq R_y(\alpha_i) \dot{\vec{\lambda}}_i + \dot{\vec{\alpha}}_i = \dot{\vec{\lambda}}_i' + \dot{\vec{\alpha}}_i \in \mathcal{F}^{M''} \quad (3.86d)$$

$$\vec{\omega}_{m/p} \triangleq \dot{\vec{\alpha}}_i \in \mathcal{F}^{M''} \quad (3.86e)$$

Eq:3.86c is an ominous and decidedly complicated result to expand and make sense of. However it can be simplified by recognizing that generalized torques for the middle ring in Eq:3.86c contain inner ring kinetic energies already introduced in Eq:3.76, but transformed to the frame $\mathcal{F}^{M''}$.

After some mathematics, Eq:3.86c can be simplified into two parts; responses pertinent to $\Delta\alpha_i$ and the transformed inner ring generalized response $R_y(\alpha_i)\vec{\tau}_\lambda(\lambda_i)$:

$$\begin{aligned}\vec{\mathbf{V}}(\lambda_i, \alpha_i) &= R_y(\alpha_i) \frac{d}{dt} \left(\frac{\partial \mathcal{L}_{n/m}}{\partial \dot{\mathbf{u}}} \right) + \left(R_y(\alpha_i)(\dot{J}'_r) R_y^{-1}(\alpha_i) \right) \dot{\alpha}_i + \left(\dot{J}''_r - R_y(\alpha_i)(\dot{J}'_r) R_y^{-1}(\alpha_i) \right) (\vec{\Omega}''_i + \dot{\lambda}'_i + \dot{\alpha}_i) \\ &+ (\dot{J}''_r) \ddot{\alpha}_i + \dot{\alpha}_i \times (\dot{J}''_r) \left(\vec{\Omega}''_i + \dot{\lambda}'_i + \dot{\alpha}_i \right) + \left(R_y(\alpha_i)(\dot{J}'_{ir}) R_y^{-1}(\alpha_i) \right) \dot{\alpha}_i + \left(\dot{J}''_{ir} - R_y(\alpha_i)(\dot{J}'_{ir}) R_y^{-1}(\alpha_i) \right) (\dot{\lambda}'_i + \dot{\alpha}_i) \\ &+ (\dot{J}''_{ir}) \ddot{\alpha}_i + \dot{\alpha}_i \times (\dot{J}''_{ir}) \left(\dot{\lambda}'_i + \dot{\alpha}_i \right) + (\dot{J}'_m) \dot{\alpha}_i + (\dot{J}'_m) \ddot{\alpha}_i + \dot{\alpha}_i \times (\dot{J}'_m) \dot{\alpha}_i \quad (3.86f)\end{aligned}$$

paying special attention to differentiate \dot{J}''_r and \dot{J}''_{ir} from Eq:3.77b and Eq:3.78b respectively with $R_y(\alpha_i)(\dot{J}'_r) R_y^{-1}(\alpha_i)$ and $R_y(\alpha_i)(\dot{J}'_{ir}) R_y^{-1}(\alpha_i)$, where the latter two terms are inertia rates of change from Eq:3.72 and Eq:3.73, but transformed to the frame $\mathcal{F}^{M''_i}$.

Generalized torques in Eq:3.86f can be further simplified by introducing combined inertial bodies $J_n = J_r + J_{ir}$ for the *entire* inner ring from Eq:2.21 and $J_p = J_m + R_x(\lambda_i)(J_n) R_x^{-1}(\lambda_i)$ for the *entire* motor module's inertia from Eq:2.24b. Using $J'_p = R_y(\alpha_i)(J_p) R_y^{-1}(\alpha_i)$ and $J'_n = R_y(\alpha_i)(J_n) R_y^{-1}(\alpha_i)$ for the net module's inertia and the entire inner ring inertia, both respectively aligned with the frame $\mathcal{F}^{M''_i}$:

$$\begin{aligned}\vec{\mathbf{V}}(\lambda_i, \alpha_i) &= R_y(\alpha_i) \vec{\mathbf{U}}(\lambda_i) + \left(R_y(\alpha_i)(\dot{J}'_n) R_y(\alpha_i) \right) \dot{\alpha}_i + \left(\dot{J}'_p - R_y(\alpha_i)(\dot{J}_p) R_y^{-1}(\alpha_i) \right) \dot{\alpha}_i \\ &+ \left(\dot{J}''_n - R_y(\alpha_i)(\dot{J}'_n) R_y^{-1}(\alpha_i) \right) \dot{\lambda}'_i + \left(\dot{J}''_r - R_y(\alpha_i)(\dot{J}'_r) R_y^{-1}(\alpha_i) \right) \vec{\Omega}''_i \\ &+ J'_p \ddot{\alpha}_i + \dot{\alpha}_i \times \left((J'_p) \dot{\alpha}_i + (J''_n) \dot{\lambda}'_i + (J''_r) \vec{\Omega}''_i \right) \quad (3.86g)\end{aligned}$$

Noting that $\dot{J}_p = \dot{J}'_r + \dot{J}'_{ir} + \dot{J}_m$ and that $\dot{J}_m = 0$, it follows that $\dot{J}_p = \dot{J}'_n$. Isolating the servo's torque response from $\Delta\alpha_i$, and again grouping inertial bodies with shared angular velocities together, the *inertia rates*, second order *inertia* and first order *gyroscopic* responses are then:

$$\begin{aligned}\vec{\tau}_\alpha(\lambda_i, \alpha_i) &= \underbrace{\left(\dot{J}'_p \dot{\alpha}_i + \left(\dot{J}''_n - R_y(\alpha)(\dot{J}'_n) R_y^{-1}(\alpha) \right) \dot{\lambda}'_i + \left(\dot{J}''_r - R_y(\alpha)(\dot{J}'_r) R_y^{-1}(\alpha) \right) \vec{\Omega}''_i \right)}_{\text{Inertia rates}} \\ &+ \underbrace{\left(J'_p \ddot{\alpha}_i + \dot{\alpha}_i \times \left((J'_p) \dot{\alpha}_i + (J''_n) \dot{\lambda}'_i + (J''_r) \vec{\Omega}''_i \right) \right)}_{\text{Inertia Gyroscopic}} \quad \in \mathcal{F}^{M''_i} \quad (3.87)\end{aligned}$$

It is important to stress that the servo's response $\vec{\tau}_\alpha(\lambda_i, \alpha_i)$ is **not** the same as the generalized torque $\vec{\mathbf{V}}(\lambda_i, \alpha_i)$ described in Eq:3.86g. The latter contains terms for the inner ring's servo response. Careful inspection could have yielded the inertia and gyroscopic components of both Eq:3.76 and Eq:3.87, however the effect of inertia time derivatives on the torque system is a far less obvious result. Each servo's respective induced torques, $\vec{\tau}_\lambda(\lambda_i)$ and $\vec{\tau}_\alpha(\lambda_i, \alpha_i)$, occur in sequential gimbal-like frames. The opposing negative responses to induced relative rotations effect the angular state dynamics in Eq:3.10d, and must be transformed to the common body frame:

$$\vec{\tau}_Q(u) = - \sum_{i=1}^4 \left(R_z(\sigma_i) R_y(\alpha_i) \vec{\tau}_\lambda(\lambda_i) + R_z(\sigma_i) \vec{\tau}_\alpha(\alpha_i, \lambda_i) \right) \quad \in \mathcal{F}^b \quad (3.88a)$$

$$= - \sum_{i=1}^4 R_z(\sigma_i) \vec{\mathbf{V}}(\lambda_i, \alpha_i) \quad (3.88b)$$

The final non-trivial torque term associated with the multibody motion which must be accounted for is the entire system's response to motion relative to the inertial frame \mathcal{F}^I , specifically considering the responses relative rotations $\Delta\lambda_i$ and $\Delta\alpha_i$ have to the net angular velocity of the entire multibody system $\vec{\omega}_b$. Such responses are an extension of the fundamental rigid 6-DOF differential equation for angular motion, reiterated from Eq:3.61:

$$\dot{\vec{\omega}}_b = (J_b^{-1}) \left(-\vec{\omega}_b \times (J_b) \vec{\omega}_b + \vec{\tau}_\mu \right) \quad \in \mathcal{F}^b \quad (3.89)$$

Before continuing with a Lagrangian formulation applied to the entire multibody vehicle, it is worth first establishing an axiom to add some clarity to the steps which follow. Consider the hypothetical rotating, non-Newtonian 2-D system illustrated in Fig:3.13.

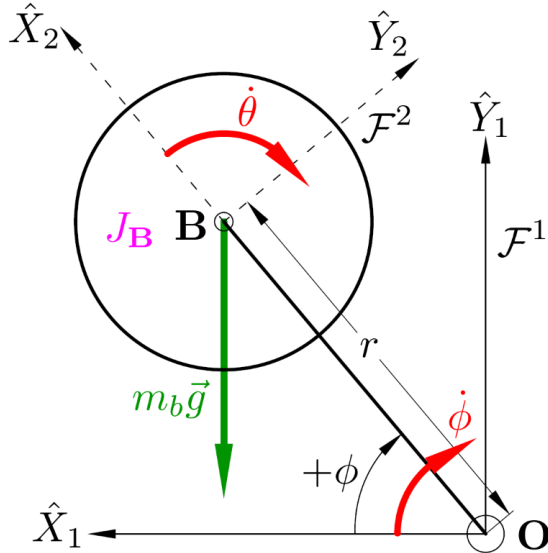


Figure 3.13: Rotating system

A massless rod of length r connects some rotational body, with a mass m_b , at point **B** to a center pivot point **O**. The principle frame \mathcal{F}^1 has axes \hat{X}_1 and \hat{Y}_1 as illustrated. The arm has a rotational velocity $\dot{\phi}$ relative to \hat{X}_1 in \mathcal{F}^1 , applied by some “motor”. Attached to the end of the rod is a secondary frame \mathcal{F}^2 with an \hat{X}_2 axis, co-linear to the rod and a perpendicular \hat{Y}_2 . The rotational body, centered at point **B**, has a rotational inertia J_B about the point (or axis) at **B**. That rotating body has a rotational velocity $\dot{\theta}$ from another “motor” relative to \mathcal{F}^2 . The question is then how to find the net torque applied to the system about point **O** in terms of angular velocities $\dot{\phi}$ and $\dot{\theta}$ and their derivatives (or accelerations)?

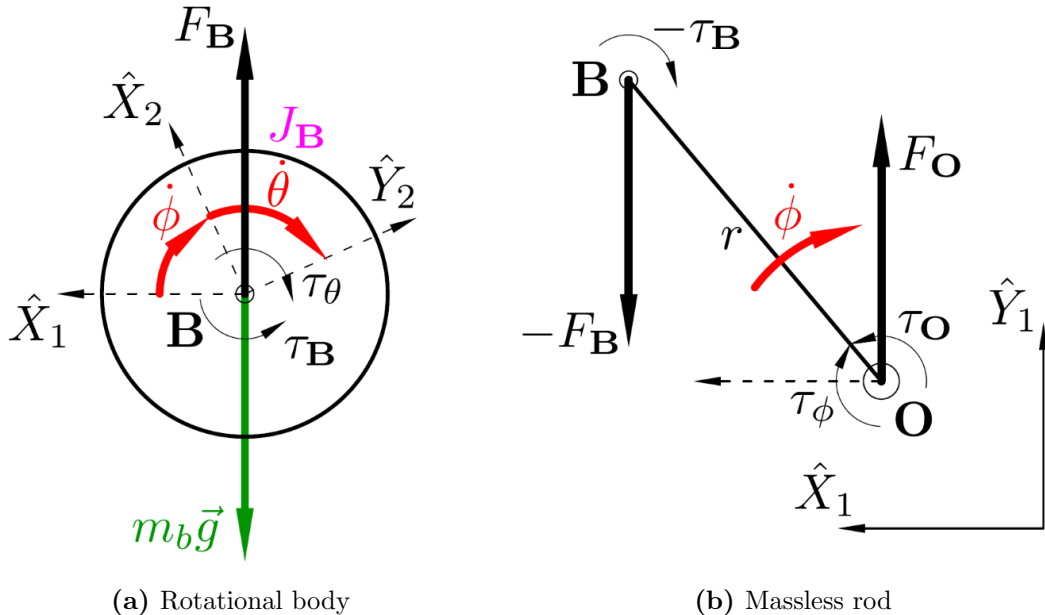


Figure 3.14: Free-body diagram for rotational system

Isolated free body diagrams for each body under consideration are illustrated in Fig:3.14. Considering the rotational body only (Fig:3.14a), the torque acting about point **B** is simply an inertia response to combined angular accelerations of $\dot{\theta}$ and $\ddot{\theta}$:

$$\tau_B = -\tau_\theta = -J_B(\ddot{\theta} + \ddot{\phi}) \quad \in \mathcal{F}^2 \quad (3.90)$$

The net force acting on the rotational body is purely the gravitational force acting through point **B** as a result of the mass m_b and some gravitational force vector $\vec{g} \in \mathcal{F}^2$:

$$F_{\mathbf{B}} = -G = -m_b \vec{g} \quad \in \mathcal{F}^2 \quad (3.91)$$

That torque and force pair, $F_{\mathbf{B}}$ and $\tau_{\mathbf{B}}$, are transferred to frame \mathcal{F}^1 through the massless rod connecting point **B** to **O**, Fig:3.14b. The net torque acting around point **O** is then comprised of three components; inferred torque from $\tau_{\mathbf{B}}$, a torque arm from force $F_{\mathbf{B}}$, and an inertia torque response to the effective “point-mass” at point **B** relative to **O**:

$$\tau_{\mathbf{O}} = -\tau_{\phi} = -\tau_{\mathbf{B}} - F_{\mathbf{B}}r \cos \phi + m_b r^2 (\ddot{\phi}) \quad \in \mathcal{F}^1 \quad (3.92)$$

The net response force acting at point **O**, $F_{\mathbf{O}}$, is of no consequence to the calculation of net torques. The “motor” applies a torque τ_{ϕ} to the rod to induce some angular acceleration $\ddot{\phi}$ on the whole system. Opposed to that angular acceleration is the torque $\tau_{\mathbf{O}}$ which acts against that rotation. The torque τ_{ϕ} acting on the system can then be simplified:

$$\tau_{\phi} = J_{\mathbf{B}}(\ddot{\theta} + \ddot{\phi}) + m_b r^2 (\ddot{\phi}) - m_b \vec{g} r \cos \phi \quad \in \mathcal{F}^1 \quad (3.93)$$

That result would not be as obvious when inferred from an energy equation. The equivalent Lagrangian for net kinetic and potential energy of the system, T and U respectively relative to \mathcal{F}^1 , would be:

$$\mathcal{L} = T(\theta, \phi) - U(\theta, \phi) \quad (3.94a)$$

$$\mathcal{L} = \frac{1}{2} \vec{\omega}_{\mathbf{B}}^T (J_{\mathbf{B}}) \vec{\omega}_{\mathbf{B}} + \frac{1}{2} \vec{\omega}_{\mathbf{O}}^T (J_{\mathbf{O}}) \vec{\omega}_{\mathbf{O}} - m_b \vec{g} r \sin \phi \quad (3.94b)$$

where $\vec{\omega}_{\mathbf{B}}$ and $\vec{\omega}_{\mathbf{O}}$ are net angular velocities of the rotational body and massless connection rod respectively. The important thing to consider is that $J_{\mathbf{O}}$, the net rotational inertia about the point **O**, is simply the point mass inertia $m_b r^2$ and not the expected parallel axis theorem $J_{\mathbf{O}} \neq J'_{\mathbf{B}} = J_{\mathbf{B}} + m_b r^2$. Expanding Eq:3.94b and applying the Euler-Lagrange formulation, using a partial derivative with respect to the path coordinate ϕ to produce the generalized torque τ_{ϕ} acting on the system:

$$\mathcal{L} = \frac{1}{2} (\dot{\theta} + \dot{\phi})^T (J_{\mathbf{B}}) (\dot{\theta} + \dot{\phi}) + (\dot{\phi}) (m_b r^2) (\dot{\phi}) - m_b (-g) r \sin \phi \quad (3.94c)$$

$$\text{Generalized forces} = \frac{d}{dt} \left(\frac{\partial \mathcal{L}}{\partial \dot{\phi}} \right) - \frac{\partial \mathcal{L}}{\partial \phi} = \vec{\tau}_{\phi} \quad (3.94d)$$

$$= \frac{d}{dt} \left((J_{\mathbf{B}}) (\dot{\theta} + \dot{\phi}) + (m_b r^2) (\dot{\phi}) \right) - m_b g r \cos \phi \quad (3.94e)$$

$$\therefore \tau_{\phi} = J_{\mathbf{B}}(\ddot{\theta} + \ddot{\phi}) + m_b r^2 (\ddot{\phi}) - m_b g r \cos \phi \quad (3.94f)$$

$$= J_{\mathbf{B}} \ddot{\theta} + J'_{\mathbf{B}} \ddot{\phi} + \tau_g \quad (3.94g)$$

where $J'_{\mathbf{B}}$ is the **parallel axis inertia** and τ_g is the gravitational torque arm contribution. The above then leads to the claim asserted from the system described in Fig:3.13:

Axiom 3.4.0.1. *A torque response opposed to angular acceleration of a doubly rotating body can be found as the contribution of the principle rotational inertia about the first axis of rotation with only the first rotational acceleration and a parallel axis inertia about the second rotational axis with the second, independent rotational acceleration. (The same torque can be found as the inertial opposition to net angular acceleration, the sum of both rotations, about the first axis and a point mass inertia opposed to the second rotation about its respective axis.)*

Returning to the net multibody system and separating the motor module from the entire body structure first (exploded bodies for *motor module 1* in Fig:3.15), only the additional contribution which the angular velocity $\vec{\omega}_b$ has on a single motor module is considered, and later introduced to the entire combined system. The Lagrangian derivation for motion relative to the inertial frame then follows.

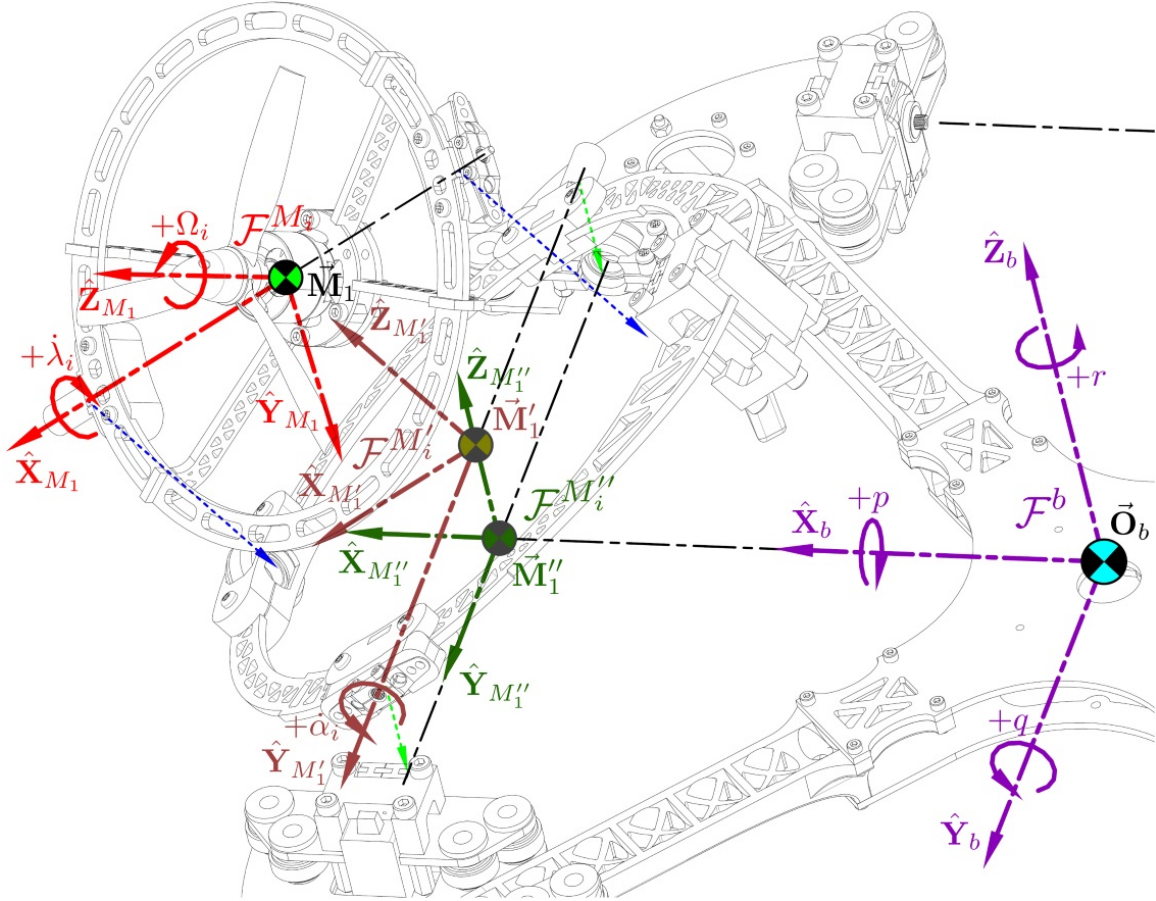


Figure 3.15: Exploded motor module inertial bodies for $\vec{\omega}_b$ response

The relative $\hat{Z}_{M''_i}$ rotation by σ_i is what differentiates the intermediate frame $\mathcal{F}^{M''}_i$ (used for calculations pertinent to Fig:3.12) and the body frame \mathcal{F}^b . The familiar rotor assembly, inner and middle ring structure's inertias from Eq:3.77a,3.78a and 3.79a have respective counterparts aligned with \mathcal{F}^b :

$$J_r''' = R_z(\sigma_i)(J_r'')R_z^{-1}(\sigma_i) = R_z(\sigma_i)R_y(\alpha_i)R_x(\lambda_i)(J_r)R_x^{-1}(\lambda_i)R_y^{-1}(\alpha_i)R_z^{-1}(\sigma_i) \quad (3.95a)$$

$$J_{ir}''' = R_z(\sigma_i)(J_{ir}'')R_z^{-1}(\sigma_i) = R_z(\sigma_i)R_y(\alpha_i)R_x(\lambda_i)(J_{ir})R_x^{-1}(\lambda_i)R_y^{-1}(\alpha_i)R_z^{-1}(\sigma_i) \quad (3.95b)$$

$$J_m'' = R_z(\sigma_i)(J_m')R_z^{-1}(\sigma_i) = R_z(\sigma_i)R_y(\alpha_i)(J_m)R_y^{-1}(\alpha_i)R_z^{-1}(\sigma_i) \quad (3.95c)$$

where σ_i in Eq:3.95 is the relative orthogonal $\hat{Z}_{M''_i}$ difference between frames $\mathcal{F}^{M''}_i$ and \mathcal{F}^b defined before in Eq:2.16 and illustrated previously in Fig:2.9. Because σ_i is constant for each $i \in [1 : 4]$, inertia rates for each component of the motor module are simply the transformations of $\dot{J}_r'', \dot{J}_{ir}''$ and \dot{J}_m' previously in Eq:3.77b,3.78b and 3.79e. Or more generally, for some inertia J constant in $\mathcal{F}^{M''}_i$, that inertia's rate in \mathcal{F}^b is:

$$\frac{d}{dt} \left(R_z(\sigma_i)(J)R_z^{-1}(\sigma_i) \right) = 0 \quad (3.96a)$$

Dropping the σ_i argument to indicate $R_z(\sigma_i)$ is a constant, the rotor, inner and middle inertia rates of change relative to the body frame \mathcal{F}^b then follow respectively:

$$\dot{J}_r''' = R_z(\dot{J}_r'')R_z^{-1} \quad (3.96b)$$

$$\dot{J}_{ir}''' = R_z(\dot{J}_{ir}'')R_z^{-1} \quad (3.96c)$$

$$\dot{J}_m'' = R_z(\dot{J}_m')R_z^{-1} \quad (3.96d)$$

Similarly, angular velocities for each separate body (rotor, inner and middle rings) in \mathcal{F}^b but relative to the inertial frame \mathcal{F}^I are; first for the rotor:

$$\vec{\omega}_r/I = \vec{\Omega}_i''' + \dot{\lambda}_i'' + \dot{\alpha}_i' + \vec{\omega}_{b/I} \in \mathcal{F}^b \quad (3.97a)$$

$$= R_z R_y(\alpha_i) R_x(\lambda_i) \vec{\Omega}_i + R_z R_y(\alpha_i) \dot{\lambda}_i + R_z \dot{\alpha}_i + \vec{\omega}_b \quad (3.97b)$$

Extending that to the inner ring's rotational velocity:

$$\vec{\omega}_{n/I} = \dot{\lambda}_i'' + \dot{\alpha}'_i + \vec{\omega}_{b/I} \in \mathcal{F}^b \quad (3.98a)$$

$$= R_z R_y(\alpha_i) \dot{\lambda}_i + R_z \dot{\alpha}_i + \vec{\omega}_{b/I} \quad (3.98b)$$

Lastly the middle ring structure has a relative angular rate:

$$\vec{\omega}_{m/I} = \dot{\alpha}'_i + \vec{\omega}_{b/I} \in \mathcal{F}^b \quad (3.99a)$$

$$= R_z \dot{\alpha}_i + \vec{\omega}_b \quad (3.99b)$$

Note that Axiom:3.4.0.1 and the parallel axis term in Eq:3.94g refer to the parallel axis difference between the *center of mass* and the resultant rotational axis. The vector difference between the rotated center of mass for a motor module $\vec{C}_p''(\lambda_i, \alpha_i)$ and the body frame origin \vec{O}_b is defined:

$$\vec{C}_p''(\lambda_i, \alpha_i) = \frac{m_n \vec{C}_n'''(\lambda_i, \alpha_i) + m_m \vec{C}_m''(\alpha_i)}{m_p} \quad (3.100a)$$

with $\vec{C}_n'''(\lambda_i, \alpha_i)$ and $\vec{C}_m''(\alpha_i)$ being rotated inner and middle ring centers of mass respectively from Eq:2.29d and Eq:2.30d:

$$\vec{C}_p''(\lambda_i, \alpha_i) = \frac{m_n R_z R_y(\alpha_i) R_x(\lambda_i) \vec{C}_n + m_m R_z R_y(\alpha_i) \vec{C}_m}{m_n + m_m} \quad (3.100b)$$

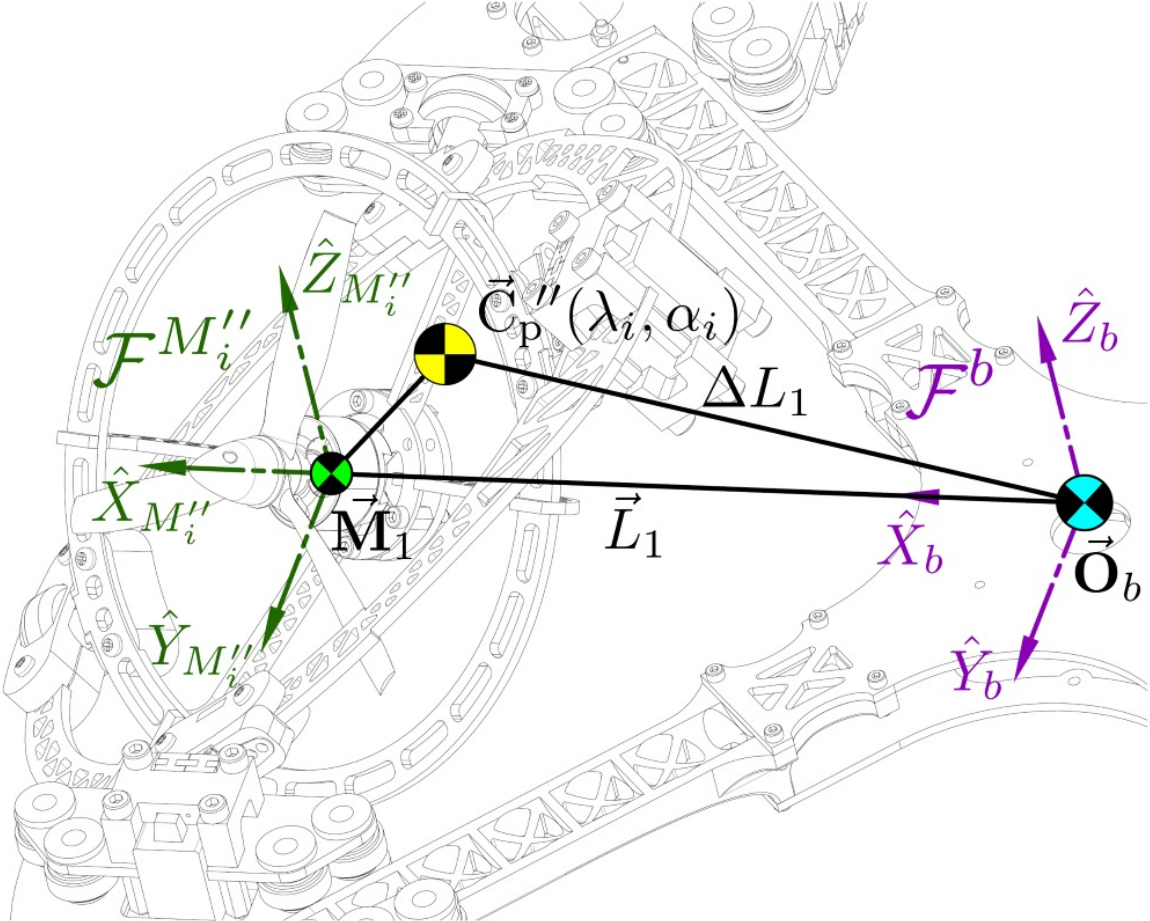


Figure 3.16: Illustration of rotated center of gravity $\vec{C}_p''(\lambda_i, \alpha_i)$

This leads to the vector difference $\Delta \vec{L}_i$, with $L = 196.15$ mm illustrated for module 1 in Fig:3.16.

$$\Delta \vec{L}_i = \vec{L}_i + \vec{C}_p''(\lambda_i, \alpha_i) \quad (3.100c)$$

The time derivative of that module's moving center of gravity, $d/dt(\vec{C}_p''(\lambda_i, \alpha_i))$ relative to the origin $\vec{\mathbf{O}}_b$, is:

$$\Delta\dot{\vec{L}}_i = \frac{d}{dt}(\vec{C}_p''(\lambda_i, \alpha_i)) \quad (3.100d)$$

$$\begin{aligned} &= \frac{1}{m_p} \left(m_n (R_z([\dot{\alpha}_i] \times R_y(\alpha_i) R_x(\lambda_i) \vec{C}_n + R_y(\alpha_i) [\dot{\lambda}_i] \times R_x(\lambda_i) \vec{C}_n) \right. \\ &\quad \left. + m_m R_z[\dot{\alpha}_i] \times R_y(\alpha_i) \vec{C}_m) \right) \end{aligned} \quad (3.100e)$$

Then, from Axiom:3.4.0.1 and the parallel axis theorem, the motor module's *point-mass* inertia J_H about the origin $\vec{\mathbf{O}}_b$ is defined, with net motor module mass $m_p = m_n + m_m$, using masses m_n and m_m from Eq:2.29a and Eq:2.30a:

$$J_H \triangleq m_p ((\Delta\vec{L}_i \cdot \Delta\vec{L}_i) \mathbb{I}_{3 \times 3} - \Delta\vec{L}_i \otimes \Delta\vec{L}_i) \quad (3.101a)$$

Or using the inner and outer products matrix definitions:

$$J_H = m_p ([\Delta\vec{L}_i]^T [\Delta\vec{L}_i] - [\Delta\vec{L}_i] [\Delta\vec{L}_i]^T) \quad (3.101b)$$

which leads to the point mass' inertia rate of change $d/dt(J_H)$:

$$\dot{J}_H = m_p ([\Delta\dot{\vec{L}}_i]^T [\Delta\vec{L}_i] + [\Delta\vec{L}_i]^T [\Delta\dot{\vec{L}}_i] - [\Delta\dot{\vec{L}}_i] [\Delta\vec{L}_i]^T - [\Delta\vec{L}_i] [\Delta\dot{\vec{L}}_i]^T) \quad (3.101c)$$

Unfortunately the rate of change of inertia, \dot{J}_H in Eq:3.101c, cannot be simplified further to a more concise form. The Lagrangian $\mathcal{L}_{p/I}$ for the energy of a single motor module about the origin $\vec{\mathbf{O}}_b$ can then be constructed, this time *including* the gravitational potential energy component:

$$\begin{aligned} \mathcal{L}_{p/I} = & \frac{1}{2} \vec{\omega}_{r/I}^T (J_r''') \vec{\omega}_{r/I} + \frac{1}{2} \vec{\omega}_{n/I}^T (J_{ir}''') \vec{\omega}_{n/I} + \frac{1}{2} \vec{\omega}_{m/I}^T (J_m'') \vec{\omega}_{m/I} + \vec{\omega}_{b/I}^T (J_H) \vec{\omega}_{b/I} \\ & + m_p \vec{G}_b \cdot (R_I^b(\eta) \vec{\mathcal{E}}_I + \Delta\vec{L}_i) \end{aligned} \quad (3.102)$$

where the term $m_p \vec{G}_b \cdot (R_I^b(\eta) \vec{\mathcal{E}}_I + \Delta\vec{L}_i)$ is the vector analogue of gravitational potential energy mgh with $R_I^b(\eta) \vec{\mathcal{E}}_I$ being the relative XYZ inertial frame position in the body frame \mathcal{F}^b relative to the body origin $\vec{\mathbf{O}}_b$. Expanding $\mathcal{L}_{p/I}$ with terms defined previously:

$$\begin{aligned} \mathcal{L}_{p/I} = & \left[\vec{\Omega}_i''' + \dot{\lambda}_i'' + \dot{\alpha}_i' + \vec{\omega}_b \right]^T (J_r''') \left[\vec{\Omega}_i''' + \dot{\lambda}_i'' + \dot{\alpha}_i + \vec{\omega}_b \right] + \left[\dot{\lambda}_i'' + \dot{\alpha}_i' + \vec{\omega}_b \right]^T (J_{ir}''') \left[\dot{\lambda}_i'' + \dot{\alpha}_i' + \vec{\omega}_b \right] \\ & \left[\dot{\alpha}_i' + \vec{\omega}_b \right]^T (J_m'') \left[\dot{\alpha}_i' + \vec{\omega}_b \right] + \vec{\omega}_b^T (m_p ([\Delta\vec{L}_i]^T [\Delta\vec{L}_i] - [\Delta\vec{L}_i] [\Delta\vec{L}_i]^T)) \vec{\omega}_b \\ & + m_p \vec{G}_b \cdot (R_I^b(\eta) \vec{\mathcal{E}}_I + \Delta\vec{L}_i) \end{aligned} \quad (3.103)$$

Applying partial derivatives of the Lagrangian formulation to $\mathcal{L}_{p/I}$ relative to the angular path coordinates $\vec{\eta}_b$ and $\vec{\omega}_b$ to calculate the generalized force $\vec{\mathbf{W}}(\vec{u}_i)$. Reiterating $\vec{\eta}_b$ is the angular orientation from Eq:2.12e, defined entirely in the body frame \mathcal{F}^b . Finally, the vector difference between the body frame's center of motion $\vec{\mathbf{O}}_b$ and the rotated motor module's center of mass $\vec{C}_p''(\lambda_i, \alpha_i)$, in Fig:3.16, is independent of the vehicle body's attitude trajectory $\vec{\eta}_b$. It follows that $\partial/\partial\vec{\eta}_b(\Delta\vec{L}_i) = 0$:

$$\vec{\mathbf{W}}(\vec{u}_i) = \frac{d}{dt} \left(\frac{\partial \mathcal{L}_{p/I}}{\partial \vec{\eta}_b} \right) - \frac{\partial \mathcal{L}_{p/I}}{\partial \vec{\eta}_b} = \frac{d}{dt} \left(\frac{\partial \mathcal{L}_{p/I}}{\partial \vec{\omega}_b} \right) - \frac{\partial \mathcal{L}_{p/I}}{\partial \vec{\eta}_b} = \vec{\tau}_M(u_i) \quad (3.104a)$$

$$\begin{aligned} &= \frac{d}{dt} \left((J_r''') \left[\vec{\Omega}_i''' + \dot{\lambda}_i'' + \dot{\alpha}_i' + \vec{\omega}_b \right] + (J_{ir}''') \left[\dot{\lambda}_i'' + \dot{\alpha}_i' + \vec{\omega}_b \right] + (J_m'') \left[\dot{\alpha}_i' + \vec{\omega}_b \right] + (J_H) \left[\vec{\omega}_b \right] \right) \\ &\quad - m_p \vec{G}_b \times \Delta\vec{L}_i \end{aligned} \quad (3.104b)$$

Then using inertia derivatives for each body from Eq:3.96b-3.96d and \dot{J}_H from Eq:3.101c, and inserting the respective relative angular velocities from Eq:3.97-3.99:

$$\begin{aligned} \vec{\tau}_M(\vec{u}_i) = & \left[(\dot{J}_r''')(\vec{\Omega}_i''' + \dot{\lambda}_i'' + \dot{\alpha}_i' + \vec{\omega}_b) \right] + \left[(J_r''')\dot{\vec{\Omega}}_i''' + \vec{\omega}_{n/I} \times (J_r''')\vec{\Omega}_i''' + (J_r''')\ddot{\lambda}_i'' + \vec{\omega}_{n/I} \times (J_r''')\dot{\lambda}_i'' \right. \\ & + (J_r''')\ddot{\alpha}_i' + \vec{\omega}_{m/I} \times (J_r''')\dot{\alpha}_i' + (J_r''')\dot{\vec{\omega}}_b + \vec{\omega}_{b/I} \times (J_r''')\vec{\omega}_b \left. \right] + \left[(\dot{J}_{ir})\dot{\lambda}_i'' + \dot{\alpha}_i' + \vec{\omega}_b \right] + \left[(J_{ir}'')\ddot{\lambda}_i'' \right. \\ & + \vec{\omega}_{n/I} \times (J_{ir}'')\dot{\lambda}_i'' + (J_{ir}'')\ddot{\alpha}_i' + \vec{\omega}_{m/I} \times (J_{ir}'')\dot{\alpha}_i' + (J_{ir}'')\dot{\vec{\omega}}_b + \vec{\omega}_{b/I} \times (J_{ir}'')\vec{\omega}_b \left. \right] + \left[(J_m'')\dot{\alpha}_i' + \vec{\omega}_{m/I} \times (J_m'')\dot{\alpha}_i' + (J_m'')\dot{\vec{\omega}}_b + \vec{\omega}_{b/I} \times (J_m'')\vec{\omega}_b \right] \\ & \left[(J_m'')\ddot{\alpha}_i' + \vec{\omega}_{m/I} \times (J_m'')\dot{\alpha}_i' + (J_m'')\dot{\vec{\omega}}_b + \vec{\omega}_{b/I} \times (J_m'')\vec{\omega}_b \right] + \left[(\dot{J}_h)\vec{\omega}_b \right] + \left[(J_H)\dot{\vec{\omega}}_b + \vec{\omega}_{b/I} \times (J_h)\vec{\omega}_b \right] \\ & - \left[m_p \vec{G}_b \times \Delta \vec{L}_i \right] \quad (3.104c) \end{aligned}$$

After expanding relative angular velocity terms; $\vec{\omega}_{n/I}$, $\vec{\omega}_{m/I}$ and $\vec{\omega}_{b/I}$ and applying some mathematics, Eq:3.104c is shown to include a transformed component of the middle ring (including the inner ring) assembly's generalized force response from Eq:3.86c.

$$\begin{aligned} \frac{d}{dt} \left(\frac{\partial \mathcal{L}_{p/I}}{\partial \vec{\omega}_b} \right) - \frac{\partial \mathcal{L}_{p/I}}{\partial \vec{\eta}_b} = & R_z \frac{d}{dt} \left(\frac{\partial \mathcal{L}_{m/p}}{\partial \vec{\mathbf{v}}} \right) + (J_r''')\vec{\omega}_b + \vec{\omega}_b \times (J_r''')\vec{\Omega}_i''' + \vec{\omega}_b \times (J_r''')\dot{\lambda}_i'' \\ & + \vec{\omega}_b \times (J_r''')\dot{\alpha}_i' + \vec{\omega}_b \times (J_r''')\vec{\omega}_b + J_r'''\dot{\vec{\omega}}_b + (J_{ir}'')\vec{\omega}_b + \vec{\omega}_b \times (J_{ir}'')\dot{\lambda}_i'' + \vec{\omega}_b \times (J_{ir}'')\dot{\alpha}_i' \\ & + \vec{\omega}_b \times (J_{ir}'')\vec{\omega}_b + (J_{ir}'')\dot{\vec{\omega}}_b + (J_m'')\vec{\omega}_b + \vec{\omega}_b \times (J_m'')\dot{\vec{\omega}}_b + (J_m'')\dot{\vec{\omega}}_b + (J_H)\vec{\omega}_b \\ & + (J_H)\dot{\vec{\omega}}_b + \vec{\omega}_b \times (J_H)\vec{\omega}_b - m_p \vec{G}_b \times \Delta \vec{L}_i \quad (3.104d) \end{aligned}$$

Combining inertial bodies with the same angular velocities and introducing inner and middle ring response terms $\vec{\tau}_\lambda(\lambda_i)$ and $\vec{\tau}_\alpha(\lambda_i, \alpha_i)$ from Eq:3.76 and Eq:3.87 respectively:

$$\begin{aligned} \vec{\tau}_M(\vec{u}_i) = & R_z \vec{\tau}_\alpha(\lambda_i, \alpha_i) + R_z R_y(\alpha) \vec{\tau}_\lambda(\lambda_i) + (\dot{J}_r''' + \dot{J}_{ir}''' + \dot{J}_m'' + \dot{J}_H) \vec{\omega}_b \\ & + (J_r''' + J_{ir}''' + J_m'' + J_H) \dot{\vec{\omega}}_b + \vec{\omega}_b \times (J_r''' + J_{ir}''' + J_m'' + J_H) \vec{\omega}_b + \vec{\omega}_b \times \left((J_r''')(\vec{\Omega}_i''' + \dot{\lambda}_i'' + \dot{\alpha}_i') \right. \\ & \left. + (J_{ir}'')(\dot{\lambda}_i'' + \dot{\alpha}_i') + (J_m'')(\dot{\alpha}_i') \right) - m_p \vec{G}_b \times \Delta L_i \quad (3.104e) \end{aligned}$$

Then $(J_r''' + J_{ir}''' + J_m'' + J_H)$ can be simplified to a parallel axis translation of the transformed net motor module inertia J'_p from Eq:2.24b, analogous to the net motor module inertia defined previously in Eq:2.27b. The net motor module's inertia, with respect to and aligned with the body frame and centered at the origin $\vec{\mathbf{O}}_b$ is:

$$\begin{aligned} (J_r''' + J_{ir}''' + J_m'' + J_H) \triangleq & R_z R_y(\alpha_i) R_x(\lambda_i) (J_r) R_x^{-1}(\lambda_i) R_y^{-1}(\alpha_i) R_z^{-1} \\ & + R_z R_y(\alpha_i) R_x(\lambda_i) (J_{ir}) R_x^{-1}(\lambda_i) R_y^{-1}(\alpha_i) R_z^{-1} + R_z R_y(\alpha_i) (J_m) R_y^{-1}(\alpha_i) R_z^{-1} + J_H \quad (3.105a) \end{aligned}$$

$$= R_z (J_p) R_z^{-1} + m_p \left([\Delta \vec{L}_i]^T [\Delta \vec{L}_i] - [\Delta \vec{L}_i] [\Delta \vec{L}_i]^T \right) = J'_{\vec{\mathbf{M}}_i} \quad (3.105b)$$

Moreover, the above can be applied to the associated inertia derivatives; \dot{J}_r''' , \dot{J}_{ir}''' , \dot{J}_m'' and \dot{J}_H . Using Eq:3.96b, 3.96c, 3.96d and 3.101c it can be shown that:

$$(\dot{J}_r''' + \dot{J}_{ir}''' + \dot{J}_m'' + \dot{J}_H) = J'_{\vec{\mathbf{M}}_i} \quad (3.105c)$$

The generalized torque acting on a single motor module, $\vec{\tau}_M(\vec{u}_i)$ from Eq:3.104e, is then found a combination of responses to servos λ_i and α_i , the inertia rates of change $\dot{J}'_{\vec{\mathbf{M}}_i}$ as a result of those rotations and finally the net response to the entire frame's angular velocity $\vec{\omega}_b$.

$$\begin{aligned} \vec{\tau}_M(\vec{u}_i) = & R_z \vec{\tau}_\alpha(\lambda_i, \alpha_i) + R_z R_y(\alpha_i) \vec{\tau}_\lambda(\lambda_i) + (\dot{J}'_{\vec{\mathbf{M}}_i}) \vec{\omega}_b + (J'_{\vec{\mathbf{M}}_i}) \dot{\vec{\omega}}_b + \vec{\omega}_b \times (J'_{\vec{\mathbf{M}}_i}) \vec{\omega}_b \\ & + \vec{\omega}_b \times \left((J_p'')\dot{\alpha}_i' + (J_n'')\dot{\lambda}_i'' + (J_r'')\vec{\Omega}_i''' \right) - m_p \vec{G}_b \times \Delta \vec{L}_i \triangleq \vec{\mathbf{W}}(\vec{u}_i) \in \mathcal{F}^b \quad (3.106) \end{aligned}$$

Consider the rigid body torque response $\vec{\tau}_y$ for the body structure's motion, J_y . That structure's inertia J_y is a constant and independent of actuator positions in $u \in \mathbb{U}$, explicitly defined in Eq:2.25d.

$$\vec{\tau}_y = (J_y)\dot{\vec{\omega}}_b + \vec{\omega}_b \times (J_y)\vec{\omega}_b - \vec{C}_y \times m_y \vec{G}_b \quad \in \mathcal{F}^b \quad (3.107)$$

The net response for the *entire* multibody system is then a sum of Eq:3.106 for modules $i \in [1 : 4]$ and $\vec{\tau}_y$ in Eq:3.107. By inspection, without constructing a complete Lagrangian for the entire system, the effective net torque $\vec{\tau}_\mu$, acting on the body frame \mathcal{F}^b is shown to be:

$$\vec{\tau}_\mu = (J_y)\dot{\vec{\omega}}_b + \vec{\omega}_b \times (J_y)\vec{\omega}_b - \vec{C}_y \times m_y \vec{G}_b + \sum_{i=1}^4 \vec{\tau}_M(\vec{u}_i) \quad \in \mathcal{F}^b \quad (3.108)$$

Recalling the net vehicle's rotational inertia $J_b(\vec{u})$, calculated as a function of the actuation matrix \vec{u} , which was defined previously in 2.31a, it follows that Eq:3.108 can be reduced by combining common inertia terms:

$$\begin{aligned} \vec{\tau}_\mu &= (J_b(\vec{u}))\dot{\vec{\omega}}_b + \vec{\omega}_b \times (J_b(\vec{u}))\vec{\omega}_b \\ &+ \sum_{i=1}^4 \left[R_z \vec{\tau}_\alpha(\lambda_i, \alpha_i) + R_z R_y(\alpha_i) \vec{\tau}_\lambda(\lambda_i) + (\dot{J}_{\vec{M}_i})\vec{\omega}_b + \vec{\omega}_b \times \left((J''_p)\dot{\vec{\alpha}}'_i + (J'''_n)\dot{\vec{\lambda}}''_i + (J'''_r)\vec{\Omega}'''_i \right) \right] \\ &\quad - m_p \vec{G}_b \times \sum_{i=1}^4 \Delta \vec{L}_i \end{aligned} \quad (3.109)$$

The external torque $\vec{\tau}_\mu$ acting on the vehicle is as a response to the commanded control action, detailed next in Ch:4. The final sum of gravitational torque contributions can be simplified to $\vec{\tau}_g$, from Eq:2.35d, which considers the *net* resultant center of gravity. Extending the angular differential equation Eq:3.10d to incorporate the multibody responses derived above:

$$\vec{\tau}_\mu = (J_b)\dot{\vec{\omega}}_b + \vec{\omega}_b \times (J_b)\vec{\omega}_b + \vec{\tau}_b(\vec{u}) - \vec{\tau}_g \quad (3.110a)$$

defines a new response torque $\vec{\tau}_b(\vec{u})$ which represents the collective responses from internal rotations relative to each body. It can be considered a nonlinear extension of the gyroscopic component of the torque $\vec{\omega}_b \times (J_b)\vec{\omega}_b$ acting on the system. That nonlinear multibody torque is defined then as follows:

$$\vec{\tau}_b(\vec{u}) \triangleq \dot{J}_b(u)\vec{\omega}_b + \sum_{i=1}^4 \left[R_z \vec{\tau}_\alpha(\lambda_i, \alpha_i) + R_z R_y(\alpha_i) \vec{\tau}_\lambda(\lambda_i) + \vec{\omega}_b \times \left((J''_p)\dot{\vec{\alpha}}'_i + (J'''_n)\dot{\vec{\lambda}}''_i + (J'''_r)\vec{\Omega}'''_i \right) \right] \quad (3.110b)$$

Using the net gravitational torque arm $\vec{\tau}_g$ defined earlier in Eq:2.35d:

$$\vec{\tau}_g \triangleq \Delta \vec{C}_G \times m_b \vec{G}_b \quad (3.110c)$$

Note that $\dot{J}_b(\vec{u})$ is another introduced term which is the sum of all motor module inertia rates from Eq:3.105c, given that body structure's inertia J_y is constant:

$$\dot{J}_b(\vec{u}) \triangleq \sum_{i=1}^4 (\dot{J}'_{\vec{M}_i}) + J_y = \sum_{i=1}^4 (\dot{J}'_{\vec{M}_i}) \quad (3.111)$$

The torque $\vec{\tau}_b(\vec{u})$ from Eq:3.110b is the most important result here. Definitions of $\vec{\tau}_\alpha(\lambda_i, \alpha_i)$ and $\vec{\tau}_\lambda(\lambda_i)$, in Eq:3.76 and Eq:3.87 respectively, were necessary to simplify and isolate different components of Eq:3.110b. The most complicated process in evaluating Eq:3.110b is calculating inertia time derivatives at each sampling interval.

3.4.2 Verification and simulation of induced model

Dynamic model verification

In spite of the rigorous mathematical approach applied to the multibody system above, physical corroboration of the proposed model(s) is still required. The systems described in Eq:3.76 for $\vec{\tau}_\lambda(\lambda_i)$, Eq:3.87 for $\vec{\tau}_\alpha(\lambda_i, \alpha_i)$ and Eq:3.110b for $\vec{\tau}_b(\vec{u})$ require further verification before an accurate and reliable simulation can be constructed based upon them. Two test rigs were designed and constructed (Fig:3.17 and Fig:3.19) to physically measure the induced torques in question. The first test rig recreates the relative motion of the inner ring actuated by the λ_i servo. Similarly the second test platform mimics the middle ring's response when driven by the outer α_i servo.

The net body response, $\vec{\tau}_b(\vec{u})$ relating to net angular body velocity $\vec{\omega}_b$ in Eq:3.110b, is harder to recreate on an isolated test rig. Such results are only discussed in the context of simulation. Considering first the innermost ring assembly, Fig:3.17 shows the test rig used to isolate and measure $\vec{\tau}_\lambda(\lambda_i)$ responses to $\Delta\lambda_i$ rotations. The inner ring is supported by two bearing assemblies, an extended shaft in the $-\hat{X}_{M_i}$ direction connects the inner ring to the driving servo block.

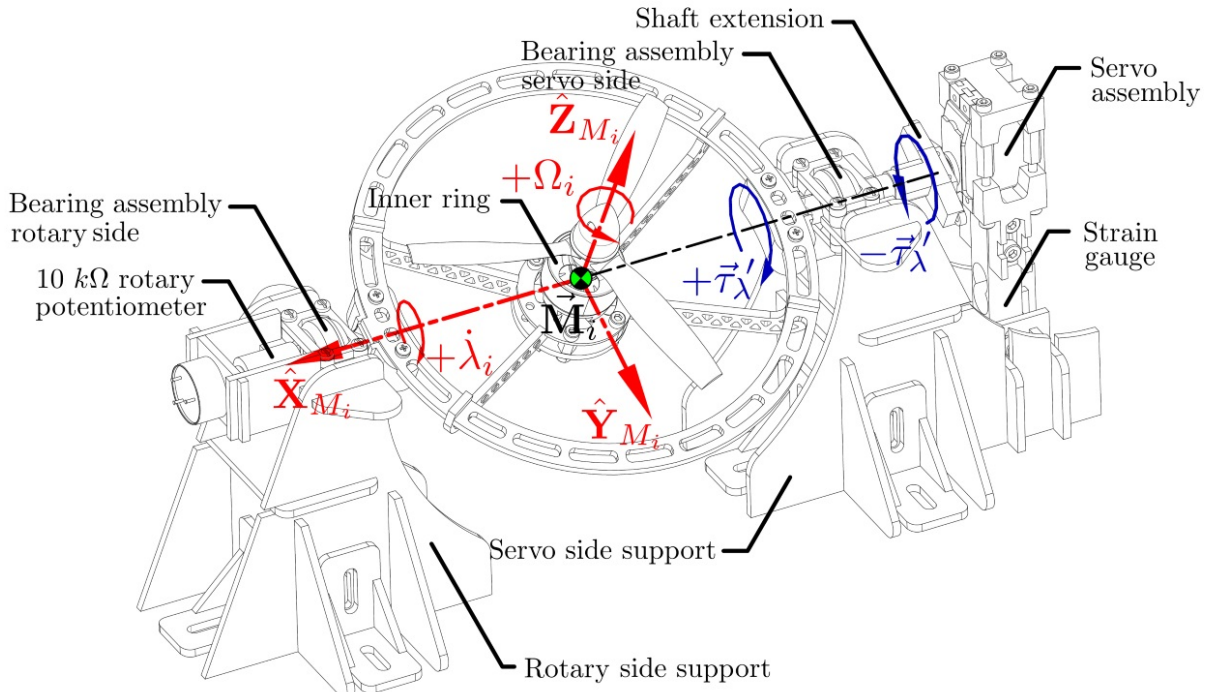


Figure 3.17: Inner ring torque test rig

Physical rotational torque $\vec{\tau}_\lambda(\lambda_i)$ is transferred through the shaft extension from the servo to the inner ring. The servo block is secured only by a vertically aligned and calibrated strain gauge (App:B.3). Deflection of the strain gauge is then proportional to the torque applied by the servo to rotate the inner ring structure. It is important to mention that whilst the bearing assembly facilitates the transfer of the servo's rotational torque, the assembly isolates only the $\hat{X}_{M'_i}$ component of the induced torque. If $\vec{\tau}'_\lambda$ is the deflection torque physically measured, its relationship with the induced torque vector $\vec{\tau}_\lambda(\lambda_i)$ is given by:

$$\vec{\tau}'_\lambda = \vec{\tau}_\lambda(\lambda_i) \cdot \hat{X}_{M'_i} \in \mathcal{F}^{M'_i} \quad (3.112)$$

One final thing to consider is that the modelled equation for $\vec{\tau}_\lambda(\lambda_i)$, previously in Eq:3.76, *does not* account for the gravitational torque from an eccentric center of gravity (Fig:2.12) or induced aerodynamic torque about the propeller's hub (Fig:3.7 and Eq:3.31b). The derivations earlier in Sec:3.4.1 introduce net gravitational torque for an effective center of gravity $\vec{\tau}_g$ into Eq:3.110a. Moreover aerodynamic drag $\vec{H}(\Omega_i)$ about the propeller's rotational axis is to be included as an additive term.

The torque response $\vec{\tau}_\lambda(\lambda_i)$ is opposed to changes of $\Delta\lambda_i$ and hence the servo's acceleration $\ddot{\lambda}_i$. That torque is from Eq:3.76 with introduced gravitational and aerodynamic drag torque components relative to the middle ring frame $\mathcal{F}^{M'_i}$:

$$\vec{\tau}_\lambda(\lambda_i) = (J'_r)\vec{\Omega}'_i + (J'_n)\dot{\lambda}_i + (J'_r)\dot{\vec{\Omega}}'_i + (J'_n)\ddot{\lambda}_i + \dot{\lambda}_i \times (J'_r)\vec{\Omega}'_i + \dot{\lambda}_i \times (J'_n)\dot{\lambda}_i \\ R_x(\lambda)(H(\Omega_i) \cdot \hat{Z}_{M_i}) + m_n(R_x(\lambda_i)\vec{C}_n) \times \vec{G}_{M'_i} \in \mathcal{F}^{M'_i} \quad (3.113)$$

The term $m_n(R_x(\lambda_i)\vec{C}_n) \times \vec{G}_{M'_i}$ is the gravitational torque from the rotated center of mass, \vec{C}_n first defined in Eq:2.29d. The torque $H(\Omega_i) \cdot \hat{Z}_{M_i}$ is the scalar projection of aerodynamic torque from Fig:3.7b onto the propeller's \hat{Z}_{M_i} axis, rotated onto the middle ring $\mathcal{F}^{M'_i}$ frame. Note the strain gauge's measured response encountered will be the negative torque response $-\vec{\tau}_\lambda(\lambda_i)$.

The plot illustrated in Fig:3.18a shows tests for the inner ring torque response at increments of relative servo step sizes: $\Delta\lambda_i = \pm[1/12\pi, 2/12\pi \dots 5/12\pi, 6/12\pi]$. A constant propeller rotational speed $\Omega_i = +6000$ RPM was used. Step changes in the propeller's speed manifest as a gyroscopic cross product in a perpendicular axis, but will not affect the projected $\hat{X}_{M'_i}$ torque $\vec{\tau}_\lambda'$ from Eq:3.112. As per convention, in the plot Fig:3.18a, $\vec{\tau}_\lambda'$ represents the **physically measured** torque on the test rig illustrated in Fig:3.17 and $\hat{\tau}_\lambda'$ is the expected **torque estimate** calculated from Eq:3.113. Both torques are the projected $\hat{X}_{M'_i}$ components of the induced torque vector.

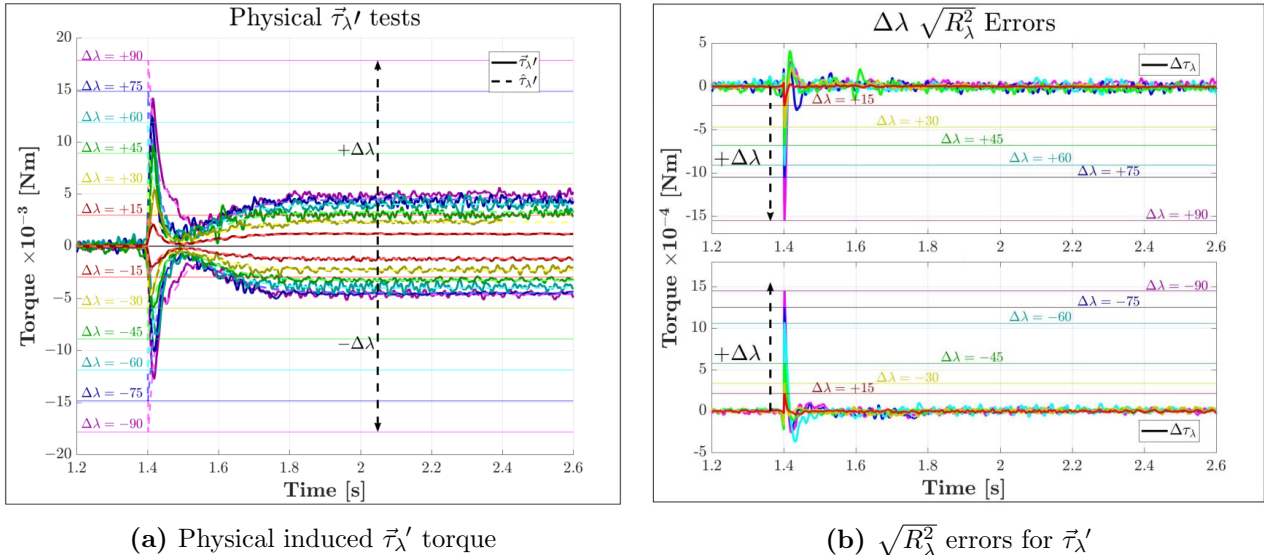


Figure 3.18: Inner ring test rig response

The error between the physically measured $\vec{\tau}_\lambda'(\lambda_i)$ and modelled $\hat{\tau}_\lambda'(\lambda_i)$ torques are shown in Fig:3.18b. Peak induced torque as a result of a commanded rotation $\Delta\lambda_i$ increases proportionally with that step size. The co-axial support bearings on the test rig, despite being de-greased and cleaned ultrasonically, still damped the faster elements of the transient torque response, moreover the overall small magnitude of measured signals meant samples were susceptible to vibration noise transformed through the mechanical structure. There is, however, a clear correlation between the simulated and physically measured signal. Within a margin of error, and considering the tolerances of the test rig, such step changes corroborate the proposed inner ring model in Eq:3.113.

Verification of the dynamics for the middle ring response requires more in-depth discussion. Unlike the inner ring's response, described in Eq:3.113, the middle ring's torque $\vec{\tau}_\alpha(\lambda_i, \alpha_i)$ from Eq:3.87 is **not equivalent** to the generalized torque response acting on the middle ring system $\vec{V}(\lambda_i, \alpha_i)$, Eq:3.86g. As mentioned previously $\vec{V}(\lambda_i, \alpha_i)$ includes a transformed component of the inner ring's generalized response $R_y(\alpha_i)\vec{U}(\lambda_i)$ from Eq:3.75a, whilst the *servo response torque* $\vec{\tau}_\alpha(\lambda_i, \alpha_i)$ **does not**.

To differentiate between the servo's response torque $\vec{\tau}_\alpha(\lambda_i, \alpha_i)$ and the physical (generalized) torque being considered and tested here, $\vec{\Gamma}_\alpha(\lambda_i, \alpha_i)$ is used to refer to the induced torque response from the middle ring assembly's net rotation.

That torque is the measured component of the middle ring response and is equivalent to the generalized torque response. Reiterating the equation for the expected generalized torque $\vec{\Gamma}_\alpha(\lambda_i, \alpha_i)$ from Eq:3.86g, now with included gravitational and aerodynamic torque components and induced torques as a result of the inner ring's rotation:

$$\begin{aligned}\vec{\Gamma}_\alpha(\lambda_i, \alpha_i) &= R_y(\alpha_i)\vec{\mathbf{U}}(\lambda_i) + (\dot{J}'_p)\dot{\alpha}_i + \left(J''_n - R_y(\alpha_i)(\dot{J}'_n)R_y^{-1}(\alpha_i) \right) \dot{\lambda}'_i + \left(J''_r - R_y(\alpha_i)(\dot{J}'_r)R_y^{-1}(\alpha_i) \right) \dot{\Omega}''_i \\ &+ (J''_p)\ddot{\alpha}_i + \dot{\alpha}_i \times \left((J'_p)\dot{\alpha}_i + (J''_n)\dot{\lambda}'_i + (J''_r)\dot{\Omega}''_i \right) + R_y(\alpha_i)R_x(\lambda_i)(H(\Omega_i) \cdot \hat{Z}_{M_i}) + m_p \vec{C}_p''(\alpha_i, \lambda_i) \times \vec{G}_{M_i''} \\ &= \vec{\mathbf{V}}(\lambda_i, \alpha_i) \in \mathcal{F}^{M_i''} \quad (3.114)\end{aligned}$$

where the term $\vec{C}_p''(\alpha_i, \lambda_i)$ is the net rotated center of gravity for the entire motor module as a function of both servo positions:

$$\vec{C}_p''(\alpha_i, \lambda_i) = \frac{m_n R_y(\alpha_i) R_x(\lambda_i) \vec{C}_n + m_m R_y(\alpha_i) \vec{C}_m}{m_m + m_n} \quad (3.115)$$

with m_m and m_n being inner and middle ring structure's respective masses, $m_m = 98$ [g] and $m_n = 92$ [g] from Sec:2.3. Fig:3.19 shows the test rig used to measure torque responses for the motor module assembly which contains both inner and middle ring assemblies. The inner ring servo λ_i was tested both at a constant $\lambda_i = 0$ and at intervals of steps with equivalent inner and middle ring servo angles.

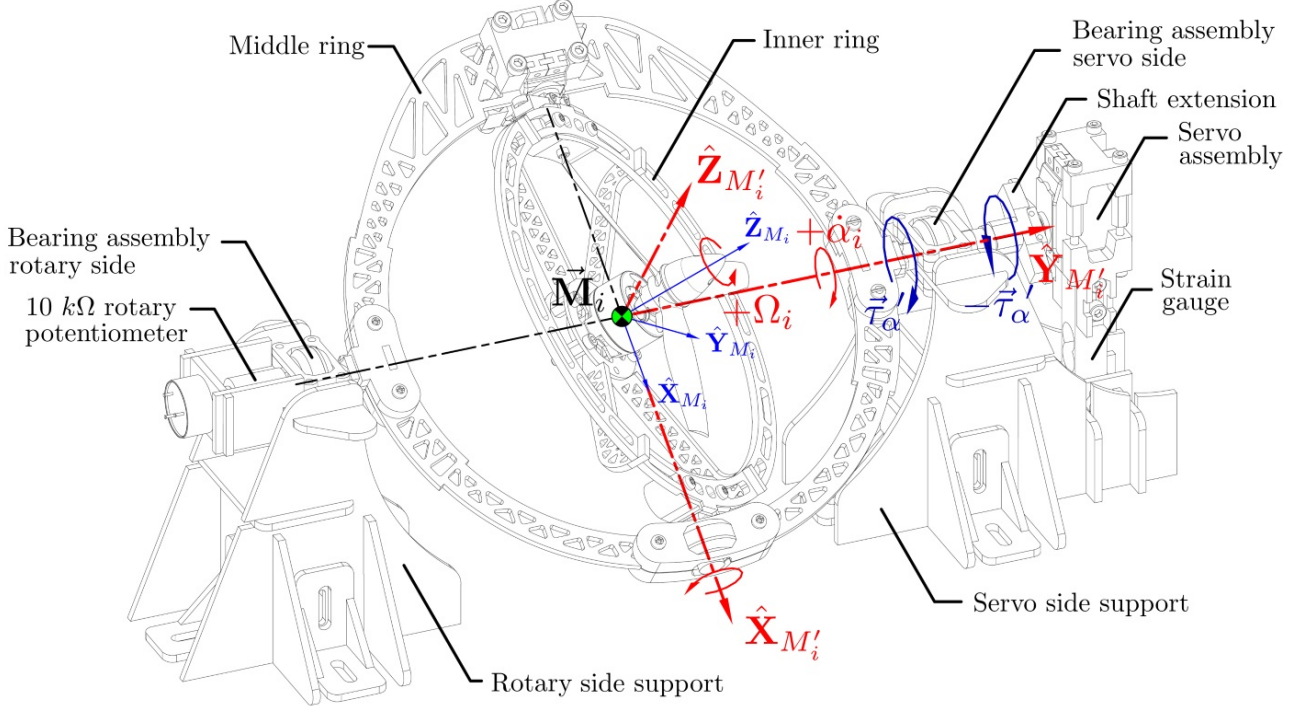


Figure 3.19: Middle ring torque test rig

The middle ring servo α_i applies an accelerating torque $\vec{\Gamma}_\alpha(\lambda_i, \alpha_i)$ to the assembly, but the test rig isolates only the $\hat{Y}_{M_i''}$ component of that torque. Because the strain gauge encounters only that axial deflection, it then deflects proportionally to the physical torque :

$$\vec{\Gamma}'_\alpha(\lambda_i, \alpha_i) = \vec{\Gamma}_\alpha(\lambda_i, \alpha_i) \cdot \hat{Y}_{M_i''} \in \mathcal{F}^{M_i''} \quad (3.116)$$

Furthermore, the inner servo's torque contribution to Eq:3.114, or $R_y(\alpha_i)\vec{\mathbf{U}}(\lambda_i)$, is small for any case where the propeller's rotational speed and the inner ring's servo speed are both roughly constant, $\dot{\Omega}_i \approx 0$ and $\dot{\lambda}_i \approx 0$. Fig:3.20a plots results for measured torque $\vec{\Gamma}'_\alpha(\lambda_i, \alpha_i)$ and expected torque estimate $\hat{\Gamma}'_\alpha(\lambda_i, \alpha_i)$ for a constant inner ring servo position $\lambda_i = 0$. Again the propeller's rotational speed was kept constant at $\Omega_i = +6000$ RPM.

The error deviation between the two measured and estimated torques is shown in Fig:3.20b, with larger fast torque spikes leading to damped errors of greater magnitude. Steps performed in Fig:3.20 at intervals $\Delta\alpha_i = \pm[1/12\pi, 2/12\pi \dots 5/12\pi, 6/12\pi]$ simply verify the middle ring's inertial contribution to the model. With no inner ring servo velocity $\dot{\lambda} \neq 0$, the complex dynamics are not completely present. It is worth noting the dissymmetry in the shape of the torque's positive and negative responses resulting from non-symmetrical inertias in J_p from Eq:2.24b.

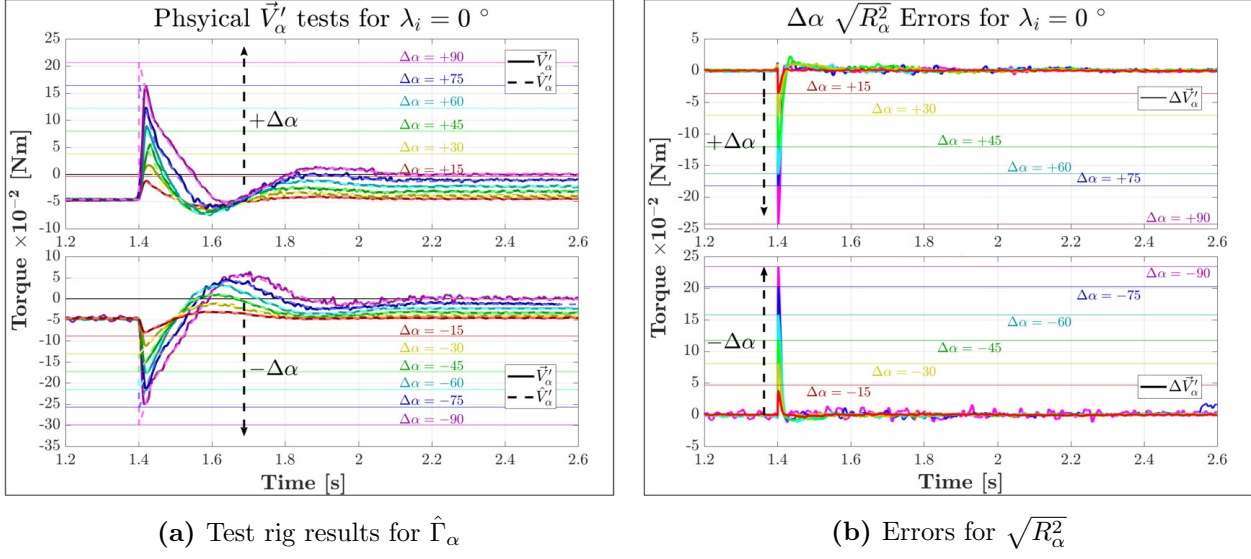


Figure 3.20: Middle ring response

The larger inertia being rotated by the α_i middle ring servo contributes towards a greater initial torque spike as a result of the angular acceleration from $\ddot{\alpha}_i$, in the order of $\times 10^{-1}$ Nm. The damping effect applied by the support bearing is more pronounced in the middle ring case, producing errors with greater magnitudes in Fig:3.20b. Without introducing a step for the inner ring λ_i , the response in Fig:3.20 is mostly a scaled version of the inner ring response in Fig:3.18.

Finally, testing combined rotations of λ_i and α_i stepped together. Fig:3.21 shows the manifestation of the complex dynamics involved in a single motor module's combined actuator action. Each interval step is performed with equal servo step sizes; $\Delta\lambda_i = \Delta\alpha_i$ for $\lambda_i, \alpha_i \in \pm[1/12\pi, 2/12\pi \dots 5/12\pi, 6/12\pi]$. Still using a constant propeller speed $\Omega_i = +6000$ rpm, the introduction of gyroscopic torque begins to affect the step response shown in Fig:3.21a. As λ_i and α_i approach $\pi/2$ rad, the propeller's rotational aerodynamic torque begins to make a contribution towards Eq:3.114 as its rotational axis aligns with the measurement axis $\hat{Y}_{M_i''}$.

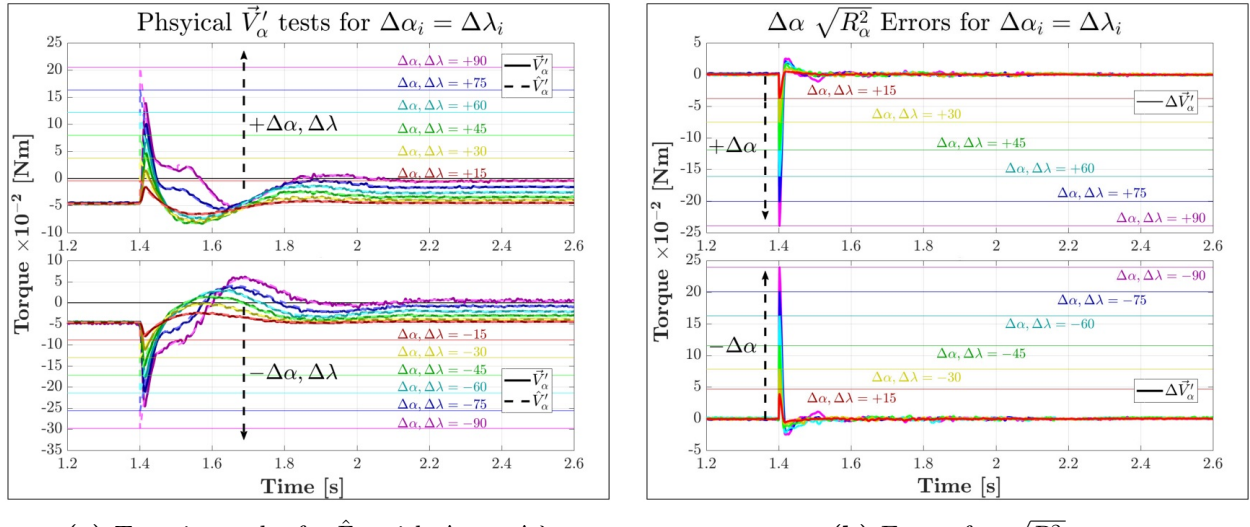


Figure 3.21: Combined middle ring response

The non-symmetrical inertia of a motor module, even at rest and due to the unbalanced servo weight in Fig:2.13, skews the response torque shown in previous tests in Fig:3.20a. Combining both servos to be actuated at the same time further skews the torque response curve. The induced gyroscopic product of both rotations constructively and destructively affects Eq:3.114 depending on the rotational sense. Only positive $\Delta\alpha_i = \Delta\lambda_i$ tests were performed, conversely $\Delta\alpha_i = -\Delta\lambda_i$ would have had a reciprocal effect. Again, the fast initial torque spike is damped by the test set-up bearings, resulting in an initial error plotted in Fig:3.21b, which subsequently reduces very quickly. Because the inner ring has a center of gravity, \vec{C}_n in Eq:2.29b, very close to the module's center of rotation, steady state torque offsets from gravitational torque contributions to $\vec{\Gamma}'(\lambda_i, \alpha_i)$ are almost independent of the inner ring λ_i servo position.

Each of the above step tests in Fig:3.18, Fig:3.20 and Fig:3.21 were performed three times and the resultant measured torques were averaged over those three tests. What is plotted are the ten sample moving averages of those combined data sets from the three independent tests for each angular step.

The above responses are pertinent to simulation and plant dependent feedback compensation. The simulation environment is structured such that the torques are produced as responses from Newtonian movement at every step interval. In due course it would be more efficient (and less stiff) for the simulation to exploit an implicit Euler [70, 141] coordinate system in lieu of the cartesian response equations developed above. However this was not implemented in Ch:6 and remains open to further testing and simulation.

Body Response Simulation Tests

To corroborate and test the presented dynamic model for the vehicle's net motion, described in Eq:3.109, a series of experimental simulations are performed using the proposed differential equations of motion and the subsequent results are discussed. The simulation environment used here is a simplified, open loop version of the one presented later in Sec:6.1. In some cases the plant inputs are reduced to net forces and torques, in other cases explicit propeller speeds and servo rotational positions are commanded as inputs. Considering the mass properties of the quadrotor design in Sec:2.1, force and torque inputs for a stable hover to be actuated by the control plant are as follows:

$$\begin{bmatrix} \vec{F}_h \\ \vec{\tau}_h \end{bmatrix} = m_b \begin{bmatrix} \vec{G}_b \\ \vec{C}_b(\vec{u}) \times \vec{G}_b \end{bmatrix} = \begin{bmatrix} [0 \ 0 \ 15.45]^T \\ [0.25 \ 0.50 \ -0.08]^T \end{bmatrix} \begin{bmatrix} [N] \\ [N.mm] \end{bmatrix} \quad (3.117)$$

where the force input \vec{F}_h acts to oppose the gravitational acceleration acting on the body and the torque $\vec{\tau}_h$ opposes the gravitational torque arm produced by the body's eccentric center of gravity. Note that Eq:3.117 does not include terms associated with rotational aerodynamic torque $\vec{H}(\Omega_i, \lambda_i, \alpha_i)$ from 3.2, such terms require feedback compensation in closed loop. Simulating hover conditions will not provide any useful insight, but the commanded plant inputs for a hovering state do provide a suitable starting values to which input offsets can be applied.

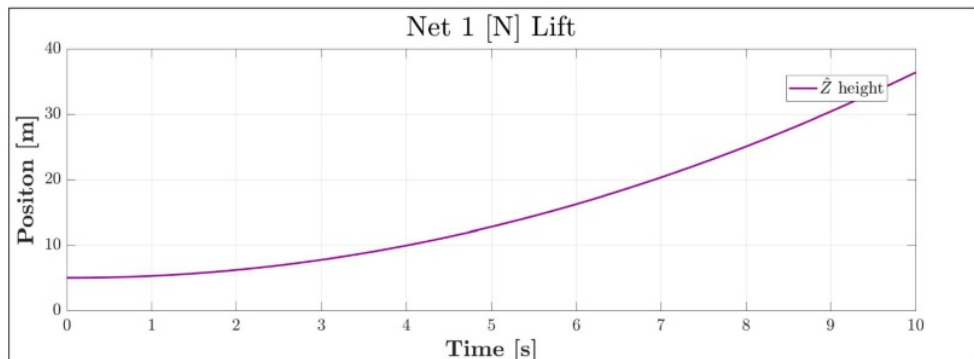


Figure 3.22: Upward lift test

Adding an extra 1 [N] of lift should result in ≈ 0.6 [m.s^{-2}] of upward acceleration being applied to the body. Fig:3.22 shows the simulation's position response to that added lift force where height is the only affected state variable. Starting from a height of 5 [m], the simulated vehicle rises to around 36.5 [m] after a time of 10 [s], as expected. A simple upward thrust test confirms the effect gravity and linear acceleration has on the model.

Testing differential torque inputs and subsequent attitude responses, a small (1%) difference between the rotational speeds of propellers 1 and 3 is applied. The differential speeds are offset from hovering conditions which command $\Omega_{1,3} = +10540$ [RPM] and $\Omega_{2,4} = -10540$ [RPM]. If the first motor module's propeller speed is reduced and the third motor module's propeller speed is increased then the net torque applied is a positive pitching torque about the body's \hat{Y}_b axis, forcing the vehicle's pitch attitude θ to increase. The applied speed offset is ± 53 [RPM] which produces an approximate differential torque $+0.3 \cdot \hat{j}$ [N.mm] about the body frame's origin \vec{O}_b .

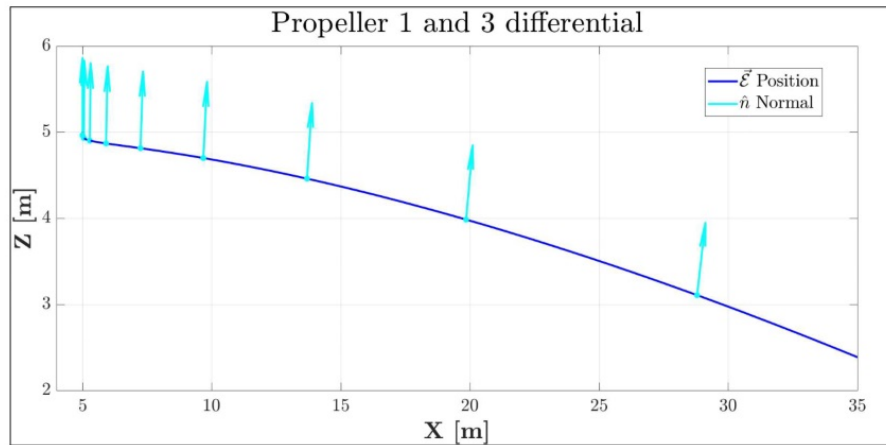


Figure 3.23: Differential torque input

Fig:3.23 shows the XZ plot of the vehicle's position following the differential propeller/torque input. The simulation starts at position $\vec{\mathcal{E}}_0 = [5 \ 5 \ 5]^T$ [m]. Over the course of a 10 [s] simulation, the applied torque slowly pitches the body's normal away from its origin whilst the \hat{X} axis displacement increases. Each normal vector is plotted at a regular time interval of 1 [s].

Then module servo rotations are applied to the first and third motor modules. Using $\lambda_{1,3} = 1^\circ$ to redirect the produced thrust vectors away from their stable hovering positions, this rotation applies an effective yaw moment about the \hat{Z}_b axis. The redirection of the two thrust vectors away from their stable hovering positions without increasing their magnitudes (propeller speeds) will adversely affect the hovering altitude. The net lift force will be reduced by the thrust vector redirection, reducing the net lift force to ≈ 15.4 [N] and applying an $\approx -26.3 \cdot \hat{k}$ [N.mm] yaw torque.

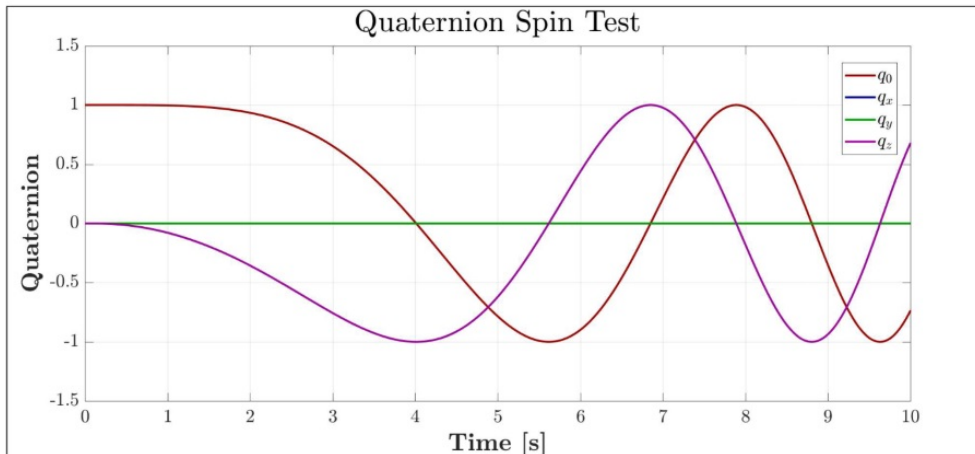


Figure 3.24: Quaternion from yaw torque

The differential torque about the \hat{Z}_b axis only affects the attitude's yaw angle ψ , but roll ϕ and pitch θ remain unchanged. Fig:3.24 shows how that yaw torque, created by redirecting motor module's thrust vectors, produces an oscillatory motion in the attitude of the plant. The reduced lift force from redirection of the two motor module thrust vectors causes the vehicle to slowly descend from its hovering height of 5 [m], shown in Fig:3.25. This particular test shows that minor perturbations away from a stable hover point causes large deviations in state variables, especially in the attitude of the plant. This leads to the conclusion that open-loop hovering stability is extremely fragile and necessitates the need for closed-loop position control to achieve the desired goal of attitude and position setpoint tracking.

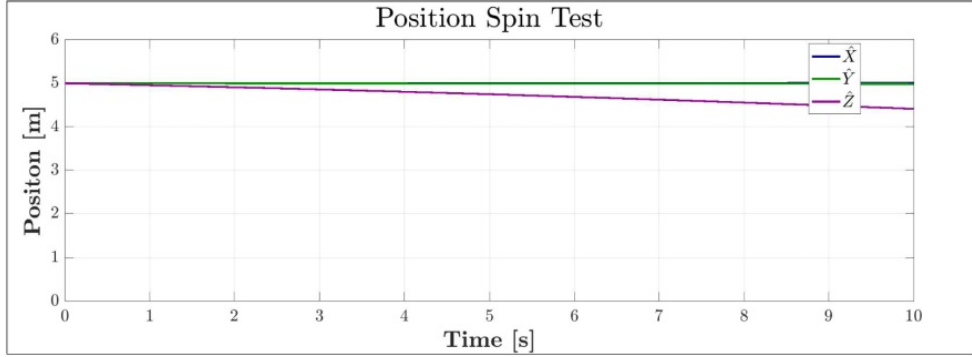


Figure 3.25: Position descent from yaw spin

Whilst none of the above simulated results are entirely unexpected, especially considering all the dynamics are derived from established fundamental theorems, the simulations and physical tests performed provide some degree of certainty to the proposed model for the multibody system. The only way to truly ascertain the absolute accuracy of the equations of motion is to compare them to physical flight test data which is, unfortunately, beyond the scope of this investigation.

3.5 Consolidated Model

The different responses detailed above, state equations from Eq:3.10a-3.10d, are now consolidated. Attitude states are lifted to $\mathbb{Q} \in \mathbb{R}^4$ using quaternions. Then nonlinear inertia and gyroscopic responses to induced perturbations are introduced, $\vec{\tau}_\lambda(\lambda_i)$ and $\vec{\tau}_\alpha(\lambda_i, \alpha_i)$ from Eq:3.76 and Eq:3.87 respectively, with nonlinear inertia terms $J_b(\vec{u})$ from Sec:2.3. Net forces and torques $\vec{F}_\mu(\vec{u})$ and $\vec{\tau}_\mu(\vec{u})$ are controllable inputs to be designed by a higher-level setpoint tracking controller discussed next in Ch:4. The exact actuator effectiveness and allocation schemes are explored thereafter in Ch:5. The vehicle's *inertial frame* position and *body frame* velocity differential equations are:

$$\dot{\vec{\mathcal{E}}}_I = Q_b^* \otimes \vec{v}_b \otimes Q_b \quad \in \mathcal{F}^I \quad (3.118a)$$

$$\dot{\vec{v}}_b = m_b^{-1} (-\vec{\omega}_b \times m_b \vec{v}_b + Q_b \otimes m_b \vec{G}_I \otimes Q_b^* + \vec{F}_\mu(\hat{u})) \quad \in \mathcal{F}^b \quad (3.118b)$$

Similarly, the vehicle's attitude quaternion rate and angular acceleration are respectively:

$$\dot{Q}_b = \frac{1}{2} Q_b \otimes \vec{\omega}_b \quad \in \mathcal{F}^I \quad (3.118c)$$

$$\dot{\vec{\omega}}_b = J_b(\vec{u})^{-1} (-\vec{\omega}_b \times J_b(\vec{u}) \vec{\omega}_b - \vec{\tau}_b(\vec{u}) + \vec{\tau}_g + \vec{\tau}_H + \vec{\tau}_\mu(\hat{u})) \quad \in \mathcal{F}^b \quad (3.118d)$$

The actuator space \vec{u} is defined as per Eq:2.18, where each actuator has its own transfer function $C(s)$ described in Sec:2.4.1, leading to an actuator state estimate \hat{u} used for control inputs $\vec{F}_\mu(\hat{u})$ and $\vec{\tau}_\mu(\hat{u})$ and feedback compensation terms.

$$\vec{u} \triangleq [\Omega_1^+, \lambda_1, \alpha_1, \dots \Omega_4^-, \lambda_4, \alpha_4] \quad \in \mathbb{U} \in \mathbb{R}^{12} \quad (3.118e)$$

Control force and torque plant inputs, $\vec{F}_\mu(\hat{u})$ and $\vec{\tau}_\mu(\hat{u})$ respectively, are a combination of Eq:3.15 with three-dimensional thrust vectors $\vec{T}(\Omega_i)$ as per the quaternion analogue of Eq:2.17. Both are later abstracted to virtual control inputs in the control allocation design Ch:5.

$$\vec{F}_\mu(\hat{u}) = \sum_{i=1}^4 \vec{T}(\Omega_i, \lambda_i, \alpha_i) = \sum_{i=1}^4 Q_{M_i}^* \otimes T(\Omega_i) \otimes Q_{M_i} \in \mathcal{F}^b \quad (3.119a)$$

$$\vec{\tau}_\mu(\hat{u}) = \sum_{i=1}^4 \vec{L}_i \times \vec{T}(\Omega_i, \lambda_i, \alpha_i) = \sum_{i=1}^4 \vec{L}_i \times (Q_{M_i}^* \otimes T(\Omega_i) \otimes Q_{M_i}) \in \mathcal{F}^b \quad (3.119b)$$

The torque term $\vec{\tau}_H$ is the net aerodynamic torque produced by the propeller's rotational velocity which is compensated for in ***feedback***, and is separated from the controllable inputs in Eq:3.119:

$$\vec{\tau}_H = \sum_{i=1}^4 \vec{H}(\Omega_i, \lambda_i, \alpha_i) = \sum_{i=1}^4 Q_{M_i}^* \otimes \vec{H}(\Omega_i) \otimes Q_{M_i} \in \mathcal{F}^b \quad (3.120)$$

Scalar thrust $T(\Omega_i)$ is a function of the propeller's rotational velocity whereas $\vec{T}(\Omega_i, \lambda_i, \alpha_i)$ is that thrust's three-dimensional counterpart in \mathcal{F}^b . Equivalently $H(\Omega_i)$ is the scalar aerodynamic torque in \mathcal{F}^{M_i} about each motor's rotor \hat{Z}_{M_i} -axis, whereas $\vec{H}(\Omega_i, \lambda_i, \alpha_i)$ is the torque vector counterpart in \mathcal{F}^b . Both thrust and aerodynamic torque terms are calculated from their respective coefficients (plotted in Fig:3.5):

$$\vec{T}(\Omega_i) = C_T(J) \rho \Omega_i^2 D^4 \cdot \hat{Z}_{M_i} \in \mathcal{F}^{M_i} \quad (3.121a)$$

$$\vec{H}(\Omega_i) = C_P(J) \rho \Omega_i^3 D^5 (1/R\Omega_i) \cdot \hat{Z}_{M_i} \in \mathcal{F}^{M_i} \quad (3.121b)$$

Recall that Ω_i for aerodynamic calculations in Eq:3.121a and Eq:3.121b has units [RPS]. The nonlinear torque responses from multibody configuration changes in Eq:3.110b are introduced as terms for feedback compensation, calculated from instantaneous actuator estimates:

$$\vec{\tau}_b(\vec{u}) \triangleq \dot{J}_b(\vec{u}) \vec{\omega}_b + \sum_{i=1}^4 \left[\vec{\tau}_\alpha'(\lambda_i, \alpha_i) + \vec{\tau}_\lambda''(\lambda_i) + \vec{\omega}_b \times \left((J_p'') \dot{\alpha}_i' + (J_n'') \dot{\lambda}_i'' + (J_r'') \dot{\Omega}_i''' \right) \right] \in \mathcal{F}^b \quad (3.122)$$

with $\vec{\tau}_\alpha'(\lambda_i, \alpha_i)$ and $\vec{\tau}_\lambda''(\lambda_i)$ both transformed to the body frame \mathcal{F}^b . Then including variable gravitational torque as a result of an eccentric center of gravity from Eq:2.34b, also dependent on the vehicle's configuration:

$$\vec{\tau}_g = \Delta \vec{C}_G \times \vec{G}_b = (\vec{O}_b - \vec{C}_b(\vec{u})) \times \vec{G}_b \in \mathcal{F}^b \quad (3.123)$$

The vehicles net rotational inertia, aligned and centered with the body frame, is calculated as a function of all actuator positions, taken from Eq:2.31a and given as:

$$\begin{aligned} J_b(\vec{u}) &= J_y' + \sum_{i=1}^4 J_n(\vec{u}_i) + \sum_{i=1}^4 J_m(\vec{u}_i) \quad \vec{u} \in \mathbb{U} \\ \vec{O}_b &\end{aligned} \quad (3.124)$$

where \vec{u}_i is the i^{th} motor module's actuator position: $\vec{u}_i \triangleq [\Omega_i \ \lambda_i \ \alpha_i]^T$ and \hat{u}_i is the position estimate subject to those actuator's transfer functions. Both attitude (either euler angles $\vec{\eta}$ or quaternions Q_b) and translational position states \vec{E}_I could indeed be combined into a single state \vec{x}_b . That could then be used for a complete state feedback control law which could potentially exploit or linearize the cross-coupling between the angular and translational plants. Such an approach would, however, dramatically increase the complexity in tuning actual control parameters (see Sec:6.2). Controllers for attitude and position loops are designed and optimized independently.

Chapter 4

Controller Development

4.1 Control Loop

The control problem is, as outlined in Ch:1, to achieve non-zero setpoint tracking (for both *attitude* and *position* states) on a quadrotor by solving the problem of its inherent underactuation. For the purposes of the subsequent controller development, the plant for some state \vec{x} is described in the following typical nonlinear state-space form in the time domain:

$$\frac{d}{dt}\vec{x} = f(\vec{x}, t) + g(\vec{x}, \vec{\nu}, t) \quad (4.1a)$$

$$\vec{y} = c(\vec{x}, t) + d(\vec{x}, \vec{\nu}, t) \quad (4.1b)$$

where the plant's dynamics are governed by state progression $f(\vec{x}, t)$ and the plant's input response $g(\vec{x}, \vec{\nu}, t)$ for a given control input $\vec{\nu}$. The latter could take the affine form $g(\vec{x}, t)\vec{\nu}$. Setpoint tracking aims for the output to track the plant's state; namely $\vec{y} = c(\vec{x}, t) \equiv \vec{x}$. The control problem is then to design a stabilizing control law \mathcal{H} for some error state difference between the desired and current state references, respectively $\vec{x}_e = \vec{x}_d - \vec{x}_b$ and:

$$\vec{\nu}_d \triangleq \mathcal{H}(\vec{x}_e, \dot{\vec{x}}_e, t) = \mathcal{H}(\vec{x}_b, \dot{\vec{x}}_b, \vec{x}_d, \dot{\vec{x}}_d, t) = \begin{bmatrix} \vec{F}_d & \vec{\tau}_d \end{bmatrix}^T \quad (4.2)$$

such that the controlled plant's error is asymptotically stabilized, or that $\lim_{t \rightarrow \infty} \vec{x}_e = \vec{0}$. Inputs \vec{F}_d and $\vec{\tau}_d$ are controller designed force and torque inputs respectively, to be applied by the actuator set. Trajectory stability conditions are defined next in Sec:4.3. Note that it is possible to combine attitude and position states into a single common trajectory reference such that its position is given by:

$$\vec{x}_b = \begin{bmatrix} \vec{\mathcal{E}}_I & Q_b \end{bmatrix}^T \quad (4.3)$$

The body's trajectory is then fully described by $\vec{x}_b(t)$ and its derivative $\dot{\vec{x}}_b(t)$. Separate control laws are developed for attitude and position tracking so both states are not combined in the context of this control project. Because the plant is overactuated, the control loop is split into two blocks; first a higher-level *setpoint tracking* controller designs a virtual control input $\vec{\nu}_d$, being net forces \vec{F}_d and torques $\vec{\tau}_d$ to act on the body. Next, a lower-level *allocator* solves for explicit actuator positions using $\vec{\nu}_d$ to physically actuate that *virtual* control input. The actuator commands control input $\vec{\nu}_c(\vec{u}_c)$ through its effectiveness function, defined in Eq:3.121, where the commanded actuator positions \vec{u}_c are subject to the transfer function $C(s)$ described in Sec:2.4.1.

$$\vec{\nu}_c = \begin{bmatrix} \vec{F}_c(\vec{u}_c) & \vec{\tau}_c(\vec{u}_c) \end{bmatrix}^T = B(\vec{x}, \vec{u}_c, t) \quad (4.4)$$

where $\vec{F}_c(\vec{u}_c)$ and $\vec{\tau}_c(\vec{u}_c)$ are the respective commanded input forces and torques actuated by \vec{u}_c .

The allocator solves for commanded actuator values \vec{u}_c such that $\vec{\nu}_c \rightarrow \vec{\nu}_d$. That allocation function, B^\dagger , can be *roughly* referred to as the effectiveness inverse:

$$\vec{u}_c = B^\dagger(\vec{x}, \vec{\nu}_d, t) \quad \in \mathbb{U} \quad (4.5)$$

This chapter derives higher-level controllers for $\vec{\nu}_d = \mathcal{H}(\vec{x}_e, \dot{\vec{x}}_e, t)$. Allocation rules are discussed next in Ch:5. A collection of attitude and position controllers is presented here and stability is proven with Lyapunov theory [86]. Each controller is compared in the context of an overactuated quadrotor plant, similarly a series of allocation schemes are presented. Propagation delays of the actuator input \vec{u}_c result from the actuator plant's transfer function $C(s)$. Those delays are assumed to have far slower time constants than the controller. If actuator estimates \hat{u}_c (incorporating the transfer functions) are used for feedback compensation calculations then major-loop controller coefficients will account for the minor-loop errors between a commanded \vec{u}_c and its estimate \hat{u}_c . Comparisons of the designed controllers as well as their explicit coefficients and efficacy are evaluated subsequently in Ch:6.

A generalized overactuated control loop consists of a series of cascaded control blocks (Fig:4.1). From the trajectory's error state \vec{x}_e , a control law designs a virtual control input $\vec{\nu}_d$ which is applied to the allocation block. The allocation law $B^\dagger(\vec{x}, \vec{\nu}_d, t)$ solves for physical actuator positions $\vec{u}_c \in \mathbb{U}$. Commanded actuator (*estimate*) positions affect a physical input $\vec{\nu}_c = B(\vec{x}, \hat{u}_c, t)$, which is an input applied to the state's dynamics, Eq:4.1. Finally the output tracking state is estimated with some filter paradigm $\hat{\vec{x}} = A(\vec{x}, t)$ which is fed back for error-state calculation (Sec:6.9).

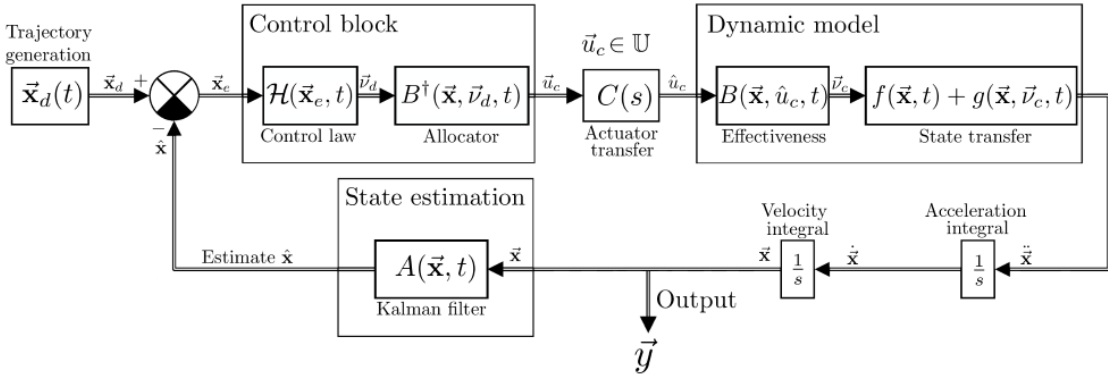


Figure 4.1: Generalized control loop with allocation

Fig:4.1 shows a generalized overactuated control loop's structure which omits many of the intricacies associated with the model in question. Some aspects of the linear system of equations for the state transfer include multibody nonlinearities, derived in Sec:3.4, which are dependent on actuator positions and rates. That generalized case is now refined in the context of an overactuated quadcopter.

4.2 Control Plant Inputs

Control inputs for the state's differential equations, from Eq:3.118, have mostly been described with net input forces and torques; $\vec{F}_\mu(\hat{u})$ and $\vec{\tau}_\mu(\hat{u})$ respectively. The relationship of the *effectiveness function* between each propeller's rotational speed and servo positions with the produced thrust vector is calculated from Eq:3.119. For some (estimated) commanded actuator position \hat{u}_c :

$$\vec{\nu}_c \triangleq \left[\vec{F}_c(\hat{u}_c) \quad \vec{\tau}_c(\hat{u}_c) \right]^T = B(\vec{x}, \hat{u}_c, t) \quad \in \mathbb{R}^6, \quad u_c \in \mathbb{U} \quad (4.6a)$$

$$\vec{F}_\mu(\hat{u}_c) = \sum_{i=1}^4 Q_{M_i}^*(\lambda_i, \alpha_i) \otimes \vec{T}(\Omega_i) \otimes Q_{M_i}(\lambda_i, \alpha_i) \quad \in \mathcal{F}^b \quad (4.6b)$$

$$\vec{\tau}_\mu(\hat{u}_c) = \sum_{i=1}^4 \vec{L}_i \times (Q_{M_i}^*(\lambda_i, \alpha_i) \otimes \vec{T}(\Omega_i) \otimes Q_{M_i}(\lambda_i, \alpha_i)) \quad \in \mathcal{F}^b \quad (4.6c)$$

As mentioned previously, a higher-level controller $\mathcal{H}(\vec{x}_e, \dot{\vec{x}}_e, t)$ designs desired net plant inputs $\vec{\nu}_d = [\vec{F}_d \quad \vec{\tau}_d]^T$ whilst a lower-level allocator commands actuator positions $\vec{u}_c = B^\dagger(\vec{x}, \vec{\nu}_d, t)$ such that $\vec{\nu}_c \rightarrow \vec{\nu}_d$. Actuator dynamics produce a tracking commanded input and not an instantaneously assumed actuator state. Separating the higher-level controller and lower-level allocator accommodates comparison between the proposed controllers and respective allocation laws. However, typical allocation rules like pseudo-inversion require an invertible relationship between plant and control inputs, detailed previously in Sec:1.2.2 and expanded on next in Sec:5.1.

The vector relationship in Eq:4.6 is not reducible to a single multiplicative relationship between the commanded actuator matrix $\vec{u}_c \in \mathbb{U} \in \mathbb{R}^{12}$ (estimated or otherwise) and the dynamic plant input $\vec{\nu}_c \in \mathbb{R}^6$. So the effectiveness function needs an extra layer of abstraction to incorporate a multiplicative relationship. Rather than calculating explicit actuator positions directly from $\vec{\nu}_d$, a set of four 3-D thrust vectors $\vec{T}_{[1:4]} \in \mathbb{R}^{1 \times 12}$ for each motor module is first calculated.

$$\vec{\nu}_c = \begin{bmatrix} \vec{F}_c(\hat{u}_c) \\ \vec{\tau}_c(\hat{u}_c) \end{bmatrix} = \begin{bmatrix} \mathbb{I}_{3 \times 3} & \mathbb{I}_{3 \times 3} & \mathbb{I}_{3 \times 3} & \mathbb{I}_{3 \times 3} \\ [\vec{L}_1]_\times & [\vec{L}_2]_\times & [\vec{L}_3]_\times & [\vec{L}_4]_\times \end{bmatrix} \begin{bmatrix} \vec{T}_1 & \vec{T}_2 & \vec{T}_3 & \vec{T}_4 \end{bmatrix}^T \quad (4.7a)$$

$$\therefore \vec{\nu}_c = B'(\vec{x}, t) \begin{bmatrix} \vec{T}_1 & \vec{T}_2 & \vec{T}_3 & \vec{T}_4 \end{bmatrix}^T \quad (4.7b)$$

$$\text{with } B'(\vec{x}, t) \triangleq \begin{bmatrix} \mathbb{I}_{3 \times 3} & \mathbb{I}_{3 \times 3} & \mathbb{I}_{3 \times 3} & \mathbb{I}_{3 \times 3} \\ [\vec{L}_1]_\times & [\vec{L}_2]_\times & [\vec{L}_3]_\times & [\vec{L}_4]_\times \end{bmatrix} \in \mathbb{R}^{12 \times 6} \quad (4.7c)$$

where $[\vec{L}_i]_\times$ is the cross product vector of the i^{th} torque arm from Eq:2.8c. Explicit actuator positions for each module $[\Omega_i, \lambda_i, \alpha_i]^T$ can then be solved for using those thrust vectors \vec{T}_i for $i \in [1 : 4]$ with some trigonometry, “undoing” the transformation applied in Eq:4.6. That trigonometric inversion is detailed later in Sec:5.2 but is described as the function R^\dagger :

$$[\Omega_i, \lambda_i, \alpha_i]^T = R^\dagger(\vec{x}, \vec{T}_i, t) \quad \text{for } i \in [1 : 4] \quad (4.8)$$

The generalized control loop illustrated in Fig:4.1 is extended to include the abstracted allocation blocks of Eq:4.7 and Eq:4.8, shown in Fig:4.2. The net control block still solves for the same actuator matrix $u \in \mathbb{U}$. The entire loop accommodates for comparison of various $B^\dagger(\vec{x}, \vec{\nu}_d, t)$ allocation rules without having to redesign the remainder of the loop’s structure.

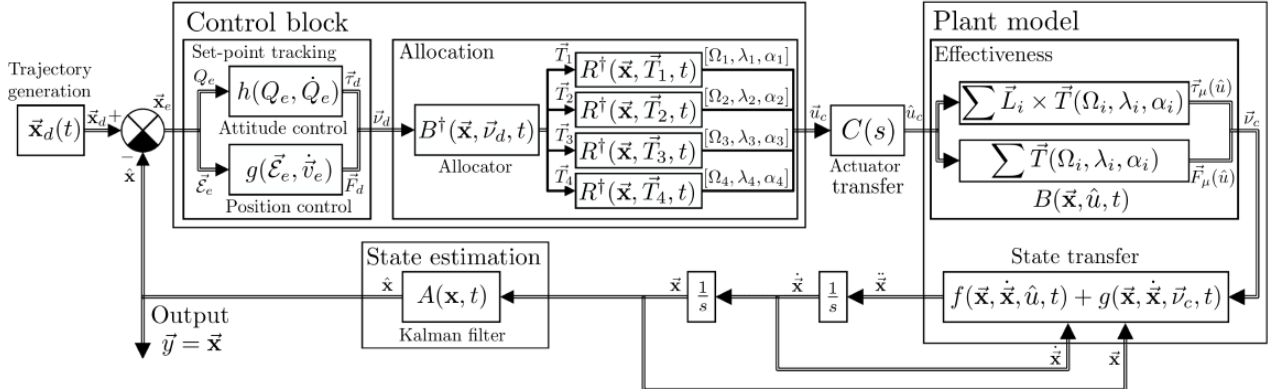


Figure 4.2: Extended control loop with overactuation

Certain blocks in Fig:4.2 use commanded actuator position estimates \hat{u}_c to calculate responses for feedback compensation. In summary, each controller designs either a net force \vec{F}_d for position or a net torque $\vec{\tau}_d$ to act on the body. Allocation rules decompose that virtual input $\vec{\nu}_d$ into four separate 3-D thrust vectors $\vec{T}_{[1:4]} \in \mathbb{R}^{1 \times 12}$, or twelve directional components. The force components are an abstracted allocation layer in place of explicit actuator positions, which are subsequently solved for using a static inverse trigonometry.

$$B^\dagger(\vec{x}, \vec{\nu}_d, t) = [T_{1x}, T_{1y}, T_{1z}, \dots, T_{4x}, T_{4y}, T_{4z}]^T \quad (4.9)$$

Each control law is co-dependent on an accompanying allocation algorithm. Traditional control loops (underactuated or well matched) typically have a unity allocation rule and as such require no consideration so they are mostly disregarded. Separate control laws for attitude and position control are presented in Section:4.6 and 4.7 respectively. Thereafter a series of allocation rules are proposed in Ch:5. Although presented independently, the controller and allocation laws are co-dependent. The stability of each controller is proven in the Lyapunov sense but explicit controller coefficients are optimized in the subsequent Ch:6, in Sec:6.2.

4.3 Stability

Before undertaking the control plant derivations, it is worth outlining definitions of control stability first. The research question aims to achieve non-zero setpoint tracking of the state's trajectory. A control loop then aims to *stabilize* the closed-loop dynamics described previously in Sec:3.5 whilst tracking particular trajectories for attitude and position setpoints, $\vec{x}_d(t) = [\vec{E}_d(t) \ Q_d(t)]^T$.

The entire system's control-loop was detailed in Sec:4.1. Stability in the context of trajectory tracking must first be defined. Generalized trajectory stability definitions are not uncommon in the context of energy-based control design, or Lyapunov theory (Sec:4.4). Stability definitions pertinent to Lyapunov's stability theorem are briefly presented here, the following is adapted from [86]. In general, for some autonomous trajectory $\vec{x}(t)$, an equilibrium point at the origin $\vec{0}$ is said to be stable (**S**) at $t = t_0$ if and only if (*iff*) the following is true:

$$\forall \varepsilon > 0, \exists \delta_0(t_0, \varepsilon) : \|\vec{x}(t_0)\| < \delta_0(t_0, \varepsilon) \quad (4.10a)$$

$$\text{and } \|\vec{x}(t)\| < \varepsilon, \forall t \geq t_0 \quad (4.10b)$$

The implication of which is that if, for some initial condition $\vec{x}(t_0)$ whose magnitude is bound by the manifold $\delta_0(t_0, \varepsilon)$, the entire subsequent trajectory of $\vec{x}(t)$ is bound from above by some other manifold ε . Generalized stability is illustrated in Fig:4.3a for a 2-D trajectory.

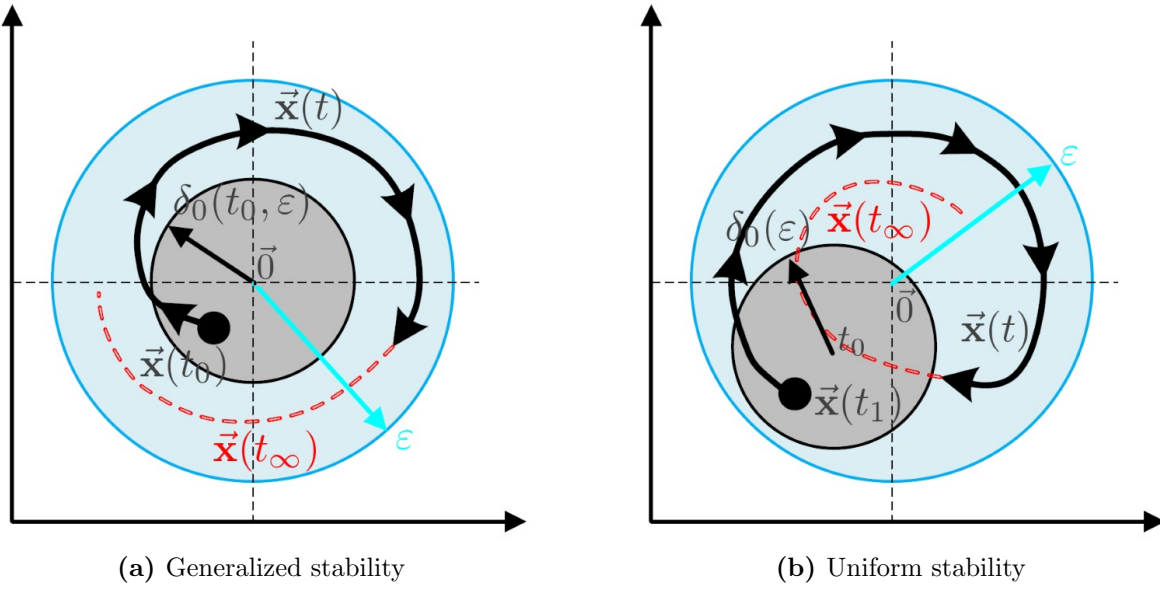


Figure 4.3: Trajectory illustrations for **S** and **US**

An equilibrium point is further said to be uniformly stable (**US**) *iff* for the time $t \in [t_0, \infty)$ the following criteria, being an extension of general stability, are met:

$$\forall \varepsilon > 0, \exists \delta_0(\varepsilon) > 0 : \|\vec{x}(t_1)\| < \delta_0(\varepsilon), \quad t_1 > t_0 \quad (4.11a)$$

$$\text{and } \|\vec{x}(t)\| < \varepsilon, \quad \forall t \geq t_1 \quad (4.11b)$$

US similarly bounds a trajectory from above by ε if the trajectory originates from within $\delta_0(\varepsilon)$. The difference is that the principle trajectory region $\delta_0(\varepsilon)$ is independent of t_0 in the case of **US**.

The two surfaces are non-concentric, a **US** trajectory is illustrated in Fig:4.3b. Uniform stability is a subset of general stability, $\mathbf{US} \subset \mathbf{S}$, however the converse is not true. Furthermore **US** is a stronger qualification of stability, each subsequent stability presented represents a stronger assertion of stability.

Extending stability definitions to include settling, an equilibrium point is said to be asymptotically stable (**AS**) iff conditions for **S** are met (Eq:4.10) and that the following holds true:

$$\exists \delta_1(t_0, \varepsilon) > 0 : \|\vec{x}(t_0)\| < \delta_1(t_0, \varepsilon) \quad (4.12a)$$

$$\text{and } \lim_{t \rightarrow \infty} \|\vec{x}(t)\| \rightarrow 0 \quad (4.12b)$$

This asserts that trajectories originating within some finer region $\delta_1(t_0, \varepsilon)$, being a subset of $\delta_0(t_0, \varepsilon)$, tend to and *asymptotically* settle at the origin. In the case of **AS** the origin is both *stable* and *attractive* (shown in Fig:4.4a). Asymptotic stability is typically the first requirement for any control law, being a stronger stability than both **US** and **S**, typically stabilizing a control setpoint's error.

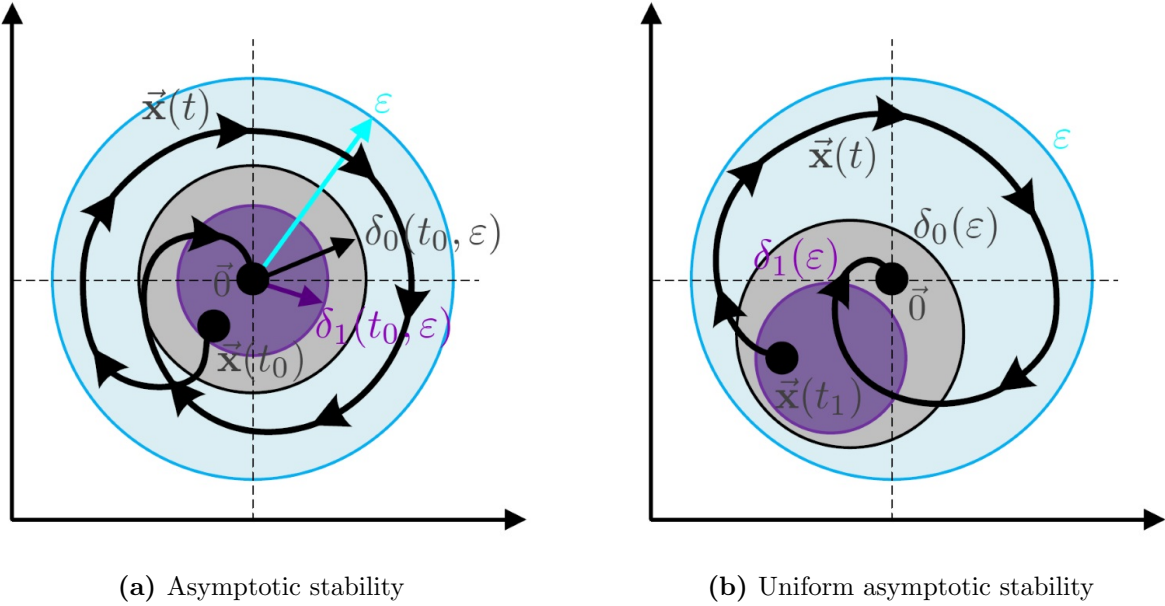


Figure 4.4: Trajectory illustrations for **AS** and **UAS**

Uniform asymptotic stability (**UAS**), an extension of asymptotic stability $\mathbf{UAS} \subset \mathbf{AS}$, occurs when the asymptotically stable bound region $\delta_1(\varepsilon)$ is independent of the principle starting time t_0 . An equilibrium point is **UAS** iff conditions for **S** are met and that:

$$\exists \delta_1(\varepsilon) > 0 : \|\vec{x}(t_1)\| < \delta_1(\varepsilon), \quad t_1 \geq t_0 \quad (4.13a)$$

$$\text{and } \lim_{t \rightarrow \infty} \|\vec{x}(t)\| \rightarrow 0 \quad (4.13b)$$

A uniformly asymptotic equilibrium point implies a stable trajectory starting within a non-concentric region, independent of the starting time t_0 , and settling to the origin (illustrated in Fig:4.4b).

A trajectory is regarded as exponentially stable (**UES**) if conditions for **UAS** are met and that there exist $\exists a, b, r$ that bound the settling of the trajectory such that:

$$\|\vec{x}(t, t_0, \vec{x}_0)\| \leq a \|\vec{x}_0\| e^{-bt}, \quad \forall \|\vec{x}_0\| \leq r \quad (4.14)$$

The term $a \|\vec{x}_0\| e^{-bt}$ bounds the worst case rate at which the trajectory settles to the origin, illustrated in Fig:4.5a. Exponential stability guarantees that the magnitude displacement of the trajectory at any given point in time is less than an explicit exponential decay. The initial point of the trajectory, \vec{x}_0 , is bound from above by some $r \triangleq \delta_1(\varepsilon)$. Moreover uniform stability is *implied* with exponential stability.

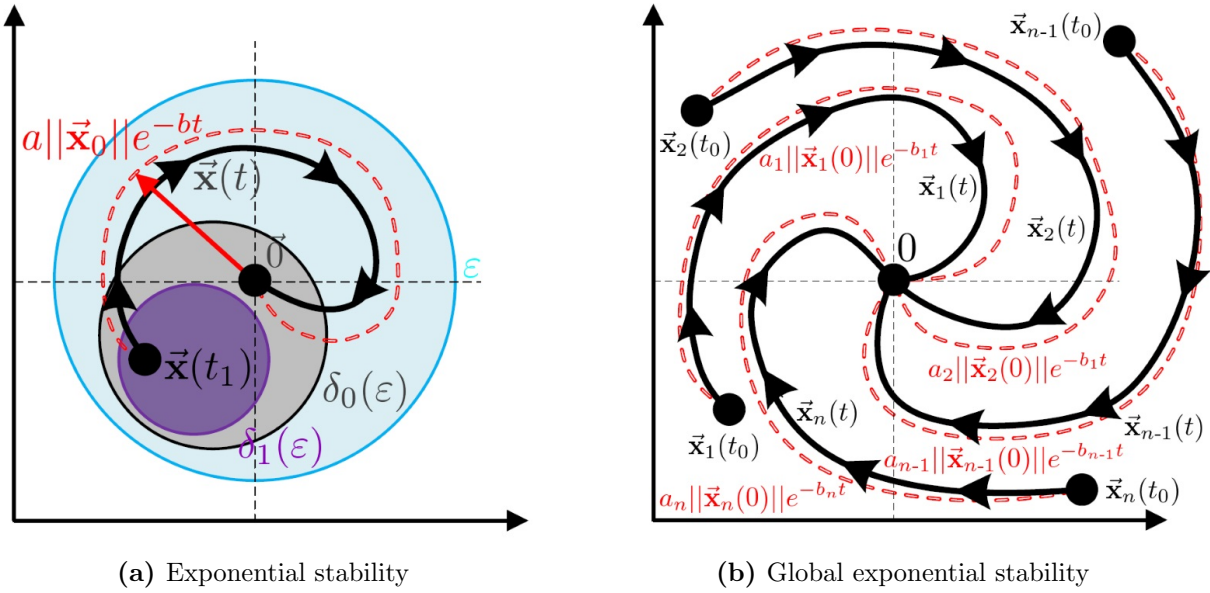


Figure 4.5: Trajectory illustrations for **UES** and **GUES**

The above definitions of stabilities are only locally defined, and so the stabilities hold true only for local trajectories, only in the case of $\vec{x}(t_0) \leq \varepsilon$. Extending **UAS** to global uniform asymptotic stability (**GUAS**), the origin's equilibrium point is **GUAS** iff conditions for **UAS** are first met, the origin is only the equilibrium point and the asymptotic approach can be extended such that:

$$\exists \delta_1(\varepsilon) > 0 : \|\vec{x}(t_1)\| < \delta_1(\varepsilon), \quad t_1 \geq t_0 \quad (4.15a)$$

$$\text{and } \lim_{t \rightarrow \infty} \|\vec{x}(t)\| \rightarrow 0, \quad \forall \vec{x}(t_0) \quad (4.15b)$$

Similarly, exponential stability can extend to the global case, shown in Fig:4.5b, but only iff **UES** conditions are first met. In the global case, the origin can be the *only equilibrium point*. Stability from Eq:4.14 is then globally:

$$\|\vec{x}(t, t_0)\| \leq a \|\vec{x}_0\| e^{-bt}, \quad \forall \|\vec{x}_0\| \quad (4.16)$$

Initial trajectory conditions are dropped in Eq:4.16 for any number of trajectories until $\vec{x}_n(t)$ each trajectory is bound by an exponential $a_n \|\vec{x}_n(0)\| e^{-b_n t}$. It follows that, irrespective of the starting point $\vec{x}_n(t_0)$ for the trajectory, the system *always* settles to the origin. **GUES** is the strongest sense of stability and provides insight into the trajectory stabilizing rate. The most desirable control design outcome is a controller which applies globally uniform exponential stability to a plant.

4.4 Lyapunov Stability Theory

Lyapunov's stability theory is an important aspect of nonlinear controller design. If the reader is unfamiliar with Lyapunov's theorem, [18, 111] each provide thorough explanations of the concept. The following is adapted from [86] and [96] and briefly outlines how Lyapunov's stability theory is used to prove (*global*) asymptotic stability for continuous time invariant systems, linear or otherwise.

The theory analyzes a generalized energy function of a system's autonomous trajectory, if the trajectory has a negative energy derivative that implies the system's energy will always dissipate towards a state of zero energy or stable equilibrium point. Lyapunov analysis is a powerful tool for stability verification because the system's trajectory itself need not be explicitly defined for stability to be determined. It is worth repeating Lyapunov fundamentals given that backstepping controllers are proposed later in Sec:4.6.3 for attitude control.

A backstepping controller enforces Lyapunov stability criteria onto the system through iterative control structure design [10, 73, 136]. In general, given a nonlinear time invariant system that follows some continually differentiable trajectory $\vec{x}(t)$, typically the trajectory is going to progress subject to some autonomous rule:

$$\dot{\vec{x}}(t) = f(\vec{x}(t)) \quad (4.17)$$

Then a generalized positive-definite function (generalized energy) or *Lyapunov function candidate (LFC)* $V(\vec{x})$ for a trajectory $\vec{x}(t)$ is constructed. A positive definite matrix M is defined such that:

$$\mathbf{z}^T M \mathbf{z} > 0 \quad \forall \mathbf{z} \neq 0 \quad (4.18)$$

As such an LFC typically, but not exclusively, has the quadratic and positive-definite form with some positive square matrix $P \in \mathbb{R}^{n \times n} > 0$:

$$V(\vec{x}) = \vec{x}^T P \vec{x}, \quad \vec{x} \in \mathbb{R}^n \quad (4.19)$$

An LFC could simply be positive semi-definite over the trajectory's path, the quadratic form is just convenient for the use of backstepping. From its definition the trajectory Eq:4.17 is continually differentiable, there is then a gradient matrix for each element of $V(\vec{x})$ in the form:

$$\nabla V(\vec{x}) \triangleq \left[\frac{\partial V(\vec{x})}{\partial x_1} \frac{\partial V(\vec{x})}{\partial x_2} \dots \frac{\partial V(\vec{x})}{\partial x_n} \right] \quad \vec{x} \in \mathbb{R}^n \quad (4.20)$$

The energy function's derivative, otherwise referred to as the *Lie derivative*, is calculated from partial derivatives in Eq:4.20 as follows:

$$\dot{V}(\vec{x}) \triangleq \nabla V(\vec{x})^T f(\vec{x}) = \frac{\partial V(\vec{x})}{\partial x_1} f_1(x_1) + \frac{\partial V(\vec{x})}{\partial x_2} f_2(x_2) + \dots + \frac{\partial V(\vec{x})}{\partial x_n} f_n(x_b) \quad (4.21)$$

Lyapunov's theorem states that if the candidate function $V(\vec{x})$ is positive definite with $V(\vec{0}) = 0$ and its derivative is strictly negative, $\dot{V}(\vec{x}) < 0 \quad \forall \vec{x}(t) \neq 0$, the system has global uniform asymptotic stability (**GUAS** from Eq:4.12). Mathematically that means, for any $\vec{x}(t)$ with $t \geq t_0$:

$$V(\vec{x}(t)) = V(\vec{x}(t_0)) + \int_{t_0}^t \dot{V}(\vec{x}(t)) dt \leq V(\vec{x}(t_0)) \quad (4.22)$$

which can be physically interpreted as the system's generalized energy (function) dissipating, irrespective of the trajectory path taken. With a strictly decreasing energy function, the system will stabilize to a state of zero energy which, naturally, is a stable equilibrium point.

$$\lim_{t \rightarrow \infty} \|V(\vec{x}(t))\| \rightarrow 0 \quad (4.23)$$

The trajectory's asymptotic stability can be extended to exponential stability boundedness, such that if the same conditions are met for asymptotic stability in Eq:4.22 and there exists some positive coefficient $\alpha > 0$ such that $\dot{V}(\vec{x}) < -\alpha V(\vec{x})$. That implies the system is globally exponentially stable and is bound in such a way that:

$$\|V(\vec{x}(t))\| \leq M e^{-\alpha t} \|V(\vec{x}(t_0))\| \quad (4.24)$$

4.5 Model Dependent and Independent Controllers

Two classes of controllers are included for the trajectory tracking control loop, both attitude and position control laws. Attitude setpoint tracking is the primary focus of this research project (Sec:4.6.1) and incorporates a more detailed schedule of controller design and evaluation. The allocation law combines both virtual control inputs from attitude and position controllers, $\vec{\nu}_d = [\vec{F}_d \ \vec{\tau}_d]^T$, to solve for explicit actuator positions.

Controller dependency on the plant's state is as a consequence of the actuator responses and complex inertial dynamics, as derived previously in Sec:3.4.1. Whilst not a prerequisite for stability, plant dependent compensation obviously improves controller performances. Independent and dependent cases are only considered for one type of controller, the most basic case proportional-derivative controller in Section:4.6.2 and tested in Sec:6.3.1. All other control laws compensate for unwanted plant dynamics in a feedback configuration.

The plant dependency makes backstepping controllers an effective controller choice for this dissertation's context. The proposed plant dependent control laws compensate for undesirable dynamics by design, basic PD and PID control structures will not. The first and most basic control solution, used as a reference case, is a PD controller for attitude and position with direct-inversion (Pseudo or Moore-Penrose inversion) allocation.

4.6 Attitude Control

4.6.1 The Attitude Control Problem

The setpoint tracking control problem for the attitude of the plant [131], is to design a stabilizing control torque $\vec{\tau}_d = h(\vec{x}_e, \dot{\vec{x}}_e, t)$ such that for any desired attitude quaternion $\forall Q_d \in \mathbb{Q}$ and an instantaneous attitude body quaternion $Q_b \in \mathbb{Q}$, the error state asymptotically stabilizes to the origin $Q_e \rightarrow [\pm 1 \vec{0}]^T$. Or that:

$$\vec{\tau}_d = h(Q_d, \dot{Q}_d, Q_b, \dot{Q}_b) \text{ such that } \lim_{t \rightarrow \infty} Q_b \rightarrow Q_d \quad (4.25)$$

Quaternion attitude error states are defined as the Hamilton product or *difference* between the desired and instantaneous quaternion attitude states, previously in Eq:3.56. Quaternion error states are multiplicative, in contrast to the subtractive relationship for Euler angle error states. The attitude error state is defined as:

$$Q_e \triangleq Q_b^* \otimes Q_d \quad (4.26)$$

The relative angular velocity error between the body frame \mathcal{F}^b and the trajectory's desired frame \mathcal{F}^d is given as $\vec{\omega}_e$. The desired angular velocity $\vec{\omega}_d$ is taken with respect to the desired angular attitude frame \mathcal{F}^d , and therefore must be first transformed back to the existing body frame.

$$\vec{\omega}_e \triangleq Q_e^* \otimes \vec{\omega}_d \otimes Q_e - \vec{\omega}_b \quad \in \mathcal{F}^b \quad (4.27a)$$

For the trajectories generated here, only first-order setpoints are commanded, hence the desired angular velocity is zero or that $\vec{\omega}_d \triangleq \vec{0}$. It follows that the angular velocity error is then simply the negative body angular velocity. It would be easy to incorporate a non-zero angular velocity setpoint to accommodate for higher-order state derivative tracking trajectories.

$$\therefore \vec{\omega}_e = -\vec{\omega}_b \Big|_{\vec{\omega}_d=\vec{0}} \quad (4.27b)$$

The time derivative for the quaternion error state is calculated from the quaternion rate definition in Eq:3.52. The quaternion error derivative \dot{Q}_e depends on the angular velocity error and is calculated:

$$\dot{Q}_e = \frac{1}{2} Q_e \otimes \vec{\omega}_e = -\frac{1}{2} Q_e \otimes \vec{\omega}_b \Big|_{\vec{\omega}_d=\vec{0}} \quad (4.28)$$

Stability proofs for each of the subsequent controllers apply Lyapunov stability theory to analyze the attitude quaternion error's trajectory. If the attitude error is asymptotically stabilized, it follows that the attitude state will track its setpoint, Eq:4.25. Typically, proposed Lyapunov Function candidates for a quaternion error trajectory all take the standard quadratic form:

$$V(Q_e) = \vec{q}_e^T \vec{q}_e + (1 - q_0)^2 \quad (4.29)$$

For Lyapunov's stability theory to be applied, a valid Lyapunov function candidate *must* be positive definite. The constraints on the quaternion trajectory LFC in Eq:4.29 are that $V(Q_e) > 0 \ \forall (Q_e) \neq 0$ and that it must be zero at the origin (in this case a zero quaternion $Q_e = [\pm 1 \vec{q}]^T$) so the requirement is that $V([\pm 1 \vec{q}]) = 0$. Unless a variable substitution is performed for the quaternion attitude error, the Lyapunov function candidate Eq:4.29 is only positive definite for a local quaternion trajectory with $q_0 \in [0 : 1]$. A variable substitution presented in [74] replaces the quaternion scalar with its absolute value, to be used as a backstepping state variable:

$$z_1 \triangleq \begin{bmatrix} 1 - |q_0| \\ \vec{q}_e \end{bmatrix} \quad (4.30a)$$

which is then used as a trajectory variable in the *positive definite* Lyapunov function candidate:

$$V(z_1) = z_1^T z_1 > 0 \ \forall z_1 \neq 0 \quad (4.30b)$$

Substitution for a quaternion scalar's absolute value makes the control law more complicated when trying to enforce backstepping iteration, shown next in Sec:4.6.3. Alternatively, limiting the quaternion error's scalar to a range $q_0 \in [0 : 1]$ reduces the "dual-coverage" quaternions have of R^3 attitudes when described in R^4 space. If one considers how an error quaternion relates to an Euler-axis rotation of an error angle θ_e about an error unit axis \hat{u}_e , from the definition of a quaternion in Eq:3.57:

$$Q_e = \begin{bmatrix} q_0 \\ \vec{q}_e \end{bmatrix} \triangleq \begin{bmatrix} \cos(\theta_e/2) \\ \sin(\theta_e/2)\hat{u}_e \end{bmatrix} \quad (4.31)$$

then a constraint applied to $q_0 \in [0 : 1]$ limits the Euler-axis error rotation $\theta_e \in [-\pi : \pi]$. In practical terms, the stability proofs for such a limited quaternion trajectory *will not* guarantee global stability in the quaternion space R^4 , *but* it will guarantee global 3-D stability in SO(3) or R^3 . That is not to say a particular controller cannot be stable for the full $q_0 \in [-1 : 1]$, the stability is only *guaranteed* for the constrained range. Because $Q = [\pm q_0 \vec{q}]$ corresponds to the same physical attitude in R^3 , the calculated quaternion error Q_e , from Eq:4.26, can be constrained with an absolute value quaternion scalar without limiting the rigid body attitude plant. Using the definition for quaternion multiplication in Eq:3.45c and the quaternion conjugate in Eq:3.46, the quaternion error is refined:

$$Q_e = \begin{bmatrix} q_0 \\ \vec{q}_e \end{bmatrix} \triangleq \begin{bmatrix} |q_{b0}q_{d0} + \vec{q}_b \cdot \vec{q}_d| \\ q_{b0}\vec{q}_d - q_{d0}\vec{q}_b - \vec{q}_b \times \vec{q}_d \end{bmatrix} \quad (4.32)$$

Using the constrained quaternion in Eq:4.32 for control calculations then ensures that global stability of the rigid body's attitude in R^3 can be guaranteed by the subsequent stability proofs. Neither the angular velocity error $\vec{\omega}_e$, nor the quaternion error derivative \dot{Q}_e , both in Eq:4.27b, are affected by the refinement.

4.6.2 Linear Controllers

PD Controller

The following control law is used as a reference case for comparing the subsequent designed controllers. It is a simple proportional-derivative (*PD*) attitude controller, adapted from [39] and applies a stability proof similar to the one derived in [131]. An attitude PD controller is proportional only to the *vector quaternion error*, so that the error is then of the same dimension as the angular velocity error, $\vec{q}_e \in R^3$. A PD controller generates the commanded torque input:

$$\vec{\tau}_{PD} = J_b(\hat{u})(K_d\vec{\omega}_e + K_p\vec{q}_e) \quad \in \mathcal{F}^b \quad (4.33)$$

where both K_d and K_p are *positive symmetrical* 3×3 gain coefficient matrices to be determined at a later stage.

Positive symmetry imposed on the coefficients in Eq:4.33 simplifies the stability proof that follows but is not necessarily a prerequisite. Because Eq:4.33 neglects the quaternion scalar error, it is therefore susceptible to unwinding. Using a positive-definite Lyapunov function candidate V_{PD} for the attitude trajectory:

$$V_{PD}(Q_e, \vec{\omega}_e) \triangleq \vec{q}_e^T \vec{q}_e + (1 - q_0)^2 + \frac{1}{2} \vec{\omega}_e^T K_p^{-1} \vec{\omega}_e > 0 \quad \forall (Q_e, \vec{\omega}_e) \neq \vec{0} \quad (4.34)$$

The origin is an equilibrium point as a result of the constrained quaternion error trajectory proposed in Eq:4.32. Then $V_{PD}([1 \vec{0}]^T, \vec{0}) = 0$, which makes it positive definite and a suitable Lyapunov function candidate. Exploiting the unit quaternion's inherent magnitude property:

$$\|Q\| \triangleq \vec{q}^T \vec{q} + q_0^2 = \vec{q}^2 + q_0^2 = 1 \quad (4.35)$$

and substituting the unit quaternion's identity and the angular velocity's error state $\vec{\omega}_e = -\vec{\omega}_b$, the proportional derivative LFC from Eq:4.34 reduces to:

$$V_{PD} = \vec{q}_e^2 + (q_0^2 - 2q_0 + 1) + \frac{1}{2} \vec{\omega}_e^T K_p^{-1} \vec{\omega}_e \quad (4.36a)$$

$$= 2(1 - q_0) + \frac{1}{2} \vec{\omega}_b^T K_p^{-1} \vec{\omega}_b \Big|_{\vec{\omega}_e = -\vec{\omega}_b} \quad (4.36b)$$

Taking the derivative of that Lyapunov Function candidate then yields:

$$\dot{V}_{PD}(Q_e, \vec{\omega}_e) = -2\dot{q}_0 + \vec{\omega}_b^T K_p^{-1} \dot{\vec{\omega}}_b \quad (4.37)$$

Then, using the error quaternion's derivative \dot{Q}_e and noting that $\vec{\omega}_e = -\vec{\omega}_b$:

$$\dot{Q}_e \triangleq \begin{bmatrix} -\frac{1}{2} \vec{q}_e^T \vec{\omega}_e \\ \frac{1}{2} ([\vec{q}_e]_\times + q_0 \mathbb{I}_{3 \times 3}) \vec{\omega}_e \end{bmatrix} \quad (4.38a)$$

$$= -\frac{1}{2} \begin{bmatrix} -\vec{q}_e^T \vec{\omega}_b \\ ([\vec{q}_e]_\times + q_0 \mathbb{I}_{3 \times 3}) \vec{\omega}_b \end{bmatrix} \quad (4.38b)$$

Substituting the error quaternion's scalar derivative \dot{q}_0 back into the LFC derivative Eq:4.37 gives:

$$\therefore \dot{V}_{PD} = -\vec{q}_e^T \vec{\omega}_b + \vec{\omega}_b^T K_p^{-1} \dot{\vec{\omega}}_b \quad (4.38c)$$

Recalling the angular velocity differential equation from Eq:3.118d for $\dot{\vec{\omega}}_b$ with a control torque input $\vec{\tau}_{PD}$ from Eq:4.33:

$$\dot{\vec{\omega}}_b = J_b^{-1}(\vec{u}) (-\vec{\omega}_b \times J_b(\vec{u}) \vec{\omega}_b - \vec{\tau}_b(\vec{u}) + \vec{\tau}_g + \vec{\tau}_H + \vec{\tau}_{PD}) \in \mathcal{F}^b \quad (4.39a)$$

Using the definition of the proportional derivative torque control law from Eq:4.33, the angular acceleration equation Eq:4.38c for $\vec{\omega}_b$ becomes:

$$\dot{\vec{\omega}}_b = J_b^{-1}(\vec{u}) (-\vec{\omega}_b \times J_b(\vec{u}) \vec{\omega}_b - \vec{\tau}_b(\vec{u}) + \vec{\tau}_g + \vec{\tau}_H) - K_d \vec{\omega}_b + K_p \vec{q}_e \quad (4.39b)$$

Substituting the above into the LFC derivative \dot{V}_{PD} in Eq:4.37 yields:

$$\dot{V}_{PD} = -\vec{q}_e^T \vec{\omega}_b + \vec{\omega}_b^T K_p^{-1} \left(-K_d \vec{\omega}_b + K_p \vec{q}_e + J_b^{-1}(\vec{u}) (-\vec{\omega}_b \times J_b(\vec{u}) \vec{\omega}_b - \vec{\tau}_b(\vec{u}) + \vec{\tau}_g + \vec{\tau}_H) \right) \quad (4.40a)$$

$$= -\vec{q}_e^T \vec{\omega}_b + \vec{\omega}_b^T \vec{q}_e - \vec{\omega}_b^T K_p^{-1} K_d \vec{\omega}_b + \vec{\omega}_b^T \left(K_p J_b(\vec{u}) \right)^{-1} (-\vec{\omega}_b \times J_b(\vec{u}) \vec{\omega}_b - \vec{\tau}_b(\vec{u}) + \vec{\tau}_g + \vec{\tau}_H) \quad (4.40b)$$

The transposed terms $\vec{q}_e^T \vec{\omega}_b$ and $\vec{\omega}_b^T \vec{q}_e$ are interchangeable so then $-\vec{q}_e^T \vec{\omega}_b + \vec{\omega}_b^T \vec{q}_e = 0$. The LFC derivative \dot{V}_{PD} then simplifies to:

$$\dot{V}_{PD} = -\vec{\omega}_b^T K_p^{-1} K_d \vec{\omega}_b + \vec{\omega}_b^T \left(K_p J_b(\vec{u}) \right)^{-1} (-\vec{\omega}_b \times J_b(\vec{u}) \vec{\omega}_b - \vec{\tau}_b(\vec{u}) + \vec{\tau}_g + \vec{\tau}_Q) \quad (4.40c)$$

Then, as long as the entire term $(-\vec{\omega}_b \times J_b(\vec{u}) \vec{\omega}_b - \vec{\tau}_b(\vec{u}) + \vec{\tau}_g + \vec{\tau}_Q)$ is negative semi-definite or $< \vec{0}$, some element of stability can be achieved. Under specific circumstances the following assumptions can be made to apply an asymptotic stability proof:

1. The inertia matrix $J_b(\vec{u})$ is approximately diagonal, which, given the inertia eigenvalues from Eq:2.32 and Eq:2.33, is reasonable. Similarly, the angular velocity can be made small with an appropriately slow trajectory such that the torque gyroscopic cross-product is negligible:

$$(-\vec{\omega}_b \times J_b(\vec{u})\vec{\omega}_b) \approx \vec{0}$$

2. The actuator rate torque response, $\vec{\tau}_b(\vec{u})$, is a second-order effect dependent on $d\vec{u}/dt$. Typically the actuator rates are going to be kept small. For small actuator step changes the inertia rates of change and servo accelerations in Eq:3.122 are small enough to be considered negligible. The assumption is then made:

$$\vec{\tau}_b(\vec{u}) \approx \vec{0}$$

3. Finally, for the sake of the stability proof, the eccentric gravitational torque arm, from a varying center of gravity $\Delta\vec{C}_G$, from Eq:3.123, is neglected. Such a situation only holds true if $\vec{u} \approx \vec{0}$ or that servo actuator positions are close to their zero positions.

$$\vec{\tau}_g \approx \vec{0}$$

All of the above assumptions are made under extraneous circumstances, the subsequent stability obviously breaks down if any of assumptions 1 through 3 fail. Stability achieved using the above plant *independent* control law is only local, and will not hold true for most of the prototype's flight envelope, which involves time varying angular velocities $\vec{\omega}_b \neq \vec{0}$.

The plant independent case is considered and simulated in Sec:6.3.1 only to demonstrate the need for plant-dependent compensation. If each of the assumptions hold true, then the unwanted dynamic terms in Eq:4.40c are negligible or $(-\vec{\omega}_b \times J_b(\vec{u})\vec{\omega}_b - \vec{\tau}_b(\vec{u}) + \vec{\tau}_g + \vec{\tau}_Q) \approx \vec{0}$, resulting in a negative definite Lyapunov function derivative. The stability proof for that very local trajectory is then:

$$\dot{V}_{PD} = -\vec{q}_e^T \vec{\omega}_b + \vec{\omega}_b^T K_p^{-1} (-K_d \vec{\omega}_b + K_p \vec{q}_e) \quad (4.41a)$$

$$= -\vec{\omega}_b^T K_p^{-1} K_d \vec{\omega}_b \quad (4.41b)$$

$$= -K_p^{-1} K_d \|\vec{\omega}_b\|^2 < 0 \quad \forall (\vec{q}_e, \vec{\omega}_e), \quad q_0 \in [0 : 1], \quad \exists (K_p^{-1}, K_d) > 0 \quad (4.41c)$$

From Lyapunov stability theorem there then exist the following limits:

$$\lim_{t \rightarrow \infty} \vec{\omega}_e \rightarrow \vec{0} \quad \therefore \lim_{t \rightarrow \infty} \vec{\omega}_b \rightarrow \vec{0} \quad (4.42a)$$

$$\lim_{t \rightarrow \infty} \vec{q}_e \rightarrow \vec{0} \quad \text{and} \quad \lim_{t \rightarrow \infty} (1 - q_0) \rightarrow 0 \quad (4.42b)$$

If $q_0 \in [0 : 1]$ then the quaternion error stabilizes $Q_e \rightarrow [1 \ \vec{0}]^T$ as $t \rightarrow \infty$. The stability shown in Eq:4.41c is only local. Introducing plant dependent compensation to the PD control law in Eq:4.33 alleviates the stringent requirements on assumptions 1 through 3, as shown subsequently. Adding compensation terms for the unwanted plants dynamics:

$$\vec{\tau}_{PD} = \underbrace{J_b(\hat{u})(K_p \vec{q}_e + K_d \vec{\omega}_e)}_{\text{Independent}} + \underbrace{\hat{\omega}_b \times J_b(\hat{u})\hat{\omega}_b + \vec{\tau}_b(\hat{u}) - \vec{\tau}_g - \vec{\tau}_Q}_{\text{Compensation}} \quad (4.43)$$

Obviously, controller errors and compensation terms rely on *state estimates*, whereas inertias and torque responses are calculated using sampled \hat{u}_c commanded actuator positions. Moreover, the quaternion attitude and angular velocity states \hat{Q}_b and $\hat{\omega}_b$ are both estimates and so a small degree of uncertainty exists. Robust stability in the case of plant-dependent uncertainty is investigated in Sec:6.6, but for now the estimates are *assumed to be free of errors and dynamics*. The resultant stability proof for the plant dependent case, Eq:4.43, is much the same as that for the independent controller, Eq:4.33. The same LFC from Eq:4.34 shows that Eq:4.41c holds globally:

$$\therefore \dot{V}_{PD} = -\vec{\omega}_b^T K_p^{-1} K_d \vec{\omega}_b \quad (4.44a)$$

$$\therefore \dot{V}_{PD} \leq -K_p K_d \|\vec{\omega}_b\|^2 < 0 \quad \forall (\vec{q}_e, \vec{\omega}_e), \quad q_0 \in [0 : 1], \quad \exists (K_p^{-1}, K_d) > 0 \quad (4.44b)$$

The inverse qualifier of K_p^{-1} in Eq:4.44a is redundant given that K_p is a symmetrical coefficient matrix. The plant-dependent controller compensates for the unwanted dynamics which the independent control otherwise assumes are inconsequential to achieve the same stability. Dynamic compensation in Eq:4.43 is simple to implement, considering the unwanted dynamics have already been quantified and corroborated in Sec:3.4.2 together with state estimate terms in Sec:2.4.1.

Auxiliary Plant Controller

Expanding on what has, in practice (Table:1.1 from Sec:1.2.1), proven to be a popular and effective controller for attitude stabilization, [128] proposed adding auxiliary signals to a PD attitude controller which guarantees an exponentially bound stable trajectory. That control law has been adapted to fit the setpoint tracking control problem considered here. Most significantly, the altered PD controller introduces terms proportional to the quaternion error's derivative, Eq:3.52, so that conditions in Eq:4.24 are met to ensure a bounding exponentially stable trajectory. Furthermore, part of the auxiliary plant is proportional to the *quaternion scalar* q_0 , a term that is otherwise neglected in the previous PD control law (Sec:4.6.2). That proportionality term ensures unnecessary quaternion unwinding of the error state is avoided. The *auxilliarily* PD control torque is calculated as a function of error states:

$$\vec{\tau}_{XPD} = \underbrace{\Gamma_2 \tilde{\Omega} + \Gamma_3 \vec{q}_e - J_b(\hat{u}) \dot{\tilde{\Omega}}}_{\text{Independent}} + \underbrace{\hat{\omega}_b \times J_b(\hat{u}) \hat{\omega}_b + \vec{\tau}_b(\hat{u}) - \vec{\tau}_g - \vec{\tau}_H}_{\text{Compensation}} \quad (4.45)$$

wherein the coefficients Γ_2 and Γ_3 are both diagonal positive $[3 \times 3]$ coefficient matrices and Γ_1 , used in Eq:4.46, is a symmetrical $[3 \times 3]$ coefficient matrix. Each gain coefficient matrix is explicitly determined later. Auxiliary signals $\tilde{\Omega}$ and $\dot{\tilde{\Omega}}$ are defined as follows; the first auxiliary term $\tilde{\Omega}$ is proportional to the quaternion error and hence its derivative $\dot{\tilde{\Omega}}$ is a quaternion rate:

$$\tilde{\Omega} \triangleq -\Gamma_1 \vec{q}_e \text{ and } \dot{\tilde{\Omega}} = -\Gamma_1 \dot{\vec{q}}_e \quad (4.46a)$$

$$\therefore \dot{\tilde{\Omega}} = -\frac{1}{2} \Gamma_1 ([\vec{q}_e]_{\times} + q_0 \mathbb{I}_{3 \times 3}) \vec{\omega}_e \quad (4.46b)$$

$$= \frac{1}{2} \Gamma_1 ([\vec{q}_e]_{\times} + q_0 \mathbb{I}_{3 \times 3}) \vec{\omega}_b \Big|_{\vec{\omega}_e = -\vec{\omega}_b} \quad (4.46c)$$

The second auxiliary term $\tilde{\Omega}$ is proportional to both quaternion vector and angular velocity errors.

$$\tilde{\Omega} \triangleq \vec{\omega}_e - \tilde{\Omega} = \vec{\omega}_e + \Gamma_1 \vec{q}_e \quad (4.47a)$$

$$= -\vec{\omega}_b + \Gamma_1 \vec{q}_e \Big|_{\vec{\omega}_e = -\vec{\omega}_b} \quad (4.47b)$$

Using an LFC similar to the basic V_{PD} function candidate from Eq:4.34, but substituting an auxiliary term $\tilde{\Omega}$ for the body's angular velocity $\vec{\omega}_b$ into the LFC, V_{XPD} is defined:

$$V_{XPD}(Q_e, \tilde{\Omega}) = \vec{q}_e^T \vec{q}_e + (1 - q_0)^2 + \frac{1}{2} \tilde{\Omega}^T (\Gamma_3^{-1} J_b(\vec{u})) \tilde{\Omega} > 0, \forall (Q_e, \tilde{\Omega}) \neq \vec{0} \quad (4.48)$$

Because the stability proof limits the attitude quaternion's scalar $q_0 \in [0 : 1]$, it follows that the trajectory's energy function is zero at the origin or $V_{XPD}([1 \vec{0}]^T, \vec{0}) = 0$. Using the simplification from a quaternion's inherent properties in Eq:4.17, the LFC from Eq:4.48 then simplifies with the following derivative:

$$V_{XPD} = 2(1 - q_0) + \frac{1}{2} \tilde{\Omega}^T (\Gamma_3^{-1} J_b(\vec{u})) \tilde{\Omega} \quad (4.49a)$$

$$\dot{V}_{XPD} = 2 \frac{1}{2} \vec{q}_e^T \vec{\omega}_e + \frac{1}{2} \dot{\tilde{\Omega}}^T (\Gamma_3^{-1} J_b(\vec{u})) \tilde{\Omega} + \frac{1}{2} \tilde{\Omega}^T (\Gamma_3^{-1} J_b(\vec{u})) \dot{\tilde{\Omega}} \quad (4.49b)$$

$$\therefore \dot{V}_{XPD} = -\vec{q}_e^T \vec{\omega}_b + \frac{1}{2} \dot{\tilde{\Omega}}^T (\Gamma_3^{-1} J_b(\vec{u})) \tilde{\Omega} + \frac{1}{2} \tilde{\Omega}^T (\Gamma_3^{-1} J_b(\vec{u})) \dot{\tilde{\Omega}} \Big|_{\vec{\omega}_e = -\vec{\omega}_b} \quad (4.49c)$$

It then follows, substituting $\dot{\tilde{\omega}}_b$ from Eq:4.47, the auxiliary derivative term $\dot{\tilde{\Omega}}$ is:

$$\dot{\tilde{\Omega}} = -\dot{\vec{\omega}}_b + \Gamma_1 \dot{\vec{q}}_e = -\dot{\vec{\omega}}_b - \dot{\tilde{\Omega}} \quad (4.50a)$$

$$\dot{\vec{\omega}}_b = J_b^{-1}(\vec{u}) (-\vec{\omega}_b \times J_b(\vec{u}) \vec{\omega}_b - \vec{\tau}_b(\vec{u}) + \vec{\tau}_g + \vec{\tau}_H + \vec{\tau}_{XPD}) \quad (4.50b)$$

$$\therefore \dot{\tilde{\Omega}} = -J_b^{-1}(\vec{u}) (-\vec{\omega}_b \times J_b(\vec{u}) \vec{\omega}_b - \vec{\tau}_b(\vec{u}) + \vec{\tau}_g + \vec{\tau}_H + \vec{\tau}_{XPD}) - \dot{\tilde{\Omega}} \quad (4.50c)$$

Substituting the auxiliary PD control law, $\vec{\tau}_{XPD}$ from Eq:4.45, into the auxiliary derivative $\dot{\tilde{\Omega}}$ gives:

$$\begin{aligned}\dot{\tilde{\Omega}} &= -J_b^{-1}(\vec{u}) \left(-\vec{\omega}_b \times J_b(\vec{u})\vec{\omega}_b - \vec{\tau}_b(\vec{u}) + \vec{\tau}_g + \vec{\tau}_H \right. \\ &\quad \left. + (\Gamma_2\tilde{\Omega} + \Gamma_3\vec{q}_e - J_b(\hat{u})\dot{\tilde{\Omega}} + \hat{\omega}_b \times J_b(\hat{u})\hat{\omega}_b + \vec{\tau}_b(\hat{u}) - \vec{\tau}_g - \vec{\tau}_H) \right) - \dot{\tilde{\Omega}} \quad (4.50d)\end{aligned}$$

$$= -J_b^{-1}(\vec{u}) \left(\Gamma_2\tilde{\Omega} + \Gamma_3\vec{q}_e - J_b(\hat{u})\dot{\tilde{\Omega}} \right) - \dot{\tilde{\Omega}} \quad (4.50e)$$

$$= J_b^{-1}(\vec{u}) \left(-\Gamma_2\tilde{\Omega} - \Gamma_3\vec{q}_e \right) \quad (4.50f)$$

From the *approximately* symmetric inertia matrix $J_b(\vec{u})$ (combined Eq:2.32 and Eq:2.33 show its ranges) and the positive symmetric and diagonal constraints imposed on the coefficient matrices Γ_1, Γ_2 and Γ_3 , the auxiliary plant $\dot{\tilde{\Omega}}$ has a transpose:

$$\dot{\tilde{\Omega}}^T = J_b^{-1}(\vec{u}) \left(-\Gamma_2\tilde{\Omega}^T - \Gamma_3\vec{q}_e^T \right) \quad (4.51)$$

Splitting the PD auxiliary plant's LFC derivative, \dot{V}_{XPD} in Eq:4.48, into components and then simplifying each individually, it follows:

$$\frac{1}{2}\dot{\tilde{\Omega}}^T \left(\Gamma_3^{-1}J_b(\vec{u}) \right) \tilde{\Omega} = \frac{1}{2} \left(-\Gamma_2\tilde{\Omega}^T - \Gamma_3\vec{q}_e^T \right) \Gamma_3^{-1}\tilde{\Omega} \quad (4.52a)$$

$$= \frac{1}{2} \left(-\tilde{\Omega}^T \Gamma_2 \Gamma_3^{-1} \tilde{\Omega} - \vec{q}_e^T \tilde{\Omega} \right) \quad (4.52b)$$

Substituting Eq:4.47 for $\vec{q}_e^T \tilde{\Omega}$ into Eq:4.52b:

$$\therefore \frac{1}{2}\dot{\tilde{\Omega}}^T \left(\Gamma_3^{-1}J_b(\vec{u}s) \right) \tilde{\Omega} = \frac{1}{2} \left(-\tilde{\Omega}^T \Gamma_2 \Gamma_3^{-1} \tilde{\Omega} + \vec{q}_e^T \vec{\omega}_b - \vec{q}_e^T \Gamma_1 \vec{q}_e \right) \Big|_{\vec{q}_e^T \tilde{\Omega} = -\vec{q}_e^T \vec{\omega}_b + \Gamma_1 \vec{q}_e^T} \quad (4.52c)$$

Similarly, for the transposed counterpart of Eq:4.52c in Eq:4.49c:

$$\frac{1}{2}\tilde{\Omega}^T \left(\Gamma_3^{-1}J_b(\vec{u}) \right) \dot{\tilde{\Omega}} = \frac{1}{2} \left(-\tilde{\Omega}^T \Gamma_2 \Gamma_3^{-1} \tilde{\Omega}^T + \vec{q}_e^T \vec{\omega}_b^T - \vec{q}_e^T \Gamma_1 \vec{q}_e^T \right) \quad (4.52d)$$

which, when substituted back into Eq:4.49c, then simplifies the LFC derivative to negative definite:

$$\begin{aligned}\therefore \dot{V}_{XPD} &= -\vec{q}_e^T \vec{\omega}_b + \frac{1}{2} \left(-\tilde{\Omega}^T \Gamma_2 \Gamma_3^{-1} \tilde{\Omega} + \vec{q}_e^T \vec{\omega}_b - \vec{q}_e^T \Gamma_1 \vec{q}_e \right) \\ &\quad + \frac{1}{2} \left(-\tilde{\Omega} \Gamma_2 \Gamma_3^{-1} \tilde{\Omega}^T + \vec{q}_e^T \vec{\omega}_b^T - \vec{q}_e^T \Gamma_1 \vec{q}_e^T \right) \quad (4.53)\end{aligned}$$

$$= -\vec{q}_e^T \Gamma_1 \vec{q}_e - \tilde{\Omega} \Gamma_2 \Gamma_3^{-1} \tilde{\Omega}^T < 0 \quad \forall(\vec{q}_e, \tilde{\Omega}), \quad q_0 \in [0 : 1], \quad \exists(\Gamma_1, \Gamma_2, \Gamma_3) > 0 \quad (4.54)$$

As such, the control law $\vec{\tau}_{XPD}$ asymptotically stabilizes the attitude plant locally for the constrained error $q_0 \in [0 : 1]$. Both $\tilde{\Omega}$ and \vec{q}_e tend to $\vec{0}$, or more specifically, the following global stability limits exist:

$$\lim_{t \rightarrow \infty} \vec{q}_e = \vec{0} \quad \text{and} \quad \lim_{t \rightarrow \infty} \tilde{\Omega} = \vec{0} \quad (4.55a)$$

Then, from the auxiliary plant definition(s) in Eq:4.47, the extended limits present themselves:

$$\lim_{t \rightarrow \infty} \vec{\omega}_b = \vec{0} \Big|_{\vec{\omega}_d = \vec{0}} \quad \text{and} \quad \lim_{t \rightarrow \infty} \tilde{\Omega} = \vec{0} \quad (4.55b)$$

$$\lim_{t \rightarrow \infty} Q_e = [1 \quad \vec{0}]^T \quad (4.55c)$$

Whilst asymptotic stability is indeed satisfactory, stronger exponential stability is obviously preferred. The stability proof for V_{XPD} can be extended to a stabilizing, exponentially bounded trajectory. From a unit quaternion's inherent definition and the constraint applied to the quaternion scalar it follows that:

$$1 - q_0 \leq 1 - q_0^2 = \|\vec{q}_e\|^2 \quad q_0 \in [0 : 1] \quad (4.56)$$

Exponential stability is a maximum boundedness proof. The relationship Eq:4.56 can then replace the quaternion scalar term $2(1 - q_0)$ in V_{XPD} as an upper bound. The LFC is then rewritten in terms of its component's norm(s) to produce a bounding inequality:

$$V_{XPD} = \vec{q}_e^T \vec{q}_e + (q_0 - 1)^2 + \frac{1}{2} \tilde{\Omega}^T (\Gamma_3^{-1} J_b(\vec{u})) \tilde{\Omega} \quad (4.57a)$$

$$\therefore V_{XPD} \leq 2 \|\vec{q}_e\|^2 + \frac{1}{2} \Gamma_3^{-1} J_b(\vec{u}) \|\tilde{\Omega}\|^2 \quad (4.57b)$$

Similarly the LFC's derivative can be written in terms of its norms as:

$$\dot{V}_{XPD} \leq -\Gamma_2 \Gamma_3^{-1} \|\tilde{\Omega}\|^2 - \Gamma_1 \|\vec{q}_e\|^2 \quad (4.57c)$$

The LFC, V_{XPD} , has a maximum such that:

$$V_{XPD} \leq \max \left\{ 2, \frac{\lambda_{\max}(\Gamma_3^{-1} J_b(\vec{u}))}{2} \right\} (\|\vec{q}_e\|^2 + \|\tilde{\Omega}\|^2) \quad (4.58)$$

where the function λ_{\max} represents the maximum eigenvalue of its argument, in this case $\Gamma_3^{-1} J_b(\vec{u})$. Similarly the *negative definite* LCF derivative is bound by the minimum:

$$\dot{V}_{XPD} \leq -\min \{ \lambda_{\min}(\Gamma_1), \lambda_{\min}(\Gamma_2 \Gamma_3^{-1}) \} (\|\vec{q}_e\|^2 + \|\tilde{\Omega}\|^2) \quad (4.59)$$

Therefore there exists some ratio $\alpha > 0$ that satisfies the relationship requirement between the LCF and its derivative, $\dot{V}_{XPD} < -\alpha V_{XPD}$, where α is defined as the ratio:

$$\alpha = \frac{\min \{ \lambda_{\min}(\Gamma_1), \lambda_{\min}(\Gamma_2 \Gamma_3^{-1}) \}}{\max \{ 2, \frac{\lambda_{\max}(\Gamma_3^{-1} J_b(\vec{u}))}{2} \}} \quad (4.60)$$

The attitude trajectory $(\vec{q}_e(t), \tilde{\Omega}(t))$ is then exponentially bounded by:

$$(\|\vec{q}_e(t)\|, \|\tilde{\Omega}(t)\|) \leq M e^{-\alpha t} (\|\vec{q}_e(0)\|, \|\tilde{\Omega}(0)\|) \quad (4.61)$$

The bounding exponential coefficient α can be found using maximum Eigen values for the maximum inertia $J_b(\vec{u}_\Lambda)$ from Eq:2.32. Using the relationship in Eq:4.61 and testing proposed controller coefficients for Γ_1 , Γ_2 and Γ_3 the settling rate can be optimized.

The above stability proof for the auxiliary attitude controller was expanded upon and derived from [128], adapted to fit attitude setpoint tracking. Introduction of the quaternion error, which is dependent on the quaternion scalar, dramatically improves controller performance. The exponential stability notably improves settling times and overshoot errors, demonstrated in Sec:6.3.2.

Interestingly, a previous paper [68] was the precursor for PD-based attitude plants with asymptotic exponential stability. That first proposed control law did not make use of any defined *auxiliary plants*, unlike Eq:4.45, however equivalent terms were effectively incorporated. The control law was developed for spacecraft attitude tracking and proposed a very similar exponentially stabilizing control scheme to that of $\vec{\tau}_{XPD}$. That controller, when changed to the notational convention used here, generates a control body torque as:

$$\vec{\tau}_{XPD}' = -\frac{1}{2} \left[([\vec{q}_e]_\times + q_0 \mathbb{I}_{3 \times 3}) \Gamma_1 + \alpha (1 - q_0 \mathbb{I}_{3 \times 3}) \right] \vec{q}_e - \Gamma_2 \vec{\omega}_b \in \mathcal{F}^b \quad (4.62)$$

Eq:4.62 could easily incorporate plant-dependent compensation to accommodate for unwanted non-linear dynamics. Both exponentially stabilizing PD controllers, from Eq:4.45 and above in Eq:4.62, share similarities with the ideal backstepping controller derived in the sequel, Eq:4.71. It is worth noting that, much like an ideal backstepping controller, if any quantities in the above stability proofs are unknown or contain errors, their stability could potentially fail.

4.6.3 Nonlinear Controllers

Backstepping controllers ([10, 72, 74]) are a popular choice for nonlinear attitude control plants. The process, through iterative design, enforces Lyapunov stability criteria to ensure asymptotic stability. A report [136] surveys the fundamentals of backstepping procedure. Ideal backstepping control (*IBC*) is a precise control solution which requires exact plant matching, something that is difficult to achieve in practice considering that most compensating feedback terms use state estimates $\hat{\mathbf{x}}(t)$ or actuator state estimates \hat{u} .

The caveat of IBC control is poor robust stability performance, being especially susceptible to plant-dependent uncertainty, [69]. Unmodelled disturbances and uncertainties could potentially drive the energy function away from stability conditions. An ideal backstepping algorithm can be extended to incorporate such uncertainties. Adaptively including disturbance and *estimate* uncertainty into the LFC energy function improves robustness (Adaptive backstepping control, *ABC*). By Lyapunov's theory, the respective estimation error terms are stabilized.

Ideal Backstepping Controller

Starting with the ideal case for the first proposed backstepping controller (similar to [74]), it is assumed the attitude plant described in Eq:3.118d from the consolidated model in Sec:3.5 exactly matches the dynamics of the physical prototype. The ideal backstepping controller aims to compensate for the plant's dynamic response to trajectory inputs perfectly. Neglecting potential uncertainties associated with the dynamic model, the aim here is to apply a stabilizing torque control law. Recalling the quaternion tracking error $Q_e = Q_b^* \otimes Q_e$ from Eq:3.56, consider the first LFC proposal for a quaternion error Q_e :

$$V_1(Q_e) = \vec{q}_e^T \vec{q}_e + (1 - q_0)^2 > 0 \quad \forall(Q_e) \neq 0 \quad (4.63)$$

The first proposed LFC is positive definite using constraints imposed on the quaternion error trajectory in Eq:4.32. After substituting in the quaternion rates, but *without* using the quaternion reduction proposed in Eq:4.36, $V_1(Q_e)$ has a derivative using Eq:4.21:

$$\dot{V}_1(Q_e) = 2\vec{q}_e^T \frac{1}{2}([\vec{q}_e]_{\times} + q_0 \mathbb{I}_{3 \times 3})\vec{\omega}_e - 2(1 - q_0)\dot{q}_0 \quad (4.64a)$$

$$= \vec{q}_e^T ([\vec{q}_e]_{\times} + q_0 \mathbb{I}_{3 \times 3})\vec{\omega}_e + (1 - q_0)\vec{q}_e^T \vec{\omega}_e \quad (4.64b)$$

Substituting the angular velocity set point $\vec{\omega}_e = -\vec{\omega}_b|_{\vec{\omega}_e=\vec{0}}$ from Eq:4.27b:

$$\therefore \dot{V}_1 = \vec{q}_e^T [\vec{q}_e]_{\times} \vec{\omega}_e + \vec{q}_e^T \vec{\omega}_e \quad (4.64c)$$

$$= -\vec{q}_e^T [\vec{q}_e]_{\times} \vec{\omega}_b - \vec{q}_e^T \vec{\omega}_b \Big|_{\vec{\omega}_e=-\vec{\omega}_b} \quad (4.64d)$$

Then a stabilizing backstepping control input $\vec{\gamma}_d$, which is a backstepping commanded input body rate for $\vec{\omega}_b$ in Eq:4.64d is chosen. Convention would have it that a backstepping stabilizing input for $\vec{\omega}_b$ would be $\vec{\omega}_d$, however $\vec{\gamma}_d$ is used here to *differentiate the backstepping stabilizing input* from the trajectory commanded angular velocity $\vec{\omega}_d$, Eq:4.27a.

The stabilizing backstepping input $\vec{\gamma}_d$ is selected such that the Lyapunov function candidate's derivative \dot{V}_1 in Eq:4.63 is negative definite when $\vec{\gamma}_d$ is substituted for $\vec{\omega}_b$.

$$\vec{\gamma}_d \triangleq \Gamma_1 \vec{q}_e \quad (4.65)$$

where Γ_1 is a symmetric positive definite gain matrix, a fact that is important to stress due to the positive definite matrix's invertability.

That backstepping input simplifies the LFC derivative \dot{V}_1 to the negative definite term:

$$\therefore \dot{V}_1 = -\vec{q}_e^T [\vec{q}_e]_{\times} \vec{\gamma}_d - \vec{q}_e^T \vec{\gamma}_d \Big|_{\vec{\omega}_b = \vec{\gamma}_d} \quad (4.66a)$$

$$= -\vec{q}_e^T [\vec{q}_e]_{\times} \Gamma_1 \vec{q}_e - \vec{q}_e^T \Gamma_1 \vec{q}_e \quad (4.66b)$$

Considering a vector cross product with itself has a zero resultant, it follows that $\vec{q}_e^T [\vec{q}_e]_{\times} = \vec{0}$. The LFC derivative \dot{V}_1 reduces:

$$\therefore \dot{V}_1 = -\vec{q}_e^T \Gamma_1 \vec{q}_e < 0 \quad \forall(Q_e), \quad \exists \Gamma_1 > 0 \quad (4.66c)$$

The stabilizing backstepping input $\vec{\gamma}_d$ then has its own associated error \vec{z}_1 because of differences between $\vec{\omega}_b$ and $\vec{\gamma}_d$.

$$\vec{z}_1 \triangleq \vec{\gamma}_d - \vec{\omega}_b = \Gamma_1 \vec{q}_e - \vec{\omega}_b \Big|_{\vec{\gamma}_d = \Gamma_1 \vec{q}_e} \quad (4.67a)$$

Defining a variable substitution for the body angular velocity $\vec{\omega}_d$ with the stabilizing backstepping input $\vec{\gamma}_d$ and its error \vec{z}_1 :

$$\vec{\omega}_b = \Gamma_1 \vec{q}_e - z_1 \quad (4.67b)$$

Substituting Eq:4.67b back into the LFC derivative:

$$\therefore \dot{V}_1 = -\vec{q}_e^T [\vec{q}_e]_{\times} (\vec{\gamma}_d - \vec{z}_1) - \vec{q}_e^T (\vec{\gamma}_d - \vec{z}_1) \quad (4.67c)$$

$$= -\vec{q}_e^T (\Gamma_1 \vec{q}_e - z_1) \Big|_{\vec{\gamma}_d = \Gamma_1 \vec{q}_e} \quad (4.67d)$$

$$= -\vec{q}_e^T \Gamma_1 \vec{q}_e + \vec{q}_e^T z_1 \quad (4.67e)$$

Introducing that error \vec{z}_1 into a second Lyapunov candidate function which extends from the first proposed energy candidate function V_1 , yields:

$$V_2(Q_e, z_1) = V_1(Q_e) + \frac{1}{2} z_1^T z_1 \quad (4.68a)$$

$$= \vec{q}_e^T \vec{q}_e + (1 - q_0)^2 + \frac{1}{2} z_1^T z_1 > 0 \quad \forall(Q_e, z_1) \neq 0 \quad (4.68b)$$

That first error z_1 has its own rate which, using the body's angular acceleration $\dot{\vec{\omega}}_b$ from earlier with but undefined input $\vec{\tau}_{IBC}$, is:

$$\dot{\vec{z}}_1 = \Gamma_1 \dot{\vec{q}}_e - \dot{\vec{\omega}}_b \quad (4.69a)$$

$$= \frac{\Gamma_1}{2} ([\vec{q}_e]_{\times} + q_0 \mathbb{I}_{3 \times 3}) \vec{\omega}_e - \dot{\vec{\omega}}_b \quad (4.69b)$$

$$= -\frac{\Gamma_1}{2} ([\vec{q}_e]_{\times} + q_0 \mathbb{I}_{3 \times 3}) \vec{\omega}_b - \dot{\vec{\omega}}_b \Big|_{\vec{\omega}_e = -\vec{\omega}_b} \quad (4.69c)$$

$$= -\frac{\Gamma_1}{2} ([\vec{q}_e]_{\times} + q_0 \mathbb{I}_{3 \times 3}) \vec{\omega}_b - J_b(\vec{u})^{-1} (-\vec{\omega}_b \times J_b(\vec{u}) \vec{\omega}_b - \vec{\tau}_b(\vec{u}) + \vec{\tau}_g + \vec{\tau}_H + \vec{\tau}_{IBC}) \quad (4.69d)$$

So using the stabilizing backstepping input's error rate $\dot{\vec{z}}_1$ from Eq:4.69d to find the second LFC's derivative \dot{V}_2 , where $\dot{V}_1 = -\vec{q}_e^T \Gamma_1 \vec{q}_e + \vec{q}_e^T \vec{z}_1$ from Eq:4.67e, gives:

$$\therefore \dot{V}_2 = \dot{V}_1 + \vec{z}_1^T \dot{\vec{z}}_1 = -\vec{q}_e^T \Gamma_1 \vec{q}_e + \vec{q}_e^T \vec{z}_1 + \vec{z}_1^T \dot{\vec{z}}_1 \quad (4.70a)$$

$$= -\vec{q}_e^T \Gamma_1 \vec{q}_e + \vec{q}_e^T \vec{z}_1 + \vec{z}_1^T \left(-\frac{\Gamma_1}{2} ([\vec{q}_e]_{\times} + q_0 \mathbb{I}_{3 \times 3}) \vec{\omega}_b - J_b^{-1}(\vec{u}) (-\vec{\omega}_b \times J_b(\vec{u}) \vec{\omega}_b - \vec{\tau}_b(\vec{u}) + \vec{\tau}_g + \vec{\tau}_H + \vec{\tau}_{IBC}) \right) \quad (4.70b)$$

$$= -\vec{q}_e^T \Gamma_1 \vec{q}_e + \vec{z}_1^T \left(\vec{q}_e - \frac{\Gamma_1}{2} ([\vec{q}_e]_{\times} + q_0 \mathbb{I}_{3 \times 3}) \vec{\omega}_b - J_b^{-1}(\vec{u}) (-\vec{\omega}_b \times J_b(\vec{u}) \vec{\omega}_b - \vec{\tau}_b(\vec{u}) + \vec{\tau}_g + \vec{\tau}_H + \vec{\tau}_{IBC}) \right) \quad (4.70c)$$

Then the precisely matched stabilizing backstepping control law, using state estimates, is as follows:

$$\vec{\tau}_{IBC} = J_b(\hat{u}) \left(\vec{q}_e - \frac{\Gamma_1}{2} ([\vec{q}_e]_\times + q_0 \mathbb{I}_{3 \times 3}) \vec{\omega}_b + \Gamma_2 \vec{z}_1 \right) + \hat{\omega}_b \times J_b(\hat{u}) \vec{\omega}_b + \vec{\tau}_b(\hat{u}) - \vec{\tau}_g - \vec{\tau}_H \quad (4.71a)$$

where Γ_2 is another positive-definite symmetric coefficient matrix. Recalling that $\vec{z}_1 = \Gamma_1 \vec{q}_e - \vec{\omega}_b$ and using the quaternion rate's vector definition from Eq:4.38a, the ideal backstepping torque control law simplifies to:

$$\therefore \vec{\tau}_{IBC} = \underbrace{J_b(\hat{u}) \left((\Gamma_1 \Gamma_2 + 1) \vec{q}_e - \Gamma_2 \hat{\omega}_b + \Gamma_1 \dot{\vec{q}}_e \right)}_{\text{Ideal backstepping}} + \underbrace{\hat{\omega}_b \times J_b(\hat{u}) \hat{\omega}_b + \vec{\tau}_b(\hat{u}) - \vec{\tau}_g - \vec{\tau}_H}_{\text{Compensation}} \in \mathcal{F}^b \quad (4.71b)$$

Substituting the backstepping control law $\vec{\tau}_{IBC}$ into the Lyapunov candidate function's derivative \dot{V}_2 in Eq:4.70c, and assuming that state estimate errors are negligible, \dot{V}_2 simplifies to negative definite:

$$\therefore \dot{V}_2 = -\vec{q}_e^T \Gamma_1 \vec{q}_e + \vec{z}_1^T \left(\vec{q}_e - \frac{\Gamma_1}{2} ([\vec{q}_e]_\times + q_0 \mathbb{I}_{3 \times 3}) \vec{\omega}_b - J_b^{-1}(\vec{u}) \left(J_b(\hat{u})(\Gamma_1 \Gamma_2 + 1) \vec{q}_e - J_b(\hat{u}) \Gamma_2 \hat{\omega}_b + J_b(\hat{u}) \Gamma_1 \dot{\vec{q}}_e \right) \right) \quad (4.72a)$$

$$= -\vec{q}_e^T \Gamma_1 \vec{q}_e + \vec{z}_1^T \Gamma_2 \left(\Gamma_1 \vec{q}_e - \hat{\omega}_b \right) \quad (4.72b)$$

$$= -\vec{q}_e^T \Gamma_1 \vec{q}_e - z_1^T \Gamma_2 z_1 < 0 \quad \forall (\vec{q}_e, z_1), \quad q_0 \in [0 : 1], \quad \exists(\Gamma_1, \Gamma_2) > 0 \quad (4.72c)$$

Because Eq:4.72c is negative definite, the following stabilizing limit then exists:

$$\lim_{t \rightarrow \infty} Q_e = \begin{bmatrix} 1 & \vec{0} \end{bmatrix}^T \quad (4.73a)$$

Furthermore, the stabilizing backstepping input error \vec{z}_1 is limited:

$$\lim_{t \rightarrow \infty} \vec{z}_1 = \Gamma_1 \vec{q}_e - \vec{\omega}_b = \vec{0} \quad (4.73b)$$

Because the quaternion error vector is stabilized $\vec{q}_e \rightarrow \vec{0}$, it follows that the angular velocity is stabilized as well ($\vec{\omega}_b \rightarrow \vec{0}$). From the definition of the angular velocity error $\vec{\omega}_e$, that error is stabilized too. There is a distinct similarity in the structure of $\vec{\tau}_{IBC}$ from Eq:4.71 to the auxiliary PD controller presented in Eq:4.45. Expanding $\vec{\tau}_{XPD}$ into state terms using the definitions of each auxiliary plant, $\tilde{\Omega}$ and $\dot{\tilde{\Omega}}$:

$$\vec{\tau}_{XPD} = (\Gamma_1 \Gamma_2 + \Gamma_3) \vec{q}_e - \Gamma_2 \hat{\omega}_b - \frac{\Gamma_1 J_b(\hat{u})}{2} ([\vec{q}_e]_\times + q_0 \mathbb{I}_{3 \times 3}) \hat{\omega}_b \quad (4.74)$$

Furthermore, using the same reasoning from Eq:4.57, the exponential stability proof is proposed in the sequel. Recall the unit quaternion bounding identity Eq:4.56:

$$1 - q_0 \leq 1 - q_0^2 = \|\vec{q}_e\|^2 \quad (4.75a)$$

The ideal backstepping Lyapunov function candidate V_2 from Eq:4.68 is then bound from above by:

$$V_{IBC} = 2(1 - q_0) + \frac{1}{2} \vec{z}_1^T \vec{z}_1 \leq 2 \|\vec{q}_e\|^2 + \frac{1}{2} \|z_1\|^2 \quad (4.75b)$$

That LFC's derivative is similarly bound from below by:

$$\dot{V}_{IBC} = -\vec{q}_e^T \Gamma_1 \vec{q}_e - \vec{z}_1^T \Gamma_2 \vec{z}_1 \leq \dot{V}_{IBC}' = -\Gamma_1 \|\vec{q}_e\|^2 - \Gamma_2 \|z_1\|^2 \quad (4.75c)$$

Then both the energy function and its derivative are bounded respectively by the following Eigen value limits:

$$V_{IBC} \leq \max \left\{ 2, \frac{1}{2} \right\} (\|\vec{q}_e\|^2 + \|z_1\|^2) \quad (4.76a)$$

$$\dot{V}_{IBC} \leq -\min \{ \lambda_{\min}(\Gamma_1), \lambda_{\min}(\Gamma_2) \} (\|\vec{q}_e\|^2 + \|z_1\|^2) \quad (4.76b)$$

The positive ratio α can then be found that proportionally relates the Lyapunov energy function V_{IBC} to its derivative \dot{V}_{IBC} such that $\dot{V}_{IBC} \leq -\alpha V_{IBC}$. That ratio α is found:

$$\alpha = \frac{\min\{\lambda_{\min}(\Gamma_1), \lambda_{\min}(\Gamma_2)\}}{2} \quad (4.77)$$

which exponentially limits the attitudes trajectory:

$$(\|\vec{q}_e(t)\|, \|z_1(t)\|) \leq M e^{-\alpha t/2} (\|\vec{q}_e(0)\|, \|z_1(0)\|) \quad (4.78)$$

The ideal backstepping controller requires exact plant matching and accounts for neither unmodelled disturbances nor measurement uncertainty. In practice, the introduction of some disturbance torque $\vec{\tau}_L$ or a measurement uncertainty could potentially drive Eq:4.70 away from negative-definite, leading to a loss of stability in the Lyapunov sense.

Adaptive Backstepping Controller

A lot of work has been done on the statistical nature of disturbance approximation and how best to adapt a nonlinear control system to the influence of unwanted disturbances, [11, 37, 51]. Only a lumped uncertainty/disturbance torque term is considered here for the adaptive case. It is assumed both plant-dependent uncertainties and estimate errors can all be included in a single lumped torque $\vec{\tau}_L$, in the body frame \mathcal{F}^b . That disturbance term is introduced to the angular acceleration dynamics:

$$\dot{\vec{\omega}}_b = J_b^{-1}(\vec{u}) (-\vec{\omega}_b \times J_b(\vec{u})\vec{\omega}_b - \vec{\tau}_b(\vec{u}) + \vec{\tau}_g + \vec{\tau}_H + \vec{\tau}_L + \vec{\tau}_{ABC}) \in \mathcal{F}^b \quad (4.79)$$

Unmodelled disturbances then act as external torques on the Lagrangian in Eq:3.9c. If the disturbance torque was known or modelled, then it could simply be compensated for in the control law $-\vec{\tau}_L$. But knowing or estimating a disturbance is difficult in practice, especially when no information about the nature of the disturbance is known. Noise compensation in sensors can be performed easily because of the known frequency spectrum which that noise occurs in. The same cannot be said for wind disturbances or large payload variations for a vehicle (large steps in inertia or mass).

An approximate disturbance observer $\hat{\tau}_L$ is used for compensation in the generated control torque $\vec{\tau}_{ABC}$. Each estimate will have its own error deviating from the physical $\vec{\tau}_L$ acting on the vehicle:

$$\Delta\hat{\tau}_L = \vec{\tau}_L - \hat{\tau}_L \quad (4.80)$$

Adaptive backstepping control introduces that observer's estimate error into a Lyapunov function candidate to develop a derivative term for $\dot{\hat{\tau}}_L$, or a *disturbance update law*, to asymptotically stabilize the estimate error. Typically, disturbance update rules are the primary contribution for satellite and generalized attitude control research papers. The statistical nature of disturbance approximation is a subject for another project. That estimate error $\Delta\hat{\tau}_L$ is then added to an LFC extended from the ideal backstepping case (previously in Eq:4.68a):

$$V_{ABC}(Q_e, z_1, \vec{L}_\Delta) = V_{IBC}(Q_e, z_1) + \frac{1}{2}\Delta\hat{\tau}_L^T \Gamma_L^{-1} \Delta\hat{\tau}_L \quad (4.81a)$$

$$= \vec{q}_e^T \vec{q}_e + (1 - q_0)^2 + \frac{1}{2}z_1^T z_1 + \frac{1}{2}\Delta\hat{\tau}_L^T \Gamma_L^{-1} \Delta\hat{\tau}_L > 0 \quad \forall(Q_e, z_1, \vec{L}_\Delta) \neq \vec{0} \quad (4.81b)$$

where Γ_L a symmetric positive definite $[3 \times 3]$ *adaptation* gain matrix. That gain determines the rate at which the system *adapts* to disturbances. The stability proof starts with the LFC rate \dot{V}_{ABC} :

$$\dot{V}_{ABC}(Q_e, z_1, \vec{L}_\Delta) = \dot{V}_{IBC}(Q_e, z_1) + \frac{1}{2}\Delta\dot{\hat{\tau}}_L^T \Gamma_L^{-1} \Delta\hat{\tau}_L + \frac{1}{2}\Delta\hat{\tau}_L^T \Gamma_L^{-1} \Delta\dot{\hat{\tau}}_L \quad (4.82)$$

Recalling the observer estimate's error $\Delta\hat{\tau}_L$ from Eq:4.80, for its derivative $\Delta\dot{\hat{\tau}}_L$, it is reasonable to assume the rate at which the physical disturbance $\vec{\tau}_L$ changes is significantly slower than that of the control system, or that $\dot{\vec{\tau}}_L \ll \dot{\hat{\tau}}_L$.

It follows that the observer error derivative depends only on the observer derivative $\dot{\hat{\tau}}_L$:

$$\therefore \Delta\dot{\hat{\tau}}_L = \dot{\vec{\tau}}_L - \dot{\hat{\tau}}_L \approx \vec{0} - \dot{\hat{\tau}}_L = -\dot{\hat{\tau}}_L \Big|_{\dot{\vec{\tau}}_L \approx \vec{0}} \quad (4.83)$$

Substituting the estimation error's derivative term back into the Lyapunov function candidate's derivative, \dot{V}_{ABC} in Eq:4.82, and expanded in Eq:4.70c, gives:

$$\begin{aligned} \dot{V}_{ABC} = & -\vec{q}_e^T (\Gamma_1 \vec{q}_e - z_1) + z_1^T \left(-\frac{\Gamma_1}{2} ([\vec{q}_e]_\times + q_0 \mathbb{I}_{3 \times 3}) \vec{\omega}_b \right. \\ & \left. - J_b^{-1}(\vec{u}) (-\vec{\omega}_b \times J_b(\vec{u}) \vec{\omega}_b - \vec{\tau}_b(\vec{u}) + \vec{\tau}_g + \vec{\tau}_H + \vec{\tau}_L + \vec{\tau}_{ABC}) \right) - \Delta\hat{\tau}_L^T \Gamma_L^{-1} \dot{\hat{\tau}}_L \end{aligned} \quad (4.84a)$$

Note that the physical disturbance term $\vec{\tau}_L$ is included in Eq:4.84a. Extending the ideal backstepping control law, $\vec{\tau}_{IBC}$ from Eq:4.71, to include a *disturbance estimate* term $\hat{\tau}_L$ for compensation:

$$\vec{\tau}_{ABC} = J_b(\hat{u}) \left((\Gamma_1 \Gamma_2 + 1) \vec{q}_e - \Gamma_2 \hat{\omega}_b + \Gamma_1 \dot{\vec{q}}_e \right) + \hat{\omega}_b \times J_b(\hat{u}) \hat{\omega}_b + \vec{\tau}_b(\hat{u}) - \vec{\tau}_g - \vec{\tau}_H - \hat{\tau}_L \in \mathcal{F}^b \quad (4.84b)$$

The adaptive backstepping Lyapunov function candidate's derivative \dot{V}_{ABC} then reduces to:

$$\dot{V}_{ABC} = \dot{V}_{IBC} - z_1^T J_b^{-1}(\vec{u}) (\vec{\tau}_L - \hat{\tau}_L) - \Delta\hat{\tau}_L^T \Gamma_L^{-1} \dot{\hat{\tau}}_L \quad (4.84c)$$

and substituting in the estimate error $\Delta\hat{\tau}_L = \vec{\tau}_L - \hat{\tau}_L$:

$$\therefore \dot{V}_{ABC} = -\vec{q}_e^T \Gamma_1 \vec{q}_e - z_1^T \Gamma_2 z_1 - z_1^T J_b^{-1}(\vec{u}) \Delta\hat{\tau}_L - \Delta\hat{\tau}_L^T \Gamma_L^{-1} \dot{\hat{\tau}}_L \quad (4.84d)$$

$$= -\vec{q}_e^T \Gamma_1 \vec{q}_e - z_1^T \Gamma_2 z_1 - \Delta\hat{\tau}_L^T \Gamma_L^{-1} (\dot{\hat{\tau}}_L + \Gamma_L J_b^{-1}(\vec{u}) z_1) \quad (4.84e)$$

The decision must then be made on how the disturbance estimate is updated such that its error $\Delta\hat{\tau}_L$ asymptotically stabilizes, or specifically that the LFC derivative \dot{V}_{ABC} is negative definite. The obvious choice for $\dot{\hat{\tau}}_L$ would be to exactly compensate for $\Gamma_L J_b^{-1}(\vec{u}) z_1$ in the LFC:

$$\dot{\hat{\tau}}_L \triangleq -\Gamma_L J_b^{-1}(\hat{u}) z_1 = -\Gamma_L J_b^{-1}(\hat{u}) (\Gamma_1 \vec{q}_e - \hat{\omega}_b) \Big|_{z_1 = \Gamma_1 \vec{q}_e - \hat{\omega}_b} \quad (4.85)$$

The disturbance is therefore compensated for and the estimate error is ensured to have asymptotic stability because V_{ABC} is positive definite.

$$\dot{V}_{ABC} = -\vec{q}_e^T \Gamma_1 \vec{q}_e - z_1^T \Gamma_2 z_1 < 0 \quad \forall (\vec{q}_e, z_1, \Delta\hat{\tau}_L), \quad q_0 \in [0 : 1], \quad \exists(\Gamma_1, \Gamma_2, \Gamma_L) > 0 \quad (4.86)$$

The same attitude stabilizing limits exist from Eq:4.86, but most importantly, now ensure the disturbance observer estimation error is stabilized:

$$\lim_{t \rightarrow \infty} \Delta\hat{\tau}_L \rightarrow \vec{0} \quad \text{and} \quad \therefore \lim_{t \rightarrow \infty} \hat{\tau}_L \rightarrow \vec{\tau}_L \quad (4.87a)$$

The gain matrix Γ_L is designed to adjust the speed of the response such that the error settles in a satisfactory time without overshoot. Fig:4.6a shows how the disturbance observer $\hat{\tau}_L$ approximates a (single axis) torque turbulence acting on the vehicle in *steady-state* hovering. Moderate damping manifests in the estimate in relation to the physical disturbance resulting in an error shown Fig:4.6b. The example shown in 4.6 contains no attitude steps nor trajectory changes. The torque turbulence, the observer and the adaptive controller's performance are all discussed later in Sec:6.6.

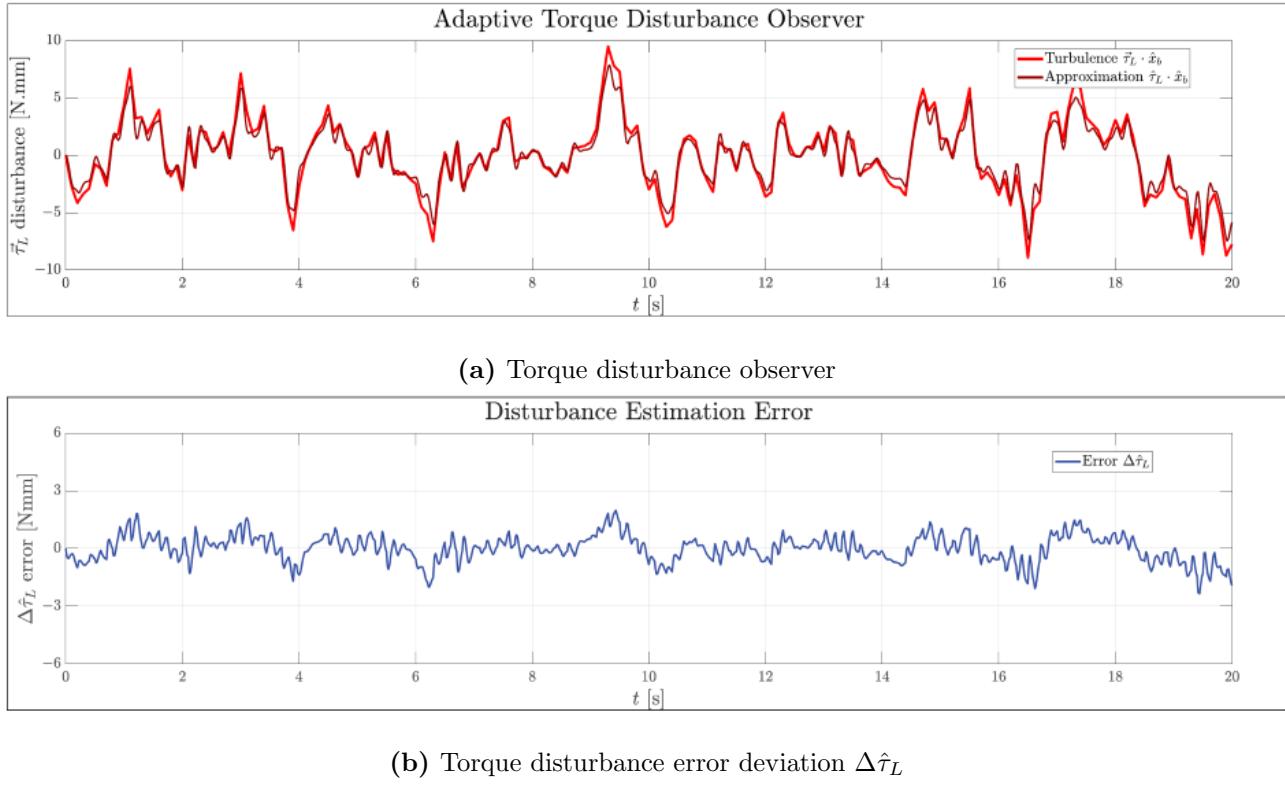


Figure 4.6: Adaptive disturbance torque observer example

4.7 Position Control

Only two plant-dependent position control laws are derived here as attitude control is the primary focus. The attitude control loop is stabilized independently from the position loop (Eq:3.118d and Eq:3.118b). Because the body's relative position is defined in the inertial frame (Eq:3.118a), but its translational velocity is defined in the body frame (Eq:3.118b), the attitude plant needs to be stabilized before the position plant can be addressed. A simple Proportional-Derivative structure is presented first as the reference case. Thereafter, an ideal backstepping controller, which is extended to an adaptive control law is derived. Recalling the differential equation for translational acceleration from Eq:3.118b:

$$\dot{\vec{v}}_b = m_b^{-1}(-\vec{\omega}_b \times m_b \vec{v}_b + m_b \vec{G}_b + \vec{F}_\mu(\hat{u})) \in \mathcal{F}^b \quad (4.88)$$

Recall that the Coriolis acceleration term $-\vec{\omega}_b \times m_b \vec{v}_b$ is what couples the position loop to the attitude plant and that \vec{G}_b is the gravitational acceleration transformed to the body frame. Most texts assume that under standard operating conditions (App:A.1), the angular velocity is small if not negligible $\vec{\omega}_b \approx \vec{0}$. It then follows that the coupled Coriolis term is assumed to be negligible when the angular velocity term is small, $\vec{\omega}_b \times m \vec{v}_b \approx \vec{0}$.

If the plant's state can be estimated with a relative degree of certainty, it is then easy to compensate for the coupled dynamics, rather than making assumptions about their influence on the system. In general, for the position control problem, translational velocity \vec{v}_b is defined in the body frame and is related to the inertial position rates through a quaternion transformation:

$$\dot{\vec{\mathcal{E}}}_b = Q_b \otimes \vec{v}_b \otimes Q_b^* \in \mathcal{F}^I \quad (4.89)$$

The difference in reference frames is an important distinction between the position and attitude state equations. Position error is calculated as the difference between a particular setpoint $\vec{\mathcal{E}}_d$ and the current body position $\vec{\mathcal{E}}_b$, which are both defined in the inertial frame:

$$\vec{\mathcal{E}}_e = \vec{\mathcal{E}}_d - \vec{\mathcal{E}}_b \in \mathcal{F}^I \quad (4.90)$$

The translational position rate error $\dot{\vec{\mathcal{E}}}_b(t)$, *not velocity error* \vec{v}_e , is calculated in the same way. Only first-order setpoints are considered for the control laws presented here, so both position rate and

velocity setpoints are zero, $\dot{\vec{\mathcal{E}}}_d = \vec{v}_d = \vec{0}$. The translational velocity error is then calculated as follows:

$$\dot{\vec{\mathcal{E}}}_e = \dot{\vec{\mathcal{E}}}_d - \dot{\vec{\mathcal{E}}}_b = -\dot{\vec{\mathcal{E}}}_b \Big|_{\dot{\vec{\mathcal{E}}}_d=\vec{0}} \in \mathcal{F}^I \quad (4.91a)$$

$$\therefore \vec{v}_e = Q_b^* \otimes (\dot{\vec{\mathcal{E}}}_d - \dot{\vec{\mathcal{E}}}_b) \otimes Q_b = -\vec{v}_b \in \mathcal{F}^b \quad (4.91b)$$

Position setpoint tracking aims is to produce a stabilizing control law $g(\vec{x}_e, \dot{\vec{x}}_e, t)$ that ensures the position tracking error asymptotically tends to $\vec{0}$. Or more formally that:

$$\vec{F}_\mu(\hat{u}) = g\left(\vec{\mathcal{E}}_d, \vec{v}_d, \vec{\mathcal{E}}_b, \vec{v}_b, t\right) \equiv g(\vec{\mathcal{E}}_e, \vec{v}_e, t) \in \mathcal{F}^b \quad (4.92a)$$

$$\text{such that } \lim_{t \rightarrow \infty} \vec{\mathcal{E}}_e \rightarrow \vec{0} \quad (4.92b)$$

4.7.1 PD Controller

Starting with a simple PD controller to be used for the reference case, plant-dependent control designs the net force proportional to both the position error and the first derivative velocity error and compensates for plant dynamics:

$$\vec{F}_{PD} = K_p \vec{\mathcal{E}}_e + K_d \dot{\vec{\mathcal{E}}}_e + \hat{\omega}_b \times m_b \hat{v}_b - m_b \vec{G}_b \in \mathcal{F}^b \quad (4.93a)$$

$$= K_p (\vec{\mathcal{E}}_d - \hat{\mathcal{E}}_b) - K_d (\dot{\hat{\mathcal{E}}}_b) + \hat{\omega}_b \times m_b \hat{v}_b - m_b \vec{G}_b \Big|_{\dot{\vec{\mathcal{E}}}_e=-\dot{\hat{\mathcal{E}}}_b} \quad (4.93b)$$

where K_p and K_d are both $[3 \times 3]$ symmetric positive definite gain coefficient matrices. Note that position and attitude state estimates are used for the controller in Eq:4.93. As with attitude state estimates, it is assumed those estimates are error free and any plant errors are incorporated into the subsequent adaptive control law presented next in Sec:4.7.2. The stability proof requires that error states are transformed to the body frame \mathcal{F}^b from their principle inertial frame \mathcal{F}^I such that the control input and error states act in a shared frame. Defining a position error state \vec{X}_e that is transformed to the body frame:

$$\vec{X}_e \triangleq Q_b \otimes (\vec{\mathcal{E}}_d - \vec{\mathcal{E}}_b) \otimes Q_b^* = \vec{X}_d - \vec{X}_b \in \mathcal{F}^b \quad (4.94a)$$

Reiterating the difference between position rates and translational velocity in Eq:3.118a, position rates:

$$\dot{\vec{X}}_e \triangleq Q_b \otimes (\dot{\vec{\mathcal{E}}}_d - \dot{\vec{\mathcal{E}}}_b) \otimes Q_b^* = -Q_b \otimes \dot{\vec{\mathcal{E}}}_b \otimes Q_b^* = -\vec{v}_b \Big|_{\dot{\vec{\mathcal{E}}}_d=\vec{0}} \quad (4.94b)$$

Quaternion derivatives for \dot{Q}_b are not considered in Eq:4.94b. Only first-order attitude setpoints were applied in Sec:4.6.2 so it is assumed quaternion rates will not affect the instantaneous transformation of translational position states. If the attitude control loop tracked non-zero angular velocities in Eq:4.27b then this would not be the case.

The control law from Eq:4.93, despite being $\in \mathcal{F}^b$ has arguments $\vec{\mathcal{E}}_e, \dot{\vec{\mathcal{E}}}_e \in \mathcal{F}^I$, which are substituted with the transformed position error \vec{X}_e and its rate $\dot{\vec{X}}_e$:

$$\vec{F}_{PD} = K_p \vec{X}_e + K_d \dot{\vec{X}}_e + \hat{\omega}_b \times m_b \hat{v}_b - m_b \vec{G}_b \in \mathcal{F}^b \quad (4.95a)$$

$$= K_p \vec{X}_e - K_d \hat{v}_b + \hat{\omega}_b \times m_b \hat{v}_b - m_b \vec{G}_b \quad (4.95b)$$

Then proposing a positive definite Lyapunov function candidate:

$$V_{PD}(\vec{X}_e, \vec{v}_e) = \frac{1}{2} \vec{X}_e^T K_p \vec{X}_e + \frac{1}{2} \vec{v}_e^T m_b \vec{v}_e > 0 \quad \forall (\vec{X}_e, \vec{v}_e) \neq \vec{0} \quad (4.96a)$$

$$= \frac{1}{2} \vec{X}_e^T K_p \vec{X}_e + \frac{1}{2} \vec{v}_b^T m_b \vec{v}_b \Big|_{\vec{v}_e=-\vec{v}_b} \quad (4.96b)$$

Calculating that LFC's derivative \dot{V}_{PD} with the PD control law substituted:

$$\dot{V}_{PD}(\vec{X}_e, \vec{v}_e) = \vec{X}_e^T K_p \dot{\vec{X}}_e + \vec{v}_b^T m_b \dot{\vec{v}}_b \quad (4.97a)$$

$$= -\vec{X}_e^T K_p \vec{v}_b + \vec{v}_b^T m_b \dot{\vec{v}}_b \quad (4.97b)$$

$$= -\vec{X}_e^T K_p \vec{v}_b + \vec{v}_b^T (-\vec{\omega}_b \times m_b \vec{v}_b + m_b \vec{G}_b + \vec{F}_{PD}) \quad (4.97c)$$

$$= -\vec{X}_e^T K_p \vec{v}_b + \vec{v}_b^T (K_p \vec{X}_e - K_d \hat{v}_b) \quad (4.97d)$$

$$\therefore \dot{V}_{PD} = -\vec{v}_b^T K_d \vec{v}_b < 0, \forall (\vec{X}_e, \vec{v}_e), \exists (K_d, K_p) > 0 \quad (4.97e)$$

The global stability asserted in Eq:4.97e holds $\forall (\vec{\mathcal{E}}_e, \dot{\vec{\mathcal{E}}}_e)$, irrespective of the transformation applied in Eq:4.94a and Eq:4.94b. The global asymptotically stabilizing limits then follow:

$$\lim_{t \rightarrow \infty} \vec{X}_e = Q_b \otimes (\vec{\mathcal{E}}_d - \vec{\mathcal{E}}_b) \otimes Q_b^* \rightarrow \vec{0} \quad (4.98a)$$

$$\therefore \lim_{t \rightarrow \infty} \vec{\mathcal{E}}_b \rightarrow \vec{\mathcal{E}}_d \quad (4.98b)$$

$$\lim_{t \rightarrow \infty} \dot{X}_e = Q_b^* \otimes (\dot{\vec{\mathcal{E}}}_d - \dot{\vec{\mathcal{E}}}_b) \otimes Q_b = -\vec{v}_b \rightarrow \vec{0} \Big|_{\dot{\vec{\mathcal{E}}}_e=0} \quad (4.98c)$$

4.7.2 Adaptive Backstepping Controller

An adaptive backstepping algorithm, analogue to the adaptive controller previously presented in Sec:4.6.3, is now applied to position control. The disturbance force term $\vec{F}_D \in \mathcal{F}^b$ represents estimate errors together with any unmodelled lumped drag *and* wind forces encountered by the vehicle in flight. That force disturbance is introduced to the position state differential Eq:4.88. Backstepping iterations for the position control loop first need to stabilize the position error, and only thereafter compensate for those disturbances (solving for an ideal backstepping controller first then adding adaptivity).

$$\dot{\vec{v}}_b = m_b^{-1} (-\vec{\omega}_b \times m_b \vec{v}_b + m_b \vec{G}_b + \vec{F}_D + \vec{F}_{ABC}) \in \mathcal{F}^b \quad (4.99)$$

The compensation for \vec{F}_D is obviously an approximation for that physical disturbance term \hat{F}_D , beginning the backstepping process for position with a position state tracking error:

$$\vec{z}_1 \triangleq \vec{\mathcal{E}}_d - \vec{\mathcal{E}}_b = \vec{\mathcal{E}}_e \in \mathcal{F}^I \quad (4.100)$$

That backstepping error has its own derivative:

$$\dot{\vec{z}}_1 = \dot{\vec{\mathcal{E}}}_e = \dot{\vec{\mathcal{E}}}_d - \dot{\vec{\mathcal{E}}}_b \quad (4.101a)$$

$$= Q_b^* \otimes (\vec{v}_d - \vec{v}_b) \otimes Q_b \quad (4.101b)$$

$$= -Q_b^* \otimes \vec{v}_b \otimes Q_b \Big|_{\vec{v}_d=\vec{0}} \quad (4.101c)$$

Transforming that error \vec{z}_1 to the body frame \mathcal{F}^b , in a similar fashion to Eq:4.94a, makes the stability proof more concise. The reference frame transformation does not affect the Layupanov candidate function's derivative as the energy function's gradient depends on its partial derivative with respect to its position trajectory only, namely $\mathcal{E}_e(t)$.

$$\vec{\zeta}_1 \triangleq Q_b \otimes \vec{z}_1 \otimes Q_b^* = Q_b \otimes (\vec{\mathcal{E}}_d - \vec{\mathcal{E}}_b) \otimes Q_b^* = \vec{X}_e \in \mathcal{F}^b \quad (4.102a)$$

$$\therefore \dot{\vec{\zeta}}_1 = Q_b \otimes \dot{\vec{z}}_1 \otimes Q_b^* = Q_b \otimes (\dot{\vec{\mathcal{E}}}_d - \dot{\vec{\mathcal{E}}}_b) \otimes Q_b^* = -\vec{v}_b \quad (4.102b)$$

Proposing the first Lyapunov function candidate $V_1(\vec{\zeta}_1)$ in terms of the tracking error:

$$V_1(\vec{\zeta}_1) = \frac{1}{2} \vec{\zeta}_1^T \vec{\zeta}_1 > 0 \quad \forall (\vec{\zeta}_1) \neq \vec{0} \quad (4.103a)$$

which has a derivative:

$$\dot{V}_1(\vec{\zeta}_1) = \vec{\zeta}_1^T \dot{\vec{\zeta}}_1 = -\vec{\zeta}_1^T \vec{v}_b \quad (4.103b)$$

The first backstepping control velocity in $\vec{\gamma}_d$ is the commanded input velocity for \vec{v}_b . Choosing $\vec{\gamma}_d$, so that when it is substituted for \vec{v}_b the LFC derivative Eq:4.103b is negative definite:

$$\gamma_d \triangleq \Gamma_1 \vec{\zeta}_1 \quad (4.104a)$$

where Γ_1 is a symmetric positive definite $[3 \times 3]$ gain coefficient matrix. That commanded backstepping input has an error between the desired $\vec{\gamma}_d$ and the angular translational velocity \vec{v}_b . The error is the second backstepping error $\vec{\zeta}_2$ and is defined:

$$\vec{\zeta}_2 \triangleq \vec{\gamma}_d - \vec{v}_b = \Gamma_1 \vec{\zeta}_1 - \vec{v}_b \quad (4.104b)$$

$$\therefore \vec{v}_b = \Gamma_1 \vec{\zeta}_1 - \vec{\zeta}_2 \quad (4.104c)$$

Substituting Eq:4.104c into the Lyapunov candidate function derivative \dot{V}_1 from Eq:4.103b gives:

$$\dot{V}_1 = -\vec{\zeta}_1^T \vec{v}_b = -\vec{\zeta}_1^T \Gamma_1 \vec{\zeta}_1 + \vec{\zeta}_1^T \vec{\zeta}_2 \quad (4.105)$$

The second backstepping error state $\vec{\zeta}_2$ has a derivative:

$$\dot{\vec{\zeta}}_2 = \dot{\vec{\gamma}}_d - \dot{\vec{v}}_b = \Gamma_1 \dot{\vec{\zeta}}_1 - \dot{\vec{v}}_b \quad (4.106a)$$

Introducing the translational acceleration differential equation for $\dot{\vec{v}}_b$ from Eq:4.99:

$$\therefore \dot{\vec{\zeta}}_2 = -\Gamma_1 \vec{v}_b - m_b^{-1}(-\vec{\omega}_b \times m_b \vec{v}_b + m_b \vec{G}_b + \vec{F}_D + \vec{F}_{IBC}) \quad (4.106b)$$

In order to stabilize the second backstepping error $\vec{\zeta}_2$, it is added as a trajectory variable to a new positive definite Lyapunov function candidate V_2 which extends from the first V_1 in Eq:4.103a:

$$V_2(\vec{\zeta}_1, \vec{\zeta}_2) = V_1(\vec{\zeta}_1) + \frac{1}{2} \vec{\zeta}_2^T \vec{\zeta}_2 \quad (4.107a)$$

$$= \frac{1}{2} \vec{\zeta}_1^T \vec{\zeta}_1 + \frac{1}{2} \vec{\zeta}_2^T \vec{\zeta}_2 > 0 \quad \forall (\vec{\zeta}_1, \vec{\zeta}_2) \neq \vec{0} \quad (4.107b)$$

That second Lyapunov function candidate has a derivative \dot{V}_2 :

$$\dot{V}_2(\vec{\zeta}_1, \vec{\zeta}_2) = \dot{V}_1(\vec{\zeta}_1) + \vec{\zeta}_2^T \dot{\vec{\zeta}}_2 = \vec{\zeta}_1^T \dot{\vec{\zeta}}_1 + \vec{\zeta}_2^T \dot{\vec{\zeta}}_2 \quad (4.108a)$$

Inserting the first LFC derivative \dot{V}_1 from Eq:4.105:

$$\therefore \dot{V}_2 = -\vec{\zeta}_1^T \Gamma_1 \vec{\zeta}_1 + \vec{\zeta}_1^T \vec{\zeta}_2 + \vec{\zeta}_2^T \dot{\vec{\zeta}}_2 \quad (4.108b)$$

Substituting the backstepping error's derivative $\dot{\vec{\zeta}}_2$ from Eq:4.106b gives:

$$\dot{V}_2 = -\vec{\zeta}_1^T \Gamma_1 \vec{\zeta}_1 + \vec{\zeta}_2^T \left(\vec{\zeta}_1 - \Gamma_1 \vec{v}_b - m_b^{-1}(-\vec{\omega}_b \times m_b \vec{v}_b + m_b \vec{G}_b + \vec{F}_D + \vec{F}_{IBC}) \right) \quad (4.108c)$$

An ideal backstepping control law, assuming that \vec{F}_D is known without errors, is then:

$$\vec{F}_{IBC} = m_b(\vec{\zeta}_1 - \Gamma_1 \hat{v}_b + \Gamma_2 \vec{\zeta}_2) + \hat{\omega}_b \times m_b \hat{v}_b - m_b \vec{G}_b - \vec{F}_D \in \mathcal{F}^b \quad (4.109a)$$

$$= m_b((1 + \Gamma_1 \Gamma_2)\vec{\zeta}_1 - (\Gamma_1 + \Gamma_2)\hat{v}_b) + \hat{\omega}_b \times m_b \hat{v}_b - m_b \vec{G}_b - \vec{F}_D \quad (4.109b)$$

where Γ_2 is another symmetric positive definite $[3 \times 3]$ coefficient gain matrix. When that backstepping control law is substituted back into \dot{V}_2 , the LFC derivative becomes negative definite:

$$\therefore \dot{V}_{IBC} = \dot{V}_2 = -\vec{\zeta}_1^T \Gamma_1 \vec{\zeta}_1 - \vec{\zeta}_2^T \Gamma_2 \vec{\zeta}_2 < 0 \quad \forall (\vec{\zeta}_1, \vec{\zeta}_2), \exists (\Gamma_1, \Gamma_2) > 0 \quad (4.109c)$$

which leads to global asymptotic stability, assuming that the disturbance term \vec{F}_D is known and can be compensated for without error. In the controller, both Γ_1 and Γ_2 are positive symmetric control coefficient matrices to be optimized.

The ideal backstepping rule and its associated Lyapunov function are now extended to incorporate an adaptive disturbance observer \hat{F}_D , similar to the adaptive backstepping attitude controller in Sec:4.6.3. The approximation leads to an estimate error $\Delta\hat{F}_D$:

$$\Delta\hat{F}_D = \vec{F}_D - \hat{F}_b \quad \in \mathcal{F}^b \quad (4.110a)$$

If it is assumed that the physical disturbance rates $\dot{\vec{F}}_D$ are far slower than the control dynamics, then $\vec{F}_D \ll \dot{\vec{F}}_D$:

$$\Delta\dot{\vec{F}}_D = \dot{\vec{F}}_D - \dot{\hat{F}}_D \approx \vec{0} - \dot{\hat{F}}_D = -\dot{\hat{F}}_D \Big|_{\vec{F}_D \approx \vec{0}} \quad (4.110b)$$

The adaptive control law then generates a force input that compensates for the phsical disturbance \vec{F}_D using the disturbance estimate \hat{F}_D :

$$\vec{F}_{ABC} = m_b(\vec{\zeta}_1 - \Gamma_1 \hat{v}_b + \Gamma_2 \vec{\zeta}_2) + \hat{\omega}_b \times m_b \hat{v}_b - m_b \vec{G}_b - \hat{F}_D \quad \in \mathcal{F}^b \quad (4.110c)$$

Proposing a Lyapunov function candidate which extends from the ideal backstepping case in Eq:4.107 to include the disturbance estimate error $\Delta\hat{F}_D$ gives:

$$V_{ABC}(\vec{\zeta}_1, \vec{\zeta}_2, \Delta\hat{F}_D) = V_{IBC}(\vec{\zeta}_1, \vec{\zeta}_2) + \frac{1}{2}\Delta\hat{F}_D^T \Gamma_D^{-1} \Delta\hat{F}_D \quad (4.111a)$$

where Γ_D (much like Γ_L in the adaptive attitude controller from Sec:4.6.3) is a symmetric positive $[3 \times 3]$ gain coefficient matrix which changes the response speed of the adaption plant. Then expanding the adaptive backstepping LFC V_{ABC} to prove it is positive definite:

$$V_{ABC} = \frac{1}{2}\vec{\zeta}_1^T \vec{\zeta}_1 + \frac{1}{2}\vec{\zeta}_2^T \vec{\zeta}_2 + \frac{1}{2}\Delta\hat{F}_D^T \Gamma_D^{-1} \Delta\hat{F}_D > 0 \quad \forall(\vec{\zeta}_1, \vec{\zeta}_2, \Delta\hat{F}_D) \neq \vec{0} \quad (4.111b)$$

Finding the LFC's derivative \dot{V}_{ABC} gives:

$$\dot{V}_{ABC} = \vec{\zeta}_1^T \dot{\vec{\zeta}}_1 + \vec{\zeta}_2^T \dot{\vec{\zeta}}_2 + \Delta\hat{F}_D^T \Gamma_D^{-1} \Delta\dot{\hat{F}}_D \quad (4.111c)$$

and substituting derivatives for $\dot{\vec{\zeta}}_2$ from Eq:4.106b and $\Delta\dot{\hat{F}}_D$ from Eq:4.110b:

$$\dot{V}_{ABC} = -\vec{\zeta}_1^T \Gamma_1 \vec{\zeta}_1 + \vec{\zeta}_2^T \left(\vec{\zeta}_1 - \Gamma_1 \vec{v}_b - m_b^{-1}(-\vec{\omega}_b \times m_b \vec{v}_b + m_b \vec{G}_b + \vec{F}_D + \vec{F}_{ABC}) \right) - \vec{D}_\Delta^T \Gamma_D^{-1} \dot{\hat{D}} \quad (4.111d)$$

Then expanding the adaptive backstepping controller generated force \vec{F}_{ABC} :

$$\dot{V}_{ABC} = -\vec{\zeta}_1^T \Gamma_1 \vec{\zeta}_1 + \vec{\zeta}_2^T \left(-\Gamma_2 \vec{\zeta}_2 - m_b^{-1}(\vec{F}_D - \hat{F}_D) \right) - \Delta\hat{F}_D^T \Gamma_D^{-1} \Delta\dot{\hat{F}}_D \quad (4.111e)$$

$$= -\vec{\zeta}_1^T \Gamma_1 \vec{\zeta}_1 - \vec{\zeta}_2^T \Gamma_2 \vec{\zeta}_2 - m_b^{-1} \vec{\zeta}_2^T \Delta\hat{F}_D - \Delta\hat{F}_D^T \Gamma_D^{-1} \Delta\dot{\hat{F}}_D \quad (4.111f)$$

$$= -\vec{\zeta}_1^T \Gamma_1 \vec{\zeta}_1 - \vec{\zeta}_2^T \Gamma_2 \vec{\zeta}_2 - m_b^{-1} \Delta\hat{F}_D^T \Gamma_D^{-1} (\Gamma_D \vec{\zeta}_2 + \Delta\dot{\hat{F}}_D) \quad (4.111g)$$

Then, a self-evident choice for the disturbance update law would be $\Delta\dot{\hat{F}}_D = -m_b^{-1} \Gamma_D \vec{\zeta}_2$, which ensures asymptotic stability:

$$\Delta\dot{\hat{F}}_D \triangleq -m_b^{-1} \Gamma_D \vec{\zeta}_2 = -m_b^{-1} \Gamma_D (\Gamma_1 \vec{\zeta}_1 - \vec{v}_b) \quad (4.112a)$$

Substituting that into the LFC derivative Eq:4.111g produces:

$$\dot{V}_{ABC} = -\vec{\zeta}_1^T \Gamma_1 \vec{\zeta}_1 - \vec{\zeta}_2^T \Gamma_2 \vec{\zeta}_2 < 0 \quad \forall(\hat{z}_1, \hat{z}_2, \vec{D}_\Delta), \quad \exists(\Gamma_1, \Gamma_2, \Gamma_\Delta) > 0 \quad (4.112b)$$

The disturbance observer tracks a general single axis directional force disturbance as illustrated in Fig:4.7a. That disturbance is a combined fluctuating wind force and vector field, the model of which is later described in Sec:6.6.2. Note that Fig:4.7 tracks an *open-loop* disturbance on a vehicle stabilized steady state. An estimation error for the deviation from the physical disturbance is plotted in Fig:4.7b.

Again there is a damping between the physical and approximated forces, no new state information is used to estimate signals in both Fig:4.6a and Fig:4.7a for attitude and position disturbances respectively. Adaptive observers in Eq:4.86 and Eq:4.112a simply introduce additional free parameters to the control loop.

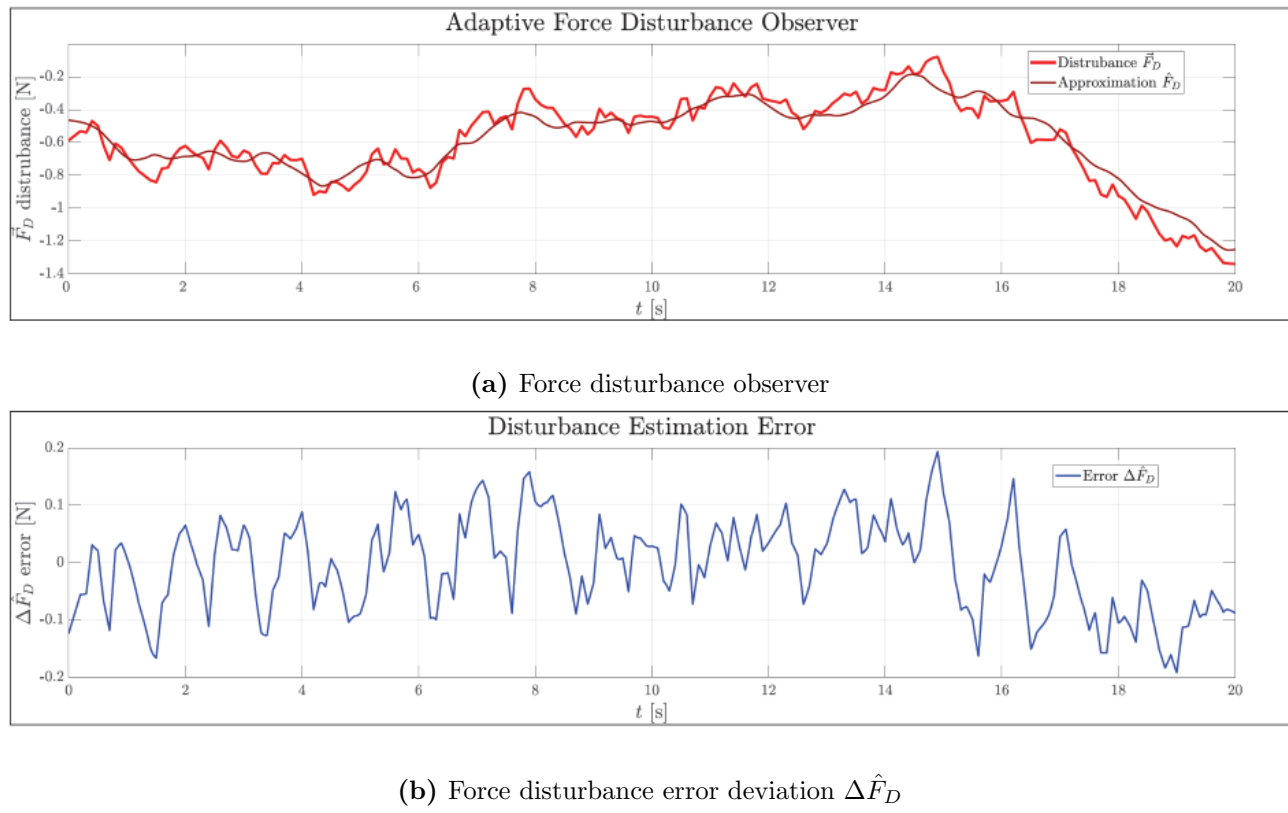


Figure 4.7: Adaptive disturbance force observer example

Chapter 5

Control Allocation Algorithm

Static allocation rules are now developed which aim to solve for actuator commands calculated from a given control input, neither adaptive nor online allocation rules are considered here. Static allocation neglects to account for individual actuator dynamics and transfer rates. Such effects are assumed to be accounted for by the major loop control coefficients, described in Ch:4, when optimized subsequently in Sec:6.2.

Higher-level attitude and position controllers (from Sec:4.6 and Sec:4.7 respectively) design a virtual control input $\mathcal{H}(\vec{x}_e, t) = \vec{\nu}_d = [\vec{F}_d \ \vec{\tau}_d]^T$ to be applied by the vehicle's actuator plant. The vehicle's mechanical overactuation was described in Sec:4.2 but a simplified allocation block, reduced from control loop diagram in Fig:4.2, is illustrated in Fig:5.1a.

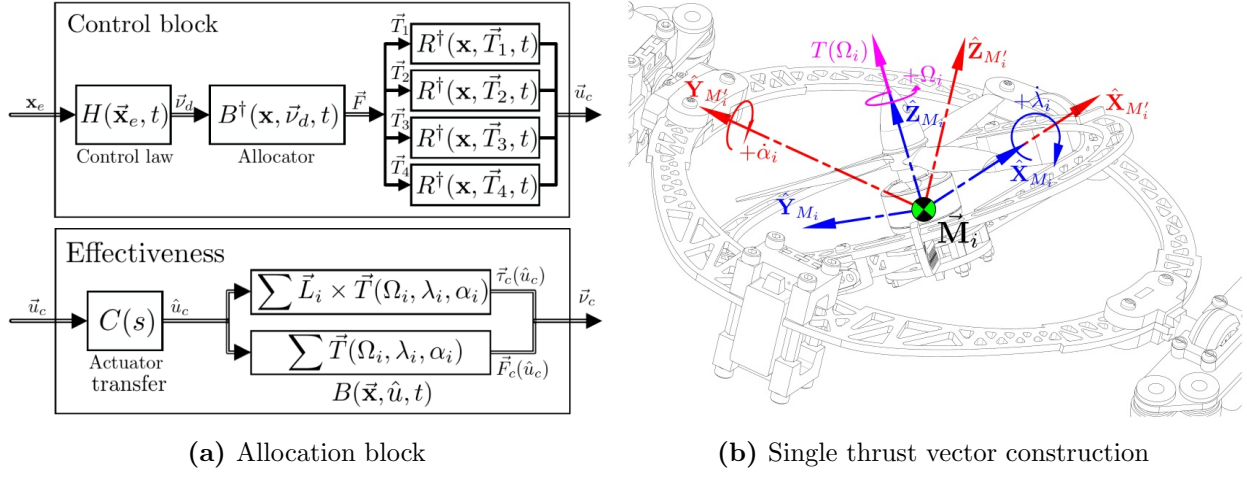


Figure 5.1: Actuator allocation

Some distribution heuristic is needed to *allocate* physical actuator positions $\vec{u}_c \in \mathbb{U}$ that command the control input $\vec{\nu}_c$, from Eq:4.6. As mentioned previously (pseudo) inversion-based allocation uses an affine actuator effectiveness function, however it is worth mentioning a multiplicative effectiveness function is *convenient* but not crucial to allocation. The allocator is abstracted to first solve for four thrust vectors which are applied by each motor module, Eq:4.7. As per convention B^\dagger represents the pseudo inverse of the allocator's effectiveness function B :

$$\vec{T}_{[1:4]} = B^\dagger(\vec{x}, t) \vec{\nu}_d = [\vec{T}_1 \ \vec{T}_2 \ \vec{T}_3 \ \vec{T}_4]^T \quad \in \mathbb{R}^{1 \times 12} \quad (5.1)$$

Each 3-D thrust vector is then used to solve for each module's propeller speed in [RPM] and both servo rotational positions in [rad], undoing the thrust vectoring (rotation) applied by the motor module's actuator structure in Fig:5.1b.

$$\vec{u}_i = [\Omega_i \ \lambda_i \ \alpha_i]^T = R^\dagger(\vec{x}, \vec{T}_i, t) \quad \text{for } i \in [1 : 4] \quad (5.2)$$

5.1 Generalized allocation

Regular, unconstrained control allocation is solved as an optimization problem, shown in [65, 100]. The aim is to minimize deviation (*slack*) \vec{s} between the virtual controller generated input $\vec{\nu}_d$ and the physically commanded control input $\vec{\nu}_c(\vec{u}_c)$, where \vec{u}_c is a commanded actuator position. For a controller's virtual input $\vec{\nu}_d = \mathcal{H}(\vec{x}_e, t)$, the problem is to optimize some cost function of the slack variable $Q(\vec{s})$:

$$\vec{s} \triangleq \vec{\nu}_d - \vec{\nu}_c(\vec{u}_c) \quad (5.3a)$$

$$\min_{\vec{u}_c \in \mathbb{U}^m, \vec{s} \in \mathbb{R}^n} (Q(\vec{s})) \text{ such that } \vec{s} = \mathcal{H}(\vec{x}_e, t) - B(\vec{x}, t, \vec{u}_c) \quad (5.3b)$$

where $\vec{u}_c \in \mathbb{U}^m$ is the dimension of the actuator set and \vec{x} , $\vec{\nu}_d$, $\vec{\nu}_c$ and \vec{s} are each the same dimension as the virtual plant's input $\in \mathbb{R}^n$, where n is the state's degree of freedom. In this case $\vec{u} \in \mathbb{U}^{12}$ for the twelve actuators and $\vec{x} \in \mathbb{R}^6$ for the 6-DOF rigid body. Typically the slack cost function $Q(\vec{s})$ in Eq:5.3b is simply the Euclidean norm of \vec{s} :

$$Q(\vec{s}) \triangleq \|\vec{s}\| = \|\vec{\nu}_d - \vec{\nu}_c(\vec{u}_c)\| \quad (5.4)$$

Overactuation implies that there exists an entire set of suitable actuator values which are all solutions to Eq:5.3. Solving for explicit actuator positions requires an introduction of a secondary cost function or minimization objective $J(\vec{x}, \vec{u}_c, t)$ to refine the solution to Eq:5.3.

$$\min_{\vec{u} \in \mathbb{U}^{12}, \vec{s} \in \mathbb{R}^6} (\|\vec{s}\| + J(\vec{x}, \vec{u}_c, t)) \text{ such that } \vec{s} = \vec{\nu}_d - \vec{\nu}_c(\vec{u}_c) \quad (5.5)$$

That secondary cost $J(\vec{x}, \vec{u}_c, t)$ and how to calculate its *explicit* minimization solution for Eq:5.5 is the subject of control allocation. Not much work has been done on overallocation for aerospace vehicles outside the field of satellite attitude control (Sec:1.2.2 for examples). Often satellites are overactuated for the sake of fault tolerance and redundancy [6, 83].

Allocation *inverts* the effectiveness of the actuator set, $B(\vec{x}, \vec{u}_c, t)$ in Eq:4.4, to find actuator positions which satisfy the virtual control input. Using pseudo-inversion to solve for an actuator command requires an affine relationship between the effectiveness function and the actuator input matrix \vec{u} , hence the abstraction layer which was introduced previously in Eq:4.7. The allocator effectiveness function, when abstracted to an affine matrix, reduces to:

$$\vec{\nu}_d = \mathcal{H}(\vec{x}_e, t) \quad (5.6a)$$

$$\vec{\nu}_c(\vec{u}_c) = B(\vec{x}, \vec{u}_c, t) = B'(\vec{x}, t)\vec{u}_c = \begin{bmatrix} \vec{F}_c(\hat{u}_c) & \vec{\tau}_c(\hat{u}_c)^T \end{bmatrix} \quad (5.6b)$$

where $\vec{F}_c(\hat{u}_c)$ and $\vec{\tau}_c(\hat{u}_c)$ are the physically allocated force and torque acting on the body as a result of the commanded actuator matrix *estimate* \hat{u}_c . The allocator solves for an actuator command setpoint \vec{u}_c which leads to actuator response estimate $\hat{u}_c = C(s)\vec{u}_c$ from the actuator block transfer function defined in Eq:2.43. In Eq:5.6 state dimensions are such that $(\vec{\nu}_d, \vec{\nu}_c) \in \mathbb{R}^n$, $\vec{u}_c \in \mathbb{U} \in \mathbb{R}^m$, and $B \in \mathbb{R}^{m \times n}$. The introduced affine abstraction $B'(\vec{x}, t)\vec{u}_c$ in Eq:4.7 makes addressing the allocation conceptually simpler, accommodating the use of inversion-based allocation laws (Sec:5.3.1-5.3.3).

5.2 Thrust vector inversion

The rotation *inversion* function $R^\dagger(\vec{x}, \vec{F}_i, t)$ to solve for physical actuator positions to be commanded $\vec{u}_c(i) = [\Omega_i \lambda_i \alpha_i]^T$ is as yet undefined. Assume for now there is some allocation rule that, from the controller input $\vec{\nu}_d$, designs four decomposed 3-D thrust vectors $\vec{T}_{[1:4]}$ to be actuated by each motor module.

It then follows that each of those four thrust vectors relate to their individual associated motor module actuator positions through a quaternion *rotation*, not transformation:

$$\vec{T}_i = Q_{M_i} \otimes \vec{T}(\Omega_i) \otimes Q_{M_i}^* \in \mathcal{F}^b \quad (5.7a)$$

$$= Q_z(\sigma_i)Q_y(\alpha_i)Q_x(\lambda_i) \otimes \vec{T}(\Omega_i) \otimes Q_x^*(\lambda_i)Q_y^*(\alpha_i)Q_z^*(\sigma_i) \quad (5.7b)$$

Where each motor's thrust vector $\vec{T}(\Omega_i)$ is calculated using blade element momentum theory thrust coefficients, Eq:3.32a with coefficients from Fig:3.5. A propeller's produced thrust is normal to its rotational plane, so in the motor module $\vec{T}(\Omega_i)$ acts in the \hat{Z}_{M_i} direction of that module's frame \mathcal{F}^{M_i} :

$$\vec{T}(\Omega_i) = [0 \ 0 \ T(\Omega_i)]^T = \begin{bmatrix} 0 \\ 0 \\ C_T(J)\rho\Omega_i^2 D^4 \end{bmatrix} \in \mathcal{F}^{M_i} \quad (5.7c)$$

Noting that quaternion rotation (or *transformation*) operators change the reference frame but retain the vector operand's magnitude, it follows that $T(\Omega_i)$, and by extension the propeller speed Ω_i , can be found:

$$|\vec{T}_i| = \sqrt{\|[T_x \ T_y \ T_z]\|} = \sqrt{T_x^2 + T_y^2 + T_z^2} = |T(\Omega_i)| = |C_T(J)\rho\Omega_i^2 D^4| \quad (5.8a)$$

$$\therefore \Omega_i = \sqrt{\frac{|\vec{T}_i|}{C_T(J)\rho D^4}} = \sqrt{\frac{\sqrt{T_x^2 + T_y^2 + T_z^2}}{C_T(J)\rho D^4}} \quad (5.8b)$$

Reversing (or *undoing*) that transformation from the motor module's frame to the body frame in Eq:5.7a:

$$\vec{T}(\Omega_i) = Q_z^*(\sigma_i)Q_y^*(\alpha_i)Q_x^*(\lambda_i) \otimes \vec{T}_i \otimes Q_x(\lambda_i)Q_y(\alpha_i)Q_z(\sigma_i) \in \mathcal{F}^{M_i} \quad (5.9a)$$

$$\therefore \vec{T}(\Omega_i) = Q_{M_i}^* \otimes \vec{T}_i \otimes Q_{M_i} \in \mathcal{F}^{M_i} \quad (5.9b)$$

Knowing only $\vec{T}(\Omega_i)$ and \vec{T}_i in the motor frame and body frame respectively requires solving for a quaternion which relates the two. If both vectors are of unit length, \check{T}_i and $\check{T}(\Omega_i)$, then the following relationship can be used to construct a relative quaternion, [75].

$$\check{T}_i \triangleq \frac{\vec{T}_i}{|\vec{T}_i|} = \frac{\vec{T}_i}{\sqrt{T_x^2 + T_y^2 + T_z^2}} \in \mathcal{F}^b \quad (5.10a)$$

$$\check{T}(\Omega_i) \triangleq \frac{\vec{T}(\Omega_i)}{|\vec{T}(\Omega_i)|} = \frac{\vec{T}(\Omega_i)}{|C_T(J)\rho\Omega^2 D^4|} = [0 \ 0 \ 1]^T \in \mathcal{F}^{M_i} \quad (5.10b)$$

$$\therefore Q_{M_i} = \begin{bmatrix} q_0 \\ \vec{q} \end{bmatrix} = \begin{bmatrix} 1 + \check{T}_i \cdot \check{T}(\Omega_i) \\ -\check{T}_i \times \check{T}(\Omega_i) \end{bmatrix} \quad (5.10c)$$

where Eq:5.10c is a quaternion operator's definition Eq:3.45b, rotating a vector around a single Euler axis, Eq:3.57, but when applied to two unit vectors. That quaternion can indeed be used to solve for relative pitch, roll and yaw Euler angles (see App:A.3). However, Eq:5.10c solves for the **shortest rotational path** between the two vectors, a sequenced ZYX rotation is by no means the shortest possible rotation. Associated $[\phi, \theta, \psi]^T$ solutions to Eq:A.16 are of no consequence when solving for the sequentially applied rotation angles $[\lambda_i, \alpha_i, \sigma_i]^T$, where σ_i is a known orthogonal multiplicate. Furthermore, when considering a sequenced ZYX quaternion, angular operands cannot be extracted without applying significantly complex trigonometric inversions:

$$Q_b \triangleq \begin{bmatrix} \cos \frac{\psi}{2} \\ 0 \\ 0 \\ \sin \frac{\psi}{2} \end{bmatrix} \otimes \begin{bmatrix} \cos \frac{\theta}{2} \\ 0 \\ \sin \frac{\theta}{2} \\ 0 \end{bmatrix} \otimes \begin{bmatrix} \cos \frac{\phi}{2} \\ \sin \frac{\phi}{2} \\ 0 \\ 0 \end{bmatrix} = \begin{bmatrix} c \frac{\psi}{2} c \frac{\theta}{2} c \frac{\phi}{2} + s \frac{\psi}{2} s \frac{\theta}{2} s \frac{\phi}{2} \\ c \frac{\psi}{2} c \frac{\theta}{2} s \frac{\phi}{2} - s \frac{\psi}{2} s \frac{\theta}{2} c \frac{\phi}{2} \\ c \frac{\psi}{2} s \frac{\theta}{2} c \frac{\phi}{2} + s \frac{\psi}{2} c \frac{\theta}{2} s \frac{\phi}{2} \\ s \frac{\psi}{2} c \frac{\theta}{2} c \frac{\phi}{2} - c \frac{\psi}{2} s \frac{\theta}{2} s \frac{\phi}{2} \end{bmatrix} = \begin{bmatrix} q_0 \\ q_x \\ q_y \\ q_z \end{bmatrix} = \begin{bmatrix} q_0 \\ \vec{q} \end{bmatrix} \quad (5.11a)$$

$$= \begin{bmatrix} c\frac{\psi}{2}c\frac{\theta}{2}c\frac{\phi}{2} + s\frac{\psi}{2}s\frac{\theta}{2}s\frac{\phi}{2} \\ c\frac{\psi}{2}c\frac{\theta}{2}s\frac{\phi}{2} - s\frac{\psi}{2}s\frac{\theta}{2}c\frac{\phi}{2} \\ c\frac{\psi}{2}s\frac{\theta}{2}c\frac{\phi}{2} + s\frac{\psi}{2}c\frac{\theta}{2}s\frac{\phi}{2} \\ s\frac{\psi}{2}c\frac{\theta}{2}c\frac{\phi}{2} - c\frac{\psi}{2}s\frac{\theta}{2}s\frac{\phi}{2} \end{bmatrix} \otimes \vec{T}(\Omega_i) \otimes \begin{bmatrix} s\frac{\psi}{2}s\frac{\theta}{2}s\frac{\phi}{2} + c\frac{\psi}{2}c\frac{\theta}{2}c\frac{\phi}{2} \\ s\frac{\psi}{2}s\frac{\theta}{2}c\frac{\phi}{2} - c\frac{\psi}{2}c\frac{\theta}{2}s\frac{\phi}{2} \\ -c\frac{\psi}{2}s\frac{\theta}{2}c\frac{\phi}{2} - s\frac{\psi}{2}c\frac{\theta}{2}s\frac{\phi}{2} \\ c\frac{\psi}{2}s\frac{\theta}{2}s\frac{\phi}{2} - s\frac{\psi}{2}c\frac{\theta}{2}c\frac{\phi}{2} \end{bmatrix} \quad (5.11b)$$

Instead, return to rotation matrices to resolve the inverse transformation and note that Euler angle equivalents for the servos are $[\phi, \theta, \psi]^T \iff [\lambda_i, \alpha_i, \sigma_i]^T$. The rotation matrix transformation from \mathcal{F}^{M_i} to \mathcal{F}^b , analogous to Eq:5.9b, is:

$$\vec{T}_i = R_z(\sigma_i)R_y(\alpha_i)R_x(\lambda_i)\vec{T}(\Omega_i) \in \mathcal{F}^b \quad (5.12a)$$

$$= \begin{bmatrix} c\sigma_i & -s\sigma_i & 0 \\ s\sigma_i & c\sigma_i & 0 \\ 0 & 0 & 1 \end{bmatrix} \begin{bmatrix} c\alpha_i & 0 & s\alpha_i \\ 0 & 1 & 0 \\ -s\alpha_i & 0 & c\alpha_i \end{bmatrix} \begin{bmatrix} 1 & 0 & 0 \\ 0 & c\lambda_i & -s\lambda_i \\ 0 & s\lambda_i & c\lambda_i \end{bmatrix} \vec{T}(\Omega_i) \quad (5.12b)$$

$$\therefore \vec{T}_i = \begin{bmatrix} c\sigma_i c\alpha_i & c\sigma_i s\alpha_i s\lambda_i - s\sigma_i c\lambda_i & c\sigma_i s\alpha_i c\lambda_i + s\sigma_i s\lambda_i \\ s\sigma_i c\alpha_i & s\sigma_i s\alpha_i s\lambda_i + c\sigma_i c\lambda_i & s\sigma_i s\alpha_i c\lambda_i - c\sigma_i s\lambda_i \\ -s\alpha_i & c\alpha_i s\lambda_i & c\alpha_i c\lambda_i \end{bmatrix} \begin{bmatrix} 0 \\ 0 \\ T(\Omega_i) \end{bmatrix} \quad (5.12c)$$

where σ_i is an orthogonal multiple applying a rotation about the \hat{Z}_b axis (Fig:2.9). Because the thrust vector $\vec{T}(\Omega_i)$ is only in the motor frame's \hat{Z}_{M_i} direction, solving for servo angles is simplified.

$$\therefore \vec{T}_i \begin{bmatrix} T_{ix} \\ T_{iy} \\ T_{iz} \end{bmatrix} = \begin{bmatrix} s\sigma_i s\lambda_i + c\sigma_i s\alpha_i c\lambda_i \\ s\sigma_i s\alpha_i c\lambda_i - c\sigma_i s\alpha_i \\ c\alpha_i c\lambda_i \end{bmatrix} T(\Omega_i) \in \mathcal{F}^b \quad (5.12d)$$

Eq:5.12d then reduces further with $R_z(\sigma_i)$ rotation matrices already defined in Eq:2.16b. The following four trigonometric relationships exist for each motor module respectively:

$$\therefore \vec{T}_{[1:4]} = \begin{bmatrix} \vec{T}_1 \\ \vec{T}_2 \\ \vec{T}_3 \\ \vec{T}_4 \end{bmatrix} = \left[\begin{bmatrix} s\alpha_1 c\lambda_1 \\ -s\lambda_1 \\ c\alpha_1 c\lambda_1 \end{bmatrix}, \begin{bmatrix} s\lambda_2 \\ s\alpha_2 c\lambda_2 \\ c\alpha_2 c\lambda_2 \end{bmatrix}, \begin{bmatrix} -s\alpha_3 c\lambda_3 \\ s\lambda_3 \\ c\alpha_3 c\lambda_3 \end{bmatrix}, \begin{bmatrix} -s\lambda_4 \\ -s\alpha_4 c\lambda_4 \\ c\alpha_4 c\lambda_4 \end{bmatrix} \right] \begin{bmatrix} T(\Omega_1) \\ T(\Omega_2) \\ T(\Omega_3) \\ T(\Omega_4) \end{bmatrix} \quad (5.13)$$

It is then a simple trigonometric inversion to solve for both λ_i and α_i . Using the thrust vector's magnitude $T(\Omega_i) = \|\vec{T}_i\|$ and implementing a four quadrant secondary arctangent2 function, where $\text{arctan2}(x, y)$ is the four-quadrant tangent inverse that results in the principle argument of the complex operand:

$$\text{arctan2}(x, y) = PR \arg(x + y\hat{i}) = \text{Arg}(x + y\hat{i}) \quad (5.14)$$

The use of a full quadrature arctangent function is to find solutions for Euler angles that are not only acute. Each inverse would otherwise need generalized reciprocal solutions with parity checks to establish which quadrant the angle occurs in. Furthermore, exploiting the fact that $\text{arctan}(x) \equiv \text{arcsin}(x/\sqrt{1-x^2})$, the servo rotational angles for motor module 1 are found:

$$\lambda_1 = \text{arctan2}\left(-T_{1y}, \sqrt{\|\vec{T}_1\|^2 - T_{1y}^2}\right) \quad (5.15a)$$

$$\alpha_1 = \text{arctan2}(T_{1x}, T_{1z}) \quad (5.15b)$$

Therefore, the secondary component of the control allocation block, $R^\dagger(\vec{x}, \vec{T}_i, t)$ from Fig:4.2 is then summarized as a single rotation inversion function (in this case for $i = 1$):

$$\begin{bmatrix} \Omega_1 \\ \lambda_1 \\ \alpha_1 \end{bmatrix} = R^\dagger(\vec{x}, \vec{T}_1, t) \triangleq \begin{bmatrix} \left(\sqrt{T_x^2 + T_y^2 + T_z^2}/C_T(J)\rho D^4\right)^{\frac{1}{2}} \\ \text{atan2}(-T_y^2, \|\vec{T}_1\| \sqrt{\|\vec{T}_1\|^2 - T_y^2}) \\ \text{atan2}(T_x, T_z \|\vec{T}_1\|) \end{bmatrix} \quad (5.16a)$$

Rotation inversion for the remaining motor modules extends from the rotations applied in Eq:5.13 which are inverted in the same process, using the *arctan2* function to produce:

$$\begin{bmatrix} \Omega_2 \\ \lambda_2 \\ \alpha_2 \end{bmatrix} = R^\dagger(\mathbf{x}, \vec{T}_2, t) \triangleq \begin{bmatrix} \left(\sqrt{T_x^2 + T_y^2 + T_z^2} / C_T(J) \rho D^4 \right)^{\frac{1}{2}} \\ \text{atan2}(T_x^2, ||\vec{T}_2|| \sqrt{||\vec{T}_2||^2 - T_x^2}) \\ \text{atan2}(T_y, T_z ||\vec{T}_2||) \end{bmatrix} \quad (5.16b)$$

$$\begin{bmatrix} \Omega_3 \\ \lambda_3 \\ \alpha_3 \end{bmatrix} = R^\dagger(\mathbf{x}, \vec{T}_3, t) \triangleq \begin{bmatrix} \left(\sqrt{T_x^2 + T_y^2 + T_z^2} / C_T(J) \rho D^4 \right)^{\frac{1}{2}} \\ \text{atan2}(T_y^2, ||\vec{T}_3|| \sqrt{||\vec{T}_3||^2 - T_y^2}) \\ \text{atan2}(-T_x, T_z ||\vec{T}_3||) \end{bmatrix} \quad (5.16c)$$

$$\begin{bmatrix} \Omega_4 \\ \lambda_4 \\ \alpha_4 \end{bmatrix} = R^\dagger(\mathbf{x}, \vec{T}_4, t) \triangleq \begin{bmatrix} \left(\sqrt{T_x^2 + T_y^2 + T_z^2} / C_T(J) \rho D^4 \right)^{\frac{1}{2}} \\ \text{atan2}(-T_x^2, ||\vec{T}_4|| \sqrt{||\vec{T}_4||^2 - T_x^2}) \\ \text{atan2}(-T_y, T_z ||\vec{T}_4||) \end{bmatrix} \quad (5.16d)$$

All that remains for the control block to be completed is a final abstracted allocation algorithm to find the thrust vectors $\vec{T}_{[1:4]}$, from the control input $\vec{\nu}_d$, to be used with Eq:5.16 to find explicit actuator commands. That allocation block $B^\dagger(\mathbf{x}, \vec{\nu}_d, t)$ is now addressed.

5.3 Allocators

5.3.1 Pseudo Inverse Allocator

The simplest control allocation solution to Eq:5.5 stems from what is categorized as *inversion*, based on controller effort optimization [65]. The requirement for an inversion-based allocation scheme is that the actuator's effectiveness function $B(\vec{\mathbf{x}}, \vec{u}, t)$ is a linear relationship which can be abstracted to $B'(\vec{\mathbf{x}}, t)\vec{u}$. The general allocation objective is to find some actuator command \vec{u}_c such that:

$$\vec{\nu}_d = \mathcal{H}(\vec{\mathbf{x}}_e, t) \quad (5.17a)$$

$$\vec{\nu}_c(\vec{u}_c) = B'(\vec{\mathbf{x}}, t)\vec{u}_c \quad (5.17b)$$

then finding an inverse B^\dagger :

$$\vec{u}_c = B^\dagger(\vec{\mathbf{x}}, t)\vec{\nu}_d \quad (5.17c)$$

which leads to the static identity:

$$\therefore \vec{\nu}_c(\vec{u}_c) = B'(\vec{\mathbf{x}}, t)B^\dagger(\vec{\mathbf{x}}, t)\vec{\nu}_d \quad (5.17d)$$

The condition for both the effectiveness matrix $B'(\vec{\mathbf{x}}, t)$ and its inverse $B^\dagger(\vec{\mathbf{x}}, t)$ is that their product produces an identity matrix:

$$B'(\vec{\mathbf{x}}, t)B^\dagger(\vec{\mathbf{x}}, t) = \mathbb{I}_{m \times m} \quad (5.17e)$$

Or more generally, and without the dependency of the affine linearity:

$$\vec{u}_c = B^\dagger(\vec{\mathbf{x}}, \vec{\nu}_d, t) \quad (5.17f)$$

$$\therefore B(\vec{\mathbf{x}}, \vec{u}_c, t)B^\dagger(\vec{\mathbf{x}}, \vec{\nu}_d, t) = \mathbb{I}_{m \times m} \quad (5.17g)$$

In Eq:5.17, the multiplicative effectiveness matrix $B'(\vec{\mathbf{x}}, t)$ has the dimension $\in \mathbb{R}^{m \times n}$. In the case of overallocation, there are more actuators than degrees of freedom, or that $m > n$ for $\vec{u} \in \mathbb{R}^m$ and $\vec{\mathbf{x}} \in \mathbb{R}^n$, then finding the inversion of $B^\dagger(\mathbf{x}, t)$ is not trivial.

Choosing the secondary allocation minimization cost, $J(\vec{x}, \vec{u}, t)$ in Eq:5.5, to be a quadratic cost function, then actuator positions \vec{u}_c to be commanded can be solved as a linear least squares problem. The quadratic least squares optimization aims to minimize controller effort (*magnitude*):

$$J(\vec{x}, \vec{u}_c, t) = \min_{\vec{u}_c \in \mathbb{U}} \frac{1}{2} (\vec{u}_c - \vec{u}_p)^T W (\vec{u}_c - \vec{u}_p) \text{ such that } \vec{\nu}_c = B'(\vec{x}, t) \vec{u}_c \quad (5.18)$$

where W is a $[12 \times 12]$ weighting matrix and \vec{u}_p is the preferred value of the actuation matrix. The least squares solution [45] to Eq:5.18 then minimizes the commanded actuator effort $\|\vec{u}_c\|_2$. In this case, because of the abstraction applied in Eq:4.7 which is reiterated next in Eq:5.21, the allocation rule solves for four thrust vectors $\vec{T}_{[1:4]}$ and *not physical actuator* servo positions and propeller rotational speeds. This means that a least squares allocation minimization minimizes those thrust magnitudes $\|\vec{T}_{[1:4]}\|$. The magnitude of each thrust vector commanded to a motor module is affected by the propeller's rotational speed Ω_i , eq:5.8. Effectively this results in an allocator that prioritizes pitching or rolling both servos λ_i and α_i over adjusting the propeller's velocity to produce input thrusts and torques.

The positive symmetrical weighting matrix W in Eq:5.18 biases certain actuators (thrust components in this case) and has units $[N^{-1}]$, creating its own class of inversion allocator presented in Sec:5.3.3. Eigenvalues of W must sum to unity for the allocation slack variable, \vec{s} in Eq:5.3, to be met, otherwise the actuator block applies its own gain to the control input. For an inversion matrix $B^\dagger(\vec{x}, t)$ actuator thrust components are found:

$$\vec{T}_{[1:4]} = \left(\mathbb{I}_{m \times m} - CB(\vec{x}, t) \right) \vec{T}_p + C \vec{\nu}_d \quad (5.19a)$$

$$C = W^{-1} B^T(\vec{x}, t) (B(\vec{x}, t) W^{-1} B^T(\vec{x}, t))^{-1} \quad (5.19b)$$

where $\vec{T}_p \in \mathbb{R}^{1 \times 12}$ are preferred thrust component values. The solution in Eq:5.19 is a *generalized inverse* with weighted actuator components and preferred values. In the case where no weightings nor preferred actuator values are specified, $W = \mathbb{I}_{n \times n}$ and $\vec{u}_p = \vec{T}_p = \vec{0}$, the solution reduces:

$$\vec{T}_{[1:4]} = B^T(\vec{x}, t) (B(\vec{x}, t) B^T(\vec{x}, t))^{-1} \vec{\nu}_d \quad (5.20a)$$

$$= B^\dagger(\vec{x}, t) \vec{\nu}_d, B^\dagger \in \mathbb{R}^{6 \times 12} \quad (5.20b)$$

The simplified case in Eq:5.20 is termed a Moore-Penrose or pseudo-inversion of the actuator effectiveness matrix $B'(\vec{x}, t)$ [77]. Pseudo-inversion is the simplest allocation rule to implement, in most cases controller effort optimization is a satisfactory constraint without any additional weights or preferred values. For an effectiveness $B'(\vec{x}, t)$ matrix defined in Eq:4.7, the pseudo-inversion is:

$$B'(\vec{x}, t) = \begin{bmatrix} \mathbb{I}_{3 \times 3} & \mathbb{I}_{3 \times 3} & \mathbb{I}_{3 \times 3} & \mathbb{I}_{3 \times 3} \\ [\vec{L}_1]_\times & [\vec{L}_2]_\times & [\vec{L}_3]_\times & [\vec{L}_4]_\times \end{bmatrix} \in \mathbb{R}^{12 \times 6} \quad (5.21a)$$

$$\therefore \vec{T}_{[1:4]} = B^T(B B^T)^{-1} \vec{\nu}_d = B^\dagger(\vec{x}, t) \vec{\nu}_d \quad (5.21b)$$

Recall that each motor module's displacement is at a distance $L_{arm} = 195.16$ [mm] from Fig:2.17. Then each module has a vector $\vec{L}_{1,3} = [\pm 195.16 \ 0 \ 0]^T$ and $\vec{L}_{2,4} = [0 \ \pm 195.16 \ 0]$. Each cross product vector in Eq:5.21a is defined from Eq:2.8c as:

$$[\vec{L}_i]_\times \triangleq \begin{bmatrix} 0 & -L_z & L_y \\ L_z & 0 & -L_x \\ -L_y & L_x & 0 \end{bmatrix} \quad (5.21c)$$

The numeric and constant pseudo-inverse matrix is then:

$$\therefore B^\dagger(\vec{\mathbf{x}}, t) = \begin{bmatrix} \frac{1}{4} & 0 & 0 & 0 & 0 & 0 \\ 0 & \frac{1}{4} & 0 & 0 & 0 & \frac{1}{4L} \\ 0 & 0 & \frac{1}{4} & 0 & \frac{-1}{2L} & 0 \\ \frac{1}{4} & 0 & 0 & 0 & 0 & \frac{-1}{4L} \\ 0 & \frac{1}{4} & 0 & 0 & 0 & 0 \\ 0 & 0 & \frac{1}{4} & \frac{1}{2L} & 0 & 0 \\ \frac{1}{4} & 0 & 0 & 0 & 0 & 0 \\ 0 & \frac{1}{4} & 0 & 0 & 0 & \frac{-1}{4L} \\ 0 & 0 & \frac{1}{4} & 0 & \frac{1}{2L} & 0 \\ \frac{1}{4} & 0 & 0 & 0 & 0 & \frac{1}{4L} \\ 0 & \frac{1}{4} & 0 & 0 & 0 & 0 \\ 0 & 0 & \frac{1}{4} & \frac{-1}{2L} & 0 & 0 \end{bmatrix} \quad (5.21d)$$

$$= \begin{bmatrix} 0.250 & 0.000 & 0.000 & 0.000 & 0.000 & 0.000 \\ 0.000 & 0.250 & 0.000 & 0.000 & 0.000 & 0.250 \\ 0.000 & 0.000 & 0.250 & 0.000 & -2.562 & 0.000 \\ 0.250 & 0.000 & 0.000 & 0.000 & 0.000 & -1.281 \\ 0.000 & 0.250 & 0.000 & 0.000 & 0.000 & 0.000 \\ 0.000 & 0.000 & 0.250 & 2.562 & 0.000 & 0.000 \\ 0.250 & 0.000 & 0.000 & 0.000 & 0.000 & 0.000 \\ 0.000 & 0.250 & 0.000 & 0.000 & 0.000 & -1.281 \\ 0.000 & 0.000 & 0.250 & 0.000 & 2.562 & 0.000 \\ 0.250 & 0.000 & 0.000 & 0.000 & 0.000 & 1.281 \\ 0.000 & 0.250 & 0.000 & 0.000 & 0.000 & 0.000 \\ 0.000 & 0.000 & 0.250 & -2.562 & 0.000 & 0.000 \end{bmatrix} \quad (5.21e)$$

Pseudo-inversion allocation guarantees that $\vec{T}_{[1:4]} = B^\dagger(\vec{\mathbf{x}}, t)\vec{\nu}_d$ produces a set of control thrust vectors $\vec{T}_{[1:4]}$ for some virtual control input $\vec{\nu}_d = \mathcal{H}(\vec{\mathbf{x}}_e, t)$ that minimizes the slack variable $\vec{s} = \vec{\nu}_d - \vec{\nu}_c(\vec{u}_c)$ when \vec{u}_c is calculated from $\vec{T}_{[1:4]}$ using Eq:5.16. Solving for $[\Omega_i, \lambda_i, \alpha_i]^T = R^\dagger(\mathbf{x}, \vec{T}_i, t)$ using Eq:5.16 constructs an actuator matrix $\vec{u}_c \in \mathbb{U} \in \mathbb{R}^{12}$ which will physically command $\vec{\nu}_c = B(\vec{\mathbf{x}}, t)\vec{u}_c$.

The actuator's effectiveness matrix $B(\vec{\mathbf{x}}, t, \vec{u})$ does not necessarily have to be static (or affine) with respect to either the state vector $\vec{\mathbf{x}}$ or time t . However it was approximated to such a static relationship to simplify the actuation process. Allocation in Eq:5.21 is the most simplified case of the least squares quadratically optimized equation for Eq:5.5 and is used as the base reference allocation law.

In certain situations it may be desirable to saturate certain actuators before exploiting other actuator plant inputs. That would entail an iterative *nested* allocation to be performed numerically online, enforcing saturation for at least some actuators and the achievement of control objectives, [65]. Such an approach is avoided here as completely saturating any actuator is not desirable, furthermore online allocation is outside the scope of applied allocation rules (only static explicit allocation rules are considered).

5.3.2 Priority Norm Inverse Allocator

Choosing a preferred actuator position from Eq:5.5 produces what is termed as a *priority norm* allocator, specifically when $\vec{u}_p = \vec{T}_p \neq \vec{0} \in \mathbb{U}$. An obvious choice for that value is the conditions required for stable hovering, those which simply keep the quadcopter airborne. There are, however, some intricacies which must be discussed with respect to what the hovering conditions are.

For a vehicle with a weight m_b , a net gravitational force acts on the vehicle through its center of gravity in the inertial frame $-m_b \vec{G}_I \in \mathcal{F}^I$. Recall hovering input forces and torques from Eq:3.117, but defined with respect to the inertial frame are as follows:

$$\vec{\nu}_H' = Q_b \otimes \vec{\nu}_H \otimes Q_b^* = m_b \begin{bmatrix} \vec{G}_I \\ \vec{C}_b(\vec{u}) \times m_b \vec{G}_I \end{bmatrix} \in \mathcal{F}^I \quad (5.22)$$

If the preferred hover conditions are taken with respect to the inertial frame as in Eq:5.22, and then the resultant preferred actuator positions are independent of the body's current or desired attitude setpoint. The control loop then naturally tends towards a rest state attitude at $Q_d = [1 \ 0]^T$ with $\vec{\nu}_H' \equiv \vec{\nu}_b$. The commanded body frame control input is equivalent to the inertial frame hovering conditions. The free body diagram in Fig:5.2 illustrates a preferred hovering condition in the inertial frame and its tendency toward a natural state at the attitude's origin.

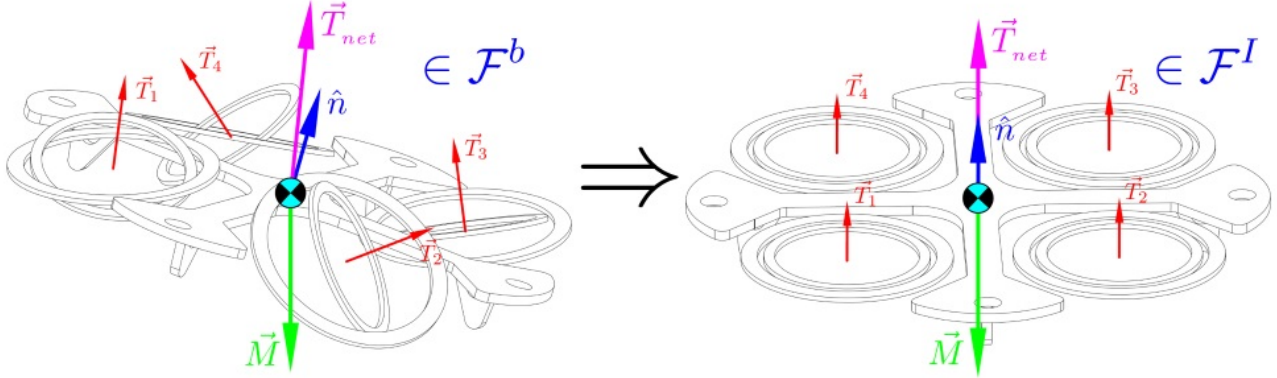


Figure 5.2: Hover conditions with respect to the inertial frame \mathcal{F}^I

Alternatively, the hover conditions could be defined with respect to the body frame, and being a function of the body's attitude, illustrated in Fig:5.3. The difference is that the body's preferred actuator positions are dependent on each instantaneous orientation. That attitude stays constant whilst the actuators are redirected to produce inertial hovering conditions, irrespective of the attitude. The preferred hovering conditions are then always dependent on the commanded attitude trajectory.

$$m_b \vec{G}_b \triangleq m_b Q_b^* \otimes \vec{G}_I \otimes Q_b \in \mathcal{F}^b \quad (5.23a)$$

$$\vec{\nu}_H = \begin{bmatrix} \vec{F}_p \\ \vec{\tau}_p \end{bmatrix} = m_b \begin{bmatrix} \vec{G}_b \\ \vec{C}_b(\vec{u}) \times \vec{G}_b \end{bmatrix} \in \mathcal{F}^b \quad (5.23b)$$

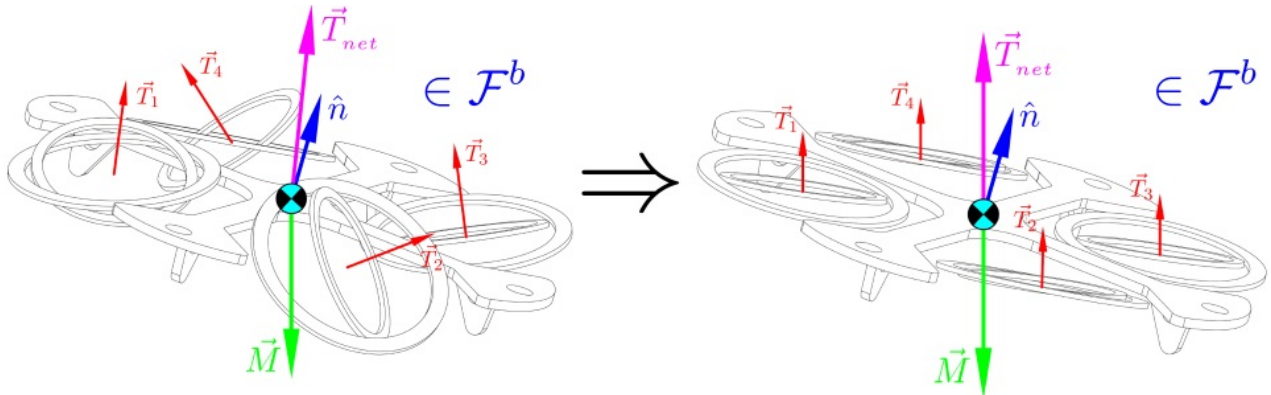


Figure 5.3: Hover conditions with respect to the body frame \mathcal{F}^b

Specific module thrust values to be commanded are then solved for using Eq:5.22 and Eq:5.23 with pseudo inversion from Eq:5.20. The two solutions are then as follows:

$$\vec{T}_p^I = B^\dagger(\mathbf{x}, \vec{\nu}_H, t) \text{ for hover in Fig:5.2} \quad (5.24a)$$

$$\vec{T}_p^b = B^\dagger(\mathbf{x}, \vec{\nu}_H, t) \text{ for hover in Fig:5.3} \quad (5.24b)$$

Both actuator preferred hovering thrust matrices are then applied to Eq:5.19 and could potentially be combined with some non-zero weighting matrix, $W \neq \mathbb{I}_{12 \times 12}$.

$$\vec{T}_{[1:4]} = (\mathbb{I}_{m \times m} - CB(\vec{x}, t))\vec{T}_p + C\vec{\nu}_d \quad (5.25a)$$

$$C = W^{-1}B^T(\vec{x}, t)(B(\vec{x}, t)W^{-1}B^T(\vec{x}, t))^{-1} \quad (5.25b)$$

Applying the inverse rotation operator R^\dagger from Eq:5.16 to the above, solves for propeller speeds and servo rotational positions in both respective cases. The physical consequences of either preferred hovering condition and its associated actuator positions are demonstrated in simulation in Sec:6.7. Priority actuator positions are not tested together with weighting matrices, the two are compared independently.

5.3.3 Weighted Pseudo-Inverse Allocator

Adding weights to the inversion in Eq:5.19, but regarding preferred actuator positions as negligible, or that $\vec{T}_p = \vec{0}$, produces a *weighted pseudo-inverse* allocator. Each weight in W biases a particular actuator's action in \vec{u} , the positive symmetrical weighting matrix is square with respect to the actuator dimension here $W \in \mathbb{R}^{12 \times 12}$, but more generally $W \in \mathbb{R}^{m \times m}$. The Moore-Penrose inversion (Eq:5.20) assumes that each actuator is weighted equally. Such a case makes the weighting matrix W diagonal identity matrix $W = \mathbb{I}_{m \times m}$.

A weighting matrix could change adaptively over time or as a result of state dependency following control faults or actuator deterioration. As long as the allocator block still produced an actuator command which met the control requirements and any actuator response dynamics were modelled, a changing allocation weight would not affect stability. The control objective of a weighted inversion is to design the explicit weighting coefficients as per some preferred heuristic or optimization. Adaptive weighting is not considered or discussed as that is out of the scope for this work and pertains more to fault tolerant control [6].

Each coefficient in W determines how the least squares solution to Eq:5.5 preferentially biases a particular thrust vector's component. Multiplication by the weighting matrix W in the quadratic allocation cost function Eq:5.18 increases the cost of a coefficient weighted actuator. Introduction of an inverted weighting matrix in the least squares solution then combines thrust vector components of the produced allocated input $\vec{T}_{[1:4]}$ to produce the control input $\vec{\nu}_d$.

$$\begin{aligned} \vec{T}_1 &\Rightarrow \begin{bmatrix} \vec{T}_1 \downarrow & \vec{T}_2 \downarrow & \vec{T}_3 \downarrow & \vec{T}_4 \downarrow \end{bmatrix} \\ &\Rightarrow \begin{bmatrix} \begin{bmatrix} W_{1:1}W_{1:2}W_{1:3} \\ W_{1:4}W_{1:5}W_{1:6} \\ W_{1:7}W_{1:8}W_{1:9} \end{bmatrix} & \begin{bmatrix} 0 & 0 & 0 \\ 0 & 0 & 0 \\ 0 & 0 & 0 \end{bmatrix} & \begin{bmatrix} W_{5:1}W_{5:2}W_{5:3} \\ W_{5:4}W_{5:5}W_{5:6} \\ W_{5:7}W_{5:8}W_{5:9} \end{bmatrix} & \begin{bmatrix} 0 & 0 & 0 \\ 0 & 0 & 0 \\ 0 & 0 & 0 \end{bmatrix} \end{bmatrix} \\ \vec{T}_2 &\Rightarrow \begin{bmatrix} \vec{T}_1 \downarrow & \vec{T}_2 \downarrow & \vec{T}_3 \downarrow & \vec{T}_4 \downarrow \end{bmatrix} \\ &\Rightarrow \begin{bmatrix} \begin{bmatrix} 0 & 0 & 0 \\ 0 & 0 & 0 \\ 0 & 0 & 0 \end{bmatrix} & \begin{bmatrix} W_{2:1}W_{2:2}W_{2:3} \\ W_{2:4}W_{2:5}W_{2:6} \\ W_{2:7}W_{2:8}W_{2:9} \end{bmatrix} & \begin{bmatrix} 0 & 0 & 0 \\ 0 & 0 & 0 \\ 0 & 0 & 0 \end{bmatrix} & \begin{bmatrix} W_{6:1}W_{6:2}W_{6:3} \\ W_{6:4}W_{6:5}W_{6:6} \\ W_{6:7}W_{6:8}W_{6:9} \end{bmatrix} \end{bmatrix} \\ \vec{T}_3 &\Rightarrow \begin{bmatrix} \vec{T}_1 \downarrow & \vec{T}_2 \downarrow & \vec{T}_3 \downarrow & \vec{T}_4 \downarrow \end{bmatrix} \\ &\Rightarrow \begin{bmatrix} \begin{bmatrix} W_{5:1}W_{5:2}W_{5:3} \\ W_{5:4}W_{5:5}W_{5:6} \\ W_{5:7}W_{5:8}W_{5:9} \end{bmatrix} & \begin{bmatrix} 0 & 0 & 0 \\ 0 & 0 & 0 \\ 0 & 0 & 0 \end{bmatrix} & \begin{bmatrix} W_{3:1}W_{3:2}W_{3:3} \\ W_{3:4}W_{3:5}W_{3:6} \\ W_{3:7}W_{3:8}W_{3:9} \end{bmatrix} & \begin{bmatrix} 0 & 0 & 0 \\ 0 & 0 & 0 \\ 0 & 0 & 0 \end{bmatrix} \end{bmatrix} \\ \vec{T}_4 &\Rightarrow \begin{bmatrix} \vec{T}_1 \downarrow & \vec{T}_2 \downarrow & \vec{T}_3 \downarrow & \vec{T}_4 \downarrow \end{bmatrix} \\ &\Rightarrow \begin{bmatrix} \begin{bmatrix} 0 & 0 & 0 \\ 0 & 0 & 0 \\ 0 & 0 & 0 \end{bmatrix} & \begin{bmatrix} W_{6:1}W_{6:2}W_{6:3} \\ W_{6:4}W_{6:5}W_{6:6} \\ W_{6:7}W_{6:8}W_{6:9} \end{bmatrix} & \begin{bmatrix} 0 & 0 & 0 \\ 0 & 0 & 0 \\ 0 & 0 & 0 \end{bmatrix} & \begin{bmatrix} W_{4:1}W_{4:2}W_{4:3} \\ W_{4:4}W_{4:5}W_{4:6} \\ W_{4:7}W_{4:8}W_{4:9} \end{bmatrix} \end{bmatrix} \end{aligned}$$

Figure 5.4: Weighting matrix biasing

Fig:5.4 groups diagonal $[3 \times 3]$ weighting coefficients $W_{1 \rightarrow 4}$ which relate to individual thrust vector direction biasing (T_{ix}, T_{iy}, T_{iz}) , whilst off-centre $[3 \times 3]$ groupings mix separate thrust terms $\vec{T}_{1 \rightarrow 4}$.

Pseudo-inversion exactly matches the virtual control input $\vec{\nu}_d = B(\mathbf{x}, \vec{u}_c, t) = \vec{\nu}_c$ so long as the actuators are not saturated and their inputs act sufficiently fast. Biasing actuators could result in gain being applied to the controller input from the allocation block. Such a case could potentially destabilize the trajectory tracking. Short of processing actuator weights online until a viable solution is found, a constraint on the nature of the weighting matrix needs to be introduced to avoid purposefully imposed control slack. So long as each thrust vector $\vec{T}_{[1:4]}$ has its own coefficient group which has row and column vectors that each sum to 1, the designed control inputs will be met, namely $\sum(W_{row}) = \sum(W_{col}) = 1$. Physically, the resultant thrusts and torque (thrust differentials) would be balanced amongst similarly directed components.

Priority biases for thrust vector components in the \hat{X}_b and \hat{Y}_b would, in theory, prioritize using pitch or roll servos, λ_i and α_i , in lieu of changing the propeller's speed Ω_i . However, given that the actuator effort in Eq:5.18 is quadratically optimized, the weighting matrix's effect is, in practice, going to be diminished. Selection of weighting coefficients needs to be designed as per some heuristic. A suitable objective (used in Sec:6.7) for the allocation block, is aiming to minimize each actuator's transfer rate which attempts to improve the net actuator block's bandwidth. A proposed set of weighting coefficients could then be simulated and penalized from actuator slew rate times together with a slack variable norm to ensure that a control objective is still met:

$$Q(\vec{s}) = \int_{t_0}^{\infty} (a \|t_{\nu_d - \nu_c} - 1\| + b \|\vec{s}\|).dt \quad (5.26)$$

where $t_{\nu_d - \nu_c}$ is a matrix of times taken for each commanded control input component of $\vec{\nu}_c(\vec{u}_c)$ to reach their desired setpoints in $\vec{\nu}_d$. That cost integral is evaluated on the body over simulations of multiple step tests in the attitude and position plant, and iteratively optimized following the combined step tests results. The weighting matrix coefficients aim to reduce the transient time for the actuator block to settle whilst ensuring stability is not compromised with the introduction of a slack penalty cost $\|\vec{s}\|$. However, actuator rates are more dependent on the rotation inverse $R^\dagger(\vec{x}, t)$ and their associated mechanical transfer functions, so the effect of a weighting matrix introduced to the allocation rule is not expected to be significant when the abstraction layer to an affine effectiveness function is introduced.

Chapter 6

Simulations and Discussion of Results

6.1 Simulator description

The proposed attitude and position control laws, together with the system's equations of motion including each actuator's transfer function, were all tested in simulation to determine a particular controller's efficacy. The rigid-body equations of motion from Sec:3.1.1, with nonlinearities from Sec:3.2 and multibody responses from Sec:3.4, were incorporated into a high-fidelity simulation environment. Closely matching the dynamics of the physical quadrotor prototype proposed in Sec:2.1, where measurement data produced by tests in Sec:3.4.2 provides a degree of confidence in the simulation's accuracy. The consolidated quaternion dynamics in Sec:3.5 formed the basis of the simulation, building a loop extended from the control structure in Fig:4.2. Each control law is optimized first without the effect of the servo's 180° saturation limit. Limiting the servos was a conscious design decision, and so its effects are investigated in Sec:6.8. For now, the servos are treated as continuous rotational actuators without saturation limits.

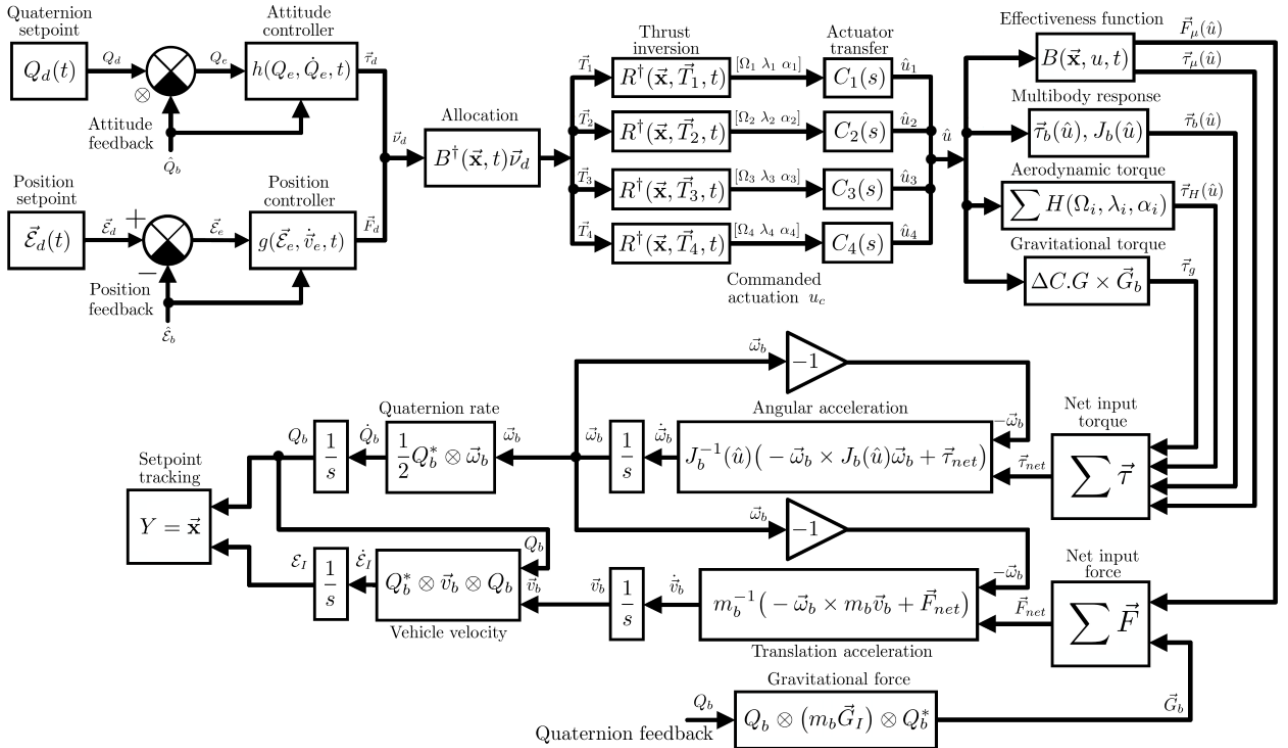


Figure 6.1: Simulation loop

An abstracted simulation loop is illustrated in Fig:6.1, incorporating both attitude and position control loops together with the additive nonlinearities. Certain feedback elements were omitted to retain clarity in the diagram, both Coriolis and gyroscopic nonlinear cross-products were included to highlight the inherent coupling between attitude and position. Not shown, but implied, is some form of state-estimation or discretization between the state-tracking output $y = \vec{x} = [\vec{\mathcal{E}}_I \ Q_b]^T$ and the feedback state estimate $\hat{\vec{x}}$ used for setpoint tracking. Discretized effects of state-estimators are discussed later in Sec:6.9. Initial conditions for each state's integrator, both position $\vec{\mathcal{E}}_I(0)$ and attitude $Q_b(0)$ origins, for their velocities $\dot{\mathcal{E}}_b$ and \dot{Q}_b (and accelerations $\ddot{\mathcal{E}}_b$ and \ddot{Q}_b in the body frame \mathcal{F}^b) are not illustrated but implied. Obviously starting conditions are important for each trajectory's simulation, but are specifically defined for each simulation in question. Actuator transfer functions from Sec:2.4.1 are combined into a bundled $C_i(S)$ block, accounting for transfer functions and nonlinear saturation limits of each motor module. Each bundled input $\vec{u}_{[1:4]}$ is similarly the projected actuator matrix:

$$\vec{u}_i = [\Omega_i \ \lambda_i \ \alpha_i] \quad \text{for } i \in [1 : 4] \quad (6.1)$$

The resultant thrust vector \vec{T}_i produced by each motor module has a net transfer function as a result of the propeller speed and servo rotation dynamics. Lastly, setpoints for both attitude and position states are either stepped or produced from an orbital trajectory. The former is used for controller optimization, whilst the latter is used for setpoint tracking performance evaluation. To discuss the question of non-zero setpoint tracking, an orbital trajectory with an increasing orbital (*chirp*) frequency generates attitude and position setpoints, illustrated in Fig:6.2.

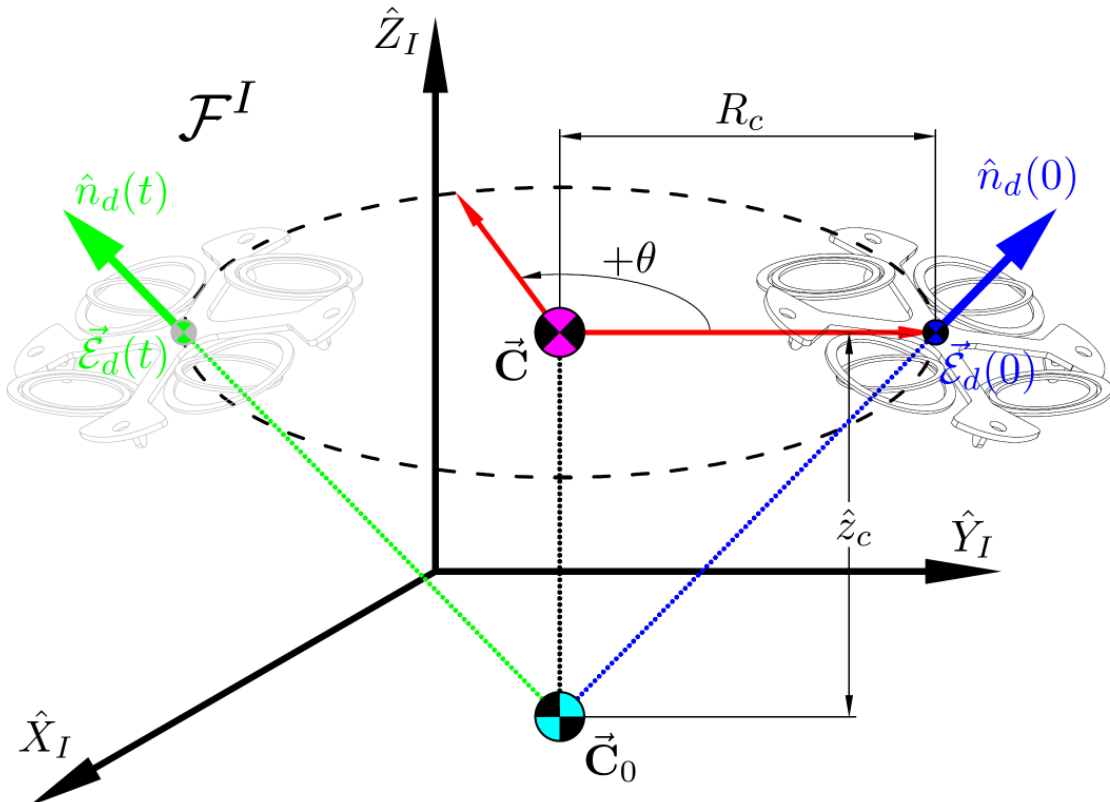


Figure 6.2: Orbital trajectory

The trajectory generates only first-order attitude and position setpoints. Furthermore, the trajectory setpoint is a body's attitude and inertial position, no actuator values for the aircraft's configuration are commanded by a trajectory. For a central point in the inertial frame $\vec{C}_0 \in \mathcal{F}^I$, the trajectory orbits with a *chirpiness* (frequency rate) of $\dot{\omega}$ [Hz.s^{-1}] around that center. The orbit is at a height of \hat{z}_c [m] and at a radius R_c [m] from the center \vec{C} . The position setpoint then follows:

$$\vec{\mathcal{E}}_d(t) = \begin{bmatrix} C_{0x} + R_c \cos(\dot{\omega}(t^2)) \\ C_{0y} + R_c \sin(\dot{\omega}(t^2)) \\ \hat{z}_c \end{bmatrix} \in \mathcal{F}^I \quad (6.2a)$$

The frequency rate $\dot{\omega}$ used in Eq:6.2a describes the rate at which a chirp generated trajectory increases. It is not the same as a body's angular velocity $\vec{\omega}_b$. By convention, a signal's frequency is annotated by ω .

The time varying trajectory's attitude setpoint is aligned with a normal vector $\hat{n}_d(t)$, banking the vehicle away from the center point \vec{C}_0 :

$$\hat{n}_d(t) \triangleq \frac{\vec{\mathcal{E}}_d(t) - \vec{C}_0}{\sqrt{\hat{z}_c^2 + R_c^2}} \quad (6.2b)$$

The normal \hat{n}_d is used to construct a quaternion setpoint $Q_d(t)$ which varies together with the orbital trajectory:

$$Q_d(t) = \left[\sin \frac{\theta(t)}{2} \quad \cos \frac{\theta(t)}{2} \hat{n}_d(t) \right]^T \quad (6.2c)$$

Whilst the trajectory equation itself may have a non-zero time derivative, both attitude and position controllers still apply the respective rate setpoints to the state variables $\dot{\vec{\mathcal{E}}}_d(t) = \vec{0}$ and $\dot{Q}_d(t) = \vec{0}$ throughout the entire trajectory, as per Eq:4.91a and Eq:4.27b. The plot in Fig:6.3 shows a chirp quaternion and attitude trajectory, $Q_d(t)$ and $\vec{\mathcal{E}}_d(t)$ respectively, over a time period of 240 [s]. The trajectory starts at $\vec{\mathcal{E}}_d(t_0) = [6 \ 6 \ 5]^T$ [m], which produces a non-zero starting attitude $Q_d(t_0) = [0.38 \ 0.42 \ 0.24 \ 0.7]^T$, Eq:6.3b.

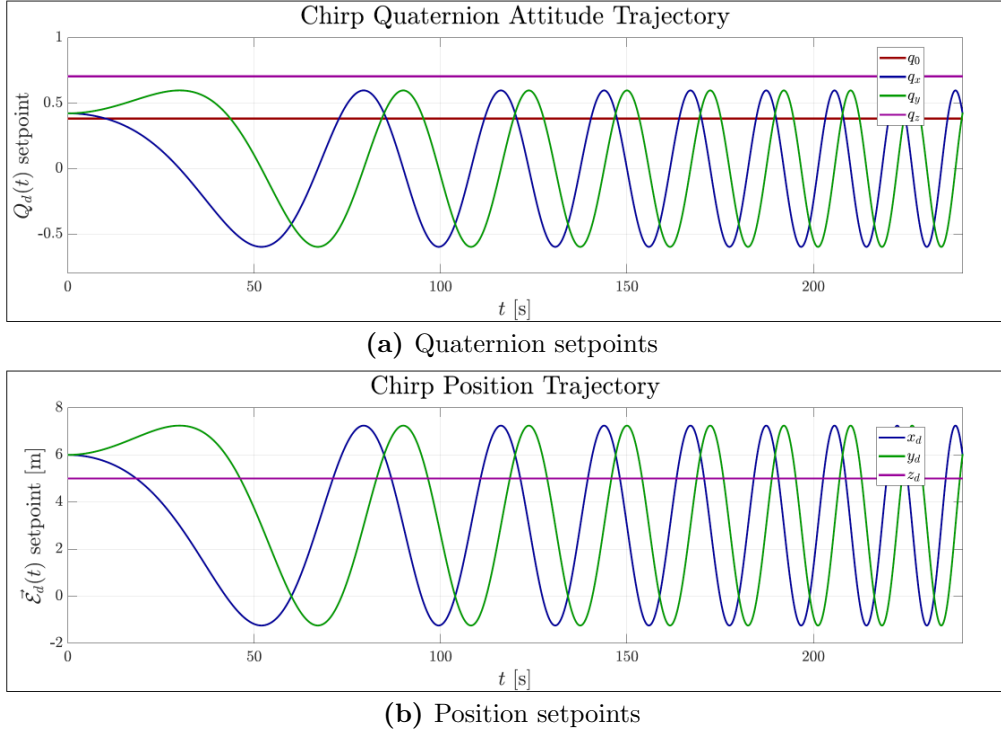


Figure 6.3: Chirp trajectory plots

6.2 Controller Tuning

Each proposed control law's proven stability (in Sec:4.6 and Sec:4.7 for attitude and position controllers respectively) demonstrates only a control law's setpoint tracking (error stability) for a time $t \rightarrow \infty$. The caveat to Lyapunov's stability theorem is that a trajectory is shown to be stabilizing, however no further insight into the controller coefficient design is provided. Often at the coefficient selection stage, a *Monte Carlo* approach is applied to select and optimize the controller coefficients.

6.2.1 Particle Swarm Optimization Algorithm

Particle swarm based optimization (*PSO*) has been shown in both [142] and [79], amongst others, to be an effective controller coefficient design tool. The algorithm treats a potential set of controller coefficients as a single *particle* which exists within some defined search space. The collection or *swarm* of possible particles explores the search space directed by both the swarm's previous performance as well as the relative performance of the swarm between each particle. In [135] the statistical nature of the swarm's trajectory is discussed, however such investigations are beyond the scope of this work.

In general, the PSO algorithm applies a *gradient-free* based search of solutions for a given optimization problem. The lack of a specified cost function gradient is an important distinction which differentiates PSO from other algorithms (note the swarm does update as per a pseudo-velocity function). Often a predefined cost function gradient is required to direct the optimization search at each interval, MatLab's fmincon [91] or Interior-Point optimizer [62] algorithms for example. Interval gradient calculations can be computationally exhaustive and reduce the rate of execution for the entire process. An optimizer's performance is directly proportional to the number of complete iterations it executes, and if an iteration has a high degree of complexity (simulation *stiffness*) its solution time is then adversely affected. The PSO algorithm is defined as follows: if there exists a set \vec{x} of k variables, $\vec{x} \in \mathbb{R}^{k \times 1}$ to be optimized, the swarm of particles (starting at particle \vec{x}_0) has an n^{th} interval position \vec{x}_n which progresses through the search space as per a velocity \vec{v}_n :

$$\vec{x}_{n+1} = \vec{v}_n + \vec{x}_n \quad (6.3a)$$

$$\vec{v}_{n+1} \triangleq w * \vec{v}_n + c_1 * r_1 (\vec{P}_{\text{best}} - \vec{x}_n) + c_2 * r_2 (\vec{G}_{\text{best}} - \vec{x}_n) \quad (6.3b)$$

where each $*$ operator in Eq:6.3b applies an element-by-element matrix coefficient multiplication. Both \vec{P}_{best} and \vec{G}_{best} are previous swarm positions where local and global optima were respectively achieved. Performance of the swarm's current interval is evaluated as per some cost function, responding to a system's dynamics. Finally r_1 and r_2 are random seeded $\mathbb{R}^{1 \times k}$ exploratory matrices which progress the search direction, biased by the two weighting coefficients c_1 and c_2 . The search is prejudiced toward local optima by c_1 , whilst c_2 directs the swarm toward global optima. Fig:6.4 illustrates how positions of both local and global optima influence subsequent velocities.

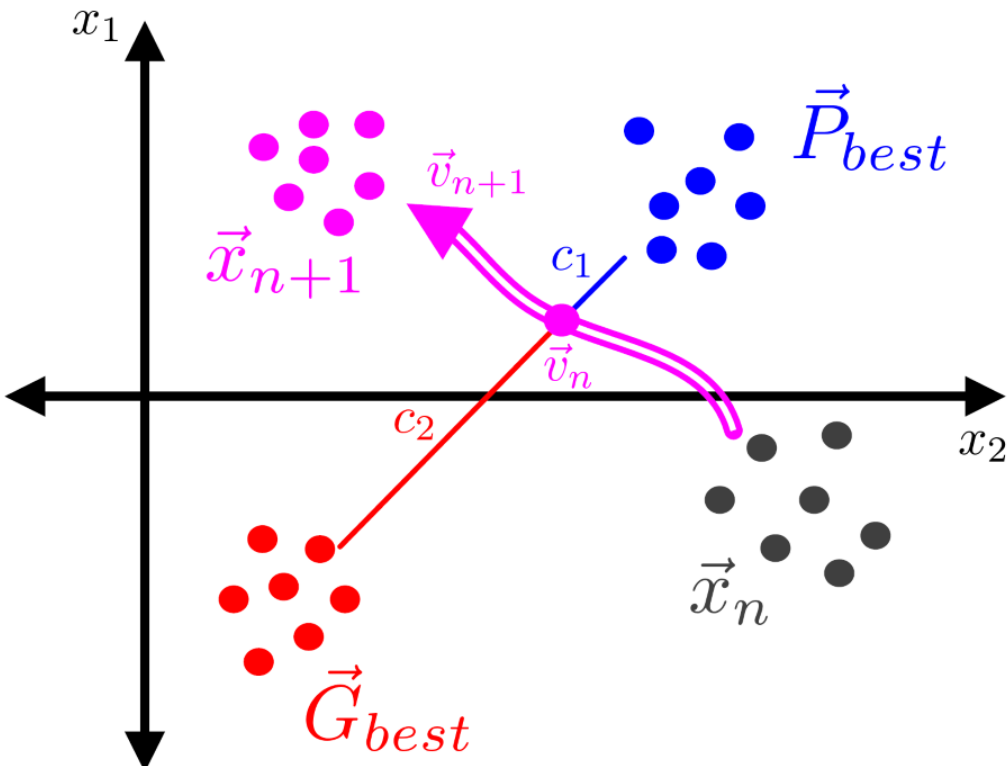


Figure 6.4: Swarm trajectory's velocity direction

The swarm's interval performance is evaluated by the response of some modelled system to the swarm's position, typically an error deviation away from some desired state. Here, the simulation described in Fig:6.1, is parsed a swarm of controller coefficients as an argument and the plant's setpoint response is simulated over a series of step tests. Particulars with regards to attitude controller optimization are discussed in Sec:6.3, thereafter position controller optimization is detailed in Sec:6.4. The objective is for zero-error setpoint tracking so each particle's coefficient performance metric calculates an integral-time-absolute-error (ITAE) cost function, [88].

$$\vec{\zeta} \triangleq \int_{t_0}^{t_\infty} t \|\vec{e}(t)\|_2 dt \quad (6.4)$$

with an error $\vec{e}(t)$ deviating from the plant's given setpoint. The ITAE integral $\vec{\zeta}$ is calculated over the entire simulation time, or an effective t_∞ . The time multiplier ensures setpoint error *and* settling time optimality, punishing overshoot and under-damped or oscillatory-like behavior. Generally a PSO algorithm progresses as in the flow diagram in Fig:6.5. Seeing that each controller was empirically proven to be stable irrespective of its trajectory, the controller will settle irrespective of the proposed interval coefficient values. A consequence of this is that starting conditions \vec{x}_0 were chosen to be a rounded set of unity.

Note that \vec{x} is a state variable in the particle swarm flow diagram Fig:6.5, \vec{j}_n was chosen to represent the swarm of particles acted on by the optimization algorithm in order to differentiate between the two.

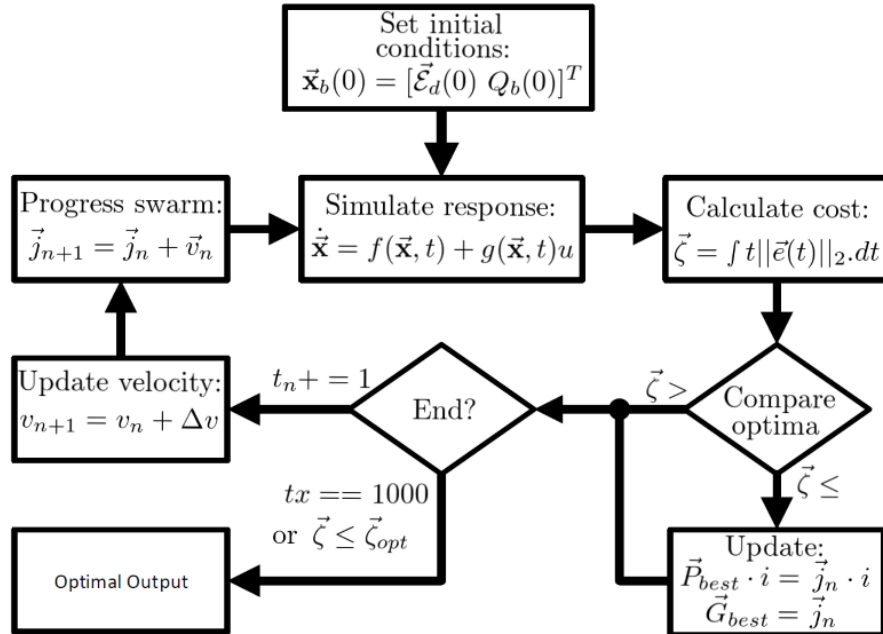


Figure 6.5: Particle swarm flow diagram

Termination conditions for the iterative optimization loop either limit the number of iteration cycles performed or break from the process once a result is regarded as sufficiently close to optimal. Each optimization loop was terminated only after a limited $tx = 1000$ iterations, testing and evaluating one thousand different swarm values for a series of stepped setpoints. With control coefficients, it is difficult to quantify how close to optimal a particular proposed set of coefficients is. As the optimizer progressed through iterations, it adapted its bias coefficients c_1 and c_2 from focusing on global optima to local optima using fractions of the iteration number, refining the way in which it searched for potential controller coefficients.

$$\vec{v}_{n+1} = \vec{v}_n + \frac{tx}{1000} * r_1(\vec{P}_{best} - \vec{x}_n) + \frac{1000 - tx}{1000} * r_2(\vec{G}_{best} - \vec{x}_n) \quad \text{for } tx \in [1 : 1000] \quad (6.5)$$

Each particle's progression was constrained such that it never violated the Lyapunov stability conditions of its respective control laws, ensuring that the coefficient matrices were kept positive definite and symmetrical.

6.3 Attitude Controllers

Attitude controllers derived in Sec:4.6 were optimized first because of their lack of coupling with the position loop. The position control loop was left in open loop with only a constant hovering force condition applied to control input \vec{F}_d for each test. Pseudo-inverse allocation, Sec:5.3.1, was applied to the control loop when testing each attitude controller. To evaluate an individual particle's performance, a number of step tests were performed. Each attitude setpoint was first defined in the Euler angle parametrization, being conceptually easier to visualize. Thereafter the attitude setpoints were converted to a desired quaternion attitude and applied to the simulation.

$$\vec{\eta}_d(t) \triangleq [\phi_d(t) \quad \theta_d(t) \quad \psi_d(t)]^T \iff Q_d(t) \quad (6.6)$$

Each of the three Euler angles were stepped in the range $[-90^\circ : +90^\circ]$ at intervals of 30° . This resulted in a test of three hundred and forty three possible attitude setpoints, making a test-space sphere as illustrated in Fig:6.6. Each attitude step was simulated for $t = 15$ [s] to allow its settling point, with an initial attitude position always set to the origin $Q_b(t_0) = [1 \ 0]$, with a *positive* quaternion scalar. The quaternion error's scalar component was limited to $q_0 \in [0 : 1]$, detailed in Eq:4.32 of Sec:4.6.1, to ensure positive definite compatibility of the proposed Lyapunov candidate functions in the control proofs. The effect of an unconstrained, negative quaternion error scalar is illustrated in Fig:6.11.

Performance for each attitude step test was evaluated by an ITAE integral for the quaternion error vector and angular velocity error. Note that each gain coefficient in a particle has its own local and global error, so the performance metric $\vec{\zeta}_q$ is a *vector*, not a scalar quantity:

$$\vec{\zeta}_Q = \int_{t=0}^{15} C_Q * t * q_0 * \|\vec{q}_e(t)\| . dt + \int_{t=0}^{15} C_\omega * t * \|\vec{\omega}_e(t)\| . dt \quad \in \mathbb{R}^3 \quad (6.7)$$

Weighting coefficients C_Q and C_ω balance priority of either quaternion or angular velocity tracking. However, tracking both were equally important and so those weights were kept at unit with respective scalar units. The cost integral in Eq:6.7 was averaged over all three hundred and forty three possible attitude steps to determine the overall performance of a proposed swarm of controller coefficients.

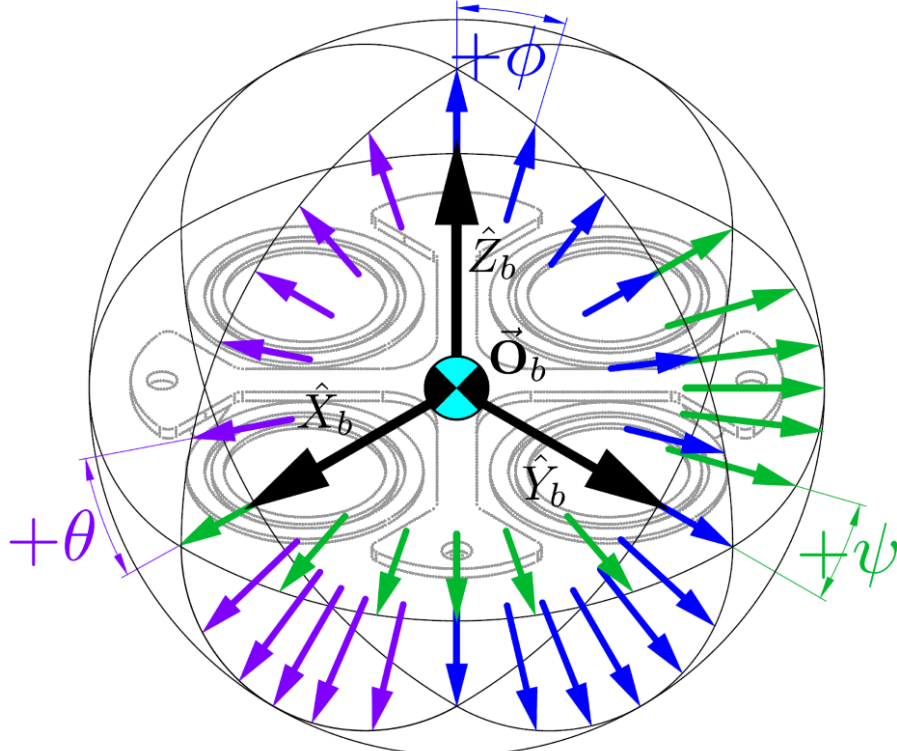


Figure 6.6: Attitude setpoint working space

The integral in Eq:6.7 produces a \mathbb{R}^3 vector result. Each coefficient in a particular controller contributes towards a local error in one of the $\hat{X}, \hat{Y}, \hat{Z}$ components, or in certain cases, a pair of axial components if the control coefficient is an off-diagonal element. A global error for the performance of each controller is simply the magnitude $\|\vec{\zeta}_Q\|$. The same global error is applicable to all controllers.

To compare the relative performance and effectiveness of each optimized control structure, a single attitude step was investigated. That attitude change was chosen to be a sizeable step in all three Euler angles to demonstrate the effect of the actuator's dynamics:

$$\vec{\eta}_d \triangleq \begin{bmatrix} \phi_d \\ \theta_d \\ \psi_d \end{bmatrix} = \begin{bmatrix} -142^\circ \\ 167^\circ \\ -45^\circ \end{bmatrix} \xleftrightarrow{Q} [-0.3254 \quad 0.2226 \quad -0.2579 \quad 0.8821]^T \quad (6.8)$$

Then each controller's settling time to 95% of its final value t_{95} and its relative angular velocity (the setpoint $\vec{\omega}_d = \vec{0}$) for such a step is calculated. Settling time, overshoot and setpoint error are all factors to consider when discussing a controller's efficacy. Lastly, the commanded (virtual) and applied input torque to the actuator set are discussed too. A feasible controller should not induce torque saturation or unachievable input rate changes.

6.3.1 PD

The first controller evaluated, the Proportional-Derivative structure, is investigated under three different circumstances. Before discussing each of the different scenarios, it is worth recalling that control structure from Sec:4.6.2. Control torque is designed by two coefficient matrices K_p and K_d :

$$\vec{\tau}_{PD} = \underbrace{J_b(\hat{u})(K_p \vec{q}_e + K_d \vec{\omega}_e)}_{Independent} + \underbrace{\hat{\omega}_b \times J_b(\hat{u}) \hat{\omega}_b + \vec{\tau}_b(\hat{u}) - \vec{\tau}_g - \vec{\tau}_H}_{Compensation} \in \mathcal{F}^b \quad (6.9)$$

The first two tests regard both coefficient matrices as purely diagonal, with no skew elements, testing the effect inclusion of plant-dependent compensation has on the controller's performance. Finally, a plant-dependent compensating PD controller is tested *with* symmetrical coefficient matrices. The diagonal coefficient matrices are defined as follows:

$$K_p \triangleq \begin{bmatrix} K_p(1) & 0 & 0 \\ 0 & K_p(2) & 0 \\ 0 & 0 & K_p(3) \end{bmatrix} \quad \text{and} \quad K_d \triangleq \begin{bmatrix} K_d(1) & 0 & 0 \\ 0 & K_d(2) & 0 \\ 0 & 0 & K_d(3) \end{bmatrix} \quad (6.10)$$

The proportional coefficient K_p acts on \vec{q}_e whilst the derivative coefficient K_d acts on $\vec{\omega}_e$, so local best positions are determined by elements of the error variable upon which each coefficient acts. A globally best position is tested simply with the magnitude $\|\vec{\zeta}_q\|$ from Eq:6.7. Then local and global best coefficient positions are updated if the minimum (best) result is improved on.

For the symmetrical coefficient case, each off-diagonal element acts on two components of the error states so that their local best positions depend on two elements of the error variables which they are related to. Then local and global coefficient positions are found when skew elements improve on *two* combined error components. The controller coefficients are structured:

$$K_p \triangleq \begin{bmatrix} K_p(1) & K_p(4) & K_p(5) \\ K_p(4) & K_p(2) & K_p(6) \\ K_p(5) & K_p(6) & K_p(3) \end{bmatrix} \quad \text{and} \quad K_d \triangleq \begin{bmatrix} K_d(1) & K_d(4) & K_d(5) \\ K_d(4) & K_d(2) & K_d(6) \\ K_d(5) & K_d(6) & K_d(3) \end{bmatrix} \quad (6.11)$$

Independent Performance

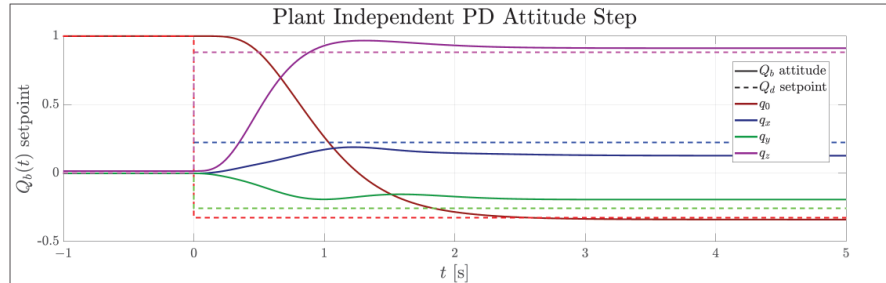
For the independent controller case, the same diagonal coefficients are used as for the plant-dependent case. The *attitude* compensation terms in Eq:6.9 are neglected to produce a plant-independent controller.

Optimizing the diagonal only PD controller produced the following coefficients:

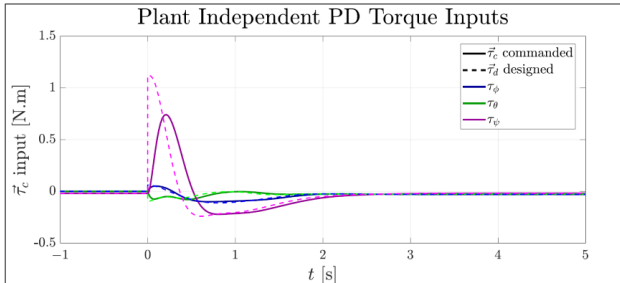
$$K_p = \begin{bmatrix} 3.5679 & 0 & 0 \\ 0 & 5.2698 & 0 \\ 0 & 0 & 6.0695 \end{bmatrix} \quad \text{and} \quad K_d = \begin{bmatrix} 9.0150 & 0 & 0 \\ 0 & 11.4848 & 0 \\ 0 & 0 & 20.1827 \end{bmatrix} \quad (6.12)$$

Fig:6.7a plots the quaternion response to an attitude step, described in Eq:6.8. The uncompensated plant never settles to its setpoint, constant steady-state errors manifest due to the uncompensated gravitational and aerodynamic torques. The plant does, however, stabilize to steady-state in $t = 3.35$ s. Fig:6.7b compares the controller designed and physically actuated input torques, $\vec{\tau}_d$ and $\vec{\tau}_c$ respectively. Actuator transfer functions produce a lagging response to those input changes. The body's angular velocity $\vec{\omega}_b \in \mathcal{F}^b$ is shown in Fig:6.7c, which changes as an attitude step is applied. Finally, Fig:6.7d plots the motor modules' actuator inputs, still with sufficient input headroom from saturation despite such a large attitude step. The actuator servos for redirection of each module's produced thrust vector are, however, rate limited.

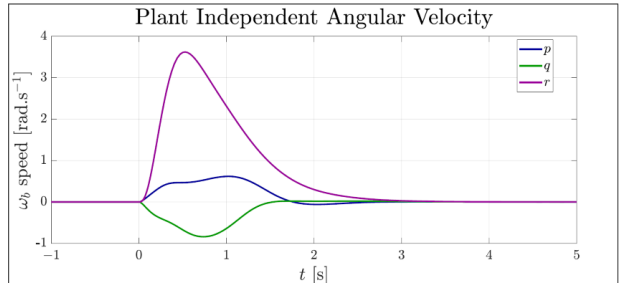
Note that module 2 and module 4 both have anti-clockwise propeller directions, represented by negative speeds in Fig:6.7d.



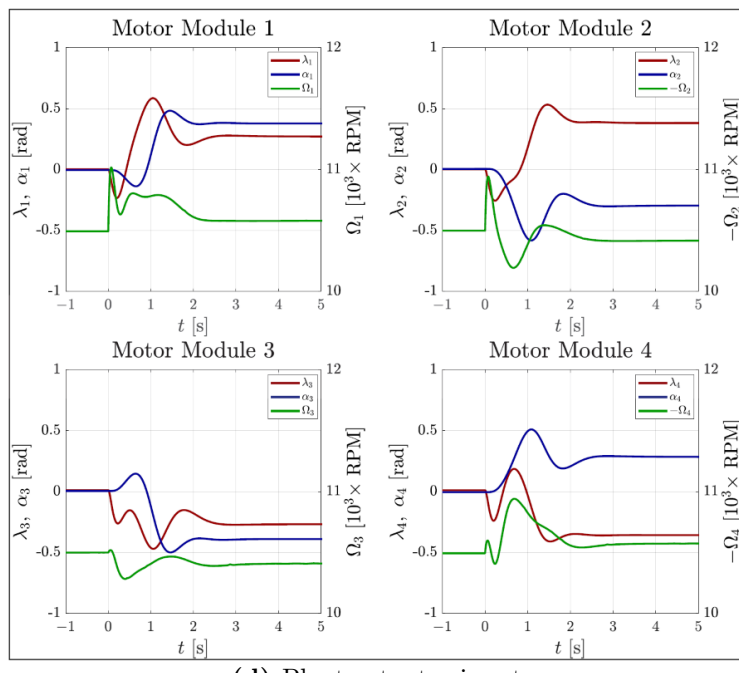
(a) Quaternion attitude step



(b) Plant input torques



(c) Angular velocity



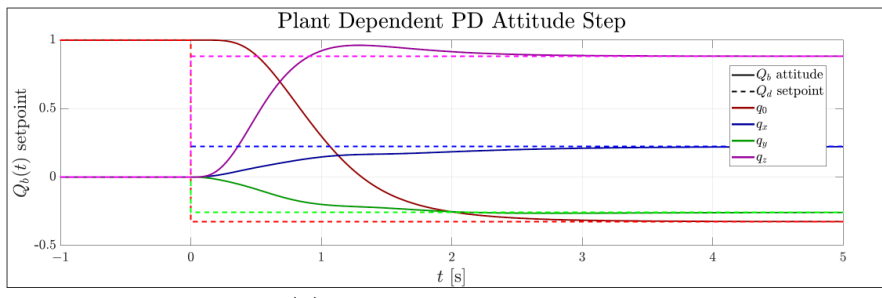
(d) Plant actuator inputs

Figure 6.7: Independent diagonal PD

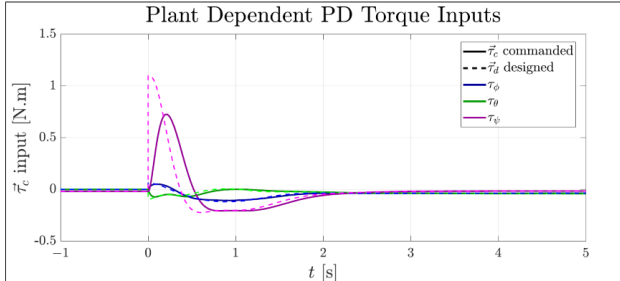
Dependent Performance

The inclusion of a plant-independent PD controller is purely for the sake of comparison, indicating the need for plant dependency to account for steady-state tracking errors (best illustrated with a trajectory test, later in Fig:6.18a). The same controller coefficients from Eq:6.12 were used to test the controller-dependent case, where the controller accounts for plant dynamics in Eq:6.9 with feedback compensation.

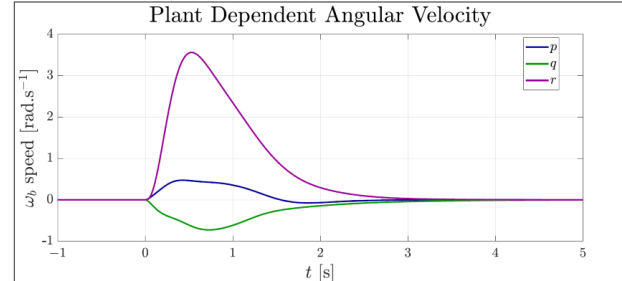
The standard quaternion attitude stepped in Fig:6.8a is applied to the PD controller with plant-dependent compensation. The attitude settles in $t_{95} = 3.0764$ s with a dynamic response much the same as that of the independent case, Fig:6.7a, however, the dependent controller removes steady-state tracking errors. The only difference is that the plant dependent controller commands a non-zero steady-state torque, illustrated by small increases in the servo actuator input rotations, shown in Fig:6.8d. It is interesting to note that the additional torque input is generated from redirection of the thrust vectors and not by increasing or decreasing the propeller speeds.



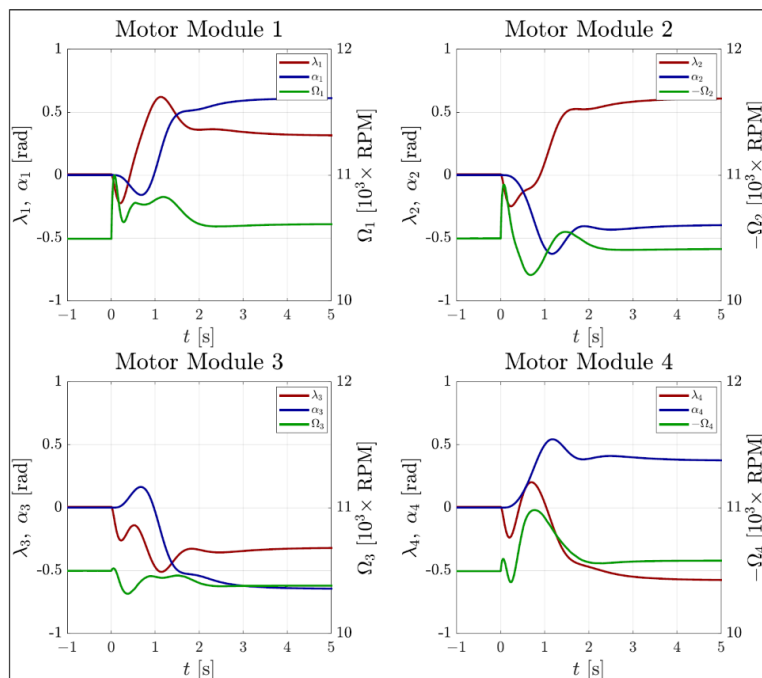
(a) Quaternion attitude step



(b) Plant input torques



(c) Angular velocity



(d) Plant actuator inputs

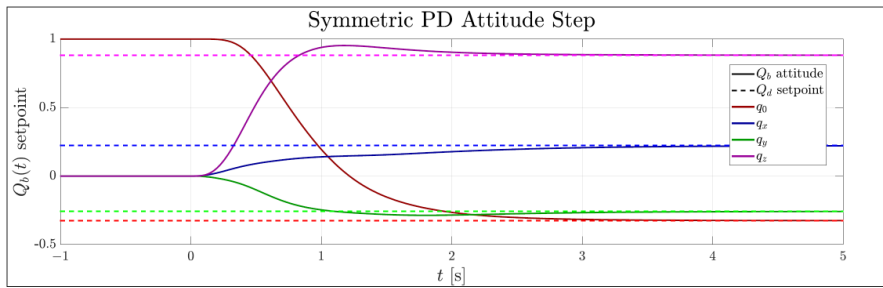
Figure 6.8: Dependent diagonal PD

Symmetric Controller Performance

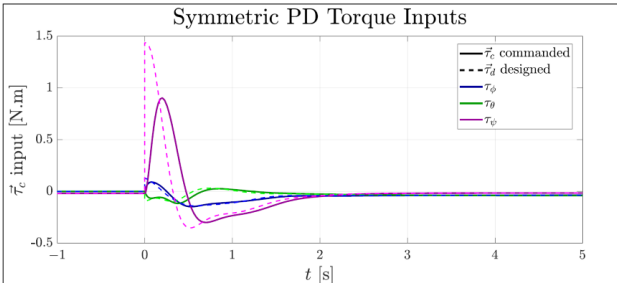
The last PD-structured attitude controller considers both coefficient matrices with non-zero off-diagonal skew elements. Eq:?? shows the structure of both symmetric matrices whose optimized coefficients were found to be:

$$K_p = \begin{bmatrix} 5.9157 & 0.4165 & 0.4714 \\ 0.4165 & 7.3141 & 0.4945 \\ 0.4714 & 0.4945 & 7.3135 \end{bmatrix} \quad \text{and} \quad K_d = \begin{bmatrix} 17.4318 & 0.45311 & 0.15258 \\ 0.45311 & 15.3569 & 0.57719 \\ 0.15258 & 0.57719 & 26.3436 \end{bmatrix} \quad (6.13)$$

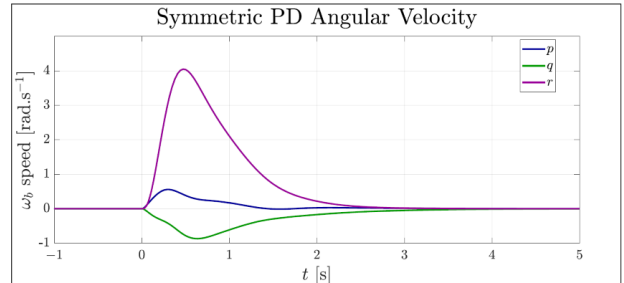
The biggest change the symmetric controller imposes is greater controller gain, $\|K_p\|_2$ and $\|K_d\|_2$ applied to quaternion and angular velocity errors. The increased gain in Eq:6.13 results in larger overshoot and, as a result, slower settling time $t_{95} = 3.2993$ [s]. Neither greater commanded torque, Fig:6.9b, nor an increased angular velocity spike, Fig:6.9c are unexpected consequences of a more aggressive control law. More coefficients to be tuned simply meant that optimization intervals to produce Eq:6.13 were perhaps not as effective at reduction of step errors as the diagonal Eq:6.12.



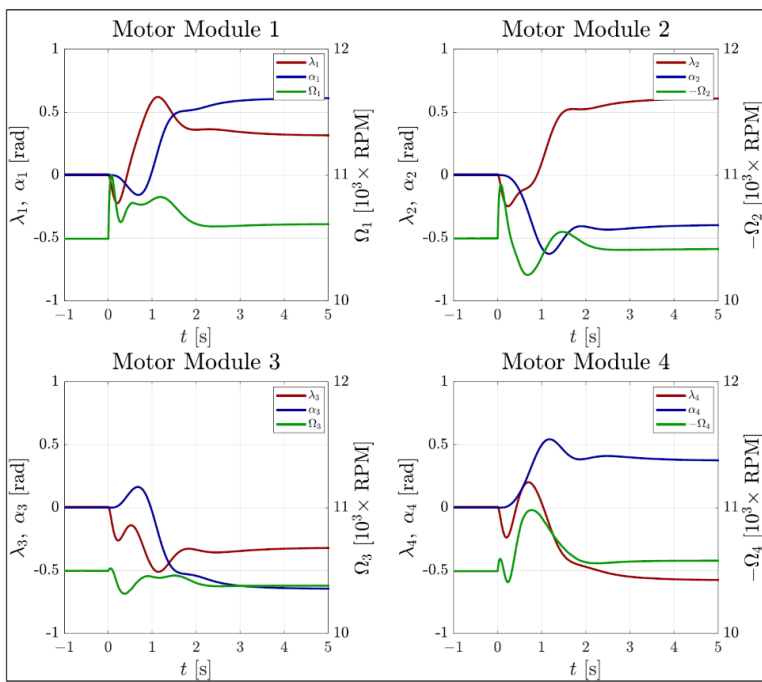
(a) Quaternion attitude step



(b) Plant input torques



(c) Angular velocity



(d) Plant actuator inputs

Figure 6.9: Dependent symmetric PD

The $[3 \times 3]$ symmetric controller's coefficients in Eq:6.13 demonstrate that improving a controller's performance is not as simple as just increasing the controller's gain. To that end, consider the diagonal plant-dependent PD controller previously detailed in Sec:6.3.1. If the gain is increased by a scale factor of 2, the settling time decreases to $t_{95} = 6.8017$ [s] from $t_{95} = 3.0764$ [s]. The attitude step for a PD controller with an increased gain is shown in Fig:6.10a, with actuator inputs shown in Fig:6.10b. More gain does not necessarily mean a faster controller.

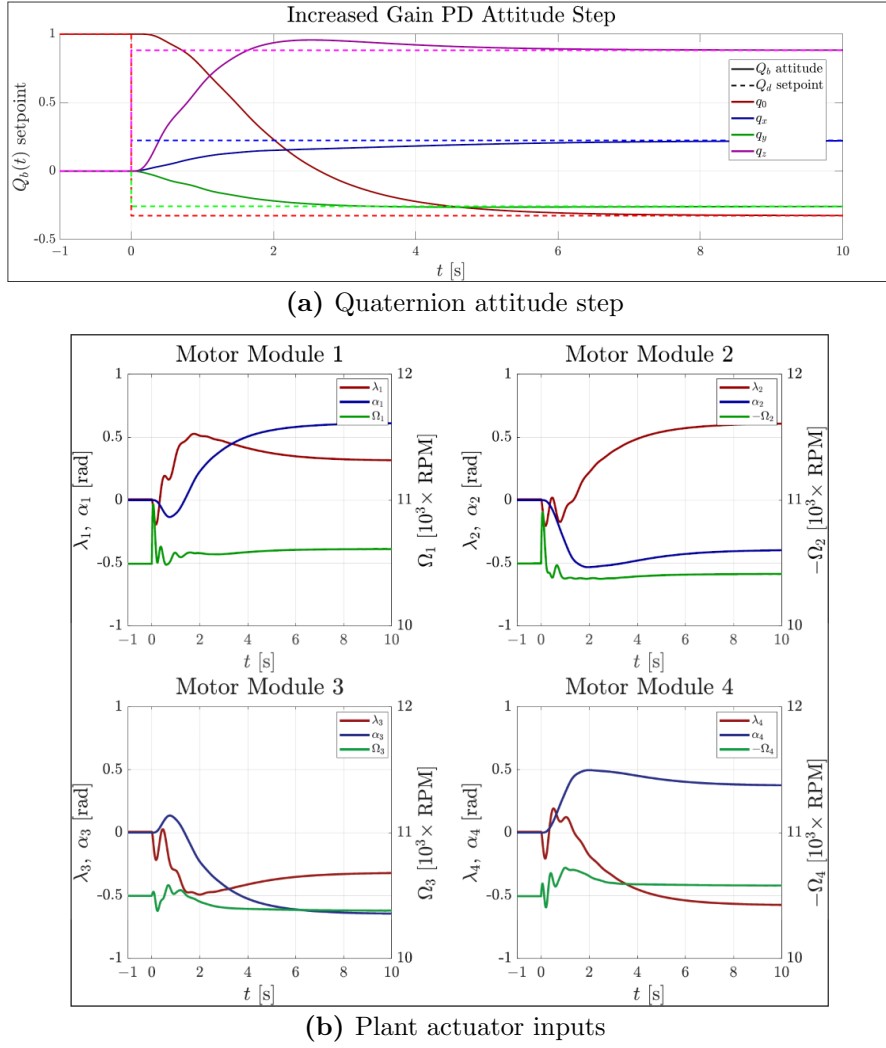


Figure 6.10: Increased gain PD

It is worth discussing the constrained quaternion error's scalar limited to $q_0 \in [0 : 1]$. That constraint was imposed during the control stability proof (Sec:4.6.1), where the constrained quaternion ensured that each proposed Lyapunov function candidate was always positive definite. Commanding the same quaternion step from Eq:6.8, however using the negative counterpart of the quaternion error's scalar $q_0 \in [-1 : 0]$, gives a step response shown in Fig:6.11. No difference is produced from using $Q_e = [\pm q_0 \vec{q}_e]^T$, despite the requirements of the stability proof. A positive definite LFC ensures suitable stability, but is by no means the *only condition* where stability is achieved.

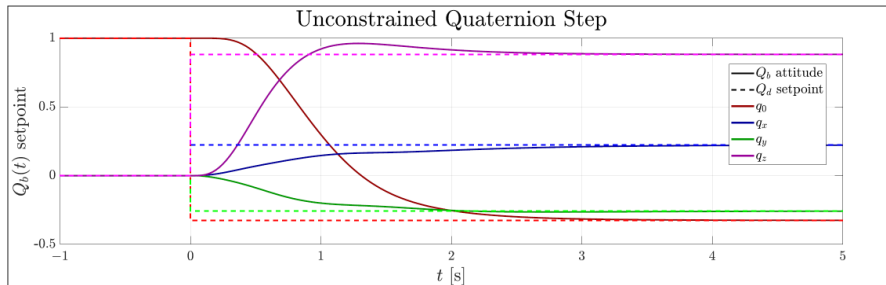


Figure 6.11: Unconstrained Error Quaternion attitude step

6.3.2 Auxiliary Plant Controller

The first of two exponentially stabilizing controllers is the auxiliary Plant controller from Sec:4.6.2. Recall that controller structure from Eq:4.45:

$$\vec{\tau}_{XPD} = \underbrace{\Gamma_2 \tilde{\Omega} + \Gamma_3 \vec{q}_e - J_b(\hat{u}) \dot{\tilde{\Omega}}}_{\text{Independent}} + \underbrace{\hat{\omega}_b \times J_b(\hat{u}) \hat{\omega}_b + \vec{\tau}_b(\hat{u}) - \vec{\tau}_g - \vec{\tau}_H}_{\text{Compensation}} \in \mathcal{F}^b \quad (6.14a)$$

where the auxiliary signals $\tilde{\Omega}$ and $\bar{\Omega}$ are defined, from Eq:4.46 and Eq:4.47 respectively, as:

$$\bar{\Omega} \triangleq -\Gamma_1 \vec{q}_e \quad \text{and} \quad \tilde{\Omega} \triangleq -\vec{\omega}_b - \bar{\Omega} \quad (6.14b)$$

In Eq:6.14a both coefficients Γ_2 and Γ_3 are $[3 \times 3]$ diagonal coefficient matrices, whilst Γ_1 is a symmetrical $[3 \times 3]$ gain matrix. Those coefficients are then structured as follows:

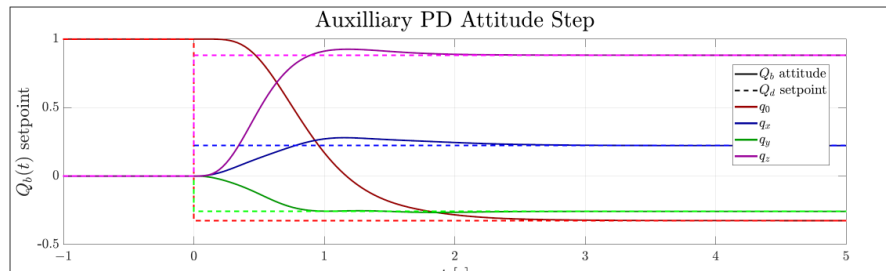
$$\begin{aligned} \Gamma_1 &\triangleq \begin{bmatrix} \Gamma_1(1) & \Gamma_1(4) & \Gamma_1(5) \\ \Gamma_1(4) & \Gamma_1(2) & \Gamma_1(6) \\ \Gamma_1(5) & \Gamma_1(6) & \Gamma_1(3) \end{bmatrix}, \quad \Gamma_2 \triangleq \begin{bmatrix} \Gamma_2(1) & 0 & 0 \\ 0 & \Gamma_2(2) & 0 \\ 0 & 0 & \Gamma_2(3) \end{bmatrix} \\ &\quad \text{and} \quad \Gamma_3 \triangleq \begin{bmatrix} \Gamma_3(1) & 0 & 0 \\ 0 & \Gamma_3(2) & 0 \\ 0 & 0 & \Gamma_3(3) \end{bmatrix} \end{aligned} \quad (6.15)$$

Global and local best positions of coefficient particles are found from the error state components on which the particular coefficients act. The first gain matrix Γ_1 acts on both \vec{q}_e and $\vec{\omega}_e$, so its local best position \vec{P}_{best} is when both errors are at their minimum. The remaining two gain matrices Γ_2 and Γ_3 act on \vec{q}_e and $\vec{\omega}_e$ respectively, so their local best positions are when each of those errors are minimized. Finally the globally best performing particle position is when $\|\vec{\zeta}\|_2$ is minimized. The control coefficients produced after $tx = 1000$ iterations are as follows:

$$\begin{aligned} \Gamma_1 &= \begin{bmatrix} 3.5924 & -0.2457 & -0.0277 \\ -0.2457 & 3.0666 & -0.0602 \\ -0.0277 & -0.0602 & 3.3809 \end{bmatrix}, \quad \Gamma_2 = \begin{bmatrix} 4.6943 & 0 & 0 \\ 0 & 4.1642 & 0 \\ 0 & 0 & 6.4109 \end{bmatrix} \\ &\quad \text{and} \quad \Gamma_3 = \begin{bmatrix} 1.1007 & 0 & 0 \\ 0 & 1.3369 & 0 \\ 0 & 0 & 1.1331 \end{bmatrix} \end{aligned} \quad (6.16)$$

Besides the stronger exponential stability, another distinctive feature of the auxiliary controller (Eq:6.15) is the introduced simulation stiffness to the control structure. Calculations for the control input at each interval became more complex as a result of the introduced error terms. Each iteration of the optimizer took longer to simulate, typically in the order of 70-80% longer, per step test.

The quaternion attitude step response is shown in Fig:6.12a, settling in $t_{95} = 2.3688$ s which is notably faster than previous tested controllers. The improved response time does, however, come at the cost of greater input torques, shown in Fig:6.12b. Moreover, commanded angular velocity change in $\vec{\omega}_b$ (Fig:6.12c) is markedly larger than that of previous controllers.



(a) Quaternion attitude step

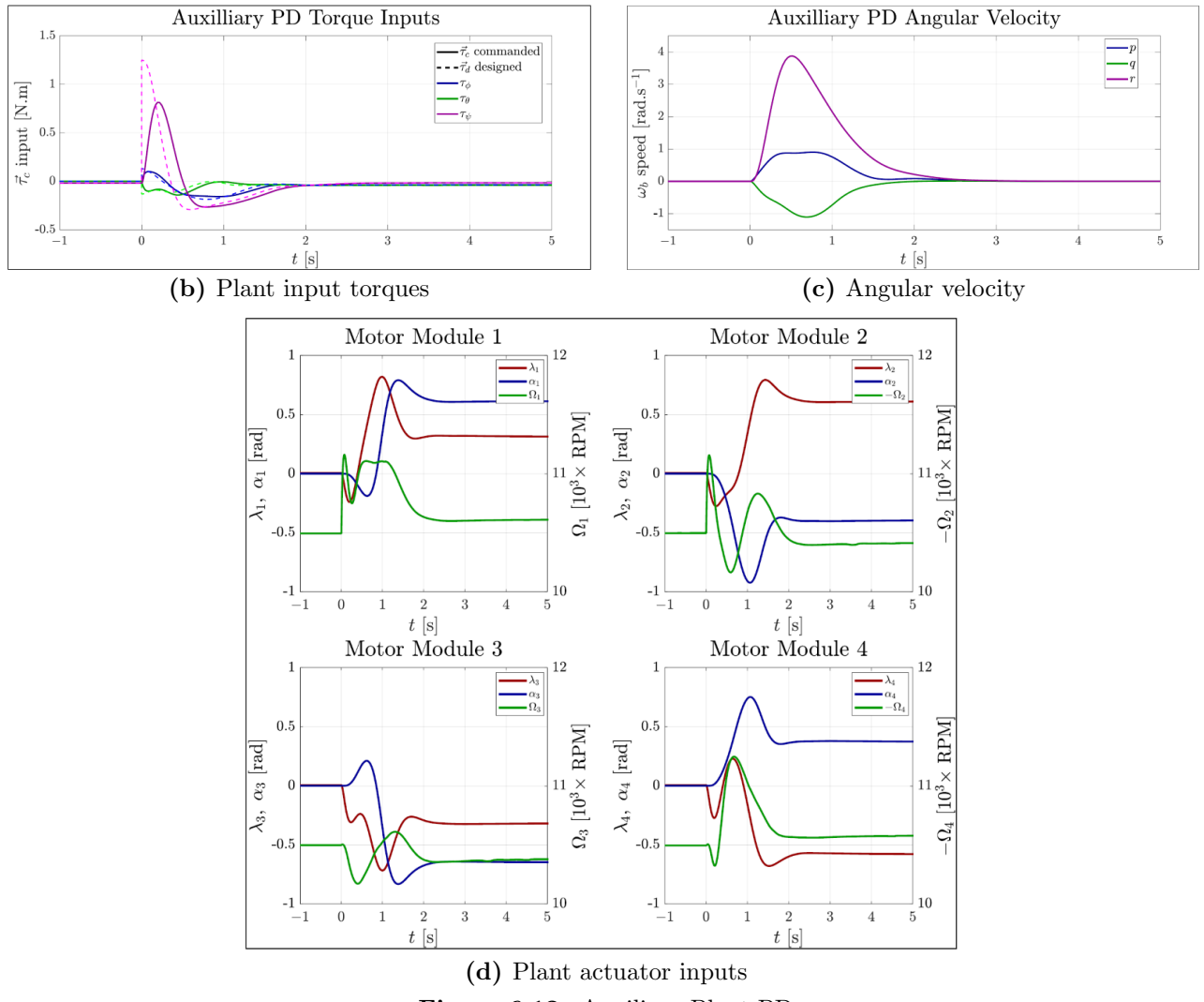


Figure 6.12: Auxiliary Plant PD

Despite the improved (23% faster) settling time the auxiliary PD controller achieves, neither the applied torque inputs (Fig:6.12b) nor the actuator commands (Fig:6.12d) are as aggressive as those of the higher gain, symmetrical PD controller (Fig:6.9b). This is a direct consequence of the *guaranteed exponentially bound error trajectory*, proven in Sec:4.6.2.

6.3.3 Ideal and Adaptive Backstepping Controllers

The second exponentially stabilizing controller and final attitude controller tested is the ideal backstepping controller. Both ideal and adaptive backstepping controllers use the same gain coefficients, the difference in structure between the two is the addition of an adaptive disturbance observer to be used for compensation. That disturbance observer and its explicit coefficients are detailed later in Sec:6.6.1. Reiterating the IBC structure from Eq:4.71:

$$\vec{\tau}_{IBC} = \underbrace{J_b(\hat{u}) \left((\Gamma_1 \Gamma_2 + 1) \vec{q}_e - \Gamma_2 \hat{\omega}_b + \Gamma_1 \dot{\vec{q}}_e \right)}_{\text{Ideal backstepping}} + \underbrace{\hat{\omega}_b \times J_b(\hat{u}) \hat{\omega}_b + \vec{\tau}_b(\hat{u}) - \vec{\tau}_g - \vec{\tau}_H}_{\text{Compensation}} \in \mathcal{F}^b \quad (6.17)$$

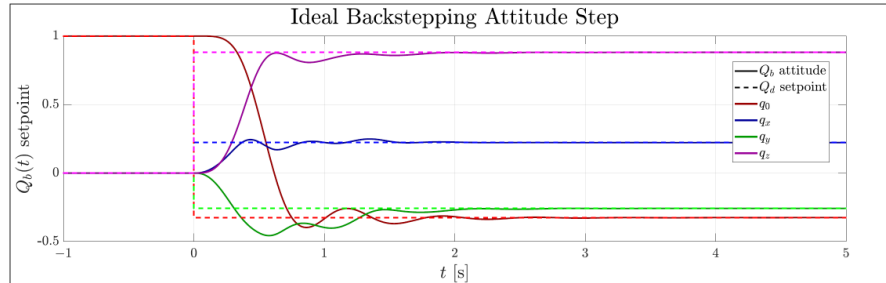
wherein the gain matrices Γ_1 and Γ_2 are both positive symmetrical 3×3 coefficient matrices:

$$\Gamma_1 \triangleq \begin{bmatrix} \Gamma_1(1) & \Gamma_1(4) & \Gamma_1(5) \\ \Gamma_1(4) & \Gamma_1(2) & \Gamma_1(6) \\ \Gamma_1(5) & \Gamma_1(6) & \Gamma_1(3) \end{bmatrix} \quad \text{and} \quad \Gamma_2 \triangleq \begin{bmatrix} \Gamma_2(1) & \Gamma_2(4) & \Gamma_2(5) \\ \Gamma_2(4) & \Gamma_2(2) & \Gamma_2(6) \\ \Gamma_2(5) & \Gamma_2(6) & \Gamma_2(3) \end{bmatrix} \quad (6.18)$$

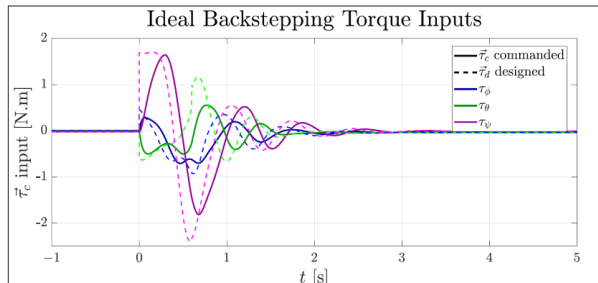
Both gain coefficient matrices act on the two error vectors \vec{q}_e and $\vec{\omega}_e$, trying to differentiate between the local and global coefficient best positions is then problematic. A particle swarm algorithm needs a clear distinction between local and global best performance positions. Equating local and global particle positions reduces the directed swarm search to a randomized *Monte Carlo* method of coefficient selection.

To avoid that reduction, Γ_1 is prioritized to control the quaternion vector error \vec{q}_e . Similarly Γ_2 is dedicated to controlling the angular velocity error $\vec{\omega}_e$. It then follows that local and global best positions, \vec{P}_{best} and \vec{G}_{best} respectively, are found in the same way as the symmetrical PD controller. When optimized, the two sets of gain coefficients are:

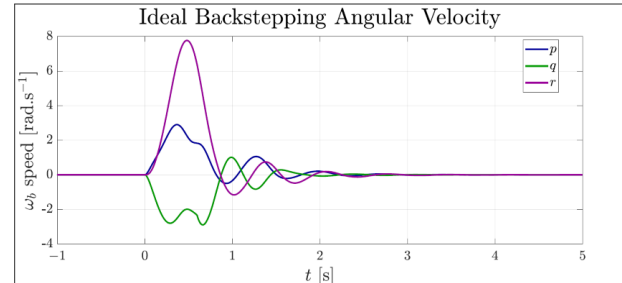
$$\Gamma_1 = \begin{bmatrix} 5.8631 & 0.0515 & 1.0221 \\ 0.0515 & 13.8375 & 0.8533 \\ 1.0221 & 0.8533 & 11.9644 \end{bmatrix} \quad \text{and} \quad \Gamma_2 = \begin{bmatrix} 9.1127 & 0.2887 & 0.1353 \\ 0.2887 & 6.8389 & 0.1971 \\ 0.1353 & 0.1871 & 2.5294 \end{bmatrix} \quad (6.19)$$



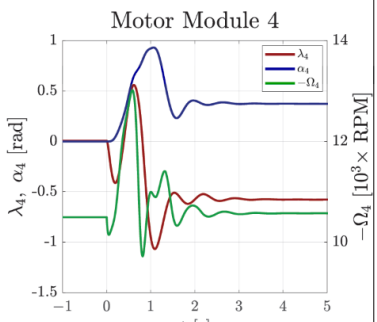
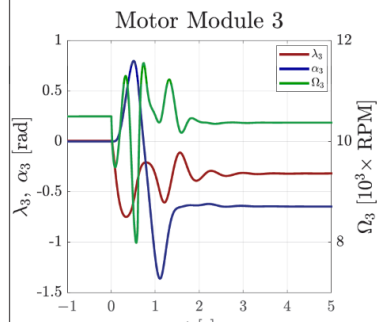
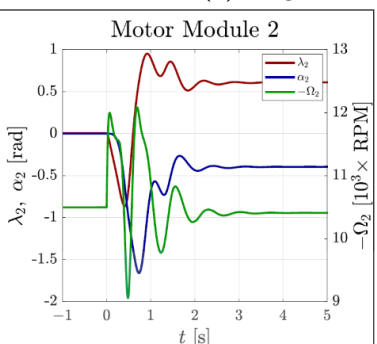
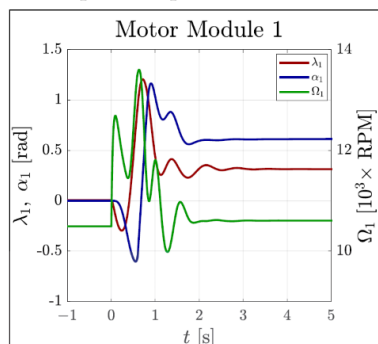
(a) Quaternion attitude step



(b) Plant input torques



(c) Angular velocity



(d) Plant actuator inputs

Figure 6.13: Ideal backstepping controller

The attitude's step response in Fig:6.13a shows a faster response with notable oscillations introduced at the settling point. The step settles in $t_{95} = 1.6403$ s, almost twice as fast as a basic PD controller. The oscillations produced at the settling point are as a result of the actuator commands (Fig:6.13d) reaching their rate limits, seen as a large difference between the commanded and physically actuated torque inputs in Fig:6.13b. Furthermore, the commanded angular velocity changes for the IBC controller are, on average, twice that of the previous control laws which then result in increased nonlinear torque responses.

The ideal backstepping controller is by far the most aggressive control law, which leads to sizeable and perhaps unsatisfactory overshoot. That aggression is due to the exact dynamic compensation applied by the attitude control and *not the applied controller gain* as is the case with the previous symmetric PD controller. Saturated rate limits of the actuators then prevent the commanded input being met by the actuated control torque. The Adaptive backstepping controller is tested and discussed later in Sec:6.6.1 in the context of robust trajectory stability, rather than stepped controller performances here.

6.4 Position Controllers

Following the attitude controller optimization, a similar approach is applied to the two proposed position control laws (in Sec:4.7). It is important to specify that, for position controller optimization, a plant dependent diagonal PD attitude controller (Sec:6.3.1) is used to stabilize the coupled attitude dynamics. To test each particle's controller coefficient performance, the attitude setpoint was kept at a constant $Q_d = [+1 \vec{0}]^T$, while various position setpoints are applied. The same basic pseudo-inversion allocator (Sec:5.3.1) is used for position control to distribute the virtual control input $\vec{\nu}_d$. Each position setpoint is defined in the inertial frame:

$$\vec{\mathcal{E}}_d(t) \triangleq [X_d(t) \quad Y_d(t) \quad Z_d(t)]^T \quad \in \mathcal{F}^I \quad (6.20)$$

A collection of position setpoints is tested, where each setpoint is positioned on the surface of a sphere at a radius of $C = 5$ [m] from a central starting point. That starting position is consistently tested at $\vec{\mathcal{E}}_0 = [5 \ 5 \ 5]^T$ [m], relative to the inertial frame's origin. Each setpoint is then stepped away from $\vec{\mathcal{E}}_0$ as per a rotated radial arm:

$$\vec{\mathcal{E}}_d(t) = \vec{\mathcal{E}}_0 + R_y(\theta_y)R_x(\phi_x) [0 \quad 0 \quad 5]^T \quad (6.21)$$

Test angles ϕ_x and θ_y rotate the radial arm C for a range $\phi_x \in [-180^\circ : 180^\circ]$ and $\theta_y \in [-90^\circ : 90^\circ]$, both at 30° increments. That results in a test space position surface illustrated in Fig:6.14, with a total of 91 position setpoints to test. Performance of each position step is evaluated with another ITAE integral for the position and translational velocity errors, both transformed into the *body frame*, \mathcal{F}^b .

$$\vec{\zeta}_{\mathcal{E}} = \int_{t=0}^{15} C_X * t * ||\vec{X}_e(t)||.dt + \int_{t=0}^{15} C_v * t * |\vec{v}_e(t)|.dt \quad (6.22)$$

As with the attitude steps, each position steps simulation is given $t = 15$ s to reach its settling point when stepped from the starting point. Weighting coefficients C_X and C_v prioritize position and velocity errors respectively, both are weighted at unity. Each particle is then stepped 91 times for position ranges described above and the resultant cost of Eq:6.22 is averaged for an overall performance metric. Only *plant-dependent compensating* position controllers are considered and optimized for the position control loop.

Not compensating for the gravitational force acceleration applied to the vehicle in its differential equation of motion, Eq:3.118b, *would* result in instability. An uncompensated gravitational force of 15.45 [N] would drive both Lyapunov function derivatives, Eq:4.97e for PD control and Eq:4.109c for backstepping control, away from stabilizing negative definite conditions.

To compare the relative performance of each optimized position controller, a constant-position step test is applied in both cases:

$$\vec{\mathcal{E}}_d = [X_d \ Y_d \ Z_d]^T = [7.5 \ 4 \ 3]^T \text{ m, } \in \mathcal{F}^I \quad (6.23)$$

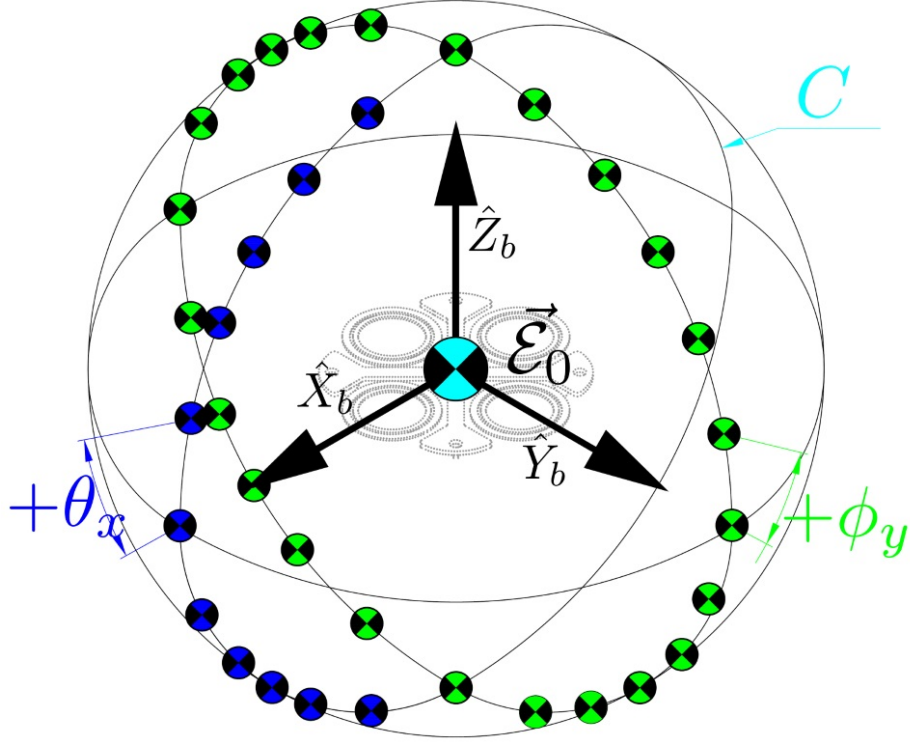


Figure 6.14: Position setpoint workspace

6.4.1 PD

The reference case for position control is the Proportional-Derivative controller, presented in Sec:4.7.1. The PD position controller designs a control force input, from Eq:4.93:

$$\vec{F}_{PD} = K_p \vec{X}_e + K_d \vec{v}_e + \hat{\omega}_b \times m_b \hat{v}_b - m_b \vec{G}_b \quad \in \mathcal{F}^b \quad (6.24)$$

where \vec{X}_e is the inertial position error $\vec{\mathcal{E}}_e \in \mathcal{F}^I$, transformed to the body frame in Eq:4.94a. Both K_p and K_d are diagonal gain coefficient matrices. Introducing symmetric $[3 \times 3]$ coefficients to the gain matrices did not yield any improvements for the attitude plant in Sec:6.3.1, so it was not investigated in the context of position control. The two coefficients for the PD controller are structured as follows:

$$K_p \triangleq \begin{bmatrix} K_p(1) & 0 & 0 \\ 0 & K_p(2) & 0 \\ 0 & 0 & K_p(3) \end{bmatrix} \quad \text{and} \quad K_d \triangleq \begin{bmatrix} K_d(1) & 0 & 0 \\ 0 & K_d(2) & 0 \\ 0 & 0 & K_d(3) \end{bmatrix} \quad (6.25)$$

Each coefficient matrix acts on the position error vector, \vec{X}_e , and the velocity error vector, \vec{v}_e , independently. The following coefficients are the result of the optimization process:

$$K_p = \begin{bmatrix} 2.4167 & 0 & 0 \\ 0 & 2.1557 & 0 \\ 0 & 0 & 2.5904 \end{bmatrix} \quad \text{and} \quad K_d = \begin{bmatrix} 3.4794 & 0 & 0 \\ 0 & 3.3846 & 0 \\ 0 & 0 & 3.8698 \end{bmatrix} \quad (6.26)$$

A step in the position loop's setpoint produces a response shown in Fig:6.15a. Stepping from the initial position to the setpoint $\vec{\mathcal{E}}_d$ described in Eq:6.8, the position step settled in $t_{95} = 4.007$ s without any overshoot.

Note that $\vec{\mathcal{E}}_d$ in Eq:6.8 is defined in the inertial frame, \mathcal{F}^I . That setpoint is transformed to the body frame as a variable substitution for \vec{X}_d for the controller error in Eq:6.24.

Not shown, but still considered, is the effect a position step has on the attitude plant's stability, which still remained stable at the origin with no deviations. Because the attitude setpoint is $\vec{Q}_d = [+1 \vec{0}]^T$, almost all the force requirement in steady-state is to oppose the gravitational downward force acting on the body, Fig:6.15b.

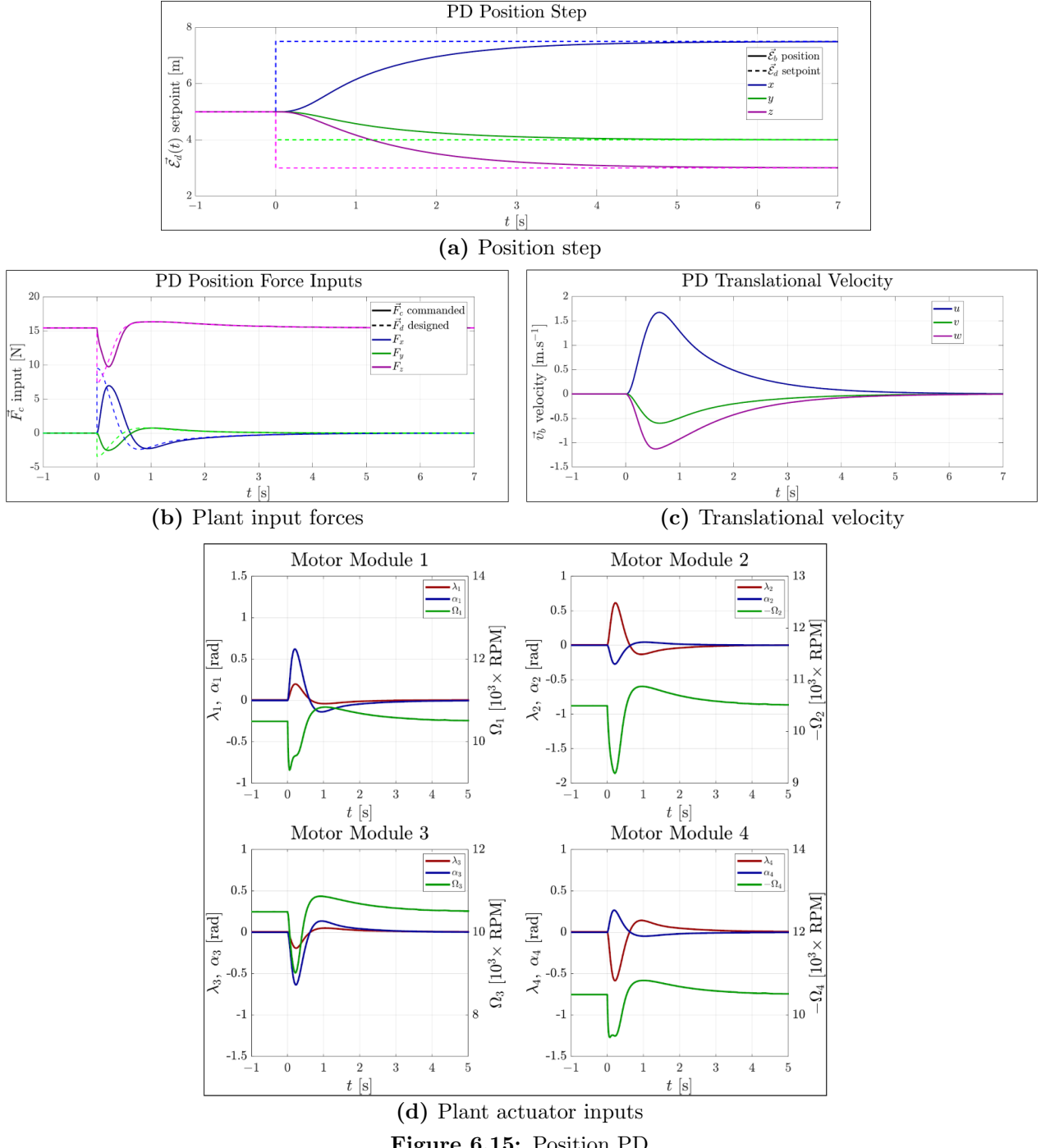


Figure 6.15: Position PD

6.4.2 Ideal and Adaptive Position Backstepping

The second and final position controller to be tested is the ideal backstabbing controller, the only exponentially stable position control law reviewed. As is the case with attitude IBC, the coefficients selected for the ideal backstepping case are used again for the adaptive case, the latter is evaluated subsequently in Sec:6.6.2. Recall the position IBC structure from Sec:4.7.2:

$$\vec{F}_{IBC} = m_b \left((1 + \Gamma_1 \Gamma_2) \vec{\zeta}_1 - (\Gamma_1 + \Gamma_2) \hat{v}_b \right) + \hat{\omega}_b \times m_b \hat{v}_b - m_b \vec{G}_b \quad \in \mathcal{F}^b \quad (6.27)$$

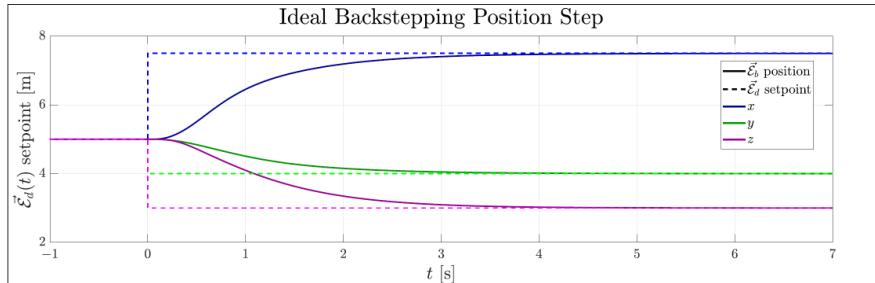
with the backstepping variable $\vec{\zeta}_1$ defined $\vec{\zeta}_1 \triangleq \vec{X}_e$, from Eq:4.102a.

The two positive symmetric coefficient gain matrices in Eq:6.27 are structured as:

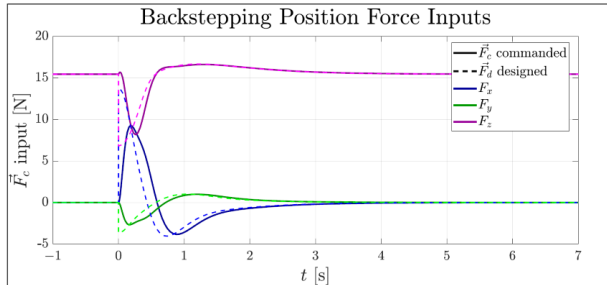
$$\Gamma_1 \triangleq \begin{bmatrix} \Gamma_1(1) & \Gamma_1(4) & \Gamma_1(5) \\ \Gamma_1(4) & \Gamma_1(2) & \Gamma_1(6) \\ \Gamma_1(5) & \Gamma_1(6) & \Gamma_1(3) \end{bmatrix} \quad \text{and} \quad \Gamma_2 \triangleq \begin{bmatrix} \Gamma_2(1) & \Gamma_2(4) & \Gamma_2(5) \\ \Gamma_2(4) & \Gamma_2(2) & \Gamma_2(6) \\ \Gamma_2(5) & \Gamma_2(6) & \Gamma_2(3) \end{bmatrix} \quad (6.28)$$

Similar to the attitude backstepping controller, the position ideal backstepping controller has gain coefficients which act on both plant's error \vec{X}_e and error rates \vec{v}_e . This makes local and global coefficient position selection difficult without adversely affecting the swarm's optimization trajectory process. Using the first coefficient matrix Γ_1 to prioritize position tracking errors \vec{X}_e , and relegating Γ_2 to settle velocity errors \vec{v}_e , the local best positions are chosen where each respective error is minimized. The optimized gain coefficients for Γ_1 and Γ_2 were then produced by the PSO algorithm:

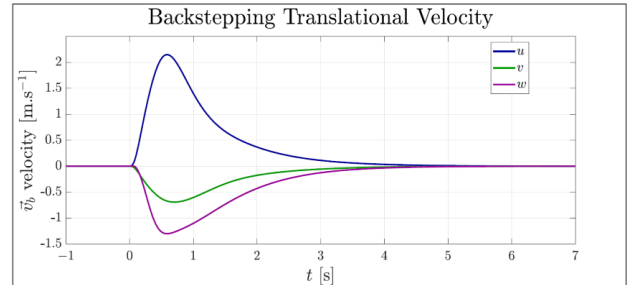
$$\Gamma_1 = \begin{bmatrix} 2.3409 & 0.1707 & -0.1644 \\ 0.1707 & 2.0493 & 0.1060 \\ -0.1644 & 0.1060 & 1.7322 \end{bmatrix} \quad \text{and} \quad \Gamma_2 = \begin{bmatrix} 1.5287 & 0.02928 & 0.0816 \\ 0.0292 & 1.4214 & -0.0410 \\ 0.0816 & -0.0410 & 1.4753 \end{bmatrix} \quad (6.29)$$



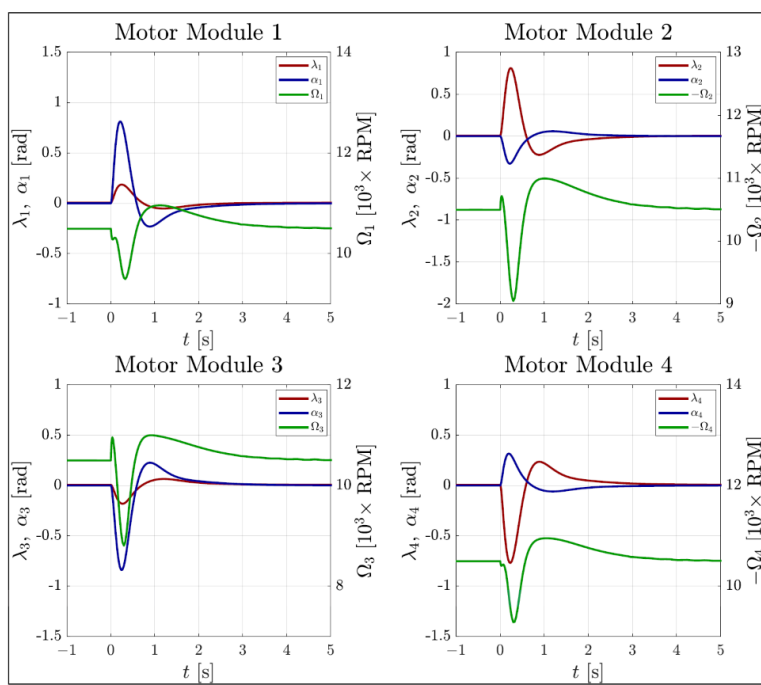
(a) Position step



(b) Plant input forces



(c) Translational velocity



(d) Plant actuator inputs

Figure 6.16: Position backstepping controller

Fig:6.16a shows how the ideal backstepping controller stabilizes and tracks a step change to the translational position setpoint. Note that the position plotted in Fig:6.16a is the relative position in the inertial frame \mathcal{F}^I , not the backstepping input $\vec{X}_e \in \mathcal{F}^b$. The ideal backstepping controller settles in $t_{95} = 2.987$ [s], faster than a regular PD position controller. The exponentially bound error trajectory improves the controller's performance but, not unexpectedly, commands greater input forces (Fig:6.16b) from larger spikes in the propeller's rotational speed, shown in Fig:6.13d.

The improved performance from the position ideal backstepping controller is due to the change in structure, increasing the PD controller's gain by a scale factor of 2 (analogous to the test performed in Fig:6.10a) and *decreases* the step's settling time from $t_{95} = 4.007$ [s] to 4.379 [s]. So improving even the conceptually simpler force-position control loop is not as easy as simply adding more gain to the control plant.

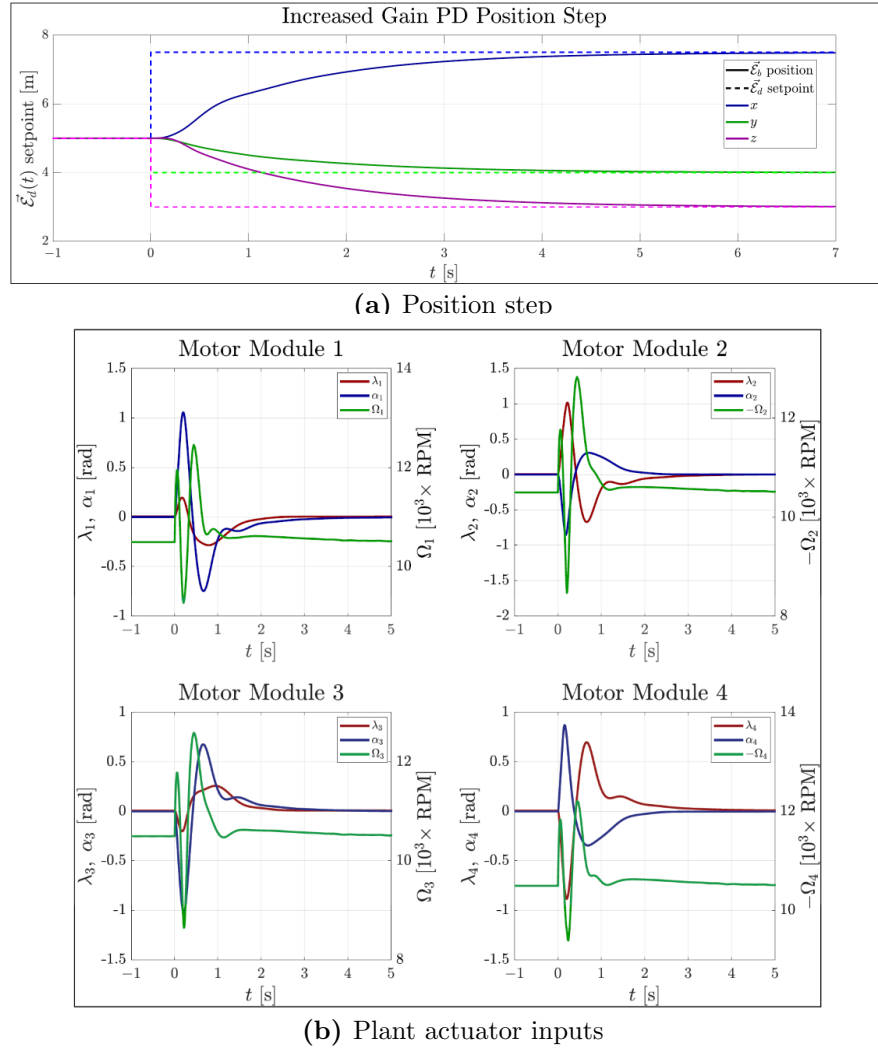


Figure 6.17: Increased gain PD position

6.5 Setpoint Control Results

None of the proposed attitude or position controllers are unstable, each one achieves the goal of setpoint tracking in the context of stepped inputs. To corroborate dynamic setpoint tracking, an increasing (*chirp*) trajectory is commanded, illustrated in Fig:6.2. The trajectory applies an increasing frequency rate of $1/60$ [$\text{Hz} \cdot \text{s}^{-1}$], starting from zero, such that at $t = 60$ [s] the trajectory orbits a central point \vec{C}_0 at a frequency of 1 [Hz]. Eventually the increasing orbital frequency will push each controller beyond its tracking limit. Only two PD *attitude* controllers are tested here, both with diagonal gain matrices (from Eq:6.12), to compare the effects of plant-dependent compensation. It was shown previously that symmetric gain coefficients yield no performance improvements for the PD case, so only diagonal coefficient matrices were used.

Furthermore, Sec:6.3.1 demonstrated that plant-independent controllers result in steady-state errors. The same is shown to be true for trajectory tracking. Adaptive backstepping controllers and their disturbance rejection properties are only discussed next in Sec:6.6. Each attitude controller is tested together with a common PD position controller, tracking the orbital XYZ position. Similarly, each position controller is tested using a simple diagonal PD controller to track the attitude. The attitude controllers have an initial step to reach the orbital attitude from their starting attitude, $Q_0 = [+1 \vec{0}]^T$. Each controller's trajectory setpoint response and its respective tracking error are plotted together in pairs.

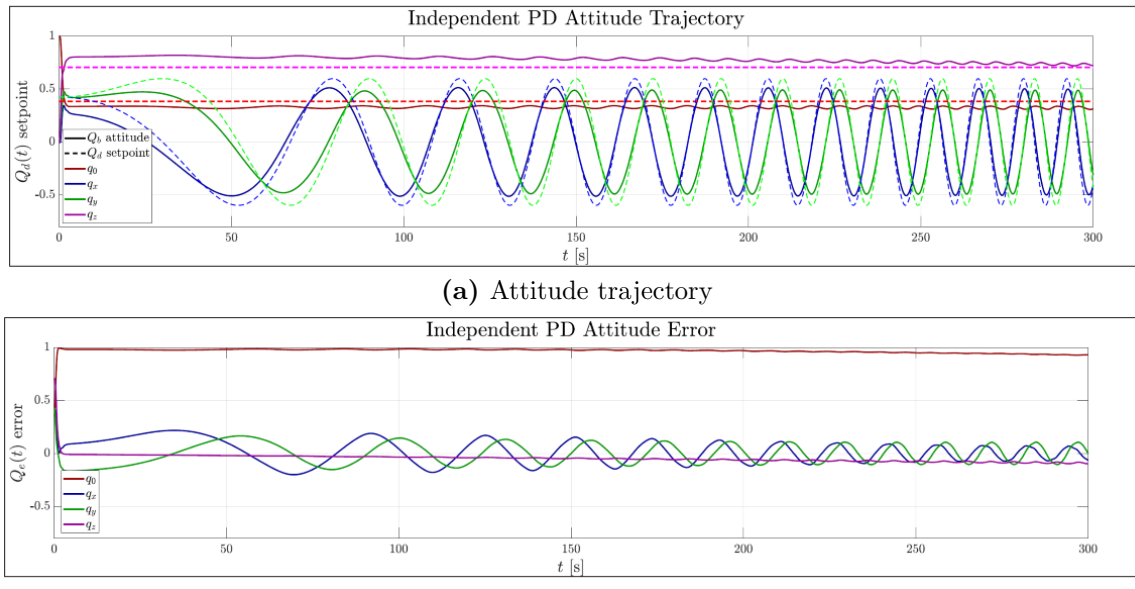


Figure 6.18: Independent PD attitude controller

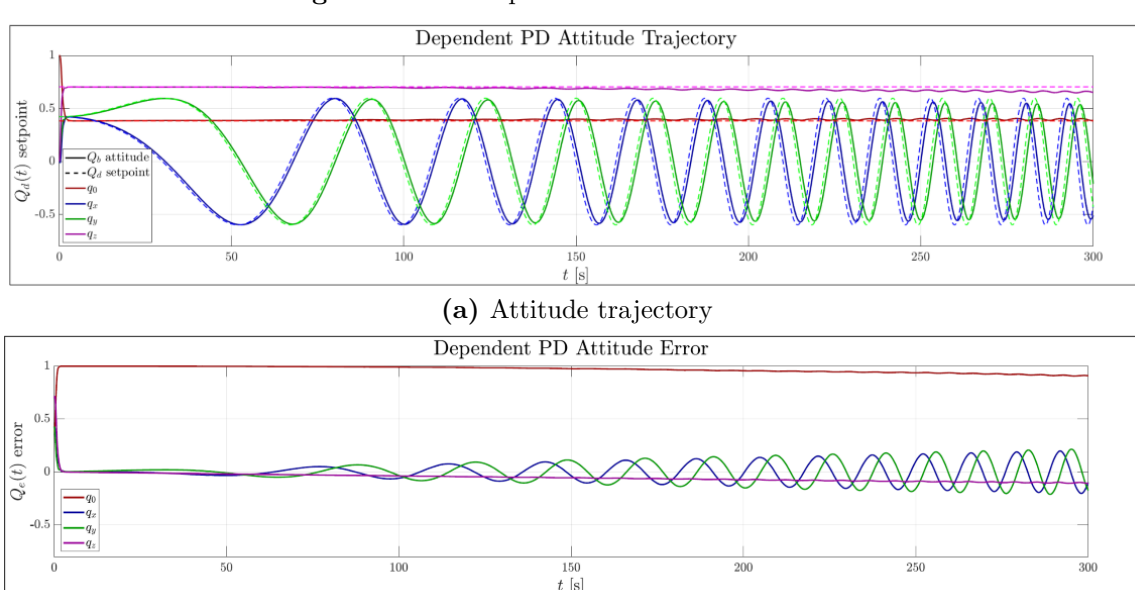
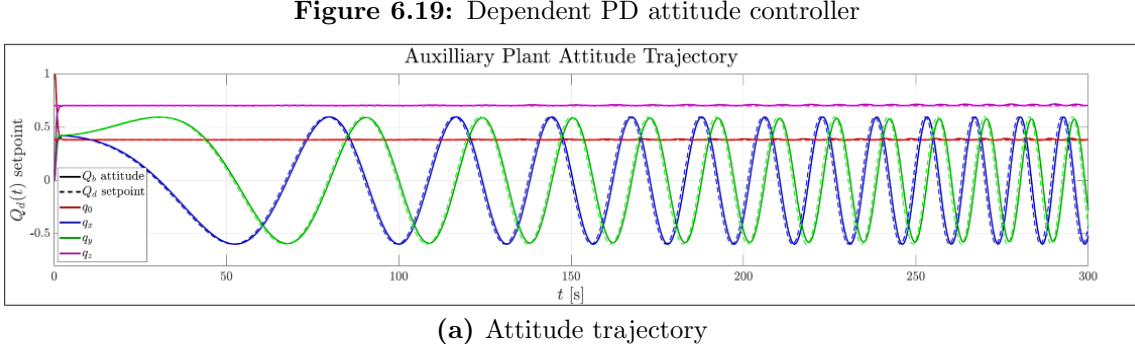
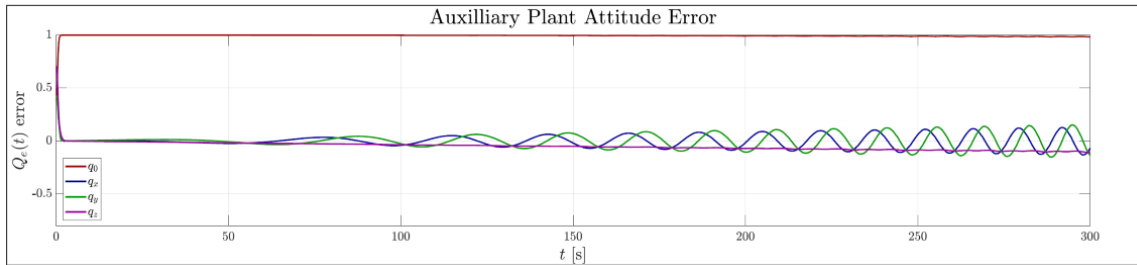
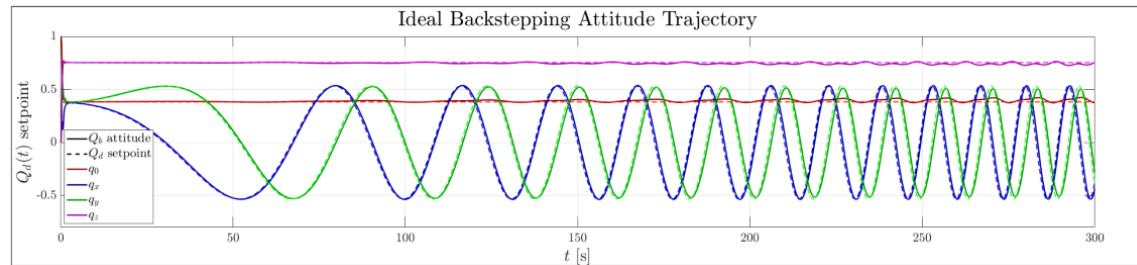


Figure 6.19: Dependent PD attitude controller

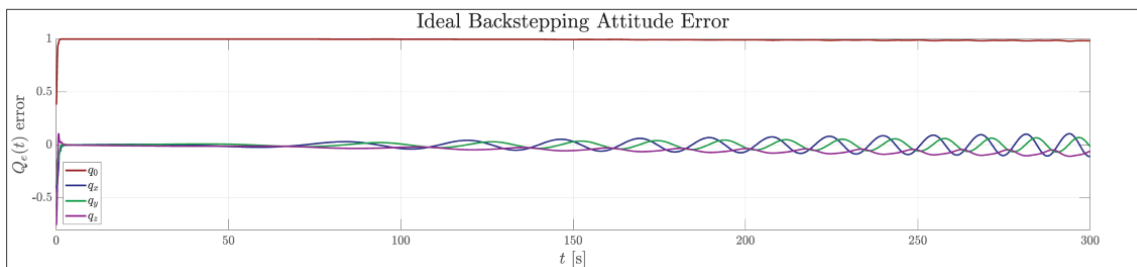




(b) Attitude trajectory error
Figure 6.20: Auxilliary PD attitude controller



(a) Attitude trajectory



(b) Attitude trajectory error
Figure 6.21: Ideal backstepping attitude controller

Interestingly, even the uncompensated (still compensating for gravitational force however) controller can still track the generated trajectory. The independent PD controller, illustrated in Fig:6.18, has a *roughly* constant quaternion error which oscillates with the trajectory setpoint. Only beyond an orbital rate of ≈ 1 [Hz], at $t = 60$ [s], does the trajectory begin to lose its stability, where the quaternion errors start to drift. Introducing plant compensation in Fig:6.19 reduces the trajectory's initial error. The plant-dependent PD controller begins to show oscillatory tracking errors at the same ≈ 1 [Hz] point and slowly drifts from its setpoint.

The exponentially stable controllers performed better and maintained approximately zero error trajectory tracking for longer. The auxiliary PD controller, Fig:6.20, starts to introduce a non-zero oscillatory tracking error at a tracking frequency only greater ≈ 1.4 [Hz], at $t = 70$ [s]. The auxiliary PD controller still maintains an acceptable error ($< 5\%$) until a trajectory rate of ≈ 3.5 [Hz] is reached at $t = 110$ [s]. The final, ideal backstepping controller in Fig:6.21 retains an error free trajectory for the longest, only introducing oscillating tracking errors at ≈ 1.8 [Hz], at $t = 80$ [s], but continues tracking the trajectory with an acceptable ($< 5\%$) error up to an orbital rate of ≈ 5.4 [Hz] until $t = 140$ [s]. Trajectory errors could be reduced (*improved*) further with the application of higher-order state-derivative trajectory setpoints for each controller with $\vec{\omega}_d \neq \vec{0}$ and $\vec{v}_d \neq \vec{0}$.

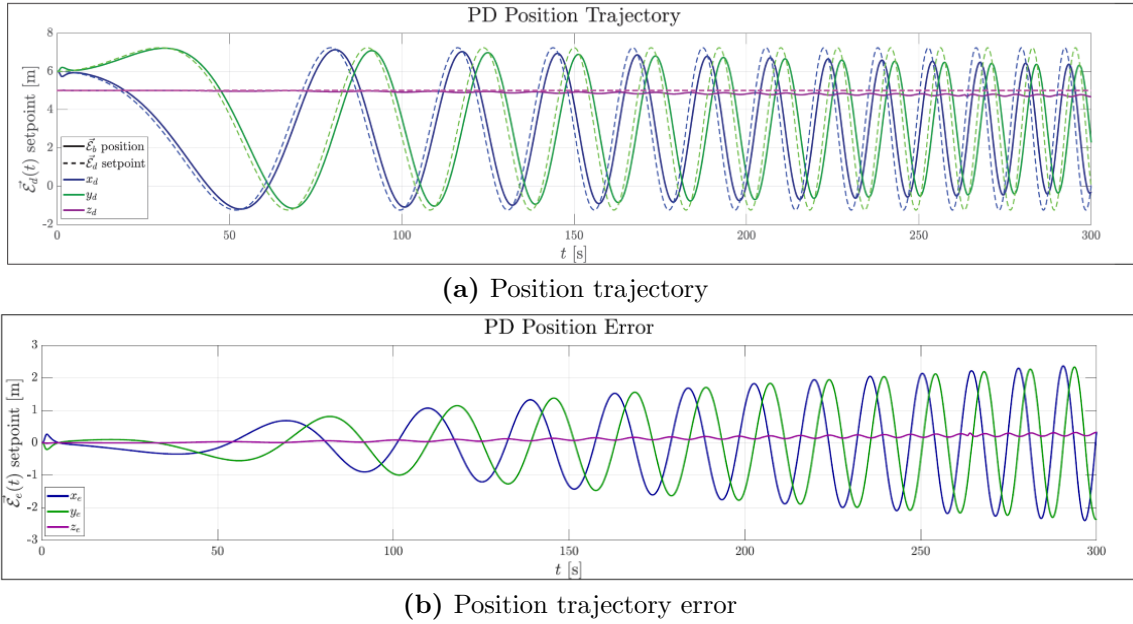


Figure 6.22: PD position controller

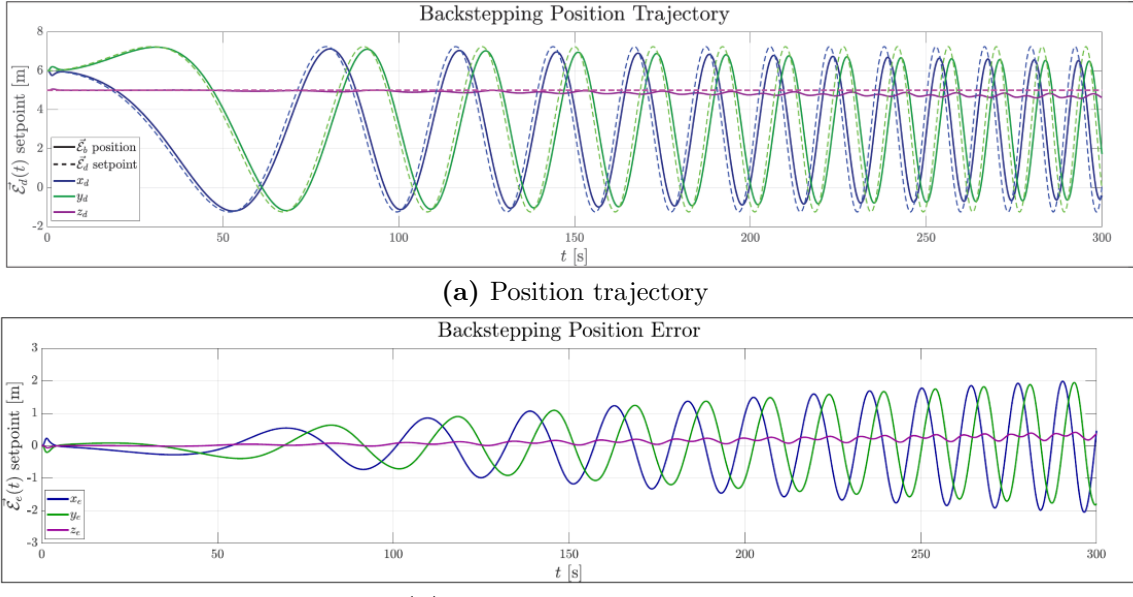


Figure 6.23: Backstepping position controller

Ideal backstepping and PD position controllers manifest a small lag behind the generated XYZ position trajectories. This is a consequence of tracking only first-order setpoints, if a velocity setpoint was applied, that tracking error would be diminished. Both controllers track the trajectory setpoint with a non-zero error from the start of the simulation. The ideal backstepping position controller does, however, track increasingly faster trajectories with a smaller error, shown in Fig:6.23b.

6.6 Robust Stability and Disturbance Rejection

Despite deriving adaptive control laws in Sec:4.6.3 and Sec:4.7.2 for attitude and position controllers respectively, each of the proposed control laws demonstrated acceptable stability under sizeable disturbances. Trajectories tested under disturbance conditions are simple oscillatory ones, similar to the trajectory setpoint illustrated in Fig:6.2 but with a *constant* orbital rate of 0.5 [Hz] applied. The purpose of the subsequent tests is to evaluate the disturbance approximator's performance, not a particular controller's trajectory tracking ability. App:C.3 shows each non-adaptive controller's trajectory response to uncompensated disturbances acting on the vehicle.

6.6.1 Torque Disturbance Rejection

Torque turbulences are difficult to define without in-depth accompanying statistical and mathematical analysis. To expedite the stability/disturbance evaluation process, torque turbulences were approximated using a Dryden Gust model, [20, 78]. That gust/wind turbulence model is designed for helicopters in hovering conditions, but the propeller span dimension was scaled accordingly. Alternatively, the Von Karman aerospace disturbance model(s) could be implemented, but that model is computationally more exhaustive. The accuracy of the turbulence model is not particularly important given that this section aims to evaluate the adaptive backstepping observer's performance at estimating a *general* disturbance. Consideration of more applicable wind and disturbance models similar to [7] remains open to further research.

Without deliberating on the details of the model, the Dryden Wind model produces turbulence signals from white noise filtered through a specified power spectrum. That power spectrum varies as per an aircraft's orientation, altitude and translational velocity. For the aircraft and trajectory under consideration here, such a disturbance model is sufficient for simulating small interference patterns. Recall the torque disturbance observer derived for the attitude backstepping plant, from Eq:4.85:

$$\dot{\vec{\tau}}_L = -\Gamma_L J_b^{-1}(\hat{u})(\Gamma_1 \vec{q}_e - \hat{\omega}_b) \quad (6.30)$$

The gain adaptivity matrix Γ_L is tuned using a PSO iteration loop, simulated in steady-state with a cost function to minimize the observer's error $\Delta \hat{\tau}_L$ over the course of a $t = 60$ [s] simulation. The resultant *diagonal* $[3 \times 3]$ adaptivity matrix is $\Gamma_L = \text{diag}(29.58, 28.43, 4.60)$. The approximator tracks an applied disturbance as shown in Fig:6.24 over a disturbance range of ± 0.2 [N.m] (which is 20% of a typical controller's commanded input for a stepped attitude from Eq:6.8) for a short steady-state test. Both pitch ϕ and roll θ torque approximator channels track the torque with a relatively small error, averaged 16% and 15% respectively. Greater deviation from the applied torque occurs in the ψ channel about the \hat{Z}_b axis, approximate 36% averaged over the short steady-state.

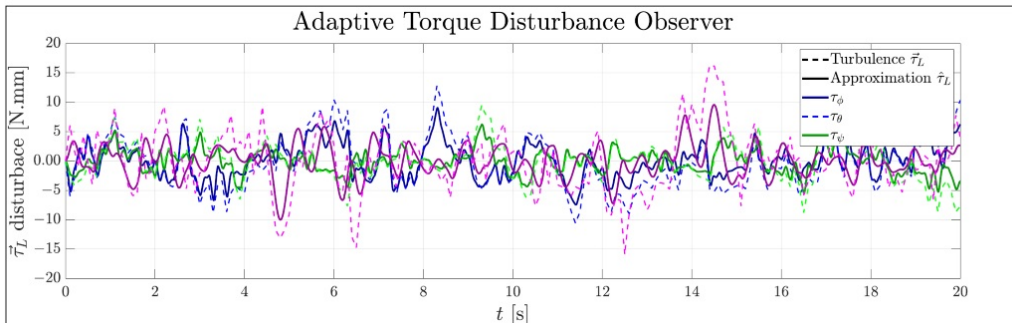


Figure 6.24: Attitude torque disturbance observer

Fig:6.25 shows the adaptive backstepping controller's attitude response over a constant orbital trajectory whilst undergoing torque turbulence. The addition of a torque observer for compensation produces a slight improvement over an uncompensated IBC controller, included in Fig:C.3c from App:C.3. The improvement a torque observer yields is diminished given that in an Ideal Backstepping case, the actuators were being rate limited (Fig:6.13d). Higher bandwidth torque inputs will not see much improvement, given that the actuators cannot apply the commanded input at a sufficient rate.

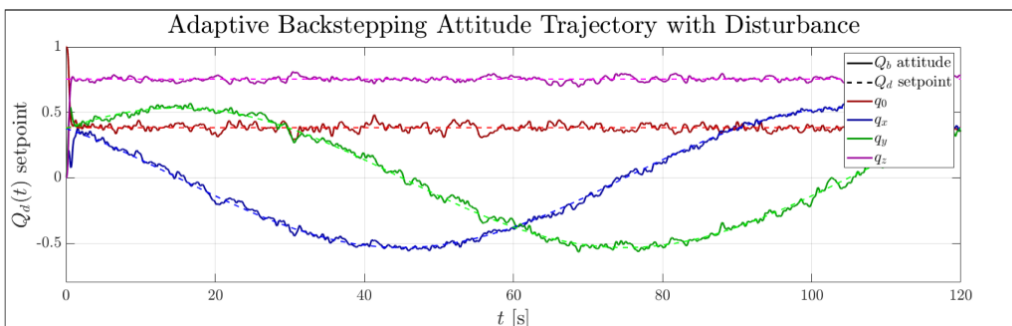


Figure 6.25: Adaptive backstepping attitude trajectory tracking

6.6.2 Disturbance Force Rejection

Force disturbances are similarly emulated in simulation using a Dryden Gust model for wind turbulent velocity generation. Additionally, a wind vector field across the inertial frame test space is also used to introduce a constant force offset throughout the trajectory simulation. The force disturbance observer, from Eq:4.112a, has an estimate update rule such that:

$$\dot{\hat{F}}_D = -m_b^{-1}\Gamma_D(\Gamma_1\vec{X}_e - \vec{v}_b) \quad (6.31)$$

where \vec{X}_e is the inertial position error transformed to the body frame, $\vec{X}_e = Q_b \otimes \vec{\mathcal{E}}_e \otimes Q_b^*$. Then Γ_D is the force disturbance observer's adaptivity $[3 \times 3]$ gain matrix. The gain matrix is chosen to minimize the force disturbance observer's error over a steady-state simulation. Using the optimized coefficients $\Gamma_D = \text{diag}(4.20, 3.84, 3.97)$, the observer tracks a force disturbance acting on the vehicle over a range of $[-4 : 8]$ N. Fig:6.26 shows how the force observer adapts to the variable force turbulence applied, the plot is taken over an entire simulation (until $t = 120$ s) to illustrate the vector field effects. Each observer channel (F_x, F_y and F_z) averaged between 5% and 10% error over the course of the simulation.

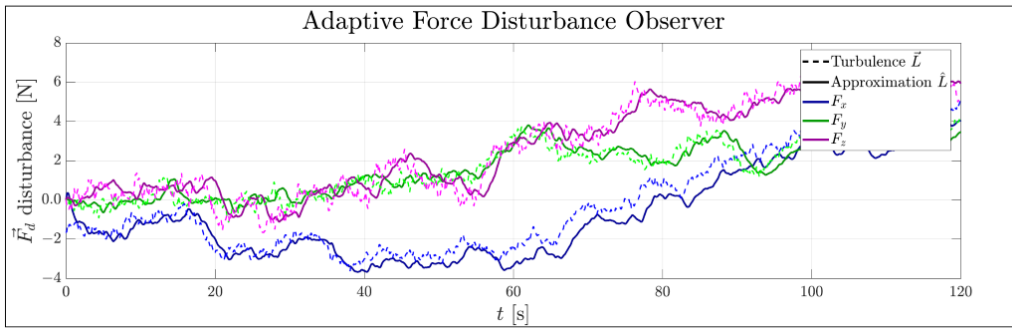


Figure 6.26: Position force disturbance observer

The position adaptive backstepping controller then tracks the inertial frame trajectory as shown in Fig:6.27. The trajectory tracking performance is improved marginally when compared to the Ideal backstepping case from Fig:C.4b. Even without adaptive disturbance compensation, the plant is stable throughout the trajectory, albeit somewhat noisy. The drawback of this particular adaptive compensation approach is that each observer is an extracted signal from existing state variables. As a result, no new information is being used to compensate the plant and as such the small signal stability is largely unaffected. The vector force field produces an oscillating error from the trajectory, despite the adaptive compensation applied to the control loop, shown in Fig:6.27.

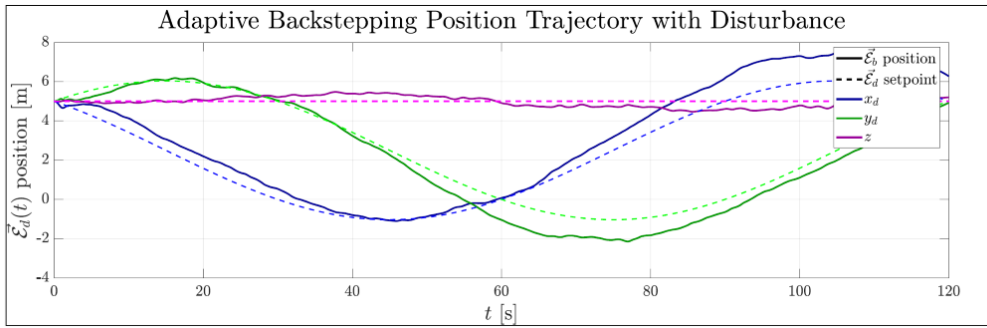


Figure 6.27: Adaptive backstepping position trajectory tracking

6.7 Allocation Tests

The various allocation rules, as derived in Ch:5, implement virtual control inputs to solve for explicit actuator positions. Each of the allocators tested here was compared to basic position and attitude PD controllers commanding a virtual input.

The abstraction applied to achieve an affine relationship required for inversion allocation (in Eq:6.32) meant that actuator transfer rates were independent of the allocation rule applied. As a result, the effect of different allocation laws is reduced.

$$\vec{v}_c = B'(\vec{x}, t)\vec{u} = \begin{bmatrix} \mathbb{I}_{3 \times 3} & \mathbb{I}_{3 \times 3} & \mathbb{I}_{3 \times 3} & \mathbb{I}_{3 \times 3} \\ [\vec{L}_1]_{\times} & [\vec{L}_2]_{\times} & [\vec{L}_3]_{\times} & [\vec{L}_4]_{\times} \end{bmatrix} \vec{T}_{[1:4]}^T \quad (6.32a)$$

$$\vec{u}_i = [\Omega_i \quad \lambda_i \quad \alpha_i]^T = R^\dagger(\vec{x}, \vec{T}_i, t) \text{ for } i \in [1 : 4] \quad (6.32b)$$

The transfer rate at which physically commanded inputs implement virtually-designed control inputs, $\vec{v}_c \rightarrow \vec{v}_d$, is affected by the thrust inversion relationship $R^\dagger(\vec{x}, t)$, not allocation rules $B'(\vec{x}, t)$. The consequence of this is that, in the context of actuator transfer rates, each allocation rule performed almost identically. Inverse solutions to Eq:5.18 solve for the quadratic least squares minimized actuator positions, so each $|\vec{T}_i|$ within the $\mathbb{R}^{1 \times 12}$ matrix $|\vec{T}_{[1:4]}|$ is minimized. The solution is a cost efficient one minimizing actuator effort. In general, psuedo-inversion, weighted and priority normalized inverse allocators each stem from Eq:5.19:

$$\vec{T}_{[1:4]} = (\mathbb{I}_{m \times m} - CB(\vec{x}, t))\vec{T}_p + C\vec{v}_d \quad (6.33a)$$

$$C = W^{-1}B^T(\vec{x}, t)(B(\vec{x}, t)W^{-1}B^T(\vec{x}, t))^{-1} \quad (6.33b)$$

A combined step of setpoints for attitude *and* position states is used to compare each allocation rule. A pseudo inverse allocator from Eq:5.20 is used as the reference case against which subsequent allocator algorithms are evaluated. The typical setpoint used for both position and attitude steps with attitude in Euler angles, $\vec{\eta}_d$ not quaternions Q_d , is:

$$\vec{x}_d = \begin{bmatrix} \vec{\mathcal{E}}_d \\ \vec{\eta}_d \end{bmatrix} = \begin{bmatrix} [7.5 \quad 4 \quad 3]^T \\ [-142 \quad 167 \quad -45]^T \end{bmatrix} \quad \begin{bmatrix} [\text{m}] \\ [{}^\circ] \end{bmatrix} \quad (6.34)$$

A pseudo-inverse allocation solves for $\vec{T}_{[1:4]}$ using $B^\dagger(\vec{x}, t)\vec{v}_d$, from Eq:5.20. Fig:6.28 shows the combined position and attitude step responses. The combined attitude and position step response with a pseudo-inverse allocator $B^\dagger(\vec{x}, t)$ settles for *both* states in $t_{95} = 5.658$ s from the state step. The commanded actuator inputs, as per the pseudo inverse allocator, are shown in Fig:6.28c.

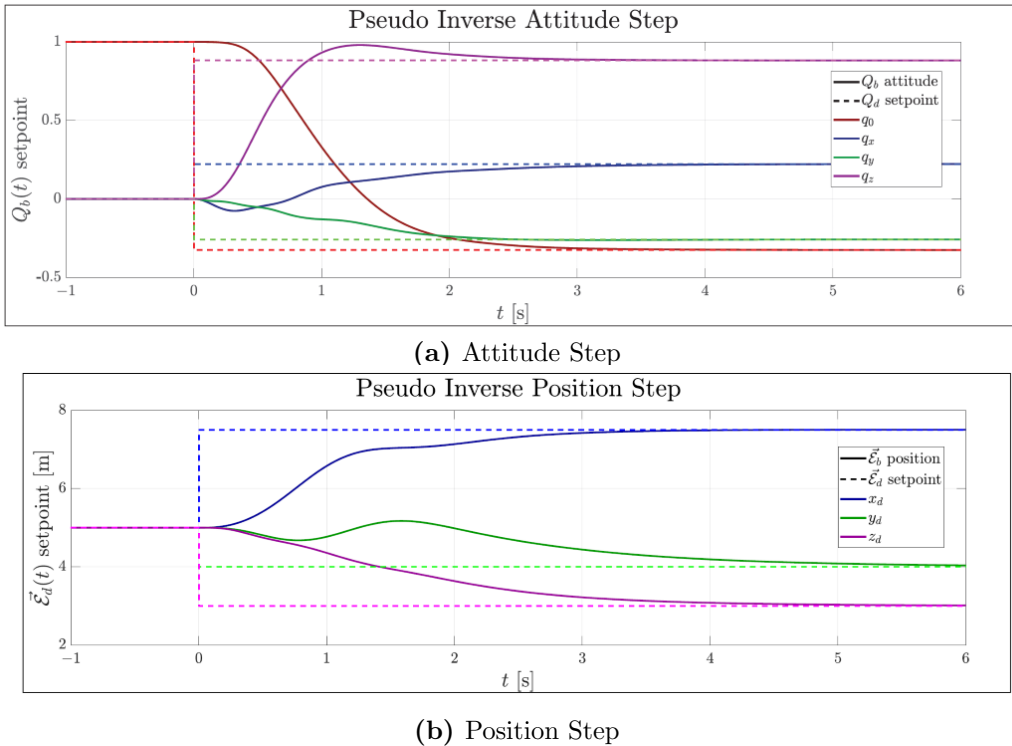
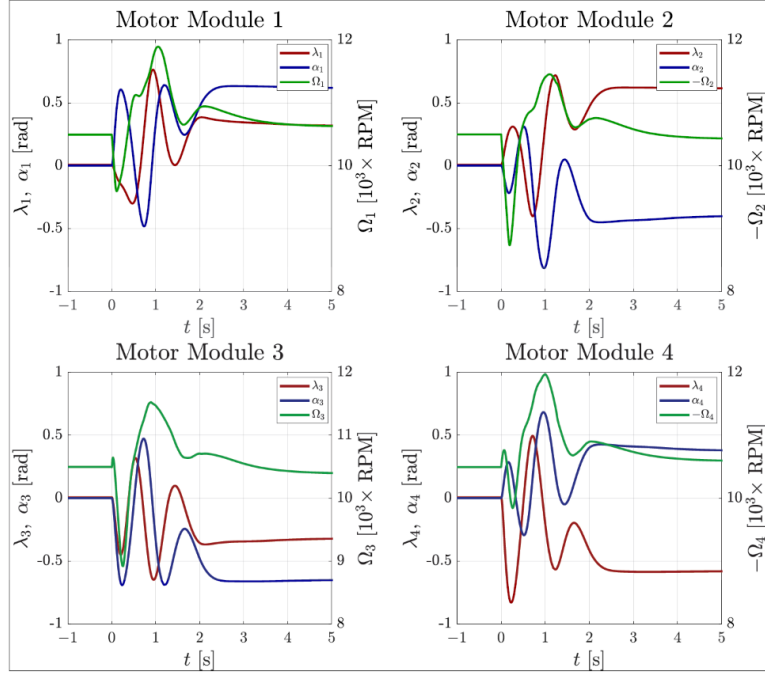


Figure 6.28: Pseudo inverse step response plot



(c) Actuator commands

Figure 6.28: Pseudo inverse step actuator response

The preferred allocator positions, described in Sec:5.3.2, are hovering conditions defined with respect to either the inertial or body frames, \mathcal{F}^I and \mathcal{F}^b respectively. At steady-state with an attitude at the origin, $Q_d = [+1 \vec{0}]^T$, the controller commands the virtual control input:

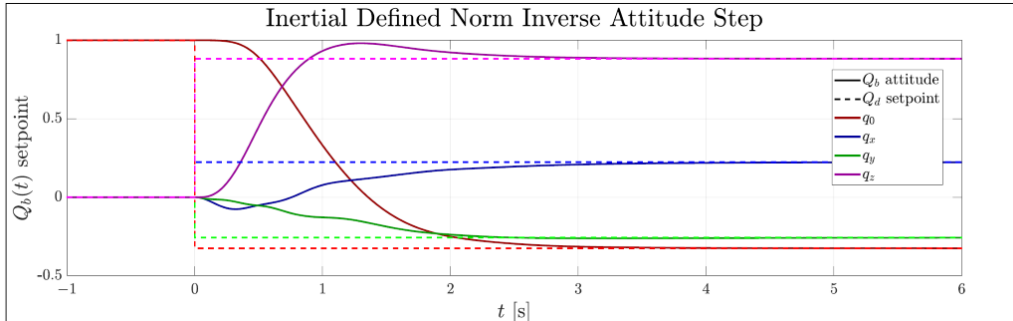
$$\vec{\nu}_p = \begin{bmatrix} \vec{F}_p \\ \vec{\tau}_p \end{bmatrix} = \begin{bmatrix} [0 \ 0 \ 15.45]^T \\ [0.25 \ 0.50 \ -1.89]^T \end{bmatrix} \begin{bmatrix} [N] \\ [N.mm] \end{bmatrix} \in \mathcal{F}^{b,I} \quad (6.35)$$

The small amount of control torque applied in Eq:6.35, about the $\hat{Z}_{I/b}$ axis, is to compensate for net gravitational torque due to the eccentric center of gravity and resultant aerodynamic torque $\vec{\tau}_H$ from the propeller's rotational velocity. Applying the pseudo inverse allocation rule to the preferred input $\vec{\nu}_p$ in Eq:6.35 produces the following actuator positions which command hovering conditions:

$$\vec{T}_p^I = B^\dagger(\mathbf{x}, t)\vec{\nu}_p = [T_{1x} \ T_{1Y} \ T_{1Z} \ \dots \ T_{4x} \ T_{4y} \ T_{4z}] \quad (6.36a)$$

$$= [[0.00 \ -0.02 \ 3.86] \ [0.02 \ 0 \ 3.86] \ [0 \ 0.02 \ 3.86] \ [-0.02 \ 0 \ 3.86]]^T \ [N] \quad (6.36b)$$

Testing the same attitude and position setpoint steps, but with preferred actuator hovering conditions relative to the inertial frame (illustrated in Fig:5.2) produces a response shown in Fig:6.29. The plant settles in $t_{95} = 5.619$ [s] with a marginally faster, but practically identical step response to the pseudo-inverse case presented before in Fig:6.28. Note that, whilst the attitude and position responses were identical, the commanded actuator inputs in Fig:6.29c are slightly less aggressive in the step's transition.



(a) Attitude Step

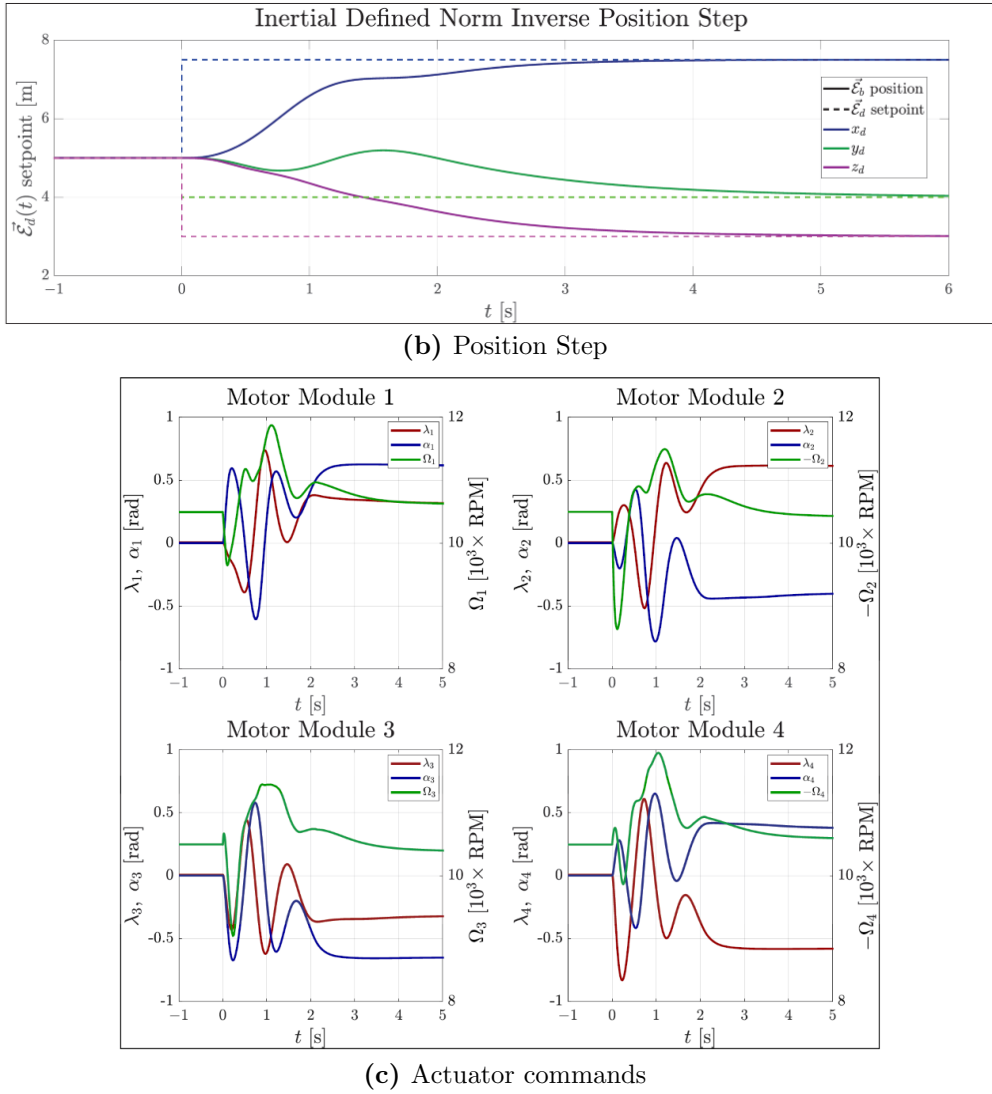
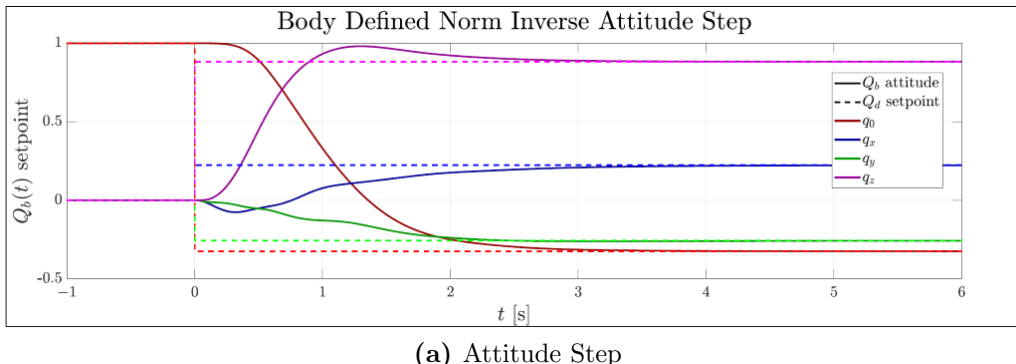


Figure 6.29: Inertial hover preferred actuator step response

Transformation of those hovering conditions in Eq:6.35 from the inertial frame to the body frame is applied through an instantaneous quaternion transformation:

$$\vec{\nu}'_p = \begin{bmatrix} Q_b \otimes \vec{F}_p \otimes Q_b^* \\ Q_b \otimes \vec{\tau}_p \otimes Q_b^* \end{bmatrix} \in \mathcal{F}^b \quad (6.37)$$

Hovering conditions are then always a function of the body's instantaneous attitude. The plant settles in a slightly improved time, $t_{95} = 5.603$ [s], with a step response plotted in Fig:6.30. The difference between the two preferred allocator positions has a small consequence on the performance of the control loop. The change in commanded actuator inputs in Fig:6.30c is almost identical to the inertial frame defined hover case. With a preferred actuator position defined in the body frame, the actuator commands are around 2% greater.



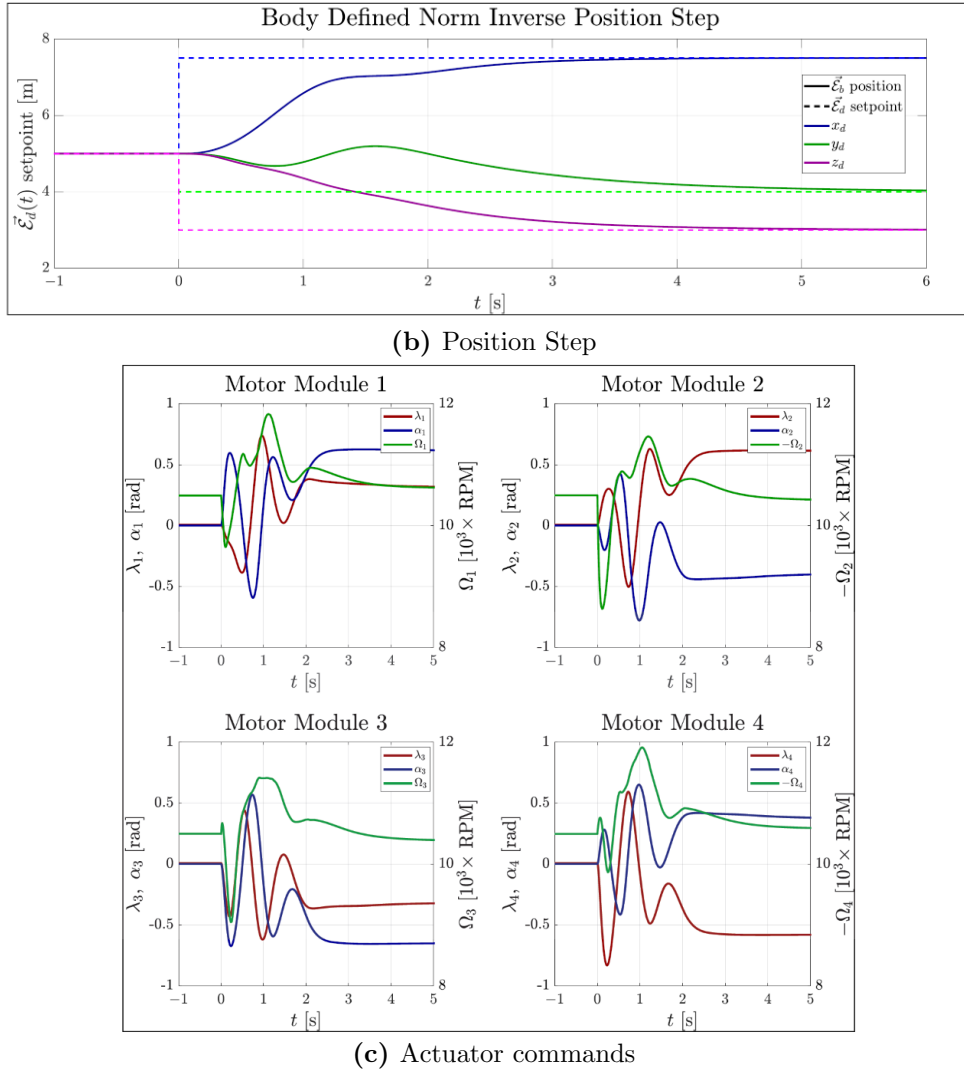


Figure 6.30: Body frame hover preferred actuator step response

The weighted actuator allocation rule, proposed in Sec:5.3.3, prioritizes the use of certain input thrust components in Eq:6.32a. The weighting matrix is a $[12 \times 12]$ set of coefficients which biases various allocators as illustrated in Fig:5.4. Note that the weighting matrix *does not* preferentially bias certain servos, it biases components of the abstracted allocation input $\vec{T}_{[1:4]}$ from Eq:5.1. The control allocator's main objective is to reduce the slack between a controller designed input $\vec{\tau}_d$ and a physically commanded input by the actuator plant $\vec{\tau}_c(\hat{u}_c)$. If the weighting matrix does not have unity Eigenvalues, it then applies a gain of its own to the control input, which could potentially alter the controller's response. Each weighting row and column in the matrix is constrained to a normalized sum, furthermore it was proposed that coefficients are selected based on an optimization as per the penalty function in Eq:5.26. The optimized allocator weighting matrix, used for $C = W^{-1}B^T(B.W^{-1}.B^T)^{-1}$ from Eq:6.33b, is found:

$$W \triangleq \begin{bmatrix} 72 & 9 & 9 \\ 9 & 72 & 9 \\ 9 & 9 & 72 \\ 0 & 0 & 0 \\ 0 & 0 & 0 \\ 0 & 0 & 0 \\ 8 & 1 & 1 \\ 1 & 8 & 1 \\ 1 & 1 & 8 \\ 0 & 0 & 0 \\ 0 & 0 & 0 \\ 0 & 0 & 0 \end{bmatrix} \begin{bmatrix} 0 & 0 & 0 \\ 0 & 0 & 0 \\ 0 & 0 & 0 \\ 72 & 9 & 9 \\ 9 & 72 & 9 \\ 9 & 9 & 72 \\ 0 & 0 & 0 \\ 0 & 0 & 0 \\ 0 & 0 & 0 \\ 8 & 1 & 1 \\ 1 & 8 & 1 \\ 1 & 1 & 8 \end{bmatrix} \begin{bmatrix} 8 & 1 & 1 \\ 1 & 8 & 1 \\ 1 & 1 & 8 \\ 0 & 0 & 0 \\ 0 & 0 & 0 \\ 0 & 0 & 0 \\ 72 & 9 & 9 \\ 9 & 72 & 9 \\ 9 & 9 & 72 \\ 0 & 0 & 0 \\ 0 & 0 & 0 \\ 0 & 0 & 0 \end{bmatrix} \begin{bmatrix} 0 & 0 & 0 \\ 0 & 0 & 0 \\ 0 & 0 & 0 \\ 8 & 1 & 1 \\ 1 & 8 & 1 \\ 1 & 1 & 8 \\ 0 & 0 & 0 \\ 1 & 8 & 1 \\ 9 & 72 & 9 \\ 9 & 9 & 72 \\ 72 & 9 & 9 \\ 9 & 72 & 9 \\ 9 & 9 & 72 \end{bmatrix} \times 10^{-3} \quad (6.38)$$

The weighted allocator's response in Fig:6.31 does not change its trajectory response at all from previous allocation rules. Furthermore, the commanded actuator inputs in Fig:6.31c are much the same as those of either preferred actuator positions. The final weighted inversion allocator, applied with Eq:6.38, settled from the attitude and position setpoint step in $t_{95} = 5.595$ [s].

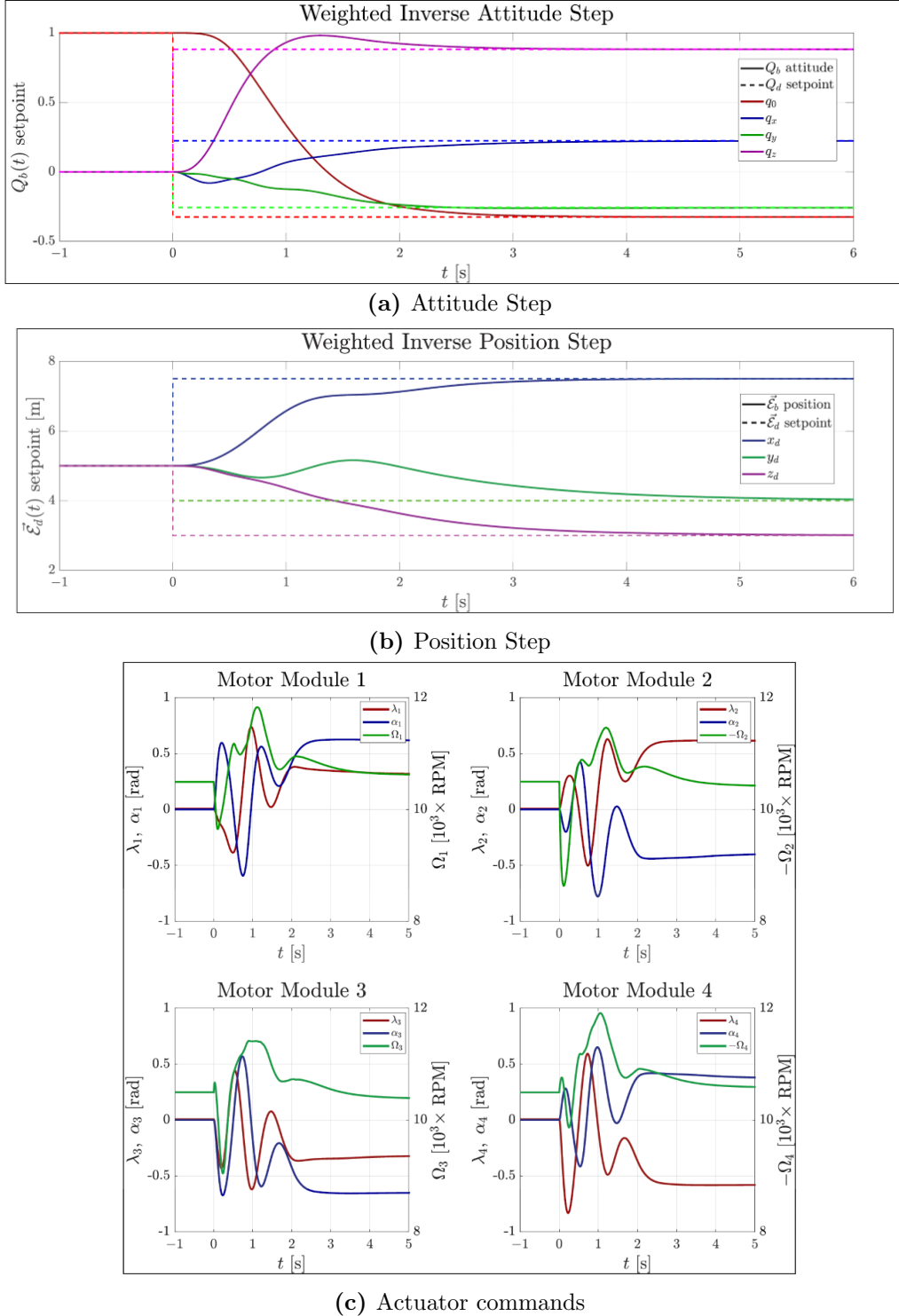


Figure 6.31: Weighted actuator allocation step response

It is not altogether unexpected that the allocation rules react in the same way. The static allocators ensure to command actuator positions which meet the control input requirement, thereby reducing the allocation slack. As a result, each allocation will perform roughly in the same way given that they apply the same secondary cost function. Moreover, pseudo inversion's requirement for an affine effectiveness relationship meant that actuator transfer functions were separated from the allocation block, this made the actuator transfer rates independent of the allocation rule applied.

6.8 Input Saturation

The introduction of a rotational limit to the actuating servos is an explicit design decision (Sec:2.4.1), the limited $\pm 90^\circ$ servos could easily be changed in the mechanical design to continuous rotation actuators. To review the effects of a non-linear saturation limit imposed on the actuator plant, a commanded setpoint must actually induce actuator saturation. The standard state setpoint step used thus far *does not* result in the servo actuators commanded beyond their $\pm 90^\circ$ limit. Each controller tested in Sec:6.3 and Sec:6.4 commands actuators to well within their limits, even without an imposed rotational saturation. Furthermore, at no point in the applied trajectory tracking loop do any of the actuators near their saturation limit. Alternatively, the following state setpoint is used:

$$\vec{x}'_d = \begin{bmatrix} \vec{\mathcal{E}}'_d \\ \vec{\eta}'_d \end{bmatrix} = \begin{bmatrix} [7.5 \ 4 \ 3]^T \\ [-142 \ 35 \ -45]^T \end{bmatrix} \begin{bmatrix} [\text{m}] \\ [^\circ] \end{bmatrix} \Leftrightarrow \begin{bmatrix} [7.5 \ 4 \ 3]^T \\ [0.1894 \ -0.874 \ -0.2649 \ -0.3605]^T \end{bmatrix} \quad (6.39)$$

The alternative attitude setpoint $\vec{\eta}'_d$ is chosen because it commands each servo beyond its $\pm\pi/2$ rotational limit. Fig:6.32 shows the step response for that commanded attitude and position setpoint when using a simple PD controller for both the position and attitude control loops.

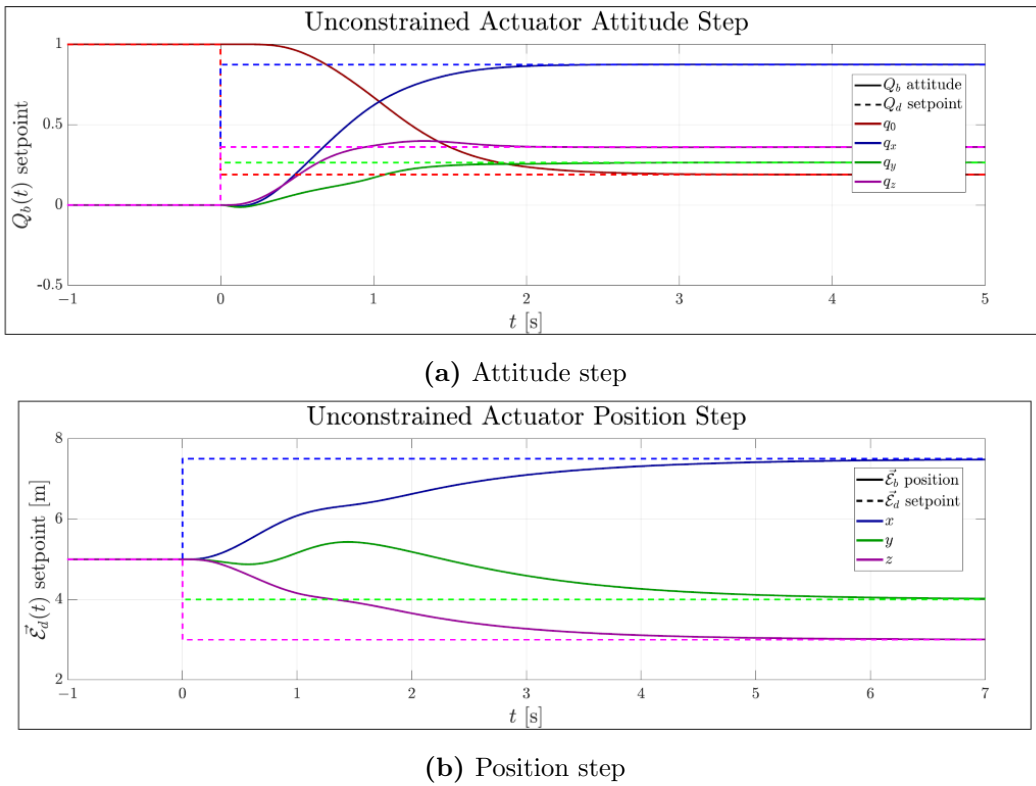
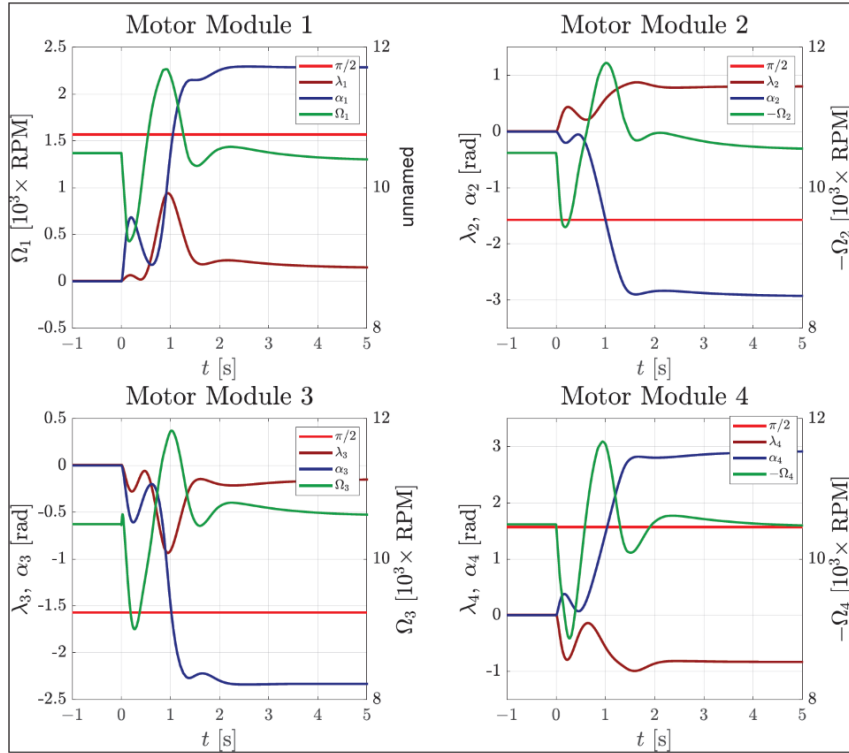


Figure 6.32: Step response without servo limits

Neither attitude nor position responses in Fig:6.32 are unexpected, even the basic PD control laws for both state tracking loops have been shown to correctly track a given setpoint. Fig:6.33 shows all twelve *unconstrained* actuator positions throughout the stepped trajectory, with highlighted $\pi/2$ rotational limits for the servos.

Each middle ring servo α_i for $i \in [1 : 4]$ settles to both above and below the $\pm\pi/2$ rotational limit. Another point to take note of is that such a large step in the servos rotational position results in a rate limited angular velocity being reached. That, however, is a consequence of the servos themselves, and can only be addressed by applying closed loop BLDC motor control in place of the servos for rotational actuation of each motor module.

**Figure 6.33:** Servo inputs without limits

Introducing the mechanical hard actuator limit to the state step in Eq:6.39 produces a step response as illustrated in Fig:6.34. The response obviously never reaches a settling point and destabilizes when the actuator saturation limits are applied.

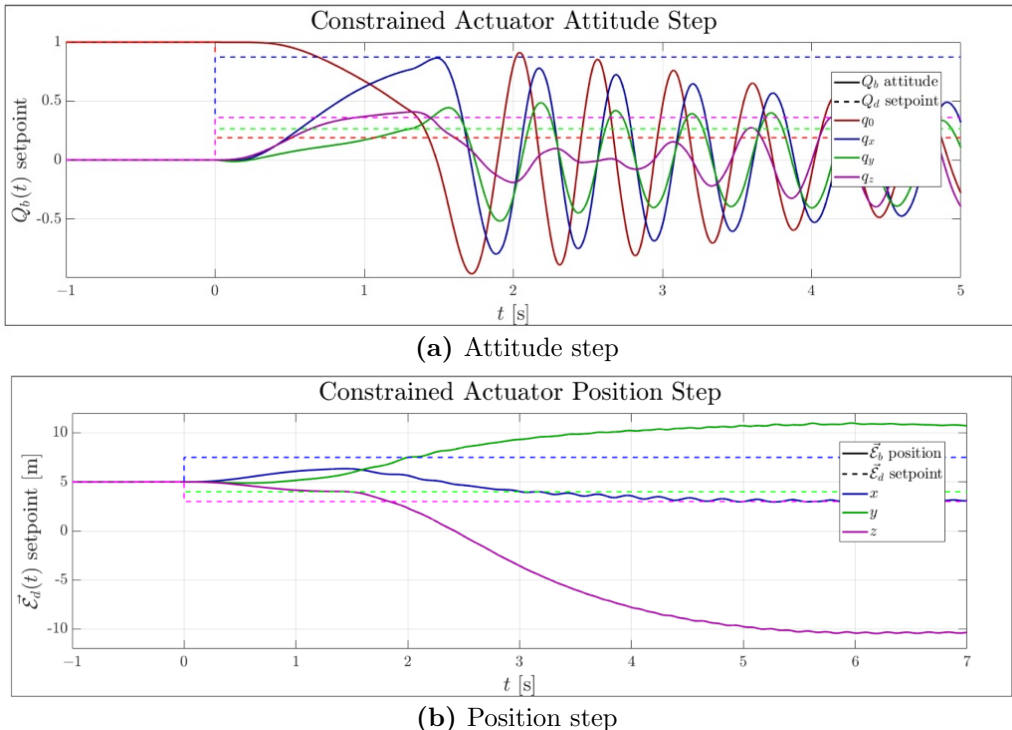
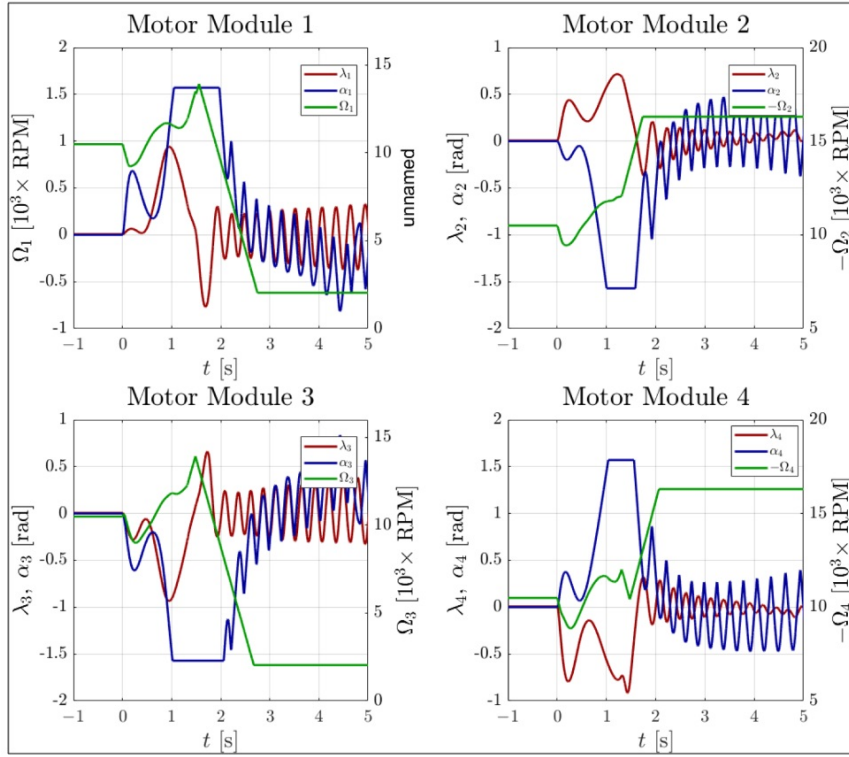
**Figure 6.34:** Step response with servo limits

Fig:6.35 shows commanded actuator inputs during the attitude and position steps. The servos reach their mechanical $\pi/2$ rotational limit, thereafter the control loop commands illegal force inputs which induce saturation of the BLDC motor blocks. The propeller speed inputs are set to their saturating limits and the actuators begin oscillating, attempting to recover. It is not the simulation that prevents the control loop from recovering, the control loop itself oscillated out and began commanding force and torque inputs far outside the feasible limits of saturation.

**Figure 6.35:** Servo inputs with limits

6.9 State Estimation

The final aspect of the control simulation to consider is the effect that state estimation has on the controller's ability to track setpoints. It was proposed, in Ch:2, that a 9-axis inertial measurement unit would sample angular rates and inertial accelerations in the body frame. Then some form of filter would fuse sensor measurements together to provide state estimates only for the vehicle's attitude. Position in the inertial frame is not approximated using only an IMU due to sensor drift. For that reason, an already available motion capture system, [110], is proposed to track the vehicle's position under testing conditions.

Such components of the embedded system loop could indeed be tested in simulation, but owing to the large amounts of noise a physical flight test would induce on those components, would not prove useful in evaluating the efficacy of the net proposed control system. Given the amount of vibrations and disturbances the prototype will undergo, simulations will not be able to accurately approximate such affects. Instead a suitable, approximated discretization is applied to the simulation's state variables used for feedback in the control loop.

Quaternion position, angular velocity and translational velocity feedback terms are discretized and sampled at a rate of 50 [Hz] with a 5 [μ s] sample delay to emulate a perfect IMU system derived from the hardware proposed (Sec:2.4). In reality, those signals would be processed by an online Kalman filter and be subject to a relative degree of noise and integral drift. The inertial position feedback is sampled at 50 [Hz] to emulate the proposed camera based state estimation from [110] with a propagation delay of 40 [μ s].

Both position and attitude control loops, testing with the basic Proportional Derivative controllers in both cases, were stable for the above proposed sampling rates. In fact, the entire system was stable for sample rates as slow as 5 [Hz], whose response for a typical attitude and position step (Eq:6.34) is plotted in Fig:6.36.

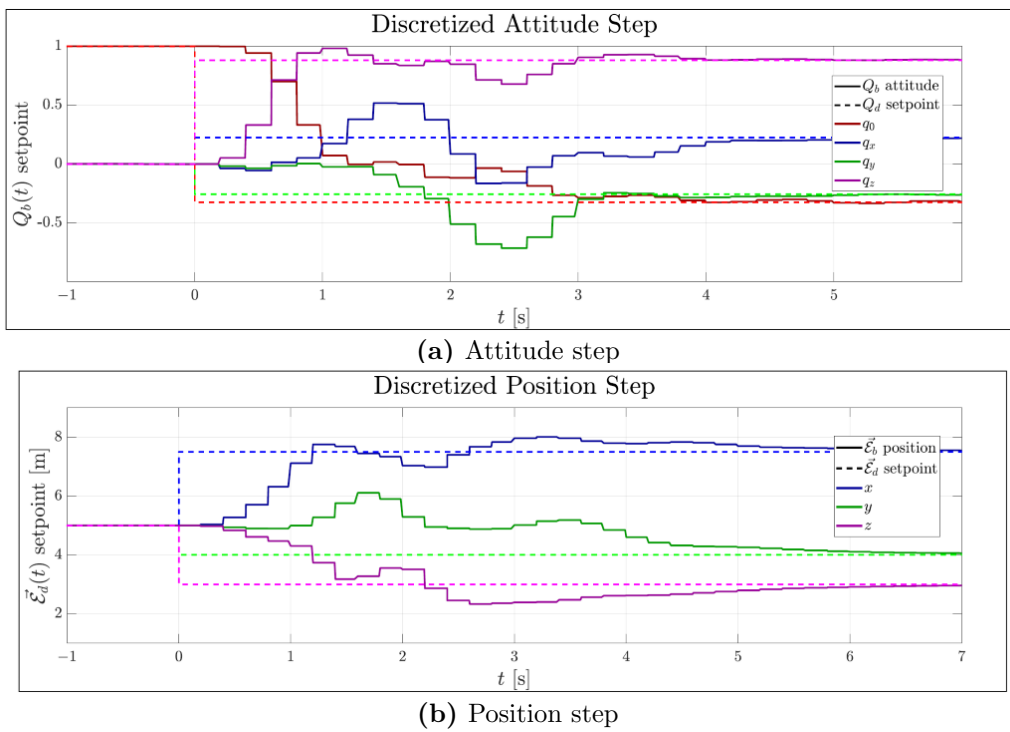


Figure 6.36: Discretized state steps

Chapter 7

Conclusions and Recommendations

The original objective for the project was to design, simulate and physically test the prototype outlined in Sec:2.1. Modeling the responses of the multibody prototype to obtain the dynamic equations of motion, derived in Sec:3.4, proved to be dramatically more complex than initially anticipated. Time varying moments of inertia (generalized in Eq:3.71d) introduced to the Lagrangian kinematics resulted in a unique problem formulation. Each actuated motor module's response to the net vehicle's dynamics (Eq:3.76,3.87 and 3.106) required multiple revisions. Each step in the derivation was tested in simulation to ensure the mathematics applied were sound. The difficulties accompanying those derivations pushed back the project's time-line significantly. As a result, it was decided to cancel the inclusion of physical flight tests. Physical implementation of the proposed control laws therefore remains open to further work. With the above being considered, the dynamic model for the system is a significant contribution of this work. The uniqueness of the multibody structure made solving for the differential equations of motion a sizeable task. A consequence of the complex dynamics was an extremely high degree of stiffness in the system which adversely affected the simulation times. Alternatively, relative coordinates could have been implemented in lieu of the used Cartesian coordinates which describe the vehicle and its configuration. Relative descriptions of each state variable could reduce the complexity in calculating instantaneous moments of inertia at each simulation interval. Moreover, implicit Euler integration could have been applied to the simulation, both changes could potentially yield simulation improvements. The cost of such changes would be to reconstruct the entire simulation environment.

The physical tests which corroborated aspects of the dynamic model (Sec:3.4.2) would ideally be extended to physical flight tests. However, considering the complexity of the system and modelling thereof, verification of the dynamics is a useful result. The time varying, non-diagonal inertias of each body in the multibody system are consequences of the design process and the cost constraint applied to the prototype. In practice, if the rigid component of the frame (J_y from Eq:2.25d) was sufficiently larger than that of the actuated (*rotating*) bodies, the relative effect of the multibody interaction responses ($\vec{\tau}_b(\hat{u})$ from Eq:3.110b) on the dynamics would be diminished.

One of the original justifications for the increased platform complexity was the improved actuator bandwidth that would accompany thrust vectoring. The hypothesis was that pitching or rolling a thrust vector would have a faster response than changing the propeller's rotational speed (see actuator transfer functions in Sec:2.4.1). The firmware changes made to the ESCs improved the brushless DC motor's transfer function's time constant significantly. The original firmware which the ESCs used by default produced an exponentially approaching speed curve rather than the standard linear relationship (illustrated in Fig:2.24). Step tests comparing changes before and after the ESC firmware was changed were not be performed. The overall constraint encountered by the actuator plant was rate (*current*) limiting imposed on the rotational servos as a result of their electrical design. That constraint limited the performance of the more aggressive ideal backstepping attitude controller, Fig:6.13. The servo rate limits prevented the motor modules from actuating fast enough, seen in the difference between controller designed and physically commanded inputs in Fig:6.13b.

The control solutions presented in this dissertation all stabilize the plant. Respective results for attitude and position controller steps (Sec:6.3 and Sec:6.4) demonstrate the improvement exponential stability yields on a controller plant. All of the control laws proposed were able to track the applied chirp trajectory for low trajectory rates. Each controller's optimization was an ITAE optimization, prioritizing settling times and overshoot errors over aggression or input magnitude. Alternatively, the optimization could apply a penalty to a proposed set of controller coefficients based on energy expenditure or induced torque response, emphasizing stability and smooth transitions over settling times. A particle swarm optimization in Sec:6.2.1 was chosen due to its simplicity and lack of an explicitly defined gradient function. More complex optimization paradigms could have potentially produced more efficient optimizations.

Certain constraints or assumptions were applied to the model in simulation. It was shown in Sec:6.8 that applying rotational limits to the actuation servo broke down the overall setpoint tracking of the control loop. Extending the actuators to accommodate for continuous rotation requires an alteration of the mechanical design and drastically improves the range of motion. The only significant assumption made on the plant's aerodynamics was neglecting to account for any propeller's down-wash becoming incident flow into other propeller. This would have a sizeable impact on the thrust plant model, requiring a complicated fluid dynamics solution to approximate for such effects. The decision to apply nonlinear state-space control to the plant prevented the use of Model Predictive control. An MPC control law could potentially better compensate for the vehicle's non-linearities, which were otherwise relegated to feedback compensation.

In conclusion, the non-zero state setpoint tracking goal was achieved by each of the control laws proposed. The control allocation rules applied did not have a notable effect on the plant's performance because of the structure applied in Sec:5.2. Finally, the dynamic model's complexity and the difficulties involved in verification of that model outweighed the control improvements shown. The thrust vectoring accommodated for unique 6-DOF trajectory tracking to be performed, however the same could have been achieved with only a single axis of rotational tilt applied to each lift propeller (similar to related projects described in Sec:1.2). The same dynamic complexities led to catastrophic failures with earlier versions of Osprey [13], the inspiration for this project. Those complexities led to the subsequent redesign of the Osprey's successor, the V-280 Valor, which has significantly smaller actuator inertias due to fewer moving parts (at the cost of more frequent maintenance).

Appendix A

Expanded Equations

A.1 Standard Quadrotor Dynamics

Following the fundamental 6-DOF equations of motion for a rigid body derived in Sec:3.1.1, the common linearizations typically applied for generic "+" configured quadrotors are now presented. Reiterating those four differential equations, Eq:3.10, which describe a rigid body's motion (using rotation matrices and not quaternions):

$$\dot{\vec{\varepsilon}} = \mathbb{R}_b^I(-\eta)\vec{v}_b \quad \in \mathcal{F}^I \quad (\text{A.1a})$$

$$\dot{\vec{v}}_b = m_b^{-1} [-\vec{\omega}_b \times m_b \vec{v}_b + m_b \mathbb{R}_I^b(-\eta) \vec{G}_I + \vec{F}_{net}] \quad \in \mathcal{F}^b \quad (\text{A.1b})$$

$$\dot{\vec{\eta}} = \Phi(\eta)\vec{\omega}_b \quad \in \mathcal{F}^{v2}, \mathcal{F}^{v1}, \mathcal{F}^I \quad (\text{A.1c})$$

$$\dot{\vec{\omega}}_b = J_b^{-1} [-\vec{\omega}_b \times J_b \vec{\omega}_b + \vec{\tau}_{net}] \quad \in \mathcal{F}^b \quad (\text{A.1d})$$

with the Euler matrix, $\Phi(\eta)$, defined in Eq:2.12i. The net heave thrust produced by motors $i \in [1 : 4]$, bound perpendicularly to the \hat{Z}_b axis, is given by:

$$\vec{T} = \sum_{i=1}^4 F(\Omega_i) \cdot \hat{Z}_b \quad \in \mathcal{F}^b \quad (\text{A.2a})$$

The simplified relationship between the thrust scalar $T(\Omega_i)$ and the propeller's rotational speed Ω_i in [RPS] is approximately quadratic:

$$F(\Omega_i) \approx k_1 \Omega_i^2 \quad (\text{A.2b})$$

Similarly, the aerodynamic torque opposing each rotating propeller, about the propellers \hat{Z}_b axis, is:

$$Q(\Omega_i) \approx k_2 \Omega_i^2 \quad (\text{A.3})$$

Coefficients k_1 & k_2 are typically determined from physical thrust tests. The controllable pitch and roll torques, τ_ϕ & τ_θ about the \hat{X}_b and \hat{Y}_b axes respectively, are generated by opposing differential lift forces. Lastly, the yaw torque, τ_ψ about the \hat{Z}_b axis, is generated from only the net response to the rotational aerodynamic propeller torques. The control torque inputs are then defined as:

$$\tau_\phi = L_{arm}(F(\Omega_1) - F(\Omega_3)) \cdot \hat{X}_b \quad (\text{A.4a})$$

$$\tau_\theta = L_{arm}(F(\Omega_2) - F(\Omega_4)) \cdot \hat{Y}_b \quad (\text{A.4b})$$

$$\tau_\psi = \sum_{i=1}^4 (-1)^i Q(\Omega_i) \cdot \hat{Z}_b \quad (\text{A.4c})$$

Then expanding the translational position and attitude state differentials, Eq:A.1b & Eq:A.1d, to their component forms (assuming the vehicle's inertial matrix J_b is diagonal):

$$\begin{pmatrix} \dot{u} \\ \dot{v} \\ \dot{w} \end{pmatrix} = \begin{pmatrix} rv - qw \\ pw - ru \\ qu - pv \end{pmatrix} + \begin{pmatrix} -g\sin(\theta) \\ g\cos(\theta)\sin(\phi) \\ g\cos(\theta)\cos(\phi) \end{pmatrix} + \frac{1}{m} \begin{pmatrix} 0 \\ 0 \\ T \end{pmatrix} \in \mathcal{F}^b \quad (\text{A.5a})$$

$$\begin{pmatrix} \dot{p} \\ \dot{q} \\ \dot{r} \end{pmatrix} = \begin{pmatrix} \frac{J_{yy}-J_{zz}}{J_{xx}} qr \\ \frac{J_{zz}-J_{xx}}{J_{yy}} pr \\ \frac{J_{xx}-J_{yy}}{J_{zz}} pq \end{pmatrix} + J_b^{-1} \begin{pmatrix} \tau_\phi \\ \tau_\theta \\ \tau_\psi \end{pmatrix} \in \mathcal{F}^b \quad (\text{A.5b})$$

Considering the size of a typical angular rate, $\vec{\omega}_b \approx \vec{0}$, the gyroscopic and Coriolis effects on the body (namely both cross product terms) are sufficiently small enough to be regarded as negligible. Assume that the body has a (*roughly*) diagonal inertial matrix. Then the following holds true around the origin when $\vec{\omega}_b \approx \vec{0}$:

$$\begin{pmatrix} rv - qw \\ pw - ru \\ qu - pv \end{pmatrix} \approx \vec{0} \quad \text{and} \quad \begin{pmatrix} \frac{J_{yy}-J_{zz}}{J_{xx}} qr \\ \frac{J_{zz}-J_{xx}}{J_{yy}} pr \\ \frac{J_{xx}-J_{yy}}{J_{zz}} pq \end{pmatrix} \approx \vec{0} \quad (\text{A.6})$$

As a result, state differentials in Eq:A.5 can then reduce to the following:

$$\begin{pmatrix} \dot{u} \\ \dot{v} \\ \dot{w} \end{pmatrix} = \begin{pmatrix} -g\sin(\theta) \\ g\cos(\theta)\sin(\phi) \\ g\cos(\theta)\cos(\phi) \end{pmatrix} + \frac{1}{m} \begin{pmatrix} 0 \\ 0 \\ T \end{pmatrix} \quad \text{and} \quad \begin{pmatrix} \dot{p} \\ \dot{q} \\ \dot{r} \end{pmatrix} = \begin{pmatrix} \frac{1}{I_x} \tau_\phi \\ \frac{1}{I_y} \tau_\theta \\ \frac{1}{I_z} \tau_\psi \end{pmatrix} \quad (\text{A.7})$$

Similarly, at an attitude near to the origin and at hovering conditions, the following simplification applies to the Euler matrix $\Phi(\eta)$:

$$\Phi(\eta) \approx \vec{1} \quad \text{for } \eta \approx \vec{0} \quad (\text{A.8})$$

and so from Eq:A.1c the body's *Euler rates* are approximately equivalent to its angular velocity:

$$(\dot{p} \quad \dot{q} \quad \dot{r})^T \approx (\ddot{\phi} \quad \ddot{\theta} \quad \ddot{\psi})^T \Rightarrow \dot{\eta} \approx \omega_b \quad (\text{A.9})$$

The above Eq:A.9 is not an insignificant result. The difficulty with Euler angle parameterization for body attitude is that each Euler angle is defined with respect to a sequential reference frame, Eq:2.12. As such, the state equations for Eq:A.5 then reduce to the following six SISO controllable plants when the vehicle's angular velocity is small:

$$\ddot{x} = (-\cos(\phi)\sin(\theta)\cos(\psi) - \sin(\phi)\sin(\psi)) \frac{1}{m} T \quad (\text{A.10a})$$

$$\ddot{y} = (-\cos(\phi)\sin(\theta)\sin(\psi) + \sin(\phi)\cos(\psi)) \frac{1}{m} T \quad (\text{A.10b})$$

$$\ddot{z} = g - (\cos(\phi)\cos(\theta)) \frac{1}{m} T \quad (\text{A.10c})$$

$$\ddot{\phi} = \frac{1}{J_{xx}} \tau_\phi \quad (\text{A.10d})$$

$$\ddot{\theta} = \frac{1}{J_{yy}} \tau_\theta \quad (\text{A.10e})$$

$$\ddot{\psi} = \frac{1}{J_{zz}} \tau_\psi \quad (\text{A.10f})$$

Typically, the simplified Eq:A.10 is abstracted to an "augmented pilot control system". In such a case the controllable inputs are abstracted to T , $\ddot{\phi}$, $\ddot{\theta}$, $\ddot{\psi}$, wherein the pilot dictates the attitude torques and net heave thrust for the quadrotor, mostly with various flavours of PD control for each channel.

A.2 Blade-Element Momentum Expansion

Expanding on the Blade-Element Momentum equations from Eq:3.27 and Eq:3.31a, the integral equations are:

$$dT = \rho 4\pi r v_\infty (1+a) a dr \quad (\text{A.11a})$$

$$dT = \frac{1}{2} a_L b c \rho (\Omega r)^2 \left(\theta - \frac{v_\infty + v_i}{\Omega r} \right) dr \quad (\text{A.11b})$$

Both Eq:A.11a-A.11b are integrals taken across the length of the propeller blade. Equating the two and defining an inflow ratio term $\lambda = \frac{v_\infty + v_i}{\Omega r} = \frac{v_\infty (1+a)}{\Omega r}$ yields the following quadratic equation:

$$\lambda^2 + \left(\frac{\sigma a_L}{8} + \lambda_c \right) \lambda - \frac{\sigma a_L}{8} \theta \frac{r}{R} = 0 \quad (\text{A.12})$$

where λ_c is the nominal free-stream inflow ratio when $v_i = 0$. Another term, σ , is defined as the propeller solidity and is given by:

$$\sigma = \frac{bc}{\pi R} \quad (\text{A.13})$$

Then, solving Eq:A.12 for λ :

$$\lambda = \sqrt{\left(\frac{\sigma a_L}{16} - \frac{\lambda_c}{2} \right)^2 + \frac{\sigma a_L}{8} \theta \frac{r}{R}} - \left(\frac{\sigma a_L}{16} - \frac{\lambda_c}{2} \right) \quad (\text{A.14})$$

So then the inflow ratio can be solved as a function of the propeller element's aerofoil profile and its static inflow factor. In static conditions, the inflow factor is:

$$\lambda = \frac{v_i}{\Omega r} = \sqrt{\frac{C_{T0}}{2}} \quad (\text{A.15})$$

Then substituting λ back into Eq:3.31a, and solving the integral produces an instantaneous thrust value. The difficulty of solving the blade-element momentum integrals is knowing the exact chord profile and local angle of attack.

A.3 Euler-Angles from Quaternions

The solution for Euler angles from an attitude quaternion is an easy trigonometric inversion. Noting that the transformation from the body frame to each motor frame follows the Z-Y-X sequence, and using an inversion solution adapted from [123] (where the transformation to quaternions is based on Shoemake's [121] definition) each quaternion can be constructed from sequenced Euler angles, as in Eq:3.51. Then, solving for each euler angle using simultaneous solutions and inverse trigonometry gives:

$$\begin{bmatrix} \phi \\ \theta \\ \psi \end{bmatrix} = \begin{bmatrix} \arctan2(2(q_0 q_x + q_y q_z), 1 - 2(q_x^2 + q_y^2)) \\ \arcsin(2(q_0 q_y - q_x q_z)) \\ \arctan2(2(q_0 q_z + q_x q_y), 1 - 2(q_y^2 + q_z^2)) \end{bmatrix} \quad (\text{A.16})$$

Appendix B

Design Bill of Materials

B.1 Parts List

Part Name	No. Used	Unit Weight[g]
Electronics		
SPRacing F3 Deluxe Flight Controller	1	8
OrangeRx 615X 2.4 GHz 6CH Receiver	1	9.8
Signal Converter SBUS-PPM-PWM	1	5.0
STLink-V2 Debugger	1	3
RotorStar Super Mini S-BEC 10A	1	30
128x96" OLED Display	1	7
XBee-Pro S1	2	4
HobbyWing XRotor 20A Opto ESC	4	15
OrangeRX RPM Sensor	4	2
HobbyKing Multi-Rotor Power Distribution Board	1	49
Motors		
Corona DS-339MG	8	32
Cobra 2208 2000KV Brushless DC	4	44.2
Frame Components		
APM Flight Controller Damping Platform	1	7
HobbyKing SK450 Replacement Arm (2 pcs)	2	51
SK450 Extended Landing Skid	1	23.25
Alloy Servo Arm (FUTABA)	8	4
10X18X6 Radial Ball Bearing	8	5
80g Damping Ball	32	≈ 0
Plastic Retainers for Damping Balls	32	≈ 0
3/5mm Aluminum Prop Adapter	4	≈ 1
6x4.5 Gemfam 3-Blade Propeller	4	6
M3 6mm Hex Nylon Spacer	8	≈ 0
M3 16mm Hex Nylon Spacer	32	≈ 0
M3 25mm Nylon Screw	128	≈ 0.08
M2.5x10mm Socket Head Cap Screw	36	≈ 0.2
M2.5x25mm Socket Head Cap Screw	20	≈ 0.6
M2.5 A-Lok Nut	16	≈ 0

Table B.1: Parts List

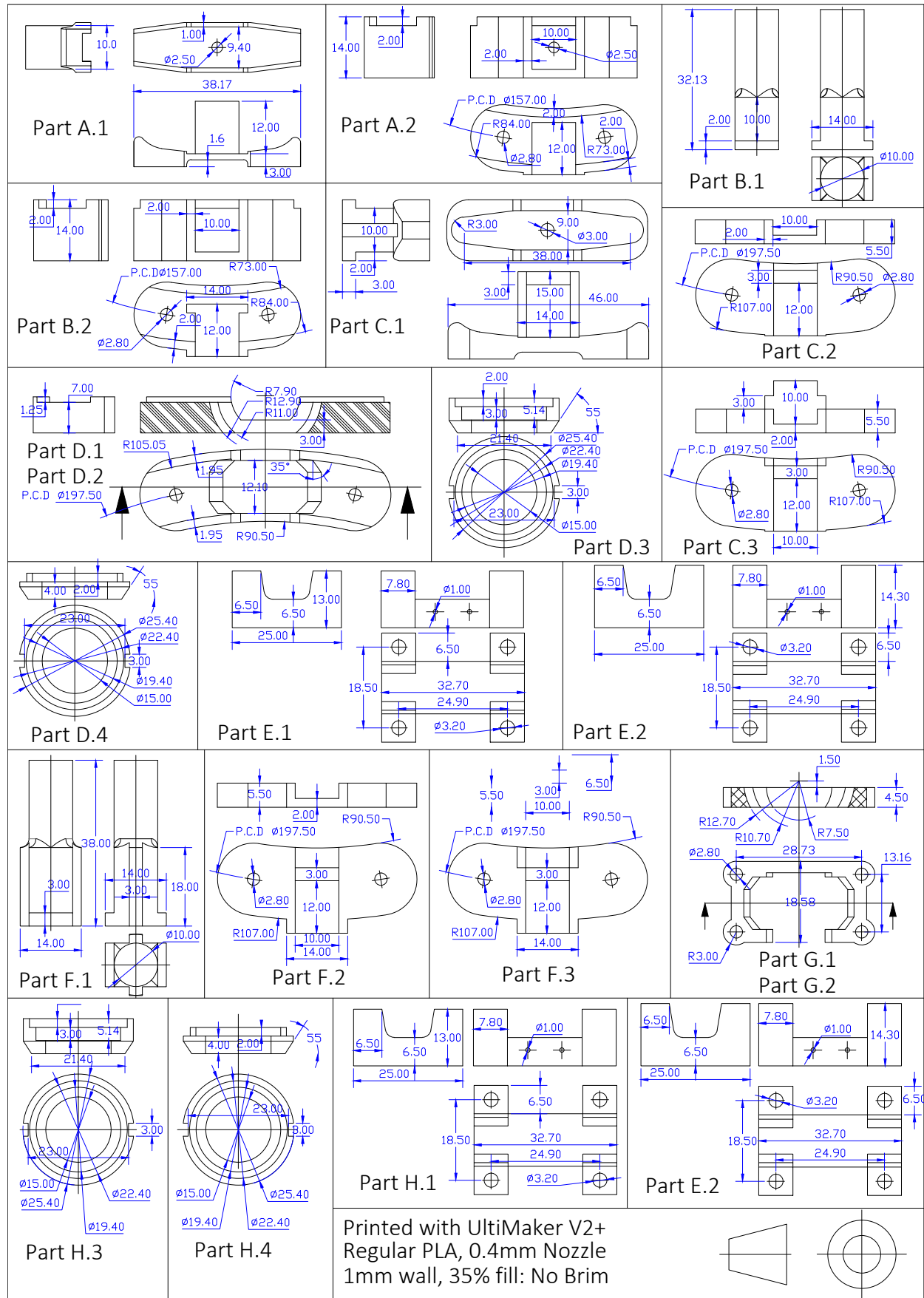


Table B.2: 3D Printed Parts

Bracket Assemblies 2

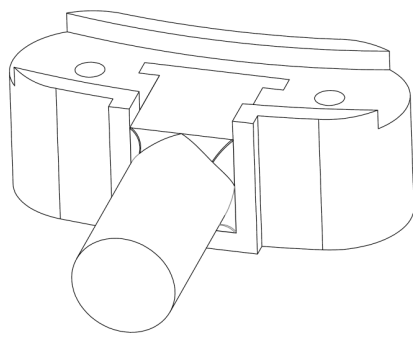


Figure B.1: Bearing Bracket Inner Ring Assembly
Parts: A.1, A.2

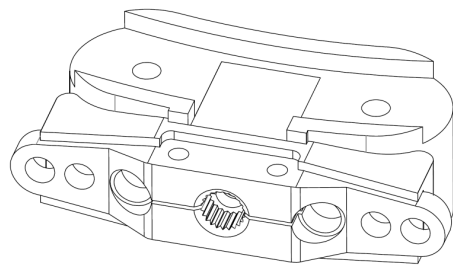


Figure B.2: Servo Bracket Inner Ring Assembly
Parts: B.1, B.2, M3 Servo Horn

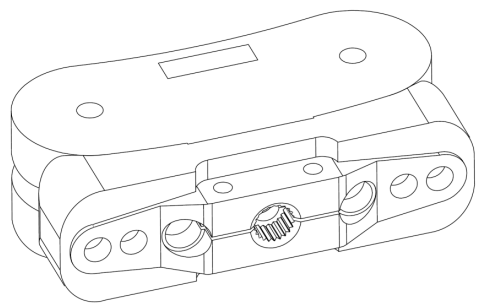


Figure B.3: Servo Bracket Middle Ring Assembly
Parts: C.1, C.2, C.3, M3 Servo Horn

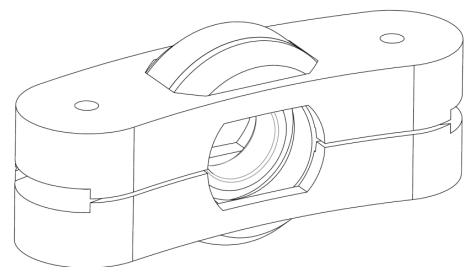


Figure B.4: Bearing Holder Middle Ring Assembly
Parts: D.1, D.2, D.3, D.4, 18-10 Bearing

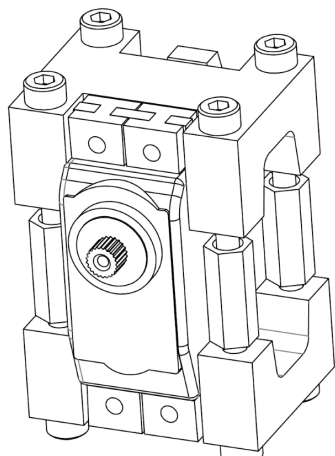


Figure B.5: Servo Mount Middle Ring Assembly
Parts: E.1, E.2, Corona Servo & Fasteners

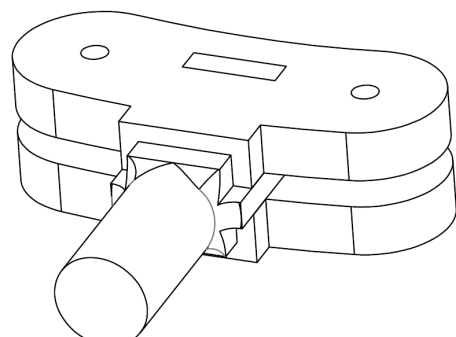


Figure B.6: Bearing Shaft Middle Ring Assembly
Parts: F.1, F.2, F.3

Table B.3: Inner & Middle Ring Assemblies

Bracket Assemblies 2

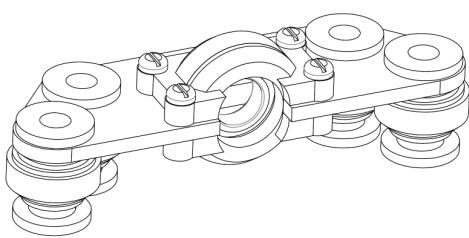


Figure B.7: Bearing Holder Damping Assembly
Parts: G.1, G.2, G.3, G.4, 18-10 Bearing, 80g
Damping Balls, Bearing Holder Damping Bracket

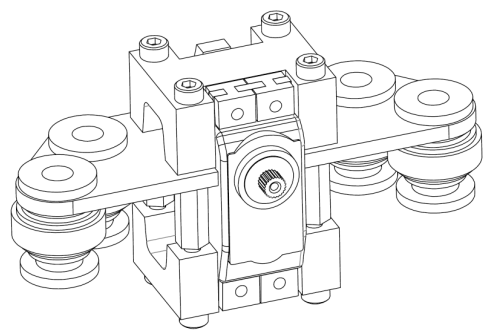


Figure B.8: Servo Mount Damping Assembly
Parts: H.1, H.2, Corona Servo & Fasteners, 80g
Damping Balls, Servo Mount Damping Bracket

Table B.4: Damping Assemblies

Laser Cut Brackets

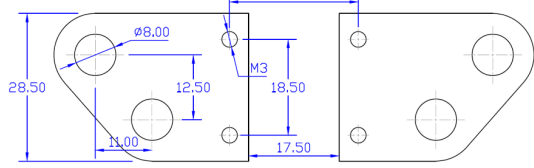


Figure B.9: Servo Mount Damping Bracket

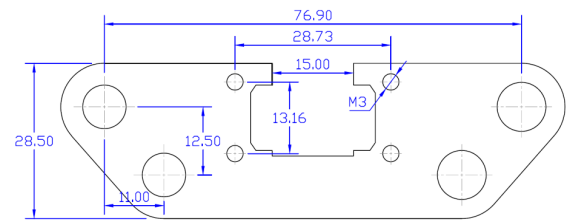


Figure B.10: Bearing Holder Damping Bracket

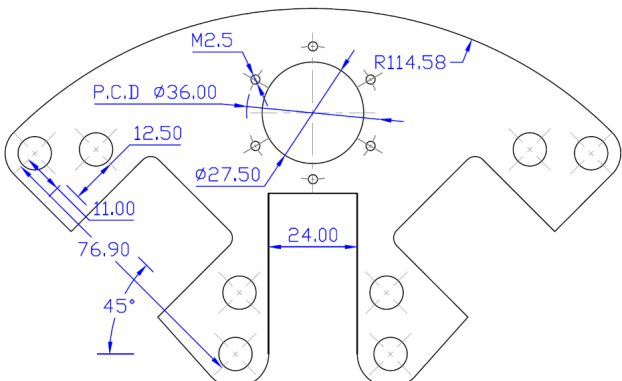


Figure B.11: Arm Mount Damping Bracket

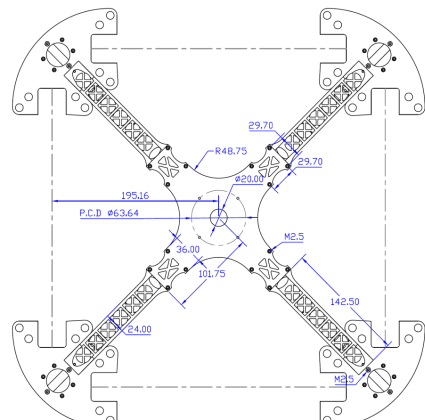


Figure B.12: Frame Brackets

Table B.5: Laser Cut Damping Brackets

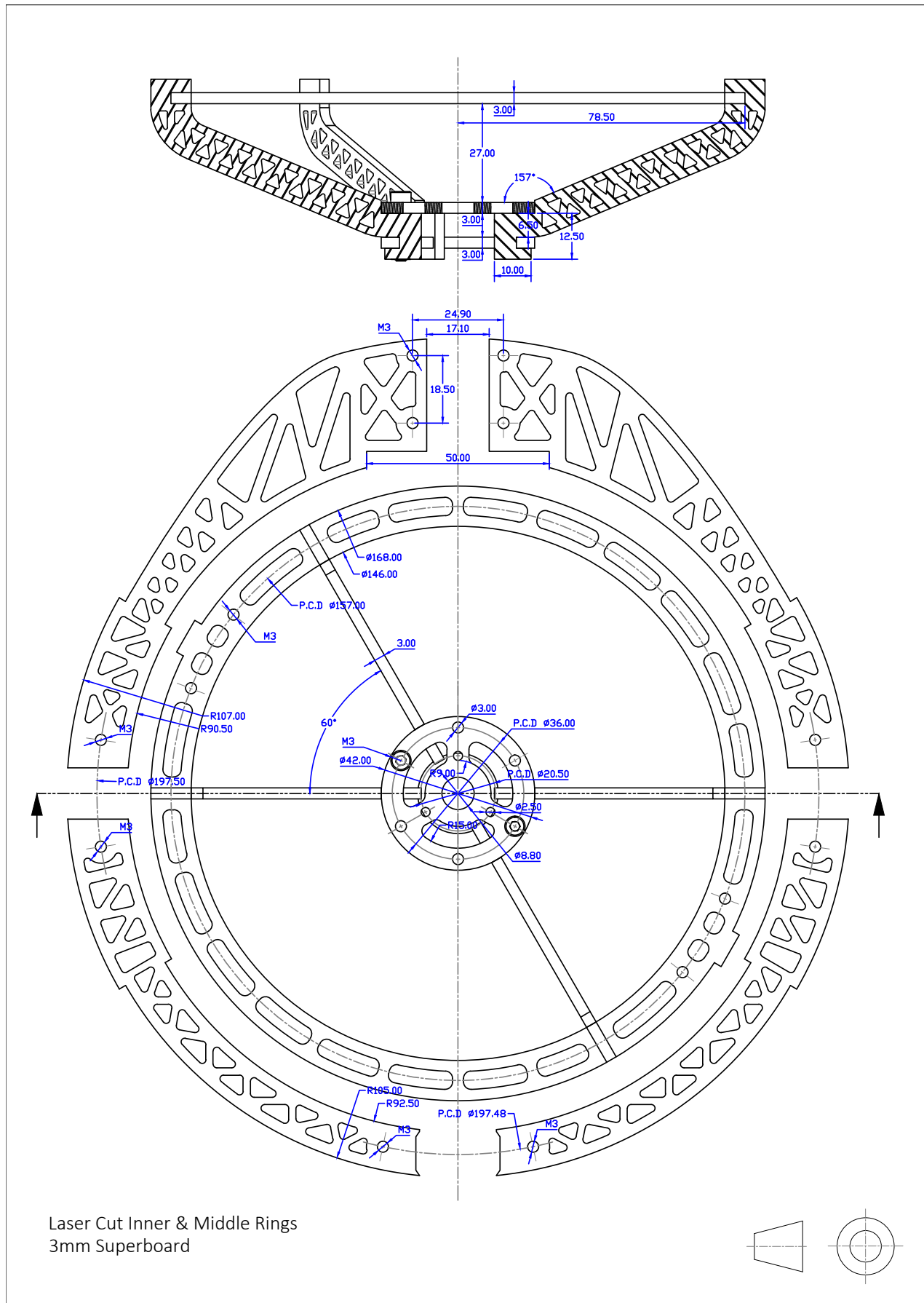


Table B.6: Laser Cut Parts

B.2 F3 Deluxe Schematic Diagram

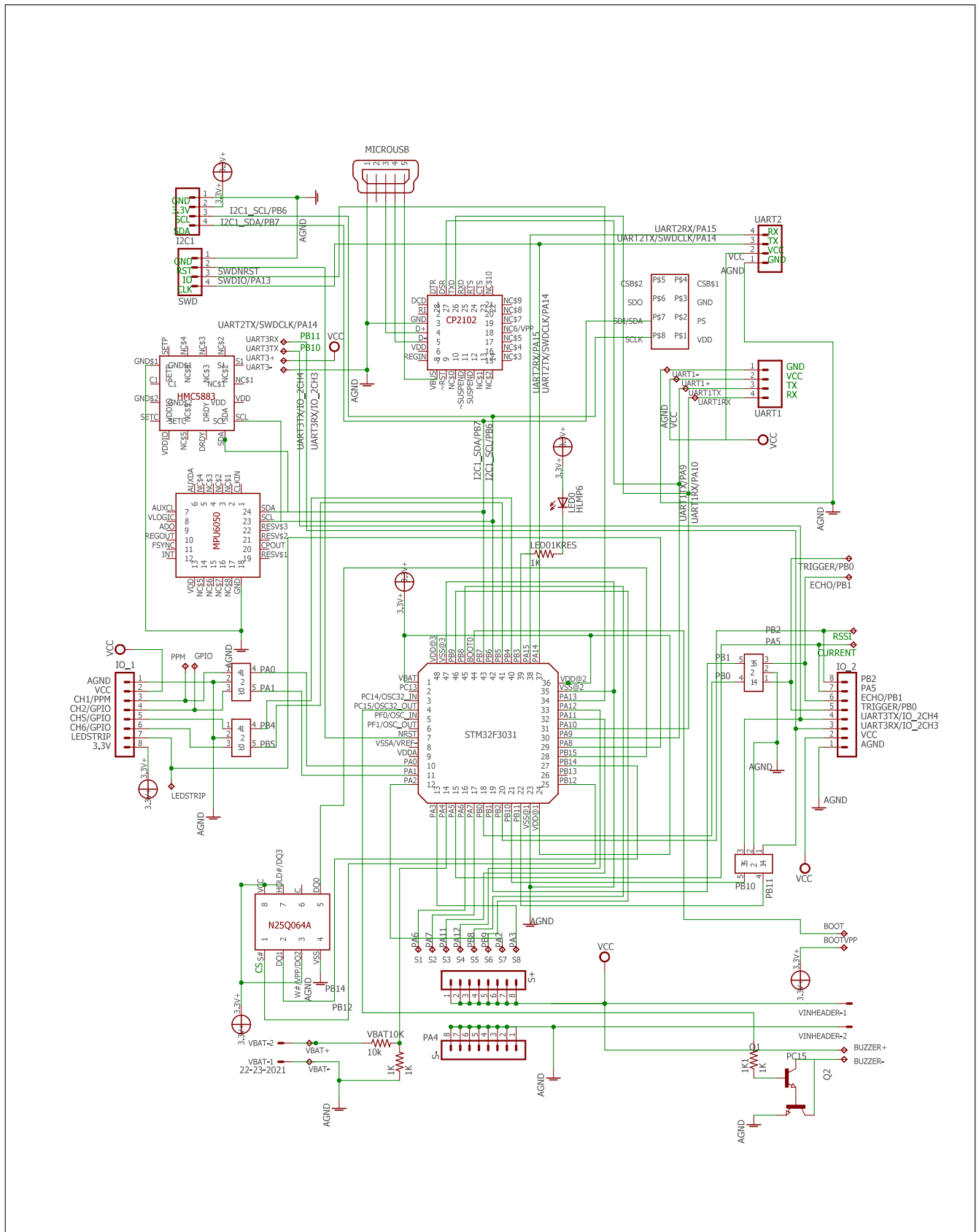


Figure B.13: F3 Deluxe Flight Controller Hardware Schematic

B.3 Strain Gauge Amplification

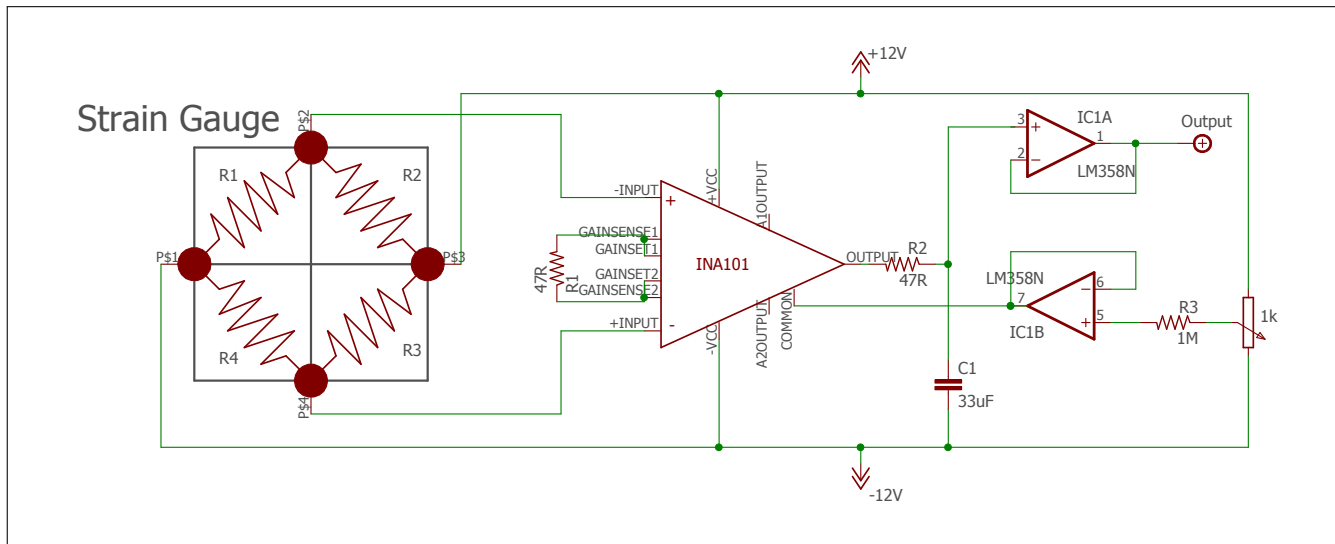


Figure B.14: Strain gauge full bridge amplifier

Appendix C

System ID Test Data

C.1 Thrust and Torque Test Data

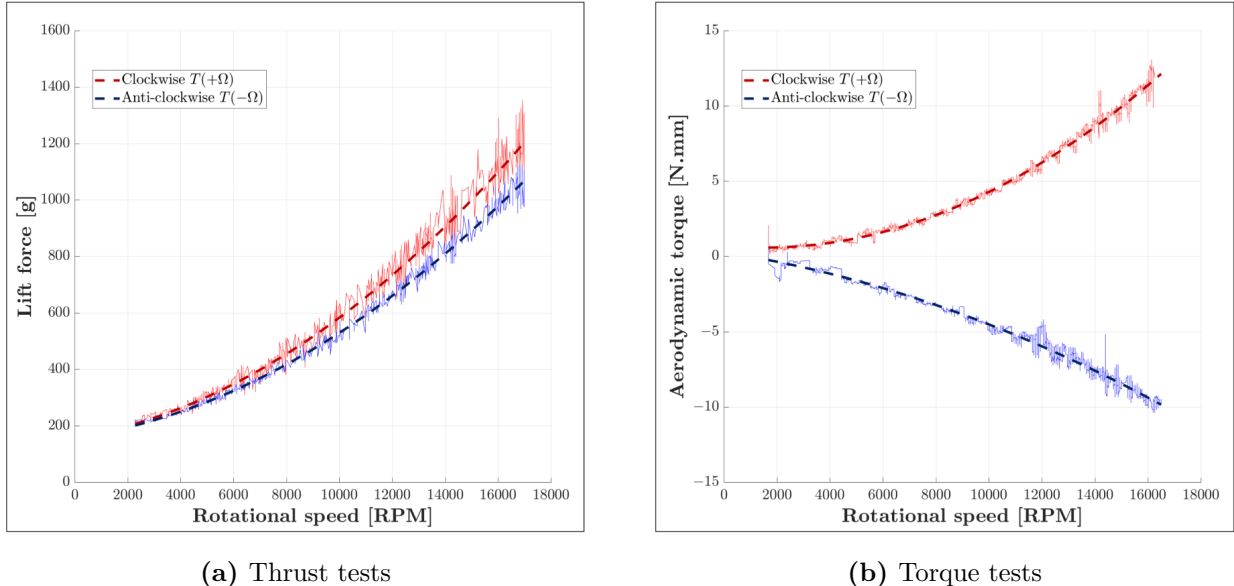


Figure C.1: Clockwise and counterclockwise rotation tests

Thrust tests in Fig:C.1a cause lateral deflection of the strain gauge thrust test rig, illustrated in Fig:3.6a. The deflection is in the direction of the propeller's rotational sense, as a result of the torque applied to the propeller. Clockwise and counter-clockwise tests were summed together and averaged to produce the thrust tests plotted in Fig:3.6.

Torque tests in Fig:C.1b show thrust deflection in the rotational torque test rig in Fig:3.7a. Upward thrust still resulted in some small deflection in the resultant measurements, so opposing clockwise and counter-clockwise results were subtracted and averaged out to produce the torque tests plotted in Fig:3.7.

C.2 Cobra CM2208-200KV Thrust Data

Cobra CM-2208/20 Motor Propeller Data										
Magnets 14-Pole	Motor Wind 20-Turn Delta	Motor Kv 2000 RPM/Volt		No-Load Current $I_o = 0.77$ Amps @ 10v	Motor Resistance $R_m = 0.076$ Ohms		I Max 20 Amps	P Max (3S) 220 W		
Stator 12-Slot	Outside Diameter 27.7 mm, 1.091 in.	Body Length 24.0 mm, 0.945 in.		Total Shaft Length 45.2 mm, 1.780 in.	Shaft Diameter 3.17 mm, 0.125 in.		Motor Weight 44.2 gm, 1.56 oz			
Test Data From Sample Motor		Input	6.0 V	8.0 V	10.0V	12.0V	Measured Kv value	Measured Rm Value		
		I_o Value	0.59 A	0.67 A	0.77 A	0.87 A	1988 RPM/Volt @ 10v	0.076 Ohms		
Prop Manf.	Prop Size	Li-Po Cells	Input Voltage	Motor Amps	Input Watts	Prop RPM	Pitch Speed in MPH	Thrust Grams	Thrust Ounces	Thrust Eff. Grams/W
APC	5.25x4.75-E	3	11.1	13.34	148.1	17,507	78.7	451	15.91	3.05
APC	5.5x4.5-E	3	11.1	13.67	151.7	17,388	74.1	456	16.08	3.01
APC	6x4-E	3	11.1	14.87	165.1	17,003	64.4	630	22.22	3.82
APC	7x4-SF	3	11.1	21.82	242.2	13,985	53.0	840	29.63	3.47
APC	7x5-E	3	11.1	24.02	266.6	13,272	62.8	797	28.11	2.99
FC	5x4.5	3	11.1	8.66	96.1	19,061	81.2	428	15.10	4.45
FC	5x4.5x3	3	11.1	12.38	137.4	17,825	76.0	534	18.84	3.89
FC	6x4.5	3	11.1	15.47	171.7	16,792	71.6	721	25.43	4.20
GemFan	5x3	3	11.1	6.67	74.0	19,801	56.3	374	13.19	5.05
HQ	5x4	3	11.1	7.13	79.1	18,182	68.9	373	13.16	4.71
HQ	5x4x3	3	11.1	9.25	102.7	17,401	65.9	449	15.84	4.37
HQ	5x4.5-BN	3	11.1	11.17	124.0	16,902	72.0	487	17.18	3.93
HQ	6x3	3	11.1	7.34	81.5	18,128	51.5	419	14.78	5.14
HQ	6x4.5	3	11.1	13.53	150.2	16,206	69.1	645	22.75	4.29
HQ	6x4.5x3	3	11.1	17.60	195.4	15,137	64.5	762	26.88	3.90
HQ	7x4	3	11.1	20.71	229.9	14,250	54.0	850	29.98	3.70
HQ	7x4.5	3	11.1	20.31	225.4	14,351	61.2	865	30.51	3.84
Prop Manf.	Prop Size	Li-Po Cells	Input Voltage	Motor Amps	Input Watts	Prop RPM	Pitch Speed in MPH	Thrust Grams	Thrust Ounces	Thrust Eff. Grams/W
APC	5.25x4.75-E	4	14.8	17.29	255.9	20,560	92.5	603	21.27	2.36
APC	5.5x4.5-E	4	14.8	17.87	264.5	20,436	87.1	635	22.40	2.40
APC	6x4-E	4	14.8	20.15	298.2	19,829	75.1	837	29.52	2.81
FC	5x4.5	4	14.8	10.89	161.2	22,511	95.9	588	20.74	3.65
FC	5x4.5x3	4	14.8	16.43	243.2	20,828	88.8	718	25.33	2.95
FC	6x4.5	4	14.8	20.09	297.3	19,809	84.4	998	35.20	3.36
HQ	4x4.5-BN	4	14.8	10.45	154.7	22,661	96.6	477	16.83	3.08
HQ	5x3	4	14.8	6.88	101.8	23,580	67.0	442	15.59	4.34
HQ	5x4	4	14.8	10.22	151.3	22,739	86.1	589	20.78	3.89
HQ	5x4x3	4	14.8	13.26	196.2	21,763	82.4	710	25.04	3.62
HQ	5x4.5-BN	4	14.8	16.10	238.3	20,899	89.1	744	26.24	3.12
HQ	6x3	4	14.8	11.06	163.7	22,512	64.0	679	23.95	4.15
HQ	6x4.5	4	14.8	19.62	290.4	19,948	85.0	982	34.64	3.38

Figure C.2: Official Test Results for Cobra Motors

C.3 Controller Disturbance Rejection

C.3.1 Attitude Controllers

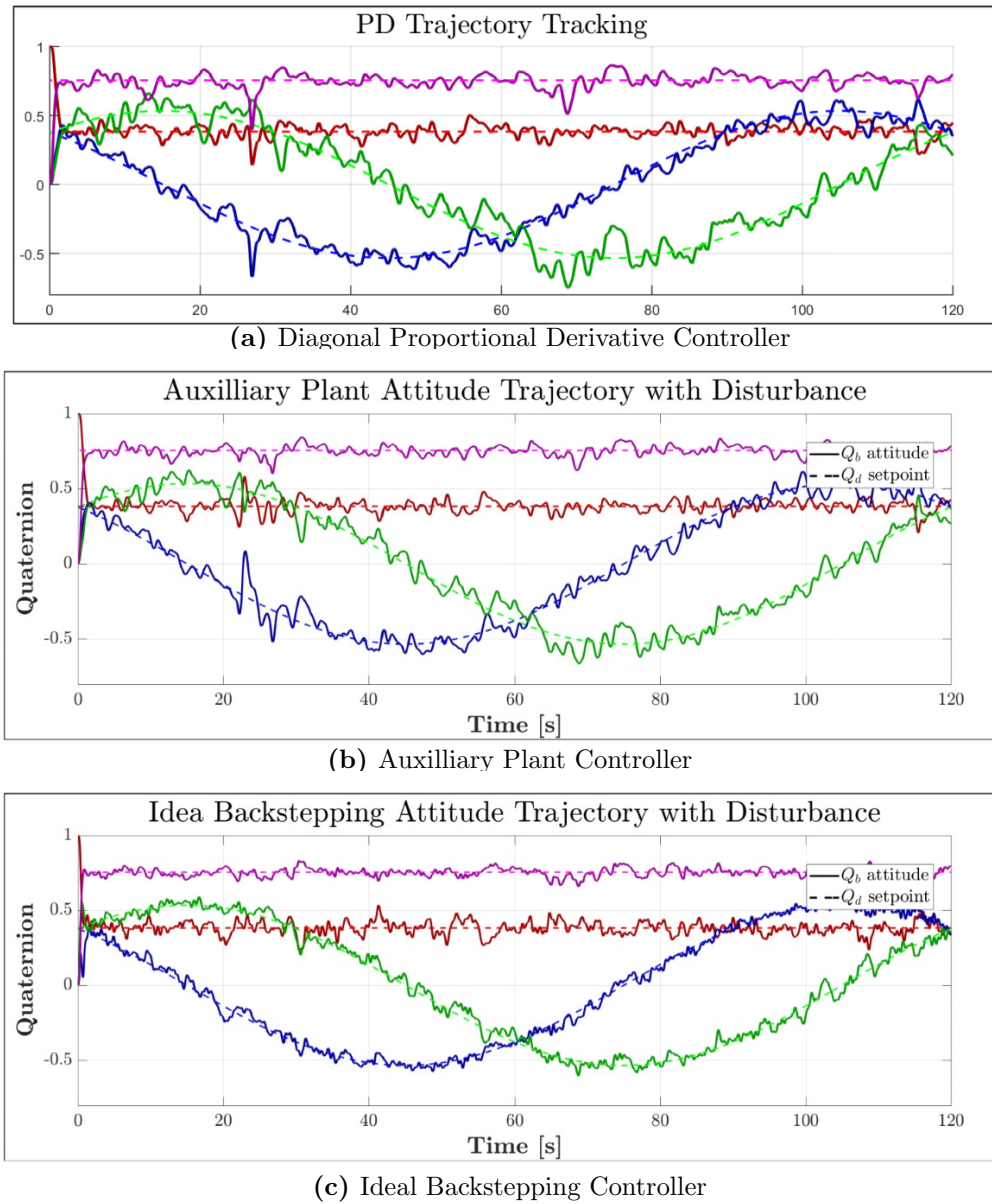


Figure C.3: Disturbances on Attitude Controllers

C.3.2 Position Controllers

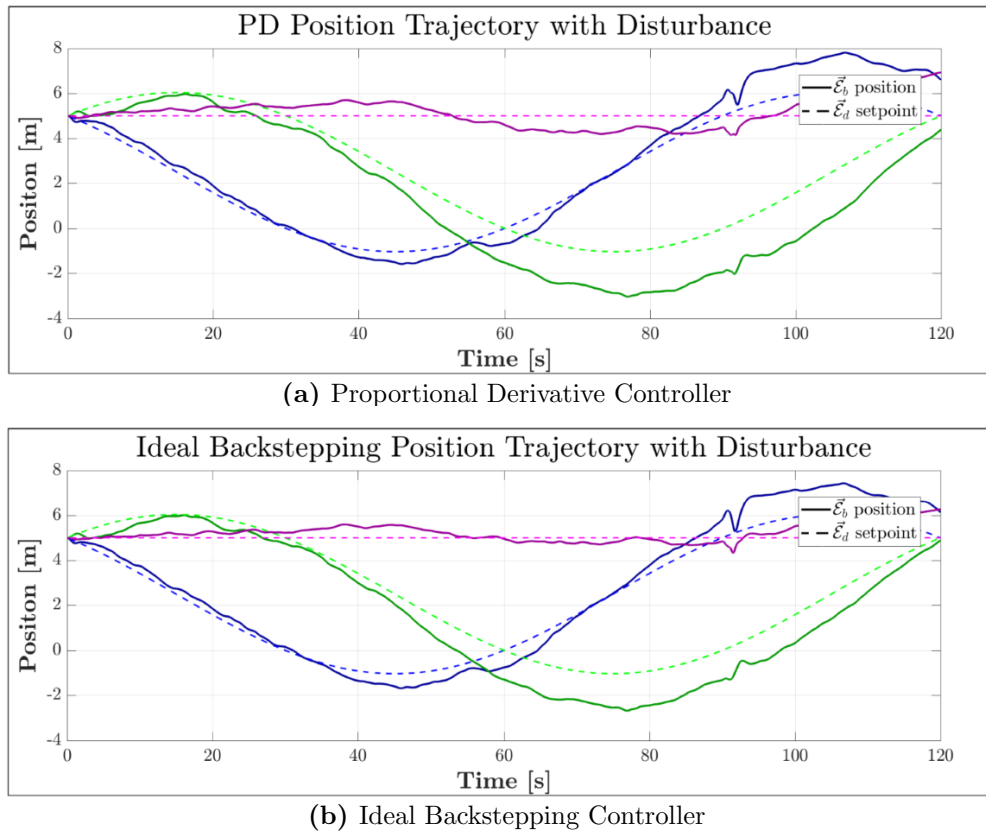


Figure C.4: Disturbances on Position Controllers

Bibliography

- [1] Parrot AG. Products: Ar drone 2.0. <https://www.parrot.com/fr/drones/parrot-ardrone-20-elite-edition#technical>, 2016. [Accessed:2017-01-16].
- [2] Y. Al-Rihani. *Development of a Dual Axis Tilt Rotorcraft UAV: Design, Prototyping and Control*. Cranfield University: School of Engineering, 2012. Masters dissertation.
- [3] N. Amiri, A. Ramirez-Serrano, and Davies R. Modelling of opposed lateral and longitudinal tilting dual-fan unmanned aerial vehicle. In *International Federation of Automatic Control*, pages 2054–2059, Milano, Italy, 8 2011. IEEE.
- [4] APM Copter. Arducopter official site. <http://www.arducopter.co.uk/>, 2016. [Accessed:2016-5-01].
- [5] E. Balasubramanian and R. Vasantharaj. Dynamic modelling and control of quadrotor. *International Journal of Engineering and Technology*, 5(1):63–39, 2 2013.
- [6] P. Baldi, B. Mogens, P. Castaldi, N Mimmo, and S. Simani. Adaptive ftc based on control allocation and fault accommodation for satellite reaction wheels. In *Conference on Control and Fault-Tolerant Systems*, volume 3, pages 672–677, Barcelona, Spain, 9 2016. IEEE.
- [7] M. Bangura and R. Mahony. Non-linear dynamic modelling for high performance control of a quadrotor. In *Australasian Conference on Robotics and Automation*, pages 1–10, Wellington, New Zealand, 12 2012. ACRA.
- [8] M. Bangura, M Melega, R. Naldi, and R. Mahony. Aerodynamics of rotor blades for quadrotors. Report, Colaboration: Australian National University & University of Bologna, 1 2016. Published:<https://arxiv.org/abs/1601.00733>.
- [9] I.Y Bar-itzhack and Y. Oshman. Attitude determination from vector observations: Quaternion estimation. In *Transactions on Aerospace and Electronic Systems*, volume 1, pages 128–137. IEEE, 1 1985.
- [10] M. Basri, A. Husain, and K. Danapalasingam. Intelligent adaptive backstepping control for mimo uncertain non-linear quadrotor helicopter systems. *Transactions of the Institute of Measurement Control*, 4(37):345–361, 9 2017.
- [11] Y. Bayiz and R. Babuska. Nonlinear disturbance compensation and reference tracking via reinforcement learning with fuzzy approximators. In *International Federation of Automatic Control*, volume 47, pages 5393–5398, Cape Town, South Africa, 8 2014. IEEE.
- [12] R. Beard. Quadrotor dynamics and control. Report, Brigham Young University, 10 2008.
- [13] R. Berler. Saving the pentagon’s killer chopper-plane. Technical report, Wired Magazine, 7 2005.
- [14] BetaFlight. Betaflight fc4 repo. Taken from the CleanFlight repo,<https://github.com/betaflight/betaflight>, 2016. [Accessed:2016-9-17].

- [15] BLHeli. Blheli master branch (silabs).
<https://github.com/bitdump/BLHeli/tree/master/SiLabs>, 2016.
[Accessed:2016-11-05].
- [16] Charles Blouin and Eric Lanteigne. Pitch control on an oblique active tilting bi-rotor. In *International Conference on Unmanned Aircraft Systems*, pages 791–799, Florida, USA, 5 2014. IEEE.
- [17] R. Bodrany, W. Steyn, and M. Crawford. In-orbit estimation of the inertia matrix and thruster parameters of uosat-12. *Control Engineering Practice*, 12:87–98, 12 2004.
- [18] Edward Boje. Lyapunov stability analysis. Report 1, University of Kwazulu-Natal: School of Electrical, Electronic and Computer Engineering, 1 2005. Course notes for: Control Systems ENEL4CN.
- [19] H. Bolandi, M. Rezaei, R. Mohsenipour, H. Nemati, and S. Smailzadeh. Attitude control of a quadcopter with optimized pid. *Intelligent Control and Automation*, (4):335–342, 8 2013.
- [20] R.M. Botez, I. Boustani, and N. Vayani. Optimal control laws for gust load alleviation. In *Proceedings of the CASI Annual Conference*, volume 46, pages 649–655, 5 1998.
- [21] S. Bouabdallah, A. Noth, and R. Siegward. Pid vs lq control techniques applied to an indoor micro quadrotor. In *International Conference on Intelligent Robots and Systems*, pages 2451–2456, Sendai, Japan, 9 2004. IEEE.
- [22] S. Bouabdallah and R. Siegward. Backstepping and sliding mode techniques applied to an indoor micro quadrotor. In *PInternational Conference on Intelligent Robots and Systems*, pages 2247–2252, 4 2005.
- [23] S. Bouabdallah and R. Siegwart. Full control of a quadrotor. In *International Conference on Intelligent Robots and Systems*, pages 153–158, California, USA, 11 2007. AIAA.
- [24] A. Bramwell, D. Balmford, and G. Done. *Bramwell's Helicopter Dynamics*, chapter 1-3, pages 1–144. Elsevier, 2 edition, 1999.
- [25] J. Brandt, R. Deters, G. Ananda, and M. Selig. Uiuc propeller data site. Univesity of Illinois Urbana-Champaign; Department of Aerospace Engineering:
<http://m-selig.ae.illinois.edu/props/propDB.html>, 2008.
[Accessed:2016-13-12].
- [26] J. Brandt and M. Selig. Propeller performance data at low reynolds numbers. *Aerospace Sciences Meeting*, 49:1–18, 1 2011.
- [27] D. Brescianini, M. Hehn, and R D'Andrea. Nonlinear quadrocopter attitude control. Technical report, Institute for Dynamic Systems and Control, ETH Zurich, 10 2013.
- [28] Z. Cai and M. S. de Queiroz. Asymptotic adaptive regulation of parametric strict-feedback systems with additive disturbance. In *American Control Conference*, volume 5, pages 3707–3712, Oregon, USA, 6 2005. IEEE.
- [29] J. Chen, A. Behal, and D. Dawson. Adaptive output feedback control for a class of mimo nonlinear systems. In *American Control Conference*, pages 5300–5306, Minnesota, USA, 6 2006. IEEE.
- [30] A.B. Chowdhury, A. Kulhare, and G. Raina. A generalized control method for tilt-rotor uav stabilization. In *International Conference on Cyber Technology in Automation, Control and Intelligent Systems*, pages 309–314, Bangkok, Thailand, 5 2012. IEEE.
- [31] CleanFlight. Cleanflight repo. <https://github.com/cleanflight/cleanflight>, 2016.
[Accessed:2016-11-13].

- [32] Dominic Clifton. Spracing f3 deluxe flight controller.
<http://seriouslypro.com/spracingf3>, 2015. [Accessed:2016-10-04].
- [33] Innov8tive Designs. Cobra cm2208/2000 motors. <http://innov8tivedesigns.com/cobra-cm-2208-20-motor-kv-2000>, 2016. [Accessed:2016-06-10].
- [34] C. Diao, B. Xian, Q. Yin, W. Zeng, H. Li, and Y. Yang. A nonlinear adaptive control approach for quadrotor uavs. In *Asian Control Conference Proceedings*, volume 8, pages 223–228, Kaohsiung, Taiwan, 8 2011. ASCC.
- [35] DJI Drones. Djis inspire one. <http://www.dji.com/product/inspire-1>, 2016. [Accessed:2016-07-10].
- [36] DJI Drones. Products: Djis phantom. <http://www.dji.com/products/phantom>, 2016. [Accessed:2016-06-12].
- [37] H. Du, G. Fan, and G. Yi. Disturbance compensated adaptive backstepping control of an unmanned seaplane. In *International Conference on Roboics and Biomimetics*, pages 1725–1730, Bali, Indonesia, 12 2014. IEEE.
- [38] Honeywell Solid State Electronics. Hmc5833 magnetometer datasheet. Advanced Information Data Sheet, 10 2010. <https://strawberry-linux.com/pub/HMC5883L.pdf>.
- [39] E. Fresk and G. Nikolakopoulos. Full quaternion based attitude control for a quadrotor. In *European Control Conference*, pages 3864–3869, Zurich, Switzerland, 7 2013. IEEE.
- [40] D. Garanin. Rotational motion of rigid bodies. Report, City University of New York, Department of Engineering, 11 2008.
- [41] P. Gasco. *Development of a Dual Axis Tilt Rotorcraft UAV: Modelling, Simulation and Control*. Cranfield University: School of Engineering, 2012. Masters dissertation.
- [42] J. Gertler. V-22 osprey tilt-rotor aircraft: Background and issues for congress. Report, Congressional Research Service, 3 2011.
- [43] GetFPV.com. Cobra 2208 2000kv bldc motor product page. <http://www.getfpv.com>, 2016. [Accessed:2017-02-19].
- [44] HiSystems GmbH. Mikrokopter quadroxl.
<http://www.mikrokopter.de/en/products/kits>, 2016. [Accessed:2016-06-13].
- [45] G. Golub and C. Van Loan. *Matrix Computations*, volume 3. Johns Hopkins University Press., 1996.
- [46] Gary R. Gress. Lift fans as gyroscopes for controlling compact vtol air vehicles: Overview and development status of oblique active tilting. In *American Helicopter Society Annual Forum*, volume 63, Virginia, USA, 5 2007. American Helicopter Society.
- [47] Karsten Groekatthfer and Zizung Yoon. Introduktion to quaternions for spacecraft attitude representation. Report, Technical University of Berlin: Department of Astronautics and Aeronautics, 5 2012.
- [48] N. Guenard, T. Hamel, and V. Moreau. Dynamic modelling and control strategy for an x4-flyer. In *International Conference on Control and Automation*, pages 141–146, Budapest, Hungary, 6 2005. IEEE.
- [49] L. Hand and J. Finch. *Analytical Mechanics*, chapter 7, pages 265–267. Cambridge University Press, 1 edition, 1998.

- [50] R. He, S. Prentice, and N. Roy. Planning in information space for a quadrotor helicopter in a gps-denied environment. In *International Conference on Robotics and Automation*, pages 1814–1820, California, USA, 5 2008. IEEE.
- [51] Y. He, H. Pei, and T. Sun. Robust tracking control of helicopters using backstepping with disturbance observers. *Asian Journal of Control*, (16):1387–1402, 10 2014.
- [52] M. Hehn and R. D’Andrea. Quadrocopter trajectory generation and control. In *International Federation of Automatic Control*, volume 44, pages 1484–1491, Milano, Italy, 9 2011. IEEE.
- [53] Drone HiTech. Xrotor 20a esc.
http://dronehitech.com/wp-content/uploads/2016/04/IMG_0524.jpg, 2016.
[Accessed:2016-11-05].
- [54] HobbyKing. Orangerx rpm sensor. http://www.hobbyking.com/hobbyking/store/_61511_Orange_RPM_Sensor.html, 2016. [Accessed:2016-10-09].
- [55] HobbyKing. Rotorstar super mini s-bec. http://www.hobbyking.com/hobbyking/store/_33987_RotorStar_Super_Mini_S_BEC_6S_10A.html, 2016.
[Accessed:2016-10-08].
- [56] HobbyKing. Signal converter module sbus-ppm-pwm.
http://www.hobbyking.com/hobbyking/store/_88384_Signal_Converter_Module_SBUS_PPM_PWM_S2PW_.html, 2016. [Accessed:2016-10-09].
- [57] HobbyKing.com. A28l 920kv brushless outrunn with variable pitch prop assembly.
https://hobbyking.com/en_us/a28l-920kv-brushless-outrunner-w-variable-pitch-prop-assembly.html?store=en_us, 2016. [Accessed:2017-19-0].
- [58] HobbyKing.com. Hobby king: The ultimate hobby experience.
<http://www.hobbyking.com/hobbyking/store/index.asp>, 2016.
[Accessed:2016-06-12].
- [59] G. Hoffmann, H. Huang, S. Waslander, and C. Tomlin. Quadrotor helicopter flight dynamics and control: Theory and experiment. In *Guidance, Navigation and Control Conference and Exhibit*, pages 1–19, South Carolina, USA, 8 2010. AIAA.
- [60] E.L Houghton and E.W Carpenter. *Aerodynamics for Engineering Students*, volume 5. Butterworth-Heinemann, 2003.
- [61] InvenSense Inc. Mpu6050 6-axis gyroscope/accelerometer datasheet. Product Specification Data Sheet, 8 2013. https://www.cdiweb.com/datasheets/invensense/MPU-6050_DataSheet_V3%204.pdf.
- [62] COIN-OR Initiative. Ipopt project home. <https://projects.coin-or.org/Ipopt>, 2017. [Accessed:2017-10-15].
- [63] Digi International. Xbee/xbee pro rf modules. Technical Data Sheet, 9 2009. <https://www.sparkfun.com/datasheets/Wireless/Zigbee/XBee-Datasheet.pdf>.
- [64] W. Jia, Z. Ming, Y. Zhiwei, and L. Bin. Adaptive back-stepping lpv control of satellite attitude maneuvers with sum of squares. In *World Congress on Intelligent Control and Automation*, volume 8, pages 1747–1752, Jinan, China, 7 2010. IEEE.
- [65] T. Johansen and T. Fossen. Control allocation - a survey. *Automatica*, 49(5):1087–1103, 5 2013.

- [66] T. Johansen, T. Fossen, and P. Tondel. Efficient optimal constraint control allocation via multi-parametric programming. *Journal of Guidance, Control and Dynamics*, (28):506–515, 5 2005.
- [67] T. Johansen and J. Tjnnns. Adaptive control allocation. *Automatica*, 44(11):2754–2765, 10 2008.
- [68] S. Joshi, A. Keklar, and J. Wen. Robust attitude stabilization of spacecraft using nonlinear feedback. In *Transactions on Automatic Control*, number 40, pages 1800–1803. IEEE, 10 1995.
- [69] J. Kabzinski and P. Mosiolek. Robust backstepping stabilization of nonlinear systems with time-varying parameters. In *Conference on Methods and Models in Automation and Robotics*, volume 22, pages 785–790, Miedzyzdroje, Poland, 8 2017. IEEE.
- [70] C. Karen-Liu and S. Jain. Tutorial on multibody dynamics. Georgia Institute of Technology: Online Course Content, Georgia, USA, 10 2012. Available at: http://www.cc.gatech.edu/~karenliu/Home_files/dynamics_1.pdf.
- [71] F. Kendoul, I. Fantoni, and R. Lozano. Modeling and control of a small autonomous aircraft having two tilting rotors. In *European Control Conference on Decision and Control*, pages 8144–8149, Seville, Spain, 12 2005. IEEE.
- [72] A. Koshkouei, A. Zinober, and K. Burnham. Adaptive sliding mode backstepping control of nonlinear systems with unmatched uncertainty. In *Conference on Decision and Control*, volume 39, pages 4765–4770, Sydney, Australia, 12 2000. IEEE.
- [73] P. Krishnamurthy and F. Khorrami. Adaptive backstepping and theta-d based controllers for a tilt-rotor aircraft. In *Mediterranean Conference on Control and Automation*, pages 540–545, Corfu, Greece, 6 2011. IEEE.
- [74] R. Kristiansen and P. Nicklasson. Satellite attitude control by quaternion-based backstepping. In *American Control Conference*, pages 907–912, Oregon, USA, 6 2005. AACC.
- [75] Jack B. Kuipers. *Quaternions and Rotation Sequences: A Primer with Application to Orbital Aerospace and Virtual Reality*, chapter 1, pages 127–143. Princeton University Press, 1 edition, 2002.
- [76] W. Lang and J. Young. Effect of inertia properties on attitude stability of nonrigid spin-stabilized spacecraft. Report, National Aeronautics and Space Administration, 4 1974.
- [77] A. Laub. The moore-penrose pseudo inverse. UCLA Math33A Course Content, Los Angeles, USA, 3 2008. Course Notes cited from <http://www.math.ucla.edu/~laub/33a.2.12s/mppseudoinverse.pdf>.
- [78] F.B Leahy. Discrete gust model for launch vehicle assessments. Report, National Aeronautics and Space Administration, 1 2008. <https://ams.confex.com/ams/presview.cgi?username=129833&password=129833&uploadid=7813>.
- [79] J. Lee, B. Min, and E. Kim. Autopilot design of tilt-rotor uav using particle swarm optimization method. In *International Conference on Control, Automation and Systems*, pages 1629–1633, Seoul, Korea, 10 2007. IEEE.
- [80] E.J Lefferts, F.L Markley, and M.D Shuster. Kalman filtering for spacecraft attitude estimation. In *AIAAS Aerospacce Sciences Megretski*, volume 20, pages 1–17, Orlando, Florida, 1 1982. AIAA.
- [81] LibrePilot. Openpilot/librepilot wiki. <http://opwiki.readthedocs.io/en/latest/index.html>, 2016. [Accessed:2016-5-04].

- [82] H. Lim, J. Park, D. Lee, and H. Kim. Build your own quadrotor. *Robotics & Automation*, pages 33–45, 9 2012.
- [83] C. Liu, B. Jiang, X. Song, and S. Zhang. Fault-tolerant control allocation for over-actuated discrete-time systems. *Journal of The Franklin Institute*, 352(6):2297–2313, 3 2015.
- [84] Kilowatt Classroom LLC. Vfd fundamentals. Report, Kilowatt Classroom LLC, 2 2003.
- [85] SteadiDrone PTY LTD. Steadidrone home. <http://www.steadidrone.com/>, 2016. [Accessed:2016-06-08].
- [86] A. Lyapunov. The general problem of the stability of motion. *International Journal of Control*, 55(3):531–773, 3 1992.
- [87] T. Madani and A. Benallegue. Backstepping control for a quadrotor helicopter. In *International Conference on Intelligent Robots and Systems*, pages 3255–3260, Beijing, China, 10 2006. IEEE.
- [88] D. Maiti, A. Acharya, M Chakraborty, and A. Konar. Tuning pid and $\pi^{\gamma}d^{\delta}$ controllers using the integral time absolute error criterion. In *International Conference on Information and Automation for Sustainability*, pages 457–462, Melbourne, Australian, 6 2008. IEEE.
- [89] I. Mandre. Rigid body dynamics using euler’s equations, rungekutta and quaternions. Unpublished, 2 2006.
- [90] C. Mantas and J. Puche. Artificial neural networks are zero-order tsk fuzzy systems. *IEE Transactions on Fuzzy Systems*, 16(3):630–644, 6 2008.
- [91] MathWorks. Optimization tool with the fmincon solver. <https://www.mathworks.com/help/optim/ug/optimization-tool-with-the-fmincon-solver.html>, 2016. [Accessed:2017-10-15].
- [92] C. Mayhew, R. Sanfelice, and A. Teel. On quaternion based attitude control and the unwinding phenomenon. In *American Control Conference*, pages 299–304, California, USA, 7 2011. ACC.
- [93] A. Mian and W. Daoboo. Modelling and backstepping-based nonlinear control of a 6dof quadrotor helicopter. *Chinese Journal of Aeronautics*, 8(21):261–268, 5 2008.
- [94] S. Napsholm. *Prototype of a Tiltrotor Helicopter*. Norwegian University of Science and Technology: Department of Engineering Cybernetics, 2013. Masters dissertation.
- [95] A. Nemati and M. Kumar. Modeling and control of a single axis tilting quadcopter. In *American Control Conference*, pages 3077–3082, Oregon, USA, 5 2014. ACC.
- [96] S. Nersersov and W. Haddad. On the stability and control of nonlinear dynamical systems via vector lyapunov functions. In *Transactions on Automatic Control*, volume 2, pages 203–215. IEEE, 2 2006.
- [97] K. Nonami, F. Kendoul, S. Suzuki, W. Wang, and D. Nakazawa. *Autonomous Flying Robots: Unmanned Aerial Vehicles and Micro Aerial Vehicles*, chapter 8, page 166. Springer Japan, 1 edition, 2010.
- [98] Kenzo Nonami, Farid Kendoul, Satoshi Suzuki, Wei Wang, and Daisuke Nakazawa. *Autonomous Flying Robots: Unmanned Aerial Vehicles and Micro Aerial Vehicles*, chapter 2, pages 44–48. Springer Japan, 1 edition, 2010.
- [99] G.P. Oliveira. Quadcopter civil applications. Master’s thesis, Informatics and Computer Engineering: University of Portugal, Portugal, 2014.

- [100] M. Oppenheimer, D. Doman, and M. Bolender. Control allocation for over-actuated systems. In *Mediterranean conference on Control and Automation*, pages 1–6, Ancona, Italy, 3 2007. IEEE.
- [101] OrangeRx. Orangerx r615x receiver. User Manual, 10 2014. Available From:<http://www.hobbyking.com/hobbyking/store/uploads/672761531X1606554X18.pdf>.
- [102] M. Orsag and S. Bogdan. Influence of forward and descent flight on quadrotor dynamics. *Recent Advances in Aircraft Technology*, pages 141–156, 2 2012.
- [103] C. Papachristos, K. Alexis, and A. Tzes. Design and experimental attitude control of an unmanned tilt-rotor aerial vehicle. In *International Conference on Advanced Robotics*, pages 465–470, Tallinn, Estonia, 6 2011. IEEE.
- [104] P.N. Patel, M.A. Patel, R.M. Faldu, and Y.R. Dave. Quadcopter for agricultural surveillance. In *Advance in Electronic and Electrical Engineering*, volume 3, pages 427–432, India, 4 2013. Research India Publications.
- [105] Google Patents. V22 osprey patent. <https://www.google.com/patents/US20110177748>, 2010. [Accessed:2017-03-03].
- [106] J. Peraire and S. Widnall. 3d rigid body dynamics: Euler angles. Lecture notes for Dynamics Course, 2009. Dynamics course notes, fall 2007.
- [107] J. Peraire and S. Widnall. 3d rigid body dynamics: The inertia tensor. Lecture notes for Dynamics Course, 2009. Dynamics course notes, fall 2007.
- [108] D. Peters. Eighth amendment of the civil aviation south african regulations. Goverment Gazette Notice, 5 2015. In Amendment to the Civil Aviation Act, 2009 (Act No.13 of 2009).
- [109] P. Pounds, R. Mahony, P. Hynes, and J. Roberts. Design of a four-rotor aerial robot. In *Australasian Conference on Robotics and Automation*, pages 145–150, Auckland, USA, 6 2002. IEEE.
- [110] A. Pretorius and E. Boje. Shutter delay estimation for a low-cost stand-alone visual tracking system. In *International Federation of Automatic Control*, pages 1–6, Telouse, France, 8 2017. IEEE.
- [111] F. Ramponi and J. Lygeros. Lecture notes on linear system theory. Technical report, Department of Information Engineering, University of Brescia, 1 2015. Course Notes cited from: http://home.mit.bme.hu/~virosztek/docs/mt_literature/LectureNotes.pdf.
- [112] O. Rawashdeh, H.C. Yang, R. AbouSleiman, and B. Sababha. Microraptor: A low cost autonomous quadrotor system. In *International Design Engineering Technical Conferences & Computers and Information in Engineering Conference*, pages 1–8, California, USA, 8 2009. American Society of Mechanical Engineers.
- [113] Anastasia Razinkove, Igor Gaponov, and Hyun-Chan Cho. Adaptive control over quadcopter uav under disturbances. In *International Conference on Control, Automation and Systems*, pages 386–390, Gyeonggi-do, Korea, 10 2014. IEEE.
- [114] M.K. Rwigema. Propeller blade element momentum theory with vortex wake deflection. In *International Congress of the Aeronautical Sciences*, pages 1–9, Nice, France, 9 2010. ICAS.
- [115] M. Ryll, H. Bulthoff, and P. Robuffo Giordano. Modelling and control of a quadrotor uav with tilting propellers. In *International Conference on Robotics and Automation*, pages 4606–4613, Minnesota, USA, 5 2012. IEEE.

- [116] M. Ryll, H. Bulthoff, and P. Robuffo Giordano. First flight tests for a quadrotor uav with tilting propellers. In *International Conference on Robotics and Automation*, pages 295–302, Karlsruhe, Germany, 5 2013. IEEE.
- [117] S. Salazar-Cruz, A. Palomino, and R. Lozano. Trajectory tracking for a four rotor mini-aircraft. In *ECC Conference on Decision and control*, pages 2505–2510, Seville, Sapin, 12 2005. IEEE.
- [118] Inc. Saleae. Logic8. <https://www.saleae.com/>, 2017. [Accessed:2017-03-12].
- [119] A. Sanchez, J. Escareo, O. Garcia, and R. Lozano. Autonomous hovering of a noncyclic tiltrotor uav: Modeling, control and implementation. In *International Federation of Automatic Control*, pages 803–808, Seoul, Korea, 6 2008. IEEE.
- [120] J. Seddon. *Basic Helicopter Aerodynamics*, chapter 2-5, pages 4–66. BSP Professional Books, 1 edition, 1990.
- [121] K. Shoemake. Quaternions. Siggraph course lecture notes, Department of Computer and Information Science; University of Pennsylvania, 1987.
- [122] P. Singla, D. Mortari, and J. Junkins. How to avoid singularity when using euler angles? *Advances in the Astronautical Sciences*, 4:1409–1426, 1 2005.
- [123] G. Slabaugh. Computing euler angles from a rotation matrix. Lecture notes, City University, London, 5 1999.
- [124] J. Sorensen. *General Momentum Thoeory for Horizontal Axis Wind Turbines*, chapter 4, pages 265–267. Cambridge University Press, 1 edition, 1998.
- [125] Measurement Speacialties. Ms5611 barometric pressure sensor. Technical Data Sheet, 10 2012. http://www.amsys.info/sheets/amsys.en.ms5611_01ba03.pdf.
- [126] STMicroElectronics. St-link/v2 in circuit debugger/programmer for stm32.
- [127] STMicroElectronics. Stm32f303 reference manual. Online Micro-Controller Reference Manual, 3 2016. http://www.st.com/content/st_com/en/products/microcontrollers/stm32-32-bit-arm-cortex-mcus/stm32f3-series/stm32f303.html?querycriteria=productId=LN1531.
- [128] A. Tayebi and S. McGilvray. Attitude stabilization of a vtol quadrotor aircraft. *Transactions on Control Systems Technology*, 14(3):562–571, 5 2006.
- [129] B. Theys, G. Dimitriadis, P. Hendrick, and J. De Schutter. Influence of propeller configuration on propulsion system efficiency of multi-rotor unmanned aerial vehicles. In *International Conference on Unmanned Aircraft Systems*, pages 195–201, Virginia, USA, 6 2016. IEEE.
- [130] S. Thornton and J. Marion. *Classical Dynamics of Particles and Systems*, chapter 7, pages 228–289. Thompson Brooks/Cole, 5 edition, 2003.
- [131] John Ting-Yung Wen and Kenneth Kreutz-Delgado. The attitude control problem. *Transactions on Automatic Control*, 36(10):1148–1162, 10 1991.
- [132] David Tong. Lagrange formalism. Lectures of Classic Dynamics, Course Notes, 2005. Classical Mechanics Notes.
- [133] P. Tsotras, M. Corless, and J. Longuski. A novel approach to the attitude control of axisymmetric spacecraft. *Automatica*, 31(8):2754–2765, 8 1995.
- [134] Ultimaker. Ultimaker v2+ product page. <https://ultimaker.com/en/products/ultimaker-2-plus#volume>, 2016. [Accessed:2016-9-11].

- [135] F. van den Berg and A. Engelbrecht. A study of particle swarm optimization particle trajectories. *Information Sciences*, 176:937–971, 2 2005.
- [136] E. van Kampen and M. M. van Paassen. Ae4301: Automatic flight control system design. Delft Centre for Systems and Control; MSc Notes, 1 2008. Course Notes cited from: <https://www.studocu.com/en/course/technische-universiteit-delft/automatic-flight-control-system-design/13152>.
- [137] A.W Vogeley. Axial-momentum theory for propellers in compressible flow. Technical Note, 1951.
- [138] R. Votel and D. Sinclair. Comparison of control moment gyros and reaction wheels for small earth-observing satellites. In *Conference on Small Satellites*, volume 26, pages 1–7, Logan, Utah, 8 2012. AIAA / Utah State University.
- [139] Tao Wang, Tao Zhao, Du Hao, and Mingxi Wang. Transformable aerial vehicle. <http://www.google.com/patents/US20140263823>, 2014. [Accessed:2017-01-16].
- [140] A Weiss, I. Kolmanovsky, D.S Bernstein, and A. Sanyal. Inertia-free spacecraft attitude control using reaction wheels. *Guidance, Control and Dynamics*, 36(14):1425–1439, 8 2013.
- [141] A. Witkin and D. Baraff. Physically based modelling: Principles and practice. CMU: Online Siggraph Course notes, 9 1997. Course Notes cited from <http://www.cs.cmu.edu/~baraff/sigcourse/>.
- [142] X. Xiaozhu, L. Zaozhen, and C. Weining. Intelligent adaptive backstepping controller design based on the adaptive particle swarm optimization. In *Chinese Control and Decision Conference*, pages 13–17, Guilin, China, 6 2009. IEEE.
- [143] S. Xin and Z. Zaojian. A fuzzy sliding mode controller with adaptive disturance approximation for an underwater robot. In *Asian Conference on Informatics in Control, Automation and Robotics*, volume 2, pages 50–53, Wuhan, China, 10 2010. IEEE.
- [144] Z. Zaheer, A. Usmani, E. Khan, and M.A Qadeer. Aerial surveillance system using uav. In *Wireless and Optical Communications Networks*, volume 13, pages 1–7, Hyderabad, India, 12 2016. IEEE.